

**Faculty of Science and Engineering  
Department of Applied Geology**

**Ultra-Precise  $^{40}\text{Ar}/^{39}\text{Ar}$  Geochronology:**  
Development of  $^{38}\text{Ar}$  cosmogenic exposure and olivine (U-Th)/He  
dating techniques; and deciphering the geochemical evolution of the  
Newer Volcanic Province, SE Australia.

**Kornelia Fieneke Oostingh**

**This thesis is presented for the Degree of  
Doctor of Philosophy  
of  
Curtin University**

**January 2017**



## DECLARATION

To the best of my knowledge and belief this thesis contains no material previously published by any other person except where due acknowledgement has been made. This thesis contains no material which has been accepted for the award of any other degree or diploma in any university.

The author acknowledges that copyright of published works contained within this thesis resides with the copyright holder(s) of those works. I warrant that I have obtained, where necessary, permission from the copyright owners to use any third-party copyright material reproduced in the thesis (e.g. questionnaires, artwork, unpublished letters), or to use any of my own published work (e.g. journal articles) in which the copyright is held by another party (e.g. publisher, co-author).

23<sup>rd</sup> of December 2016

---

Kornelia Fieneke Oostingh

---

Date

## ABSTRACT

The availability of accurate and precise geochronology data is of paramount importance to better understand geological and geomorphological processes on Earth. In this thesis, an example of this is provided, as the results of an integrated study towards the geochemistry and geochronology of the small, intraplate Newer Volcanic Province (NVP) in southeast Australia are given. New and existing major and trace element data as well as Sr, Nd and Pb isotope data show that the volcanic products within the NVP are the result of a temporally and perhaps even spatially changing mantle source within the geodynamic process of edge driven convection with shear driven upwelling of magma. Older (95 Ma – 19 Ma) central volcanoes are most likely generated by small degrees of partial melting of a mixed mantle source reflected by 10% calci-carbonatite metasomatised sub-continental lithospheric mantle veins melting into Indian mid-ocean ridge basalt followed by 20% fractional crystallization. Nd and Pb isotope data of younger (< 7 Ma) volcanics show that the mantle source eventually changed to a more depleted, garnet-rich composition. The two youngest series of volcanics in the NVP: the valley-filling lava flows of the Newer Plains series and the overlying lava shields, scoria cones and maars of the Newer Cones series were subjected to rigorous sampling for  $^{40}\text{Ar}/^{39}\text{Ar}$  geochronology to gain a better insight into the geodynamic variation over time, as reliable age data were lacking for the NVP. The Newer Plains were sampled from two cores and ages ranged from  $3.76 \pm 0.01$  Ma to  $4.32 \pm 0.03$  Ma ( $2\sigma$ ; all sources of uncertainties included), with the production rate of volcanism apparently decreasing post-4 Ma. These volcanic products, which show the effects of 5% of crustal contamination in their geochemical composition, are interpreted as being generated by the geodynamic process of edge driven convection with shear driven upwelling with added thermal input of the Cosgrove track mantle plume which migrated along the NVP at the time of Newer Plains eruption. The Newer Cones series showed  $^{40}\text{Ar}/^{39}\text{Ar}$  ages ranging from  $1290 \pm 20$  ka to  $41.1 \pm 2.2$  ka ( $2\sigma$ ) and are probably derived from a source that represent small (5 – 10%) degrees of partial melting from a mixture of depleted, anhydrous, Indian MORB type spinel lherzolite and enriched, hydrous spinel lherzolite metasomatised by alkaline melts. It is furthermore shown that the spatial distribution of these volcanic features is strongly dependent on existing basement structures; in particular the major faults that are northward extensions of the major Tasman Fault Zone south of the NVP. An observed apparent westerly progressing age trend in the onset of volcanism suggests that sinistral movement along

the Tasman Fault Zone and resulting E – W migration of stress potentially aided the geodynamic process of edge driven convection in facilitating magma upwelling throughout the NVP.

Cosmogenic exposure dating techniques can provide insight into the timescales of post-eruptive land surface processes such as e.g. erosion and climate change. In this study, cosmogenic  $^{38}\text{Ar}$  derived from spallation reactions on Ca and K is further investigated, as this stable isotope promises to be a significant tool to obtain rates of landscape evolution over long periods of time. Strategically sampled and irradiated pyroxene minerals from Mt Elephant in the NVP show statistically significant cosmochrons for which a geologically meaningful combined apparent exposure age of  $319 \pm 183$  ka ( $2\sigma$ ) was obtained, using a  $^{38}\text{Ar}$  production rate (Ca) of 250 atoms/g Ca/y. Extremely promising for the further development of this technique is the advancement in analytical precision that can be obtained by using the new generation multi-collector ARGUS VI mass spectrometer. It is shown that it is now possible to determine cosmogenic  $^{38}\text{Ar}$  abundances above background values, as well as discriminate  $^{38}\text{Ar}/^{36}\text{Ar}$  ratios ( $1\sigma$  absolute precision of  $\pm 0.3\%$ ) from the non-cosmogenic background value. Apatite from West-Australian granite batholites is less promising as a target for cosmogenic  $^{38}\text{Ar}$  exposure dating, as these suffer from strong natural and reactor-induced Cl interferences as well as a strong nucleogenic contribution from the U and Th rich host rock.

New geochronology techniques are required when conventional techniques cannot be applied, due to e.g. alteration of phases of interest. (U-Th)/He dating of olivine phenocrysts has potential due to the abundance of olivine in mafic rocks, the retention of He in olivine at temperatures of interest and the resistance of olivine to weathering. However, research so far has been extremely limited and suffered from analytical complexity. Using a simplified methodology, it is shown here that fresh olivine phenocrysts from the Ellendale E9 lamproite deposit (West Australia) yielded three (U-Th)/He ages of  $18.7 \pm 5.2$  Ma,  $18.7 \pm 5.6$  Ma and  $34 \pm 13$  Ma; equivalent to phlogopite  $^{40}\text{Ar}/^{39}\text{Ar}$  ages within uncertainty [ $22.37 \pm 0.03$  Ma ( $2\sigma$ ),  $22.40 \pm 0.03$  Ma ( $2\sigma$ ) and  $22.42 \pm 0.04$  Ma ( $2\sigma$ )]. Hence, (U-Th)/He dating of olivine phenocrysts could be a viable new geochronology technique, given that problems with incomplete sample recovery and potential volatilization of parental isotopes during heating can be overcome.

## ACKNOWLEDGEMENTS

This research would not have been possible without the support of the following people:

- My supervisor Fred Jourdan – thank you for your continuous support and words of encouragement throughout the long journey. Your knowledge and enthusiasm on every subject was inspiring and kept me going when times were hard. I am thankful for all the time and effort you have put into guiding me along the path of  $^{40}\text{Ar}/^{39}\text{Ar}$  geochronology.
- My supervisors Brent McInnes and Pete Kinny – many thanks for placing all your trust in me. I've always felt to be a valuable part of Curtin University and the laboratories.
- Collaborative researchers Martin Danišik, Noreen Evans and Brad McDonald – you have all invested way more time in me than you will ever get credits for; please know that I'm grateful for the knowledge, guidance and support you've given me throughout the years.
- Collaborative researchers Renaud Merle, Massimo Chiaradia, David Phillips and Erin Matchan – I've learned lots from the many discussions we had while trying to make sense of the geochemistry and the geochronology of southeast Australia.
- Technical staff at Curtin University: Celia Mayers, Adam Frew, Zdenka Martelli, Andrew Todd, Tanya Jude-Eton and Andy Wieczorek – my PhD would not have been complete without you; and the hours (months!) spend picking grains, working the ARGUS and sharing laughter with you will always remain some of my fondest memories of the past years.
- My colleagues Bryant, Vicky, Nishka and Camilla – many thanks for providing a listening ear during lunchtime whenever I needed to vent.
- My friends in the Netherlands: Alwina, Francien, Marijn, Okke, Jort, Timmy and Jaap; my friends in Australia: Nynke, Carlijn, Eline, Solange, Emmelie, Kerstin, Linda, Birgitta, Irene and Stefanie, and Meeghan and Tushar in Malaysia – I can't express how grateful I am for your friendship – I think it has kept me sane.
- My family – lovely, sweet parents; thank you for always believing in me and supporting me. Sisters; thanks for setting such great examples!
- Cat Zazzles – for listening to all my practice talks and providing mental support.

- My husband Quintijn – you are and will be the most important person in my life, even if you will have to share some of my love with our son Art. This thesis is dedicated to you.

## LIST OF PUBLICATIONS INCLUDED AS PART OF THIS THESIS

This thesis compiles a collection of research papers that were either accepted or under review at the time of writing of this document. The relation between each paper is outlined in the Introductory Chapter 1, whereas Chapter 2 provides the necessary theoretical background to all geochronology techniques presented. All papers have Statement of Authorships in Appendix A, and published Paper 1 is reprinted with permission of the journal in Appendix A as well.

The formatting of each chapter within this thesis may appear to vary, and may differ to the published form based on the requirements and formatting guidelines of each individual journal and this thesis. Due to the nature of this thesis as a composite of peer-reviewed manuscripts there is a degree of repetition throughout.

Paper 1: Oostingh K. F., Jourdan F., Merle R. and Chiaradia M. (2016) *Spatio-temporal Geochemical Evolution of the SE Australian Upper Mantle Deciphered from the Sr, Nd and Pb Isotope Compositions of Cenozoic Intraplate Volcanic Rocks*. *J. Petrol.* **57**, 1509–1530.

Available at:

<http://www.petrology.oxfordjournals.org/lookup/doi/10.1093/petrology/egw048>.

Paper 2: Oostingh, K. F., Jourdan, F., Matchan, E. L. & Phillips, D. (2017).  *$^{40}\text{Ar}/^{39}\text{Ar}$  geochronology reveals rapid change from plume-assisted to stress-dependent volcanism in the Newer Volcanic Province, SE Australia*. *Geochemistry, Geophysics, Geosystems* **18**, 1065–1089.

Available at:

<http://onlinelibrary.wiley.com/doi/10.1002/2016GC006601/full>

Paper 3: Oostingh K. F., Jourdan F., Danišik M. and Evans N. J. *Advancements in cosmogenic  $^{38}\text{Ar}$  exposure dating of terrestrial rocks*. *Geochim. Cosmochim. Acta.*; **in revision**.

Paper 4: Oostingh K. F., Danišik M., Evans N. J., Jourdan F., McDonald B. J. and McInnes B. I. A. (2017) *(U-Th)/He dating of olivine phenocrysts in the K-rich Ellendale olivine lamproite, Western Australia*. *Aust. J. Earth Sci.* **under revi**.



## LIST OF ADDITIONAL PUBLICATIONS RELEVANT TO THIS THESIS

The following two titles are references to conference abstracts where part of the research outlined in this thesis was presented.

Oostingh K. F., Jourdan F., Phillips D. and Matchan E. L. (2015) *Ultra-precise  $^{40}\text{Ar}/^{39}\text{Ar}$  geochronology and  $^{38}\text{Ar}$  exposure dating on young basalts from the Newer Volcanic Province, Australia*. In Goldschmidt 2015 Conference Abstracts

Oostingh K. F., Jourdan F., Danišík M. and Evans N. J. (2016) *Terrestrial cosmogenic  $^{38}\text{Ar}$  dating*. In Thermochronology and Noble Gas Geochemistry and Geochronology Organization Workshop 2016: TANG30 (eds. M. Danišík, F. Jourdan, C. Talavera, and B. I. A. McInnes).

## TABLE OF CONTENTS

DECLARATION .....	i
ABSTRACT .....	ii
ACKNOWLEDGEMENTS .....	iv
LIST OF PUBLICATIONS INCLUDED AS PART OF THIS THESIS .....	vi
LIST OF ADDITIONAL PUBLICATIONS RELEVANT TO THIS THESIS .....	vii
TABLE OF CONTENTS .....	viii
LIST OF FIGURES .....	xiii
LIST OF TABLES.....	xix
Chapter 1 Introduction .....	1
1.1. Geological Background .....	2
1.1.1. The Newer Volcanic Province .....	3
1.1.2. Lamproites .....	5
1.2. Aim and objectives .....	6
1.3. Thesis structure .....	7
1.4. References.....	9
Chapter 2 Theoretical background of geochronology techniques used in this study.....	13
2.1. $^{40}\text{Ar}/^{39}\text{Ar}$ geochronology.....	13
2.1.1. Fundamentals of K-Ar and $^{40}\text{Ar}/^{39}\text{Ar}$ dating .....	13
2.1.2. Neutron irradiation.....	15
2.1.3. Gas extraction .....	16
2.1.4. Data regression and presentation .....	17
2.1.5. Applicability of the $^{40}\text{Ar}/^{39}\text{Ar}$ geochronology technique .....	19
2.2. Cosmogenic $^{38}\text{Ar}$ geochronology.....	20
2.2.1. Fundamentals of cosmogenic exposure dating .....	20
2.2.2. Cosmogenic $^{38}\text{Ar}$ and the ‘cosmochron diagram’ .....	22
2.2.3. Applicability of the cosmogenic $^{38}\text{Ar}$ geochronology technique .....	24
2.3. (U-Th)/He dating .....	24
2.3.1. Fundamentals of (U-Th)/He dating.....	25
2.3.2. Applicability of basalt (U-Th)/He dating.....	28
2.4. References.....	28
Chapter 3 Spatio-temporal geochemical evolution of the SE Australian upper mantle deciphered from Sr, Nd and Pb isotopes of Cainozoic intraplate volcanics .....	32
3.1. Abstract.....	32
3.2. Introduction.....	33
3.3. Overview of Cainozoic magmatism in South East Australia.....	35

3.3.1. Older Volcanics .....	35
3.3.2. Euroa Volcanics .....	35
3.3.3. Newer Volcanics .....	36
3.4. Geological setting and sample descriptions .....	36
3.5. Methods.....	37
3.6. Results.....	44
3.6.1. Major elements.....	44
3.6.2. Trace elements .....	46
3.6.3. Sr, Nd and Pb isotopes .....	49
3.7. Discussion.....	52
3.7.1. Geochemical comparison between the Newer Cones and the Older Volcanics, Euroa Volcanics and Newer Plains. ....	52
3.7.2. Petrogenesis .....	55
3.7.3. Mantle source compositions.....	60
3.7.4. Geodynamics.....	64
3.8. Conclusion .....	67
3.9. Acknowledgements.....	67
3.10. References.....	68
Chapter 4 $^{40}\text{Ar}/^{39}\text{Ar}$ geochronology reveals rapid change from plume-assisted to stress-dependent volcanism in the Newer Volcanic Province, SE Australia.....	75
4.1. Abstract.....	75
4.2. Introduction.....	76
4.3. Geological setting and sample description.....	78
4.4. Methods.....	80
4.4.1. $^{40}\text{Ar}/^{39}\text{Ar}$ geochronology .....	80
4.4.2. Spatial analyses of the Newer Cones .....	84
4.5. Results.....	86
4.5.1. $^{40}\text{Ar}/^{39}\text{Ar}$ geochronology .....	86
4.5.2. Spatial analysis.....	99
4.6. Discussion .....	100
4.6.1. Comparison with existing K/Ar, $^{40}\text{Ar}/^{39}\text{Ar}$ and cosmogenic isotope ages .....	100
4.6.2. Comparison with cosmogenic ages.....	102
4.6.3. Implications of new $^{40}\text{Ar}/^{39}\text{Ar}$ isotope data .....	103
4.6.4. Spatial analyses.....	103
4.7. Spatio-temporal constraints on NVP volcanism .....	104
4.7.1. Mantle source migration?.....	106
4.7.2. Tectonic controls? .....	107

4.8. Conclusion .....	108
4.9. Acknowledgements .....	109
4.10. References .....	109
Chapter 5 Advancements in cosmogenic $^{38}\text{Ar}$ exposure dating of terrestrial rocks .....	118
5.1. Abstract .....	118
5.2. Introduction .....	119
5.3. Geological setting and sample description .....	120
5.3.1. Southeast Australian pyroxene .....	121
5.3.2. West-Australian apatite .....	122
5.4. Analytical Methodology .....	123
5.4.1. Sample preparation and irradiation .....	123
5.4.2. Argon gas extraction and analysis .....	123
5.4.3. Data reduction and exposure age calculation .....	124
5.4.4. Apatite (U-Th)/He analysis .....	126
5.4.5. ELA-ICP-MS analysis .....	126
5.5. Results .....	126
5.5.1. Degassing characteristics .....	126
5.5.2. Cosmochron characteristics .....	128
5.5.3. Apatite (U-Th)/He ages .....	132
5.5.4. Apatite $^{40}\text{Ar}/^{39}\text{Ar}$ ages .....	132
5.6. Discussion .....	133
5.6.1. Analytical advancement .....	133
5.6.2. Multiple degassing domains .....	139
5.6.3. Pyroxene as a potential cosmogenic exposure dating tool .....	139
5.6.4. Apatite as a potential cosmogenic exposure dating tool .....	143
5.6.5. Applicability of cosmogenic $^{38}\text{Ar}$ exposure dating .....	147
5.7. Conclusions .....	148
5.8. Acknowledgements .....	148
5.9. References .....	148
Chapter 6 (U-Th)/He dating of olivine phenocrysts in the K-rich Ellendale olivine lamproite, Western Australia .....	152
6.1. Abstract .....	152
6.2. Introduction .....	153
6.2.1. Theoretical background .....	153
6.3. Sample description .....	155
6.4. Analytical methodology .....	156
6.4.1. $^{40}\text{Ar}/^{39}\text{Ar}$ geochronology .....	157

6.4.2. (U-Th)/He geochronology.....	158
6.5. Results.....	159
6.5.1. $^{40}\text{Ar}/^{39}\text{Ar}$ geochronology.....	159
6.5.2. (U-Th)/He geochronology.....	162
6.6. Discussion.....	164
6.6.1. $^{40}\text{Ar}/^{39}\text{Ar}$ versus (U-Th)/He dating.....	164
6.6.2. Future implications.....	166
6.7. Conclusion.....	167
6.8. Acknowledgements.....	167
6.9. References.....	168
Chapter 7 THESIS CONCLUSIONS.....	173
Chapter 8 BIBLIOGRAPHY.....	176
APPENDIX A. FIRST AUTHOR JOURNAL PUBLICATIONS.....	198
APPENDIX B. SUPPLEMENTARY DATA CHAPTER 3 – MAJOR AND TRACE ELEMENT DATA.....	260
APPENDIX C. SUPPLEMENTARY DATA CHAPTER 3 – ISOTOPE DATA.....	267
APPENDIX D. SUPPLEMENTARY DATA CHAPTER 4 – $^{40}\text{Ar}/^{39}\text{Ar}$ ISOTOPE ABUNDANCES NEWER PLAINS.....	269
APPENDIX E. SUPPLEMENTARY DATA CHAPTER 3 – $^{40}\text{Ar}/^{39}\text{Ar}$ ISOTOPE ABUNDANCES NEWER CONES.....	278
APPENDIX F. SUPPLEMENTARY DATA CHAPTER 4 - K/CA DIAGRAMS AND THIN SECTION PHOTOS OF THE NEWER PLAINS.....	307
APPENDIX G. SUPPLEMENTARY DATA CHAPTER 4 - K/CA DIAGRAMS AND THIN SECTION PHOTOS OF THE NEWER CONES.....	310
APPENDIX H. SUPPLEMENTARY DATA CHAPTER 5 – PYROXENE SAMPLES.....	317
APPENDIX I. SUPPLEMENTARY DATA CHAPTER 5 – APATITE THIN SECTIONS.....	319
APPENDIX J. SUPPLEMENTARY DATA CHAPTER 5 – ISOTOPE ABUNDANCES PYROXENE SAMPLES.....	321
APPENDIX K. SUPPLEMENTARY DATA CHAPTER 5 – ISOTOPE ABUNDANCES APATITE SAMPLES.....	328
APPENDIX L. SUPPLEMENTARY DATA CHAPTER 5 – DEGASSING SPECTRA ALL PYROXENE SAMPLES.....	334
APPENDIX M. SUPPLEMENTARY DATA CHAPTER 5 – DEGASSING SPECTRA ALL APATITE SAMPLES.....	336
APPENDIX N. SUPPLEMENTARY DATA CHAPTER 5 – COSMOCHRONS ALL CL-CORRECTED APATITE SAMPLES.....	338
APPENDIX O. SUPPLEMENTARY DATA CHAPTER 6 – ISOTOPE ABUNDANCES E9 PHLOGOPITE.....	340
APPENDIX P. SUPPLEMENTARY DATA CHAPTER 6 – ADDITIONAL $^{40}\text{Ar}/^{39}\text{Ar}$ AR DATA SERBIAN AND SPANISH LAMPROITES.....	344

Sample description.....	345
Results.....	346
Discussion.....	347
References.....	347
Supplementary Data – relative abundances of K-rich phases.....	348

## LIST OF FIGURES

- Figure 1.1.** Location map of the Newer Volcanic Province within the eastern Australian Cainozoic volcanic region. Colours offshore represent bathymetry, with red colours indicative of higher areas; the Tasmanids and Lord Howe seamount chains are easily visible. Onshore, the black areas indicate the location of Central Volcanoes, whereas the grey areas indicate the location of lava fields. After Knesel et al. (2008). ..... 3
- Figure 1.2** Graph depicting the relation between latitude ( $^{\circ}$ S) and K-Ar age (Ma) of the central volcanoes, lava fields and the Tasmanids and Lord Howe seamount chains. After Vasconcelos et al. (2008). ..... 4
- Figure 1.3** Simplified cross-section of a lamproite deposit. Depth of the feeder system is approximately 1000m. After Mitchell and Bergman (1991). ..... 5
- Figure 2.1** Energy states of the dual decay of potassium. After McDougall and Harrison (1999) ..... 13
- Figure 2.2.** Potential apparent age plateaus and K/Ca spectra generated during step-heating for a) closed system; b) open system; c) sericite alteration and d) excess  $^{40}\text{Ar}$ . ..... 18
- Figure 2.3.** Example of an inverse isochron diagram for sample VIC38 (see also Chapter 4). ..... 19
- Figure 2.4.** Cascade of secondary particle production resulting from the interaction of GCR with particles in the Earth's atmosphere.  $e^-$  = electron;  $e^+$  = positron;  $\gamma$  = gamma ray or photon;  $\nu$  = neutrino;  $\mu$  = muon;  $n$  = neutron;  $p$  = proton;  $\kappa$  = kaon. After (Gosse and Phillips, 2001). ..... 20
- Figure 2.5.** Typical cosmochron diagram. See text for discussion of main components. ..... 23
- Figure 2.6.** The effect of long  $\alpha$ -stopping distances on helium retention. After (Farley, 2002). ..... 26
- Figure 2.7.** Closure temperature as a function of cooling rate for spherical bodies of varying radius ( $r$ ). After (Hart, 1984) ..... 27
- Figure 3.1.** (a) Location of the Newer Volcanic Province in Victoria and its youngest expression (Mt Gambier and Mt Shank) in South Australia. The Tasman Line (T), the Gawler Craton, as well as the Delamerian and Lachlan fold belts are indicated. (b) Enlarged section of (a) indicating the approximate extent of the Newer Volcanics Province in grey; the 4,5–1Ma Newer Plains are located stratigraphically below the <1Ma Newer Cones. The 10–5Ma Euroa Volcanics are indicated by cross-hatching. The 95–19Ma Older Volcanics are indicated in black. The dashed line represents the approximate outline of the Selwyn Block at depth (Cayley et al., 2011). (c) Simplified outcrop of the volumetrically dominant Western Plains sub-province indicated in dark grey and location of samples. Indicated in light grey is the Central Highlands sub-province; this is an area of slightly older volcanism (Aziz-ur-Rahman & McDougall, 1972). The black dashed line represents the approximate westernmost outline of the Selwyn block at depth. Major faults are indicated by dashed red lines: C, Colac lineament; H, Hummocks fault; Y, Yarramyljip fault; E, Escondida fault; M, Moyston fault; A, Avoca fault; W, Mt William fault. .... 33

**Figure 3.2.** Total alkalis–silica (TAS) diagram after Le Bas et al. (1986). Older Volcanics and Newer Plains data are from Price et al. (1997, 2014); Euroa Volcanics data are from Paul et al. (2005); Newer Cones literature data are from Frey et al. (1978), McDonough et al. (1985), Vogel & Keays (1997), Foden et al. (2002), Demidjuk et al. (2007), Van Otterloo et al. (2014) and Boyce et al. (2015). Dashed line represents the alkaline–sub-alkaline division of Irvine & Baragar (1971). ..... 44

**Figure 3.3.** Major element variation diagrams, all data normalized to 100% on a volatile-free basis. Mg-number calculated as the atomic ratio of  $[100\text{Mg}/(\text{Mg} + 0.85*\text{Fe}_{\text{tot}})]$ . Data sources as in Fig. 3. 2. .... 45

**Figure 3.4.** (a–f) Trace element plots vs Mg-number for all series; data sources as in Fig. 2. Basanite samples VIC03, VIC09 and VIC25 are indicated in (a); (g): La/Nb vs Ba/Nb; the Primitive Mantle value is from Sun & McDonough (1989). Samples F1-111, 40, 42, 212, 300 and 301 (Price et al., 1997) are indicated. (h) Ce/Pb vs Nb/U after Hofmann et al. (1986); the grey field represents the Ce/Pb ( $25 \pm 5$ ) and Nb/U ( $47 \pm 10$ ) ratios in both ocean island basalt (OIB) and mid-ocean ridge basalt (MORB); average continental crust is indicated (Nb/U = 10; Ce/Pb = 4; Taylor & McLennan, 1995). ..... 47

**Figure 3.5.** Primitive mantle normalized trace element patterns for the Newer Volcanics compared with the Older Volcanics. Typical ocean island basalt (OIB; Sun & McDonough, 1989) is indicated with a black dashed line. Basanite samples VIC03, VIC09 and VIC25 indicated are indicated by blue lines. Data sources as in Fig. 3.2. .... 48

**Figure 3.6.** Rare earth element (REE) C1 chondrite (Sun & McDonough, 1989) normalized patterns. Typical ocean island basalt (OIB; Sun & McDonough, 1989) is indicated with a black dashed line. Basanite samples VIC03, VIC09 and VIC25 are indicated by blue lines. Data sources as in Fig. 3.2. 48

**Figure 3.7.**  $(^{87}\text{Sr}/^{86}\text{Sr})_i$ ,  $(^{143}\text{Nd}/^{144}\text{Nd})_i$ ,  $(^{207}\text{Pb}/^{204}\text{Pb})_i$  and  $(^{208}\text{Pb}/^{204}\text{Pb})_i$  vs Mg-number [atomic ratio of  $100 \text{Mg}/(\text{Mg} + 0.85*\text{Fe}_{\text{tot}})]$ . All isotope data are corrected to initial values; Newer Cones 500 – 41 ka, Newer Plains 4.6 – 1 Ma, Euroa Volcanics 7 Ma; Older Volcanics 95 – 19 Ma. Error bars ( $2\sigma$ ) are indicated in (c), but are smaller than the symbols for the  $^{87}\text{Sr}/^{86}\text{Sr}$ ,  $^{143}\text{Nd}/^{144}\text{Nd}$  and  $^{208}\text{Pb}/^{204}\text{Pb}$  isotope data. Published Pb isotope data for the Newer Cones are limited to recent studies of Mt Rouse (Boyce et al., 2015) and Mt Gambier (Van Otterloo et al., 2014); the respective fields are indicated in (c) and (d). No major element data are available for the basalts analysed for Pb isotope composition by Cooper & Green (1969). Other data sources are as in Fig. 3.2. .... 49

**Figure 3.8.** (a)  $(^{87}\text{Sr}/^{86}\text{Sr})_i$  vs  $(^{143}\text{Nd}/^{144}\text{Nd})_i$ , showing the mantle array in green and approximate locations of mantle end-members. Indicated are fields for Newer Volcanic Province spinel lherzolite (pink) and garnet pyroxenite (purple) xenoliths (McDonough et al., 1985; Griffin et al., 1988; O'Reilly & Griffin, 1988; Yaxley et al., 1991; Powell et al., 2004) as well as Group 0 anhydrous xenoliths (cross-hatched), Group 1 CO<sub>2</sub> fluid metasomatized (black star), Group 2 alkaline melt metasomatized (white star) and Group 3 carbonatite metasomatized xenoliths (diagonal lines) after Stolz & Davies (1988). (b)  $(^{207}\text{Pb}/^{204}\text{Pb})_i$  vs  $(^{206}\text{Pb}/^{204}\text{Pb})_i$  and (c)  $(^{208}\text{Pb}/^{204}\text{Pb})_i$  vs  $(^{206}\text{Pb}/^{204}\text{Pb})_i$  indicating fields for xenoliths after Stolz & Davies (1988). NHRL, Northern Hemisphere Reference Line. Newer Cones literature data are from Cooper & Green (1969), Stolz & Davies (1988), Van Otterloo et al. (2014) and Boyce et al. (2015). .... 51

**Figure 3.9.** Models for trace element fractionation during nonmodal partial melting of Newer Volcanic Province xenolith compositions (Griffin et al., 1988; Stolz & Davies, 1988; Yaxley et al., 1991) with either added garnet (continuous line) or added spinel (dashed line), using the equation



from Shaw (1970). Only basalt samples are plotted for which less than 5% fractional crystallization is inferred. Compositions are normalized to chondrite after Sun & McDonough (1989). Trace element distribution coefficients are from McKenzie & O’Nions (1983). Starting modal composition: continuous line: 56 wt % olivine, 25 wt % orthopyroxene, 11 wt % clinopyroxene, 2 wt % garnet, 6 wt % amphibole and La/Yb = 11; dashed line: 56 wt % olivine, 25 wt % orthopyroxene, 11 wt % clinopyroxene, 1 wt % spinel, 7 wt % amphibole and La/Yb<sup>1/4</sup>15. Melting mode modified from Walter (1998): ol 0.08, opx -0.19, cpx 0.81, gt 0.15 and sp 0.15. Data sources as in Fig. 3.2. Numbers in rectangles indicate per cent melting..... 54

**Figure 3.10.** MELTS (Ghiorso & Sack, 1995) modelling results for (a) and (c) the Newer Cones and (b) the Older Volcanics, Euroa Volcanics and Newer Plains. Data sources as in Fig. 3.2. Continuous lines represent isobaric (1 kbar) cooling (from 1200 to 800°C) of a dry magma, fO<sub>2</sub> = QFM + 1; dashed line represents isobaric (1 kbar) cooling (from 1200 to 800°C) of a dry magma, fO<sub>2</sub> = QFM + 2. .... 56

**Figure 3.11.** (a) Sr (ppm) vs <sup>87</sup>Sr/<sup>86</sup>Sr for all Newer Cones samples showing EC-RAXFC modelling using input parameters as in Table 3.3. (b) Enlarged section of (a) showing EC-RAXFC modelling results for the Newer Plains (Price et al., 1997, 2014) using input parameters as in Table 3.3. The continuous and dashed lines represent assimilation and fractional crystallization of average upper and lower crust (Taylor & McLennan, 1995), respectively..... 59

**Figure 3.12.** (<sup>207</sup>Pb/<sup>204</sup>Pb)<sub>i</sub> vs (<sup>143</sup>Nd/<sup>144</sup>Nd)<sub>i</sub> for samples interpreted to represent magmas unaffected by crustal assimilation showing: (a) calculated mixing line (Vollmer, 1976) between Indian MORB-source mantle and melts derived by 1% (blue continuous line) and 5% (blue dashed line) partial melting of Group 3 xenoliths; (b) calculated mixing line between Indian MORB-source mantle and the most primitive sample (Mg-number = 67) of the Older Volcanics (green continuous line); (c) calculated mixing line between Group 0 and Group 2 xenoliths. It should be noted that the Euroa Volcanics plot in two groups. The Seven Creek West samples (Paul et al., 2005) are indicated. .... 61

**Figure 3.13.** (a) Interpreted temporal geodynamic evolution of the mantle below SE Australia (after Kaislaniemi & Van Hunen, 2014). Thickness to the base of the lithosphere after Davies & Rawlinson (2014). (b) Enlarged section. Decompression melting at the base of the lithosphere results in preferential melting of metasomatized veins and mixing of the resultant enriched partial melts with Indian MORB-source mantle (MORB-A) thereby generating the magmas parental to the Older Volcanics. (c) Mixing of MORB-A with the alkaline melts represented by the Older Volcanics results in a slightly modified Indian MORB-source mantle (MORB-B). (d) Prolonged periods of melting will deplete the SCLM of calcio-carbonatite metasomatized veins. (e) Continued edge-driven convection with shear causes thermal erosion of the base of the lithosphere, incorporating depleted SCLM within MORB-B. The resultant melts have the potential to incorporate enriched vein material from the SCLM en route to the surface ..... 65

**Figure 4.1** Map of the Newer Volcanic Province and sample locations. (a) Approximate extent of the Newer Volcanic Province, indicating sub-provinces Central Highlands, Western Plains and Mt Gambier. Also indicated are major structural elements (red lines): T = Tartwaup fault, H = Hummocks fault, Y = Yarramyljup fault, E = Escondida fault, M = Moyston fault, A = Avoca fault, MW = Mount Williams fault, C = Colac lineament. (b) Enlarged section of (a) showing the approximate outcrop of Newer Plains in light grey and some relevant Newer Cone flows in dark grey. Indicated are sample locations (exact coordinates can be found in Table 4.1 and Table 4.2) and the resulting <sup>40</sup>Ar/<sup>39</sup>Ar ages (± 2σ)..... 76

- Figure 4.2.** Stratigraphic logs of bores PRC-006 and Kororoit-16, indicating the depth of samples and their associated  $^{40}\text{Ar}/^{39}\text{Ar}$  age ( $2\sigma$  errors). These ages were used to calculate production rates (thick red lines; m/Ma) and associated  $2\sigma$  errors (grey outlines) using IsoPlot (Ludwig, 2012). The production rate of VIC46 and VIC47 is apparent only due to poor correlation in IsoPlot between two closely located points. .... 79
- Figure 4.3.** (a) Plane polarized and (b) cross polarized image of VIC18 (Newer Cones basalt). (c) Plane polarized and (d) cross polarized image of VIC48 (Newer Plains basalt). .... 81
- Figure 4.4.** Examples of volcanic alignment and geomorphology interpretations. (a) Satellite image of Mt Eccles and (b) interpreted alignment direction. (c) Satellite image of Lake Cartcarrong (maar) and (d) interpreted elongation of the maar structure with preferred orientation. .... 85
- Figure 4.5.** Summary of Newer Plains step-heating analyses; apparent age plateau and inverse isochron diagrams. Plateau ages (bold) are inverse isochron intercept ( $^{40}\text{Ar}/^{36}\text{Ar}$ ) corrected. Mini-plateaus (50 - 70% cumulative  $^{39}\text{Ar}$ ) are indicated in italics. All ages are reported with  $2\sigma$  uncertainty. The material analysed was groundmass for all samples. .... 87
- Figure 4.6.** Summary of Newer Cones step-heating analyses; apparent age plateau and inverse isochron diagrams. Plateau ages (bold) are inverse isochron intercept ( $^{40}\text{Ar}/^{36}\text{Ar}$ ) corrected. Mini-plateaus (50 - 70% cumulative  $^{39}\text{Ar}$ ) are indicated in italics. All ages are reported to a  $2\sigma$  uncertainty. Groundmass was analysed for all samples except VIC22B (glass). .... 90
- Figure 4.7.** Qualitative Euclidean distance nearest neighbour density map of the NVP, indicated are the four clusters resulting from this analysis; darker colours represent higher densities. Also indicated are major and minor crustal structures as well as structural zones. .... 100
- Figure 4.8.** Rose diagrams of volcanic alignments; (a) – (d): rose diagrams of the four clusters as derived from visual interpretation of volcanic centres. (e) – (f): rose diagrams of the four clusters as derived from automated two-point azimuth analysis (Le Corvec et al., 2013b). .... 101
- Figure 4.9.** Longitude versus age diagrams. (a) Newer Plains results and literature data. K-Ar data from; Aziz-ur-Rahman and McDougall, 1972; Gray and McDougall, 2009; McDougall et al., 1966;  $^{40}\text{Ar}/^{39}\text{Ar}$  age from Hare et al, 2005a. (b) Newer Cones results and literature data (Matchan and Phillips, 2014, 2011; Matchan et al., 2016). Note that  $2\sigma$  errors for our data are often smaller than the size of the symbols used. .... 105
- Figure 4.10.** Cartoon illustrating the generation of the Newer Plains (top right) due to the interplay of complex 3D lithospheric thickness and the Cosgrove track mantle plume (dashed red line; Davies et al., 2015) and the generation of the Newer Cones (lower left) as a response to movement along the Tasman Fracture Zone. Ages of the Newer Cones have been subdivided into three groups: 0 – 100 ka, 100 – 500 ka and > 500 ka to illustrate the age progression towards the West. Lithosphere thicknesses from Davies and Rawlinson (2015). Note that there are much more eruption centres present (however undated) in the NVP that are not represented on this map. .... 106
- Figure 5.1.** (a) Location map of Mt Elephant in Southeast Australia. (b) Sampling location on top of Mt Elephant (looking South). (c-f) Panoramic photos show the absence of major shielding. .... 121

- Figure 5.2.** (a) Location map of the granite inselbergs in West-Australia; Gorge Rock (VIC100), King's Rock (VIC101 and VIC102) and Jilakin Rock (VIC103). (b-d) Panoramic photos of sample locations show the horizontal sampling surface and the absence of any shielding factors..... 122
- Figure 5.3.** Degassing patterns of (a) typical pyroxene and (b) typical apatite. The top diagram displays isotopic abundance (in fA) for  $^{37}\text{Ar}$  (grey line, open circles) and  $^{38}\text{Ar}$  (red line, closed squares). Note the exponential scale and the order of magnitude difference between the  $^{37}\text{Ar}$  and  $^{38}\text{Ar}$  signal. The middle diagram displays the  $^{38}\text{Ar}/^{36}\text{Ar}$  ratio and associated  $2\sigma$  error. Note that the size of the symbols is larger than the error for the apatite. The green line in the  $^{38}\text{Ar}/^{36}\text{Ar}$  graphs represents the UNCT value of  $0.18826 \pm 0.00018$  (Renne et al., 2001). The lower diagram displays the K/Ca ratio calculated after the  $^{39}\text{Ar}/^{37}\text{Ar}$  ratio..... 127
- Figure 5.4.** Cosmochron diagrams for irradiated pyroxene. Data in grey forms outliers to the main trend and are not used in the construction of the cosmochron..... 130
- Figure 5.5.** Cosmochron diagrams for irradiated apatite. Data in grey forms outliers to the main trend and are not used in the construction of the cosmochron..... 131
- Figure 5.6.**  $^{40}\text{Ar}/^{39}\text{Ar}$  apparent age diagram of sample VIC100 – apatite; the total fusion age of this sample is 1.4 Ga. Note that this age does not represent the formation age of this rock in any case; but rather provides an estimate of the integral theoretical duration of  $^{40}\text{Ar}$  (and thus nucleogenic  $^{38}\text{Ar}$ ) retention in the rock since formation. .... 132
- Figure 5.7.** Cosmochron comparison diagrams between (a) and meteorite pyroxene samples analysed on the MAP 250-50 mass spectrometer (Kennedy et al., 2013) and (b) and terrestrial pyroxene analysed on the ARGUSVI. The difference in analytical precision is obvious. .... 133
- Figure 5.8.** Calculated potential analytical uncertainty on the exposure age that can be obtained with the new generation multi-collector mass spectrometers. Indicated two potential ages as discussed in the text..... 134
- Figure 5.9.** (a) Cosmochron diagram for the combined pyroxene samples VIC63, VIC64, VIC65 and VIC66. (b) Age comparison diagram between the individual pyroxene samples, the combined exposure age and the  $^{40}\text{Ar}/^{39}\text{Ar}$  eruption age..... 140
- Figure 5.10.** Cosmochron diagrams of typical apatite showing the difference in isotopic abundance for (a) the uncorrected data vs (b) natural and reactor-derived Cl-corrected data. .... 144
- Figure 5.11.** Cosmochron diagrams to compare exposure ages derived from irradiated apatite samples and non-irradiated samples with  $^{38}\text{Ar}/^{36}\text{Ar}$  taken from non-irradiated degassing experiment and  $^{37}\text{Ar}/^{36}\text{Ar}$  taken from corresponding irradiated aliquot. It can be seen that the irradiated samples have extremely high  $^{38}\text{Ar}$  values which are most likely derived from reactor-induced chlorogenic interferences. The artificially constructed cosmochron slope of the non-irradiated apatite samples is thought to be more geologically meaningful and a statistically significant ( $p > 0.05$ ) exposure age can be obtained for sample VIC102ap\_unirr at  $2.7 \pm 0.5$  Ma. .... 145
- Figure 5.12.** Relative contribution of nucleogenic  $^{38}\text{Ar}$  (in %) on the total  $^{38}\text{Ar}$  abundance over a range of potential formation ages of a rock and different exposure ages. .... 147

<b>Figure 6.1.</b> Simplified location map of the Ellendale lamproite field after Jaques et al (1986). Major geological units are distinguished by different colours. Major faults are indicated by red lines. Lamproite deposits are indicated by a star.....	156
<b>Figure 6.2.</b> Thin section images of an olivine phenocryst in the Ellendale E9 sample. (a) Plane polarized light and (b) cross polarized light.....	158
<b>Figure 6.3.</b> Age spectra of the three E9 phlogopite aliquots. The size of the error box represents a $2\sigma$ uncertainty on the apparent age. ....	162
<b>Figure 6.4.</b> Age comparison between (U-Th)/He ages of six olivine aliquots and the ultra-precise weighted mean $^{40}\text{Ar}/^{39}\text{Ar}$ age of the three phlogopite aliquots of sample Ellendale E9. All errors are $2\sigma$ . ....	164
<b>Figure 6.5.</b> Ellendale E9 olivine phenocrysts (a) before and (b) after three days of air abrasion used to remove the outer edge of $20\ \mu\text{m}$ from the grains to overcome $\alpha$ -implantation effects from the U and Th rich lamproite groundmass. ....	165
<b>Figure P.0.1.</b> Simplified location map of the Spanish and Serbian lamproite occurrences. ....	345
<b>Figure P.0.2.</b> Thin section photographs (cross polars) of (b) sample BK13/B and (c) sample 03V14. ....	345
<b>Figure P.0.3.</b> Age spectra and K/Ca diagrams for relevant phases for K-rich phases analysed. ....	346

## LIST OF TABLES

<b>Table 2.1.</b> Interference reactions producing argon during neutron irradiation. Q values (MeV) and target isotope abundance (atom%) are given in italics in the parentheses. The arrows represent $\beta$ - decay in all cases. After McDougall and Harrison (1999). .....	16
<b>Table 3.1.</b> Major (wt %) and trace element (ppm) analyses of Newer Volcanic Province basalts. ....	39
<b>Table 3.2</b> Sr – Nd – Pb isotope data for the Newer Cones .....	50
<b>Table 3.3.</b> Input parameters for EC-RAXFC modelling, thermal parameters and standard upper and lower crustal composition after Bohrsen and Spera (2002).....	58
<b>Table 4.1.</b> Summary of $^{40}\text{Ar}/^{39}\text{Ar}$ results for the Newer Plains basalts. Data in italics are derived from mini-plateaus (50 - 70% $^{39}\text{Ar}$ released) and are considered minimum ages only. * No plateau age is calculated, as the correlation of the inverse isochron diagram .....	89
<b>Table 4.2.</b> Summary of $^{40}\text{Ar}/^{39}\text{Ar}$ results for the Newer Cones basalts. Data in italics are derived from mini-plateaus (50% - 70% $^{39}\text{Ar}$ released) and are considered minimum ages only. Mt Buninyong is the only volcano analysed which is located in the Central Highlands.....	96
<b>Table 5.1.</b> Apatite (U-Th)/He results. Th, $^{232}\text{Th}$ ; ng, nanogram; U, $^{238}\text{U}$ ; Sm, $^{147}\text{Sm}$ ; He, $^4\text{He}$ in ncc at STP; ncc, nano cubic centimetre; TAU, total analytical uncertainty, Ft, alpha recoil correction factor after Farley et al., 1996. Data in italics is excluded for the calculation of the mean weighted average age.....	136
<b>Table 5.2.</b> Cosmochron characteristics and resulting exposure ages for all irradiated samples. The $(^{38}\text{Ar}/^{36}\text{Ar})_{\text{cosmogenic}}$ ratio is 1.49 for the apatite samples and 2.17 for the pyroxene samples. The alpha-coefficient is 0.52 for all samples. A P38(Ca) of $\sim 250$ (high latitude, sea level) was used to calculate all exposure ages. Exposure ages derived from statistically meaningful cosmochrons are indicated in bold, apparent exposure ages are indicated in italics. See text for discussion on the Cl correction of the apatite samples.....	142
<b>Table 5.3.</b> Composition of apatite (VIC100, VIC101, VIC102 and VIC103) and pyroxene (VIC63) samples as derived from averaging two-spot (apatite) and four-spot (pyroxene) ELA-ICP-MS analysis. ....	143
<b>Table 6.1.</b> Summary of $^{40}\text{Ar}/^{39}\text{Ar}$ results of three phlogopite aliquots for Ellendale E9.....	161
<b>Table 6.2.</b> (U-Th)/He degassing summary (all blank subtracted) and resulting ages.....	163
<b>Table P.0.1.</b> Summary of $^{40}\text{Ar}/^{39}\text{Ar}$ results of various K-rich mineral phases of the lamproite samples. Data in italics are derived from mini-plateaus (50% - 70% $^{39}\text{Ar}$ released) and are considered minimum ages only. ....	347



## Chapter 1 Introduction

The scientific community always strives to provide an accurate and reliable temporal framework for geological phenomena. The most readily available example is the age of the Earth itself. From the first estimates of the age of the Earth (Thomson, 1899), radiometric dating techniques have been indispensable to derive a geologically meaningful age of the Earth from meteorites (Patterson, 1956) consistent with the age of very old Australian zircons (Compston and Pidgeon, 1986). The availability of reliable geochronological data is of paramount importance to correctly interpret geological, geochemical and geomorphological processes in terrestrial as well as extra-terrestrial systems. There is an ongoing progression in the field of geochronology; where new techniques are being continuously developed and advances in instrumental sensitivity allow for the determination of more accurate and precise ages.

The focus of this thesis is to better understand Australia's igneous geology and geomorphology; the timescales and rates on which volcanic activity and landscape evolution has taken place throughout geological history. Better understanding of this leads to, e.g. better understanding of the underlying processes that have caused volcanism, potentially even leading to assessment of locations and timeframes of future volcanism. Here, we improve upon, and further develop existing geochronology techniques:  $^{40}\text{Ar}/^{39}\text{Ar}$  dating of young mafic rocks; (U-Th)/He dating of olivine phenocrysts; and cosmogenic  $^{38}\text{Ar}$  exposure dating of terrestrial rocks, to achieve this goal.

Although the  $^{40}\text{Ar}/^{39}\text{Ar}$  geochronology technique (McDougall and Harrison, 1999) is widely applied on K-rich phases, new generation multi-collector mass spectrometers, such as the Thermofisher™ ARGUSVI used in this study, prove to be a game-changer where accuracy and precision of the resulting ages are concerned. It has been shown that the ARGUSVI is capable of yielding ages with an order of magnitude better precision as compared to previous generation mass spectrometers (VG3600; Matchan and Phillips, 2014). The importance of having accurate and precise ages available to better understand the spatial and temporal distribution of volcanism is shown in Chapter 4. Not only does this study massively improve on the existing geochronological database of an intraplate volcanic province in which accurate age data is either lacking or restricted to unreliable K-Ar data, but it is shown that the availability of precise ages is key to interpret timescales of volcanism and its relation to the complex geodynamic setting in the area.

The cosmogenic  $^{38}\text{Ar}$  exposure dating technique, although widely used in extra-terrestrial settings (e.g. Kennedy *et al.*, 2013; Levine *et al.*, 2007), has not yet been applied on Earth but for two publications (Niedermann *et al.*, 2007; Renne *et al.*, 2001) and a single, unpublished PhD thesis (Knight, 2006). Nevertheless, this technique could be extremely valuable in determining the timing of surface processes using Ca-rich or K-rich minerals in rock; such as the timing of past seismic activity by dating calcite on exposed fault planes; rates of erosion; the onset of glacial retreat and the timescales of climate change. As  $^{38}\text{Ar}$  is stable; it can be used on timescales beyond that of other, unstable, cosmogenic exposure dating techniques such as  $^{10}\text{Be}$ ,  $^{26}\text{Al}$  and  $^{36}\text{Cl}$ . However, development of cosmogenic  $^{38}\text{Ar}$  exposure dating has long suffered from the difficulty to both distinguish cosmogenic  $^{38}\text{Ar}$  from the high terrestrial atmospheric background value and to discriminate between multiple argon reservoirs in a mineral. In Chapter 5 we show the results of using irradiated (Merrill and Turner, 1966) pyroxene and apatite from strategically sampled locations in southeast and southwest Australia, for cosmogenic  $^{38}\text{Ar}$  analysis on the multi-collector ARGUSVI mass spectrometer with both  $^{38}\text{Ar}$  and  $^{36}\text{Ar}$  determined using the instruments' ultra-sensitive compact discrete dynode. This approach allows simultaneous analysis of both daughter ( $^{38}\text{Ar}$ ) and 'proxy-parent' ( $^{37}\text{Ar}$ ) isotopes; step-heating and associated statistical analysis of individual degassing steps; discrimination between multiple argon reservoirs in a sample and discrimination between atmospheric  $^{38}\text{Ar}$  and cosmogenic  $^{38}\text{Ar}$ .

(U-Th)/He dating of olivine phenocrysts could be a valuable tool to date igneous processes when minerals suitable for dating with more generic geochronology techniques are either absent or altered. However, the methodology as currently proposed (Aciego *et al.*, 2007, 2010) suffers from analytical complexity and incapability in determining precise helium concentrations. We present a simplified methodology for more accurate and precise (U-Th)/He age analysis of olivine phenocrysts in Chapter 6, using the Alphachron™ mass spectrometer by Australian National Instruments/CSIRO for He degassing experiments and calibrating the resulting ages against high-precision  $^{40}\text{Ar}/^{39}\text{Ar}$  ages on phlogopite from K-rich lamproites from northwest Australia.

### 1.1. Geological Background

Here, the wider geological context of the sampling locations is described and the importance of the availability of geochronological data of these regions highlighted. Detailed geological descriptions; including rock types, basement geology, geological structures etc. of the Newer Volcanic Province can be found in Chapter 3 (Sections 3.3 and 3.4) and Chapter 4 (Section 4.4).



## 1.1.1. The Newer Volcanic Province

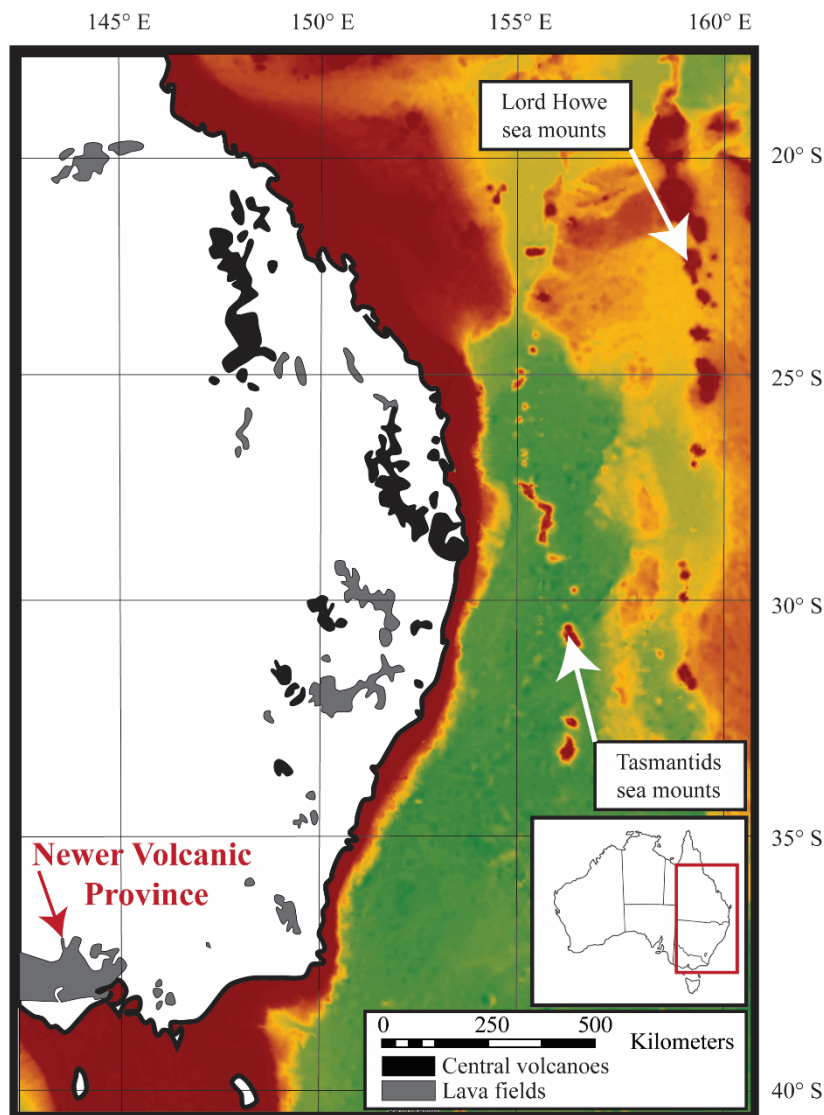


Figure 1.1. Location map of the Newer Volcanic Province within the eastern Australian Cenozoic volcanic region. Colours offshore represent bathymetry, with red colours indicative of higher areas; the Tasmantids and Lord Howe seamount chains are easily visible. Onshore, the black areas indicate the location of Central Volcanoes, whereas the grey areas indicate the location of lava fields. After Knesel *et al.* (2008).

The Newer Volcanic Province (NVP) is part of a widespread zone of Cenozoic volcanism along the eastern margin of Australia (Figure 1.1). Volcanic regions along this margin have been subdivided into three distinct groups: 1) central volcanic provinces 30–100 km in diameter; 2) lava fields consisting of thick (up to 1000 m) basaltic flows and smaller volcanic features such as lava shields, scoria cones and maars; and 3) a single leucite occurrence (Wellman and McDougall, 1974). Although upwelling mantle plumes have been proposed in earlier literature as an explanation for lava field volcanism (Sutherland *et al.*, 2014; Wellman

and McDougall, 1974), recent insights into thickness variations of the underlying lithosphere have put forward the model of Edge Driven Convection (King and Anderson, 1998) for magmatic upwelling in the NVP region (Davies and Rawlinson, 2014; Demidjuk *et al.*, 2007). Xenolith studies have shown that the NVP is underlain by a heavily metasomatised sub-continental lithospheric mantle (Griffin *et al.*, 1988; O'Reilly and Griffin, 1988; Stolz and Davies, 1988). The majority of geochemical studies towards the NVP basalts were limited to major and trace elements only (e.g. Day, 1983; Irving and Green, 1976; McDonough *et al.*, 1985; O'Reilly and Zhang, 1995) and limited Sr isotope data on the lava fields in the NVP (Price *et al.*,

1997) which suggested that the enriched geochemical signature of the lava plains basalts could potentially be linked to geochemical variations in the underlying lithosphere. In Chapter 3 an integrated major and trace element and Sr, Nd and Pb isotope study towards the geochemical composition of the NVP basalts is presented, in which not only the geochemistry of the lava plains is considered, but also that of the older central volcanoes and the younger scoria cones, lava shields and maars (Oostingh *et al.*, 2016). The high resolution of especially Pb isotopes permits differentiation between geochemically distinct mantle sources far better than major and trace element geochemistry only. Detailed knowledge of magmatic provenance is essential for the correct geological interpretation of geochronology data; as we will show in Chapter 4.

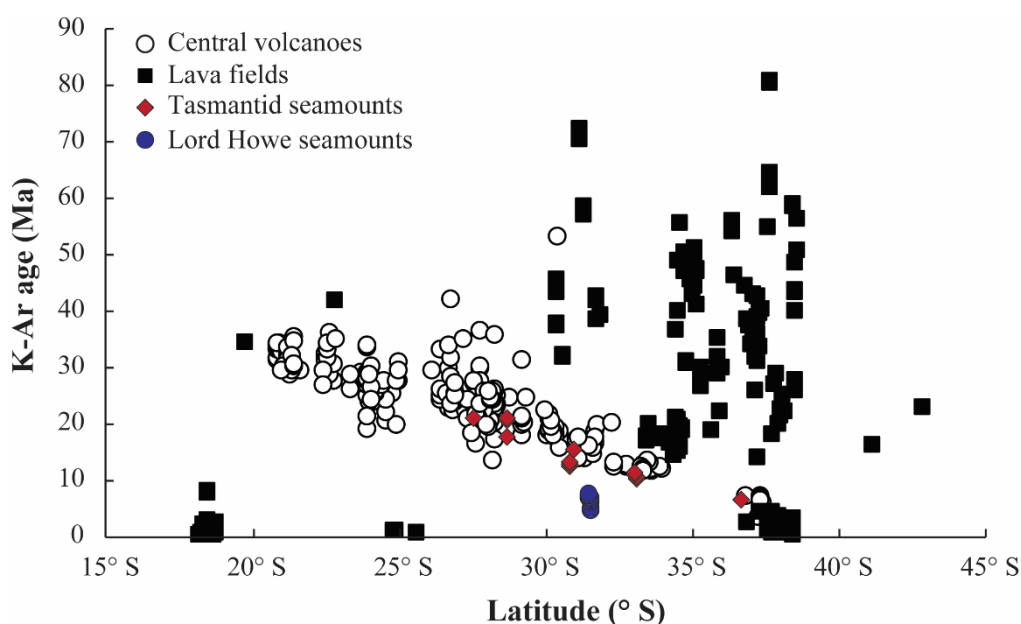


Figure 1.2 Graph depicting the relation between latitude ( $^{\circ}$ S) and K-Ar age (Ma) of the central volcanoes, lava fields and the Tasmantids and Lord Howe seamount chains. After Vasconcelos *et al.* (2008)

The NVP is the youngest ( $< 5$  Ma) expression of lava field volcanism within the larger region of Cenozoic volcanism in east Australia. Most of the geochronology research in this region has been restricted to K-Ar studies, limited  $^{40}\text{Ar}/^{39}\text{Ar}$  and

fission track dating and few studies using Rb-Sr, U-Pb, cosmogenic isotopes,  $^{14}\text{C}$  and TL (Vasconcelos *et al.*, 2008). The presence of an apparent K-Ar age trend within the Central volcanoes parallel to trends of existing hotspot trails, such as the Lord Howe Rise and Tasmantids seamount chains (Figure 1.2), has led researchers to propose that the large central volcanic provinces were generated by magmatic upwelling along Earth's longest continental hotspot track; the Cosgrove track (Davies *et al.*, 2015). Lack of any spatio-temporal correlation between and within lava field provinces - such as the NVP - makes volcanism in these regions more enigmatic to explain. Most of the geochronology data in the NVP is represented by K-Ar ages on lava plains (Cohen, 2007). K-Ar dating will only provide reliable eruption ages if the samples are completely unaltered; sample splits

for K and Ar analysis are homogenous; and if the initial trapped  $^{40}\text{Ar}/^{36}\text{Ar}$  ratio is within the range of the air value [ $298.56 \pm 0.31$ ; as measured by Lee *et al.* (2006)].  $^{40}\text{Ar}/^{39}\text{Ar}$  geochronology provides more reliable age data and analysis with the new generation ARGUSVI mass spectrometer offers the resolution to distinguish a potential age progression in the onset of volcanism within the NVP (Oostingh *et al.*, 2017; Chapter 4). Hence it is shown that the process of Edge Driven Convection alone is probably not enough to ultimately trigger volcanism in such a localized area as the NVP (Davies *et al.*, 2015), and a complex interplay between the arrival of the Cosgrove track mantle plume and the existing mantle convection by Edge Driven Convection is proposed to explain lava field volcanism (Oostingh *et al.*, 2017; Chapter 4).

The detailed  $^{40}\text{Ar}/^{39}\text{Ar}$  geochronology of eastern Australia's Cenozoic volcanic features as presented in this study could furthermore aid in investigating the geomorphic and climatic processes that shaped the Australian continent. Reliable geochronology data will provide a framework for the interpretation of Cenozoic tectonic uplift and denudation data (Aziz-ur-Rahman and McDougall, 1972; Gurnis *et al.*, 1998; Sandiford, 2007; Wellman, 1974); as well as eastern Australia's climatic record, biological evolution and human occupation (Tedford *et al.*, 1975; Wellman and McDougall, 1974). For example; a study is currently being undertaken at the University of Melbourne using  $^{40}\text{Ar}/^{39}\text{Ar}$  ages of the Tower Hill tuff generated during this research to investigate periods of human occupation of this region; indicated by tools found in the tuff layers of this volcano (Matchan *et al.*, in prep).

### 1.1.2. Lamproites

Lamproites are K and Mg-rich, ultramafic igneous rocks ( $\text{K}_2\text{O}/\text{Na}_2\text{O} > 3$  [molar ratio]), that can be found as flows, cinder cones, dykes, sills and diatremes in a variety of geological and tectonic environments. Lamproite diatremes often resemble a typical sherbet-glass shape (Figure 1.3; Bergman, 1987; Mitchell and Bergman, 1991). These rocks are generated from a strongly depleted mica-harzburgite source (Foley and Peccerillo, 1992) in the garnet-stability field (previous amount of  $\sim 20\%$  partial melting), which

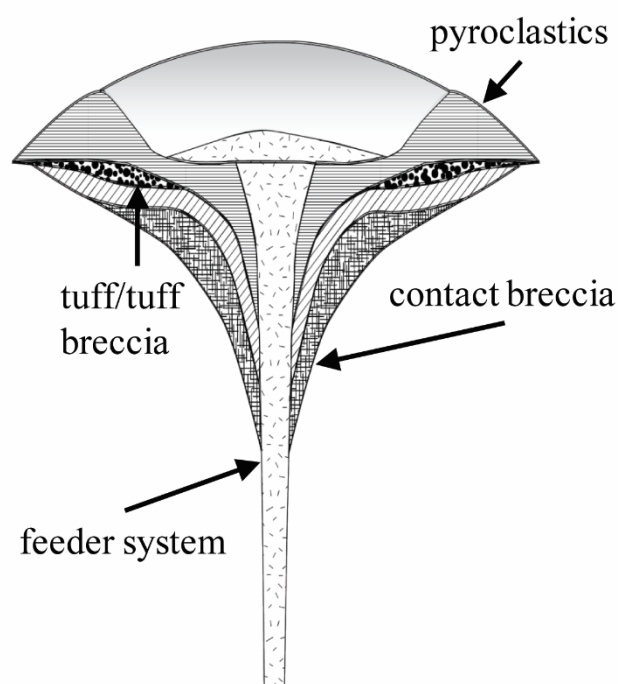


Figure 1.3 Simplified cross-section of a lamproite deposit. Depth of the feeder system is approximately 1000m. After Mitchell and Bergman (1991).

was later enriched by a metasomatic melt rich in light REE and other incompatible elements (Tainton and McKenzie, 1994). Their spatial distribution suggests that lamproite occurrences are strongly dependent on pre-existing geological structures within the lithosphere (Jaques and Milligan, 2004). More detailed information about the petrogenesis of the individual lamproite occurrence studied in this thesis can be found in Chapter 6, Section 6.3. Lamproites are distinguished from kimberlites and other K-rich rocks based on their mineralogical composition. They are characterized by the presence of typical primary phases such as 1) titanium (2-10 wt% TiO<sub>2</sub>), aluminium-poor phenocrystic phlogopite (5-12 wt% Al<sub>2</sub>O<sub>3</sub>); 2) poikilitic phlogopite in the groundmass (5-10 wt% TiO<sub>2</sub>); 3) titanium (3-5 wt% TiO<sub>2</sub>) potassium (4-6 wt%) richterite, 4) forsteritic olivine, 5) aluminium-poor (<1 wt% Al<sub>2</sub>O<sub>3</sub>) and sodium-poor (<1 wt% Na<sub>2</sub>O) diopside, 6) iron-rich (1-4 wt% Fe<sub>2</sub>O<sub>3</sub>) leucite and 7) iron-rich (1-5 wt% Fe<sub>2</sub>O<sub>3</sub>) sanidine. Minor and common accessory phases include priderite [(K,Ba)(Ti,Fe<sup>3+</sup>)<sub>8</sub>O<sub>16</sub>], wadeite [K<sub>2</sub>ZrSi<sub>3</sub>O<sub>9</sub>], apatite [Ca<sub>5</sub>(PO<sub>4</sub>)<sub>3</sub>F], perovskite [CaTiO<sub>3</sub>], magnesiochromite [MgCr<sub>2</sub>O<sub>4</sub>], titanium magnesiochromite [(Mg,Ti)Cr<sub>2</sub>O<sub>4</sub>], magnesian titaniferous magnetite [(Mg, Fe<sup>2+</sup>)(Ti,Fe<sup>3+</sup>)<sub>2</sub>O<sub>4</sub>], jeppeite [(K,Ba)<sub>2</sub>(Ti,Fe<sup>3+</sup>)<sub>6</sub>O<sub>13</sub>], armalcolite [(Mg,Fe<sup>2+</sup>)Ti<sub>2</sub>O<sub>5</sub>], shcherbakovite [(K,Ba,Na)KNaTi<sub>2</sub>O(OH)(Si<sub>4</sub>O<sub>12</sub>)], ilmenite [Fe<sup>2+</sup>TiO<sub>3</sub>] and enstatite [Mg<sub>2</sub>Si<sub>2</sub>O<sub>6</sub>] (Woolley *et al.*, 1996).

These rocks are considered ideal candidates for the further development of the (U-Th/He) dating technique on olivine phenocrysts because of their distinct mineralogy and geomorphology. They both contain K-rich phases suitable for <sup>40</sup>Ar/<sup>39</sup>Ar dating, as well as fresh olivine phenocrysts suitable for (U-Th)/He dating. The rapid ascent of magma from depth, and small size of resulting intrusions (~50 m diameter; Mitchell and Bergman, 1991) ensures rapid and simultaneous cooling of all phases; which will thus most likely all represent a similar age. Importantly; partition coefficients for U are generally high in lamproite rocks (K<sub>d</sub> = 0.0012) for olivine phenocrysts, as compared to less alkaline rocks (K<sub>d</sub> = 0.0001; McKenzie and O’Nions, 1991) due to a favourably larger M2 site (Foley and Jenner, 2004). Hence, smaller sample aliquots are required for reliable U and Th analysis; facilitating better dissolution of degasses olivine samples and improving the duration and accuracy of analysis.

## 1.2. Aim and objectives

The aim of this thesis is to better understand the igneous geology and geomorphology of Australia, focusing on the intraplate Newer Volcanic Province, SE Australia; for which both existing as well as relatively new geochronology techniques are improved upon and further developed.

These aims are addressed by several sub-objectives, which are represented by the following chapters:

- 1) To gain insight in the current status of  $^{40}\text{Ar}/^{39}\text{Ar}$  geochronology, cosmogenic  $^{38}\text{Ar}$  exposure dating and (U-Th)/He dating techniques and their applicability (Chapter 2).
- 2) To get a better understanding of magmatic provenance and geological processes in the Newer Volcanic Province, SE Australia (Chapter 3).
- 3) To better understand the timescales of volcanism in the Newer Volcanic Province, SE Australia and to gain insight in the spatial and temporal distribution of volcanism within this province (Chapter 4).
- 4) To better understand the timescales of geomorphic processes (e.g. erosion) in Australia by further developing cosmogenic  $^{38}\text{Ar}$  exposure dating (Chapter 5).
- 5) To be able to determine timing of volcanism in situations where conventional dating techniques are not sufficient; by developing a simplified method for (U-Th)/He dating on olivine phenocrysts using K-rich lamproite from Ellendale, western Australia (Chapter 6).

### 1.3. Thesis structure

The thesis opens with an Introduction (Chapter 1), which stresses the importance of improving upon existing and further developing new geochronology techniques to better understand the igneous and geomorphic past of Australia. Furthermore, the Introduction provides a brief geological context of the sampling locations, where the focus is on the larger regional geological setting not discussed in the relevant chapters. The main body of the thesis comprises chapters 2 – 6; of these, Chapter 3 is published in *Journal of Petrology*, Chapter 4 is currently under review in *Geology, Geochemistry, Geosystems (G-Cubed)*, Chapter 5 is currently under review in *Geochimica et Cosmochimica Acta*; and Chapter 6 is under review in *The Australian Journal of Earth Sciences*. Copies of the published manuscripts can be found in Appendix A, together with the publishers' copyright as well as co-author approvals of all submitted manuscripts.

*Chapter 2. Theoretical background of geochronology techniques used in this study.* This Chapter ensures a thorough understanding of the fundamental principles, analytical techniques and applicability of  $^{40}\text{Ar}/^{39}\text{Ar}$  geochronology, cosmogenic  $^{38}\text{Ar}$  exposure dating and (U-Th)/He dating, as is required to correctly interpret the data presented in Chapters 4 – 6.

*Chapter 3: Spatio-temporal geochemical evolution of the SE Australian upper mantle deciphered from Sr, Nd and Pb isotopes of Cainozoic intraplate volcanics.* This chapter provides a wider geological overview of the Newer Volcanic Province and presents a new geological model for the

composition of the magma source. The novelty of this research is that it combines a large amount of geochemical data from multiple datasets with new major and trace element and isotope analysis on the Newer Cones series. Such a part review/part analytical manuscript was not yet published and proves key to discovering a geochemical change of the underlying magma source over time. This knowledge is extremely important to correctly interpret spatial and temporal trends in magmatism based on ultra-precise  $^{40}\text{Ar}/^{39}\text{Ar}$  geochronology presented in Chapter 4.

*Chapter 4. Ultra-precise  $^{40}\text{Ar}/^{39}\text{Ar}$  geochronology reveals rapid change from plume-assisted to stress-dependent volcanism in the Newer Volcanic Province, SE Australia.* This chapter provides more than 20 new, ultra-precise  $^{40}\text{Ar}/^{39}\text{Ar}$  ages for both the Newer Plains as well as the Newer Cones series in the Newer Volcanic Province, SE Australia. Furthermore, it presents a spatial analysis of the distribution and geomorphology of volcanic features in the region, to better understand and interpret the age trends observed. This research is novel as it is the first large-scale study of  $^{40}\text{Ar}/^{39}\text{Ar}$  ages in the region, and one of the few studies that combines geochronology with spatial analysis. The advantage of performing such a large-scale study is exemplified by the observation of a progressive age trend in volcanism from east to west not previously described in the literature. Several potential hypotheses that address this age trend are discussed in Chapter 4, of which that of migrating stress fits best with the spatial trends of volcanism in the area.

*Chapter 5. Advancements towards  $^{38}\text{Ar}$  exposure dating of terrestrial rocks.* This chapter showcases the major improvement in analytical precision that can be obtained with the ARGUSVI mass spectrometer, which proves to be absolutely essential to derive statistically meaningful cosmochrons on terrestrial pyroxene. The chapter is methodology-focused and discusses the degassing characteristics and exposure ages derived on two sample sets: very young (< 1 Ma) pyroxene minerals from Mt Elephant in the Newer Volcanic Province, SE Australia; and very old (~ 2.5 Ga) apatite minerals from the Yilgarn granite bornhardts in the wheatbelt region of SW Australia. As this chapter presents an entirely novel technique, it includes a detailed theoretical background of  $^{38}\text{Ar}$  cosmogenic exposure dating, a detailed methodological approach and a detailed discussion of all the variables and unknowns present during the calculation of an exposure age.

*Chapter 6. (U-Th)/He dating of olivine phenocrysts in K-rich lamproites.* This chapter presents the first-ever results of (U-Th)/He dating of olivine phenocrysts from ultramafic rocks (lamproites). As this study represents the third study towards (U-Th)/He dating of olivine phenocrysts, it heavily focuses on the methodological development and theoretical background of (U-Th)/He dating in general.  $^{40}\text{Ar}/^{39}\text{Ar}$  dating of lamproites from the Ellendale E9 deposit in northwest Australia was

performed, as well as (U-Th)/He dating of olivine phenocrysts which partially overlap within error with the  $^{40}\text{Ar}/^{39}\text{Ar}$  phlogopite age.

#### 1.4. References

Aciego, S. M., DePaolo, D. J., Kennedy, B. M., Lamb, M. P., Sims, K. W. W. & Dietrich, W. E. (2007). Combining [ $^3\text{He}$ ] cosmogenic dating with U–Th/He eruption ages using olivine in basalt. *Earth and Planetary Science Letters* 254, 288–302.

Aciego, S. M., Jourdan, F., DePaolo, D. J., Kennedy, B. M., Renne, P. R. & Sims, K. W. W. (2010). Combined U–Th/He and  $^{40}\text{Ar}/^{39}\text{Ar}$  geochronology of post-shield lavas from the Mauna Kea and Kohala volcanoes, Hawaii. *Geochimica et Cosmochimica Acta*. Elsevier Ltd 74, 1620–1635.

Aziz-ur-Rahman & McDougall, I. (1972). Potassium-Argon ages on the Newer Volcanics of Victoria. *Proceedings of the Royal Society of Victoria* 85.

Bergman, S. C. (1987). Lamproites and other potassium-rich igneous rocks: a review of their occurrence, mineralogy and geochemistry. Geological Society, London, Special Publications 30, 103–190.

Cohen, B. E. (2007). High-Resolution  $^{40}\text{Ar}/^{39}\text{Ar}$  geochronology of intraplate volcanism in eastern Australia. PhD thesis; University of Queensland.

Compston, W. & Pidgeon, R. T. (1986). Jack Hills, evidence of more very old detrital zircons in Western Australia. *Nature* 321, 766–769.

Davies, D. R. & Rawlinson, N. (2014). On the origin of recent intraplate volcanism in Australia. *Geology* 1–4.

Davies, D. R., Rawlinson, N., Iaffaldano, G. & Campbell, I. H. (2015). Lithospheric controls on magma composition along Earth's longest continental hotspot track. *Nature*.

Day, R. A. (1983). *Petrology and Geochemistry of the Older Volcanics, Victoria: distribution, characterization, and petrogenesis*. Monash University, Clayton, Victoria.

Demidjuk, Z., Turner, S., Sandiford, M., George, R., Foden, J. & Etheridge, M. (2007). U-series isotope and geodynamic constraints on mantle melting processes beneath the Newer Volcanic Province in South Australia. *Earth and Planetary Science Letters* 261, 517–533.

Foley, S. F. & Jenner, G. A. (2004). Trace element partitioning in lamproitic magmas—the Gaussberg olivine leucitite. *Lithos* 75, 19–38.

Foley, S. F. & Peccerillo, A. (1992). Potassic and ultrapotassic magmas and their origin. *Lithos* 28, 181–185.

Griffin, W. L., O'Reilly, S. Y. & Stabel, A. (1988). Mantle metasomatism beneath western Victoria, Australia: II. Isotopic geochemistry. *Geochimica et Cosmochimica Acta* 52, 449–459.

Gurnis, M., Müller, R. D. & Moresi, L. N. (1998). Cretaceous Vertical Motion of Australia and the Australian Antarctic Discordance. *Science* 279, 1499 LP-1504.

- Irving, A. J. & Green, D. H. (1976). Geochemistry and petrogenesis of the newer basalts of Victoria and South Australia. *Journal of the Geological Society of Australia: An International Geoscience Journal of the Geological Society of Australia* 23, 45–66.
- Jaques, A. L. & Milligan, P. R. (2004). Patterns and controls on the distribution of diamondiferous intrusions in Australia. *Lithos* 77, 783–802.
- Kennedy, T., Jourdan, F., Bevan, A. W. R., Mary Gee, M. A. & Frew, A. (2013). Impact history of the HED parent body(ies) clarified by new  $^{40}\text{Ar}/^{39}\text{Ar}$  analyses of four HED meteorites and one anomalous basaltic achondrite. *Geochimica et Cosmochimica Acta*. Elsevier Ltd 115, 162–182.
- King, S. D. & Anderson, D. L. (1998). Edge-driven convection. *Earth and Planetary Science Letters* 160, 289–296.
- Knight, K. B. (2006). Argon geochronology. University of California.
- Knesel, K. M., Cohen, B. E., Vasconcelos, P. M. & Thiede, D. S. (2008). Rapid change in drift of the Australian plate records collision with Ontong Java plateau. *Nature* 454, 754–7.
- Lee, J. B., Marti, K., Severinghaus, J. P., Kawamura, K., Yoo, H. & Kim, J. S. (2006). A redetermination of the isotopic abundances of atmospheric Ar. *Geochimica et Cosmochimica Acta* 70, 4507–4512.
- Levine, J., Renne, P. R. & Muller, R. A. (2007). Solar and cosmogenic argon in dated lunar impact spherules. *Geochimica et Cosmochimica Acta* 71, 1624–1635.
- Matchan, E. L. & Phillips, D. (2014). High precision multi-collector  $^{40}\text{Ar}/^{39}\text{Ar}$  dating of young basalts: Mount Rouse volcano (SE Australia) revisited. *Quaternary Geochronology*. Elsevier Ltd.
- Matchan, E. L., Phillips, D., Jourdan, F. & Oostingh, K. F. (n.d.). New insights into earliest Aboriginal presence in SE Australia from high-precision  $^{40}\text{Ar}/^{39}\text{Ar}$  dating of young volcanic eruptions. *Nature Letters*.
- McDonough, W. F., McCulloch, M. T. & Sun, S. S. (1985). Isotopic and geochemical systematics in Tertiary-Recent basalts from southeastern Australia and implications for the evolution of the sub-continental lithosphere. *Geochimica et Cosmochimica Acta* 49, 2051–2067.
- McDougall, I. & Harrison, T. M. (1999). *Geochronology and thermochronology by the  $^{40}\text{Ar}/^{39}\text{Ar}$  method*. Oxford University Press.
- McKenzie, D. & O’Nions, R. K. (1991). Partial Melt Distributions from Inversion of Rare Earth Element Concentrations. *Journal of Petrology* 32, 1021–1091.
- Merrihue, C. & Turner, G. (1966). Potassium-Argon dating by activation with fast neutrons. *Journal of Geophysical Research* 71, 2852–2857.
- Mitchell, R. H. & Bergman, S. C. (1991). *Petrology of Lamproites*. Plenum Press, New York.
- Niedermann, S., Schaefer, J., Wieler, R. & Naumann, R. (2007). The production rate of cosmogenic  $^{38}\text{Ar}$  from calcium in terrestrial pyroxene. *Earth and Planetary Science Letters* 257, 596–608.
- O’Reilly, S. Y. & Griffin, W. L. (1988). Mantle metasomatism beneath western Victoria, Australia: I. Metasomatic processes in Cr-diopside lherzolites. *Geochimica et Cosmochimica Acta* 52, 433–447.



- O'Reilly, S. Y. & Zhang, M. (1995). Geochemical characteristics of lava-field basalts from eastern Australia and inferred sources: connections with the subcontinental lithospheric mantle? *Contributions to Mineralogy and Petrology* 121, 148–170.
- Oostingh, K. F., Jourdan, F., Matchan, E. L. & Phillips, D. (2017).  $^{40}\text{Ar}/^{39}\text{Ar}$  geochronology reveals rapid change from plume-assisted to stress-dependent volcanism in the Newer Volcanic Province, SE Australia. *Geochemistry, Geophysics, Geosystems* 18, 1065–1089.
- Oostingh, K. F., Jourdan, F., Merle, R. & Chiaradia, M. (2016). Spatio-temporal Geochemical Evolution of the SE Australian Upper Mantle Deciphered from the Sr, Nd and Pb Isotope Compositions of Cenozoic Intraplate Volcanic Rocks. *Journal of Petrology* 57, 1509–1530.
- Patterson, C. (1956). Age of meteorites and the earth. *Geochimica et Cosmochimica Acta*. Pergamon 10, 230–237.
- Price, R. C., Gray, C. M. & Frey, F. A. (1997). Strontium isotopic and trace element heterogeneity in the plains basalts of the Newer Volcanic Province, Victoria, Australia. *Geochimica et Cosmochimica Acta* 61, 171–192.
- Renne, P. R., Farley, K. A., Becker, T. A. & Sharp, W. D. (2001). Terrestrial cosmogenic argon. *Earth and Planetary Science Letters* 188, 435–440.
- Sandiford, M. (2007). The tilting continent: A new constraint on the dynamic topographic field from Australia. *Earth and Planetary Science Letters* 261, 152–163.
- Stolz, A. J. & Davies, G. R. (1988). Chemical and isotopic evidence from spinel lherzolite xenoliths from episodic metasomatism of the upper mantle beneath southeastern Australia. *Journal of Petrology Spec. Vol.*, 303–330.
- Sutherland, F. L., Graham, I. T., Hollis, J. D., Meffre, S., Zwingmann, H., Jourdan, F. & Pogson, R. E. (2014). Multiple felsic events within post-10 Ma volcanism, Southeast Australia: inputs in appraising proposed magmatic models. *Australian Journal of Earth Sciences*. Taylor & Francis 61, 241–267.
- Tainton, K. M. & McKenzie, D. (1994). The Generation of Kimberlites, Lamproites, and their Source Rocks. *Journal of Petrology* 35, 787–817.
- Tedford, R. H., Banks, M. R., Kemp, N. R., McDougall, I. A. & Sutherland, F. L. (1975). Recognition of the oldest known fossil marsupials from Australia. *Nature* 255, 141–142.
- Thomson, W. (1899). The age of the Earth as an abode fitted for life. *Journal of the Transactions of the Victoria Institute* 31, 11–38.
- Vasconcelos, P. M., Knesel, K. M., Cohen, B. E. & Heim, J. A. (2008). Geochronology of the Australian Cenozoic: a history of tectonic and igneous activity, weathering, erosion, and sedimentation. *Australian Journal of Earth Sciences* 55, 865–914.
- Wellman, P. (1974). Potassium-argon ages on the Cainozoic Volcanic rocks of Eastern Victoria, Australia. *Journal of the Geological Society of Australia* 21, 359–376.
- Wellman, P. & McDougall, I. (1974). Cainozoic igneous activity in eastern Australia. *Tectonophysics* 23, 49–65.

Woolley, A. R., Bergman, S. C., Edgar, A. D., Le Bas, M. J., Mitchell, R. H., Rock, N. M. S. & Scott-Smith, B. H. (1996). Classification of Lamprophyres, Lamproites, Kimberlites, and the Kalsilitic, Melilitic, and Leucitic rocks. *The Canadian Mineralogist* 34, 175–186.

## Chapter 2 Theoretical background of geochronology techniques used in this study.

### 2.1. $^{40}\text{Ar}/^{39}\text{Ar}$ geochronology.

#### 2.1.1. Fundamentals of K-Ar and $^{40}\text{Ar}/^{39}\text{Ar}$ dating

The  $^{40}\text{Ar}/^{39}\text{Ar}$  geochronology method (Merrihue and Turner, 1966) is an adaptation of the potassium-argon (K-Ar) dating method which was developed more than 50 years ago (McDougall and Harrison, 1999). K-Ar dating is based on the natural occurrence of  $^{40}\text{K}$  in minerals, which is a radioactive isotope with a half-life ( $t_{1/2}$ ) of 1253 Ma. This  $^{40}\text{K}$  isotope undergoes dual decay to both  $^{40}\text{Ca}$  and radiogenic  $^{40}\text{Ar}$  ( $^{40}\text{Ar}^*$ ; Figure 2.1). An ideal, simple rock, such as an undisturbed (unaltered) volcanic rock erupting at the Earth's surface and completely void of pre-existing magmatic  $^{40}\text{Ar}$  in its structure (degassed), will start to quantitatively accumulate radiogenic  $^{40}\text{Ar}$  after cooling. Measurement of the parent isotope  $^{40}\text{K}$  and daughter isotope  $^{40}\text{Ar}$ , combined with the known rate of radioactive decay hence allows the calculation of an age; which will reflect the time since cooling (eruption) of the rock (McDougall and Harrison, 1999). Other than radiogenic argon, non-radiogenic argon might be present in the sample and comprises:

1) Trapped argon; which is the argon incorporated within a rock or mineral at the time of its formation or during a subsequent event; if a rock or mineral is completely degassed and equilibrated with the atmosphere during formation, the trapped argon component has atmospheric composition. However, true trapped compositions

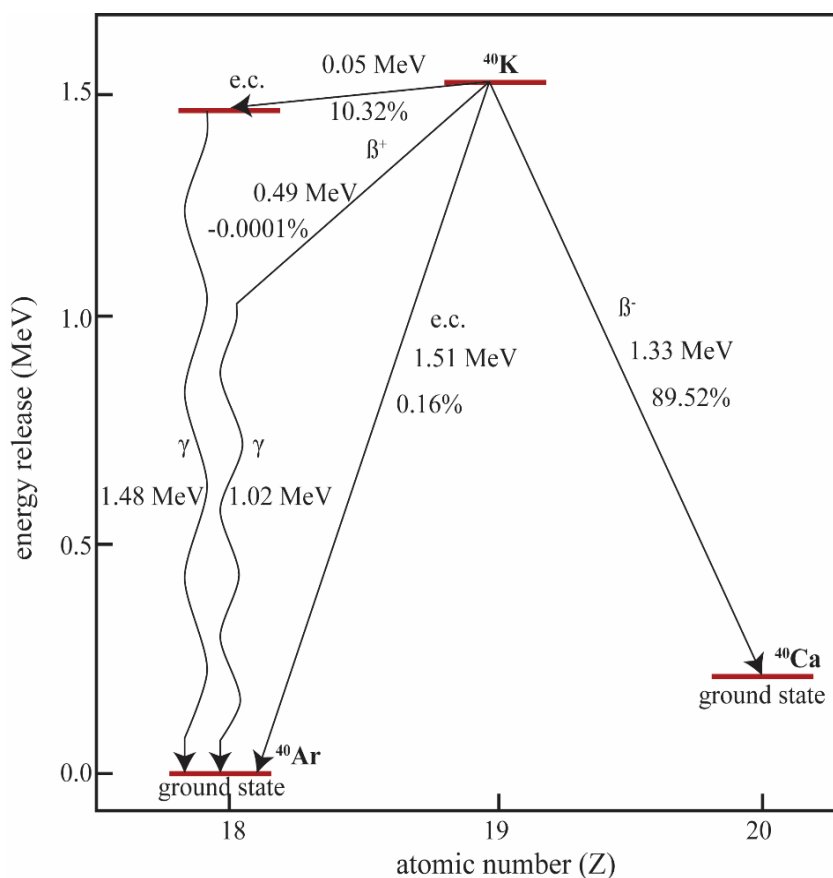


Figure 2.1 Energy states of the dual decay of potassium. After McDougall and Harrison (1999)

might differ from atmospheric composition, in which case the trapped argon might also include either excess argon or inherited argon from contamination.

2) Cosmogenic argon; which is argon produced from cosmic-ray interaction with target nuclei such as potassium, calcium, iron, titanium, nickel and chlorine by either spallation reactions or neutron capture; see Chapter 5.

3) Neutron-induced argon; which is argon derived from neutron interference reactions on chlorine, potassium and calcium during irradiation of a rock or mineral.

K-Ar measurements are laborious, as daughter isotope  $^{40}\text{Ar}$  is analysed via gas extraction and mass spectrometry, whereas parent isotope  $^{40}\text{K}$  is analysed via dissolution chemistry followed by mass spectrometry. This methodology requires a large amount of sample material for analysis ( $> 1$  g) and can potentially introduce large analytical errors. Most importantly, the K-Ar dating technique does not provide information on the potential of loss or addition of  $^{40}\text{Ar}$  to the mineral in case of an open system. Furthermore, the composition of trapped argon isotopes initially present in the mineral requires an assumption which cannot be verified.

The  $^{40}\text{Ar}/^{39}\text{Ar}$  geochronology method provides a solution to the challenges of the K-Ar dating method outlined above. Potassium has three naturally occurring isotopes;  $^{39}\text{K}$  ( $93.2581 \pm 0.0029$  %),  $^{40}\text{K}$  ( $0.001167 \pm 0.00004$  %) and  $^{41}\text{K}$  ( $6.7302 \pm 0.0029$  %) (Garner *et al.*, 1975). In both the K-Ar as well as the  $^{40}\text{Ar}/^{39}\text{Ar}$  dating technique, the underlying assumption is that the ratio between these isotopes remains constant in rocks and minerals (McDougall and Harrison, 1999). To enable  $^{40}\text{Ar}/^{39}\text{Ar}$  dating, a sample is exposed to a neutron flux in a reactor, which converts part of the  $^{39}\text{K}$  in the sample to  $^{39}\text{Ar}$ . The  $^{39}\text{Ar}$  isotope produced is considered a ‘proxy-parent’, as  $^{39}\text{Ar}$  is directly linked to  $^{40}\text{K}$  using the constant ratio of  $^{39}\text{K}$  and  $^{40}\text{K}$  in nature. The efficiency of the transformation in the reactor is measured by exposing a fluence monitor standard of known K-Ar age to the same neutron flux and comparing the  $^{40}\text{Ar}^*/^{39}\text{Ar}_\text{K}$  ratio of the sample with that of the fluence monitor standard. Calculation of the age can be obtained by using the standard age equation for radioactive decay:

$$t = \frac{1}{\lambda} \ln \left( 1 + J \frac{^{40}\text{Ar}^*}{^{39}\text{Ar}_\text{K}} \right) \quad (1)$$

Where  $\lambda$  is the decay constant (Renne *et al.*, 2010) and J is the irradiation parameter dependent on the duration of the irradiation, the neutron flux and the neutron capture cross section. The parameter J can be obtained by rearranging the age equation and irradiating a sample of known age:

$$J = \frac{(\exp\lambda t) - 1}{^{40}\text{Ar}^*/^{39}\text{Ar}_K} \quad (2)$$

Due to the ability of simultaneously measuring both parent and daughter isotope (as well as other argon isotopes:  $^{36}\text{Ar}$ ,  $^{37}\text{Ar}$  and  $^{38}\text{Ar}$ ), smaller sample sizes are required, the analytical error is much smaller and assumptions on initial argon isotopes trapped in the rock or mineral can be verified.

### 2.1.2. Neutron irradiation.

During irradiation in the nuclear reactor, incident particles react with the target nucleus to produce one or more other nuclei and potential other particles. For the conversion of  $^{39}\text{K}$  into ‘proxy-parent’  $^{39}\text{Ar}$ , the reaction is:



Where Q represents the energy released (McDougall and Harrison, 1999). Fast neutrons are required for this conversion; therefore, irradiation needs to take place in a nuclear reactor where fast-neutron fluxes in the  $10^{12} - 10^{14}$  n/cm<sup>2</sup>/s are available. We have used the Oregon State CLICIT TRIGA reactor for all our irradiations where samples are placed in the core of the reactor. This reactor is cadmium (Cd) shielded, as cadmium is used to eliminate slow neutrons that can produce unwanted neutron interferences.

However, fast neutrons can produce interfering isotopes of argon produced from reactions on calcium, potassium, argon and chlorine in the samples (Table 2.1). These reactor induced interferences are routinely corrected by application of interference corrections obtained from long-term exposure of K, Ca and Cl bearing salts and glasses in the specific reactor. We will quote the correction values applied in each relevant chapter.

Another effect that could influence the concentration of  $^{39}\text{Ar}$  generated during irradiation is nuclear recoil (Jourdan and Renne, 2014; Onstott *et al.*, 1995). Nuclear recoil is defined as the displacement of  $^{39}\text{Ar}_K$  from the original lattice site of the parental  $^{39}\text{K}$  during irradiation. Although it is generally assumed that  $^{39}\text{Ar}$  formed from  $^{39}\text{K}$  is distributed in the same manner as  $^{40}\text{K}$  in the sample, small differences are possible as  $^{39}\text{Ar}$  recoil distances are typically  $\sim 0.2\mu\text{m}$  (Renne *et al.*, 2005). This effect is particularly relevant for fine-grained or even glassy samples. The age spectra of such samples is often ‘saddle-shaped’, with high ages found in the early stages of gas release due to  $^{39}\text{Ar}_K$  recoil from grain boundaries and unrealistically low apparent ages in final stages of gas release (McDougall and Harrison, 1999).

Ar isotope produced	Target element			
	Calcium	Potassium	Argon	Chlorine
$^{36}\text{Ar}$	$^{40}\text{Ca}(n,n\alpha)^{36}\text{Ar}$ (-7.04, 96.94)			$^{35}\text{Cl}(n,\gamma)^{36}\text{Cl} \rightarrow ^{36}\text{Ar}$ (+8.58, 75.77)
$^{37}\text{Ar}$	$^{40}\text{Ca}(n,\alpha)^{37}\text{Ar}$ (+1.75, 96.94)	$^{39}\text{K}(n,nd)^{37}\text{Ar}$ (-15.99, 93.26)	$^{36}\text{Ar}(n,\gamma)^{37}\text{Ar}$ (+8.79, 0.337)	
$^{38}\text{Ar}$	$^{42}\text{Ca}(n,n\alpha)^{38}\text{Ar}$ (-6.25, 0.65)	$^{39}\text{K}(n,d)^{38}\text{Ar}$ (-4.16, 93.26) $^{41}\text{K}(n,\alpha)^{38}\text{Cl} \rightarrow ^{38}\text{Ar}$ (-0.12, 6.73)	$^{40}\text{Ar}(n,nd)^{38}\text{Cl} \rightarrow ^{38}\text{Ar}$ (-18.38, 99.60)	$^{37}\text{Cl}(n,\gamma)^{38}\text{Cl} \rightarrow ^{38}\text{Ar}$ (+6.11, 24.23)
$^{39}\text{Ar}$	$^{42}\text{Ca}(n,\alpha)^{39}\text{Ar}$ (+0.34, 0.65)	$^{39}\text{K}(n,p)^{39}\text{Ar}$ (+0.22, 93.26)	$^{38}\text{Ar}(n,\gamma)^{39}\text{Ar}$ (+6.60, 0.063)	
	$^{43}\text{Ca}(n,n\alpha)^{39}\text{Ar}$ (-7.59, 0.14)	$^{40}\text{K}(n,d)^{39}\text{Ar}$ (-5.36, 0.01167)	$^{40}\text{Ar}(n,d)^{39}\text{Cl} \rightarrow ^{39}\text{Ar}$ (-10.30, 99.60)	
$^{40}\text{Ar}$	$^{43}\text{Ca}(n,\alpha)^{40}\text{Ar}$ (+2.28, 0.14)	$^{40}\text{K}(n,p)^{40}\text{Ar}$ (+2.29, 0.01167)		
	$^{44}\text{Ca}(n,n\alpha)^{40}\text{Ar}$ (-8.85, 2.09)	$^{41}\text{K}(n,d)^{40}\text{Ar}$ (-5.58, 6.73)		

Table 2.1. Interference reactions producing argon during neutron irradiation.  $Q$  values (MeV) and target isotope abundance (atom%) are given in italics in the parentheses. The arrows represent  $\beta$ -decay in all cases. After McDougall and Harrison (1999).

### 2.1.3. Gas extraction

The analysis of irradiated samples offers another advantage; the sample can be step-heated and the relation of parent and daughter isotope as well as the K/Ca ratio of the sample can be closely monitored for each temperature increment. Here, higher temperatures reflect the release of gas from deeper within the sample. The West Australian Argon Isotope Facility, John de Laeter Centre, Curtin University (WAAIF) where all argon geochronology experiments in this thesis were performed, uses a 100 W Photon Machines Fusions 10.6 CO<sub>2</sub> laser to incrementally heat the samples. The gas extracted for each step is then purified using a series of getters in a custom-build extra low-volume (240 cc) stainless steel extraction line. Argon isotope analysis is performed with the multi-collector ARGUSVI mass spectrometer from ThermoFisher© operating in static mode.

Extracted and purified argon gasses are ionized using a Nier-type electron-bombardment ion source which forms positively charged ion beams of different mass/energy ratio. These ion beams are then accelerated and deflected based on mass using a sector magnet as the radius of the path described by ions of the same energy - but different mass to charge ratio - varies according to the square root of the mass to charge ratio in a magnetic field (McDougall and Harrison, 1999), which means the heavier isotopes have a larger path radius. As the ARGUSVI is a multi-collector mass spectrometer, the multiple paths of the various argon isotopes can be measured simultaneously. This mass spectrometer contains five Faraday detectors (typically used for  $^{40}\text{Ar}$ ,  $^{39}\text{Ar}$ ,  $^{38}\text{Ar}$  and  $^{37}\text{Ar}$  analysis) and a single ion counting compact discrete dynode (CDD; typically used for  $^{36}\text{Ar}$ ) which has an ion counting efficiency of  $> 80\%$ . For each gas extraction step, typically ten cycles of peak-hopping are used to determine the raw output data (in fA), with a typical integration time of 33s for each mass. After expansion in the ionization chamber, the isotope counts are recorded as a function of time, after which the trend resulting from the ten cycles are regressed to time zero. The data at time zero is then corrected for the baseline (instrument noise detected off-peaks), mass discrimination factor as well as instrumental backgrounds. The mass discrimination of each detector within the collector system is determined each day; the Faraday cups contain an internal electronic calibration to calibrate for slight offsets in the peak of each mass, whereas the CDD is calibrated each day for its actual yield using a series of air aliquots. The instrumental background is routinely measured every fourth sample (Chapter 4) or even more often (Chapter 5). Finally, the data is corrected for decay since time of irradiation, which is most significant for  $^{37}\text{Ar}$  ( $t_{1/2} = 35$  days) and  $^{39}\text{Ar}$  ( $t_{1/2} = 269$  y).

#### 2.1.4. Data regression and presentation

All raw data generated in this thesis has been exported and regressed using the ArArCalc algorithm (Koppers, 2002). Here, raw data is corrected for the relevant J-value and reactor dependent neutron interferences. ArArCalc calculates an apparent age for each temperature step, which can be plotted in an age spectrum diagram of cumulative  $^{39}\text{Ar}$  released (%) versus apparent age.

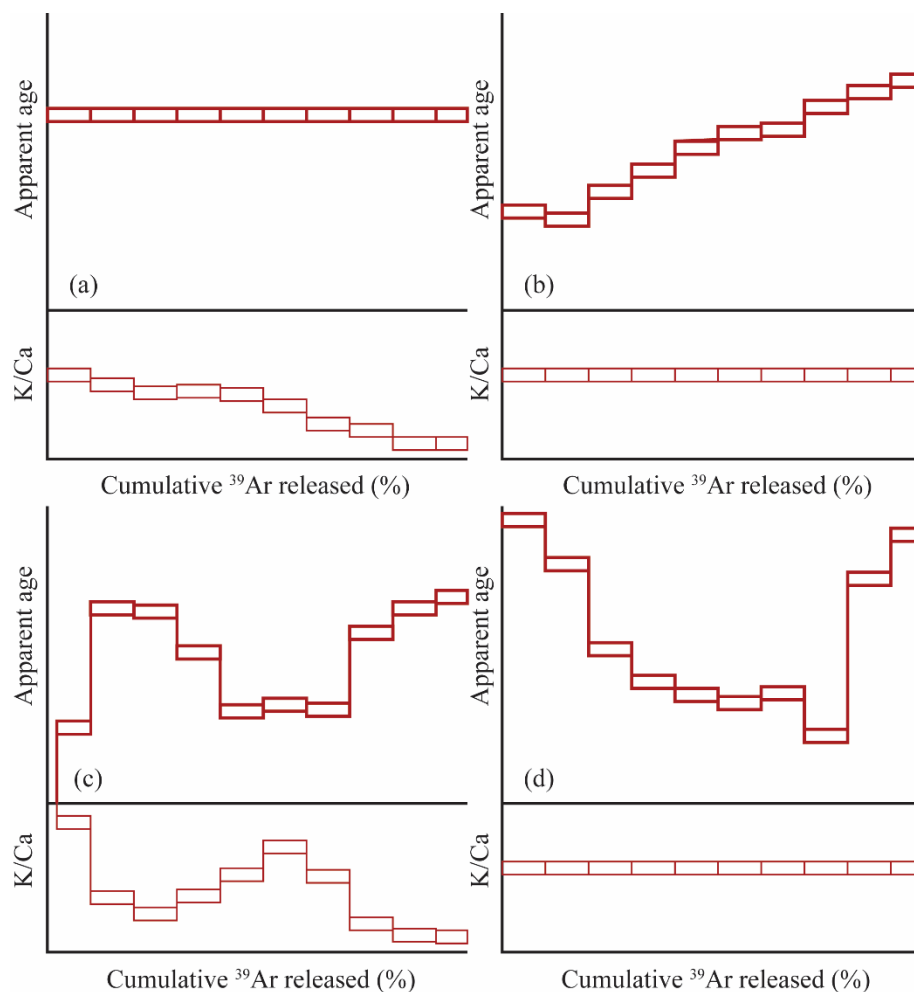


Figure 2.2. Potential apparent age plateaus and K/Ca spectra generated during step-heating for a) closed system; b) open system; c) sericite alteration and d) excess  $^{40}\text{Ar}$ .

Plateau ages are defined as including  $> 70\%$  of released  $^{39}\text{Ar}$  from at least 3 subsequent steps with  $^{40}\text{Ar}/^{39}\text{Ar}$  ratios within error of the  $2\sigma$  confidence level and satisfying a probability of fit (P) based on the  $\chi^2$  test distribution of at least 0.05 (Figure 2.2a; see for a description Jourdan et al., 2009).

When these criteria are not met, a sample is thought to have been extracted from an isotopically open system.  $^{40}\text{Ar}^*$  loss due to diffusion will cause a convex-shaped age spectrum (Figure 2.2b). A

tilde ( $\sim$ ) - shaped age spectrum (Figure 2.2c) with corresponding disturbed Ca/K ratios is present when plagioclase is altered to sericite (Verati and Jourdan, 2014) or when the sample has been affected by recoil effects (Jourdan *et al.*, 2009b). Excess or inherited  $^{40}\text{Ar}^*$  often results in a saddle-shaped (Figure 2.2d) age spectrum, where early and late degassing steps give anomalously high ages (Kelley, 2002). Excess argon is that component of  $^{40}\text{Ar}$  that is present in the sample other than trapped, atmospheric  $^{40}\text{Ar}$  and that present because of radioactive decay.

Another way of presenting the data obtained during step-heating is by using a three-isotope diagram, of which the inverse isochron ( $^{39}\text{Ar}/^{40}\text{Ar}$  versus  $^{36}\text{Ar}/^{40}\text{Ar}$ ; Figure 2.3) is the most useful (Roddick, 1978; Turner, 1971). Ideally, for a closed system, samples plotted in this diagram form a linear correlation, where the x-intercept corresponds to the pure radiogenic component of the sample and the y-intercept to the pure trapped (atmospheric + excess or initial) component of the sample (McDougall and Harrison, 1999). If no excess or initial  $^{40}\text{Ar}$  is present in the sample, the y-intercept



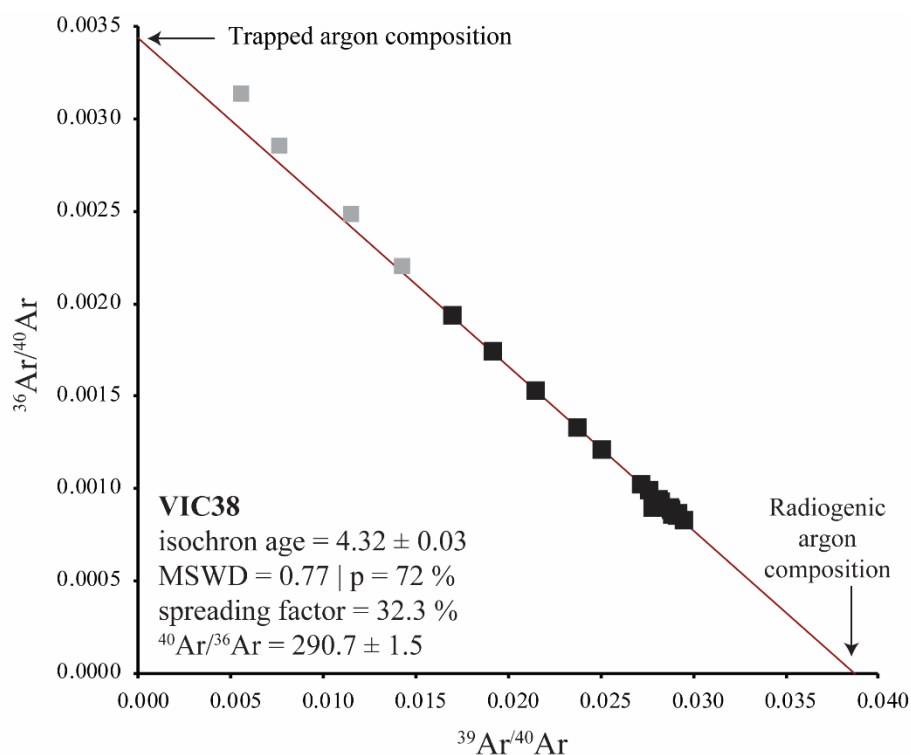


Figure 2.3. Example of an inverse isochron diagram for sample VIC38 (see also Chapter 4).

should correspond to the atmospheric  $^{40}\text{Ar}/^{36}\text{Ar}$  ratio determined to be  $298.56 \pm 0.31$  (Lee *et al.*, 2006). Therefore, use of the inverse isochron will provide an independent evaluation of the composition of trapped  $^{40}\text{Ar}$  in the sample, for which  $^{40}\text{Ar}/^{39}\text{Ar}$  age corrected. The age calculated from an inverse isochron diagram, unlike that calculated from the age spectra, is not affected by trapped argon

$^{40}\text{Ar}/^{36}\text{Ar}$  ratios that are different from the atmospheric ratio and may thus contribute to a better age interpretation (Kuiper, 2002). We will provide an example of the impact of using inverse isochron y-intercept values to correct plateau ages to obtain a more meaningful result in Chapter 4.

#### 2.1.5. Applicability of the $^{40}\text{Ar}/^{39}\text{Ar}$ geochronology technique

Any rock or mineral can be dated with the  $^{40}\text{Ar}/^{39}\text{Ar}$  geochronology technique given that potassium contents are sufficiently high (or the rock is sufficiently old) so that radiogenic argon can be detected within the limits of the currently available instrumentation. The technique has been successfully applied on both extra-terrestrial samples (e.g. Cohen *et al.*, 2001; Turner, 1971) and terrestrial rocks and minerals; from dating impact structures: e.g. Jourdan *et al.*, 2009b, to archeological applications: e.g. Morgan *et al.*, 2009. Ideally, minerals are used that retain argon in their lattice sites, as it is most likely that these minerals have retained their radiogenic argon quantitatively at temperatures experienced in the geological environment. However, experiments on dating retentive, K-poor minerals such as pyroxene are currently being undertaken (Ware *et al.*, 2015). Naturally, it is important to consider the resulting ages derived from  $^{40}\text{Ar}/^{39}\text{Ar}$  in their wider geological context, of which we will give an example in Chapter 4.

2.2. Cosmogenic <sup>38</sup>Ar geochronology

2.2.1. Fundamentals of cosmogenic exposure dating

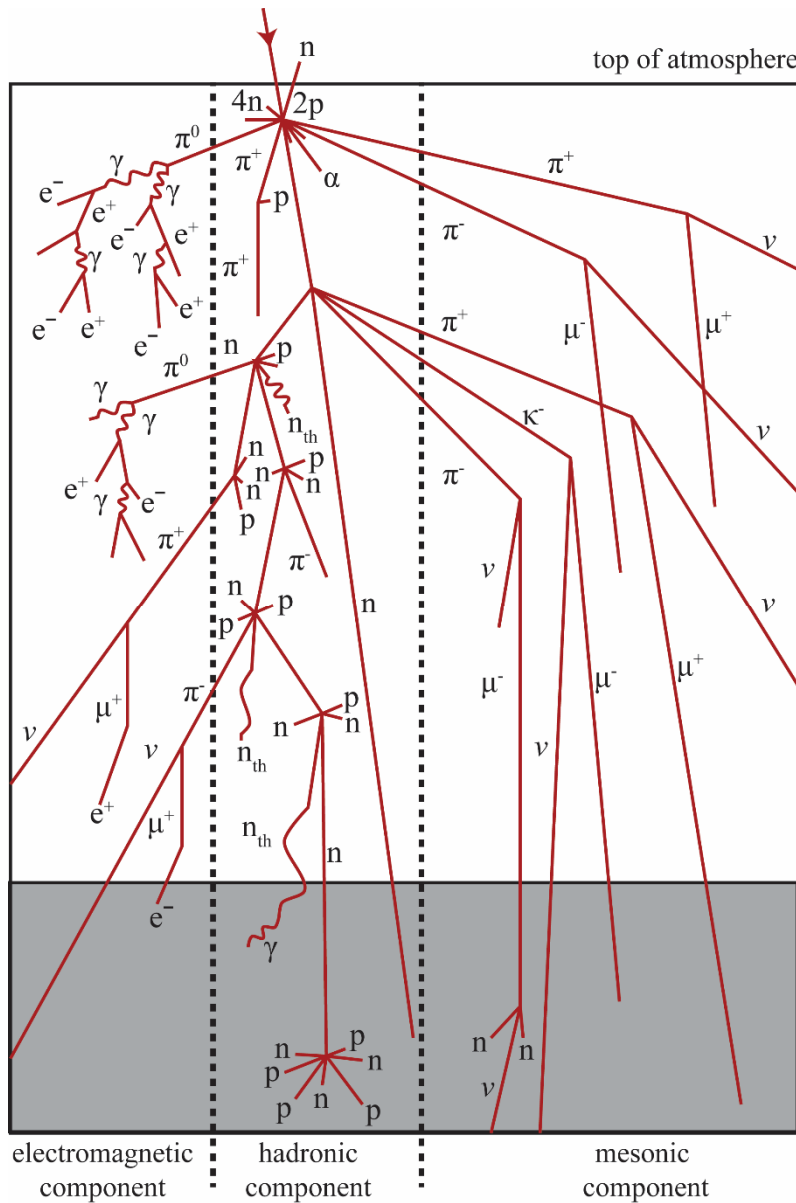


Figure 2.4. Cascade of secondary particle production resulting from the interaction of GCR with particles in the Earth’s atmosphere. e<sup>-</sup> = electron; e<sup>+</sup> = positron; γ = gamma ray or photon; ν = neutrino; μ = muon; n = neutron; p = proton; κ = kaon. After (Gosse and Phillips, 2001).

Cosmic rays are originating from the galactic cosmic radiation (GCR) which contains high energy (~1 GeV to ~ 10<sup>10</sup> GeV) nucleons which have sufficient energy to interact with nuclei in the top layers of the Earth’s atmosphere (see for a review of terrestrial cosmogenic exposure dating; Dunai, 2010; Gosse and Phillips, 2001; Niedermann, 2002). Following deflection due to the Earth’s geomagnetic field, particles enter the atmosphere and cascade down as secondary radiation, which comprises an electromagnetic (electrons) component, a hadronic (neutrons and protons) component and a mesonic (muons) component (Lal and Peters, 1967; Figure 2.4). In turn, these nuclei will interact with target elements in a rock or mineral, where production is based on the type of cosmic ray particles involved, the nuclear cross section σ (energy dependent probability for a given particle interaction to occur),

the flux (φ) of particles with a given energy (E) and the density (N) of target atoms (Knight, 2006). Production decreases with depth (the attenuation depth Λ) according to the relation:

$$P(z) = P(0) * e^{-\frac{\rho z}{\Lambda}} \tag{1}$$

Where ρ is the density of a rock and z is the depth.

The intensity of the cosmic rays entering the Earth's atmosphere is not isotropic as in space, and production rates vary both temporally and spatially. Temporal variations occur predominantly due to variations in the primary GCR flux and variations due to solar modulation, whereas spatial differences in the production rates are caused by the effects of the geomagnetic field and variations in atmospheric shielding (Gosse and Phillips, 2001). Disagreement between potassium exposure ages and  $^{36}\text{Cl}$ - $^{36}\text{Ar}$ ,  $^{10}\text{Be}$ - $^{21}\text{Ne}$  and  $^{26}\text{Al}$ - $^{21}\text{Ne}$  exposure age pairs on iron meteorites, led to the conclusion that the primary GCR flux of the last 10 Ma is approximately 28% higher than the average value (Lavielle et al., 1999). Some explanations of this temporal variation include a change in the galactic cosmic ray intensity, movement of the Earth through different interstellar fluxes or the effect of short-term shock waves from nearby supernovae (Gosse and Phillips, 2001). The 11-year and 27-year variations in sun spot activity (solar modulation) have an effect on the primary GCR flux, as this flux is partly deflected by the interplanetary magnetic field, which is generated by the sun and transported by the solar wind (Ahluwalia, 2003). Empirical measurements show that the primary GCR flux (and thus also the resulting secondary flux) at low latitudes comprises higher energy particles than the flux at high latitudes, as the geomagnetic cut-off rigidity (the minimum rigidity - or momentum of a particle per charge – required of an approaching particle of a given charge to penetrate the magnetic field and interact with the upper atmosphere) is strongly latitude-dependent. Below latitude  $58^\circ$ , changes in the geomagnetic dipole moment may result in significant changes in the GCR flux to a site at a given time. The changes in the geomagnetic dipole moment might result from 1) paleo-intensity variations of the geomagnetic field, 2) the effects of reversals and excursions and 3) secular variations in the Earth's dipole axis position ('polar wander'). Lastly, changes in the effective atmospheric depth can also impact the temporal variation in particle fluxes. For example; tectonic uplift of a sample over time will place the sample at decreasing atmospheric depths (Brook et al., 1995). It is also thought that the changing atmospheric thickness and characteristics due to climate change might play a role (Carslaw et al., 2002).

Relevant production rates are challenging to obtain due to the difficulties outlined above. Estimates of production rates for a given isotopic system might be determined 1) experimentally, by laboratory experiments of exposure of slabs of known composition, 2) geologically, by measuring the cosmogenic isotope concentration of a sample with a simple exposure history [see Chapter 5]; and 3) numerically, by computed simulation of potential interactions (e.g. Dep et al., 1994; Masarik and Beer, 1999, 2009; Masarik and Reedy, 1995; Masarik et al., 1986). Once determined or calculated, production rates are given to the reference condition of a horizontal surface on a flat plain at high

latitude ( $> 70^\circ$ ) at sea level. All samples obtained from other latitudes and altitudes yielding production rates or used in the calculation of exposure ages must be scaled to this reference condition. Scaling factors include: 1) spatial shielding accounting for the altitude and latitude dependence of the secondary nuclear flux (Dunai, 2000; Lal, 1991); 2) topographic shielding where a sloping surface might partially obstruct incoming particles from the secondary flux; 3) surface covering where snow, soil and/or vegetation can obstruct the incoming secondary particle flux and lastly 4) sample thickness (Gosse and Phillips, 2001; Niedermann, 2002). Thus, the concentration of cosmogenic nuclide  $N_m$  dependent on time, is:

$$\frac{dN_m}{dt} = P_{t,m}(Z) - \lambda_m N_m \quad (2)$$

Where  $P$  is the production rate at depth ( $Z$ ) and  $\lambda_m$  is the decay constant for nuclide  $m$  ( $1/y$ ).

Following this; the concentration of cosmogenic nuclide  $N_m$  as a function of depth ( $Z$ ), time ( $t$ ) and erosion ( $\epsilon$ ) is:

$$N_m(Z, t, \epsilon) = S_{el} S_T S_s \sum_q \frac{J_q}{\epsilon / (AL)_q + \lambda_m} \left[ \exp\left(-\frac{Z_0 - \epsilon t}{(AL)_q}\right) - \exp\left(-\lambda_m t - \frac{Z_0}{(AL)_q}\right) \right] \quad (3)$$

Where  $S_{el}$ ,  $S_T$  and  $S_s$  are scaling factors concerned with elevation and latitude, shielding by topography and shielding by cover;  $J_q$  is the production rate coefficient (atoms/g target element/y) and  $(AL)_q$  the attenuation length (Gosse and Phillips, 2001). In this research, we have performed strategic sampling, where samples were selected based on their chemical composition and location to greatly simplify the equation above. We have targeted spallation-dominated reactions, where the resulting nuclides are stable ( $^{38}\text{Ar}$ ), from top surfaces on which the erosion rate can be considered negligible (Chapter 5). The equation above thus becomes linear with time ( $t$ ):

$$N_{m,s}(t) = S_{el} Q_s P_{m,s} t \quad (4)$$

Where  $Q_s$  is the ratio of the production rate integrated over the thickness of a sample to the surface production rate, from spallogenic reactions only (Gosse and Phillips, 2001). Note that we assume that for our samples, scaling based on topography and cover is assumed to be negligible.

### 2.2.2. Cosmogenic $^{38}\text{Ar}$ and the ‘cosmochron diagram’

Cosmogenic  $^{38}\text{Ar}$  ( $^{38}\text{Ar}_{\text{cos}}$ ) is predominantly produced from spallation reactions on potassium [ $^{39}\text{K}(n,pn)^{38}\text{Ar}$ ], calcium [ $^{40}\text{Ca}(n,2pn)^{38}\text{Ar}$ ] and iron [ $^{56}\text{Fe}(n,8p11n)^{38}\text{Ar}$ ] as well as from negative muon capture reactions on potassium [ $^{39}\text{K}(\mu^-,n)^{38}\text{Ar}$ ] and calcium [ $^{40}\text{Ca}(\mu^-,pn)^{38}\text{Ar}$ ], all of which are elements found in major rock-forming minerals. Reactions on titanium and nickel are considered

minor (Niedermann, 2002). Although widely applied in extra-terrestrial studies (e.g. Levine et al., 2007; Turner et al., 1971), application of this system to terrestrial samples has been hampered by the high concentration of  $^{38}\text{Ar}$  in the atmosphere ( $\sim 6$  ppm), which can be present as trapped argon within a sample. In theory, data can be corrected for this trapped component by correcting to the uniform non-cosmogenic terrestrial (UNCT) composition of  $^{38}\text{Ar}/^{36}\text{Ar}$  of  $0.18826 \pm 0.00018$  (Renne et al., 2001). However, resolving  $^{38}\text{Ar}$  from  $^{36}\text{Ar}$  is complex due to 1) cosmogenic production of  $^{36}\text{Ar}$  and 2) time dependent  $^{36}\text{Ar}$  production due to  $\beta^-$  decay of  $^{36}\text{Cl}$  with a half-life ( $t_{1/2}$ ) of  $\sim 3 \times 10^5$  y. This has resulted in the absence of any published studies which perform exposure age dating based on  $^{38}\text{Ar}_{\text{cos}}$ .

In this study, the neutron irradiation technique has been applied (Merrihue and Turner, 1966; Turner et al., 1971) to better understand degassing behaviour of minerals with respect to  $^{38}\text{Ar}$  and  $^{36}\text{Ar}$ , as well as to investigate the potential of deriving statistically significant exposure ages based on cosmogenic  $^{38}\text{Ar}$ . During neutron irradiation, parental isotope  $^{40}\text{Ca}$  is converted into  $^{37}\text{Ar}$  via;

$^{40}\text{Ca}(n,\alpha)^{37}\text{Ar}$  ( $t_{1/2} = 35$  days). Due to this very short half-life, it is expected that no  $^{37}\text{Ar}$  is initially present in the sample and that the  $^{37}\text{Ar}$  can be used as a proxy for the parent isotope concentration, given that the reaction efficiency is determined by co-irradiating a standard sample of known age (flux monitor). As this allows for simultaneous release of both parent and daughter isotope, gas extraction of neutron irradiated samples can be performed with step-heating, which provides a wealth of information about the degassing behaviour of a sample. Resulting data can be plotted in a ‘cosmochron diagram’ (Figure 2.5; Levine et al., 2007), which displays the mixing line between the atmospheric (y-intercept) and the cosmogenic (x-intercept) component of the argon released as a function of  $^{37}\text{Ar}$ . The slope of the mixing line is a function of  $^{38}\text{Ar}/^{37}\text{Ar}$  (and thus  $^{38}\text{Ar}/^{40}\text{Ca}$  by proxy), whereas the value of the y-intercept provides an independent measure of the assumed composition of

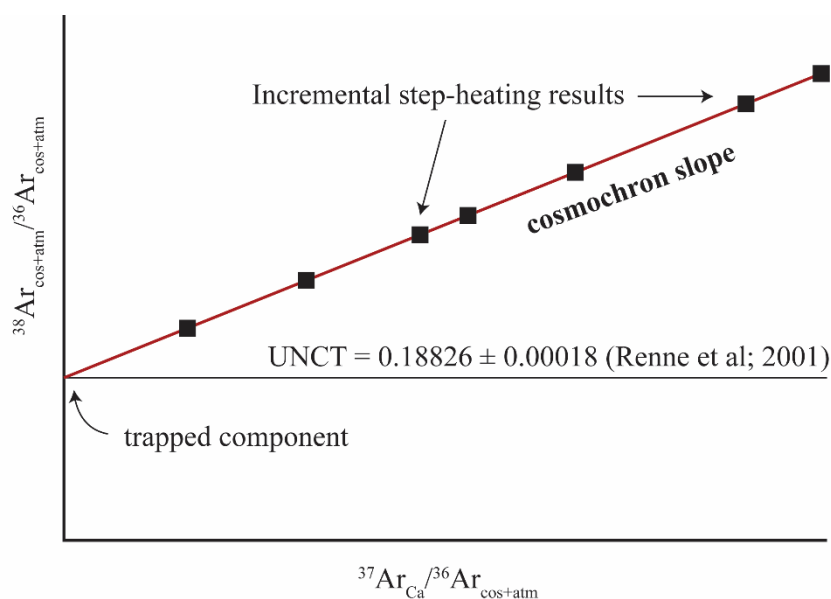


Figure 2.5. Typical cosmochron diagram. See text for discussion of main components.

atmospheric  $^{38}\text{Ar}/^{36}\text{Ar}$  present in the sample. Deviations of this ratio from the UNCT of  $0.18826 \pm 0.00018$  (Renne et al., 2001) implies complexity of the sample which can then be accounted for. Combination of the slope, the production rate  $P(^{38}\text{Ar}/^{36}\text{Ar})_{\text{cos}}$  and the true value of the atmospheric  $^{38}\text{Ar}/^{36}\text{Ar}$  composition allows calculation of the exposure age of the sample in which the true errors of both the analysis, and the uncertainties associated with the production rate and the atmospheric ratio can be fully propagated. The production rate for the  $^{40}\text{Ca}(n, 2p)^{38}\text{Ar}$  reaction is still widely debated. Theoretical estimates based on the cross-sections of the spallation reaction yielded a production rate of  $\sim 200$  atoms/g Ca/y at high latitudes ( $> 70^\circ$ ) and sea-level (Lal, 1991). Experimental data using a variety of minerals yielded a much higher ratio of  $\sim 300$  atoms/g Ca/y (Knight, 2006), however, errors on this rate are estimated to be 50%. Recent experimental work on pyroxene from Antarctic Ferrar dolerite yielded production rates ranging from  $191 \pm 21$  atoms/g Ca/y to  $254 \pm 28$  atoms/g Ca/y (Niedermann et al., 2007).

### 2.2.3. Applicability of the cosmogenic $^{38}\text{Ar}$ geochronology technique

Applications of terrestrial cosmogenic exposure dating using other isotope systems have included (but are not limited to); reconstruction of Quaternary ice volumes; dating of volcanic events; providing time controls on palaeoseismic events; determination of surface uplift rates, erosion and incision rates; dating meteorite impacts and the determination of rates of landscape and soil evolution (Gosse and Phillips, 2001 and references therein).

$^{38}\text{Ar}_{\text{cos}}$  exposure dating offers some advantages over existing cosmogenic exposure dating techniques. As  $^{38}\text{Ar}$  is a stable isotope, this dating technique offers a larger time range of applicability as compared to the short-lived isotope systems such as  $^{10}\text{Be}$ ,  $^{26}\text{Al}$  and  $^{36}\text{Cl}$  (Renne et al., 2001). Furthermore, as  $^{38}\text{Ar}_{\text{cos}}$  exposure dating is performed on Ca-rich or K-rich rocks, elements comprised in many major rock-forming minerals, potential applications could be; determination of erosion rates on carbonate rocks, fault exposure dating by means of dating Ca-rich veins, constraining the timing of tsunami's by dating exposed  $\text{CaCO}_3$  on oceanic rocks deposited on land, and exposure dating of fresh volcanic pyroxenes in otherwise altered surrounding rock. Naturally, the largest advantage of  $^{38}\text{Ar}_{\text{cos}}$  exposure dating is the potential of irradiating the sample and obtaining independent information about the accuracy and precision and well as the statistical meaning of the exposure age derived.

### 2.3. (U-Th)/He dating

(U-Th)/He dating has received renewed attention for two main reasons; 1) it could prove a viable alternative to other dating techniques, as the instrument sensitivity for U, Th and He is high, and 2) when applied to various minerals of a geological system, it could provide information on the cooling

history of this system, due to different rates of diffusive He loss from individual minerals (Farley, 2002). Due to its omnipresence in many rocks as well as its retentive behaviour for helium, olivine is a suitable candidate for (U-Th)/He dating applications. However, published work on this subject is extremely limited with two published studies only (Aciego et al., 2003, 2010), which used an expansive instrumental methodology on very young rocks (Aciego et al., 2007); yielding results that are not always concordant with existing  $^{40}\text{Ar}/^{39}\text{Ar}$  ages and thus hard to interpret (Aciego et al., 2010).

### 2.3.1. Fundamentals of (U-Th)/He dating

Radiogenic  $^4\text{He}$  ( $\alpha$  particles) are produced by radioactive decay of  $^{238}\text{U}$ ,  $^{235}\text{U}$ ,  $^{232}\text{Th}$  as well as from  $^{147}\text{Sm}$ , the latter contribution usually negligible. The ingrowth equation for the generation of  $^4\text{He}$  over time (t) is:

$$^4\text{He} = 8 * ^{238}\text{U}(e^{\lambda_{238}t} - 1) + 7 * \left(\frac{^{238}\text{U}}{137.88}\right)(e^{\lambda_{235}t} - 1) + 6 * ^{232}\text{Th}(e^{\lambda_{232}t} - 1) \quad (5)$$

Where uranium, thorium and helium are the present-day concentrations, the coefficients represent the number of  $\alpha$  particles released by each decay step,  $\lambda$  is the decay constant ( $\lambda_{238} = 1.551 \times 10^{-10} \text{ yr}^{-1}$ ,  $\lambda_{235} = 9.849 \times 10^{-10} \text{ yr}^{-1}$ ,  $\lambda_{232} = 4.948 \times 10^{-11} \text{ yr}^{-1}$ ) and the value of 1/137.88 represents the present-day  $^{235}\text{U}/^{238}\text{U}$  ratio (Mamyrin and Tolstikhin, 1984). To calculate a meaningful age using this equation, there are several assumptions to bear in mind; 1) initial  $^4\text{He}$  is absent from the sample, 2) the sample is in secular equilibrium with respect to the daughters in the decay chain; 3) information about the retentive qualities for helium of the mineral being dated is known.

For volcanic phenocrysts of interest to this study (Chapter 6), assumption 1 is often invalid. At the time of eruption, phenocrysts will have  $^3\text{He}$  and  $^4\text{He}$  from magmatic sources and atmospheric sources; often present in fluid-inclusions. During cooling, nucleogenic  $^3\text{He}$  produced by Li ( $^6\text{Li}(n,\alpha)^3\text{H}$  followed by  $^3\text{H}^{\beta^-} \rightarrow ^3\text{He}$ ; Mamyrin and Tolstikhin, 1984) as well as radiogenic  $^4\text{He}$  generated via the reaction above starts to form in situ in the phenocryst. Furthermore, if the phenocryst is within 1 meter of the Earth's surface, there will be a combined in situ production of both cosmogenic and radiogenic/nucleogenic  $^3\text{He}$  and  $^4\text{He}$ . A common approach to resolve the various helium components is to crush the sample in vacuo and determine the subsequently released  $^4\text{He}$  concentrations and  $^3\text{He}/^4\text{He}$  ratios, followed by heating of the sample to release radiogenic/nucleogenic  $^3\text{He}$  and  $^4\text{He}$ , cosmogenic  $^3\text{He}$  and  $^4\text{He}$  as well as residual atmospheric or magmatic  $^3\text{He}$  and  $^4\text{He}$  (Aciego et al., 2007). It has been shown that in vacuo crushing of olivine and pyroxene phenocrysts quantitatively retains the cosmogenic and nucleogenic/radiogenic  $^3\text{He}$  and  $^4\text{He}$ , given that the size fraction is  $> 10 \mu\text{m}$  and temperature during crushing is kept to a minimum ( $< 300^\circ\text{C}$ ; Blard et al., 2008). Thus, during

high temperature gas extraction of a sample, it is assumed that  ${}^4\text{He}_{\text{rad}} = {}^4\text{He}_{\text{tot}} - {}^4\text{He}_{\text{cos}} - {}^4\text{He}_{\text{res}}$ , where  ${}^4\text{He}_{\text{rad}}$  is the radiogenic helium produced from decay of uranium and thorium,  ${}^4\text{He}_{\text{tot}}$  is the total fraction of  ${}^4\text{He}$  released during gas extraction,  ${}^4\text{He}_{\text{cos}}$  is helium from cosmogenic sources and  ${}^4\text{He}_{\text{res}}$  is residual  ${}^4\text{He}$  from atmospheric or magmatic sources not released during in vacuo crushing. Strategic sampling, where samples are obtained from deeper levels below the Earth's surface is the easiest way to avoid the cosmogenic contribution of  ${}^4\text{He}$ . Otherwise, the production rate of  ${}^4\text{He}$  from cosmic rays (60 atoms/g target element/y; Lal, 1991) is  $\sim 3$  orders of magnitude lower than the  ${}^4\text{He}_{\text{rad}}$  production rate (Aciego et al., 2007) and can thus safely be neglected for surface samples, given that the sample is sufficiently old. Ignoring the presence of residual  ${}^3\text{He}$  and  ${}^4\text{He}$  from atmospheric and/or magmatic sources resulting from undercrushing of the sample will result in overestimated ages. Crushed samples can be analysed and corrected for the presence of  ${}^4\text{He}_{\text{res}}$  by incorporating a low temperature ( $300^\circ\text{C}$ ) gas extraction step, where any gas released which will represent  ${}^4\text{He}_{\text{res}}$  derived from fluid inclusions.

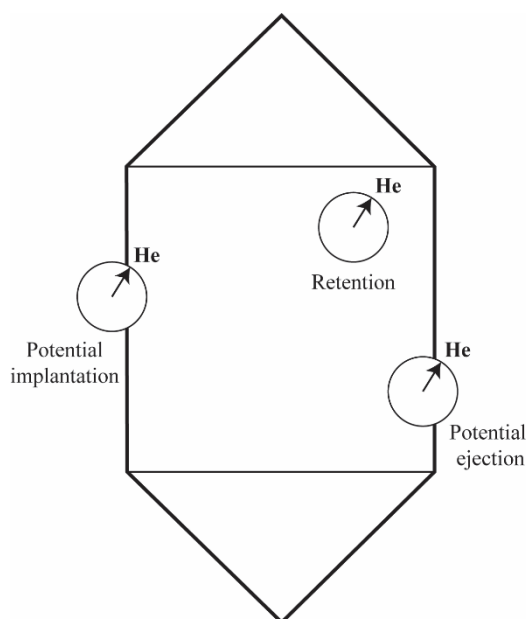


Figure 2.6. The effect of long  $\alpha$ -stopping distances on helium retention. After (Farley, 2002).

The  $\alpha$  particles generated by decay of uranium and thorium are sufficiently energetic that they can travel up to  $20\ \mu\text{m}$ , which results in a potential spatial offset between the parent and daughter isotopes. Such inconsistencies are of major concern at the grain boundary (Figure 2.6), as potential  $\alpha$ -implantation or  $\alpha$ -ejection can occur, resulting in overestimated or underestimated ages respectively. This effect can be corrected for, either using a quantitative model to calculate the correction factor ( $F_t$ ) based on the grain size and geometry (Farley et al., 1996), or by physically abrading the outer  $20\ \mu\text{m}$  of the sample (Min et al., 2006). These latter authors have shown that physical removal of the outer  $20\ \mu\text{m}$  of sufficiently large grains corresponds to an alpha-implantation correction factor  $F_t$

(Farley et al., 1996) approaching unity.

As the (U-Th)/He system is based on decay of multiple long-lived parents, and  $\alpha$  particles are emitted throughout the decay series and not just by the final daughter; the issue of secular disequilibrium arises for young samples ( $< \sim 1\ \text{Ma}$ ; Beattie, 1993; Farley et al., 2002). Here, intermediate daughter nuclides in the actinide decay chain may become fractionated from each other, which yield largely



overestimated or underestimated ages, depending on the initial isotopic activity ratio. The effect is strongest for intermediate daughter isotope  $^{230}\text{Th}$  ( $t_{1/2} = \sim 75$  ka). Naturally, long magma residence times largely obliterate the effects of secular disequilibrium. To gain insight into potential secular disequilibrium of a system as well as estimate magma residence times, it is often recommended to co-analyse multiple minerals from a single geological system (Farley et al., 2002). As the samples discussed in Chapter 6 are  $\gg 1$  Ma, we do not need to correct for secular disequilibrium, which can introduce errors up to 50% of final (U-Th)/He ages.

It has been shown that helium is quantitatively retained within the olivine and pyroxene mineral structure at surface temperatures (Aciego et al., 2003, 2007; Niedermann, 2002). However, slowly cooled samples might have undergone helium diffusion. Diffusivity is usually expressed by the Arrhenius relationship:

$$\frac{D}{a^2} = \frac{D_0}{a^2} e^{-E_a/RT} \quad (6)$$

Where  $D$  is the diffusivity,  $D_0$  is the diffusivity at infinite temperature,  $a$  is the diffusion domain radius,  $E_a$  is the activation energy (kcal/mole),  $R$  is the gas constant and  $T$  the temperature in Kelvin. For a single diffusion domain, measurements of  $\ln(D/a^2)$  as a function of  $1/T$  will plot on a straight line, with the slope  $-E_a/R$  and intercept  $\ln(D_0/a^2)$ . For olivine at low temperatures ( $150^\circ\text{C} - 600^\circ\text{C}$ ) it has been shown that helium diffusion obeys this Arrhenius relationship, with very low diffusivities at environmental temperatures around  $1 \times 10^{-22}$  cm<sup>2</sup>/s ( $E_a = 25 \pm 4$  kcal/mole; Trull et al., 1991). At mantle temperatures ( $\sim 1200^\circ\text{C} - 1350^\circ\text{C}$ ), diffusion of helium in olivine is relatively fast at  $2.2 \times 10^{-8}$  cm/s ( $E_a = 120 \pm 30$  kcal/mole; Hart, 1984) to  $5.3 \times 10^{-9}$  cm<sup>2</sup>/s ( $E_a = 100 \pm 4.8$  kcal/mole; Trull and Kurz, 1993), which suggest that phenocrysts are readily degassed from any magmatic helium. However, the presence of trapped magmatic helium in samples (e.g. Aciego et al., 2003, 2007), released during in vacuo crushing, suggests that some

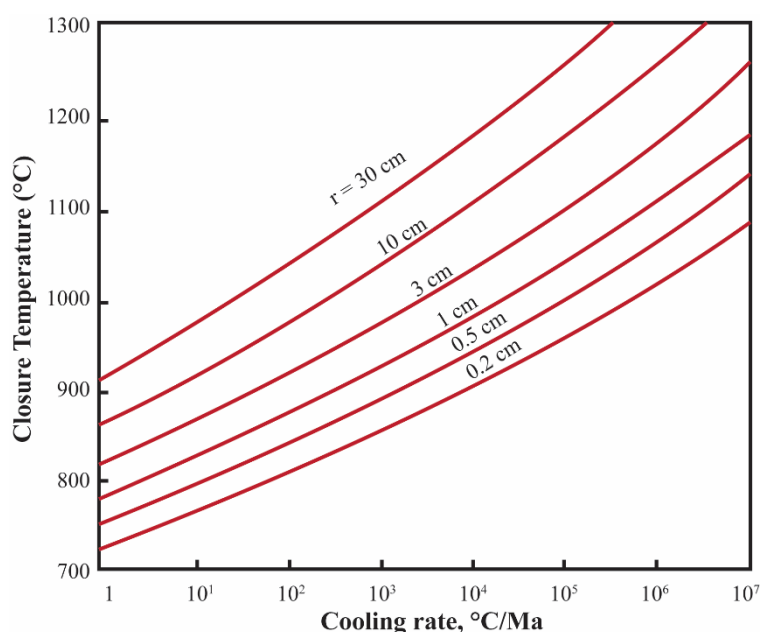


Figure 2.7. Closure temperature as a function of cooling rate for spherical bodies of varying radius ( $r$ ). After (Hart, 1984)

diffusion of helium in olivine is relatively fast at  $2.2 \times 10^{-8}$  cm/s ( $E_a = 120 \pm 30$  kcal/mole; Hart, 1984) to  $5.3 \times 10^{-9}$  cm<sup>2</sup>/s ( $E_a = 100 \pm 4.8$  kcal/mole; Trull and Kurz, 1993), which suggest that phenocrysts are readily degassed from any magmatic helium. However, the presence of trapped magmatic helium in samples (e.g. Aciego et al., 2003, 2007), released during in vacuo crushing, suggests that some

magmatic helium is retained in phenocrysts forming at magmatic temperatures. Based on the diffusion parameters above, Hart (1984) constructed a diagram of cooling rate ( $^{\circ}\text{C}/\text{Ma}$ ) versus closure temperature ( $^{\circ}\text{C}$ ) for a suite of differently sized spherical bodies (Figure 2.7). For the grain sizes used in this study ( $\sim 300\ \mu\text{m}$ ) and the expected fast cooling rate of  $10^7\ ^{\circ}\text{C}/\text{Ma}$  for a small ( $\sim 50\ \text{m}$ ) intrusion (see Chapter 6), the closing temperature for helium in olivine is about  $1000 - 1100\ ^{\circ}\text{C}$ . It is shown that  $\text{CO}_2$ -rich and  $\text{H}_2\text{O}$ -rich peridotite melts (characteristics of lamproites – the host rock of interest of this study; Chapter 6 and Section 1.1.2) have solidus temperatures below  $1000\ ^{\circ}\text{C}$  between 20 – 30 GPa (Foley et al., 2009), which implies that trapped magmatic helium will be retained in olivine phenocrysts during formation of such rocks.

### 2.3.2. Applicability of basalt (U-Th)/He dating

Based on helium retention experiments (Hart, 1984; Trull *et al.*, 1991; Trull and Kurz, 1993); the most promising minerals for (U-Th)/He dating in basalts are clinopyroxene and olivine (Aciego *et al.*, 2007). Clinopyroxene should have higher uranium and thorium concentrations, but the effect of its mineral structure on diffusivity are not yet fully understood (Lippolt and Weigel, 1988). Therefore, olivine might be the most straightforward candidate to date basaltic rocks with low potassium abundances; submarine basalts in which K-rich phases will be severely altered; samples containing inherited Ar; or samples that have been incompletely degassed.

## 2.4. References

- Aciego, S., Kennedy, B. M., DePaolo, D. J., Christensen, J. N. & Hutcheon, I. (2003). U-Th/He age of phenocrystic garnet from the 79 AD eruption of Mt. Vesuvius. *Earth and Planetary Science Letters* 216, 209–219.
- Aciego, S. M., DePaolo, D. J., Kennedy, B. M., Lamb, M. P., Sims, K. W. W. & Dietrich, W. E. (2007). Combining [3He] cosmogenic dating with U–Th/He eruption ages using olivine in basalt. *Earth and Planetary Science Letters* 254, 288–302.
- Aciego, S. M., Jourdan, F., DePaolo, D. J., Kennedy, B. M., Renne, P. R. & Sims, K. W. W. (2010). Combined U–Th/He and  $^{40}\text{Ar}/^{39}\text{Ar}$  geochronology of post-shield lavas from the Mauna Kea and Kohala volcanoes, Hawaii. *Geochimica et Cosmochimica Acta*. Elsevier Ltd 74, 1620–1635.
- Ahluwalia, H. S. (2003). Solar wind modulation of galactic cosmic rays. *Geophysical Research Letters* 30, 1133.
- Beattie, P. (1993). The generation of uranium series disequilibria by partial melting of spinel peridotite: constraints from partitioning studies. *Earth and Planetary Science Letters* 117, 379–391.
- Blard, P.-H., Puchol, N. & Farley, K. A. (2008). Constraints on the loss of matrix-sited helium during vacuum crushing of mafic phenocrysts. *Geochimica et Cosmochimica Acta* 72, 3788–3803.

- Brook, E. J., Brown, E. T., Kurz, M. D., Ackert Jr, R. P., Raisbeck, G. M. & Yiou, F. (1995). Constraints on Age, Erosion, and Uplift of Neogene Glacial Deposits in the Transantarctic-Mountains Determined From in-Situ Cosmogenic Be-10 and Al-26. *Geology* 23, 1063–1066.
- Carslaw, K. S., Harrison, R. G. & Kirkby, J. (2002). Cosmic Rays, Clouds, and Climate. *Science* 298, 1732–1737.
- Cohen, B. A., Snyder, G. A., Hall, C. M., Taylor, L. A. & Nazarov, M. A. (2001). Argon-40-argon-39 chronology and petrogenesis along the eastern limb of the Moon from Luna 16, 20 and 24 samples. *Meteoritics and Planetary Science* 36, 1345–1366.
- Dep, L., Elmore, D., Fabryka-Martin, J., Masarik, J. & Reedy, R. C. (1994). Production rate systematics of in-situ-produced cosmogenic nuclides in terrestrial rocks: Monte Carlo approach of investigating  $^{35}\text{Cl}$  ( $n, \gamma$ )  $^{36}\text{Cl}$ . *Nuclear Instruments and Methods in Physics Research Section B: Beam Interactions with Materials and Atoms* 92, 321–325.
- Dunai, T. J. (2000). Scaling factors for production rates of in situ production cosmogenic nuclides: a critical reevaluation. *Earth and Planetary Science Letters* 176, 157–169.
- Dunai, T. J. (2010). *Cosmogenic Nuclides, Principles, Concepts and Applications in the Earth Surface Sciences*. Cambridge University Press.
- Farley, K. A. (2002). (U-Th)/He Dating: Techniques, Calibrations, and Applications. *Reviews in Mineralogy and Geochemistry* 47, 819–844.
- Farley, K. A., Kohn, B. P. & Pillans, B. (2002). The effects of secular disequilibrium on (U-Th)/He systematics and dating of Quaternary volcanic zircon and apatite. *Earth and Planetary Science Letters* 201, 117–125.
- Farley, K. A., Wolf, R. A. & Silver, L. T. (1996). The effects of long alpha-stopping distances on (U-Th)/He ages. *Geochimica et Cosmochimica Acta* 60, 4223–4229.
- Foley, S. F., Yaxley, G. M., Rosenthal, A., Buhre, S., Kiseeva, E. S., Rapp, R. P. & Jacob, D. E. (2009). The composition of near-solidus melts of peridotite in the presence of CO<sub>2</sub> and H<sub>2</sub>O between 40 and 60 kbar. *Lithos*. Elsevier B.V. 112, 274–283.
- Garner, E. L., Murphy, J., Gramlich, J. W., Paulsen, P. J. & Barnes, I. L. (1975). Absolute isotopic abundance ratios and atomic weight of a reference sample of potassium. *Journal of Research of the National Institute of Standards and Technology* 79A, 713–725.
- Gosse, J. C. & Phillips, F. M. (2001). Terrestrial in situ cosmogenic nuclides: theory and application. *Quaternary Science Reviews* 20, 1475–1560.
- Hart, S. R. (1984). He diffusion in olivine. *Earth and Planetary Science Letters* 70, 297–302.
- Jourdan, F. & Renne, P. R. (2014). Neutron-induced  $^{37}\text{Ar}$  recoil ejection in Ca-rich minerals and implications for  $^{40}\text{Ar}/^{39}\text{Ar}$  dating. *Geological Society, London, Special Publications* 378, 33–52.
- Jourdan, F., Renne, P. R. & Reimold, W. U. (2009a). An appraisal of the ages of terrestrial impact structures. *Earth and Planetary Science Letters* 286, 1–13.

- Jourdan, F., Renne, P. R. & Reimold, W. U. (2009b). An appraisal of the ages of terrestrial impact structures. *Earth and Planetary Science Letters*. Elsevier B.V. 286, 1–13.
- Kelley, S. P. (2002). Excess argon in K–Ar and Ar–Ar geochronology. *Chemical Geology* 188, 1–22.
- Knight, K. B. (2006). Argon geochronology. University of California.
- Koppers, A. A. P. (2002). ArArCALC - software for  $^{40}\text{Ar}/^{39}\text{Ar}$  age calculations. *Computer and Geosciences* 28, 605–619.
- Kuiper, Y. (2002). The interpretation of inverse isochron diagrams in  $^{40}\text{Ar}/^{39}\text{Ar}$  geochronology. *Earth and Planetary Science Letters* 203, 499–506.
- Lal, D. (1991). Cosmic ray labeling of erosion surfaces: in situ nuclide production rates and erosion models. *Earth and Planetary Science Letters* 104, 424–439.
- Lal, D. & Peters, B. (1967). Cosmic Ray Produced Radioactivity on the Earth. In: Sitte, K. (ed.) *Kosmische Strahlung II / Cosmic Rays II*. Berlin, Heidelberg: Springer Berlin Heidelberg, 551–612.
- Lavielle, B., Marti, K., Jeannot, J., Nishiizumi, K. & Caffee, M. W. (1999). The  $^{36}\text{Cl}$  –  $^{36}\text{Ar}$  –  $^{40}\text{K}$  –  $^{41}\text{K}$  records and cosmic ray production rates in iron meteorites. *Earth and Planetary Science Letters* 170, 93–104.
- Lee, J. B., Marti, K., Severinghaus, J. P., Kawamura, K., Yoo, H. & Kim, J. S. (2006). A redetermination of the isotopic abundances of atmospheric Ar. *Geochimica et Cosmochimica Acta* 70, 4507–4512.
- Levine, J., Renne, P. R. & Muller, R. A. (2007). Solar and cosmogenic argon in dated lunar impact spherules. *Geochimica et Cosmochimica Acta* 71, 1624–1635.
- Lippolt, H. J. & Weigel, E. (1988).  $^4\text{He}$  diffusion in  $^{40}\text{Ar}$ -retentive minerals. *Geochimica et Cosmochimica Acta* 52, 1449–1458.
- Mamyrin, B. A. & Tolstikhin, I. N. (1984). Helium isotopes in nature. Elsevier.
- Masarik, J. & Beer, J. (1999). Simulation of particle fluxes and cosmogenic nuclide production in the earth atmosphere. *Journal of Geophysical Research* 104, 12099–12111.
- Masarik, J. & Beer, J. (2009). An updated simulation of particle fluxes and cosmogenic nuclide production in the Earth's atmosphere. *Journal of Geophysical Research: Atmospheres* 114, 1–9.
- Masarik, J., Emrich, P., Povinec, P. & Tokar, S. (1986). Monte Carlo simulation of cosmogenic nuclide production. *Nuclear Instruments and Methods in Physics Research B* 17, 483–489.
- Masarik, J. & Reedy, R. C. (1995). Terrestrial cosmogenic-nuclide production systematics calculated from numerical simulations. *Earth and Planetary Science Letters* 136, 381–395.
- McDougall, I. & Harrison, T. M. (1999). Geochronology and thermochronology by the  $^{40}\text{Ar}/^{39}\text{Ar}$  method. Oxford University Press.
- Merrihue, C. & Turner, G. (1966). Potassium-Argon dating by activation with fast neutrons. *Journal of Geophysical Research* 71, 2852–2857.

- Min, K., Reiners, P. W., Wolff, J. A., Mundil, R. & Winters, R. L. (2006). (U-Th)/He dating of volcanic phenocrysts with high-U-Th inclusions, Jemez Volcanic Field, New Mexico. *Chemical Geology* 227, 223–235.
- Morgan, L. E., Renne, P. R., Taylor, R. E. & WoldeGabriel, G. (2009). Archaeological age constraints from extrusion ages of obsidian: Examples from the Middle Awash, Ethiopia. *Quaternary Geochronology*. Elsevier Ltd 4, 193–203.
- Niedermann, S. (2002). Cosmic-Ray-Produced noble gases in terrestrial rocks: dating tools for surface processes. *Reviews in Mineralogy and Geochemistry* 47, 731–784.
- Niedermann, S., Schaefer, J., Wieler, R. & Naumann, R. (2007). The production rate of cosmogenic  $^{38}\text{Ar}$  from calcium in terrestrial pyroxene. *Earth and Planetary Science Letters* 257, 596–608.
- Onstott, T. C., Miller, M. L., Ewing, R. C., Arnold, G. W. & Walsh, D. S. (1995). Recoil refinements : Implications for the  $^{40}\text{Ar} / ^{39}\text{Ar}$  dating technique. *Geochimica et Cosmochimica Acta* 59, 1821–1834.
- Renne, P. R., Farley, K. A., Becker, T. A. & Sharp, W. D. (2001). Terrestrial cosmogenic argon. *Earth and Planetary Science Letters* 188, 435–440.
- Renne, P. R., Knight, K. B., Nomade, S., Leung, K. N. & Lou, T. P. (2005). Application of deuterium-deuterium (D-D) fusion neutrons to  $^{40}\text{Ar}/^{39}\text{Ar}$  geochronology. *Applied Radiation and Isotopes* 62, 25–32.
- Renne, P. R., Mundil, R., Balco, G., Min, K. & Ludwig, K. R. (2010). Joint determination of  $^{40}\text{K}$  decay constants and  $^{40}\text{Ar}^*/^{40}\text{K}$  for the Fish Canyon sanidine standard, and improved accuracy for  $^{40}\text{Ar}/^{39}\text{Ar}$  geochronology. *Geochimica et Cosmochimica Acta* 74, 5349–5367.
- Roddick, J. C. (1978). The application of isochron diagrams in  $^{40}\text{Ar}/^{39}\text{Ar}$  dating: a discussion. *Earth and Planetary Science Letters* 41, 233–244.
- Trull, T. W. & Kurz, M. D. (1993). Experimental measurements of  $^3\text{He}$  and  $^4\text{He}$  mobility in olivine and clinopyroxene at magmatic temperatures. *Geochimica et Cosmochimica Acta* 57, 1313–1324.
- Trull, T. W., Kurz, M. D. & Jenkins, W. J. (1991). Diffusion of cosmogenic  $^3\text{He}$  in olivine and quartz : implications for surface exposure dating. *Earth and Planetary Science Letters* 103, 241–256.
- Turner, G. (1971). Ar-40-Ar-39 ages from the lunar maria. *Earth and Planetary Science Letters* 11, 169–191.
- Turner, G., Huneke, J. C., Podosek, F. A. & Wasserburg, G. J. (1971).  $^{40}\text{Ar}$ - $^{39}\text{Ar}$  ages and cosmic ray exposure of Apollo-14 samples. *Earth and Planetary Science Letters* 12, 19–35.
- Verati, C. & Jourdan, F. (2014). Modelling effect of sericitization of plagioclase on the  $^{40}\text{K}/^{40}\text{Ar}$  and  $^{40}\text{Ar}/^{39}\text{Ar}$  chronometers: implication for dating basaltic rocks and mineral deposits. *Geological Society, London, Special Publications* 378, 155–174.
- Ware, B. D., Jourdan, F. & Vinnicombe, K. (2015). High Precision  $^{40}\text{Ar}/^{39}\text{Ar}$  Geochronology of Large Igneous Provinces: The Tasmanian Dolerites of the Ferrar LIP. *Goldschmidt Abstracts* 3360.

## Chapter 3 Spatio-temporal geochemical evolution of the SE Australian upper mantle deciphered from Sr, Nd and Pb isotopes of Cainozoic intraplate volcanics<sup>1</sup>

### 3.1. Abstract

Intraplate basaltic volcanic rocks ranging in age from Late Cretaceous to Holocene are distributed across southeastern Australia in Victoria and eastern South-Australia. They comprise four provinces differentiated on the basis of age and spatial distribution. The youngest of these (< 4.6 Ma) is the Newer Volcanic Province (NVP) which incorporates lava flows, scoria cones and maars, distributed across western and central Victoria into South-Australia. The oldest eruptives belong to the 95 – 19 Ma Older Volcanic Province, which comprises basaltic lava flows and shallow intrusions distributed across eastern and central Victoria. When examined within the broader framework of geochemical data available for Cretaceous to Cainozoic intraplate volcanism in south eastern Australia, new major, minor, trace and Sr, Nd and Pb isotope analyses of volcanic rocks from the NVP suggest that these rocks originated from a distinctively different source as compared to that of the Older Volcanics. We propose that the magmas represented by the Older Volcanics originated from low degrees of partial melting of a mixed source of Indian mid-ocean ridge basalt (MORB) and calci-carbonatite metasomatised sub-continental lithospheric mantle (SCLM), followed by up to 20% fractional crystallization. The magmas of the youngest (<500 ka) suite of the NVP (the Newer Cones) were generated by up to 13% partial melting of a garnet-rich source, followed by similar degrees of fractional crystallization. We also suggest that the temporally intermediate Euroa Volcanics (~7 Ma) reflect chemical evolution from the source of the Older Volcanics to that of the Newer Cones. Furthermore, energy-constrained recharge, assimilation and fractional crystallisation (EC-RA<sub>x</sub>FC) modelling suggests that the Sr isotope signature of the ~4.6 - 1 Ma Newer Plains component of the NVP can be explained by up to 5% upper crustal assimilation. On the basis of these results and literature xenolith data, we propose a geodynamic model involving decompression melting of metasomatised veins at the base of the SCLM generating the Older Volcanics and modifying the initial asthenosphere of Indian MORB isotope character. This was followed by thermal erosion and entrainment of the resulting depleted SCLM into the modified Indian MORB mantle generating the

---

<sup>1</sup> This Chapter was accepted as a paper in *Journal of Petrology* the 28<sup>th</sup> of July, 2016. Oostingh, K. F., Jourdan, F., Merle, R. & Chiaradia, M. (2016). *Spatio-temporal Geochemical Evolution of the SE Australian Upper Mantle Deciphered from the Sr, Nd and Pb Isotope Compositions of Cenozoic Intraplate Volcanic Rocks*. *Journal of Petrology* **57**, 1509–1530.

Newer Cones. Such a model is in agreement with recent geophysical observations in the area suggesting edge driven convection with shear driven upwelling as potential geodynamic model resulting in temporal upwelling in the region.

### 3.2. Introduction

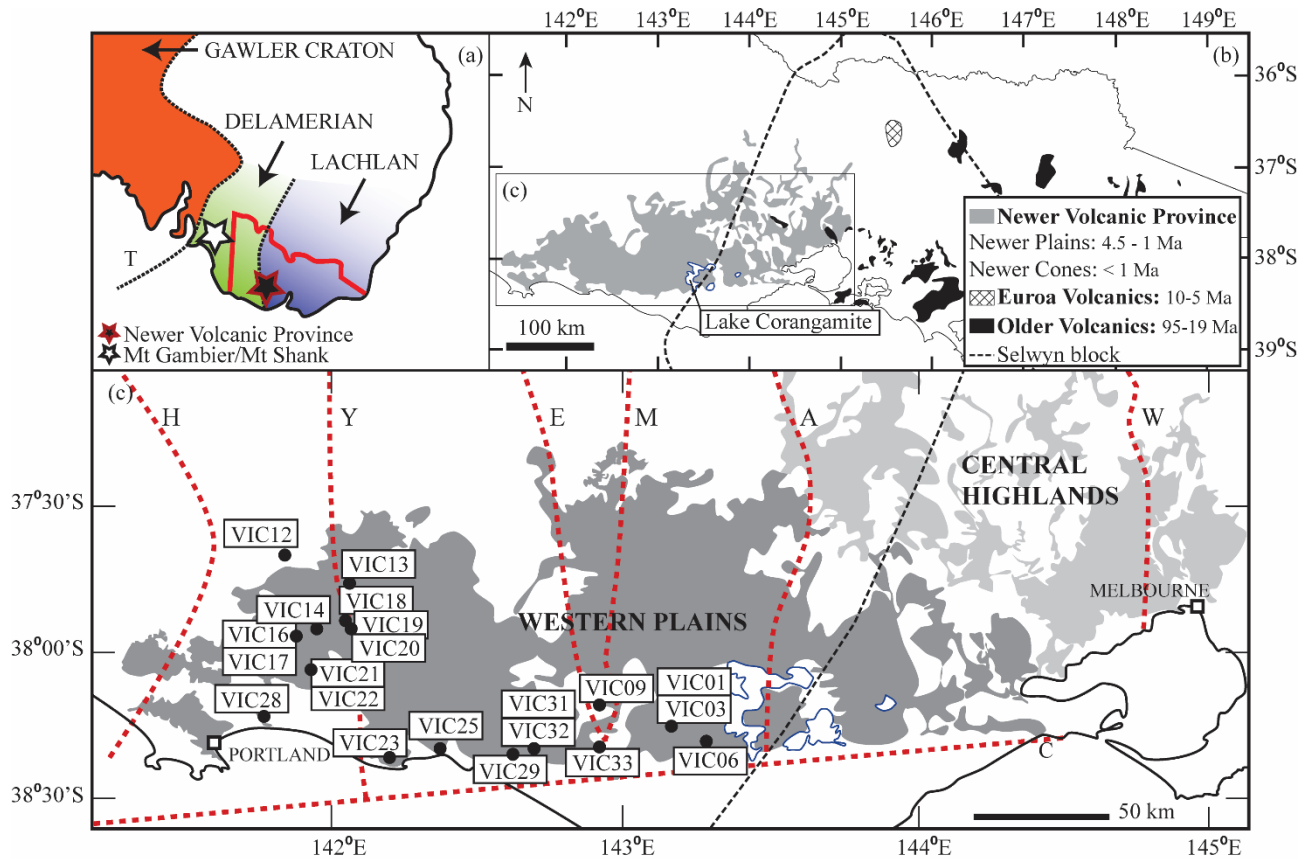


Figure 3.1. (a) Location of the Newer Volcanic Province in Victoria and its youngest expression (*Mt Gambier* and *Mt Shank*) in South Australia. The *Tasman Line* (T), the *Gawler Craton*, as well as the *Delamerian* and *Lachlan* fold belts are indicated. (b) Enlarged section of (a) indicating the approximate extent of the *Newer Volcanics Province* in grey; the 4.5–1Ma *Newer Plains* are located stratigraphically below the <1Ma *Newer Cones*. The 10–5Ma *Euroa Volcanics* are indicated by cross-hatching. The 95–19Ma *Older Volcanics* are indicated in black. The dashed line represents the approximate outline of the *Selwyn Block* at depth (Cayley et al., 2011). (c) Simplified outcrop of the volumetrically dominant *Western Plains* sub-province indicated in dark grey and location of samples. Indicated in light grey is the *Central Highlands* sub-province; this is an area of slightly older volcanism (Aziz-ur-Rahman & McDougall, 1972). The black dashed line represents the approximate westernmost outline of the *Selwyn block* at depth. Major faults are indicated by dashed red lines: C, *Colac lineament*; H, *Hummocks fault*; Y, *Yarramylyp fault*; E, *Escondida fault*; M, *Moyston fault*; A, *Avoca fault*; W, *Mt William fault*.

Cainozoic intraplate volcanism in south east Australia was initiated during breakup of Gondwana and subsequent rapid northward rifting of the Australian plate from 40 Ma onward (Veevers, 1986). In Victoria and South Australia, volcanism is represented by the 95 – 19 Ma *Older Volcanics* and the eruptive products found in the *Newer Volcanic Province* (NVP; Figure 3.1); the 4.5 – 1 Ma *Newer Plains* and the < 1 Ma *Newer Cones*. Furthermore, a 10 – 5 Ma volcanic area of similar age to the

largely felsic rocks of the Macedon-Trentham volcanic province (Price *et al.*, 2003) and with spatial affinities of both the westernmost extent of the Older Volcanics and the easternmost extent of the Newer Volcanics is located near the town of Euroa (Figure 3.1; hereafter the Euroa Volcanics after Paul *et al.*, 2005). The NVP is subdivided into two distinct regions based on geomorphology: the Central Highlands and Western Plains (Figure 3.1). The presence of hot springs (Cartwright *et al.*, 2002) suggests that the province is still active. Nevertheless, the source and provenance of the Older Volcanics, the Newer Plains and Newer Cones basalts are still a matter of debate (Demidjuk *et al.*, 2007; O'Reilly and Zhang, 1995; Price *et al.*, 1997, 2014; Zhang *et al.*, 1999). Enriched geochemical signatures for the Newer Plains with spatially variable Sr isotope data corresponding to the location of both the Moyston Fault and the Selwyn Block (Figure 3.1) led Price *et al.* (1997, 2014) to suggest that the lithosphere had an important control on observed geochemical variation between the series. It is now well-established that the region is underlain by a complex Palaeozoic basement (Cayley *et al.*, 2011) as well as metasomatised and heterogeneous sub continental lithospheric mantle (SCLM) (Griffin *et al.*, 1988; Handler *et al.*, 1997; O'Reilly and Griffin, 1988; Stolz and Davies, 1988; Yaxley *et al.*, 1991). Pb isotopes systematics are thought to resolve source variations at much higher resolution than Sr and Nd isotopes and trace element systematics (e.g. Ewart, 2004), however, Pb isotope data is only available for basalts of the Older Volcanics (Price *et al.*, 2014), the suite of rocks around the town of Euroa (Paul *et al.* (2005) and two individual eruption centres of the Newer Cones; Mt Rouse (Boyce *et al.*, 2015) and Mt Gambier (Van Otterloo *et al.*, 2014). However, single eruptions can represent discrete and compositionally distinct magma batches, resulting in considerable geochemical variation within and between eruption centres, stressing the need for larger scale geochemical investigations to understand the processes involved in monogenetic volcanism (McGee *et al.*, 2013). Here, we present new major and trace element analyses and Pb, Sr and Nd isotope data for 11 volcanic centres and their associated flows of the Newer Cones, which, with a relatively young age span from around 500 000 to 5000 years (Blackburn *et al.*, 1982; Matchan and Phillips, 2011, 2014), represent a proxy for the current geochemical composition of the mantle beneath south east Australia. Recent ultra-precise  $^{40}\text{Ar}/^{39}\text{Ar}$  age dating on these samples confirms these ages, and exemplifies the major age difference between the ~ 4 Ma Newer Plains (Gray and McDougall, 2009) and the < 500 000 ka Newer Cones in the NVP (Oostingh *et al.*, 2015). Combined data from the Older Volcanics, Euroa Volcanics and the Newer Plains and Newer Cones allow us to resolve spatial and temporal source variations and differences in magmatic processes in order to elucidate the origin of south east Australian Cainozoic magmatism.



### 3.3. Overview of Cainozoic magmatism in South East Australia

#### 3.3.1. Older Volcanics

Day (1989, 1983) subdivided the limited outcrops of the Older Volcanics (Figure 3.1) into fifteen separate fields on the basis of major and trace element analyses and outcrop distribution which display a continuum of compositions from nephelinites to quartz-tholeiitic basalts showing no spatial and temporal correlation between basalt type and location or age. Even though K – Ar dating suggests that volcanism has been almost continuous from 95 Ma up to 19 Ma (Wellman, 1974), individual volcanic fields show a more restricted age range, leading Day (1989, 1983) to subdivide the Older Volcanics into four groups: Group 1 (95 Ma – 55 Ma), Group 2 (59 Ma – 38 Ma), Group 3 (44 Ma – 31 Ma) and Group 4 (29 Ma – 19 Ma). Recently published major and trace element results as well as Sr, Nd and Pb isotope data (Price *et al.*, 2014) suggest that the Older Volcanics are derived from a tri-component source of depleted mantle (DM) and enriched (EMI and EMII) mantle components. Enrichment in incompatible trace elements and light rare earth elements (LREE) over heavy rare earth elements (HREE) in the Older Volcanics can be explained by partial melting of a complex spectrum of mantle compositions followed by limited fractional crystallization and potential minor crustal assimilation (Price *et al.*, 2014). These authors also recognized two groups within high Mg-number samples with subtle variations in trace elements potentially derived from depleted mantle mixing with different metasomatised components with either 2-3% EMI or 1% calci-carbonatite composition.

#### 3.3.2. Euroa Volcanics

The Euroa region represents a key location, as it has spatial affinities with both the Older Volcanics and Newer Plains and Newer Cones basalts as well as the small felsic flows, domes, plugs and spines of the Macedon – Trentham region (Paul *et al.*, 2005; Figure 3.1b) and is located on a N – S trend of more felsic magmatism (8 – 5 Ma; Wellman and McDougall, 1974). These more evolved rocks (mugearite to trachyte) have been previously interpreted as the southernmost extent of the New South Wales leucitite suite; a north-south trending linear chain of volcanic centres proposed as a trace of hotspot volcanism (Davies *et al.*, 2015; Nelson *et al.*, 1986). However, work by Paul *et al.* (2005) revealed that the geochemical characteristics of the Euroa Volcanics are distinct from the New South Wales leucitites, questioning the extension of potential hotspot related extrusives into Victoria. Geochemical similarities of these Euroa Volcanics with both the Older Volcanics and Newer Plains and Newer Cones basalts suite (Price *et al.*, 2014), suggest a common source. Their age range and location provide an additional constraint on the temporal and spatial variability of this source and magmatic processes.

### 3.3.3. Newer Volcanics

The youngest expressions of intraplate volcanism are the < 4.6 Ma (Aziz-ur-Rahman and McDougall, 1972; Gray and McDougall, 2009; McDougall *et al.*, 1966) alkaline basaltic volcanic products of the Newer Plains and Newer Cones series in the NVP (Figure 3.1a and b) covering around 15 000 – 20 000 km<sup>2</sup> of Victoria and South Australia (Boyce, 2013; Price *et al.*, 2003) and comprising more than 704 eruption points from > 416 volcanic centres (Boyce, 2013). In the Central Highlands sub-province, scoria cones and lava shield volcanoes have produced valley flows and small lava plains. In the volumetrically dominant Western Plains sub-province, thin, ~4.6 to 1 Ma old lava flows (Gray and McDougall, 2009; the Newer Plains) cover the basement of Palaeozoic sediments and granites, whereas a younger (< 10 – 300 ka; Aziz-ur-Rahman and McDougall, 1972) volcanic phase is characterized by small (< 100 m high) scoria cones, maars and lava shields with associated flows (the Newer Cones; Price *et al.*, 2003). These younger cones are alkalic lavas and have strong incompatible element enrichment, whereas the underlying Newer Plains comprise less enriched transitional to tholeiitic rock types (Price *et al.*, 2003).

### 3.4. Geological setting and sample descriptions

The NVP is restricted between 141°E - 145°E and 37°S – 38.5°S and is underlain by a complex Palaeozoic basement consisting of a series of eastward younging stacked fold belts of deformed and metamorphosed rocks of the Delamerian and Lachlan orogenies occurring east of the Tasman Line which subdivides the Palaeozoic basement from the Proterozoic Gawler Craton (Figure 1a). An important structural domain is the early Ordovician continental crust of the inferred Selwyn basement block within the southern Lachlan Orogen (Cayley *et al.*, 2011), which underlies most of the Older Volcanics, but is absent from the basement below our samples of the Newer Volcanics of the Western Plains that were sampled west of Lake Corangamite (Figure 3.1b).

We focused our sampling efforts on the volumetrically dominant Western Plains sub-province in the NVP, targeting the young Newer Cones. Although extensive literature data are available on the petrology and major and trace element geochemistry of these Newer Cones (see Price *et al.*, 2003 and references therein), isotope data are scarce. A recent study by Price *et al.* (2014) as well as work by Paul *et al.* (2005) provided isotope data on the Older Volcanics, Newer Plains and Euroa Volcanics; which highlights the need for an updated dataset on the Newer Cones to expand the current isotope geochemical database available for localized volcanic centres (Boyce *et al.*, 2015; Van Otterloo *et*

*al.*, 2014). We targeted young scoria cones and lava shields and their flows at: Mt Leura (VIC03); Mt Porndon (VIC06); Mt Noorat (VIC09); Mt Pierrepont (VIC13); Mt Napier (VIC18, VIC19 and VIC20) and its Harman flow (VIC14, VIC16 and VIC17); the flow from Mt Rouse (VIC23); the Tower Hill complex (VIC25); Mt Eccles (VIC21 and VIC22) and its Tyrendarra flow (VIC28) and Staughton Hill (VIC33) as well as a smaller, yet unnamed cone GEOVIC ME-2 (Boyce, 2013; VIC31 and VIC32) which we will refer to as Mt Boomerang, and the flow at Hopkins Falls that cannot be linked to a clear eruptive centre (VIC29). Samples are typically dark grey, cryptocrystalline basalt with fresh plagioclase laths and fresh olivine visible in hand specimen and minor vesicularity; in the case of flows, vesicles are commonly aligned. Samples VIC19 and VIC22 represent scoriaceous samples with very fine, glassy groundmass, whereas VIC25 represents a volcanic bomb within tuff layers at the Tower Hill complex. Mantle xenoliths (cm-scale) are present in samples VIC03, VIC09 and VIC31 and VIC32 and olivine glomerocrysts occur in samples VIC29 and VIC33. All samples are devoid of any alteration in thin section. Principal mineral phases observed are phenocrysts of olivine, plagioclase and clino-pyroxene in groundmass containing laths of plagioclase and Fe-Ti oxides.

### 3.5. Methods

Samples were pulverised in an agate pestle and mortar. The major, minor and trace elements of 20 samples were analysed for major elements at Intertek Genalysis Laboratories, Perth, using X-ray fluorescence (XRF) and this was followed by standard dissolution techniques and analysis of solutions for trace elements by inductively coupled plasma mass spectrometry (ICP-MS). Internal standards SARM1 and SY-4 were used for the major elements and SY-4, OREAS25a, OREAS25b and GBW07105 for the trace elements. All major (XRF) and trace (ICP-MS) analyses proved to have an internal and external precision better than 5% at the 95% confidence level ( $2\sigma$ ), except for V and Zr which show precision  $>5\%$  ( $2\sigma$ ) for the standards reported.

Strontium, Nd and Pb isotopes were analysed on a subset of 9 samples at the Department of Earth Sciences (University of Geneva, Switzerland) using the method described in Chiaradia *et al.* (2011) and a Thermo Neptune PLUS Multi-Collector ICP-MS in static mode. Ratios used for internal fractionation were  $^{88}\text{Sr}/^{87}\text{Sr} = 8.375209$  for the  $^{87}\text{Sr}/^{86}\text{Sr}$ ,  $^{146}\text{Nd}/^{144}\text{Nd} = 0.7219$  for the  $^{143}\text{Nd}/^{144}\text{Nd}$  ratio and  $^{203}\text{Tl}/^{205}\text{Tl} = 0.418922$  for the three Pb ratios (a Tl standard solution was added to the sample). The  $^{144}\text{Sm}$  interference on  $^{144}\text{Nd}$  was monitored on mass  $^{147}\text{Sm}$  and corrected by using a  $^{144}\text{Sm}/^{147}\text{Sm}$  value of 0.206700 and  $^{204}\text{Hg}$  interference on  $^{204}\text{Pb}$  was corrected by monitoring  $^{202}\text{Hg}$ .

External standards used were SRM987 ( $^{87}\text{Sr}/^{86}\text{Sr} = 0.710248$ , long-term external reproducibility: 10 parts per million (ppm)), JNdi-1 ( $^{143}\text{Nd}/^{144}\text{Nd} = 0.512115$  (Tanaka *et al.*, 2000) long-term external reproducibility: 10 ppm), and SRM981 (Baker *et al.*, 2004) for Pb (long-term external reproducibility of 0.0048% for  $^{206}\text{Pb}/^{204}\text{Pb}$ , 0.0049% for  $^{207}\text{Pb}/^{204}\text{Pb}$  and 0.0062% for  $^{208}\text{Pb}/^{204}\text{Pb}$ ). Based on the systematic discrepancy between the measured and proposed Sr, Nd and Pb isotope ratios of the above standards, sample values were further corrected for external fractionation by a value of -0.039‰, +0.047‰ and +0.5‰ amu respectively.

	VIC03	VIC06	VIC09	VIC12	VIC13	VIC14	VIC16	VIC17	VIC18	VIC19
Location	Mt Leura	Mt Porndon	Mt Noorat	Wannon Falls	Mt Pierre-point	Harman flow	Harman flow	Harman flow	Mt Napier	Mt Napier
LAT (dec degrees)	-38.25	-38.30	-38.18	-37.67	-37.77	-37.92	-37.94	-37.94	-37.89	-37.89
LONG (dec degrees)	143.16	143.28	142.92	141.84	142.06	141.95	141.88	141.88	142.05	142.05
<i>Major elements (wt%)</i>										
SiO <sub>2</sub>	44.06	50.68	46.87	49.57	51.19	49.62	48.54	48.88	50.02	50.47
Al <sub>2</sub> O <sub>3</sub>	12.86	13.97	14.11	14.45	14.21	14.50	13.78	13.57	15.28	15.42
TiO <sub>2</sub>	3.22	2.13	2.76	1.88	1.83	1.82	2.09	2.03	2.34	2.32
Fe <sub>2</sub> O <sub>3</sub>	14.37	12.23	13.20	11.65	11.53	12.23	12.29	12.16	11.71	11.46
MnO	0.17	0.16	0.17	0.15	0.15	0.15	0.16	0.16	0.15	0.15
MgO	9.72	8.05	7.45	9.27	8.07	7.76	9.94	10.21	6.75	6.46
CaO	8.34	8.46	7.37	8.40	8.41	8.66	8.98	8.98	8.29	8.45
Na <sub>2</sub> O	4.37	3.48	4.96	3.51	3.45	3.45	3.21	3.30	4.09	3.91
K <sub>2</sub> O	2.26	1.16	2.76	1.16	0.92	0.92	1.08	1.13	1.39	1.39
Cr <sub>2</sub> O <sub>3</sub>	0.04	0.04	0.03	0.04	0.05	0.04	0.05	0.05	0.02	0.02
P <sub>2</sub> O <sub>5</sub>	1.29	0.44	1.02	0.41	0.33	0.33	0.45	0.43	0.50	0.43
LOI	-0.69	-0.59	-0.83	-0.35	0.02	0.25	-0.34	-0.65	-0.52	-0.44
Total	100.10	100.30	100.00	100.18	100.19	99.77	100.28	100.30	100.06	100.09
Mg-no.	61	61	57	65	62	60	65	66	57	57

Table 3.1. Major (wt %) and trace element (ppm) analyses of Newer Volcanic Province basalts.

<i>Trace Elements (ppm)</i>	<b>VIC03</b>	<b>VIC06</b>	<b>VIC09</b>	<b>VIC12</b>	<b>VIC13</b>	<b>VIC14</b>	<b>VIC16</b>	<b>VIC17</b>	<b>VIC18</b>	<b>VIC19</b>
Rb	51.1	27.6	48.4	19.8	17.9	14.8	14.7	20.6	28.0	25.7
Ba	590.4	240.8	557.9	296.6	267.8	258.1	307.6	303.4	342.2	368.6
Th	6.4	3.1	7.1	2.8	2.2	2.1	2.8	2.8	3.0	3.2
Nb	78.2	28.8	77.8	31.7	25.2	23.5	30.2	29.2	34.3	34.2
Sr	1044.3	477.0	1095.6	670.4	466.5	475.1	529.9	536.5	609.9	627.4
Hf	7.9	4.6	9.0	4.1	3.6	3.3	3.7	3.6	4.3	4.6
Zr	311	166	363	154	138	124	142	135	169	176
Y	26.2	21.6	23.4	19.9	20.6	19.8	19.1	19.1	21.4	21.9
Pb	5.3	2.8	6.7	2.1	2.7	1.9	2.1	3.4	2.3	2.7
Ta	4.7	1.7	5.2	1.9	1.5	1.5	1.8	1.7	2.1	2.1
U	1.8	0.9	2.0	0.6	0.5	0.1	0.7	0.6	0.7	0.8
Sc	13.0	18.0	11.0	19.0	18.0	18.0	19.0	18.0	15.0	16.0
V	197	185	161	180	153	171	192	188	192	191
Cr	236	245	176	285	308	286	293	304	101	103
Co	63.5	49.1	49.4	53.7	51.5	55.7	55.0	56.5	43.4	62.1
Ni	230.8	149.0	157.1	195.2	209.0	214.4	216.6	224.1	109.0	101.8
La	65.0	23.3	59.5	22.5	18.1	17.8	21.3	22.1	25.0	25.6
Ce	133.8	49.0	117.7	44.8	37.3	35.7	45.1	44.0	49.9	50.7
Pr	15.5	6.2	14.2	5.5	4.8	4.5	5.6	5.4	6.3	6.2
Nd	62.9	26.0	54.7	23.5	20.5	18.9	24.0	23.0	25.5	27.3
Sm	12.0	6.1	10.7	5.3	5.0	4.7	5.3	5.3	5.8	5.9

Table 3.1. Continued.

	<b>VIC03</b>	<b>VIC06</b>	<b>VIC09</b>	<b>VIC12</b>	<b>VIC13</b>	<b>VIC14</b>	<b>VIC16</b>	<b>VIC17</b>	<b>VIC18</b>	<b>VIC19</b>
Eu	4.1	2.0	3.5	1.8	1.7	1.7	1.9	1.8	2.1	2.1
Gd	10.3	6.0	9.5	5.1	5.2	5.2	5.5	5.3	6.1	6.0
Tb	1.3	0.9	1.3	0.8	0.8	0.7	0.8	0.8	0.8	0.9
Dy	6.5	4.9	5.8	4.1	4.2	4.2	4.2	4.1	4.5	4.7
Ho	1.1	0.8	1.0	0.7	0.8	0.8	0.8	0.7	0.8	0.8
Er	2.4	2.3	2.2	2.0	2.0	2.0	1.9	1.9	2.1	2.1
Tm	0.3	0.3	0.3	0.2	0.2	0.3	0.2	0.2	0.3	0.3
Yb	1.6	1.7	1.3	1.3	1.4	1.5	1.6	1.6	1.6	1.6
Lu	0.2	0.2	0.2	0.2	0.2	0.2	0.2	0.2	0.2	0.2
	<b>VIC20</b>	<b>VIC21</b>	<b>VIC22</b>	<b>VIC23</b>	<b>VIC25</b>	<b>VIC28</b>	<b>VIC29</b>	<b>VIC31</b>	<b>VIC32</b>	<b>VIC33</b>
Location	Mt Napier	Mt Eccles	Mt Eccles	Mt Rouse flow	Tower Hill	Tyrendarra flow	Hopkins Falls	GEOVIC ME-2	GEOVIC ME-2	Stoughton Hill
LAT (dec degrees)	-37.92	-38.06	-38.06	-38.36	-38.33	-38.22	-38.35	-38.33	-38.33	-38.32
LONG (dec degrees)	142.07	141.93	141.93	142.20	142.37	141.77	142.62	142.69	142.69	142.92
<i>Major elements (wt%)</i>										
SiO <sub>2</sub>	49.93	46.16	46.87	48.11	46.44	48.20	46.70	45.47	45.56	46.51
Al <sub>2</sub> O <sub>3</sub>	14.64	14.09	13.35	14.15	13.78	14.11	13.19	13.19	13.18	12.88
TiO <sub>2</sub>	2.24	2.60	2.36	2.29	2.46	2.22	2.45	2.81	2.76	2.40
Fe <sub>2</sub> O <sub>3</sub>	11.73	12.91	13.20	12.80	13.05	12.99	13.18	12.99	12.77	13.37
MnO	0.15	0.17	0.17	0.16	0.17	0.17	0.17	0.17	0.16	0.17

Table 3.1. Continued.

	VIC20	VIC21	VIC22	VIC23	VIC25	VIC28	VIC29	VIC31	VIC32	VIC33
MgO	7.84	7.92	10.10	8.87	8.86	8.68	11.01	10.60	10.48	11.12
CaO	8.58	9.66	9.19	9.03	8.79	8.75	9.05	9.01	9.16	9.05
Na <sub>2</sub> O	3.78	3.69	3.27	3.43	4.07	3.69	3.32	3.45	3.44	3.05
K <sub>2</sub> O	1.34	1.62	1.44	1.15	2.17	1.51	1.37	1.77	1.77	1.33
Cr <sub>2</sub> O <sub>3</sub>	0.03	0.04	0.05	0.04	0.03	0.04	0.05	0.04	0.05	0.05
P <sub>2</sub> O <sub>5</sub>	0.48	0.85	0.61	0.45	0.82	0.58	0.58	0.62	0.62	0.57
BaO	0.05	0.05	0.04	0.04	0.06	0.05	0.05	0.05	0.05	0.04
SO <sub>3</sub>	0.01	0.04	0.07	0.01	0.05	0.02	0.01	0.02	0.03	0.01
LOI	-0.74	0.32	-0.61	-0.43	-0.52	-0.74	-0.87	-0.11	0.07	-0.47
Total	100.06	100.11	100.11	100.10	100.24	100.26	100.25	100.08	100.10	100.09
Mg-no.	61	59	64	62	61	61	66	66	66	66
<i>Trace Elements (ppm)</i>										
Rb	26.5	31.8	27.5	21.9	44.8	30.9	25.4	33.6	35.3	23.9
Ba	350.1	457.2	350.3	278.2	518.5	390.6	354.9	411.8	399.8	344.9
Th	2.9	4.2	3.2	2.8	5.3	3.7	3.0	4.3	4.6	2.7
Nb	33.0	56.1	39.0	32.7	61.7	45.6	38.4	51.8	52.3	37.1
Sr	578.1	959.0	661.2	592.6	876.4	670.8	677.8	709.3	717.7	587.7
Hf	4.2	5.4	4.3	4.4	7.3	5.2	4.5	5.7	6.0	4.5
Zr	160	228	169	173	279	202	168	224	225	171
Y	20.7	25.6	20.6	21.0	25.5	23.0	20.9	21.6	21.9	21.3
Pb	2.5	2.8	2.3	2.2	4.0	2.9	3.1	2.8	3.1	1.6
Ta	2.1	3.3	2.3	2.1	3.9	2.8	2.4	3.5	3.4	2.3

Table 3.1. Continued.



	VIC20	VIC21	VIC22	VIC23	VIC25	VIC28	VIC29	VIC31	VIC32	VIC33
U	0.8	1.3	0.9	0.8	1.5	0.9	0.9	1.1	1.3	0.7
Sc	17.0	19.0	18.0	20.0	17.0	18.0	19.0	18.0	19.0	19.0
V	191	219	203	200	194	189	208	221	231	204
Cr	171	242	282	273	205	238	311	281	295	367
Co	48.6	49.1	60.2	55.9	53.1	49.8	62.2	63.3	60.5	64.4
Ni	137.9	136.9	228.8	175.7	174.1	166.3	245.6	231.8	213.9	276.7
La	24.6	43.2	29.4	24.5	47.8	33.5	29.2	36.9	37.1	27.3
Ce	49.4	86.4	59.2	50.8	96.6	66.8	60.7	73.5	74.0	56.0
Pr	6.2	10.2	7.2	6.3	11.5	8.1	7.6	8.9	8.8	7.1
Nd	26.3	43.2	30.5	26.2	46.0	32.9	31.4	35.2	36.6	29.1
Sm	5.8	8.6	6.6	5.8	8.8	6.7	6.6	7.3	7.4	6.3
Eu	2.1	2.9	2.3	2.0	3.0	2.4	2.3	2.4	2.5	2.3
Gd	5.7	8.6	6.4	5.7	7.9	7.0	6.4	7.2	6.9	6.4
Tb	0.8	1.1	0.9	0.8	1.1	0.9	0.9	0.9	0.9	0.9
Dy	4.5	5.6	4.8	4.5	5.7	4.9	4.6	5.0	4.9	4.7
Ho	0.8	1.0	0.8	0.8	1.0	0.9	0.8	0.9	0.9	0.8
Er	2.1	2.3	2.1	2.0	2.4	2.2	2.0	2.2	2.2	2.0
Tm	0.2	0.3	0.2	0.2	0.3	0.3	0.2	0.3	0.3	0.2
Yb	1.5	1.7	1.5	1.7	1.6	1.8	1.2	1.5	1.5	1.4
Lu	0.2	0.2	0.2	0.2	0.2	0.2	0.2	0.2	0.2	0.2

Table 3.1. Continued.

### 3.6. Results

All our new analyses of Newer Cones samples have loss on ignition (LOI) < 2 weight percentage (wt%) (Table 3.1) and major element data have been normalised to 100% on a volatile-free basis. (Appendix B (major and trace elements) and Appendix C (Sr, Nd and Pb isotopes)). For comparison, we have also plotted the whole rock major and trace element concentrations of the GEOROC database and data from Boyce et al (2015), Price et al (2014) and Van Otterloo et al (2014) for Cretaceous and Cainozoic intraplate volcanic rocks of south eastern Australia. We have not used data for altered samples with LOI > 3 wt% or without LOI recorded as the quality of the data cannot be assessed.

#### 3.6.1. Major elements

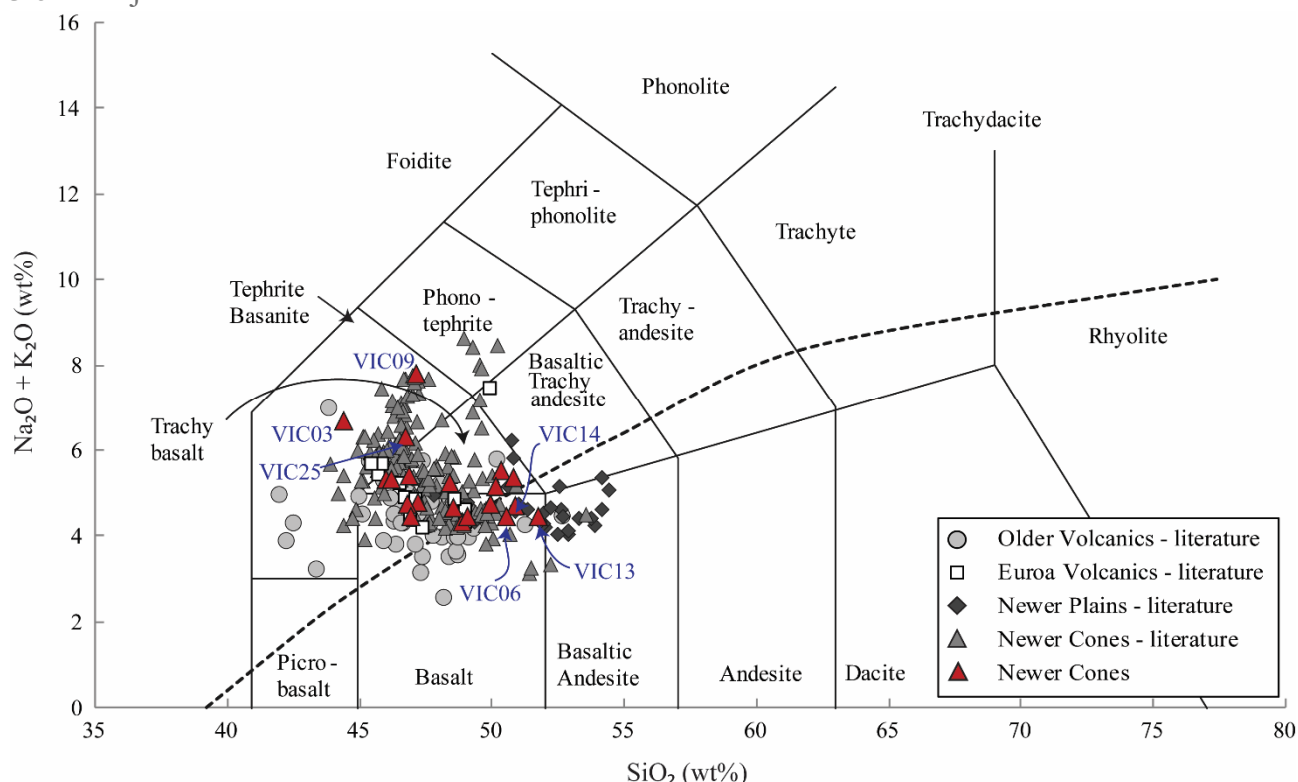


Figure 3.2. Total alkali-silica (TAS) diagram after Le Bas et al. (1986). Older Volcanics and Newer Plains data are from Price et al. (1997, 2014); Euroa Volcanics data are from Paul et al. (2005); Newer Cones literature data are from Frey et al. (1978), McDonough et al. (1985), Vogel & Keays (1997), Foden et al. (2002), Demidjuk et al. (2007), Van Otterloo et al. (2014) and Boyce et al. (2015). Dashed line represents the alkaline-sub-alkaline division of Irvine & Baragar (1971).

On a total-alkali-silica (TAS) diagram (Figure 3.2; Le Bas et al., 1986), the data obtained from this study overlap with published data on the Newer Cones, with all samples except for VIC06, VIC13 and VIC14 plotting above the alkaline – sub alkaline division line of Irvine and Baragar (1971). Seventeen Newer Cones samples plot within the basalt and trachy-basalt fields, with three samples (VIC03, VIC09 and VIC25) classifying as basanite based on CIPW norm calculation. Data for sample VIC09, ( $\text{SiO}_2$  of 47.1 wt% and total alkali composition of 7.8 wt%) overlap with those published for

Mt Gambier and Mt Shank (Figure 3.1a; Demidjuk et al., 2007; Foden et al., 2002; McDonough et al., 1985) which is the westernmost and youngest suite of volcanic rocks of the NVP. Except for these three basanites, our analyses of the Newer Cones show a narrow range in  $\text{Na}_2\text{O} + \text{K}_2\text{O}$  (wt%).

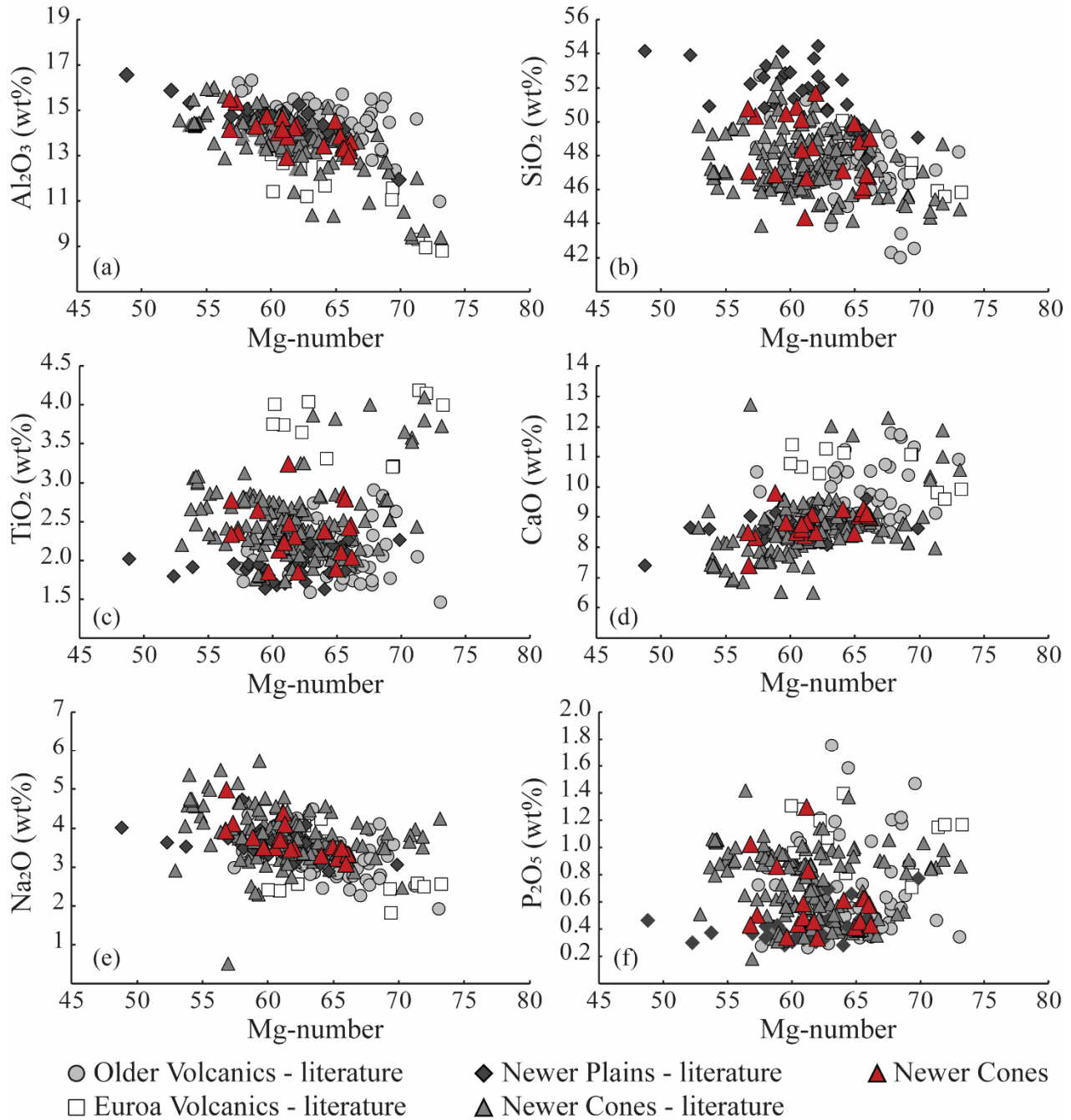


Figure 3.3. Major element variation diagrams, all data normalized to 100% on a volatile-free basis. Mg-number calculated as the atomic ratio of  $[100\text{Mg}/(\text{Mg} + 0.85\text{Fe}_{\text{tot}})]$ . Data sources as in Fig. 2.

Our samples define a positive covariation between  $\text{Al}_2\text{O}_3$  concentrations and Mg-number [atomic ratio of  $100\text{Mg}/(\text{Mg} + 0.85\text{Fe}_{\text{tot}})$ ] suggesting progressive differentiation, with our data overlapping

Al<sub>2</sub>O<sub>3</sub> concentrations of literature data on the Newer Cones (Figure 3.3a-f; Boyce *et al.*, 2015; Demidjuk *et al.*, 2007; Ellis, 1976; Foden *et al.*, 2002; Frey *et al.*, 1978; McBride *et al.*, 2001; McDonough *et al.*, 1985; Van Otterloo *et al.*, 2014; Vogel and Keays, 1997). Furthermore, our samples show TiO<sub>2</sub> concentrations up to 3.2 wt% which is lower than those reported for the youngest eruptives in South Australia (Mt Watch and Mt McIntyre; Foden *et al.*, 2002; McDonough *et al.*, 1985; Vogel and Keays, 1997). Our Newer Cones samples are also distinguished from these rocks by their lower CaO content (7.4 – 9.8 wt%).

### 3.6.2. Trace elements

Whole rock Mg-numbers of our Newer Cones samples range between 57 and 66 and Ni, Cr and Co concentrations are between 102 – 277 ppm, 101 – 367 ppm and 49 – 64 ppm respectively. The samples show no trend in trace element contents versus Mg-number (Figure 3.4a-f), but for the positive covariation between Ni concentration and increasing Mg-number. This spread is mainly caused by basanite samples VIC03, VIC09 and VIC25 which are significantly enriched in incompatible trace elements such as La (47.8 – 65 ppm) and Rb (44.8 – 51.1 ppm) as compared to La (< 37 ppm) and Rb (< 34 ppm) for the other Newer Cones samples. Basanites aside, our samples show a restricted range in trace element concentrations overlapping with literature data on samples from this region, again except for the suite from Mt Schank and Mt Gambier (Demidjuk *et al.*, 2007; Foden *et al.*, 2002; Van Otterloo *et al.*, 2014). On a La/Nb versus Ba/Nb diagram the data cluster around the Primitive Mantle ratio (La/Nb: 0.9 and Ba/Nb: 9; Sun and McDonough, 1989, Figure 3.4g). On a Ce/Pb versus Nb/U diagram, 18 of our 20 Newer Cones samples fall within the range defined for mid-ocean ridge basalt (MORB) and ocean island basalt (OIB) (Hofmann *et al.*, 1986, Figure 3.4h), except for VIC14 which shows an extremely high Nb/U ratio of 235 due to depletion of this sample in U (0.1 ppm versus > 0.5 ppm for the other samples) and VIC06 which trends slightly towards the continental crust value (Taylor and McLennan, 1995). The samples show a typical OIB trace element signature on a normalised extended element diagram (Figure 3.5) with relative enrichment of incompatible elements Rb, Ba, Th, U, Nb and LREEs compared to primitive mantle, as well as negative Pb and positive Nb anomalies. The basanites (VIC03, VIC09 and VIC25) show a greater enrichment in LREEs when compared to the trachy-basalts and (sub-) alkaline basalts with La/Lu ratios (normalized to C1 chondrites) of >25. C1 Chondrite normalized REE patterns (Figure 3.6; Sun and McDonough, 1989) furthermore show light rare earth element (LREE) versus middle rare earth element (MREE) and MREE/HREE enrichment for all Newer Cones samples.

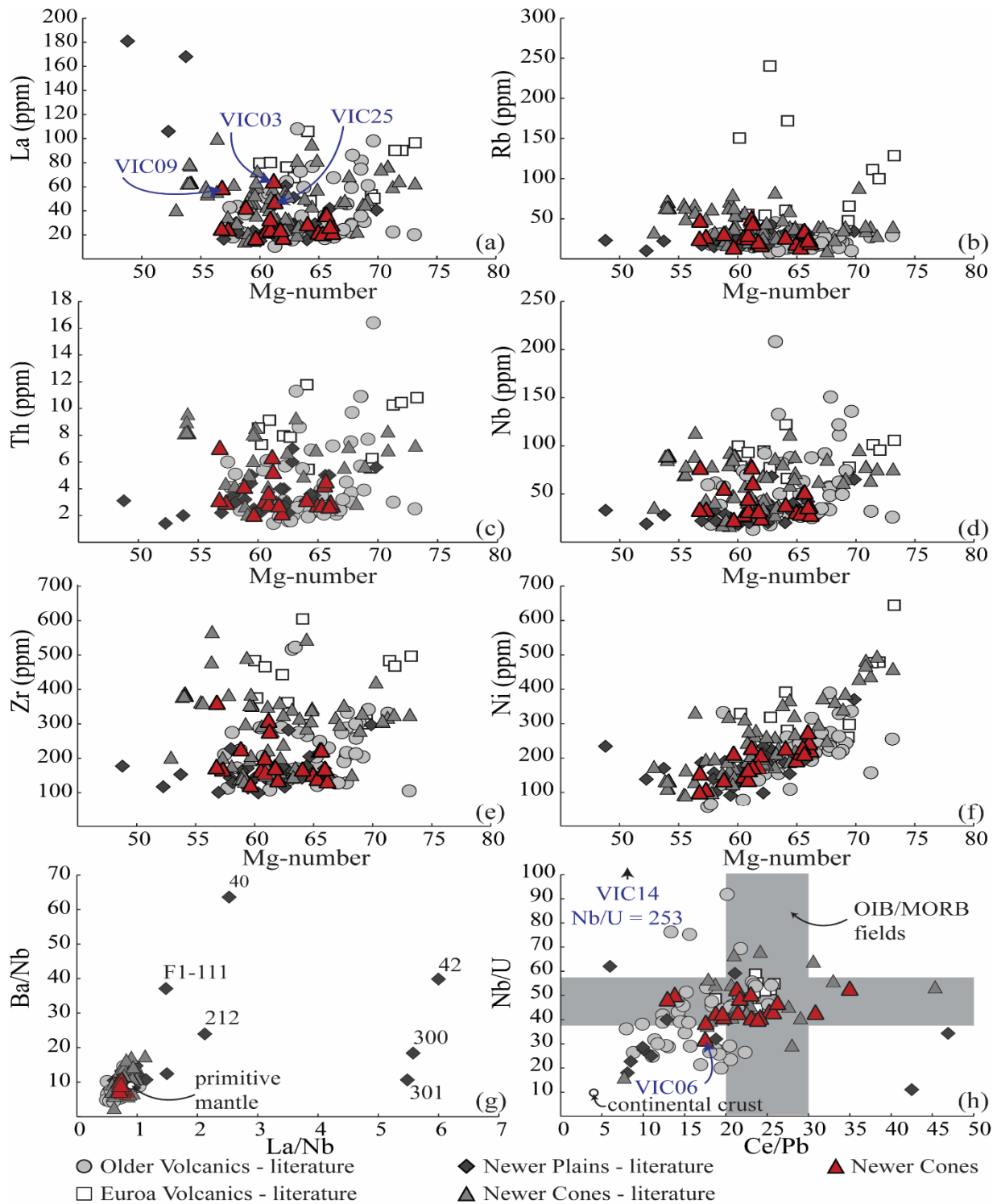


Figure 3.4. (a–f) Trace element plots vs Mg-number for all series; data sources as in Fig. 2. Basalt samples VIC03, VIC09 and VIC25 are indicated in (a); (g): La/Nb vs Ba/Nb; the Primitive Mantle value is from Sun & McDonough (1989). Samples F1-111, 40, 42, 212, 300 and 301 (Price et al., 1997) are indicated. (h) Ce/Pb vs Nb/U after Hofmann et al. (1986); the grey field represents the Ce/Pb ( $25 \pm 5$ ) and Nb/U ( $47 \pm 10$ ) ratios in both ocean island basalt (OIB) and mid-ocean ridge basalt (MORB); average continental crust is indicated (Nb/U = 10; Ce/Pb = 4; Taylor & McLennan, 1995).

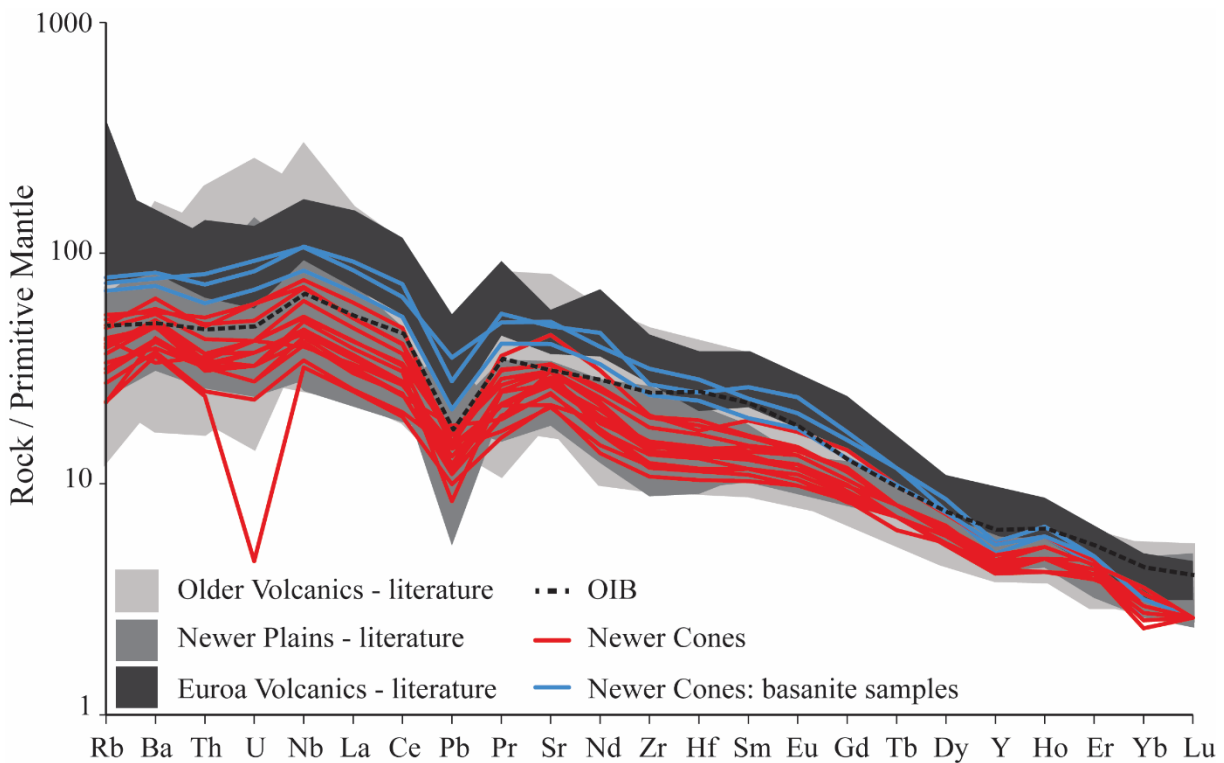


Figure 3.5. Primitive mantle normalized trace element patterns for the Newer Volcanics compared with the Older Volcanics. Typical ocean island basalt (OIB; Sun & McDonough, 1989) is indicated with a black dashed line. Basanite samples VIC03, VIC09 and VIC25 indicated are indicated by blue lines. Data sources as in Fig. 2.

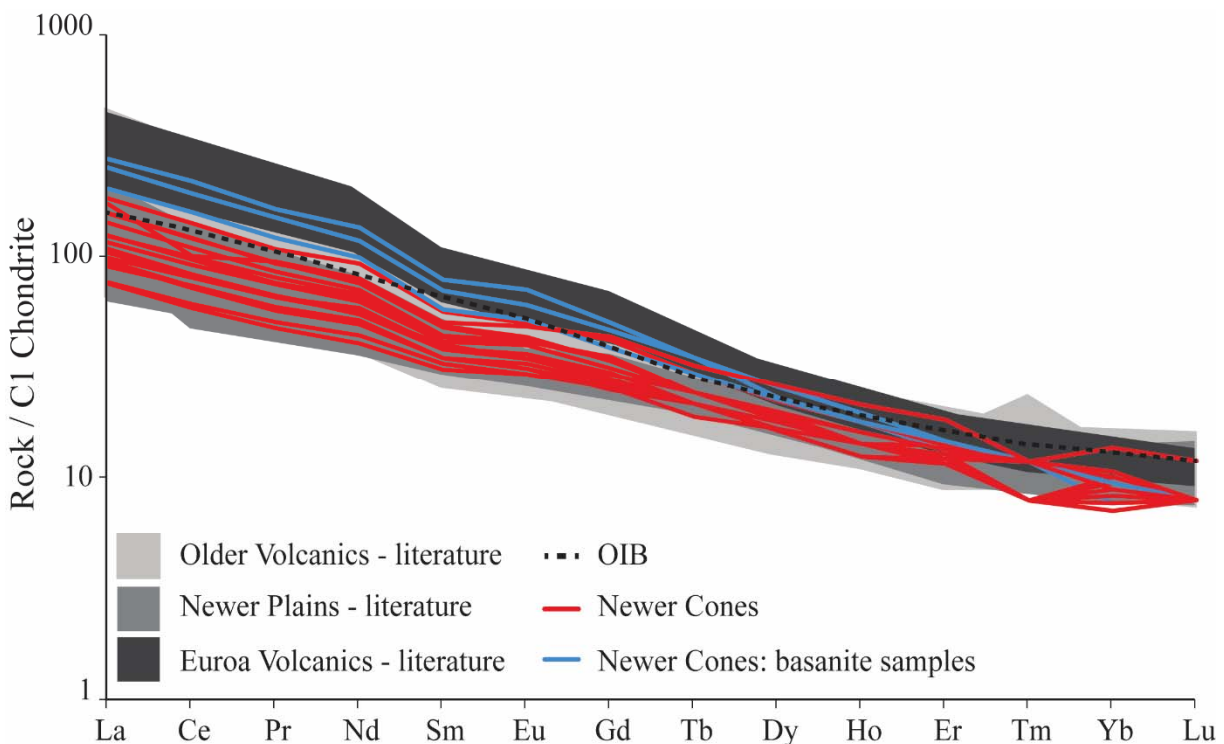


Figure 3.6. Rare earth element (REE) CI chondrite (Sun & McDonough, 1989) normalized patterns. Typical ocean island basalt (OIB; Sun & McDonough, 1989) is indicated with a black dashed line. Basanite samples VIC03, VIC09 and VIC25 are indicated by blue lines. Data sources as in Fig. 2.

## 3.6.3. Sr, Nd and Pb isotopes

Isotope ratios were corrected to initial values using new  $^{40}\text{Ar}/^{39}\text{Ar}$  ages for these samples (Oostingh *et al.*, 2015). For all samples, isotope age correction yields initial values that are indistinguishable from the measured values with differences ranging between 0.00012% and 0.00001% from the analysed isotope composition.

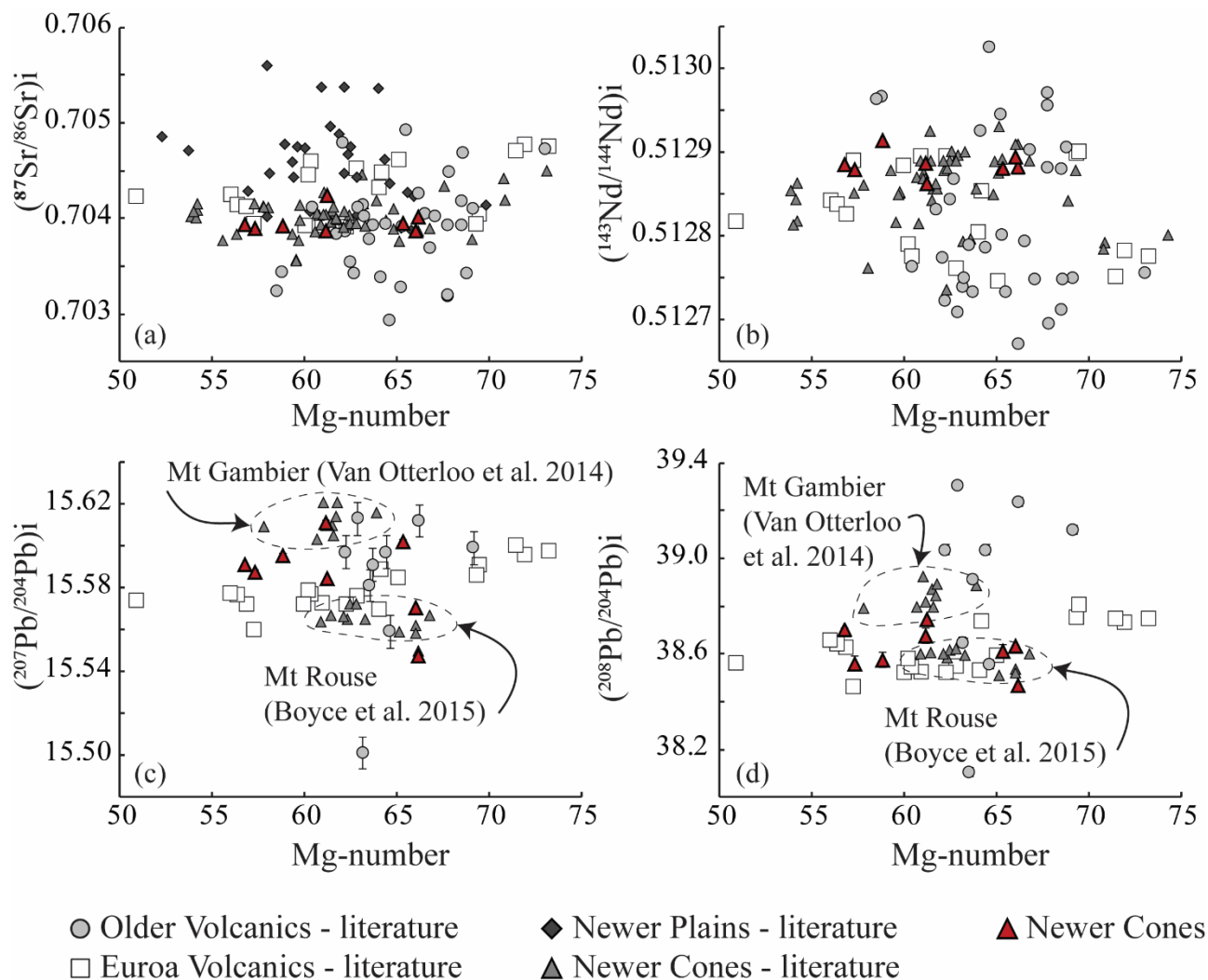


Figure 3.7.  $(^{87}\text{Sr}/^{86}\text{Sr})_i$ ,  $(^{143}\text{Nd}/^{144}\text{Nd})_i$ ,  $(^{207}\text{Pb}/^{204}\text{Pb})_i$  and  $(^{208}\text{Pb}/^{204}\text{Pb})_i$  vs Mg-number [atomic ratio of 100 Mg/(Mg + 0.85\*Fe<sub>tot</sub>)]. All isotope data are corrected to initial values; Newer Cones 500 – 41 ka, Newer Plains 4.6 – 1 Ma, Euroa Volcanics 7 Ma; Older Volcanics 95 – 19 Ma. Error bars ( $2\sigma$ ) are indicated in (c), but are smaller than the symbols for the  $^{87}\text{Sr}/^{86}\text{Sr}$ ,  $^{143}\text{Nd}/^{144}\text{Nd}$  and  $^{208}\text{Pb}/^{204}\text{Pb}$  isotope data. Published Pb isotope data for the Newer Cones are limited to recent studies of Mt Rouse (Boyce *et al.*, 2015) and Mt Gambier (Van Otterloo *et al.*, 2014); the respective fields are indicated in (c) and (d). No major element data are available for the basalts analysed for Pb isotope composition by Cooper & Green (1969). Other data sources are as in Fig. 2.

The samples define a relatively narrow range of  $(^{87}\text{Sr}/^{86}\text{Sr})_i$  ratios from 0.70387 for VIC03 to 0.70424 for VIC25 ( ) for a wide range of Mg-number (Figure 3.7) as well as a narrow range in  $(^{143}\text{Nd}/^{144}\text{Nd})_i$  compositions ranging from 0.51281 to 0.51286.

	Sr ppm	Nd ppm	Pb ppm	$^{87}\text{Sr}/^{86}\text{Sr}$	$^{143}\text{Nd}/^{144}\text{Nd}$	$^{206}\text{Pb}/^{204}\text{Pb}$	$2\sigma$	$^{207}\text{Pb}/^{204}\text{Pb}$	$2\sigma$	$^{208}\text{Pb}/^{204}\text{Pb}$	$2\sigma$
<b>VIC03</b>	1044.3	62.90	5.3	0.70387	0.51284	18.8333	5.95E-06	15.6112	1.23E-03	38.6758	3.13E-02
<b>VIC06</b>	477.0	26.00	2.8	0.70455	0.51278	18.7927	7.32E-06	15.6359	1.17E-02	38.8884	2.88E-02
<b>VIC09</b>	1095.6	54.70	6.7	0.70394	0.51284	18.7441	6.10E-06	15.5909	1.08E-03	38.7035	2.75E-02
<b>VIC16</b>	529.9	24.00	2.1	0.70396	0.51283	18.5334	3.91E-08	15.6019	6.82E-06	38.6134	1.95E-04
<b>VIC17</b>	536.5	23.00	3.4	0.70401	0.51283	18.4525	4.75E-08	15.5472	4.19E-06	38.4706	1.40E-04
<b>VIC18</b>	69.9	25.50	2.3	0.70390	0.51283	18.5041	7.09E-06	15.5876	1.10E-03	38.5615	3.36E-02
<b>VIC21</b>	959.0	43.20	2.8	0.70392	0.51286	18.5348	3.99E-08	15.5952	1.08E-05	38.5757	2.49E-04
<b>VIC25</b>	876.4	46.00	4.0	0.70424	0.51281	18.6453	8.45E-07	15.5846	1.92E-04	38.7449	4.86E-03
<b>VIC29</b>	677.8	31.40	3.1	0.70388	0.51284	18.6072	9.58E-06	15.5706	1.00E-04	38.6349	2.39E-03

Table 3.2 Sr – Nd – Pb isotope data for the Newer Cones



When plotted on a  $(^{87}\text{Sr}/^{86}\text{Sr})_i$  versus  $(^{143}\text{Nd}/^{144}\text{Nd})_i$  diagram, all samples are located on the mantle array (Figure 3.8a), trending towards Bulk Silicate Earth (BSE; Zindler and Hart, 1986). Our samples show high  $(^{207}\text{Pb}/^{204}\text{Pb})_i$  and  $(^{208}\text{Pb}/^{204}\text{Pb})_i$  ratios for a given  $(^{206}\text{Pb}/^{204}\text{Pb})_i$  value; ranging from 15.5472 to 15.6112 and 38.4702 to 38.7449 respectively.  $(^{208}\text{Pb}/^{204}\text{Pb})_i$  ratios show a narrow spread in the data over a wide range of Mg-number values, whereas the  $(^{207}\text{Pb}/^{204}\text{Pb})_i$  and  $(^{206}\text{Pb}/^{204}\text{Pb})_i$  ratios show similar patterns and are slightly more scattered (Figure 3.7). When plotted on the respective  $(^{206}\text{Pb}/^{204}\text{Pb})_i$  versus  $(^{207}\text{Pb}/^{204}\text{Pb})_i$  and  $(^{208}\text{Pb}/^{204}\text{Pb})_i$  diagrams, most of the samples plot above and parallel to the northern hemisphere reference line (NHRL; Figure 3.8b and 3.8c). When plotted on a  $(^{207}\text{Pb}/^{204}\text{Pb})_i$  versus  $(^{143}\text{Nd}/^{144}\text{Nd})_i$  diagram (Figure 3.8d) it can be seen that the Newer Cones trend towards HIMU end-member compositions, whereas the Older Volcanics trend towards EMII.

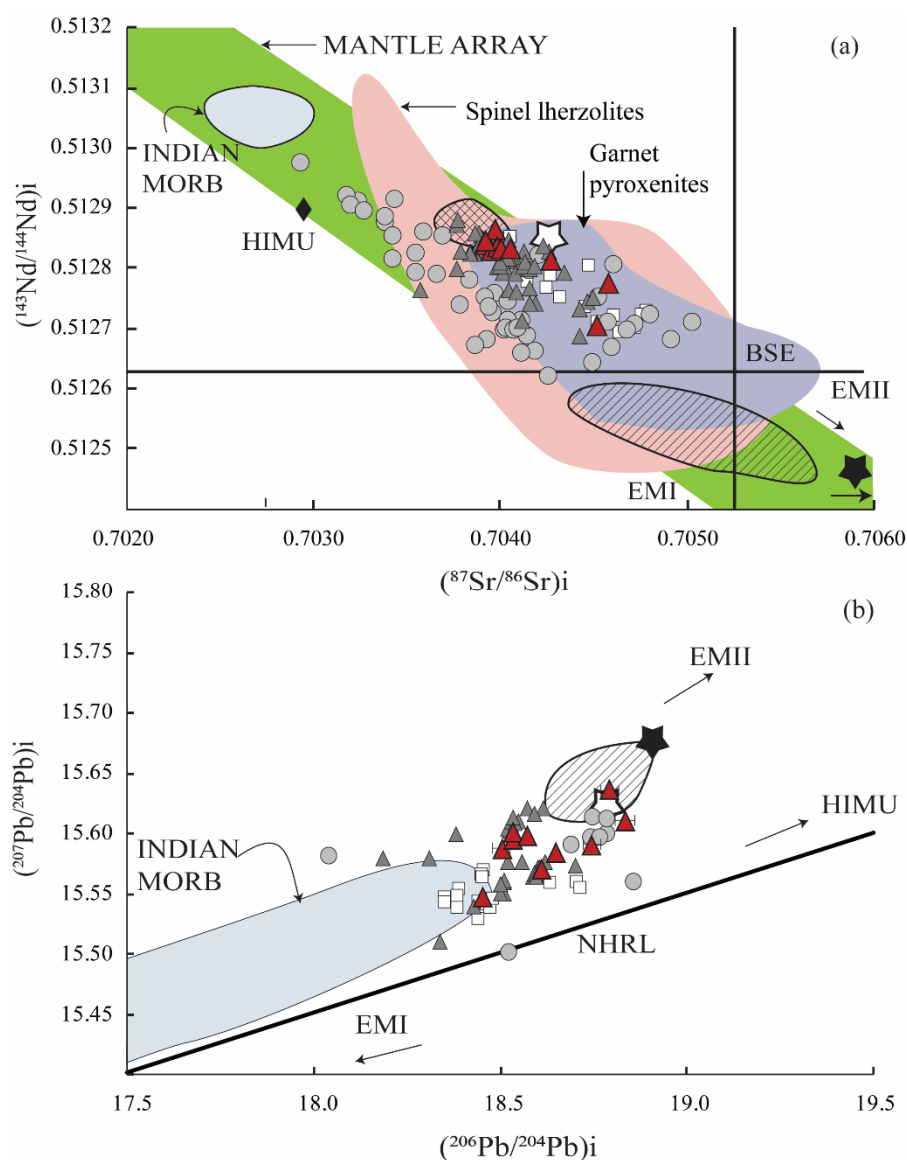
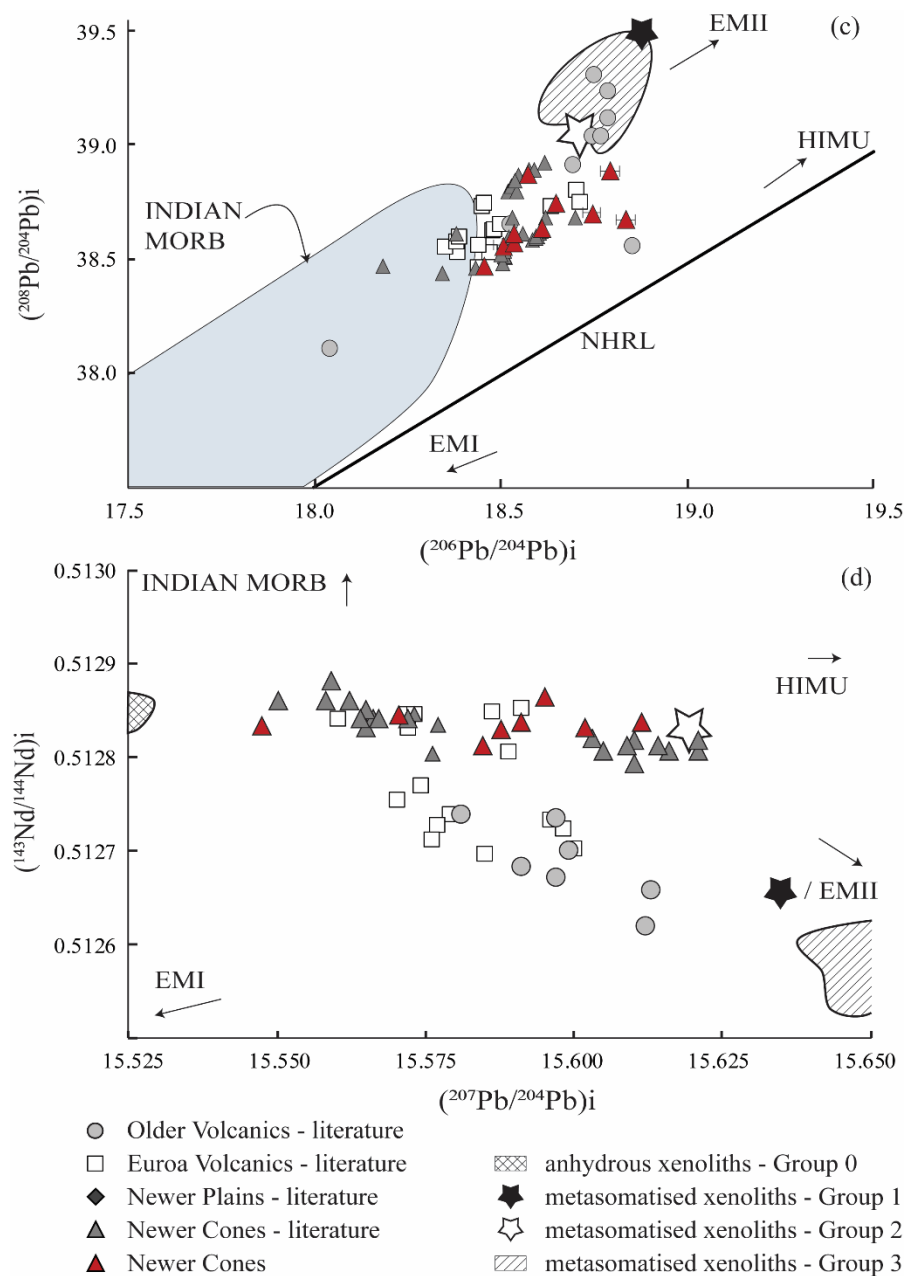


Figure 3.8. (a)  $(^{87}\text{Sr}/^{86}\text{Sr})_i$  vs  $(^{143}\text{Nd}/^{144}\text{Nd})_i$ , showing the mantle array in green and approximate locations of mantle end-members. Indicated are fields for Newer Volcanic Province spinel lherzolite (pink) and garnet pyroxenite (purple) xenoliths (McDonough et al., 1985; Griffin et al., 1988; O'Reilly & Griffin, 1988; Yaxley et al., 1991; Powell et al., 2004) as well as Group 0 anhydrous xenoliths (cross-hatched), Group 1  $\text{CO}_2$  fluid metasomatized (black star), Group 2 alkaline melt metasomatized (white star) and Group 3 carbonatite metasomatized xenoliths (diagonal lines) after Stolz & Davies (1988). (b)  $(^{207}\text{Pb}/^{204}\text{Pb})_i$  vs  $(^{206}\text{Pb}/^{204}\text{Pb})_i$  and (c)  $(^{208}\text{Pb}/^{204}\text{Pb})_i$  vs  $(^{206}\text{Pb}/^{204}\text{Pb})_i$ , indicating fields for xenoliths after Stolz & Davies (1988). NHRL, Northern Hemisphere Reference Line. Newer Cones literature data are from Cooper & Green (1969), Stolz & Davies (1988), Van Otterloo et al. (2014) and Boyce et al. (2015).



(d)  $(^{207}\text{Pb}/^{204}\text{Pb})_i$  vs  $(^{143}\text{Nd}/^{144}\text{Nd})_i$  showing the isotopic variation in the Older Volcanics, Euroa Volcanics and Newer Cones, as well as the isotope composition of various mantle end-members: enriched mantle I (EMI), enriched mantle II (EMII) and HIMU (High- $\mu$ ; high  $^{238}\text{U}/^{204}\text{Pb}$ ) (Stracke et al., 2005), and the isotope compositions of the various groups of mantle xenoliths from Stolz & Davies (1988). Other data sources as in Fig. 2.

### 3.7. Discussion

#### 3.7.1. Geochemical comparison between the Newer Cones and the Older Volcanics, Euroa Volcanics and Newer Plains.

##### 3.7.1.1. Major and trace elements

The Newer Cones data overlap with those for the Older Volcanics and Euroa Volcanics in the alkaline field of the TAS diagram, whereas the Newer Plains show a more sub-alkaline geochemical composition. All series show a wide range in major element compositions, in particular, a negative correlation between  $\text{Al}_2\text{O}_3$  or  $\text{Na}_2\text{O}$  and  $\text{MgO}$  contents and slight positive correlation between  $\text{CaO}$

and MgO content that indicates fractional crystallization of olivine and clino-pyroxene without plagioclase. Similar trends are observed for the Newer Cones, Newer Plains and the Older Volcanics. The Euroa Volcanics are distinct from the other groups showing lower Al<sub>2</sub>O<sub>3</sub> and Na<sub>2</sub>O compositions and higher MgO, TiO<sub>2</sub> and CaO contents, similar to those of the suite of Newer Cones in South Australia (Figure 3.3).

Compared to the Newer Cones, the Euroa Volcanics show an enriched signature for highly and moderately incompatible trace elements, with Rb values up to ~240 ppm and Zr values up to ~605 ppm. Whereas the Newer Plains generally show a restricted range in Mg-number and trace element composition except for some outliers, the Older Volcanics display constant variation with Mg-numbers of 57 – 73 and a wide spread in trace element concentration (Th: 1.4 – 16.1 ppm, Zr: 105 – 523 ppm, Nb: 20 – 208 ppm) except for their narrow range of Rb concentration around 25 ppm (Figure 4). Six Newer Plains samples (40, 42, 212, 300, 300 and F1-111; Price *et al.*, 1997) show extreme La/Nb enrichment of 1.5 – 6 with four of those (40, 42 and 212) also having high Ba/Nb ratios of 23.95 – 63.58, indicative of fluid metasomatism (Price *et al.*, 1997). The other series show a gradual trend with the Older Volcanics having the lowest La/Nb and Ba/Nb ratios (~0.5 and ~6 respectively; Figure 4g), while the Euroa Volcanics overlap with our Newer Cones data having La/Nb of ~0.7 and Ba/Nb of ~8, followed by the Newer Plains which have the most extreme enrichment. All groups show enrichment in Ni (Figure 3.4f) for increasing Mg-number. A major part of the Newer Plains as well as some of the Older Volcanics trend towards the average Continental Crust value (Taylor and McLennan, 1995) on a Ce/Pb versus Nb/U diagram (Figure 3.4h), suggestive of crustal contamination. Older Volcanics and the Euroa Volcanics have very similar OIB-type trace element characteristics, with negative Pb and positive Nb anomalies (Figure 3.5). These anomalies are absent in some of the Newer Plains basalts, which instead show a positive U anomaly for some samples. Figure 3.6 shows that the Older Volcanics and Newer Plains have C1 chondrite normalized REE patterns similar to those of the Newer Cones, whereas the Euroa Volcanics are characterized by higher LREE enrichment.

#### 3.7.1.2. Sr, Nd and Pb isotopes

Strontium and Nd data for the Newer Cones overlap with published data (Figure 3.7a – b). Our Pb isotope data overlap with the recently published data for Mt Rouse (Boyce *et al.*, 2015), an individual volcanic centre of the Newer Cones. However, Pb isotope data for Mt Gambier show slightly higher values (Van Otterloo *et al.*, 2014). So far, isotope data for the Newer Plains are limited to (<sup>87</sup>Sr/<sup>86</sup>Sr)<sub>i</sub> only (Price *et al.*, 1997), which shows higher isotopic ratios as compared to the other series for a wide

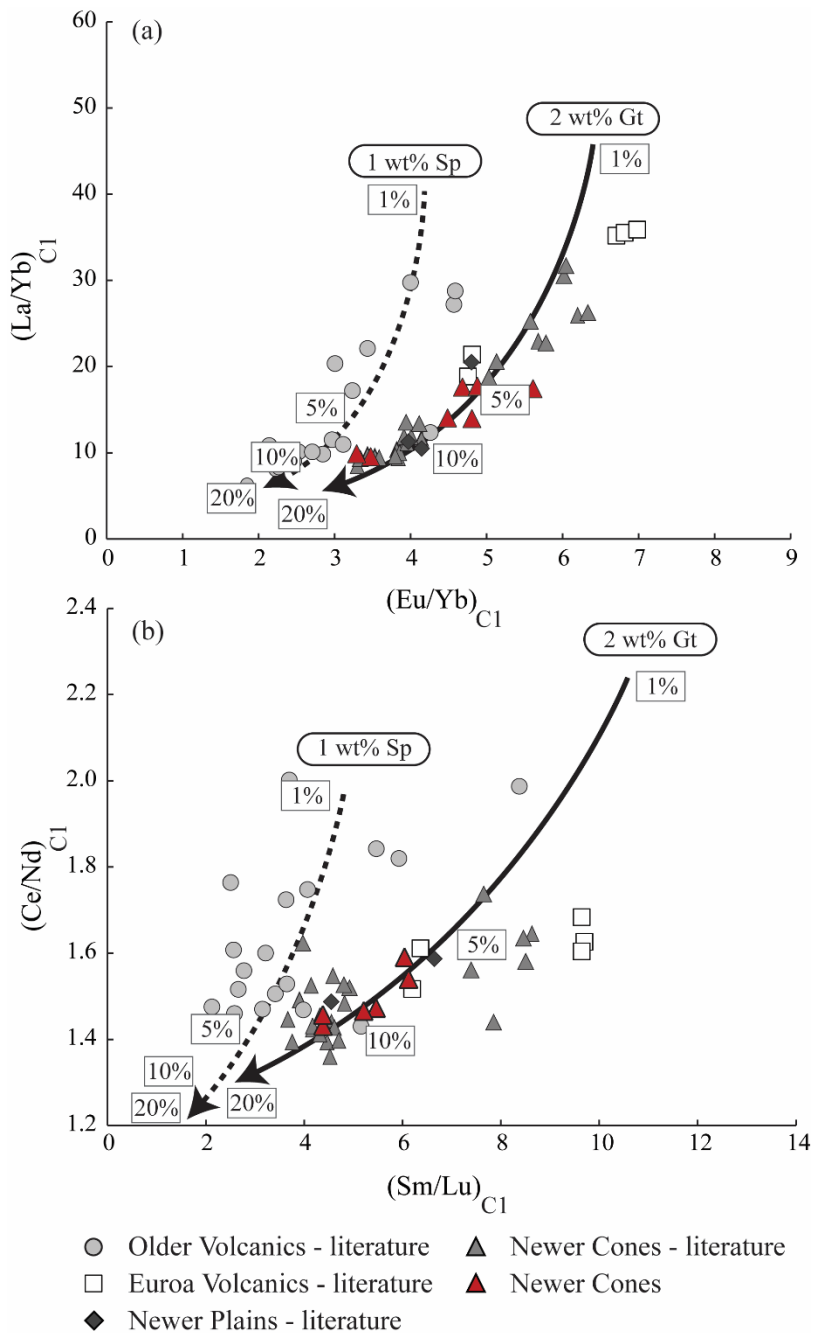


Figure 3.9. Models for trace element fractionation during nonmodal partial melting of Newer Volcanic Province xenolith compositions (Griffin et al., 1988; Stolz & Davies, 1988; Yaxley et al., 1991) with either added garnet (continuous line) or added spinel (dashed line), using the equation from Shaw (1970). Only basalt samples are plotted for which less than 5% fractional crystallization is inferred. Compositions are normalized to chondrite after Sun & McDonough (1989). Trace element distribution coefficients are from McKenzie & O’Nions (1983). Starting modal composition: continuous line: 56 wt % olivine, 25 wt % orthopyroxene, 11 wt % clinopyroxene, 2 wt % garnet, 6 wt % amphibole and  $La/Yb = 11$ ; dashed line: 56 wt % olivine, 25 wt % orthopyroxene, 11 wt % clinopyroxene, 1 wt % spinel, 7 wt % amphibole and  $La/Yb = 15$ . Melting mode modified from Walter (1998): ol 0.08, opx -0.19, cpx 0.81, gt 0.15 and sp 0.15. Data sources as in Fig. 2. Numbers in rectangles indicate per cent melting.

range in Mg-number (Figure 3.7a). Our Newer Cones data generally show a narrower range in Sr, Nd and Pb isotope compositions compared to those of the Older Volcanics and Euroa Volcanics (Figure 3.7a-d). These two series show more scatter than our new data but none of the series display an obvious trend in the Mg-number versus initial isotopic ratios plots (Figure 3.7a-d). As observed by Price et al. (2014), all series overlap on the mantle array in a  $(^{87}Sr/^{86}Sr)_i$  versus  $(^{143}Nd/^{144}Nd)_i$  isotope diagram, with the Older Volcanics defining a steeper slope (Figure 3.8a). There is no obvious correlation with trace element signatures and isotope variation, as the difference in Sr-Nd isotope trends for the Older Volcanics is independent of Ce/Pb and Nb/U ratio, as are the high Sr isotope

values for the Newer Plains. Pb isotope data for our data display a parallel trend along the NHRL that is also observed for the Older Volcanics and Euroa Volcanics (Figure 3.8b and 3.8c). A  $(^{207}\text{Pb}/^{204}\text{Pb})_i$  versus  $(^{143}\text{Nd}/^{144}\text{Nd})_i$  diagram (Figure 3.8d) shows that the Older Volcanics, Euroa Volcanics and Newer Cones data trend towards xenoliths of different isotopic composition (Stolz and Davies, 1988), indicative of a heterogeneous source.

### 3.7.2. Petrogenesis

#### 3.7.2.1. Partial melting

Distinct isotope and trace element compositions differentiate the Older Volcanics from the Euroa Volcanics and the Newer Cones and Newer Plains series, as illustrated by the different trends between the series on bivariate REE ratio diagrams (Figure 3.9a and b). Whereas the Euroa Volcanics and Newer Cones and Newer Plains show a narrow range in LREE/MREE  $((\text{La}/\text{Sm})_{\text{C1}}$  of 2.5 – 5) and high MREE/HREE  $((\text{Sm}/\text{Yb})_{\text{C1}}$  of 3 – 9.5), the Older Volcanics show a slightly wider range in LREE/MREE  $((\text{La}/\text{Sm})_{\text{C1}}$  of 2.5 – 6) and lower MREE/HREE  $((\text{Sm}/\text{Yb})_{\text{C1}}$  of 2 – 6) values. Trace element behaviour in all series is independent of Mg-number variations (Figure 3.4) and therefore, the observed trends cannot be explained by either fractional crystallization or contamination processes. On the contrary, the different trends observed among the Cretaceous and Cainozoic intraplate basalts of south eastern Australia are most likely caused by subtle variations of the melting modalities of their respective sources.

To test the melting conditions, we have used the standard equation from Shaw (1970) which describes trace element distribution during partial melting. The model was applied only to samples with less than 5 % fractional crystallization. A wide range of published trace element concentrations for peridotite xenoliths from the NVP (Foden *et al.*, 2002; Frey and Green, 1974; O'Reilly and Griffin, 1984; Yaxley *et al.*, 1997) was used to constrain the composition of the potential initial source. We found that the trace element distribution patterns of the Newer Cones, Newer Plains and Euroa Volcanics are best represented by up to ~ 15% batch melting of a hydrated, garnet-bearing lherzolite source with a modal composition of 57 wt% olivine, 25 wt% orthopyroxene, 11 wt% clinopyroxene, 6 wt% amphibole and 2 wt% garnet (La: 0.26 ppm, La/Yb: 15, La/Sm: 2). However, the Older Volcanics are better represented by smaller degrees (5 – 10%) of batch melting of a hydrated, spinel-bearing lherzolite source with a modal composition of 55 wt% olivine, 25 wt% orthopyroxene, 11 wt% clinopyroxene, 8 wt% amphibole and 1 wt% spinel (La: 0.35 ppm, La/Yb: 15, La/Sm: 1; Figure 3.9a and b). These results indicate that over time, the mantle source beneath south east Australia

became more enriched in MREE, and degrees of partial melting as well as depth of melting slightly increased. These degrees of partial melting are slightly higher than those suggested for different intraplate volcanic centres in similar settings, such as, for example, 5 – 7% for lava shields at Jeju Island volcanic field in Korea (Brenna *et al.*, 2010) and 2 – 3% for alkaline basalts in the Auckland Volcanic field (McGee *et al.*, 2011). It is important to note that for this modelling we have assumed that the source region is predominantly homogeneous; however, trends in isotope variation diagrams are an indication that source heterogeneity might have played an important role in the petrogenesis of south eastern Australian intraplate basalts. Therefore, the degrees of partial melting found for all series most likely indicate maximum values.

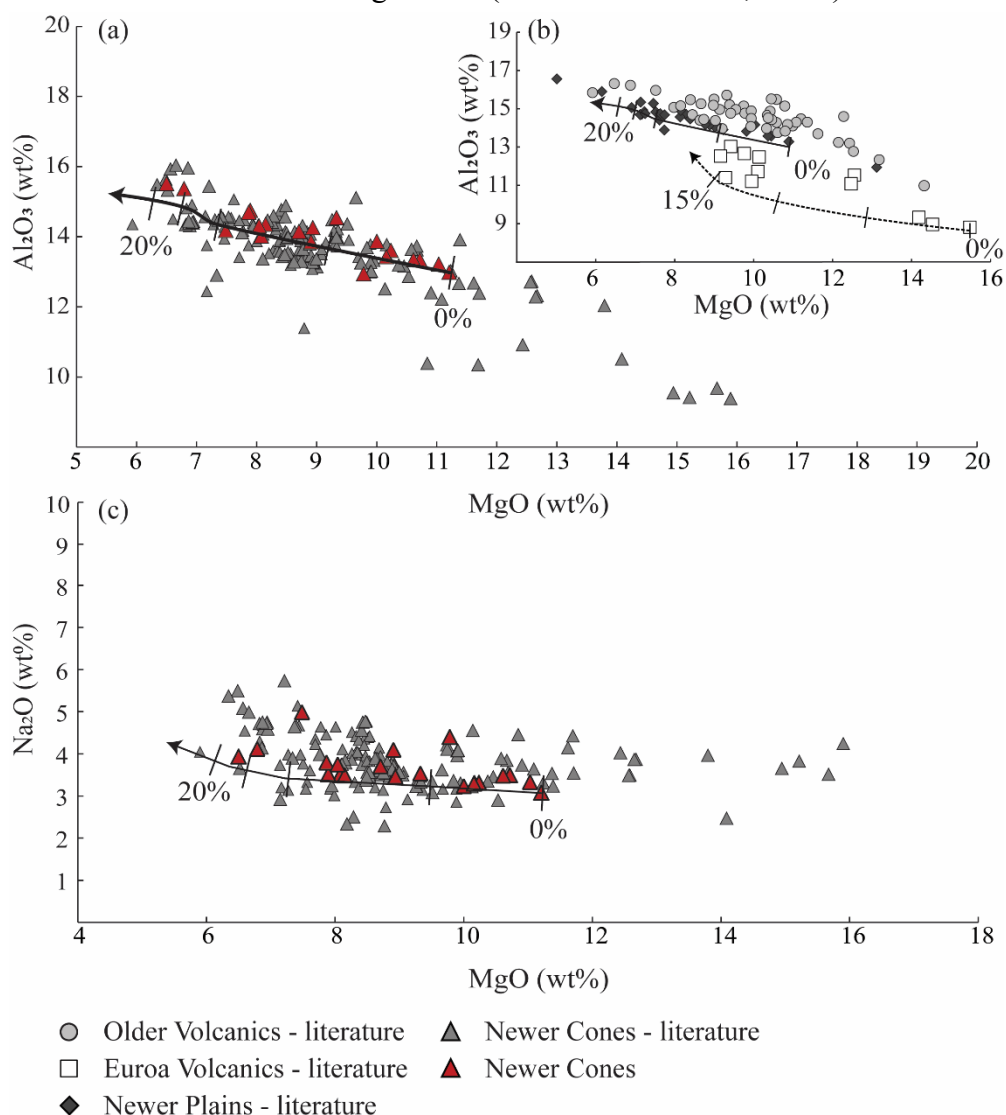
### 3.7.2.2. Fractional crystallization

Covariation on major element variation diagrams as well as parallel REE patterns on chondrite (C1) normalized REE diagrams suggests that all series might have undergone fractional crystallization.

We used the MELTS algorithm (Ghiorso and Sack, 1995) to test this

Figure 3.10. MELTS (Ghiorso & Sack, 1995) modelling results for (a) and (c) the Newer Cones and (b) the Older Volcanics, Euroa Volcanics and Newer Plains. Data sources as in Fig. 2. Continuous lines represent isobaric (1 kbar) cooling (from 1200 to 800°C) of a dry magma,  $fO_2 = QFM + 1$ ; dashed line represents isobaric (1 kbar) cooling (from 1200 to 800°C) of a dry magma,  $fO_2 = QFM + 2$ .

Tick marks represent 5% steps.



hypothesis for the Newer Cones sample suite and further quantify the extent of fractional crystallization for all series. We have used model parameters for isobaric cooling at low pressure (1 kbar) from 1200 to 800°C [ $fO_2 = \text{QFM}$  (quartz – fayalite – magnetite)] using our least differentiated sample VIC33 (MgO = 11.2 wt%; Ni = 277 ppm, Cr = 367 ppm) as starting composition. Figure 3.10a shows that the magmas represented by the Newer Cones basalts could have been generated by up to 20% fractional crystallization of olivine and clino-pyroxene. This process led the remaining liquid to be progressively enriched in  $Al_2O_3$ . A few other Newer Cones samples previously studied have probably undergone similar amounts of fractional crystallization, but were potentially generated from a more primitive initial composition. The Older Volcanics as well as the Newer Plains show similar trends to the Newer Cones on MgO versus  $Al_2O_3$  diagrams, and these can also be explained by up to 20% fractional crystallization using physical conditions similar to those applicable to the Newer Cones (isobaric cooling at low pressure (1 kbar) from 1200 to 800°C,  $fO_2 = \text{QFM}$ ). The Euroa Volcanics show a different trend, possibly because of plagioclase crystallization in the more evolved melts. These rocks have high MgO contents, however, olivine compositions are in good agreement with minerals that crystallized in equilibrium with liquids having compositions similar to bulk rock analyses of these rocks, indicating that these rocks are unlikely to be cumulates (Paul *et al.*, 2005). MELTS modelling is compatible with these rocks being formed in a slightly more reducing environment ( $fO_2 = \text{QFM} + 2$ ) using melting conditions similar to those applied in other cases (isobaric at 1 kbar, 1200 to 800°C). However, deviation from the modelled fractionation trend for some Euroa samples suggests that these results are indicative only. Paul *et al.* (2005) reported the presence of leucite in some of the most primitive samples, which could indicate derivation of the Euroa Volcanics from a more alkaline-rich source, or the generation of under-saturated melts by a lower degree of melting.

#### 3.7.2.3. Crustal contamination

The basement below South Australia and Victoria is both complex in structure as well as stratigraphy, as it contains fragments of Neoproterozoic continental crust incorporated into eastward younging Palaeozoic subduction-accretionary systems. Furthermore, it includes Cambrian – Ordovician oceanic boninitic and MORB-type tholeiitic volcanic rocks as well as deep-ocean sedimentary rocks and arc-related volcanic rocks (Cayley *et al.*, 2011). McBride *et al.* (2001) suggested on the basis of osmium isotopes that the Newer Plains ( $^{187}\text{Os}/^{188}\text{Os}$ :  $0.18096 \pm 52$  to  $0.4456 \pm 22$ ) basalts might have been crustally contaminated (upper continental crust having much higher  $^{187}\text{Os}/^{188}\text{Os}$  of approximately 1.4 based on a  $^{187}\text{Re}/^{188}\text{Os}$  isotope ratio of 34.4; Peucker-Ehrenbrink and Jahn (2001)), in contrast to the Newer Cones which display  $^{187}\text{Os}/^{188}\text{Os}$  ratios compatible with a derivation from an

uncontaminated OIB-like source ( $^{187}\text{Os}/^{188}\text{Os}$  of  $0.13423 \pm 33$  and  $0.13677 \pm 37$ ). A narrow range of ( $^{87}\text{Sr}/^{86}\text{Sr}$ )<sub>i</sub> compositions over a wide range of Mg-number (73 – 54) and Ce/Pb and Nb/U ratios similar to OIB and MORB (Figure 3.4) shows that most of the Newer Cones and Euroa Volcanics are indeed unlikely to have been affected by crustal contamination. On the other hand, negative covariation between Sr isotopes and Sr element concentration as well as non-OIB or MORB Ce/Pb and Nb/U ratios (Hofmann *et al.*, 1986) for the Older Volcanics, Newer Plains and one Newer Cones sample (VIC06) suggest that contamination by upper or lower continental crust might have affected at least some of these basalts.

	<b>Thermal parameters</b>			
	<i>Upper Crust</i>	<i>Lower Crust</i>		
Magma liquidus temperature, $T_{l,m}$	1280°C	1320°C	Crystallization enthalpy, $\Delta h_{c_{ry}}$ (J/kg)	396000
Magma initial temperature, $T_m^0$	1280°C	1320°C	Isobaric specific heat of magma, $C_{p,m}$ (J/kg per K)	1484
Assimilant liquidus temperature, $T_{l,a}$	1000°C	1100°C	Fusion enthalpy, $\Delta h_{fus}$ (J/kg)	270000
Assimilant initial temperature, $T_a^0$	300°C	600°C	Isobaric specific heat of assimilant, $C_{p,a}$ (J/kg per K)	1370
Solidus temperature, $T_s$	900°C	950°C		
Equilibrium temperature, $T_{eq}$	980°C	980°C		
	<b>Compositional parameters</b>			
	<i>Newer Cones</i>		<i>Newer Plains</i>	
	<i>Upper Crust</i>	<i>Lower Crust</i>	<i>Upper Crust</i>	<i>Lower Crust</i>
	Sr	Sr	Sr	Sr
Magma initial conc. (ppm), $C_m^0$	1095.6	1095.6	718	718
Magma isotope ratio, $\epsilon_m$	0.70394	0.70394	0.70415	0.70415
Magma trace element distribution coefficient, $D_m$	1.5	1.5	1.5	1.5
Enthalpy of trace element distribution coefficient, $\Delta H_m$	-	-	-	-
Assimilant initial conc. (ppm), $C_a^0$	350	230	350	230
Assimilant isotope ratio, $\epsilon_a$	0.722	0.7100	0.722	0.7100
Assimilant trace element distribution coefficient, $D_a$	1.5	0.05	1.5	0.05
Enthalpy of trace element distribution reaction, $\Delta H_a$	-	-	-	-

Table 3.3. Input parameters for EC-RAxFC modelling, thermal parameters and standard upper and lower crustal composition after Bohrsen and Spera (2002)

We have used the energy-constrained recharge, assimilation and fractional crystallization (EC-RAxFC) algorithm (Bohrson and Spera, 2001; Spera, 2001) to investigate the possible extent of crustal assimilation on these potentially contaminated rocks. Due to the complexity of the crust as outlined above, we have used values for average upper and lower continental crust (Taylor and



McLennan, 1995) instead of detailed compositions for each individual structural zone. Table 3.3 provides the thermal and compositional input parameters used for the modelling.

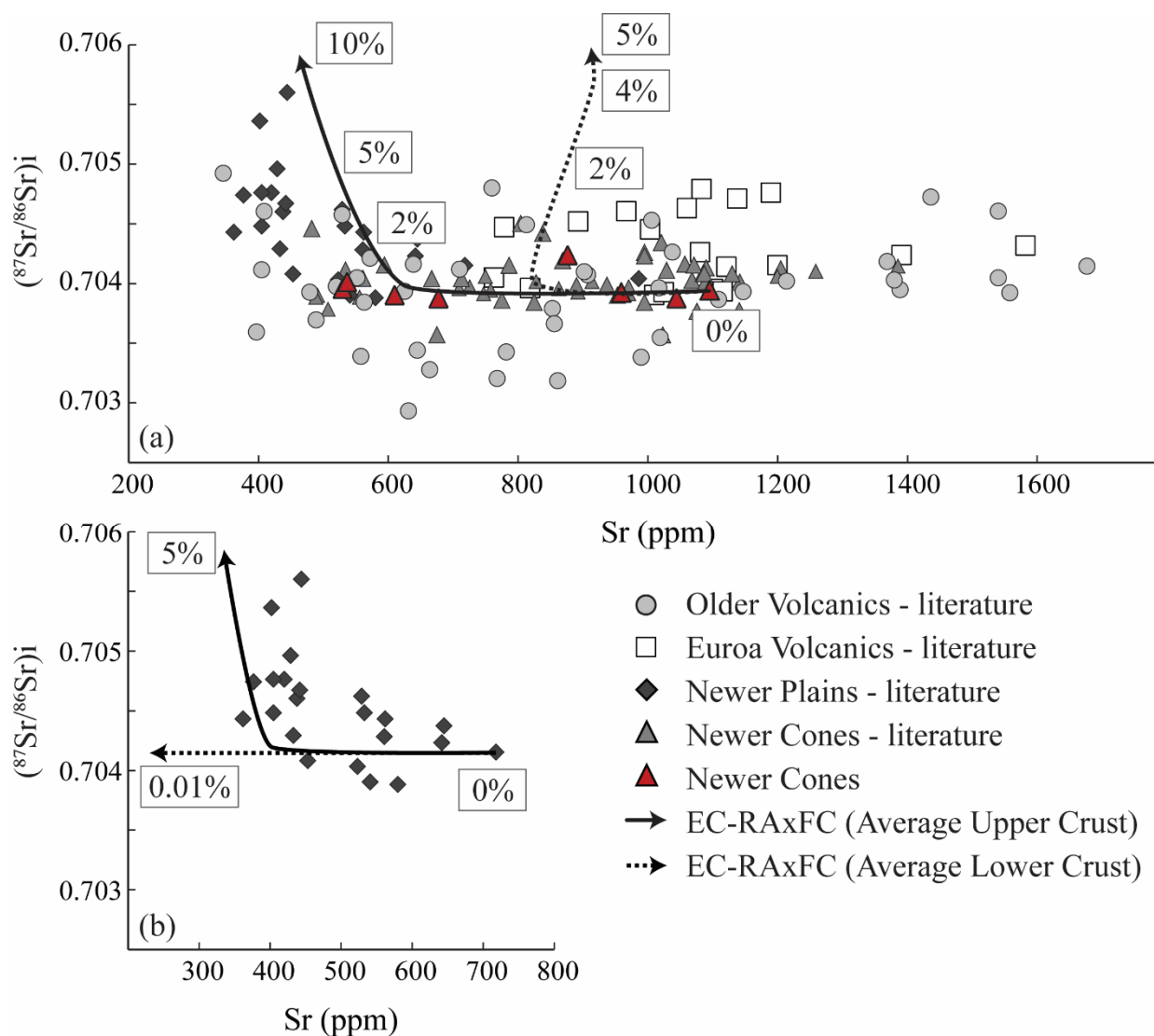


Figure 3.11. (a) Sr (ppm) vs  $^{87}\text{Sr}/^{86}\text{Sr}$  for all Newer Cones samples showing EC-RAXFC modelling using input parameters as in Table 3.3. (b) Enlarged section of (a) showing EC-RAXFC modelling results for the Newer Plains (Price et al., 1997, 2014) using input parameters as in Table 3.3. The continuous and dashed lines represent assimilation and fractional crystallization of average upper and lower crust (Taylor & McLennan, 1995), respectively.

The Newer Cones do not show any correlation between Sr and  $(^{87}\text{Sr}/^{86}\text{Sr})_i$  other than that expected of fractional crystallization, suggesting that crustal contamination was either absent or well below 1% (Figure 3.11a). The Euroa Volcanics show a similar narrow range in Sr isotope composition over a wide range of Sr element concentrations. Any covariation in Sr isotope composition versus Sr element concentration is also absent for the Older Volcanics. However,  $(^{87}\text{Sr}/^{86}\text{Sr})_i$  values for the Newer Plains roughly increase for decreasing Sr concentration, which can be satisfactorily modelled by up to 5%

assimilation of average upper continental crust using the most primitive composition among these basalts (Figure 3.11b). Whereas the majority of the Newer Plains Sr isotope composition is suggestive of crustal assimilation, as they show high Sr initial ratios, most of the Older Volcanics, Euroa Volcanics and the majority of the Newer Cones appear to be uncontaminated, as mentioned above. Their initial Sr, Nd and Pb isotope ratios are likely reflecting mantle source characteristics. Whereas a slightly low Nb/U ratio for VIC06 is suggestive of significant crustal contamination, depletion in U for VIC14 is indicative of potential fluid interaction and thus alteration; these samples are therefore omitted from the following discussion.

### 3.7.3. Mantle source compositions

#### 3.7.3.1. Identifying potential mantle end-members

Even though agreement exists over the involvement of partial melting and open (assimilation) and closed (fractional crystallization) processes contributing to the geochemical characteristics of the basalts of the Older Volcanics, Euroa Volcanics and Newer Plains and Newer Cones, the possible contribution of the lithosphere and asthenosphere in terms of mantle sources remains contentious. Whereas some authors favour partial melting of asthenosphere, either of homogenous composition (Paul *et al.*, 2005) or changing over time (Zhang *et al.*, 1999), others argue for melting of the lithospheric mantle and entrainment of this melt into the convecting asthenosphere (Price *et al.*, 1997, 2014).

The south eastern Australian lithospheric mantle has been extensively sampled with spinel lherzolites and garnet pyroxenites, which have undergone up to three metasomatic events, being represented in xenolith suites of many of the Newer Cones (Griffin *et al.*, 1988; McDonough and McCulloch, 1987; O'Reilly and Griffin, 1988; Powell *et al.*, 2004; Stolz and Davies, 1988; Yaxley *et al.*, 1991). On a ( $^{87}\text{Sr}/^{86}\text{Sr}$ )<sub>i</sub> versus ( $^{143}\text{Nd}/^{144}\text{Nd}$ )<sub>i</sub> isotope diagram (Figure 3.8a) the Newer Cones and the Euroa Volcanics overlap with isotope compositions of south east Australian spinel lherzolites or garnet pyroxenites. Some samples of the Older Volcanics have less radiogenic ( $^{87}\text{Sr}/^{86}\text{Sr}$ )<sub>i</sub> compositions trending toward Indian MORB compositions (Figure 3.8a). This suggests that a mantle source such as Indian MORB asthenosphere can be considered as one of the end-members for these rocks, which is in agreement with our trace element modelling (Figure 3.9).

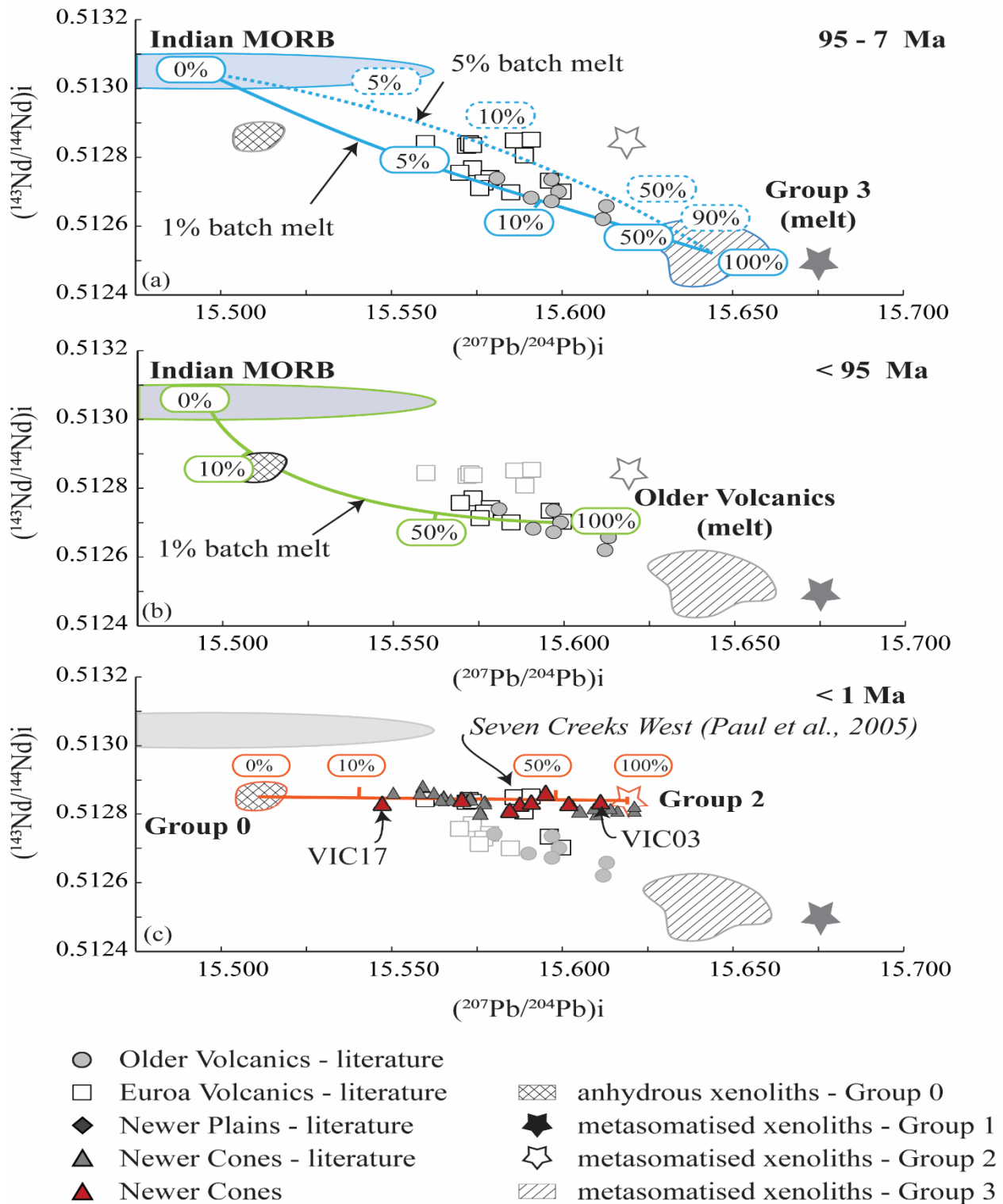


Figure 3.12.  $(^{207}\text{Pb}/^{204}\text{Pb})_i$  vs  $(^{143}\text{Nd}/^{144}\text{Nd})_i$  for samples interpreted to represent magmas unaffected by crustal assimilation showing: (a) calculated mixing line (Vollmer, 1976) between Indian MORB-source mantle and melts derived by 1% (blue continuous line) and 5% (blue dashed line) partial melting of Group 3 xenoliths; (b) calculated mixing line between Indian MORB-source mantle and the most primitive sample (Mg-number = 67) of the Older Volcanics (green continuous line); (c) calculated mixing line between Group 0 and Group 2 xenoliths. It should be noted that the Euroa Volcanics plot in two groups. The Seven Creek West samples (Paul et al., 2005) are indicated.

As far as we are aware, only Stolz and Davies (1988) have presented Pb isotope data on the xenoliths of the NVP and these have heterogeneous compositions, which are representative of the upper mantle beneath the region. These authors have subdivided spinel lherzolites from Mount Gnotuk and Lake Bullenmerri into four different suites based on their trace element and isotope compositions: Group 0: depleted, anhydrous xenoliths with Pb isotope composition similar to the isotopically distinct Indian MORB (Rehkamper and Hofmann, 1997); Group 1: enriched, anhydrous xenoliths probably metasomatised by CO<sub>2</sub>-rich fluids with Pb isotope composition trending towards EMII; Group 2: hydrous xenoliths probably metasomatised by interaction between alkaline magmas and the depleted anhydrous xenoliths with Pb isotope composition similar to Group 3, but having lower Sr isotope and higher Nd isotope compositions respectively, and Group 3: hydrous xenoliths metasomatised later by fluids originating from deeper levels in the mantle with Pb isotope composition similar to Group 2, but having higher Sr isotope and lower Nd isotope compositions (Stolz and Davies, 1988). The metasomatic agent for this last group is suspected to be calci-carbonate fluid (Stolz and Davies, 1988), and Sr-Nd isotope compositions of this group overlap with those of Group B of Powell et al (2004) which is interpreted as having undergone carbonatite metasomatism. Price et al (2014) also indicated the potential for 1% calci-carbonate fluid to have been added to depleted mantle to generate the range of Older Volcanics with distinctive negative K anomalies.

The difference between the three basalt groups is expressed in a (<sup>207</sup>Pb/<sup>204</sup>Pb)<sub>i</sub> versus (<sup>143</sup>Nd/<sup>144</sup>Nd)<sub>i</sub> diagram, where there is a clear distinction between the trends of the Newer Cones, Euroa Volcanics and Older Volcanics (Figure 3.12a). As a consequence, we propose that the isotopic compositions of the Older Volcanics and part of the Euroa Volcanics can be explained by binary mixing between a mantle source similar to the depleted asthenosphere source of the Indian MORBs and a metasomatised lithospheric mantle represented by Group 3 xenoliths. In contrast, the isotopic signature of the Newer Cones is more consistent with binary mixing between mantle sources similar to the Group 0 and Group 2 xenoliths. We modelled this mixing using the equation of Vollmer (1976). Figure 3.12a (blue lines) shows that the range of Older Volcanics isotope compositions can be generated by mixing of Indian MORB type melts (<sup>143</sup>Nd/<sup>144</sup>Nd = 0.51303, <sup>207</sup>Pb/<sup>204</sup>Pb = 15.486 (taking average compositions for Indian MORB reported in Stracke et al., 2003), [Nd] = 9 ppm and [Pb] = 0.6 ppm (Sun and McDonough, 1989)) and small degree partial melt derived from the Group 3 xenoliths (<sup>143</sup>Nd/<sup>144</sup>Nd = 0.512523, <sup>207</sup>Pb/<sup>204</sup>Pb = 15.6424 (Stolz and Davies, 1988)). Trace element concentrations used for mixing modelling of the Group 3 xenoliths were [Nd] = 167.78 ppm and [Pb] = 13.68 ppm and Nd = 85.24 ppm and Pb = 3.17 ppm as derived from calculations on 1% and 5%

batch melting of the most primitive Group 3 xenolith (MgO = 41.02 wt%, [Ni] = 2072 ppm, [Cr] = 5967 ppm) respectively (Stolz and Davies, 1988). It is shown that Older Volcanics with low  $^{143}\text{Nd}/^{144}\text{Nd}$  isotope ratio for a given  $^{207}\text{Pb}/^{204}\text{Pb}$  isotope ratio can be derived from a source resulting from Indian MORB to which 5 to 10% of only small amounts of Group 3 melts are added (1% partial melting from the original peridotite), whereas the Older Volcanics with slightly higher  $^{143}\text{Nd}/^{144}\text{Nd}$  isotope ratio for a given  $^{207}\text{Pb}/^{204}\text{Pb}$  isotope ratio are more likely derived from a source resulting from mixing of Indian MORB and up to 40% Group 3 melts (5% partial melting).

Stolz and Davies (1988) Group 0 depleted, anhydrous xenoliths have Pb isotope compositions similar to Indian MORB, but have slightly higher and lower Sr and Nd isotope compositions respectively. We propose that subsequent interaction of Indian MORB melts with the alkaline melts that generated the Older Volcanics could have generated Group 0 xenoliths. Mixing between the most primitive of the Older Volcanics [ $(^{143}\text{Nd}/^{144}\text{Nd})_i = 0.5127$ ,  $(^{207}\text{Pb}/^{204}\text{Pb})_i = 15.599$ , Mg-number = 69 (Price *et al.*, 2014)] and Indian MORB with composition as above shows that adding approximately 10% alkaline melt to Indian MORB lowers the Nd isotope composition towards that of the Group 0 xenoliths (Figure 3.12b – green line).

The Newer Cones, however, show contrasting behaviour having a very narrow range in Nd isotope compositions for a given  $(^{207}\text{Pb}/^{204}\text{Pb})_i$  and forming a trend between Group 0 and Group 2 xenoliths. Mixing between Group 0 ( $^{143}\text{Nd}/^{144}\text{Nd} = 0.51285$ ,  $^{207}\text{Pb}/^{204}\text{Pb} = 15.507$ , [Nd] = 1.36 ppm and [Pb] = 0.019 ppm) and Group 2 ( $^{143}\text{Nd}/^{144}\text{Nd} = 0.512841$ ,  $^{207}\text{Pb}/^{204}\text{Pb} = 15.619$ , [Nd] = 4.86 ppm and [Pb] = 0.059 ppm (Stolz and Davies, 1988) shows that VIC17 can be generated by only 10% addition of Group 2 into the depleted anhydrous mantle, whereas VIC03 can be generated by higher degrees of mixing (~80 % of Group 2; Figure 3.12c). There is no direct evidence that carbonatite metasomatised xenoliths (Group 3) have had much influence in the generation of the Newer Cones basalts.

The Euroa Volcanics are divided into two groups, where the majority approximately follows the trend of the Older Volcanics (Figure 3.12a), whereas the data for samples of Seven Creeks West (Paul *et al.*, 2005) overlap with our data on the Newer Cones (Figure 3.12c). It would be interesting to measure the age of the samples from the Seven Creeks as an old age would imply that they originated from the same process as the Older Volcanics, as described above, whereas ages similar to the Newer Cones would indicate that they derived from mixing between Group 0 and Group 2 lithospheric mantles.

In summary, whereas the 95 – 19 Ma Older Volcanics as well as part of the Euroa Volcanics have compositions indicating basalt generation from a source with isotope characteristics similar to that of a mixture between Indian MORB and small degrees of partial melt derived from Group 3 (carbonatite metasomatised) xenoliths, the (< 1 Ma) Newer Plains and perhaps the remainder of the Euroa Volcanics show basalt generation that can be explained entirely by melting of a distinctively different suite of source materials comprising modified Indian MORB (Group 0) and alkaline-melt metasomatised xenoliths (Group 2). Our model compares well, and is an extension of the model by Price *et al.* (2014) who suggested mixing of 1 % calci-carbonate fluid to the depleted mantle to generate the geochemical signature of the Older Volcanics.

#### 3.7.4. Geodynamics

Recent teleseismic tomography (Davies and Rawlinson, 2014), using variations in P-wave speed, revealed the presence of a low-velocity anomaly in the upper mantle which spatially corresponds to the surface extent of the NVP. Such an anomaly is indicative of the presence of elevated temperatures (mantle plume) and/or a region of partial melt in the upper mantle (Davies and Rawlinson, 2014), the latter hypothesis being preferred due to the limited topographic response in the region (Demidjuk *et al.*, 2007). The U/Th disequilibria showing a  $^{230}\text{Th}$  excess of 12-57 % (Demidjuk *et al.*, 2007) are suggestive of dynamic melting in the upwelling upper asthenosphere rather than static batch melting within the lithosphere, an interpretation that is supported by magnetotelluric sounding that provides evidence for decompression melting in the upper asthenosphere (Aivazpourporgou *et al.*, 2015). It is thought that this upwelling is triggered by 3D thickness variations of the lithosphere, creating edge driven convection (King and Anderson, 1998). Rapid plate movement from 40 Ma onward after the separation of Antarctica and Australia (Veevers, 1986) resulted in a fast, northward plate movement of 6.5 cm/year (Sella *et al.*, 2002). As this plate movement is perpendicular to a step in lithospheric thickness (Demidjuk *et al.*, 2007) and plate movement is > 1 cm/year; edge driven convection with shear resulting in shear driven upwelling is postulated to be the geodynamic cause of NVP magmatism (Conrad *et al.*, 2011). Convection cell sizes on the order of 150 – 200 km are observed during edge driven convection with shear driven upwelling (King and Anderson, 1998), which is comparable to the spatial extent of volcanism in south east Australia. Recent edge driven convection modelling for the Moroccan Cainozoic volcanic province (Kaislaniemi and Van Hunen, 2014) shows that upwelling mantle; 1) facilitates decompression melting removing the hydrous mantle components; and 2) erodes the bottom of the mantle entraining the residual depleted lithosphere. Furthermore, this study found that edge driven convection with shear produces convection rolls with axes perpendicular to lithosphere thickness steps. The complex lithosphere configuration beneath

Victoria, with a stacked alternation of continental (Delamerian) and continental/oceanic (Lachlan) crust as well as a locally constrained continental section of the Selwyn block within the Lachlan fold

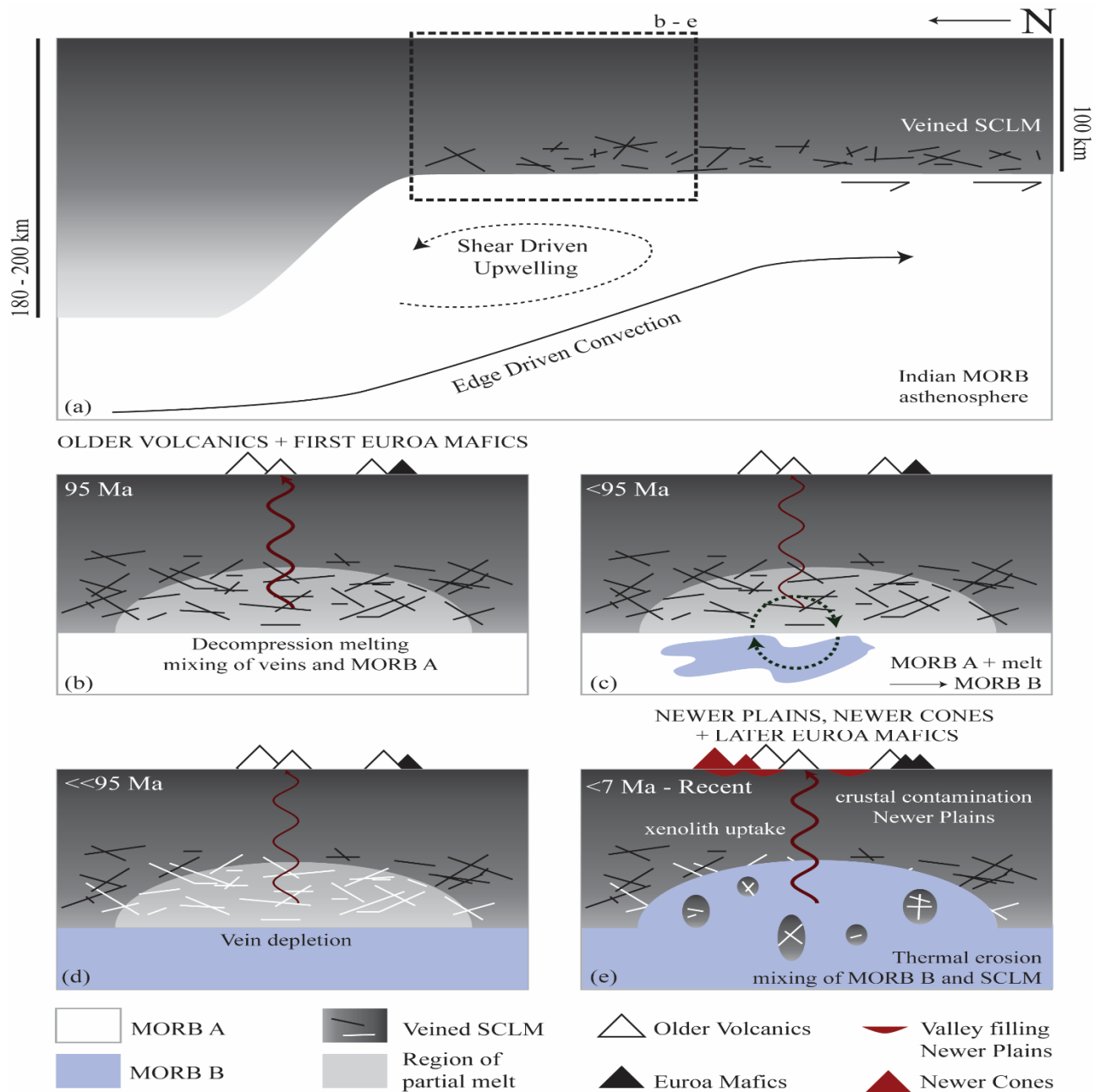


Figure 3.13. (a) Interpreted temporal geodynamic evolution of the mantle below SE Australia (after Kaislaniemi & Van Hunen, 2014). Thickness to the base of the lithosphere after Davies & Rawlinson (2014). (b) Enlarged section. Decompression melting at the base of the lithosphere results in preferential melting of metasomatized veins and mixing of the resultant enriched partial melts with Indian MORB-source mantle (MORB-A) thereby generating the magmas parental to the Older Volcanics. (c) Mixing of MORB-A with the alkaline melts represented by the Older Volcanics results in a slightly modified Indian MORB-source mantle (MORB-B). (d) Prolonged periods of melting will deplete the SCLM of calcio-carbonatite metasomatized veins. (e) Continued edge-driven convection with shear causes thermal erosion of the base of the lithosphere, incorporating depleted SCLM within MORB-B. The resultant melts have the potential to incorporate enriched vein material from the SCLM en route to the surface

belt, potentially generates a complex 3D configuration of convection rolls, capable of variably focusing the loci of upwelling and associated magmatism in the region.

Figure 3.13a shows a schematic representation of our interpretation of the processes leading to the genesis of the Older Volcanics, Euroa Volcanics, Newer Plains and Newer Cones magmatism. Using the different xenolith groups as proxies for larger scale mantle structures [Group 0 = modified Indian MORB (“MORB – B”); Group 2 = depleted SCLM and Group 1/ Group 3 = veined SCLM] we can deduce the spatial and temporal variations of the mantle beneath south east Australia. We suggest that at the time of earliest basalt generation (Figure 3.13b), the mantle beneath Victoria consisted of an Indian MORB-type asthenosphere (MORB-A) and a veined, Group 3-type SCLM (O’Reilly and Griffin, 1988). Such veins can have solidus temperatures up to 200°C lower than their surrounding wall rock (Foden *et al.*, 2002) and will melt first during decompression melting at the base of the SCLM. Mixing of these veins with upwelling Indian MORB potentially resulted in the distinct  $(\text{Sm}/\text{Yb})_{\text{C1}}$ ,  $(\text{Eu}/\text{Yb})_{\text{C1}}$  and Pb and Nd isotope signatures of the Older Volcanics and part of the Euroa Volcanics. Prolonged periods of decompression melting could have caused minor modification of the Indian MORB-type asthenosphere (MORB-B) due to mixing of alkaline melts with this source as evidenced by the Group 0 xenolith composition (Stolz and Davies, 1988; Figure 3.12b, Figure 3.13c). Furthermore, ongoing vein melting in the region of decompression melting would have purged the SCLM of enriched Group 3 veins, leaving a more depleted residual SCLM (Figure 3.13d).

As upwelling and shear persisted (Figure 3.13e), thermal erosion of the depleted residual SCLM potentially resulted in lithosphere delamination and mixing of this depleted SCLM with modified Indian MORB-type asthenosphere; which in turn was the source of the basalts of the Newer Plains and Newer Cones. High rates of partial melting following lithosphere delamination could have resulted in the volumetrically dominant, tholeiitic Newer Plains. As the magmas represented by these rocks are relatively depleted in incompatible elements compared to the Newer Cones, assimilation and crustal contamination would have affected isotope and trace element compositions of the Newer Plains more than the compositions of the Newer Cones. Both of these slightly deeper melts might have taken up shallow enriched metasomatised xenoliths of all groups that were unaffected by the decompression melting *en route* to the surface, as suggested by the presence of abundant and compositionally variable mantle xenoliths within the Newer Cones. Such a model is in agreement with recent geophysical observations in the province as well as with the wide range of pressures calculated for both Older Volcanics and Newer Cones basalt generation (1.5 - 4.5 GPa; Price *et al.*, 2014).



### 3.8. Conclusion

New major and trace element as well as Sr, Nd and Pb isotope data on the youngest expression of Cretaceous to Cainozoic volcanism in south east Australia, suggests spatial and long-term temporal geochemical and geodynamic variations within the mantle below. We find that basalts of the < 1 Ma Newer Cones were generated by approximately 5 to 10% partial melting of a garnet-spinel mantle source; the composition of which can be represented by mixing of depleted, anhydrous, Indian MORB type spinel lherzolite and enriched, hydrous spinel lherzolite metasomatised by alkaline melts. The resulting melts evolved by fractional crystallisation. According to our modelling, up to 20% of crystallisation is required to reach the composition of our samples. EC-RA<sub>x</sub>FC modelling shows that the Newer Cones magmas were not affected by crustal assimilation processes. Conversely, enriched trace element and isotope signatures of < 4.6 Ma Newer Plains can be modelled by up to 5% assimilation of standard upper crust. The ~ 7 Ma Euroa Volcanics represent basaltic magmas generated by smaller degrees of both partial melting (10%) and fractional crystallization (15%). Their Pb and Nd isotopes suggest a variable source which we interpret to reflect a progressive temporal change from the source of the Older Volcanics to the source of the Newer Cones. The 95 – 19 Ma old Older Volcanics have trace element and Sr-Nd-Pb isotope signatures that are very distinct from those of the other series and their source can be modelled by adding approximately 10% of melts derived from small degrees of partial melting of carbonatite metasomatised vein material to a composition similar to that of Indian MORB. We suggest that the temporal variation in the mantle source can be explained by the geodynamical model of edge driven convection with shear. The primary magmas of the Older Volcanics were formed by decompression melting that favoured the partial melting of hydrous carbonatite metasomatised veins. Subsequent thermal erosion and entrainment of the depleted SCLM in the locally slightly enriched upper asthenosphere resulted in the eruption of the Euroa Volcanics, Newer Plains and Newer Cones.

### 3.9. Acknowledgements

Prof David Phillips and Dr Erin Matchan of the University of Melbourne as well as David Taylor of the Geological Survey of Victoria are thanked for their assistance in the field. Michèle Senn (University of Geneva) is thanked for performing the column chemistry for the Sr, Nd and Pb isotope analyses. Richard C. Price (University of Waikato), Lucy McGee (Universidad de Chile) and an anonymous reviewer provided constructive reviews and Richard Price and Majorie Wilson are thanked for editorial handling. The support of TiGER and the department Applied Geology at Curtin

University of Technology is gratefully acknowledged. This research was funded by Australian Research Council Discovery grant DP130100517.

### 3.10. References

Aivazpourporgou, S., Thiel, S., Hayman, P. C., Moresi, L. N. & Heinson, G. (2015). Decompression melting driving intraplate volcanism in Australia: Evidence from magnetotelluric sounding. *Geophysical Research Letters* 42, 1–9.

Aziz-ur-Rahman & McDougall, I. (1972). Potassium-Argon ages on the Newer Volcanics of Victoria. *Proceedings of the Royal Society of Victoria* 85.

Baker, J., Peate, D., Waight, T. & Meyzen, C. (2004). Pb isotopic analysis of standards and samples using a  $^{207}\text{Pb}$ - $^{204}\text{Pb}$  double spike and thallium to correct for mass bias with a double-focusing MC-ICPMS. *Chemical Geology* 211, 275–303.

Blackburn, G., Allison, G. B. & Leaney, F. W. J. (1982). Further evidence on the age of tuff at Mt Gambier, South Australia. *Transactions of the Royal Society of South Australia* 106, 163–167.

Bohrson, W. A. & Spera, F. J. (2001). Energy-Constrained Open-System Magmatic Processes II: Application of Energy- Constrained Assimilation – Fractional Crystallization (EC-AFC) Model to Magmatic Systems. *Journal of Petrology* 42, 1019–1041.

Boyce, J. (2013). The Newer Volcanics Province of southeastern Australia: a new classification scheme and distribution map for eruption centres. *Australian Journal of Earth Sciences* 60, 449–462.

Boyce, J. A., Nicholls, I. A., Keays, R. R. & Hayman, P. C. (2015). Composition and volatile contents of parental magmas of Mt. Rouse, a polymagmatic volcano in the Newer Volcanics intraplate basaltic province, SE Australia. *Contributions to Mineralogy and Petrology* 169, 1–21.

Brenna, M., Cronin, S. J., Smith, I. E. M., Sohn, Y. K. & Németh, K. (2010). Mechanisms driving polymagmatic activity at a monogenetic volcano, Udo, Jeju Island, South Korea. *Contributions to Mineralogy and Petrology* 160, 931–950.

Cartwright, I., Weaver, T., Tweed, S., Ahearne, D., Cooper, M., Czapnik, K. & Tranter, J. (2002). Stable isotope geochemistry of cold CO<sub>2</sub>-bearing mineral spring waters, Daylesford, Victoria, Australia: Sources of gas and water and links with waning volcanism. *Chemical Geology* 185, 71–91.

- Cayley, R. A. et al. (2011). Crustal architecture of central Victoria: results from the 2006 deep crustal reflection seismic survey. *Australian Journal of Earth Sciences* 58, 113–156.
- Chiaradia, M., Muntener, O. & Beate, B. (2011). Enriched Basaltic Andesites from Mid-crustal Fractional Crystallization, Recharge, and Assimilation (Pilavo Volcano, Western Cordillera of Ecuador). *Journal of Petrology* 52, 1107–1141.
- Conrad, C. P., Bianco, T. A., Smith, E. I. & Wessel, P. (2011). Patterns of intraplate volcanism controlled by asthenospheric shear. *Nature Geoscience*. Nature Publishing Group 4, 317–321.
- Cooper, J. A. & Green, D. H. (1969). Lead isotope measurements on lherzolite inclusions and host basanites from Western Victoria, Australia. *Earth and Planetary Science Letters* 6, 69–76.
- Davies, D. R. & Rawlinson, N. (2014). On the origin of recent intraplate volcanism in Australia. *Geology* 1–4.
- Davies, D. R., Rawlinson, N., Iaffaldano, G. & Campbell, I. H. (2015). Lithospheric controls on magma composition along Earth's longest continental hotspot track. *Nature*.
- Day, R. A. (1983). *Petrology and Geochemistry of the Older Volcanics, Victoria: distribution, characterization, and petrogenesis*. Monash University, Clayton, Victoria.
- Day, R. A. (1989). East Australian Volcanic Geology; Victoria and South Australia. In: Johnson, R. W. (ed.) *Intraplate volcanism of Eastern Australia and New Zealand*. Australian Academy of Science, 132–142.
- Demidjuk, Z., Turner, S., Sandiford, M., George, R., Foden, J. & Etheridge, M. (2007). U-series isotope and geodynamic constraints on mantle melting processes beneath the Newer Volcanic Province in South Australia. *Earth and Planetary Science Letters* 261, 517–533.
- Ellis, D. J. (1976). High pressure cognate inclusions in the Newer Volcanics of Victoria. *Contributions to Mineralogy and Petrology* 58, 149–180.
- Ewart, A. (2004). Petrology and Geochemistry of Early Cretaceous Bimodal Continental Flood Volcanism of the NW Etendeka, Namibia. Part 1: Introduction, Mafic Lavas and Re-evaluation of Mantle Source Components. *Journal of Petrology* 45, 59–105.
- Foden, J., Song, S. H., Turner, S., Elburg, M., Smith, P. B., Van der Steldt, B. & Van Penglis, D. (2002). Geochemical evolution of lithospheric mantle beneath S.E. South Australia. *Chemical Geology* 182, 663–696.

Frey, F. A. & Green, D. H. (1974). The mineralogy, geochemistry and origin of lherzolite inclusions in Victorian basanites. *Geochimica et Cosmochimica Acta* 38, 1023–1059.

Frey, F. A., Green, D. H. & Roy, S. D. (1978). Integrated Models of Basalt Petrogenesis: A Study of Quartz Tholeiites to Olivine Melilitites from South Eastern Australia Utilizing Geochemical and Experimental Petrological Data. *Journal of Petrology* 19, 463–513.

Ghiorso, M. S. & Sack, R. O. (1995). Chemical mass transfer in magmatic processes IV. A revised and internally consistent thermodynamic model for the interpolation and extrapolation of liquid-solid equilibria in magmatic systems at elevated temperatures and pressures. *Contributions to Mineralogy and Petrology* 119, 197–212.

Gray, C. M. & McDougall, I. (2009). K-Ar geochronology of basalt petrogenesis, Newer Volcanic Province, Victoria. *Australian Journal of Earth Sciences* 56, 245–258.

Griffin, W. L., O'Reilly, S. Y. & Stabel, A. (1988). Mantle metasomatism beneath western Victoria, Australia : II . Isotopic geochemistry. *Geochimica et Cosmochimica Acta* 52, 449–459.

Handler, M. R., Bennett, V. C. & Esat, T. M. (1997). The persistence of off-cratonic lithospheric mantle: Os isotopic systematics of variably metasomatised southeast Australian xenoliths. *Earth and Planetary Science Letters* 151, 61–75.

Hofmann, A. W., Jochum, K. P., Seufert, M. & White, W. M. (1986). Nb and Pb in oceanic basalts: new constraints on mantle evolution. *Earth and Planetary Science Letters* 79, 33–45.

Irvine, T. N. & Baragar, W. R. A. (1971). A Guide to the Chemical Classification of the Common Volcanic Rocks. *Canadian Journal of Earth Sciences* 8, 523–548.

Kaislaniemi, L. & Van Hunen, J. (2014). Dynamics of lithosphere thinning and mantle melting by edge-driven convection; application to the Moroccan Atlas mountains. *Geochemistry, Geophysics, Geosystems* 15, 3175–3189.

King, S. D. & Anderson, D. L. (1998). Edge-driven convection. *Earth and Planetary Science Letters* 160, 289–296.

Le Bas, M. J., Le Maitre, R. W., Streckeisen, A. & Zanettin, B. (1986). A chemical classification of volcanic rocks based on the total alkali vs. silica diagram. *Journal of Petrology* 27, 745–750.

- Matchan, E. L. & Phillips, D. (2011). New  $^{40}\text{Ar}/^{39}\text{Ar}$  ages for selected young (<1 Ma) basalt flows of the Newer Volcanic Province, southeastern Australia. *Quaternary Geochronology*. Elsevier B.V 6, 356–368.
- Matchan, E. L. & Phillips, D. (2014). High precision multi-collector  $^{40}\text{Ar}/^{39}\text{Ar}$  dating of young basalts: Mount Rouse volcano (SE Australia) revisited. *Quaternary Geochronology*. Elsevier Ltd.
- McBride, J. S., Lambert, D. D., Nicholls, I. A. & Price, R. C. (2001). Osmium Isotopic Evidence for Crust – Mantle Interaction in the Genesis of Continental Intraplate Basalts from the Newer Volcanics Province, Southeastern Australia. *Journal of Petrology* 42, 1197–1218.
- McDonough, W. F. & McCulloch, M. T. (1987). The southeast Australian lithospheric mantle: isotopic and geochemical constraints on its growth and evolution. *Earth and Planetary Science Letters* 86, 327–340.
- McDonough, W. F., McCulloch, M. T. & Sun, S. S. (1985). Isotopic and geochemical systematics in Tertiary-Recent basalts from southeastern Australia and implications for the evolution of the sub-continental lithosphere. *Geochimica et Cosmochimica Acta* 49, 2051–2067.
- McDougall, I., Allsopp, H. L. & Chamalaun, F. H. (1966). Isotopic dating of the newer volcanics of Victoria, Australia, and geomagnetic polarity epochs. *Journal of Geophysical Research* 71, 6107–6118.
- McGee, L. E., Beier, C., Smith, I. E. M. & Turner, S. P. (2011). Dynamics of melting beneath a small-scale basaltic system: A U-Th-Ra study from Rangitoto volcano, Auckland volcanic field, New Zealand. *Contributions to Mineralogy and Petrology* 162, 547–563.
- McGee, L. E., Smith, I. E. M., Millet, M. A., Handley, H. K. & Lindsay, J. M. (2013). Asthenospheric control of melting processes in a monogenetic basaltic system: A case study of the Auckland volcanic field, New Zealand. *Journal of Petrology* 54, 2125–2153.
- McKenzie, D. & O’Nions, R. K. (1983). Mantle reservoirs and ocean island basalts. *Nature* 301, 229 – 231.
- Nelson, D. R., McCulloch, M. T. & Sun, S. S. (1986). The origins of ultrapotassic rocks as inferred from Sr, Nd and Pb isotopes. *Geochimica et Cosmochimica Acta* 50, 231–245.

O'Reilly, S. Y. & Griffin, W. L. (1984). Sr isotopic heterogeneity in primitive basaltic rocks, southeastern Australia: correlation with mantle metasomatism. *Contributions to Mineralogy and Petrology* 87, 220–230.

O'Reilly, S. Y. & Griffin, W. L. (1988). Mantle metasomatism beneath western Victoria, Australia: I. Metasomatic processes in Cr-diopside lherzolites. *Geochimica et Cosmochimica Acta* 52, 433–447.

O'Reilly, S. Y. & Zhang, M. (1995). Geochemical characteristics of lava-field basalts from eastern Australia and inferred sources: connections with the subcontinental lithospheric mantle? *Contributions to Mineralogy and Petrology* 121, 148–170.

Oostingh, K. F., Jourdan, F., Phillips, D. & Matchan, E. L. (2015). Ultra-precise  $^{40}\text{Ar}/^{39}\text{Ar}$  geochronology and  $^{38}\text{Ar}$  exposure dating on young basalts from the Newer Volcanic Province, Australia. *Goldschmidt 2015 Conference Abstracts*.

Paul, B., Hergt, J. M. & Woodhead, J. D. (2005). Mantle heterogeneity beneath the Cenozoic volcanic provinces of central Victoria inferred from trace-element and Sr, Nd, Pb and Hf isotope data. *Australian Journal of Earth Sciences* 52, 243–260.

Peucker-Ehrenbrink, B. & Jahn, B. (2001). Rhenium-osmium isotope systematics and platinum group element concentrations: Loess and the upper continental crust. *Geochemistry Geophysics Geosystems* 2.

Powell, W., Zhang, M., O'Reilly, S. Y. & Tiepolo, M. (2004). Mantle amphibole trace-element and isotopic signatures trace multiple metasomatic episodes in lithospheric mantle, western Victoria, Australia. *Lithos* 75, 141–171.

Price, R. C., Gray, C. M. & Frey, F. A. (1997). Strontium isotopic and trace element heterogeneity in the plains basalts of the Newer Volcanic Province, Victoria, Australia. *Geochimica et Cosmochimica Acta* 61, 171–192.

Price, R. C., Nicholls, I. A. & Day, A. (2014). Lithospheric influences on magma compositions of late Mesozoic and Cenozoic intraplate basalts (the Older Volcanics) of Victoria, south-eastern Australia. *Lithos*. Elsevier B.V. 206-207, 179–200.

Price, R. C., Nicholls, I. A. & Gray, C. M. (2003). Cainozoic igneous activity. In: Birch, W. D. (ed.) *Geology of Victoria*. Geological Society of Australia (Victoria Division), 361–375.

- Rehkamper, M. & Hofmann, A. W. (1997). Recycled ocean crust and sediment in Indian Ocean MORB. *Earth and Planetary Science Letters* 147, 93–106.
- Sella, G. F., Dixon, T. H. & Mao, A. (2002). REVEL: A model for Recent plate velocities from space geodesy. *Journal of Geophysical Research* 107.
- Shaw, D. M. (1970). Trace element fractionation during anatexis. *Geochimica et Cosmochimica Acta* 34, 237–243.
- Spera, F. J. (2001). Energy-Constrained Open-System Magmatic Processes I: General Model and Energy-Constrained Assimilation and Fractional Crystallization (EC-AFC) Formulation. *Journal of Petrology* 42, 999–1018.
- Stolz, A. J. & Davies, G. R. (1988). Chemical and isotopic evidence from spinel lherzolite xenoliths from episodic metasomatism of the upper mantle beneath southeastern Australia. *Journal of Petrology Spec. Vol.*, 303–330.
- Stracke, A., Bizimis, M. & Salters, V. J. M. (2003). Recycling oceanic crust: Quantitative constraints. *Geochemistry, Geophysics, Geosystems* 4.
- Stracke, A., Hofmann, A. W. & Hart, S. R. (2005). FOZO, HIMU, and the rest of the mantle zoo. *Geochemistry, Geophysics, Geosystems* 6, n/a–n/a.
- Sun, S. S. & McDonough, W. F. (1989). Chemical and isotopic systematics of oceanic basalts: implications for mantle composition and processes. *Geological Society, London, Special Publications* 42, 313–345.
- Tanaka, T., Togashi, S., Kamioka, H., Amakawa, H., Kagami, H. & Hamamoto, T. (2000). JNdi-1: a neodymium isotopic reference in consistency with LaJolla neodymium. *Chemical Geology* 168, 279–281.
- Taylor, S. R. & McLennan, S. M. (1995). The geochemical evolution of the continental crust. *Reviews of Geophysics* 33, 241–265.
- Van Otterloo, J., Raveggi, M., Cas, R. A. F. & Maas, R. (2014). Polymagmatic Activity at the Monogenetic Mt Gambier Volcanic Complex in the Newer Volcanics Province, SE Australia: New Insights into the Occurrence of Intraplate Volcanic Activity in Australia. *Journal of Petrology* 55, 1317–1351.

- Veevers, J. J. (1986). Breakup of Australia and Antarctica estimated as mid-Cretaceous ( $95 \pm 5$  Ma) from magnetic and seismic data at the continental margin. *Earth and Planetary Science Letters* 77, 91–99.
- Vogel, D. C. & Keays, R. R. (1997). The petrogenesis and platinum-group element geochemistry of the Newer Volcanic Province, Victoria, Australia. *Chemical Geology* 136, 181–204.
- Vollmer, R. (1976). Rb-Sr and U-Th-Pb systematics of alkaline rocks: the alkaline rocks from Italy. *Geochimica et Cosmochimica Acta* 40, 283–295.
- Walter, M. J. (1998). Melting of Garnet Peridotite and the Origin of Komatiite and Depleted Lithosphere. *Journal of Petrology* 39, 29–60.
- Wellman, P. (1974). Potassium-argon ages on the Cainozoic Volcanic rocks of Eastern Victoria, Australia. *Journal of the Geological Society of Australia* 21, 359–376.
- Wellman, P. & McDougall, I. (1974). Cainozoic igneous activity in eastern Australia. *Tectonophysics* 23, 49–65.
- Yaxley, G. M., Crawford, A. J. & Green, D. H. (1991). Evidence for carbonatite metasomatism in spinel peridotite xenoliths from western Victoria, Australia. *Earth and Planetary Science Letters* 107, 305–317.
- Yaxley, G. M., Kamenetsky, V. S., Green, D. H. & Falloon, T. J. (1997). Glasses in mantle xenoliths from western Victoria, Australia, and their relevance to mantle processes. *Earth and Planetary Science Letters* 148, 433–446.
- Zhang, M., O'Reilly, S. Y. & Chen, D. (1999). Location of Pacific and Indian mid-ocean ridge-type mantle in two time slices: Evidence from Pb, Sr, and Nd isotopes for Cenozoic Australian basalts. *Geology* 27, 39.
- Zindler, A. & Hart, S. R. (1986). Chemical geodynamics. *Annual review of earth and planetary sciences* 14, 493–571.



## Chapter 4 $^{40}\text{Ar}/^{39}\text{Ar}$ geochronology reveals rapid change from plume-assisted to stress-dependent volcanism in the Newer Volcanic Province, SE Australia<sup>2</sup>

### 4.1. Abstract

Here, we present  $^{40}\text{Ar}/^{39}\text{Ar}$  ages of volcanic features in the Cenozoic intraplate Newer Volcanic Province in southeast Australia. The < 5 Ma volcanic products in the Newer Volcanic Province can be subdivided into tholeiitic, valley-filling Newer Plains basalts and alkaline scoria cones, lava shields and maars of the Newer Cones series. Plateau ages range from  $3.76 \pm 0.01$  Ma to  $4.32 \pm 0.03$  Ma ( $2\sigma$ ; all sources of uncertainties included) for the Newer Plains series, with production rates of volcanism decreasing post 4 Ma. We suggest that magmatism is related to the complex interplay of magma upwelling due to edge driven convection and the Cosgrove track mantle plume located in the northeast of the province at 6.5 – 5 Ma. Plateau ages range from  $1290 \pm 20$  ka to  $41.1 \pm 2.2$  ka ( $2\sigma$ ) for the Newer Cones series, with a diffuse age progression in the onset of volcanism for these features from east to west. Analyses of the distribution and geomorphology of these volcanic features indicates a strong control of basement faults on volcanism, reflected in alignment of volcanic features along Palaeozoic north – south oriented basement faults in the east and Cretaceous northwest – southeast oriented extensional features in the west. This age progression can be explained by a westerly migration of stress derived from the left-lateral strike-slip Tasman Fracture Zone. This suggests that the general mechanism of volcanism changed from upwelling due to plume-assisted edge driven convection prior to  $\sim 4$  Ma to stress-dependent upwelling at around 1.3 Ma.

---

<sup>2</sup>. This Chapter was accepted as a paper in *Geochemistry, Geophysics and Geosystems* on the 17<sup>th</sup> of February 2017. Oostingh, K. F., Jourdan, F., Matchan, E. L. & Phillips, D. (2017).  $^{40}\text{Ar}/^{39}\text{Ar}$  geochronology reveals rapid change from plume-assisted to stress-dependent volcanism in the Newer Volcanic Province, SE Australia. *Geochemistry, Geophysics, Geosystems* **18**, 1065–1089.

## 4.2. Introduction

The Newer Volcanic Province (NVP; Price et al., 2003) is a relatively small, intraplate volcanic province which covers an area of around 19 000 km<sup>2</sup> (Boyce, 2013) with basaltic rocks in the densely populated area west of Melbourne in south eastern Australia (141° E - 145° E and 37° S – 38.5° S; Figure 4.1a). It is sub-divided into three zones; the Central Highlands sub-province, the Western Plains sub-province and the Mt. Gambier region in South Australia (Figure 4.1a). There are two geomorphological and geochemical distinct types of Cenozoic volcanism in the area: older (> 1 Ma; Gray and McDougall, 2009) valley filling Newer Plains basalts, as well as the younger Newer Cones series, comprising maars, scoria cones, lava shields and their associated flows.

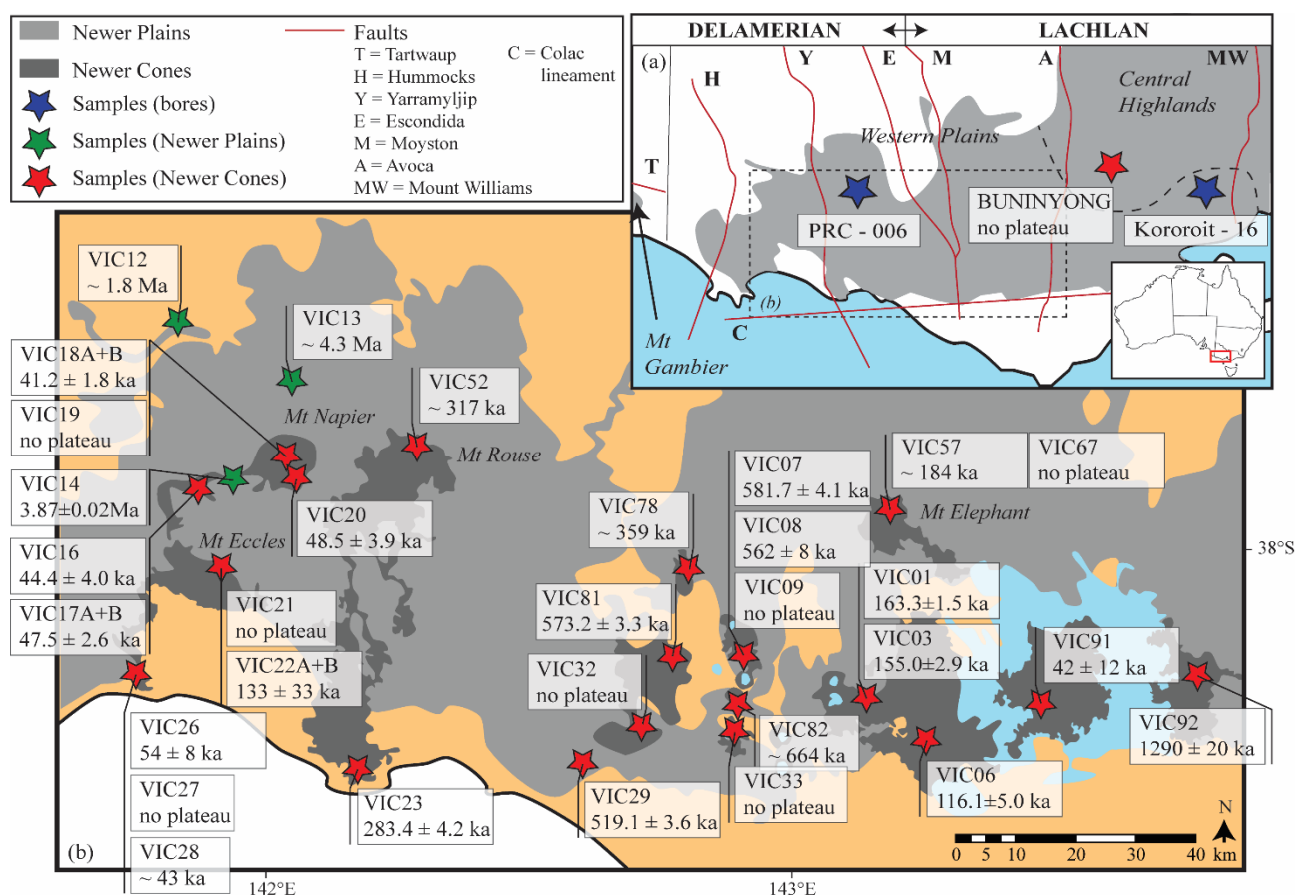


Figure 4.1 Map of the Newer Volcanic Province and sample locations. (a) Approximate extent of the Newer Volcanic Province, indicating sub-provinces Central Highlands, Western Plains and Mt Gambier. Also indicated are major structural elements (red lines): T = Tartwaup fault, H = Hummocks fault, Y = Yarramylyjup fault, E = Escondida fault, M = Moyston fault, A = Avoca fault, MW = Mount Williams fault, C = Colac lineament. (b) Enlarged section of (a) showing the approximate outcrop of Newer Plains in light grey and some relevant Newer Cone flows in dark grey. Indicated are sample locations (exact coordinates can be found in Table 1 and Table 2) and the resulting  $^{40}\text{Ar}/^{39}\text{Ar}$  ages ( $\pm 2\sigma$ ).

The NVP is considered dormant on the basis of  $\delta^{13}\text{C}$  value of  $\text{CO}_2$  gas found in mineral waters in the area (Cartwright et al., 2002), with the last volcano, Mt Schank in the Gambier region (Figure 4.1a), erupting ~ 5 ka ago; based on thermoluminescence dating of quartz from a beach deposit overlain by

the Mt Schank lava flow (Smith and Prescott, 1987). Therefore, it is of paramount importance to have reliable age data available to better understand the distribution and timeframe of volcanism in the NVP. Furthermore, age data can provide a geochronological framework for regional climate reconstructions based on lake (e.g. Mooney, 1997; Harle et al., 2002; Wilkins et al., 2013) and swamp (Crowley and Kershaw, 1994) sediments that formed as a result of disrupted drainage pathways by basalt flows. Accurate ages can also be used to constrain the geodynamic origin of the province, which is still a matter of debate (Demidjuk et al. 2007; Davies & Rawlinson 2014; Price et al. 2014; Oostingh et al. 2016), and to test if any spatio-temporal migration of the main loci of volcanism occurred within the NVP.

Currently, the majority of available geochronological data in the NVP were either derived by K – Ar dating (N = 147; e.g. Aziz-ur-Rahman and McDougall, 1972; Gray and McDougall, 2009; McDougall et al., 1966; Singleton et al., 1976) and a few cosmogenic exposure ( $^{21}\text{Ne}$  and  $^{36}\text{Cl}$ ; n = 6; Stone *et al.*, 1997; Gillen *et al.*, 2010) and  $^{40}\text{Ar}/^{39}\text{Ar}$  ages (n = 9; Hare et al., 2005a; Matchan and Phillips, 2014, 2011; Matchan et al., 2016; see for a review on available geochronology Vasconcelos et al., 2008). K – Ar dating suggests continuous volcanism throughout the NVP from *ca.* 4.6 Ma to present. These data suggest that three volumetric dominant stages can be resolved: 4.6 – 3.0 Ma, dominated by tholeiitic eruptions; 3.0 – 1.8 Ma, ranging from transitional hawaiites to basaltic icelandites and 1.8 Ma - present, with volcanism becoming more alkalic (Price *et al.*, 1997, 2003). Whereas cosmogenic exposure dating provides minimum ages only due to potential erosion and shielding (Gosse & Phillips, 2001), K-Ar dating will only provide reliable eruption ages if the samples are completely unaltered; sample splits for K and Ar analysis are homogenous; and if the initial trapped  $^{40}\text{Ar}/^{36}\text{Ar}$  ratio is within the range of the air value [ $298.56 \pm 0.31$ ; as measured by Lee et al. (2006) and independently confirmed by Mark et al. (2011)]. As we will demonstrate in this study, both assumptions are often erroneous for the NVP basalts, questioning the reliability of the existing age data.

$^{40}\text{Ar}/^{39}\text{Ar}$  geochronology is currently widely accepted as an accurate dating technique for a wide variety of geological samples (McDougall and Harrison, 1999). New generation mass spectrometers such as the multi-collector ARGUS VI equipped with five ultra-sensitive Faraday collectors and one ion-counting compact discrete dynode (CDD) have shown to increase accuracy and precision of analyses of young basalt; due to improved knowledge of the trapped  $^{40}\text{Ar}/^{36}\text{Ar}$  ratio, while decreasing required sample quantity and the time of sample preparation and analysis (Matchan *et al.*, 2016; Matchan and Phillips, 2014). In this work, we will present 19 new  $^{40}\text{Ar}/^{39}\text{Ar}$  ages from 16 individual

eruptive centres and associated flows of the Newer Cones series, as well as 4 new ages from the Newer Plains basalts found in the Western Plains sub-province of the NVP. Furthermore, we evaluate the distribution and spatial characteristics of eruptive centres in the NVP to assess potential relationships between location, geochemistry and eruption age.

#### 4.3. Geological setting and sample description

The onset of predominantly basaltic volcanism in southeast Australia is associated with rifting due to break-up of Australia and Antarctica from Gondwana in the Late Jurassic, and occurred intermittently from 190 Ma onwards with the youngest expression of volcanism in the NVP representing a volumetric peak ranging from *ca.* 4.6 Ma to *ca.* 5 ka (Blackburn et al. 1982; Price et al. 2003). The geodynamic model of edge driven convection (King and Anderson, 1998) accompanied by shear driven upwelling (Conrad et al., 2010) due to fast northward plate motions of the Australian plate (Sella et al., 2002; 6 cm/year) and complex 3D lithospheric thickness variations (Fishwick et al. 2008; Davies & Rawlinson, 2014; Rawlinson, Kennett, et al. 2015) has been proposed to explain the occurrence of volcanism in southeast Australia (Demidjuk et al. 2007; Price et al. 2014; Oostingh et al. 2016).

Volcanic products are underlain by a complex Palaeozoic basement consisting of a series of eastward younging stacked fold belts of deformed and metamorphosed rocks of the Delamerian orogeny (Cambrian to Ordovician) and Lachlan orogeny (Late Ordovician to Carboniferous) as well as rift-related late Mesozoic – Cenozoic sedimentary basins (Gray *et al.*, 2003). A major lithospheric structure in the region is the north – south trending Moyston Fault Zone, which forms the boundary between the early-Palaeozoic Delamerian orogeny in the east and the Lachlan orogeny in the west (Figure 4.1a; Graeber et al., 2002). Other major structures are the roughly north – south trending fault zones bordering the major structural divisions within the Delamerian and Lachlan fold belts: the Hummocks and Yarramylyjup faults within the Delamerian orogeny, the Avoca fault between the Stawell and Bendigo Zones and the Mt. William fault between the Bendigo and Melbourne Zones (Figure 4.1a - see Figure 4.7 for main structural zones; Gray et al., 2003). Sediments of the east – west trending Otway basin underlie the NVP basalts in the South, in which Late Cretaceous extension resulted in west north west – east south east trending structures such as the Tartwaup fault system (Lesti *et al.*, 2008). The east – west striking Colac lineament marks the southern extent of the NVP volcanics (Figure 4.1a). The area is currently in a slight compressional stress regime ( $S_{Hmax}$  oriented N150°) which followed a period of inversion tectonics during the Pliocene and Quaternary (Dickinson et al. 2002; Sandiford 2003; Sandiford et al. 2004).

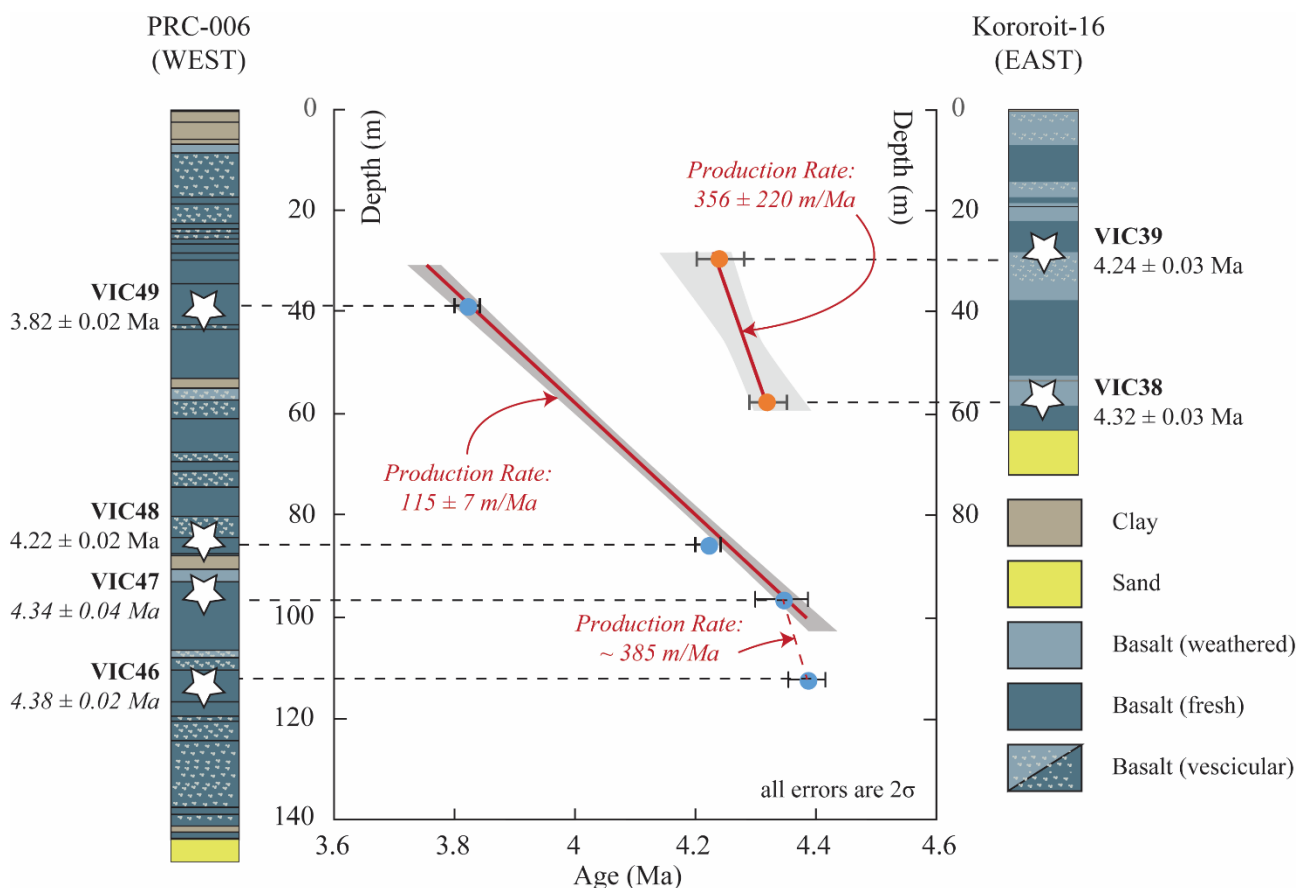


Figure 4.2. Stratigraphic logs of bores PRC-006 and Kororoit-16, indicating the depth of samples and their associated  $^{40}\text{Ar}/^{39}\text{Ar}$  age ( $2\sigma$  errors). These ages were used to calculate production rates (thick red lines; m/Ma) and associated  $2\sigma$  errors (grey outlines) using IsoPlot (Ludwig, 2012). The production rate of VIC46 and VIC47 is apparent only due to poor correlation in IsoPlot between two closely located points.

Previous dating efforts (McDougall et al. 1966; Aziz-ur-Rahman & McDougall 1972; Gray & McDougall, 2009) concentrated on the valley-filling Newer Plains basalts, as  $< 1$  Ma low-K tholeiitic rocks were typically difficult to date with the previous generations of instruments. We sampled 9 Newer Plains basalts (Figure 4.1 and Figure 4.2) for  $^{40}\text{Ar}/^{39}\text{Ar}$  dating. VIC12 was sampled from a supposedly older flow at Wannan Falls, whereas VIC13 represents a tholeiitic bomb of underlying Newer Plains within the scoria cone of Mt Pierrepont (Figure 4.1b). VIC14 was sampled from a quarry excavating basalt located stratigraphically below the young flows of Mt Napier (Figure 4.1b). We have sampled fresh mafic rocks from well Kororoit 16 (see Figure 4.1a for location) at two different depth intervals: 60 m (VIC38) and 30 m (VIC39) as well as from PRC-6 (Yalimba 20002; see Figure 4.1a for location) at four different depth intervals: 112 m (VIC46); 97 m (VIC47), 86 m (VIC48) and 39 m (VIC49) to determine the eruption rates of the Newer Plains basalts (Figure 4.2). We focused the remainder of our sampling efforts on the stratigraphically younger scoria cones and lava shield volcanoes as well as associated lava flows (Newer Cones series) and a single maar (VIC82; Terang maar). We sampled a wide range of volcanic features in the volumetrically dominant Western

Plains sub-province, aiming for a wide longitudinal range in sample locations. A total of 29 samples were collected from 16 individual cones and their flows (Figure 4.1a and b; Table 4.1 and Table 4.2). In all cases it was possible to sample fresh rock from either recently exposed outcrops in quarries and road cuts, or from at least 0.5 m depth to avoid both the effects of cosmogenic exposure and production of  $^{38}\text{Ar}_c$  as well as alteration on flow surfaces. Samples VIC06, VIC26, VIC27 and VIC28 were taken at the same location - but deeper levels - of the Gillen et al (2010) and Stone et al (1997) cosmogenic exposure dating sites. Most rocks are represented by dark grey, cryptocrystalline basalt with slight to moderate vesicularity, often directional in the case of flows. Thin section analysis shows that samples are generally unaltered (Figure 4.3), having glassy to fine grained groundmass containing plagioclase laths and Fe-Ti oxides. The Newer Cones are characterized by the presence of unaltered plagioclase, olivine and clino-pyroxene phenocrysts, whereas a few of the older Newer Plains samples show minor alteration indicated by slight iddingsitisation of olivine as well as occasional zeolite infill of vesicles.

#### 4.4. Methods

##### 4.4.1. $^{40}\text{Ar}/^{39}\text{Ar}$ geochronology

###### 4.4.1.1. *Sample preparation and irradiation*

All samples were crushed to cm-scale using a hydraulic press, after which fresh separates were further crushed to several hundred  $\mu\text{m}$  in size in a Tungsten - Carbide ring mill. The resulting crushate was sieved to yield the fraction of interest (355 - 500  $\mu\text{m}$ ) and washed multiple times with DI in a sonic bath. Approximately 200 - 500 mg of groundmass grains was handpicked for each sample using a binocular stereomicroscope; which is a quantity that allows for replicate analysis following irradiation. Glassy scoria was handpicked for sample VIC22B. Separates were leached with methanol and diluted HF (2N) for 5 minutes, followed by duplicate DI washes to remove any silicate phases, and loaded into aluminium discs wrapped in aluminium foil. These discs were stacked together and placed in quartz tubes along with the fully inter-calibrated flux monitor Fish Canyon Tuff sanidine for which an age of  $28.294 \pm 0.036$  Ma is adopted (Renne *et al.*, 2011). Samples were irradiated for 20 minutes at the Cadmium-Lined In-Core Irradiation Tube (Cd shielded to minimize undesirable nuclear interference reactions) at the Oregon State TRIGA reactor, USA.

###### 4.4.1.2. *Gas extraction and analysis*

$^{40}\text{Ar}/^{39}\text{Ar}$  step-heating analyses were performed with the ultra-high precision new generation multi-collector mass spectrometer ARGUSVI from Thermofisher© (Phillips and Matchan, 2013) at the

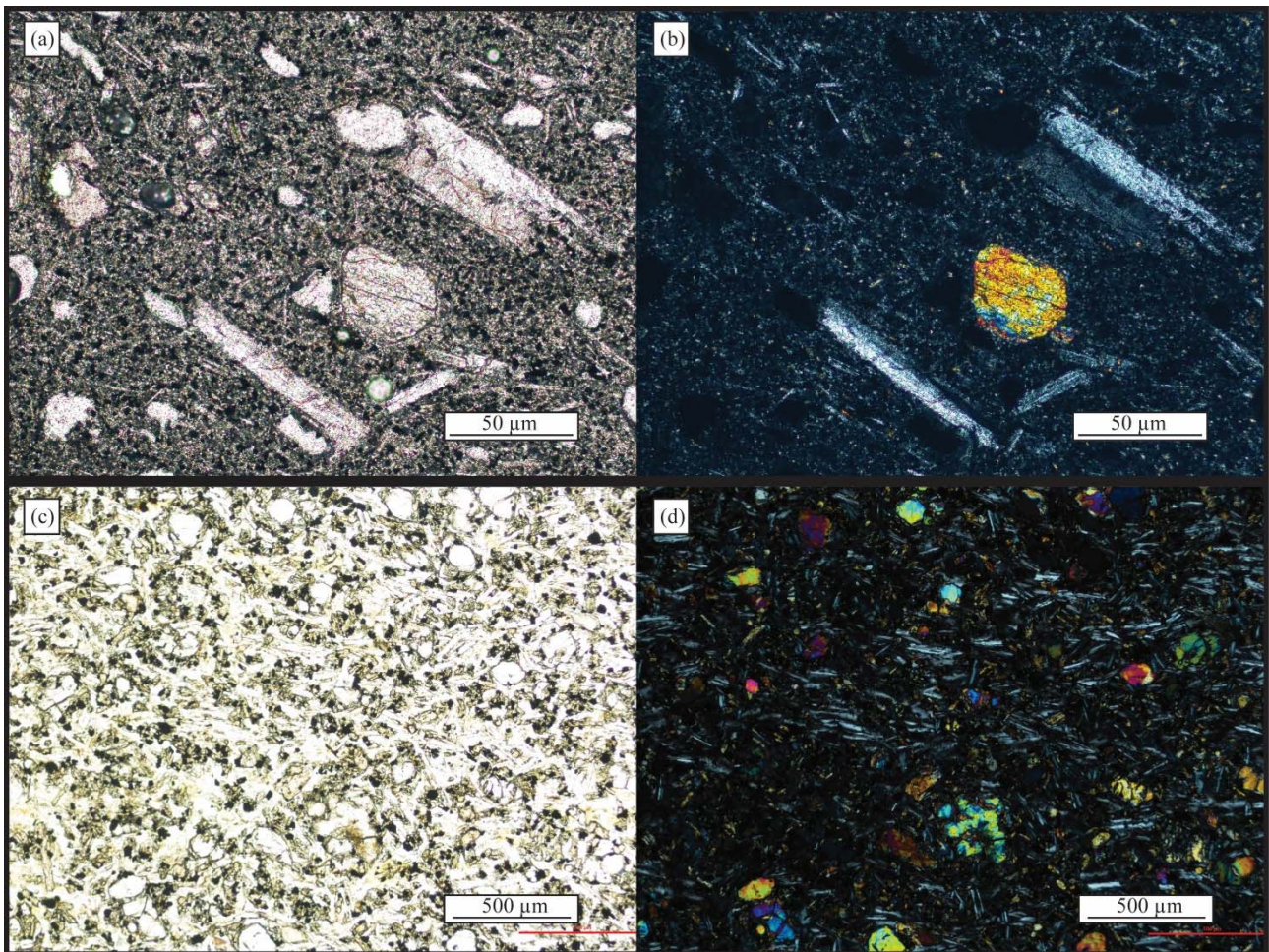


Figure 4.3. (a) Plane polarized and (b) cross polarized image of VIC18 (Newer Cones basalt). (c) Plane polarized and (d) cross polarized image of VIC48 (Newer Plains basalt).

West Australian Argon Isotope Facility, Curtin University, Perth. Approximately 100 – 150 mg of five irradiated groundmass separates was placed as a single layer in a custom-made high-grade aluminium sample disk and loaded into the sample chamber connected to a custom-built, extra low volume (240 cc), stainless steel gas extraction line coupled to the low volume (600 cc) ARGUSVI mass spectrometer. The ARGUSVI contains 5 Faraday detectors and a CDD (compact discrete dynode) ion counting electron multiplier, which allows for simultaneous analysis of all 5 Argon isotopes (Matchan and Phillips, 2014). The sample and extraction line were baked at 120° C for at least 12 h to reach acceptable ultra-high vacuum (UHV) background levels. Each sample was step-heated with a 100 W Photon Machines Fusions 10.6 CO<sub>2</sub> laser using a homogenized 4 mm beam between 3 – 40 % laser power (max. power of 55 W), whereas standards were fused in a single step. The beam was jogged over the sample for approximately one minute to homogenise the temperature gradient between grains.

Resulting gases were purified using a polycold electrical cryocooler, a liquid nitrogen condensation trap, a SAES GP50 getter operating at 450°C, a AP10 SAES getter operating at 450°C and a AP10 SAES getter operating at room temperature. The purified gases were analysed in static mode on the ARGUSVI mass spectrometer. Measurements were performed in multi-collector mode with  $^{37}\text{Ar}$ ,  $^{38}\text{Ar}$ ,  $^{39}\text{Ar}$  and  $^{40}\text{Ar}$  analysed on four Faraday detectors and  $^{36}\text{Ar}$  analysed on the CDD. The relative abundance of each mass was simultaneously measured during 10 cycles of 33 seconds integration time for each mass. These Faraday detectors incorporate high gain amplifier circuits that allow for gains of  $10^{12} \Omega$  resistors on mass 40, 38 and 37, and  $10^{13} \Omega$  on mass 39, as well as a high dynamic range due to an improved measurement range of 50,000 fA. The CDD has an ion counting efficiency of > 95% relative to the Faraday cup set to mass 40, with inherent noise levels lower than 10 counts per minute (cpm). Half of the experiments were run with  $10^{12} \Omega$  resistors for all masses, whereas the other half was run with a  $10^{13} \Omega$  resistor for mass 39. Faraday detectors are routinely calibrated each day to correct for slight offsets in the peak for each isotopic mass either by exposure to a standard electrical current (in case of  $10^{12} \Omega$  resistors for all masses), or with a 2900 fA air shot (in case of  $10^{13} \Omega$  resistor for mass 39), whereas the CDD is calibrated each day for its actual yield by running a series of four air aliquots.

Argon isotope results are corrected for system blanks, mass discrimination, radioactive decay and reactor-induced interference reactions. System blanks were measured every fourth sample. Mass discrimination was closely monitored via an automated air pipette system before and after each step-heating experiment assuming an atmospheric  $^{40}\text{Ar}/^{36}\text{Ar}$  ratio of  $298.56 \pm 0.31$  (Lee *et al.*, 2006; Mark *et al.*, 2011). The J-value for all specific levels was calculated by averaging the mean ( $^{40}\text{Ar}^*/^{39}\text{Ar}$ ) ratios from total fusion analysis of four aliquots of FC sanidine bracketing the sample. Mass discrimination and J-values ranged from  $0.992121 \pm 0.00019$  to  $0.996254 \pm 0.00019$  per Dalton (atomic mass unit) and  $0.0000932 \pm 0.0000002$  (0.205%) to  $0.0000972 \pm 0.0000004$  (0.375%) respectively. We used correction factors obtained from prolonged analysis of K-Ca-Cl glass/salts at the Oregon State TRIGA reactor:  $(^{39}\text{Ar}/^{37}\text{Ar})_{\text{Ca}} = (7.60 \pm 0.09) \times 10^{-4}$ ;  $(^{36}\text{Ar}/^{37}\text{Ar})_{\text{Ca}} = (2.70 \pm 0.02) \times 10^{-4}$ ;  $(^{40}\text{Ar}/^{39}\text{Ar})_{\text{K}} = (7.30 \pm 0.90) \times 10^{-4}$ ; and  $(^{38}\text{Ar}/^{39}\text{Ar})_{\text{K}} = (1.24 \pm 0.004) \times 10^{-2}$  (Jourdan and Renne, 2007).

Data regression and age calculation was performed using the ArArCALC algorithm (Koppers, 2002). Plateau ages are defined as including > 70% of released  $^{39}\text{Ar}$  from at least 3 subsequent steps with  $^{40}\text{Ar}/^{39}\text{Ar}$  ratios within error of the  $2\sigma$  confidence level and satisfying a probability of fit (P) based on the  $\chi^2$  test distribution of at least 0.05 (see for a description Jourdan *et al.*, 2009). Plateau ages were



calculated using the optimisation model of Renne et al. (2010) and the standard ages (Fish Canyon sanidine:  $28.294 \pm 0.036$  Ma) and decay constants of Renne et al. (2011) as well as the atmospheric argon composition of Lee et al. (2006) using the mean of all the plateau steps, each weighted by the inverse variance of their individual analytical error. Uncertainties were calculated using error propagation of uncertainties associated with the mean and plateau ages and J-value and are reported at the  $2\sigma$  confidence level.

All ages reported in the text correspond to plateau ages corrected for deviations from the atmospheric  $^{40}\text{Ar}/^{36}\text{Ar}$  ratio of Lee et al. (2006). Typically, plateau age calculations for young volcanic rocks involve correction of the  $^{40}\text{Ar}$  contribution from atmosphere using these authors'  $^{40}\text{Ar}/^{36}\text{Ar}$  value of 298.56, assuming that the initial trapped ratio has an atmospheric composition. Multiple measurements of the NVP basalts showed that this assumption is not always valid, with ratios both above and below the atmospheric  $^{40}\text{Ar}/^{36}\text{Ar}$  values, respectively indicating excess argon or air fractionation during cooling or potential isobaric interferences on mass 36. In addition, the standard plateau age calculation does not propagate the uncertainty of the measurement of this trapped ratio, thus likely underestimating the true age uncertainty. Therefore, the inverse isochron ( $^{40}\text{Ar}/^{39}\text{Ar}$  vs.  $^{40}\text{Ar}/^{36}\text{Ar}$ ) age, which accounts for both the trapped ratio value and its uncertainty, provides a more accurate representation of the crystallization age of the rock. However, most publications on young volcanics, including each publication on the Newer Volcanic Province, only provide (model) plateau ages (Hare *et al.*, 2005a; Matchan *et al.*, 2016; Matchan and Phillips, 2011, 2014). In this study, in addition to providing inverse isochron ages, we use the  $^{40}\text{Ar}/^{36}\text{Ar}$  value and its uncertainty as measured by the inverse isochron, to correct for the true value of the trapped ratio. Note that this approach tends to yield better  $\chi^2$  statistics due to larger errors on each step, but as only inverse isochron  $^{40}\text{Ar}/^{36}\text{Ar}$  values derived from an isochron fit with probability of fit ( $p$ ) > 5 % were taken for the correction, we avoided having plateau ages calculated from statistically insignificant inverse isochrons. In cases where the  $p$ -value of the inverse isochron was lower than 5%, no plateau age was calculated. The uncertainty of the trapped ratio value is then propagated in the final age uncertainty; which is therefore generally larger than the uncertainty derived from using the standard plateau age model, but smaller than the uncertainty derived from using the inverse isochron. In the text and discussion, we choose to report the corrected plateau ages, as this allows an easier comparison in terms of uncertainty with published ages, all calculated using the standard plateau approach, but is statistically more accurate considering the fact that most studies do not propagate the uncertainty of the trapped ratio in their calculation. In addition, the plateau representation allows ready assessment

of the amount of gas included in the age calculation. Both the inverse isochron and corrected-plateau ages are given in Table 4.1 and Figure 4.5 for the Newer Plains and Table 4.2 and Figure 4.6 for the Newer Cones.

#### 4.4.2. Spatial analyses of the Newer Cones

##### 4.4.2.1. Regional analysis

We used the database of Boyce (2013) in which 416 individual volcanic centres are recorded with 704 eruption points. These authors merged the database of Geoscience Victoria with existing databases (Singleton & Joyce, 1970; Rosengren, 1994) using both Google Earth and the Department of Primary Industries Seamless Geology ArcGIS layers to identify volcanic features. Contrasting to previously used databases for volcanic alignment analysis solely based on satellite imagery (e.g. Lesti et al., 2008), a large amount of the volcanic centres proposed by Boyce (2013) has been confirmed by ground truthing. For the regional scale density analysis, we used the projected XY coordinates of the 416 individual centres as to not over-represent volcanic centres with multiple eruption points.

Population density analysis of the entire NVP was performed using the Euclidean nearest neighbour point pattern analysis incorporated in the spatial analyst tool pack of the ArcGIS - ArcMap 10.3.1 software suite using a circular area around each point with radius of 25 km to visualize regional scale patterns and an output cell size corresponding to the approximate areal extent of volcanic features which are typically 1 to 12 km in diameter (Hare *et al.*, 2005b). Four clusters (see sections 4.2 and 5.4 and Figure 4.7) were visually identified.

##### 4.4.2.2. Cluster analysis

We performed quantitative point pattern analysis of the four high volcanic density clusters visually identified using the Geological Image Analysis Software suite (GIAS; Beggan and Hamilton, 2010). This MATLAB operated script allows automated sample size dependent nearest neighbour (NN) point pattern analysis to quantify the degree of randomness between the points using parameters R and c (Beggan and Hamilton, 2010). Parameter R is calculated as the ratio between the actual mean NN distance ( $r_a$ ) and the expected mean NN distance ( $r_e$ ). The expected mean NN distance  $r_e$  is dependent on the input population density,  $\rho_0$ , given as the number of objects  $N$  divided over the area  $A$  of the feature field. The expected standard error of the Poisson distribution,  $\sigma_e$  is given as  $[0.26136/\sqrt{(N * \rho_0)}]$ . Parameter c is calculated as  $(r_a - r_e)/\sigma_e$  (Clark and Evans, 1954). An ideal set of random Poisson distributed volcanic centres would have an R value of 1 and a c value of 0, whereas values of  $R < 1$  or  $R > 1$  would respectively indicate that volcanoes are more closely spaced or more randomly distributed than expected.

## 4.4.2.3. Alignment analysis

To test the dependence on geological structure for the volcanic centres within clusters, information of the shape of each volcanic vent is as useful as information about its location (Paulsen and Wilson, 2010). We used both visual (e.g. Lesti et al., 2008) as well as automated (e.g. Cebriá et. al., 2011)

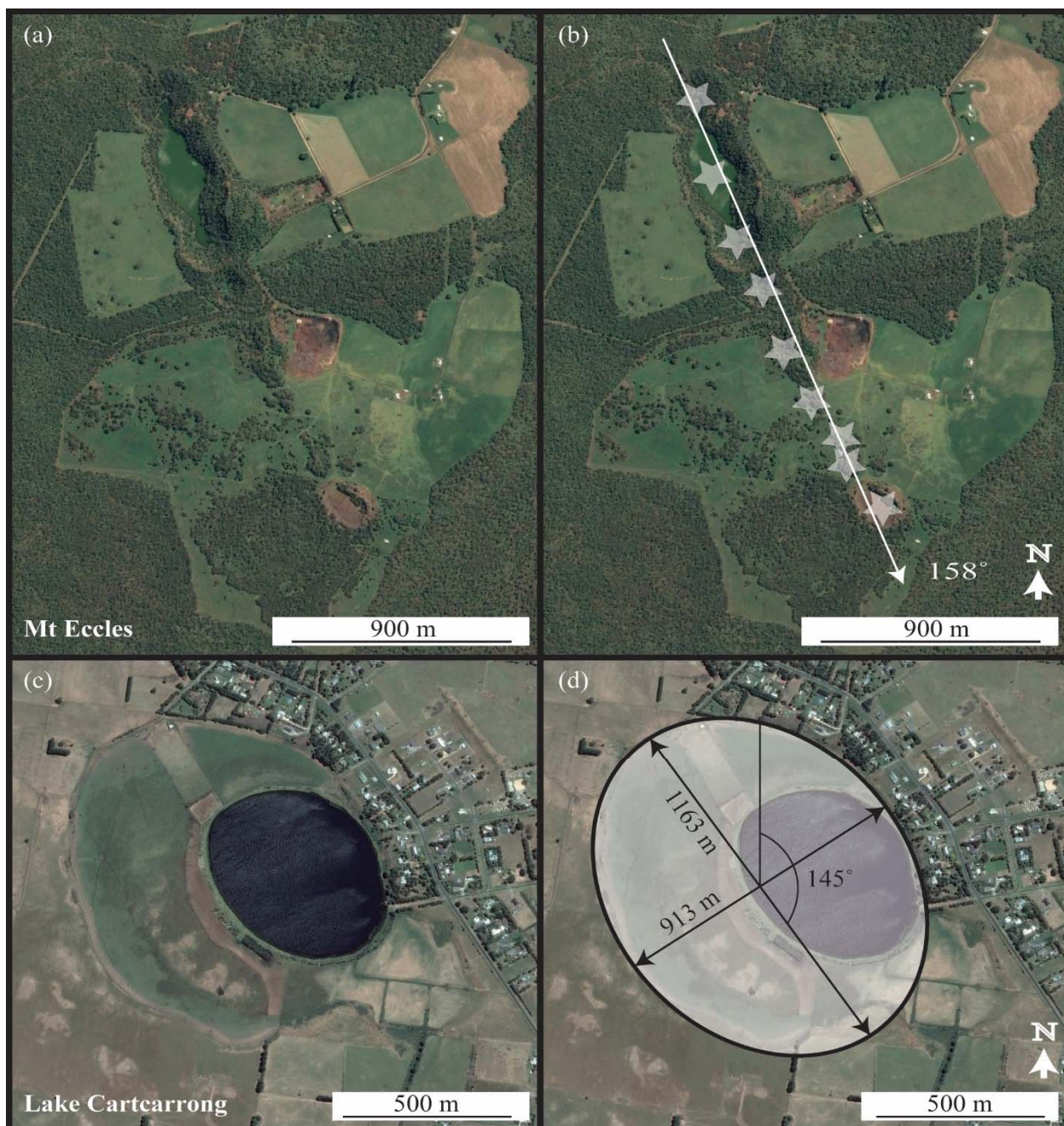


Figure 4.4. Examples of volcanic alignment and geomorphology interpretations. (a) Satellite image of Mt Eccles and (b) interpreted alignment direction. (c) Satellite image of Lake Cartcarrong (maar) and (d) interpreted elongation of the maar structure with preferred orientation.

techniques to identify potential alignments between volcanic centres and assess the shape of individual volcanoes. For the visual interpretation of volcanic shapes, we printed satellite imagery of each centre on a large format to find shapes pointing towards underlying structures, such as elongated

cones, clefted crests and aligned eruption points (Figure 4.4; Paulsen and Wilson, 2010). Using a grading scheme (1 = direct observation of elongation/cleft from complete outcrop, 2 = direct observation of elongation/cleft from incomplete outcrop, 3 = elongation derived from topography, 4 = elongation derived from surrounding structures) as well as a ratio larger than 1.2 for the elliptical maximum and minimum axis, we derived elongation information with associated azimuth direction on a number of volcanic centres within each cluster. GEOrient software (Holcombe, 2010) was used to plot azimuth directions of alignments, where we chose to only use azimuths derived from grade 1 and grade 2 observations.

A fully automated analysis of small scale alignments within each cluster can be achieved by using the MATLAB script developed by Le Corvec *et al.* based on two-point azimuth point pattern analysis (Le Corvec *et al.*, 2013a, 2013b). We investigated potential alignments between more than three eruption points, allowing a width tolerance of 100 – 200 m, as this is a typical surface expression of the scale of crustal faults at depth. Furthermore, we used an individual length tolerance for the maximum distance allowed between volcanic centres along a single alignment, based on the relation between density of the volcanic field (as derived from the GIAS analysis) and the minimum number of resulting artefacts which for which we used the relation:  $-2527 * \ln(x) - 36895$  ( $x$ : population density; Le Corvec *et al.*, 2013). GEOrient software (Holcombe, 2010) was used to plot azimuth directions of alignments using bins of 10 degrees.

## 4.5. Results

### 4.5.1. $^{40}\text{Ar}/^{39}\text{Ar}$ geochronology

#### 4.5.1.1. Newer Plains basalts

We were able to derive statistically significant ages for four of the nine Newer Plains samples (Figure 4.1a, Figure 4.2 and Figure 4.5; Table 4.1) with plateau ages ranging from  $3.82 \pm 0.02$  Ma (VIC49) to  $4.32 \pm 0.03$  Ma (VIC38).

The Newer Plains samples yielded  $^{40}\text{Ar}/^{36}\text{Ar}$  trapped ratios ranging from  $290.7 \pm 1.5$  to  $313.5 \pm 4.5$ , relative to the atmospheric ratio of  $298.56 \pm 0.31$  (Lee *et al.*, 2006). Samples VIC12, VIC14, VIC46 and VIC47 only yielded a mini-plateau (50 – 70% cumulative  $^{39}\text{Ar}$ ; Jourdan *et al.*, 2007). Mini-plateau ages are less robust than their plateau counter-parts and should be taken with caution. They might indicate the true crystallization age, but can also represent maximum or minimum age values,

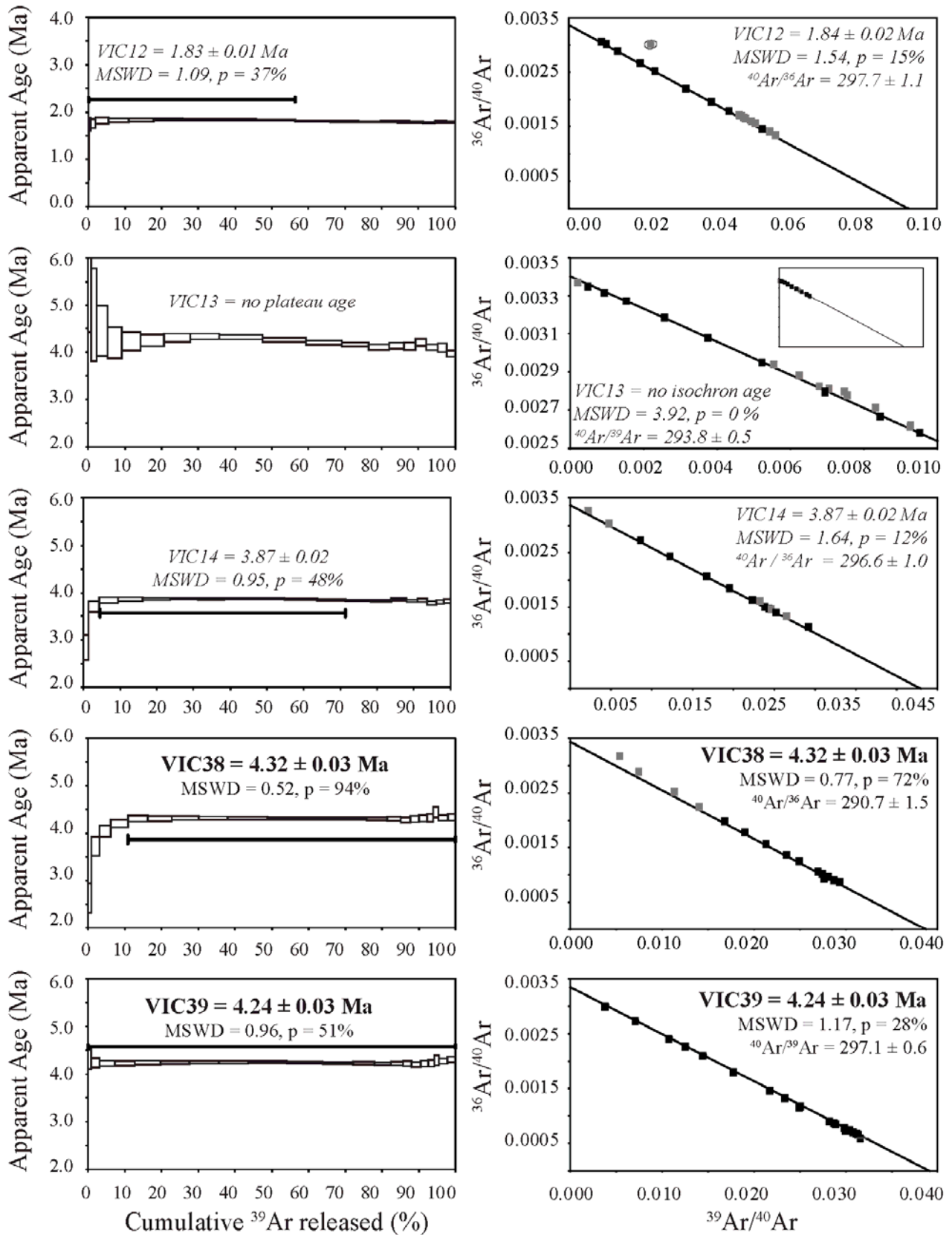


Figure 4.5. Summary of Newer Plains step-heating analyses; apparent age plateau and inverse isochron diagrams. Plateau ages (**bold**) are inverse isochron intercept ( $^{40}\text{Ar}/^{36}\text{Ar}$ ) corrected. Mini-plateaus (50 - 70% cumulative  $^{39}\text{Ar}$ ) are indicated in italics. All ages are reported with  $2\sigma$  uncertainty. The material analysed was groundmass for all samples.

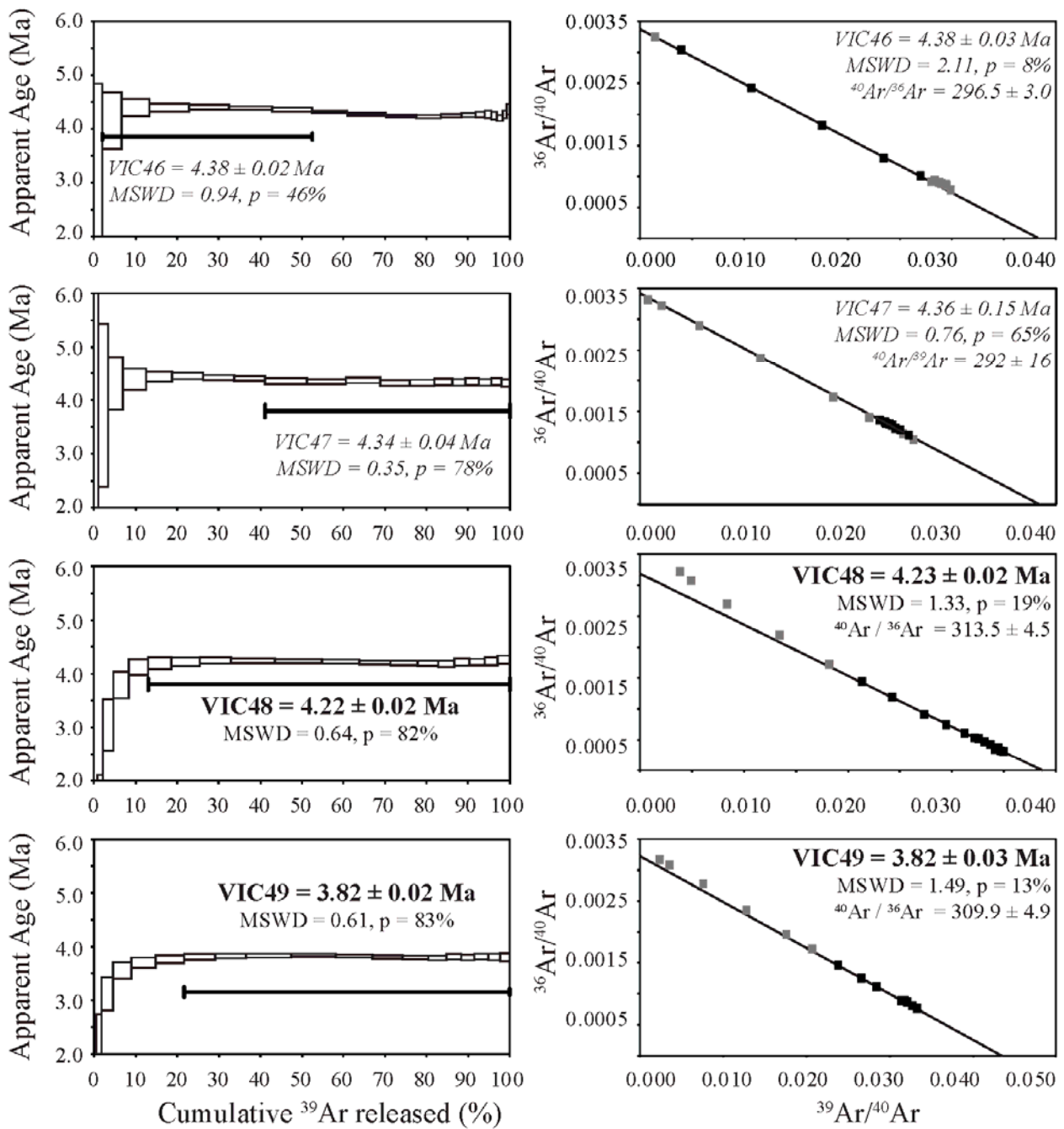


Figure 4.5. Continued.

as the probability of fit for the inverse isochron was lower than 5%. Figure 4.5 shows a summary of the apparent age spectra and inverse isochron diagrams for the Newer Plains basalts. Full step-heating analyses as well as all age and isochron spectra can be found in Appendix D and Appendix F respectively.

Unit	Sample characteristics			Plateau characteristics				Inverse Isochron characteristics					
	Sample No	min eral	X (dec. degrees)	Y (dec. degrees)	Plateau age (Ma, $\pm 2\sigma$ )	Total $^{39}\text{Ar}$ released (%)	MS WD	P	Inverse Isochron age (Ma, $\pm 2\sigma$ )	n	$^{40}\text{Ar}/^{36}\text{Ar}$ intercept ( $\pm 2\sigma$ )	MS WD	P
Wannon Falls	VIC12	GM	141.840	-37.674	1.83 $\pm$ 0.01	56.32	1.09	0.37	1.84 $\pm$ 0.02	9	297.7 $\pm$ 1.1	1.54	0.15
Mt Pierre-point Napier area old flow	VIC13	GM	142.060	-37.770	no plateau age*				no isochron age		293.8 $\pm$ 0.5	3.92	0.00
	VIC14	GM	141.948	-37.923	3.87 $\pm$ 0.02	67.11	0.95	0.48	3.87 $\pm$ 0.02	9	296.6 $\pm$ 1.0	1.64	0.12
Kororoit-16	VIC38	GM	144.38	-37.44	<b>4.32 <math>\pm</math> 0.03</b>	89.18	0.54	0.94	<b>4.32 <math>\pm</math> 0.03</b>	17	290.7 $\pm$ 1.5	0.77	0.72
	VIC39	GM	144.38	-37.44	<b>4.24 <math>\pm</math> 0.03</b>	100.00	0.96	0.51	<b>4.24 <math>\pm</math> 0.03</b>	21	297.1 $\pm$ 0.6	1.17	0.28
	VIC46	GM	142.339	-37.823	4.38 $\pm$ 0.02	50.60	0.94	0.46	4.38 $\pm$ 0.03	6	296.5 $\pm$ 3.0	2.11	0.08
	VIC47	GM	142.339	-37.823	4.34 $\pm$ 0.04	58.86	0.35	0.78	4.36 $\pm$ 0.15	11	292 $\pm$ 16	0.76	0.65
PRC-6	VIC48	GM	142.339	-37.823	<b>4.22 <math>\pm</math> 0.02</b>	87.02	0.64	0.82	<b>4.23 <math>\pm</math> 0.02</b>	14	313.5 $\pm$ 4.5	1.33	0.19
	VIC49	GM	142.339	-37.823	<b>3.82 <math>\pm</math> 0.02</b>	78.41	0.61	0.83	<b>3.82 <math>\pm</math> 0.02</b>	13	309.9 $\pm$ 4.9	1.49	0.13

Table 4.1. Summary of  $^{40}\text{Ar}/^{39}\text{Ar}$  results for the Newer Plains basalts. Data in italics are derived from mini-plateaus (50 - 70%  $^{39}\text{Ar}$  released) and are considered minimum ages only. \* No plateau age is calculated, as the correlation of the inverse isochron diagram

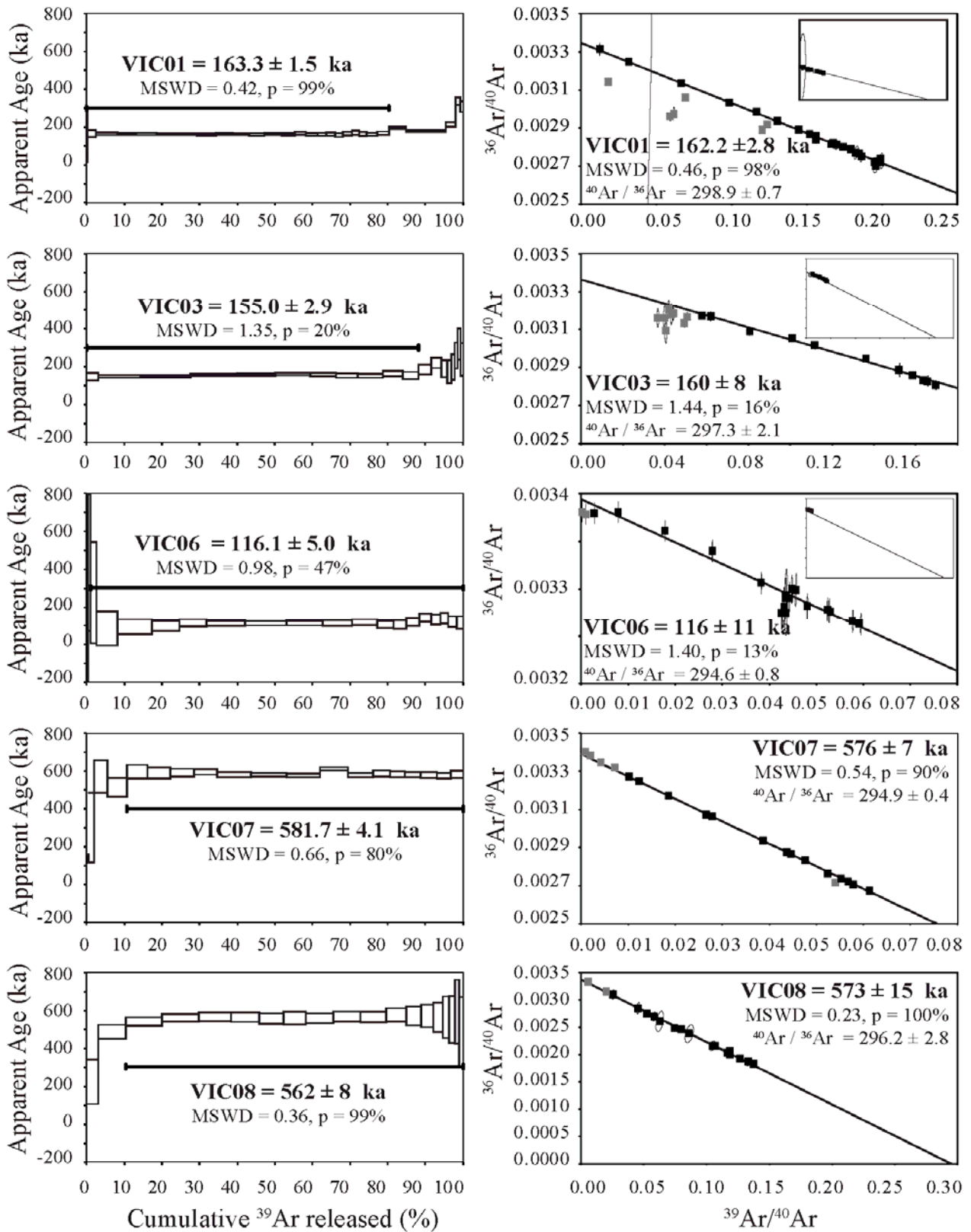


Figure 4.6. Summary of Newer Cones step-heating analyses; apparent age plateau and inverse isochron diagrams. Plateau ages (**bold**) are inverse isochron intercept ( $^{40}\text{Ar}/^{36}\text{Ar}$ ) corrected. Mini-plateaus (50 - 70% cumulative  $^{39}\text{Ar}$ ) are indicated in italics. All ages are reported to a  $2\sigma$  uncertainty. Groundmass was analysed for all samples except VIC22B (glass).



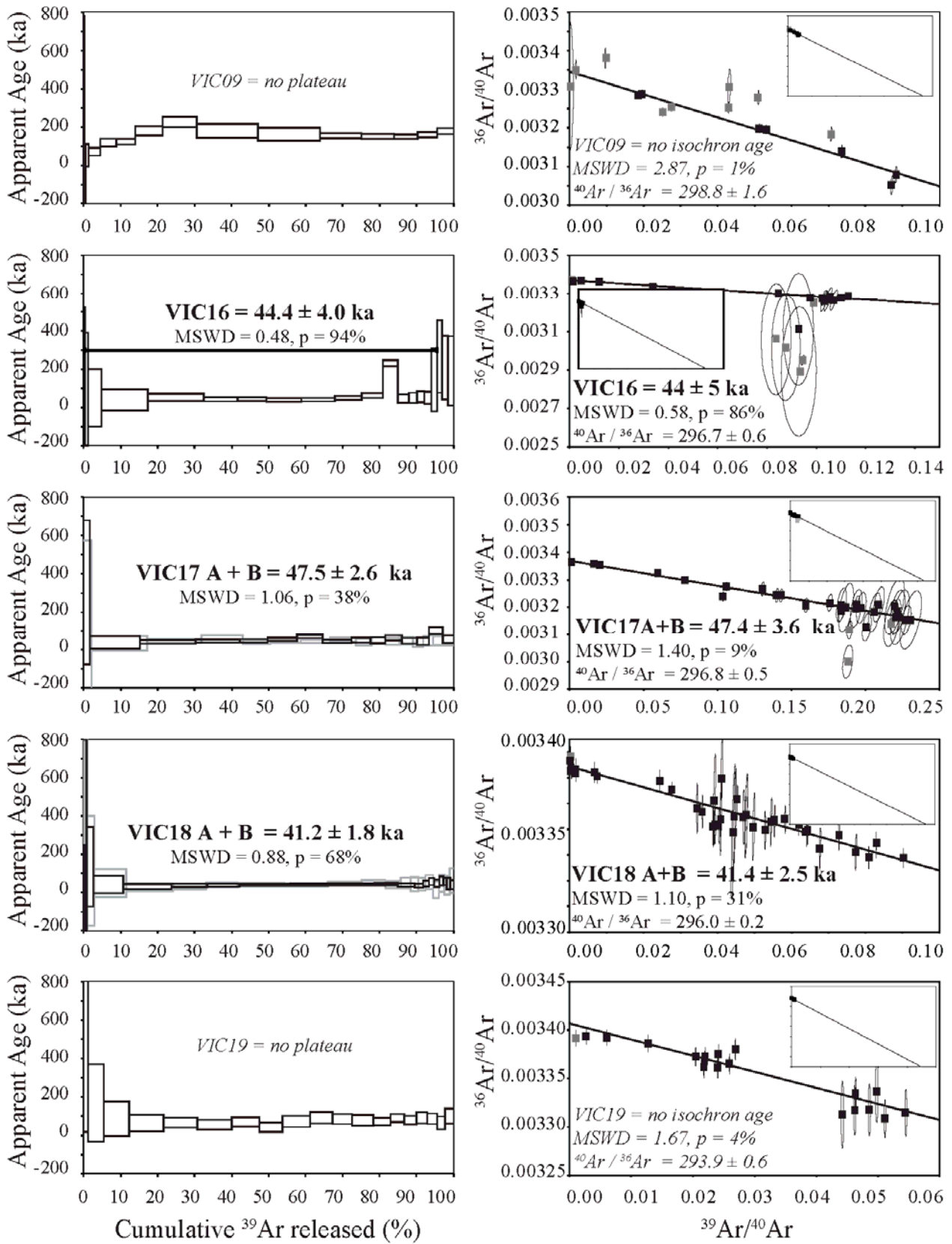


Figure 4.6. Continued

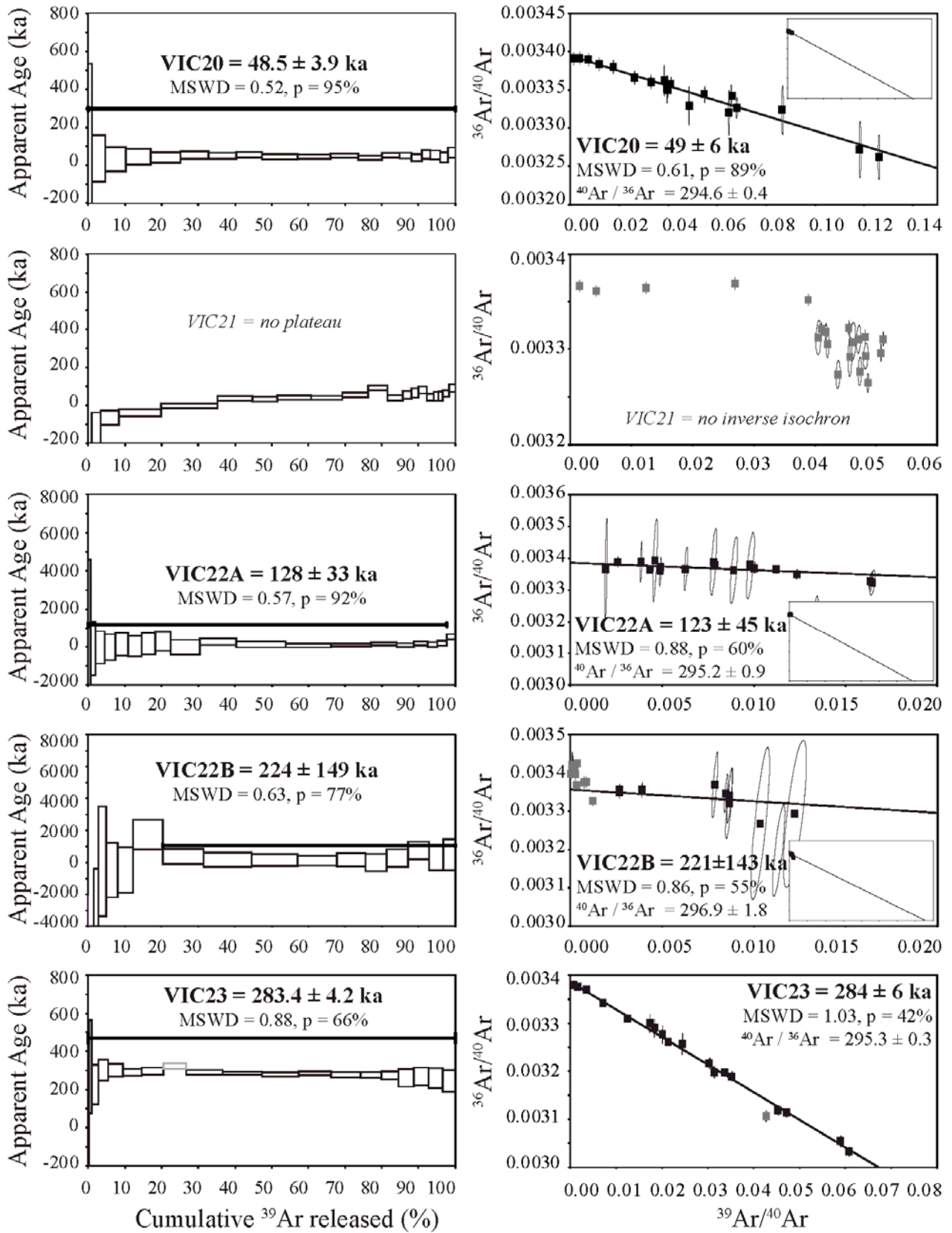


Figure 4.6. Continued

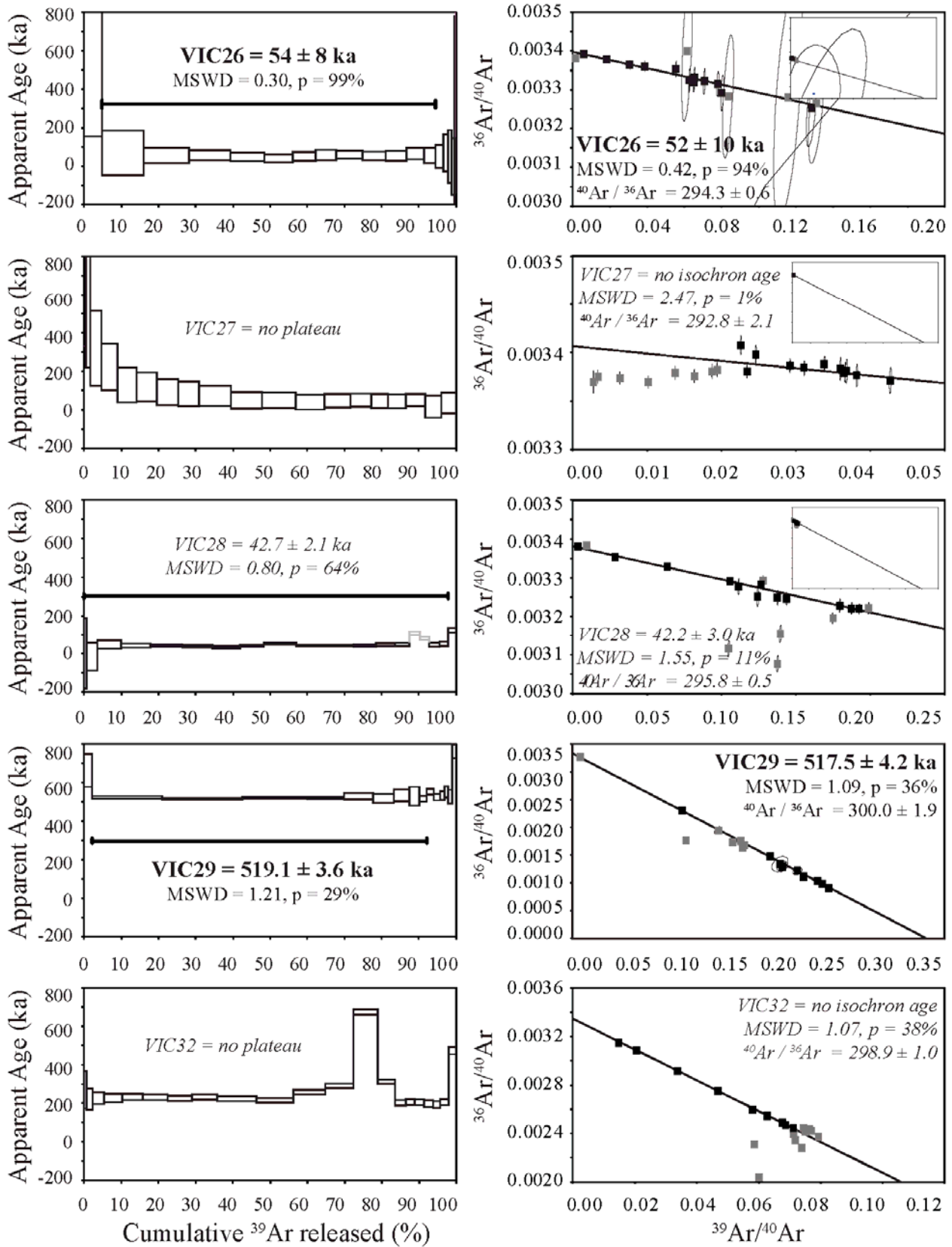


Figure 4.6. Continued.

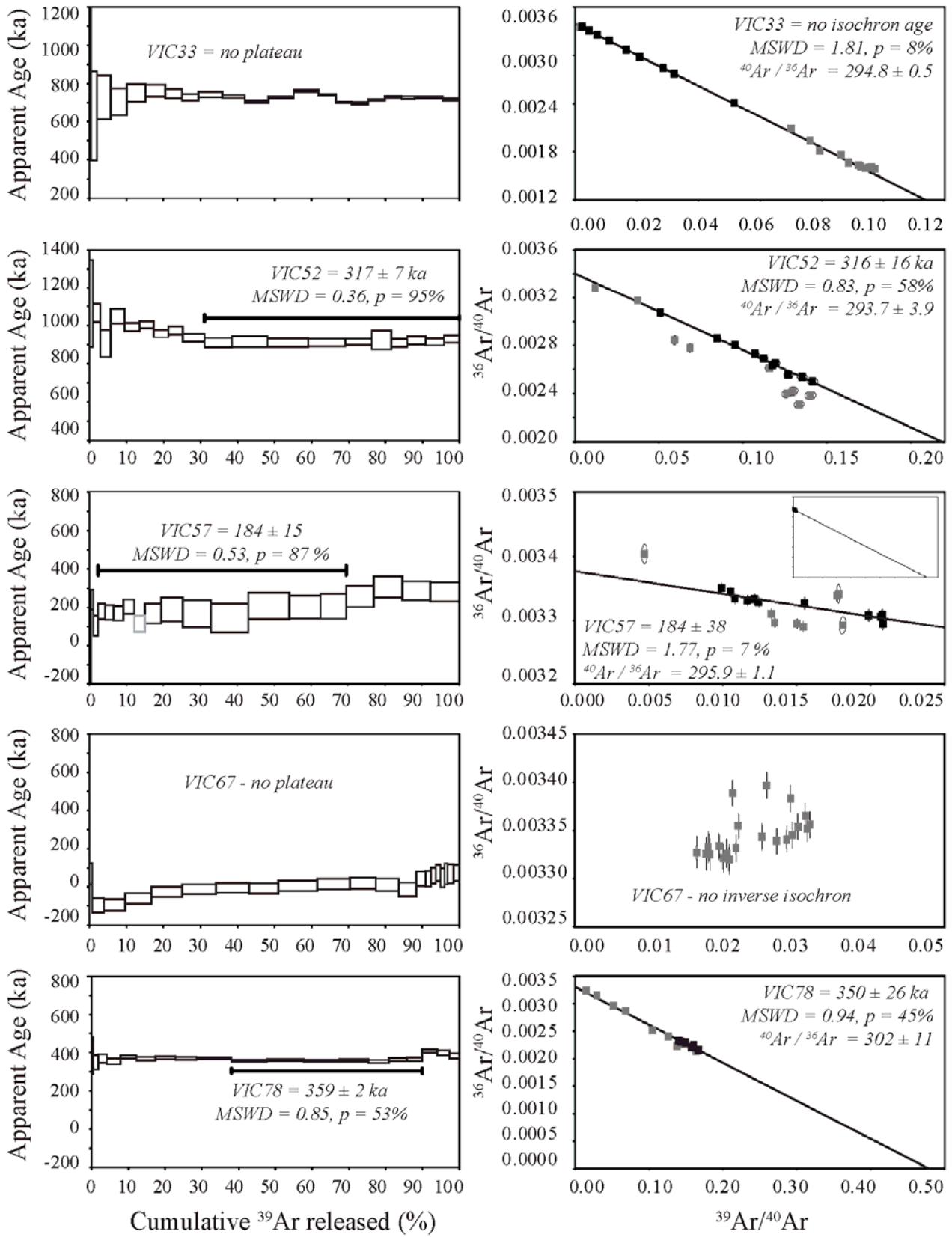


Figure 4.6. Continued.

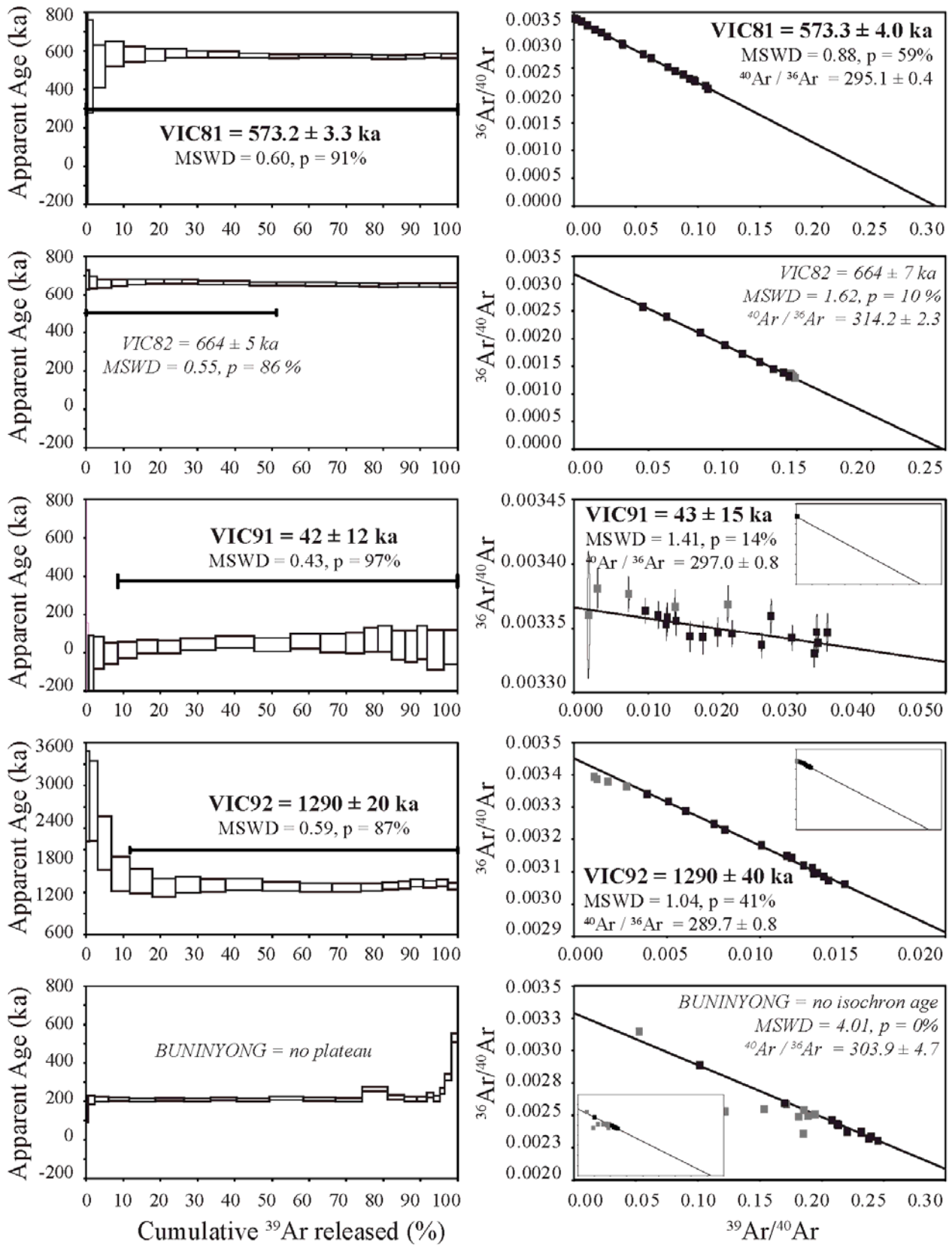


Figure 4.6. Continued.

Unit	Sample characteristics				Plateau characteristics				Inverse Isochron characteristics				
	Sample No	mine-ral	X (dec. degrees)	Y (dec. degrees)	Plateau age (ka, $\pm 2\sigma$ )	Total $^{39}\text{Ar}$ released (%)	MS WD	P	Inverse Isochron age (ka, $\pm 2\sigma$ )	n	$^{40}\text{Ar}/^{36}\text{Ar}$ intercept ( $\pm 2\sigma$ )	MS WD	P
Mt Buninyong	BUNY	GM	143.923	-37.653		no plateau age*			no isochron age		303.9 $\pm$ 4.7	4.01	0.00
Mt Leura	VIC01	GM	143.163	-38.247	<b>163.3 <math>\pm</math> 1.5</b>	80.28	0.42	0.99	<b>162.2 <math>\pm</math> 2.8</b>	23	298.9 $\pm$ 0.7	0.46	0.98
	VIC03	GM	143.163	-38.247	<b>155.0 <math>\pm</math> 2.9</b>	88.25	1.35	0.20	<b>160 <math>\pm</math> 8</b>	11	297.3 $\pm$ 2.1	1.44	0.16
Mt Porndon	VIC06	GM	143.281	-38.302	<b>116.1 <math>\pm</math> 5.0</b>	99.02	0.98	0.47	<b>116 <math>\pm</math> 11</b>	18	294.6 $\pm$ 0.8	1.40	0.13
	VIC07	GM	142.923	-38.180	<b>581.7 <math>\pm</math> 4.1</b>	81.86	0.66	0.80	<b>576 <math>\pm</math> 7</b>	14	294.9 $\pm$ 0.4	0.54	0.90
Mt Noorat	VIC08	GM	142.923	-38.180	<b>562 <math>\pm</math> 8</b>	89.60	0.36	0.99	<b>573 <math>\pm</math> 15</b>	17	296.2 $\pm$ 2.8	0.23	1.00
	VIC09	GM	142.923	-38.180		no plateau age			no isochron age		298.8 $\pm$ 1.6	2.87	0.01
	VIC16	GM	141.884	-37.939	<b>44.4 <math>\pm</math> 4.0</b>	85.48	0.48	0.94	<b>44 <math>\pm</math> 5</b>	14	296.7 $\pm$ 0.6	0.58	0.86
	VIC17A	GM	141.883	-37.938	<b>47.2 <math>\pm</math> 3.6</b>	86.26	1.10	0.36	<b>46.7 <math>\pm</math> 5.0</b>	12	296.7 $\pm$ 0.6	1.45	0.15
	VIC17B	GM	141.883	-37.938	<b>47.9 <math>\pm</math> 3.9</b>	100.00	1.09	0.36	<b>48 <math>\pm</math> 6</b>	16	296.9 $\pm$ 0.9	1.48	0.11
	<b>weighted mean age for VIC17: 47.5 <math>\pm</math> 2.6 ka</b>												
Mt Napier	VIC18A	GM	142.050	-37.887	<b>41.1 <math>\pm</math> 2.2</b>	100.00	1.21	0.24	<b>41.2 <math>\pm</math> 3.1</b>	20	296.1 $\pm$ 0.3	1.46	0.09
	VIC18B	GM	142.050	-37.887	<b>41.6 <math>\pm</math> 4.1</b>	99.83	0.58	0.92	<b>41 <math>\pm</math> 6</b>	19	295.8 $\pm$ 0.4	0.69	0.81
	<b>weighted mean age for VIC18: 41.2 <math>\pm</math> 1.8 ka</b>												
	VIC19	GM	142.050	-37.887		no plateau age			no isochron age		293.9 $\pm$ 0.6	1.67	0.04
	VIC20	GM	142.068	-37.919	<b>48.5 <math>\pm</math> 3.9</b>	100.00	0.52	0.95	<b>49 <math>\pm</math> 6</b>	19	294.6 $\pm$ 0.4	0.61	0.89

Table 4.2. Summary of  $^{40}\text{Ar}/^{39}\text{Ar}$  results for the Newer Cones basalts. Data in italics are derived from mini-plateaus (50% - 70%  $^{39}\text{Ar}$  released) and are considered minimum ages only. Mt Buninyong is the only volcano analysed which is located in the Central Highlands

Unit	Sample characteristics				Plateau characteristics				Isochron characteristics				
	Sample No	mine-ral	X (dec. degrees)	Y (dec. degrees)	Plateau age (ka, ±2σ)	Total <sup>39</sup> Ar released (%)	MS WD	P	Isochron age (ka, ±2σ)	n	<sup>40</sup> Ar/ <sup>36</sup> Ar intercept (±2σ)	MSWD	P
	VIC21	GM	141.930	-38.060		no age plateau					no inverse isochron		
	VIC22A	GM	141.927	-38.061	<b>128 ± 33</b>	97.64	0.57	0.92	<b>123 ± 45</b>	18	295.2 ± 0.9	0.88	0.60
	VIC22B	GL	141.927	-38.061	<b>224 ± 149</b>	79.73	0.63	0.77	<b>221 ± 143</b>	10	296.9 ± 1.8	0.86	0.55
Mt Eccles	<b>weighted mean age for VIC22: 133 ± 33 ka</b>												
	VIC26	GM	141.769	-38.219	<b>54 ± 8</b>	89.74	0.30	0.99	<b>52 ± 10</b>	12	294.3 ± 0.6	0.42	0.94
	VIC27	GM	141.769	-38.219		no plateau age			no isochron age		292.8 ± 2.1	2.47	0.01
	VIC28	GM	141.768	-38.219	42.7 ± 2.1	67.16	0.80	0.64	42.2 ± 3.0	12	295.8 ± 0.5	1.55	0.11
	VIC23	GM	142.197	-38.362	<b>283.4 ± 4.2</b>	93.85	0.88	0.66	<b>284 ± 6</b>	18	295.3 ± 0.3	1.03	0.42
Mt Rouse	VIC52	GM	142.371	-38.099	317 ± 7	68.97	0.36	0.95	316 ± 16	10	293.7 ± 3.9	0.83	0.58
Hopkins Falls	VIC29	GM	142.618	-38.349	<b>519.1 ± 3.6</b>	89.90	1.21	0.29	<b>517.5 ± 4.2</b>	9	300.0 ± 1.9	1.09	0.36
Hopkins Falls RD	VIC32	GM	142.691	-38.330		no plateau age			no isochron age		298.9 ± 1.0	1.07	0.38
Staughton Hill	VIC33	GM	142.916	-38.318		no plateau age			no isochron age		294.8 ± 0.5	1.81	0.08
Mt Elephant	VIC57	GM	143.200	-37.956		no plateau age			no isochron age		288.9 ± 2.5	2.24	0.02
	VIC67	GM	143.199	-37.969		no age plateau <sup>†</sup>					no inverse isochron		
Mt Shadwell	VIC78	GM	142.817	-38.050	359 ± 2	51.93	0.85	0.53	350 ± 26	7	350 ± 26	0.94	0.45
Two Sisters	VIC81	GM	142.792	-38.188	<b>573.2 ± 3.3</b>	100.00	0.60	0.91	<b>573.3 ± 4.0</b>	19	295.1 ± 0.4	0.88	0.59

Table 4.2. Continued.

Unit	Sample characteristics			Plateau characteristics			Isochron characteristics						
	Sample No	mine ral	X (dec. degrees)	Y (dec degrees)	Plateau age (ka, $\pm 2\sigma$ )	Total $^{39}\text{Ar}$ released (%)	MS WD	P	Isochron age (ka, $\pm 2\sigma$ )	n	$^{40}\text{Ar}/^{36}\text{Ar}$ intercept ( $\pm 2\sigma$ )	MS WD	P
Terang Maar	VIC82	GM	142.915	-38.250	664 $\pm$ 5	51.25	0.55	0.86	664 $\pm$ 7	11	314.2 $\pm$ 2.3	1.62	0.10
Alvie	VIC91	GM	143.503	-38.247	42 $\pm$ 12	91.54	0.43	0.97	43 $\pm$ 15	16	297.0 $\pm$ 0.8	1.41	0.14
Mt Gellibrand	VIC92	GM	143.503	-38.247	1290 $\pm$ 20	88.32	0.59	0.87	1290 $\pm$ 40	15	289.7 $\pm$ 0.8	1.04	0.41

Table 4.2. Continued.



#### 4.5.1.2. Newer Cones basalt

Nineteen of the 32 Newer Cones samples yielded statistically significant plateau ages (Figure 4.6; Table 4.2), ranging from  $41.1 \pm 2.2$  ka (VIC18A) to  $1290 \pm 20$  ka (VIC92). Replicate analyses of samples VIC17, VIC18 and VIC22 allowed us to calculate mean weighted ages of  $47.5 \pm 2.6$  ka,  $41.2 \pm 1.8$  ka and  $133 \pm 33$  ka respectively. These samples yielded  $^{40}\text{Ar}/^{36}\text{Ar}$  trapped ratios ranging from  $288.9 \pm 2.5$  to  $301 \pm 8$ . Most samples are characterized by sub-atmospheric  $^{40}\text{Ar}/^{36}\text{Ar}$  ratios (e.g.  $293.9 \pm 0.6$  for VIC19). Furthermore, some samples have a very low spreading factor along the inverse isochron diagram (Jourdan *et al.*, 2009a) of only a few percent or less, for example; 0.6% for VIC91. Samples VIC28, VIC52, VIC57, VIC78 and VIC82 only yielded mini-plateaus between 50% and 70% cumulative  $^{39}\text{Ar}$  released. No inverse isochron corrected plateau age could be obtained for Mt Buninyong (BUNYG), VIC09, VIC19, VIC27, VIC32 and VIC33 due to the statistically poor fit of their inverse isochrons. No inverse isochron or plateau age could be derived for samples VIC21 and VIC67. The two aliquots of sample VIC22 show indistinguishable ages of  $128 \pm 33$  ka for sample VIC22A (groundmass) and  $224 \pm 149$  ka for sample VIC22B (glass). A summary of the apparent age spectra and inverse isochron diagrams for the Newer Cones basalts can be found in Figure 4.6, whereas full step-heating analyses and all age and isochron spectra can be found in the Appendix E and Appendix G.

#### 4.5.2. Spatial analysis

Regional scale point density analysis reveals the presence of four distinct clusters of higher density within the NVP region: the Mt Gambier, Western Plains West, Western Plains East and the Central Highlands clusters (Figure 4.7). GIAS analysis results indicate that eruption points within all four clusters show a non-random distribution with R values of 0.581 for the Gambier cluster, 0.512 for the Western Plains West cluster, 0.447 for the Western Plains East cluster and 0.710 for the Central Highlands cluster.

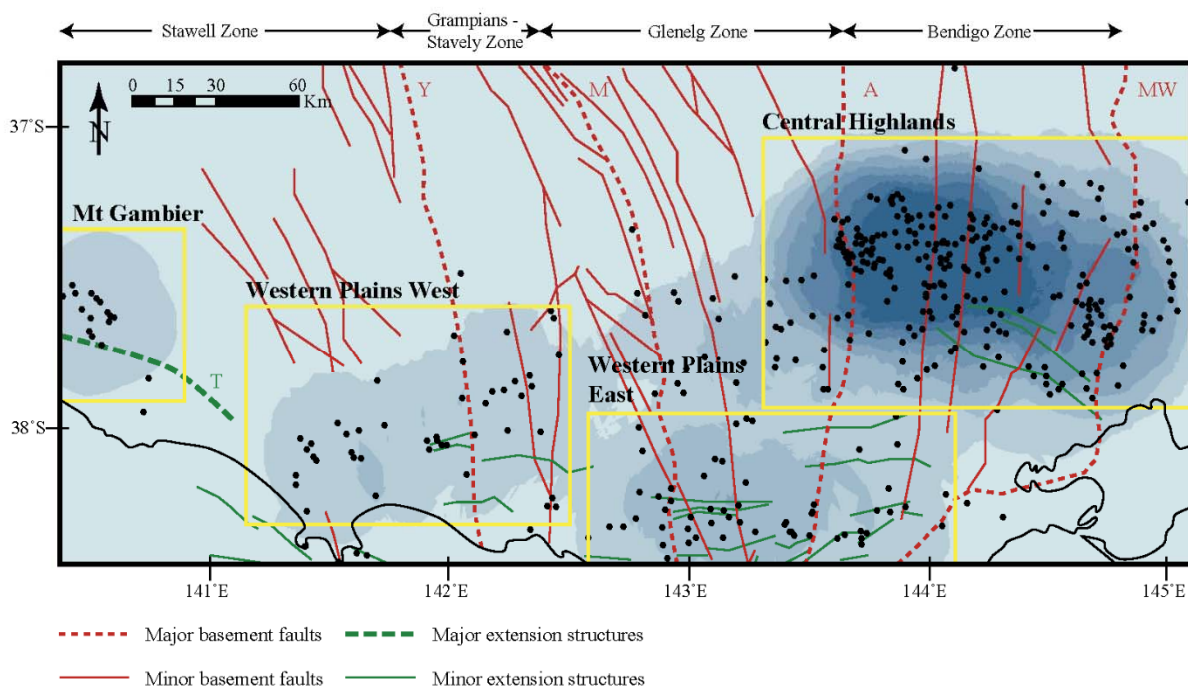


Figure 4.7. Qualitative Euclidean distance nearest neighbour density map of the NVP, indicated are the four clusters resulting from this analysis; darker colours represent higher densities. Also indicated are major and minor crustal structures as well as structural zones.

Visual interpretation of individual volcanic centres shows that for all clusters, volcanic features show elongation in a preferred azimuth direction (Figure 4.8a-d; Mt Gambier:  $130^{\circ}\text{N} - 140^{\circ}\text{N}$  ( $n = 9$ ), Western Plains West:  $140^{\circ} - 150^{\circ}$  ( $n = 20$ ), Western Plains East:  $10^{\circ} - 30^{\circ}$  ( $n = 31$ ) and Central Highlands:  $0^{\circ} - 10^{\circ}$  ( $n = 65$ ). These azimuth directions are confirmed in two clusters by the results of the automated two-point azimuth analysis (Figure 4.8e-h: Western Plains West:  $140^{\circ} - 150^{\circ}$  ( $n = 6695$ ) and the Western Plains East:  $10^{\circ} - 30^{\circ}$  ( $n = 2371$ ). The alignment azimuth found in Mt Gambier is oriented slightly more east – west at  $110^{\circ} - 130^{\circ}$  ( $n = 1757$ ), whereas the Central Highland cluster shows two preferential alignment directions at  $80^{\circ} - 90^{\circ}$  and  $140^{\circ} - 150^{\circ}$  ( $n = 1151$ ).

## 4.6. Discussion

### 4.6.1. Comparison with existing K/Ar, $^{40}\text{Ar}/^{39}\text{Ar}$ and cosmogenic isotope ages

#### 4.6.1.1. Newer Plains basalts

Extensive K-Ar geochronology on the Newer Plains basalts (Aziz-ur-Rahman and McDougall, 1972; Gray and McDougall, 2009; McDougall *et al.*, 1966; Singleton *et al.*, 1976) has suggested ongoing volcanism from 4.6 Ma to present, with peak volcanic activity from 3 – 1.8 Ma. Our nine samples show that all ages but one ( $\sim 1.8$  Ma) range from 3.8 to 4.3 Ma, which is significantly older than the age range reported for the volumetric peak of Newer Plains volcanism. This could be due to the fact that most K-Ar sampling has taken place on basalt flows close to the surface which are potentially

altered; from boulders in pastures as well as shallow quarries, whereas most of our samples were derived from fresh, mostly unaltered drill core.

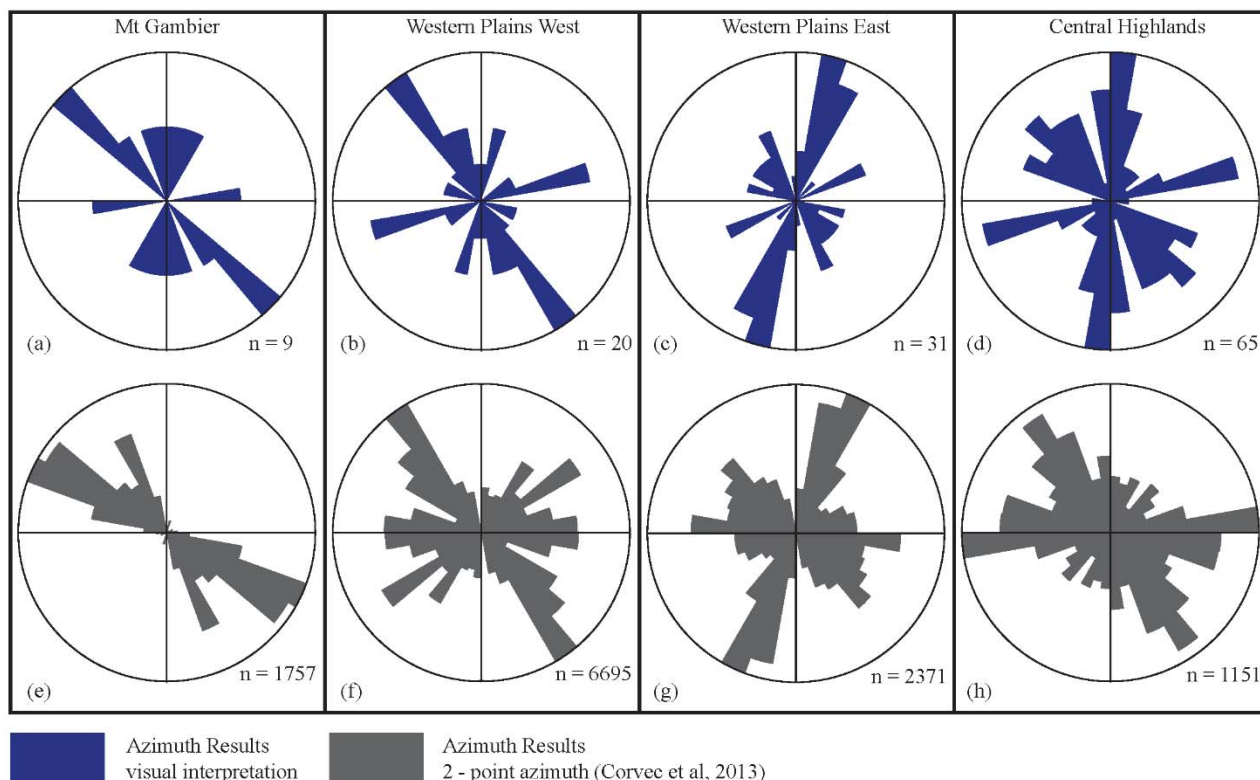


Figure 4.8. Rose diagrams of volcanic alignments; (a) – (d): rose diagrams of the four clusters as derived from visual interpretation of volcanic centres. (e) – (f): rose diagrams of the four clusters as derived from automated two-point azimuth analysis (Le Corvec *et al.*, 2013b).

Furthermore, the degassing characteristics of our samples are important for the interpretation of published K-Ar ages, as the K-Ar dating technique is not able to recognize (and correct for) non-atmospheric  $^{40}\text{Ar}/^{36}\text{Ar}$  ratios and alteration effects. Hence, the reliability of K-Ar ages proves to be questionable. Five out of 9 samples analysed show non-atmospheric  $^{40}\text{Ar}/^{36}\text{Ar}$  ratios, plotting either above ( $313.5 \pm 3.5$ : VIC48;  $309.9 \pm 4.9$ : VIC49) or below ( $293.8 \pm 0.5$ : VIC13;  $296.6 \pm 1.1$ : VIC14;  $297.1 \pm 0.6$ : VIC39) the given atmospheric ratio of  $298.56 \pm 0.31$  (Lee *et al.*, 2006). Whereas supra-atmospheric values can be explained by the presence of excess  $^{40}\text{Ar}$ , sub-atmospheric values are more difficult to explain. For fresh, young volcanic rocks, this observation is best explained in terms of isotopic mass fractionation of argon of atmospheric composition during exchange with the magma before or during eruption (Jourdan *et al.*, 2012; McDougall and Harrison, 1999; Renne *et al.*, 2009). Low  $^{40}\text{Ar}/^{36}\text{Ar}$  ratios can also be due to isobaric interferences during analysis on mass 36 for Cl-rich samples; however, this explanation is unlikely as 1) atmospheric  $^{40}\text{Ar}/^{36}\text{Ar}$  ratios for other young basalts are routinely obtained in this laboratory using this specific instrumental setup; and 2) isobaric

interferences are not expected to be consistent throughout the samples due to natural zoning of Cl and associated multiple isotopic reservoirs in a rock, which is not observed in the linear correlation of the inverse isochrons.

#### 4.6.1.2. Newer Cones basalts

Most of the ages available for the Newer Cones basalts are based on  $^{40}\text{Ar}/^{39}\text{Ar}$  results and are hence much more reliable than the K/Ar data available for the Newer Plains. However, published  $^{40}\text{Ar}/^{39}\text{Ar}$  ages of the Newer Cones are still very scarce, with only 8 ages available in the literature (Matchan *et al.*, 2016; Matchan and Phillips, 2011, 2014). From this restricted database, several ages have been reinvestigated in this study in an attempt to directly compare with ages generated in a different laboratory. Our age of the Mt Rouse flow (VIC23) is in agreement with a recently published  $^{40}\text{Ar}/^{39}\text{Ar}$  age on Mt Rouse analysed using a similar analytical set-up by Matchan and Phillips (2014). These authors derived a weighted mean age of  $284.4 \pm 1.8$  ka from multiple aliquots, which statistically overlaps with our age of  $283.4 \pm 4.2$  ka from a single aliquot. Furthermore, our age of  $519.1 \pm 3.6$  ka for the Hopkins Falls flow (VIC29) is in agreement with, and an order of magnitude more precise than, the age of  $535 \pm 27$  previously reported for the youngest of two flows at this location (Matchan and Phillips, 2011) measured using the previous generation of noble gas mass spectrometers. Our relatively imprecise but statistically correct plateau age of  $184 \pm 23$  ka for Mount Elephant (VIC57) supports the recently published hypothesis based on geomorphic observations that this volcano is between 390 ka and 40 ka old (Matchan *et al.*, 2016).

#### 4.6.2. Comparison with cosmogenic ages

Samples VIC06 (Mt Porndon), VIC16 (Harman flow – Mt Napier) and VIC26 (Tyrendarra flow – Mt Eccles) yield  $^{40}\text{Ar}/^{39}\text{Ar}$  plateau ages of  $116.1 \pm 5$  ka,  $44.4 \pm 4.0$  ka and  $54 \pm 8$  ka respectively and allow comparison with the cosmogenic  $^{21}\text{Ne}$  (Gillen *et al.*, 2010) and  $^{36}\text{Cl}$  (Stone *et al.*, 1997) exposure ages reported in literature. Exposure ages of  $53 \pm 5$  ka ( $^{21}\text{Ne}$ ) and  $58.5 \pm 5$  ka ( $^{36}\text{Cl}$ ) for Mt Porndon,  $37 \pm 5$  ka ( $^{21}\text{Ne}$ ) and  $31.9 \pm 2.4$  ka ( $^{36}\text{Cl}$ ) for the Harman flow and  $36 \pm 3$  ka ( $^{21}\text{Ne}$ ) for the Tyrendarra flow show that the cosmogenic ages are systematically younger than the crystallization age. Cosmogenic exposure dating is strongly dependent on assumptions concerning the erosion rate, the amount of shielding of a sample (tree cover, rocks), and the production rate of cosmogenic isotopes at a certain latitude (Gosse and Phillips, 2001; Niedermann, 2002). Considering that all these parameters used to calculate the exposure age are well constrained, the best explanation for the discrepancy between exposure ages and eruption ages is that the samples have been temporally shielded by vegetation, as lake deposits in the NVP show alternating periods of wetting and drying over the past 50 ka (Edney *et al.*, 1990; Harle, 1997). In any case, our results show that when using

cosmogenic exposure dating as a tool, one should keep in mind that the results only indicate how long a given surface has been exposed to the bombardment of cosmic rays, not when the lava flow has erupted. Hence, exposure ages should always be treated as minimum age when used as a proxy to date the formation age of a given layer.

#### 4.6.3. Implications of new $^{40}\text{Ar}/^{39}\text{Ar}$ isotope data

##### 4.6.3.1. Production rate of volcanism – Newer Plains

The two plateau ages ( $4.22 \pm 0.02$  Ma at 85.8 m; VIC48 and  $3.82 \pm 0.02$  Ma at 39 m; VIC49) as well as the mini-plateau ages of  $4.34 \pm 0.04$  Ma at 96.6 m for VIC47 and  $4.38 \pm 0.02$  Ma at 112 m for VIC46 were used to constrain the production rate of volcanism in core PRC-006. It can be seen in Figure 4.2 that the production rate of volcanism for PRC-006 appears to be non-linear; with an apparent rate of  $\sim 385$  m/Ma for the lower section and a rate of  $115 \pm 7$  m/Ma for the upper section. The two ages of  $4.32 \pm 0.03$  Ma at 58 m (VIC38) and  $4.24 \pm 0.04$  Ma at 29.5 m (VIC39) resulted in a relatively imprecise production rate of  $356 \pm 220$  m/Ma ( $2\sigma$ ) for core Kororoit-16 (Figure 4.2). This suggests that the production rates of volcanism throughout the NVP were relatively high before  $\sim 4$  Ma, after which a decreased rate of production is suggested by the trend recorded by PRC-006 post 4 Ma. Recent work has suggested the presence of a mantle plume ('Cosgrove track') to the northeast of the NVP at around 6.5 - 5 Ma (Davies *et al.*, 2015). We suggest that the potential higher production rates before  $\sim 4$  Ma could therefore be a consequence of the increased temperature of the mantle due to thermal contribution of this mantle plume. Southward migration of this mantle plume (Figure 4.10) over time potentially caused the thermal effects from the mantle plume to the existing process of edge-driven convection to decrease and eventually terminate. Rigorous  $^{40}\text{Ar}/^{39}\text{Ar}$  dating and eruption rate calculation of Newer Plains basalts throughout the NVP is required to further test this hypothesis.

##### 4.6.4. Spatial analyses

Clustering of volcanic centres within an intraplate setting has been recorded for other volcanic provinces such as Armenia [R = 0.63], Daringanga, Mongolia [R = 0.86], Es Safa, Syria [R = 0.63], Pali Aike, Chile – Argentina [R = 0.57] and St Michael, USA [R = 0.60] (Le Corvec *et al.*, 2013). The number, location and extent of our clusters does not correspond well with the six clusters proposed for the NVP by Lesti and co-workers (2008), which were based on the location of volcanic features from the database of Rosengren (1984) as well as from visual interpretation of satellite imagery. However, their interpretation of 683 volcanic points includes many circular, maar-like structures in the North West of the NVP. These features are located to the north of the northernmost extent of the sedimentary basement of the Otway basin, and are most likely not of volcanic origin, but potentially are dry salt lakes instead. Recent re-assessment of volcanic features in the NVP has

stressed the need for ground truthing to confirm features interpreted from satellite imagery (Boyce *et al.*, 2014). Clustering of volcanic features on a large scale is generally interpreted to be an indication of the geological structures in the sub-surface, such as the location and shape of the underlying magma source (e.g. Brenna *et al.*, 2010) and/or the (elastic) thickness of the underlying lithosphere (Vogt, 1974; Mohr and Wood, 1976; Mazzarini, 2004). Geophysical imaging (Fishwick *et al.*, 2008; Davies and Rawlinson, 2014; Rawlinson *et al.*, 2015b) has shown that the lithosphere in southeast Australia has a complex 3D thickness configuration, caused by the stacking of both continental and oceanic crustal fragments in the Delamerian and Lachlan fold belts, as well as the incorporation of exotic crustal blocks such as the Selwyn Block (Cayley, 2011; Cayley *et al.*, 2011). Magneto-telluric sounding has shown that distinct regions of partial melt are currently present in the upper mantle below the NVP (Aivazpourporgou *et al.*, 2015), spatially overlapping with our Central Highlands and Western Plains East clusters, but not with the Mt Gambier and Western Plains East cluster.

Alignment of volcanic centres in the NVP and Mt Gambier region has previously been ascribed to a dependence of magma ascent on major north – south trending basement faults as well as northwest – southeast trending Cretaceous extensional structures (Bishop, 2007; Lesti *et al.*, 2008; Holt *et al.*, 2013; Van Otterloo *et al.*, 2013). Our results show that volcanism in the Mt Gambier region is aligned along the west northwest – east southeast Mesozoic extensional features such as the Tartwaup Fault, whereas volcanism in the Western Plains West cluster is aligned north northwest – south southeast, similar to the major basement fault direction of the Glenelg and Grampians – Stavely Zones ( $160^\circ$  –  $170^\circ$ ). Volcanism in both the Western Plains East and Central Highlands clusters is preferentially aligned along the north – south trending basement faults of the Bendigo Zone rather than along the trend of faults ( $150^\circ$  –  $160^\circ$ ) in the Stawell Zone (Figure 4.7 and Figure 4.8a-h). Our analyses using the new database and automated point pattern analysis show that volcanism in the NVP is strongly dependent on basement structures, which is in agreement with previous findings of Lesti *et al.* (2008).

#### 4.7. Spatio-temporal constraints on NVP volcanism

Figure 4.9a shows that the predominantly tholeiitic Newer Plains erupted synchronous throughout the entire Newer Volcanic Province, starting at around 4.5 Ma. This distribution agrees with volcanism predominantly caused by edge driven convection and aided by the thermal contribution of a migrating plume. Figure 4.10a provides an illustration of the potential complex interplay between lithosphere of variable thickness (Davies and Rawlinson, 2014) and the approximate location of the mantle plume at 6.5 – 5 Ma (Davies *et al.*, 2015).

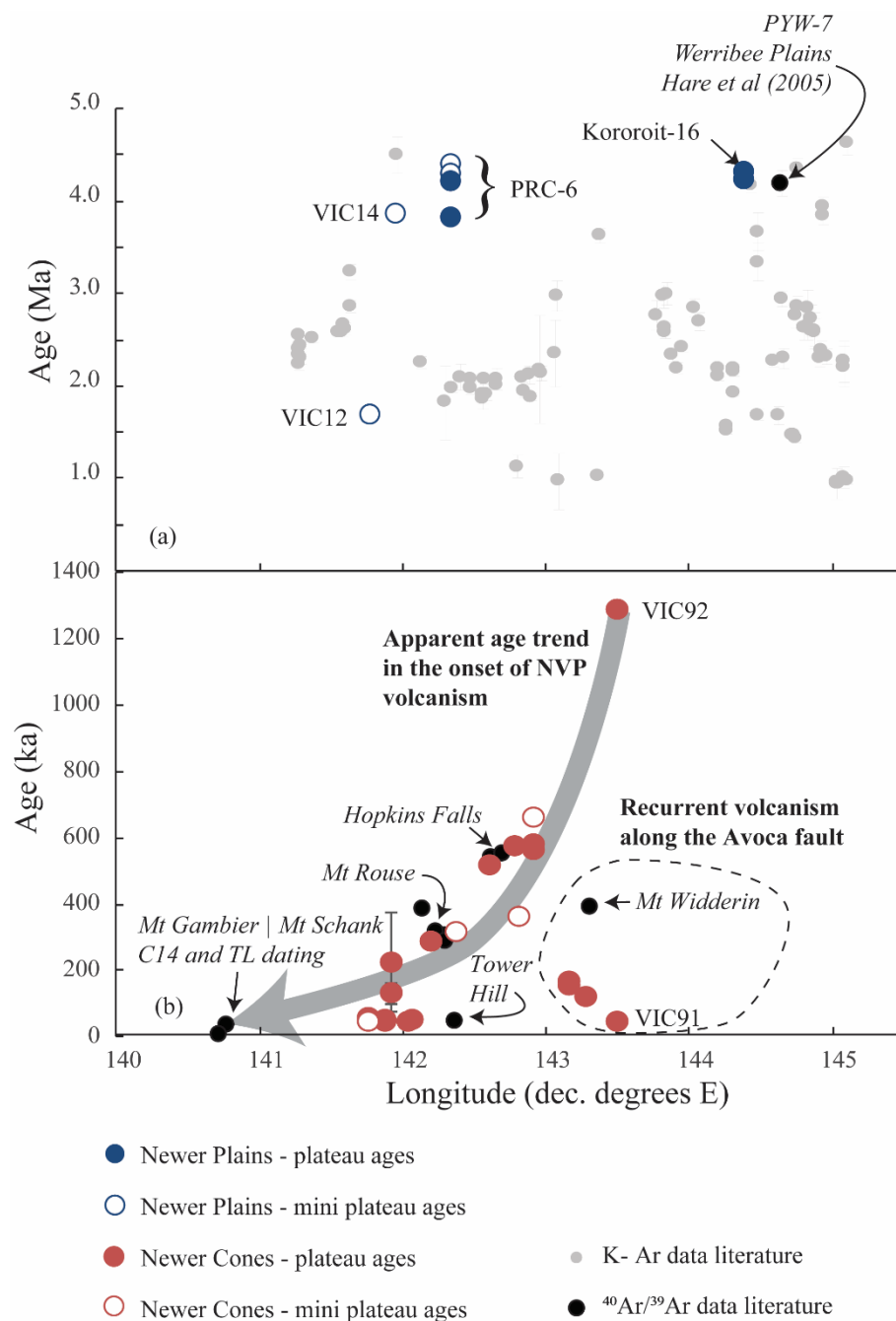


Figure 4.9. Longitude versus age diagrams. (a) Newer Plains results and literature data. K-Ar data from; Aziz-ur-Rahman and McDougall, 1972; Gray and McDougall, 2009; McDougall et al., 1966;  $^{40}\text{Ar}/^{39}\text{Ar}$  age from Hare et al, 2005a. (b) Newer Cones results and literature data (Matchan and Phillips, 2014, 2011; Matchan et al., 2016). Note that  $2\sigma$  errors for our data are often smaller than the size of the symbols used.

Figure 4.9b shows that the predominantly alkaline Newer Cones display a potential age progression in the onset of volcanism from east to west in an otherwise much more diffuse trend of volcanism as compared to the Newer Plains. Specific space-time clusters are apparent; with a cluster of 600 ka old volcanism at longitude  $143^\circ$  E, ages around 40 ka at longitude  $142^\circ$  E and a few younger ages again at higher longitudes (around  $143.5^\circ$  E). Nevertheless, no older ( $> 500$  ka) ages are found in the westernmost part of the NVP ( $141^\circ - 143^\circ$  E), and the age progression fits well with young ( $\sim 5 - 27$  ka) ages found in the westernmost Mt Gambier region (Blackburn et al., 1982; Smith and Prescott, 1987). The apparent age progression in the onset of

volcanism can potentially be explained either by deep sub-surface processes such as spatial migration of the thermal mantle source or by shallow sub-surface constraints such as the availability of suitable pathways for magma transport through the crust. Here, we will discuss some potential causes for the apparent age progression of the Newer Cones basalts. Note that our age data only represents a

relatively small number of volcanic centres present in this area, and more rigorous  $^{40}\text{Ar}/^{39}\text{Ar}$  geochronology towards the other centres is required to fully investigate this hypothesis.

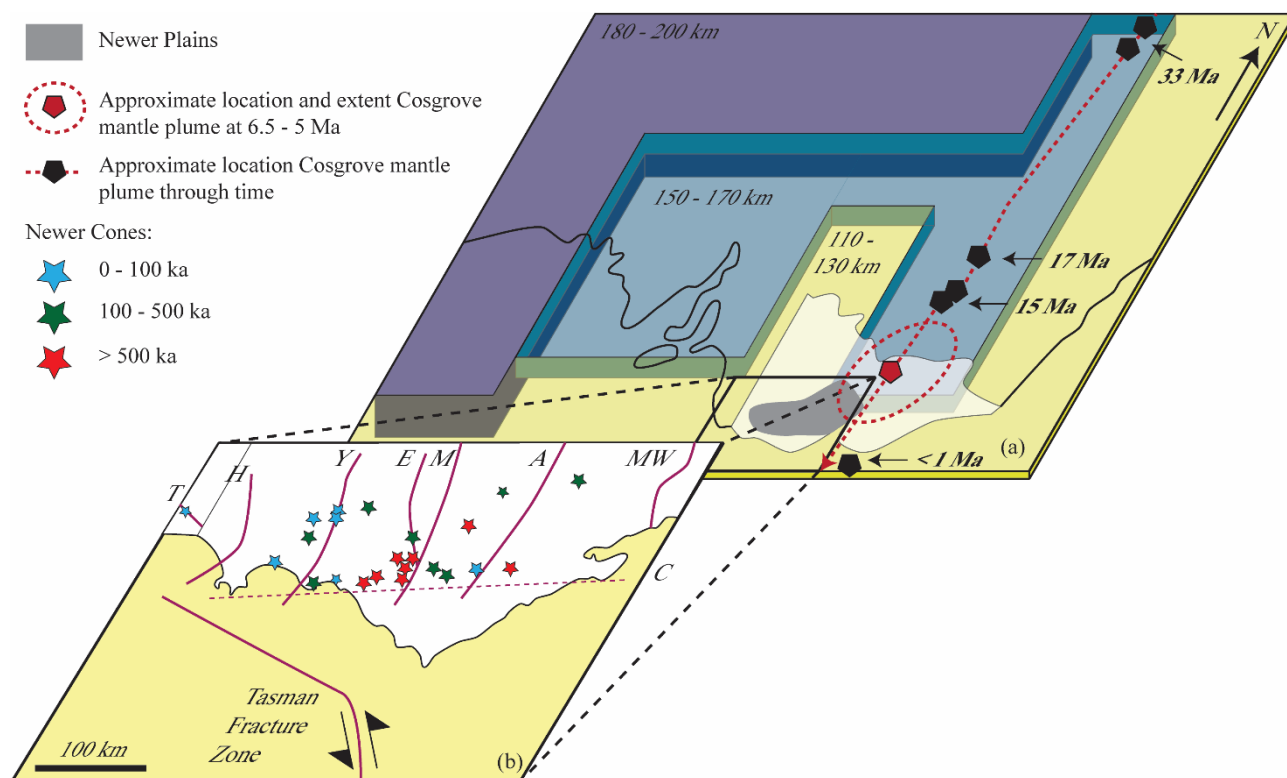


Figure 4.10. Cartoon illustrating the generation of the Newer Plains (top right) due to the interplay of complex 3D lithospheric thickness and the Cosgrove track mantle plume (dashed red line; Davies *et al.*, 2015) and the generation of the Newer Cones (lower left) as a response to movement along the Tasman Fracture Zone. Ages of the Newer Cones have been subdivided into three groups: 0 – 100 ka, 100 – 500 ka and > 500 ka to illustrate the age progression towards the West. Lithosphere thicknesses from Davies and Rawlinson (2015). Note that there are much more eruption centres present (however undated) in the NVP that are not represented on this map.

#### 4.7.1. Mantle source migration?

Age progression of volcanic eruption centres is usually linked to migration of the plate over a static mantle plume, such as proposed for the classic Hawaiian Islands hotspot trail (Morgan, 1972). However, for the NVP we observe an age progression (east to west) perpendicular to the direction of plate motion (south to north), thus incompatible with the hotspot track model. Furthermore, isotope geochemistry has shown that the Newer Cones most likely originated from the shallow rather than the deep asthenosphere; as distinct high  $(^{207}\text{Pb}/^{204}\text{Pb})_i$  ratios for a given  $(^{143}\text{Nd}/^{144}\text{Nd})_i$  value suggest large degrees of mixing of metasomatised Sub Continental Lithospheric Mantle into a mantle source similar to Indian MORB in composition (Oostingh *et al.*, 2016). The distinct major and trace element and isotope signatures (Oostingh *et al.*, 2016), U-Th disequilibria (Demidjuk *et al.*, 2007) and



geophysical data (Davies and Rawlinson, 2014) of the NVP basalts are best explained by the geodynamic model of edge driven convection (King and Anderson, 1998) aided by shear driven upwelling (Conrad *et al.*, 2011), resulting in localized upwelling of shallow mantle at the trailing edge of an anomalous thick block of lithosphere (Figure 4.10a). It is still possible that the age progression is caused by a migrating roll of fertile mantle material from east to west, caused by an east to west motion of the shallow mantle during shear assisted upwelling caused by the complex 3D lithospheric thickness variations below the NVP (Fishwick *et al.*, 2008; Rawlinson *et al.*, 2015b) during edge driven convection. In such a scenario, one would expect that such a fertile mantle patch is now located in the west, at the approximate location of the youngest volcanism. However, a region of partial melt (or fertile mantle material) is currently present in the east rather than the west (Aivazpourporgou *et al.*, 2015) based on the identification of a low-resistivity zone beneath the Bendigo and Stawell zones by magneto-telluric sounding. Hence, migration of the mantle source fails to explain the observed age trend within the NVP.

#### 4.7.2. Tectonic controls?

The alignment of volcanoes along north – south trending basement structures in the east and northwest – southeast trending extension structures in the west as observed from our spatial analyses, suggests that the lithosphere had a major control on volcanism in the NVP. Such a dependence of volcanism on faults could potentially explain the age progression of the Newer Cones volcanoes from east to west in the NVP. The present-day Australian continent is not tectonically inert, and southeast Australia represents one of the regions with highest seismic activity and widespread neo-tectonism (Sandiford, 2003; Hillis *et al.*, 2008) which could have triggered volcanism in the NVP (Lesti *et al.*, 2008). It has been shown that this neo-tectonism initiated in the Mid-Miocene, resulting in large-scale basin inversion (Dickinson *et al.*, 2002) and continued in the Quaternary, with ~ 120 ka dune deposits showing evidence of deformation (Sandiford, 2003), suggesting the presence of a tectonically active region during eruption of the Newer Cones volcanoes. Stress modelling has suggested that the onset of neo-tectonism can be associated with the formation of the Southern Alps in New Zealand (Sandiford *et al.*, 2004). Thermal erosion of the Sub Continental Lithospheric Mantle (Price *et al.*, 2014; Oostingh *et al.*, 2016) beneath southeast Australia could have played a role in weakening the intraplate lithosphere, facilitating neo-tectonism and allowing upwelling of magma through the crust along reactivated faults. A similar process can be observed in the northern Alpine foreland in Europe; which is an intraplate region in a compressional stress regime with active neo-tectonism (Cloetingh *et al.*, 2005) and associated volcanism. Lesti *et al.* (2008) suggested that left lateral strike-slip opening of the major north - south trending faults in the NVP caused by movement along the Tasman Fracture

Zone (Figure 4.10b; a major sinistral transform fault) triggered magmatism in the area. Loci of maximum stress and subsequent reactivation of faults could potentially migrate from east to west throughout the NVP, due to the left-lateral nature of the Tasman Fracture Zone; resulting in the observed age progression of the onset of volcanism in the NVP. The space-time clustering of our Newer Cones age data, as well as the age progression of the onset of volcanism from east to west and recurrent volcanism around longitude  $143.5^\circ$  E suggests that stress derived from movement of the Tasman Fracture Zone is not accommodated evenly throughout the NVP, with data suggesting that major faults such as the Avoca fault (longitude  $143^\circ$  E) were reactivated multiple times (Figure 4.10b). The Avoca Fault - and to a lesser degree the Moyston Fault - form spatial extensions of the north - south component of the Tasman Fracture Zone (see Figure 1 of Gibson *et al.*, 2013). Therefore, movement along the Tasman Fracture Zone might have been preferentially accommodated along those two faults, explaining the frequent reactivation of these faults as reflected in the wide range of ages for volcanic features around longitude  $143^\circ$  E (Figure 4.9b).

#### 4.8. Conclusion

$^{40}\text{Ar}/^{39}\text{Ar}$  dating of Cainozoic intraplate basalts in the Newer Volcanic Province in southeast Australia shows a fast change in the mode of magma generation. Ages of 3.8 to 4.3 Ma for valley filling tholeiitic Newer Plains basalts and relatively high production rates of volcanism prior to  $\sim 4$  Ma show that these rocks were probably generated by the interplay of magma upwelling due to edge driven convection and additional thermal contribution of the Cosgrove track mantle plume located in the northeast of the area at 6.5 – 5 Ma. No spatial age progression can be observed within the Newer Plains.

The stratigraphically overlying volcanic scoria cones, lava shield and associated flows as well as maars of the Newer Cones are significantly younger, with ages ranging from 1.3 Ma (this work) to  $\sim 5$  ka for Mt Schank (Smith and Prescott, 1987). Detailed structural analysis of the distribution and geomorphic characteristics of these features shows a strong dependence of magmatism derived from shallow mantle melting and subsequent upwelling due to edge driven convection with shear on existing north - south oriented Palaeozoic basement faults and northwest - southeast oriented Cretaceous extension structures. An apparent age progression of the onset of volcanism from east to west suggests that volcanism was dependent on reactivation of major faults due to a westerly progression of stress derived from movement along the Tasman Fracture Zone, with recurrent reactivation of volcanism along major faults over time. Although our data is still limited, we suggest that volcanism in the NVP changed from being driven by edge driven convection with added thermal

input of the Cosgrove track mantle plume resulting in the Newer Plains ('plume-driven') prior to ~ 4 Ma; to localization of volcanism by neo-tectonism along a westerly progressing front in the onset of volcanism resulting in the Newer Cones ('stress-dependent') starting at approximately 1.3 Ma.

#### 4.9. Acknowledgements

David Taylor of the Geological Survey Victoria is thanked for his assistance in the field. Adam Frew, Zdenka Martelli and Celia Mayers of WAAIF are thanked for their assistance during sample preparation. Julie Boyce (Monash University) as well as Nicholas Le Corvec (Lunar and Planetary Institute) are thanked for discussion. Benjamin Cohen (UQ) is thanked for sharing his geochronology database. Darren Mark (SUERC) and Anthony Koppers (OSU) are thanked for their reviews, which have significantly improved the quality of this publication. Janne Blichert-Toft is thanked for editorial handling. The support of TiGER and the department Applied Geology at Curtin University of Technology is gratefully acknowledged. This research was funded by Australian Research Council Discovery grant DP130100517.

#### 4.10. References

- Aivazpourporgou, S., Thiel, S., Hayman, P.C., Moresi, L.N., Heinson, G., 2015. Decompression melting driving intraplate volcanism in Australia: Evidence from magnetotelluric sounding. *Geophys. Res. Lett.* 42, 1–9. doi:10.1002/2014GL060088
- Aziz-ur-Rahman, McDougall, I., 1972. Potassium-Argon ages on the Newer Volcanics of Victoria. *Proc. R. Soc. Victoria* 85.
- Beggan, C., Hamilton, C.W., 2010. New image processing software for analyzing object size-frequency distributions, geometry, orientation, and spatial distribution. *Comput. Geosci.* 36, 539–549. doi:10.1016/j.cageo.2009.09.003
- Bishop, M.A., 2007. Point pattern analysis of eruption points for the Mount Gambier volcanic sub-province: A quantitative geographical approach to the understanding of volcano distribution. *Area* 39, 230–241. doi:10.1111/j.1475-4762.2007.00729.x
- Blackburn, G., Allison, G.B., Leaney, F.W.J., 1982. Further evidence on the age of tuff at Mt Gambier, South Australia. *Trans. R. Soc. South Aust.* 106, 163–167.
- Boyce, J., 2013. The Newer Volcanics Province of southeastern Australia: a new classification scheme and distribution map for eruption centres. *Aust. J. Earth Sci.* 60, 449–462. doi:10.1080/08120099.2013.806954

- Boyce, J., Keays, R.R., Nicholls, I.A., Hayman, P., 2014. Eruption centres of the Hamilton area of the Newer Volcanics Province, Victoria, Australia: pinpointing volcanoes from a multifaceted approach to landform mapping. *Aust. J. Earth Sci.* 1–20. doi:10.1080/08120099.2014.923508
- Brenna, M., Cronin, S.J., Smith, I.E.M., Sohn, Y.K., Németh, K., 2010. Mechanisms driving polymagmatic activity at a monogenetic volcano, Udo, Jeju Island, South Korea. *Contrib. to Mineral. Petrol.* 160, 931–950. doi:10.1007/s00410-010-0515-1
- Cartwright, I., Weaver, T., Tweed, S., Ahearne, D., Cooper, M., Czapnik, K., Tranter, J., 2002. Stable isotope geochemistry of cold CO<sub>2</sub>-bearing mineral spring waters, Daylesford, Victoria, Australia: Sources of gas and water and links with waning volcanism. *Chem. Geol.* 185, 71–91. doi:10.1016/S0009-2541(01)00397-7
- Cayley, R.A., 2011. Exotic crustal block accretion to the eastern Gondwanaland margin in the Late Cambrian-Tasmania, the Selwyn Block, and implications for the Cambrian-Silurian evolution of the Ross, Delamerian, and Lachlan orogens. *Gondwana Res.* 19, 628–649. doi:10.1016/j.gr.2010.11.013
- Cayley, R.A., Korsch, R.J., Moore, D.H., Costelloe, R.D., Nakamura, A., Willman, C.E., Rawling, T.J., Morand, V.J., Skladzien, P.B., O’Shea, P.J., 2011. Crustal architecture of central Victoria: results from the 2006 deep crustal reflection seismic survey. *Aust. J. Earth Sci.* 58, 113–156. doi:10.1080/08120099.2011.543151
- Cebriá, J.M., Martín-Escorza, C., López-Ruiz, J., Morán-Zenteno, D.J., Martiny, B.M., 2011. Numerical recognition of alignments in monogenetic volcanic areas: Examples from the Michoacán-Guanajuato Volcanic Field in Mexico and Calatrava in Spain. *J. Volcanol. Geotherm. Res.* 201, 73–82. doi:10.1016/j.jvolgeores.2010.07.016
- Clark, P.J., Evans, F.C., 1954. Distance to Nearest Neighbor as a Measure of Spatial Relationships in Populations. *Ecology* 35, 445–453.
- Cloetingh, S., Ziegler, P.A., Beekman, F., Andriessen, P.A.M., Hardebol, N., Dezes, P., 2005. Intraplate deformation and 3D rheological structure of the Rhine Rift System and adjacent areas of the northern Alpine foreland. *Int. J. Earth Sci.* 94, 758–778. doi:10.1007/s00531-005-0502-3
- Conrad, C.P., Bianco, T.A., Smith, E.I., Wessel, P., 2011. Patterns of intraplate volcanism controlled by asthenospheric shear. *Nat. Geosci.* 4, 317–321. doi:10.1038/ngeo1111

- Conrad, C.P., Wu, B., Smith, E.I., Bianco, T.A., Tibbetts, A., 2010. Shear-driven upwelling induced by lateral viscosity variations and asthenospheric shear: A mechanism for intraplate volcanism. *Phys. Earth Planet. Inter.* 178, 162–175. doi:10.1016/j.pepi.2009.10.001
- Crowley, G.M., Kershaw, A.P., 1994. Late Quaternary environmental change and human impact around Lake Bolac, Western Victoria, Australia. *J. Quat. Sci.* 9, 367–377. doi:10.1002/jqs.3390090407
- Davies, D.R., Rawlinson, N., 2014. On the origin of recent intraplate volcanism in Australia. *Geology* 1–4. doi:10.1130/G36093.1
- Davies, D.R., Rawlinson, N., Iaffaldano, G., Campbell, I.H., 2015. Lithospheric controls on magma composition along Earth's longest continental hotspot track. *Nature*. doi:10.1038/nature14903
- Demidjuk, Z., Turner, S., Sandiford, M., George, R., Foden, J., Etheridge, M., 2007. U-series isotope and geodynamic constraints on mantle melting processes beneath the Newer Volcanic Province in South Australia. *Earth Planet. Sci. Lett.* 261, 517–533. doi:10.1016/j.epsl.2007.07.006
- Dickinson, J.A., Wallace, M.W., Holdgate, G.R., Gallagher, S.J., Thomas, L., 2002. Origin and Timing of the Miocene-Pliocene Unconformity in Southeast Australia. *J. Sediment. Res.* 72, 288–303. doi:10.1306/082701720288
- Edney, P.A., Kershaw, A.P., De Deckker, P., 1990. A late Pleistocene and Holocene vegetation and environmental record from Lake Wangoom, Western Plains of Victoria, Australia. *Palaeogeogr. Palaeoclimatol. Palaeoecol.* 80, 325–343.
- Fishwick, S., Heintz, M., Kennett, B.L.N., Reading, A.M., Yoshizawa, K., 2008. Steps in lithospheric thickness within eastern Australia, evidence from surface wave tomography. *Tectonics* 27, 1–17. doi:10.1029/2007TC002116
- Gibson, G.M., Totterdell, J.M., White, L.T., Mitchell, C.H., Stacey, A.R., Morse, M.P., Whitaker, A., 2013. Pre-existing basement structure and its influence on continental rifting and fracture zone development along Australia's southern rifted margin. *J. Geol. Soc. London.* 170, 365–377. doi:10.1144/jgs2012-040
- Gillen, D., Honda, M., Chivas, A.R., Yatsevich, I., Patterson, D.B., Carr, P.F., 2010. Cosmogenic  $^{21}\text{Ne}$  exposure dating of young basaltic lava flows from the Newer Volcanic Province, western Victoria, Australia. *Quat. Geochronol.* 5, 1–9. doi:10.1016/j.quageo.2009.08.004

- Gosse, J.C., Phillips, F.M., 2001. Terrestrial in situ cosmogenic nuclides: theory and application. *Quat. Sci. Rev.* 20, 1475–1560. doi:10.1016/S0277-3791(00)00171-2
- Graeber, F.M., Houseman, G.A., Greenhalgh, S.A., 2002. Regional teleseismic tomography of the western Lachlan Orogen and the Newer Volcanic Province, southeast Australia. *Geophys. J. Int.* 149, 249–266. doi:10.1046/j.1365-246X.2002.01598.x
- Gray, C.M., McDougall, I., 2009. K-Ar geochronology of basalt petrogenesis, Newer Volcanic Province, Victoria. *Aust. J. Earth Sci.* 56, 245–258. doi:10.1080/08120090802547066
- Gray, D.R., Foster, D.A., Morand, V.J., Willman, C.E., Cayley, R.A., Spaggiari, C. V., Taylor, D.H., Gray, C.M., VandenBerg, A.H.M., Hendrickx, M.A., Wilson, C.J.L., 2003. Structure, metamorphism, geochronology and tectonics of Palaeozoic rocks - interpreting a complex, long-lived orogenic system., in: Birch, W.D. (Ed.), *Geology of Victoria*. Geological Society of Australia, pp. 15–71.
- Hare, A.G., Cas, R.A.F., Musgrave, R., Phillips, D., 2005a. Magnetic and chemical stratigraphy for the Werribee Plains basaltic lava flow-field, Newer Volcanics Province, southeast Australia: implications for eruption frequency. *Aust. J. Earth Sci.* 52, 41–57. doi:10.1080/08120090500100069
- Hare, A.G., Cas, R.A.F., Musgrave, R., Phillips, D., 2005b. Magnetic and chemical stratigraphy for the Werribee Plains basaltic lava flow-field, Newer Volcanics Province, southeast Australia: implications for eruption frequency. *Aust. J. Earth Sci.* 52, 41–57. doi:10.1080/08120090500100069
- Harle, K.J., 1997. Late Quaternary vegetation and climate change in southeastern Australia: palynological evidence from marine core E55-6. *Paleogeography, Paleoclimatology, Paleoecol.* 131, 465–483.
- Harle, K.J., Heijnis, H., Chisari, R., Kershaw, a. P., Zoppi, U., Jacobsen, G., 2002. A chronology for the long pollen record from Lake Wangoom, western Victoria (Australia) as derived from uranium/thorium disequilibrium dating. *J. Quat. Sci.* 17, 707–720. doi:10.1002/jqs.684
- Hillis, R.R., Sandiford, M., Reynolds, S.D., Quigley, M.C., 2008. Present-day stresses, seismicity and Neogene-to-Recent tectonics of Australia's "passive" margins: intraplate deformation controlled by plate boundary forces, in: Johnson, H., Dore, A.G., Gatliff, R.W., Holdsworth, R., Lundin, E.R., Ritchie, J.D. (Eds.), *Geological Society, London, Special Publications*. The Geological Society of London, pp. 71–90. doi:10.1144/SP306.3
- Holcombe, R., 2010. *GEORient* - structural geology software.

- Holt, S.J., Holford, S.P., Foden, J., 2013. New insights into the magmatic plumbing system of the South Australian Quaternary Basalt province from 3D seismic and geochemical data. *Aust. J. Earth Sci.* 60, 797–817. doi:10.1080/08120099.2013.865143
- Jourdan, F., Féraud, G., Bertrand, H., Watkeys, M.K., 2007. From flood basalts to the inception of oceanization: Example from the  $^{40}\text{Ar}/^{39}\text{Ar}$  high-resolution picture of the Karoo large igneous province. *Geochemistry, Geophys. Geosystems* 8. doi:10.1029/2006GC001392
- Jourdan, F., Renne, P.R., 2007. Age calibration of the Fish Canyon sanidine  $^{40}\text{Ar}/^{39}\text{Ar}$  dating standard using primary K–Ar standards. *Geochim. Cosmochim. Acta* 71, 387–402. doi:10.1016/j.gca.2006.09.002
- Jourdan, F., Renne, P.R., Reimold, W.U., 2009. An appraisal of the ages of terrestrial impact structures. *Earth Planet. Sci. Lett.* 286, 1–13. doi:10.1016/j.epsl.2009.07.009
- Jourdan, F., Sharp, W.D., Renne, P.R., 2012.  $^{40}\text{Ar}/^{39}\text{Ar}$  ages for deep (~3.3 km) samples from the Hawaii Scientific Drilling Project, Mauna Kea volcano, Hawaii. *Geochemistry, Geophys. Geosystems* 13. doi:10.1029/2011GC004017
- King, S.D., Anderson, D.L., 1998. Edge-driven convection. *Earth Planet. Sci. Lett.* 160, 289–296. doi:10.1016/S0012-821X(98)00089-2
- Koppers, A.A.P., 2002. ArArCALC - software for  $^{40}\text{Ar}/^{39}\text{Ar}$  age calculations. *Comput. Geosci.* 28, 605–619.
- Le Corvec, N., Bebbington, M.S., Lindsay, J.M., McGee, L.E., 2013a. Age, distance, and geochemical evolution within a monogenetic volcanic field: Analyzing patterns in the Auckland Volcanic Field eruption sequence. *Geochemistry, Geophys. Geosystems* 14, 3648–3665. doi:10.1002/ggge.20223
- Le Corvec, N., Spörl, K.B., Rowland, J., Lindsay, J.M., 2013b. Spatial distribution and alignments of volcanic centers: Clues to the formation of monogenetic volcanic fields. *Earth-Science Rev.* 124, 96–114. doi:10.1016/j.earscirev.2013.05.005
- Lee, J.B., Marti, K., Severinghaus, J.P., Kawamura, K., Yoo, H., Kim, J.S., 2006. A redetermination of the isotopic abundances of atmospheric Ar. *Geochim. Cosmochim. Acta* 70, 4507–4512. doi:10.1016/j.gca.2006.06.1563

- Lesti, C., Giordano, G., Salvini, F., Cas, R.A.F., 2008. Volcano tectonic setting of the intraplate, Pliocene-Holocene, Newer Volcanic Province (southeast Australia): Role of crustal fracture zones. *J. Geophys. Res.* 113. doi:10.1029/2007JB005110
- Mark, D.F., Stuart, F.M., de Podesta, M., 2011. New high-precision measurements of the isotopic composition of atmospheric argon. *Geochim. Cosmochim. Acta* 75, 7494–7501. doi:http://dx.doi.org/10.1016/j.gca.2011.09.042
- Matchan, E.L., Joyce, E.B., Phillips, D., 2016. A new  $^{40}\text{Ar}/^{39}\text{Ar}$  eruption age for the Mount Widderin volcano, Newer Volcanic Province, Australia, with implications for eruption frequency in the region. *Aust. J. Earth Sci.* 99, 1–12. doi:10.1080/08120099.2016.1156576
- Matchan, E.L., Phillips, D., 2011. New  $^{40}\text{Ar}/^{39}\text{Ar}$  ages for selected young (<1 Ma) basalt flows of the Newer Volcanic Province, southeastern Australia. *Quat. Geochronol.* 6, 356–368. doi:10.1016/j.quageo.2011.03.002
- Matchan, E.L., Phillips, D., 2014. High precision multi-collector  $^{40}\text{Ar}/^{39}\text{Ar}$  dating of young basalts: Mount Rouse volcano (SE Australia) revisited. *Quat. Geochronol.* doi:10.1016/j.quageo.2014.02.005
- Mazzarini, F., 2004. Volcanic vent self-similar clustering and crustal thickness in the northern Main Ethiopian Rift. *Geophys. Res. Lett.* 31, 1–4. doi:10.1029/2003GL018574
- McDougall, I., Allsopp, H.L., Chamalaun, F.H., 1966. Isotopic dating of the newer volcanics of Victoria, Australia, and geomagnetic polarity epochs. *J. Geophys. Res.* 71, 6107–6118. doi:10.1029/JZ071i024p06107
- McDougall, I., Harrison, T.M., 1999. *Geochronology and thermochronology by the  $^{40}\text{Ar}/^{39}\text{Ar}$  method.* Oxford University Press.
- Mohr, P.A., Wood, C.A., 1976. Volcano spacings and lithospheric attenuation in the Eastern Rift of Africa. *Earth Planet. Sci. Lett.* 33, 126–144. doi:10.1016/0012-821X(76)90166-7
- Mooney, S., 1997. A fine-resolution palaeoclimatic reconstruction of the last 2000 years, from Lake Keilambete, southeastern Australia. *The Holocene* 7, 139–149. doi:10.1177/095968369700700202
- Morgan, W.J., 1972. Deep mantle convection plumes and plate motions. *Am. Assoc. Pet. Geol. Bull.* 2, 203–213.
- Niedermann, S., 2002. Cosmic-Ray-Produced noble gases in terrestrial rocks: dating tools for surface processes. *Rev. Mineral. Geochemistry* 47, 731–784. doi:10.2138/rmg.2002.47.16



- Oostingh, K.F., Jourdan, F., Merle, R., Chiaradia, M., 2016. Spatio-temporal Geochemical Evolution of the SE Australian Upper Mantle Deciphered from the Sr, Nd and Pb Isotope Compositions of Cenozoic Intraplate Volcanic Rocks. *J. Petrol.* 57, 1509–1530. doi:10.1093/petrology/egw048
- Paulsen, T.S., Wilson, T.J., 2010. New criteria for systematic mapping and reliability assessment of monogenetic volcanic vent alignments and elongate volcanic vents for crustal stress analyses. *Tectonophysics* 482, 16–28. doi:10.1016/j.tecto.2009.08.025
- Phillips, D., Matchan, E.L., 2013. Ultra-high precision  $^{40}\text{Ar}/^{39}\text{Ar}$  ages for Fish Canyon Tuff and Alder Creek Rhyolite sanidine: New dating standards required? *Geochim. Cosmochim. Acta* 121, 229–239. doi:10.1016/j.gca.2013.07.003
- Price, R.C., Gray, C.M., Frey, F.A., 1997. Strontium isotopic and trace element heterogeneity in the plains basalts of the Newer Volcanic Province, Victoria, Australia. *Geochim. Cosmochim. Acta* 61, 171–192. doi:10.1016/S0016-7037(96)00318-3
- Price, R.C., Nicholls, I.A., Day, A., 2014. Lithospheric influences on magma compositions of late Mesozoic and Cenozoic intraplate basalts (the Older Volcanics) of Victoria, south-eastern Australia. *Lithos* 206–207, 179–200. doi:10.1016/j.lithos.2014.07.027
- Price, R.C., Nicholls, I.A., Gray, C.M., 2003. Cainozoic igneous activity, in: Birch, W.D. (Ed.), *Geology of Victoria*. Geological Society of Australia (Victoria Division), pp. 361–375.
- Rawlinson, N., Kennett, B.L.N., Salmon, M., Glen, R.A., 2015a. Origin of Lateral Heterogeneities in the Upper Mantle Beneath South-east Australia from Seismic Tomography, in: Khan, A., Deschamps, F. (Eds.), *The Earth's Heterogeneous Mantle*. Springer Geophysics, pp. 47–78. doi:10.1007/978-3-319-15627-9
- Rawlinson, N., Pilia, S., Young, M., Salmon, M., Yang, Y., 2015b. Crust and upper mantle structure beneath southeast Australia from ambient noise and teleseismic tomography. *Tectonophysics*. doi:10.1016/j.tecto.2015.11.034
- Renne, P.R., Balco, G., Ludwig, K.R., Mundil, R., Min, K., 2011. Response to the comment by W.H. Schwarz et al. on “Joint determination of  $^{40}\text{K}$  decay constants and  $^{40}\text{Ar}^*/^{40}\text{K}$  for the Fish Canyon sanidine standard, and improved accuracy for  $^{40}\text{Ar}/^{39}\text{Ar}$  geochronology” by P.R. Renne et al. (2010). *Geochim. Cosmochim. Acta* 75, 5097–5100. doi:10.1016/j.gca.2011.06.021

- Renne, P.R., Cassata, W.S., Morgan, L.E., 2009. The isotopic composition of atmospheric argon and  $^{40}\text{Ar}/^{39}\text{Ar}$  geochronology: Time for a change? *Quat. Geochronol.* 4, 288–298. doi:10.1016/j.quageo.2009.02.015
- Renne, P.R., Mundil, R., Balco, G., Min, K., Ludwig, K.R., 2010. Joint determination of  $^{40}\text{K}$  decay constants and  $^{40}\text{Ar}^*/^{40}\text{K}$  for the Fish Canyon sanidine standard, and improved accuracy for  $^{40}\text{Ar}/^{39}\text{Ar}$  geochronology. *Geochim. Cosmochim. Acta* 74, 5349–5367. doi:10.1016/j.gca.2010.06.017
- Rosengren, N., 1994. Eruption points of the Newer Volcanics Province - an inventory and evaluation of scientific significance. Melbourne.
- Sandiford, M., 2003. Neotectonics of southeastern Australia; linking Quaternary faulting record with seismicity and in situ stress. *Geol. Soc. Aust. Spec. Publ.* 22, 101–113. doi:10.1130/0-8137-2372-8.107
- Sandiford, M., Wallace, M., Coblenz, D.D., 2004. Origin of the in situ stress field in south-eastern Australia. *Basin Res.* 16, 325–338. doi:10.1111/j.1365-2117.2004.00235.x
- Sella, G.F., Dixon, T.H., Mao, A., 2002. REVEL: A model for Recent plate velocities from space geodesy. *J. Geophys. Res.* 107. doi:10.1029/2000JB000033
- Singleton, O.P., Joyce, E.B., 1970. Catalogue of the post-Miocene volcanoes of Victoria, Australia. Prepared for the IAVCEI Catalogue of post-Miocene Volcanoes of the World.
- Singleton, O.P., McDougall, I., Mallett, C.W., 1976. The Pliocene-Pleistocene boundary in Southeastern Australia. *J. Geol. Soc. Aust.* 23, 299–311. doi:10.1080/00167617608728943
- Smith, B.W., Prescott, J.R., 1987. Thermoluminescence dating of the eruption at Mt Schank, South Australia. *Aust. J. Earth Sci.* 34, 335–342. doi:10.1080/08120098708729415
- Stone, J., Peterson, J.A., Fifield, L.K., Cresswell, R.G., 1997. Cosmogenic Chlorine-36 exposure ages for two basalt flows in the Newer Volcanics Province, Western Victoria. *Proc. R. Soc. Victoria* 109, 121–131.
- Van Otterloo, J., Cas, R.A.F., Sheard, M.J., 2013. Eruption processes and deposit characteristics at the monogenetic Mt. Gambier Volcanic Complex, SE Australia: implications for alternating magmatic and phreatomagmatic activity. *Bull. Volcanol.* 75, 1–21. doi:10.1007/s00445-013-0737-y

Vasconcelos, P.M., Knesel, K.M., Cohen, B.E., Heim, J.A., 2008. Geochronology of the Australian Cenozoic: a history of tectonic and igneous activity, weathering, erosion, and sedimentation. *Aust. J. Earth Sci.* 55, 865–914. doi:10.1080/08120090802120120

Vogt, P.R., 1974. Volcano spacing, fractures, and thickness of the lithosphere. *Earth Planet. Sci. Lett.* 21, 235–252. doi:10.1016/0012-821X(74)90159-9

Wilkins, D., Gouramanis, C., De Deckker, P., Fifield, L.K., Olley, J.M., 2013. Holocene lake-level fluctuations in Lakes Keilambete and Gnotuk, southwestern Victoria, Australia. *The Holocene* 23, 784–795. doi:10.1177/0959683612471983

## Chapter 5 Advancements in cosmogenic $^{38}\text{Ar}$ exposure dating of terrestrial rocks<sup>3</sup>

### 5.1. Abstract

Cosmogenic exposure dating of Ca-rich minerals using  $^{38}\text{Ar}$  on terrestrial rocks could be a valuable new dating tool to determine timescales of geological surface processes on Earth. Here, we show that advancement in analytical precision, using the new generation multi-collector ARGUSVI mass spectrometer on irradiated pyroxene and apatite samples, allows determination of cosmogenic  $^{38}\text{Ar}$  abundances above background values, as well as discrimination of  $^{38}\text{Ar}/^{36}\text{Ar}$  ratios ( $1\sigma$  absolute precision of  $\pm 0.3\%$ ) from the non-cosmogenic background value. Four statistically significant cosmochron ( $^{38}\text{Ar}/^{36}\text{Ar}$  vs  $^{37}\text{Ar}/^{36}\text{Ar}$ ) diagrams could be constructed for southeast Australian pyroxene samples from the Mt Elephant scoria cone for which a combined apparent exposure age of  $319 \pm 183$  ka ( $2\sigma$ ) was obtained when using a  $^{38}\text{Ar}$  production rate (Ca) of 250 atoms /g Ca/ yr. This exposure age overlaps within error with the known  $^{40}\text{Ar}/^{39}\text{Ar}$  eruption age of  $184 \pm 15$  ka ( $2\sigma$ ). Although apatite shows much larger  $^{38}\text{Ar}$  abundances than pyroxene, our modelling and analyses of unirradiated apatite suggest that apatite suffers from both natural and reactor-derived chlorogenic as well as nucleogenic contributions of  $^{38}\text{Ar}$ . Hence, we suggest that cosmogenic  $^{38}\text{Ar}$  exposure dating on irradiated Ca-rich (and eventually K-rich), but Cl-free, terrestrial minerals is a potential valuable and accessible tool to determine geological surface processes on timescales of a few Ma. Calculations show that with the new generation multi-collector mass spectrometers an analytical uncertainty better than 5% ( $2\sigma$ ) can be achieved on samples with expected exposure ages of  $> 4$  Ma.

---

<sup>3</sup> This Chapter was submitted as a paper to *Geochimica et Cosmochimica Acta* on December 22<sup>nd</sup>, 2016 and is currently being revised for publication.

## 5.2. Introduction

Primary galactic cosmic radiation interacts with nuclei of atoms in the upper layers of the Earth's atmosphere, resulting in a secondary particle flux cascading down on the Earth's surface (Gosse and Phillips, 2001) and interacting with elements such as Ca and K, which are constituents of major rock-forming minerals. Daughter isotope  $^{38}\text{Ar}$  is predominantly produced from parent isotopes  $^{40}\text{Ca}$  and  $^{40}\text{K}$  (both approximately 200 atoms/g/y), and minor Fe, Ti and Cl (e.g., 1.7 atoms/g Fe/y; Lal, 1991), when a fast incoming particle of the secondary cosmic ray flux creates a nuclear reaction in which a target nucleus in the upper few cm of the Earth's surface loses two protons and one neutron (Niedermann, 2002). Cosmogenic  $^{38}\text{Ar}$  exposure dating could be an invaluable dating tool to determine exposure ages and related information such as erosion rates, complementing the spectrum of existing exposure dating techniques such as  $^3\text{He}$ ,  $^{10}\text{Be}$ ,  $^{21}\text{Ne}$ ,  $^{26}\text{Al}$  and  $^{36}\text{Cl}$ . As  $^{38}\text{Ar}$  is stable, the technique can be applied to date surfaces on timescales beyond that of other, unstable, cosmogenic exposure dating techniques (Renne *et al.*, 2001). Although widely used in extra-terrestrial applications for decades (e.g. Kennedy *et al.*, 2013; Levine *et al.*, 2007; Shuster and Cassata, 2015; Turner *et al.*, 1971), cosmogenic  $^{38}\text{Ar}$  dating of terrestrial rocks has long been considered impracticable; mainly because the technique suffered from high atmospheric  $^{38}\text{Ar}$  background on Earth, as well as the presence of multiple  $^{38}\text{Ar}$  reservoirs in a single sample; trapped (magmatic)  $^{38}\text{Ar}$  and cosmogenic  $^{38}\text{Ar}$  (Niedermann *et al.*, 2007).

Advances in the previous generation of analytical instruments (e.g. MAP 250-50; VG5400) finally allows detection of cosmogenic  $^{38}\text{Ar}$  above instrumental and background values in terrestrial samples (Renne *et al.*, 2001). These authors measured Ca-rich samples (fluor-apatites and a fluorite) from the Granite Harbor Intrusive Suite in the Transantarctic Mountains, and derived  $^{38}\text{Ar}/^{36}\text{Ar}$  values as high as  $0.2894 \pm 0.0029$  ( $1\sigma$ ); resolvable from their air pipette results of the atmospheric  $^{38}\text{Ar}/^{36}\text{Ar}$  ratio of  $0.18816 \pm 0.00023$  ( $1\sigma$ ). Furthermore, step-heating analysis showed that incrementally increasing laser power yields progressive enrichment in  $^{38}\text{Ar}/^{36}\text{Ar}$  ratios, suggesting that  $^{38}\text{Ar}_{\text{cos}}$  is tightly restrained in the sample (Renne *et al.*, 2001).

The standard approach to cosmogenic  $^{38}\text{Ar}$  dating requires the measurement of the concentration of total  $^{38}\text{Ar}$  in a sample and subsequent correction for the trapped, atmospheric  $^{38}\text{Ar}$  contribution. The composition of the trapped argon in terrestrial samples is mostly assumed to be atmospheric, and an  $^{38}\text{Ar}/^{36}\text{Ar}$  value of  $0.18826 \pm 0.00023$  (Renne *et al.*, 2001) is generally used to correct the data. However, the true value of the trapped  $^{38}\text{Ar}/^{36}\text{Ar}$  ratio can differ due to e.g. isotopic mass fractionation (Jourdan *et al.*, 2012; Kaneoka, 1980; Oostingh *et al.*, 2017). Neutron irradiation (Merrihue and

Turner, 1966; Turner *et al.*, 1971) of target material converting parental isotope  $^{40}\text{Ca}$  into a ‘proxy-parent’  $^{37}\text{Ar}$  allows simultaneous analysis of parent and daughter isotopes; and facilitates direct measurement of the true trapped  $^{38}\text{Ar}/^{36}\text{Ar}$  ratio during step-wise heating and gas extraction of irradiated samples. Similar to the normal isochron technique used in  $^{40}\text{Ar}/^{39}\text{Ar}$  dating, step-wise degassing of irradiated samples allows construction of a parental relative abundance versus daughter relative abundance diagram, as well as testing of the statistical concordance of a dataset. Such a diagram has been proposed early on by Turner *et al.* (1971) and is currently applied exclusively to cosmogenic exposure dating on meteorites. It has relatively recently been called a *cosmochron diagram* (Levine *et al.*, 2007) and reflects a mixture between both  $^{36}\text{Ar}$  and  $^{38}\text{Ar}$  not related to any  $^{37}\text{Ar}$  released (trapped argon), and  $^{36}\text{Ar}$ ,  $^{38}\text{Ar}$  and  $^{37}\text{Ar}$  present in a certain proportion (cosmogenic argon). The slope of the correlation trend (the *cosmochron*) as well as the true value of the trapped  $^{38}\text{Ar}/^{36}\text{Ar}$  component (y-intercept) can be used to calculate a cosmogenic exposure age in which all uncertainties of analysis and data correction can be fully propagated.

In this study we used the new generation multi-collector ARGUS VI mass spectrometer (ThermoFisher™) to construct the first ever published cosmochrons for apatite and pyroxene from strategically selected samples collected from basaltic volcanic rocks in SE Australia (Oostingh *et al.*, 2016, 2017; Price *et al.*, 2003) and well exposed granite inselbergs in West Australia (Twidale and Bourne, 1998). The unprecedented precision the ARGUS VI offers as compared to the previous generation of mass spectrometers (Matchan and Phillips, 2014), allowed us to target the various argon reservoirs in these samples and quantify these by step-wise degassing of non-irradiated and irradiated samples. Furthermore, we explored the significance of our results in the framework of available and new geochronological data. Finally, in the light of our results, we will expand on which geological contexts would benefit the most from cosmogenic  $^{38}\text{Ar}$  dating in comparison to more established cosmogenic techniques.

### 5.3. Geological setting and sample description

When using cosmogenic produced isotopes to calculate exposure ages, sample-specific corrections concerning erosion rates, shielding from incoming rays due to boulders or vegetation and the effective attenuation length for the incoming particle in the target material are required (Niedermann, 2002). We have strategically sampled unshielded material from the top few cm of exposed, horizontal rock, thus discarding the need for shielding and attenuation corrections which could potentially introduce errors in the exposure age calculation up to ~20% (Gosse and Phillips, 2001). Furthermore, to avoid

cosmogenic  $^{38}\text{Ar}$  produced from spallation reactions on potassium, we have focused our research on the K-poor minerals apatite  $[\text{Ca}_5(\text{PO}_4)_3(\text{F}, \text{Cl}, \text{OH})]$  and pyroxene  $[(\text{Mg},\text{Fe})\text{CaSi}_2\text{O}_6 - \text{Ca}_2\text{Si}_2\text{O}_6]$ .

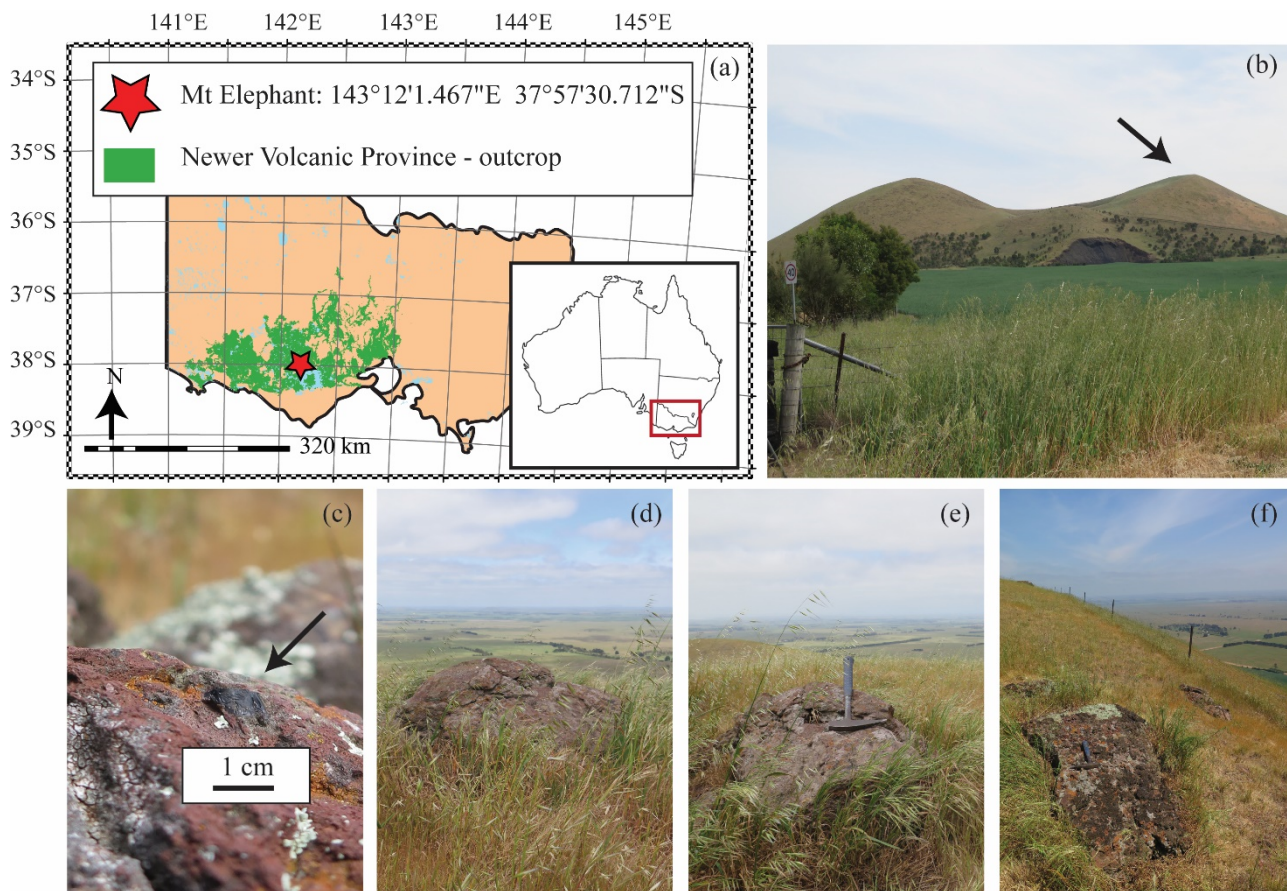


Figure 5.1. (a) Location map of Mt Elephant in Southeast Australia. (b) Sampling location on top of Mt Elephant (looking South). (c-f) Panoramic photos show the absence of major shielding.

### 5.3.1. Southeast Australian pyroxene

Mt Elephant (Figure 5.1b) is part of a dominantly monogenetic suite of scoria cones, lava shields and maars comprising the Newer Volcanic Province, SE Australia (Figure 5.1a). Groundmass from Mt Elephant has recently been dated by  $^{40}\text{Ar}/^{39}\text{Ar}$  techniques to be  $184 \pm 15$  ( $2\sigma$ ) ka (Oostingh *et al.*, 2017), which provides a maximum age limit on  $^{38}\text{Ar}$  exposure dating. We sampled fresh, cm-scale sized pyroxene phenocrysts (Figure 5.1c) at six locations (VIC61, VIC62, VIC64, VIC65 and VIC66 (augite) and VIC63 (diopside)) around the western part of the rim of the Mt Elephant (Figure 5.1d-f). Thin section images can be found in Appendix H. These phenocrysts were fully exposed on the rim of the volcano, with no shielding from flora, boulders or surrounding topography. We acknowledge that accounting for erosion rates and complex shielding is required to obtain an accurate and precise cosmogenic exposure age; however, this is beyond the scope of this methodological development study.

## 5.3.2. West-Australian apatite

Gorge rock (VIC100), King's Rock (VIC101 and VIC102) and Jilakin Rock (VIC103) are examples of Archean granite outcrops located in SW Australia (Figure 5.2a), thought to be exposed as early as the Cenozoic, as their geomorphology suggest that they pre-date the Eocene laterite soil (Twidale and Bourne, 1998).

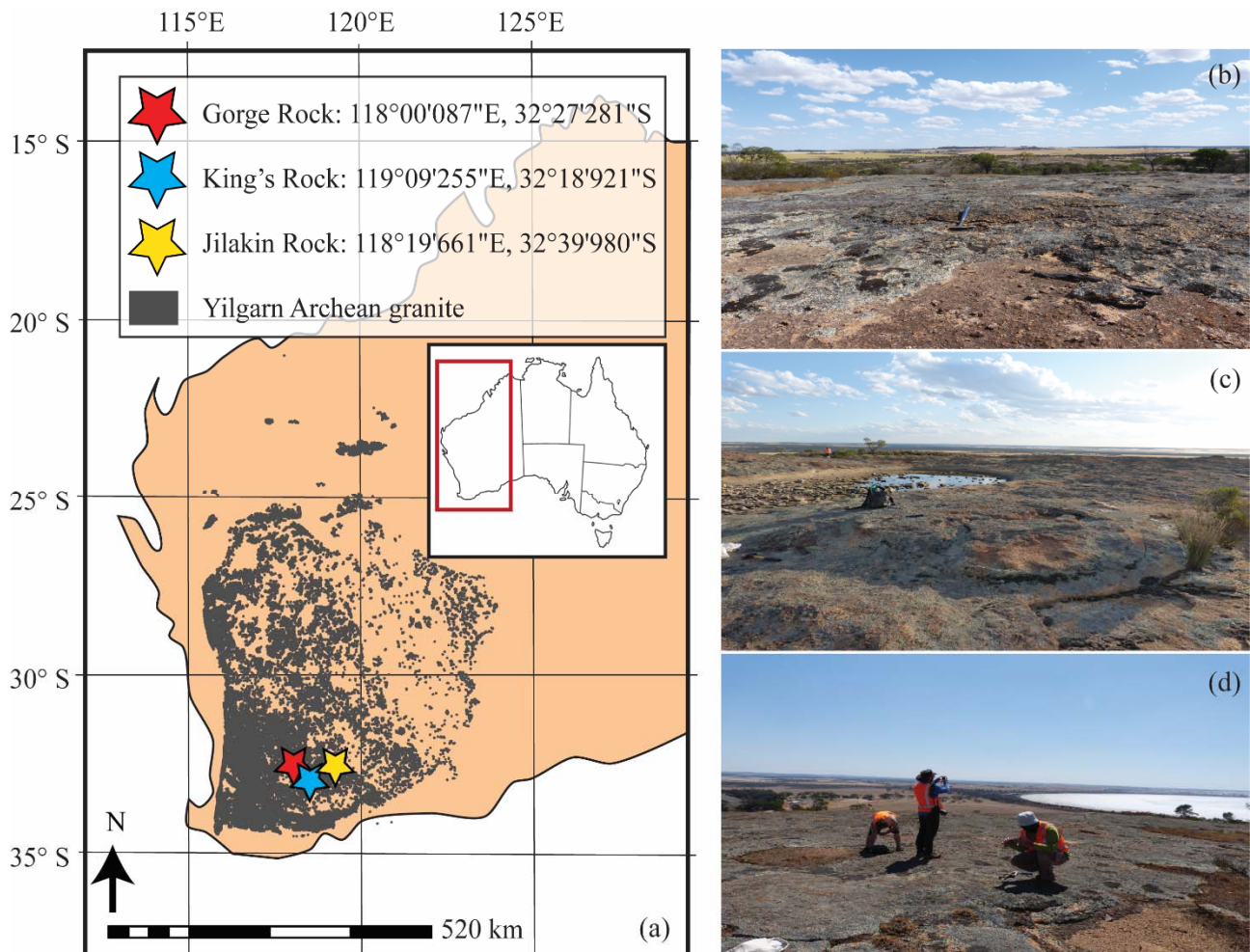


Figure 5.2. (a) Location map of the granite inselbergs in West-Australia; Gorge Rock (VIC100), King's Rock (VIC101 and VIC102) and Jilakin Rock (VIC103). (b-d) Panoramic photos of sample locations show the horizontal sampling surface and the absence of any shielding factors.

Cosmogenic nuclide ( $^{10}\text{Be}$  and  $^{26}\text{Al}$ ) analysis of comparable landforms in north Australia suggest that these granite outcrops are some of the most stable land surfaces on Earth, thought to have experienced erosion of only a few decimetres over the past few million years (Bierman and Caffee, 2002). We sampled a few kg of fresh granite from upper ~10 cm layers at the very top of each outcrop, limiting the impact of any shielding (Figure 5.2b-d). Thin section images can be found in Appendix I.



## 5.4. Analytical Methodology

### 5.4.1. Sample preparation and irradiation

#### 5.4.1.1. Pyroxene samples

Pyroxene grains extracted from surrounding altered scoria were carefully crushed to the 125 - 212  $\mu\text{m}$  size fraction using an agate mortar and pestle, allowing easy handling of radioactive material while minimizing the amount of interfering (fluid) inclusions. Depending on the availability of material between 80 and 300 mg of inclusion-free fresh pyroxene grains were handpicked using a binocular stereomicroscope; the resulting separate consisting of fresh, transparent dark green to green pyroxene (Appendix H). Separates were leached with diluted HF (2N) for 5 minutes to remove adhering scoria, followed by multiple DI washes. Each sample as well as four bracketing Fish Canyon Tuff sanidine standards ( $28.294 \pm 0.036$  Ma; Renne *et al.*, 2011) were loaded into a high-grade aluminium disc, wrapped in aluminium foil and placed in a quartz tube, followed by 20 minutes irradiation in the Cd-shielded (to avoid undesirable nuclear interference reactions) Cadmium-Lined-In-Core-Irradiation-Tube (CLICIT), Oregon State TRIGA reactor, USA.

#### 5.4.1.2. Apatite samples

Euhedral apatite grains were liberated from the granite matrix using SelFrag<sup>TM</sup> high voltage pulse power fragmentation. The fragmented granite was sieved to the 125 – 212  $\mu\text{m}$  size fraction of interest and subjected to a series of magnetic and density separation techniques to concentrate apatite minerals. Optically fresh apatite grains were carefully handpicked using a binocular stereomicroscope, and the resulting concentrate was subjected to 5 minutes of methanol and dilute HF (2N) leaching followed by multiple DI washes to remove adhering silicate phases. An aliquant of samples VIC100 and VIC102 was separated for degassing experiments of non-irradiated sample material, these samples will be referred to as VIC100ap\_unirr and VIC102ap\_unirr. Between 200 and 300 mg of each sample, as well as bracketing GA1550 biotite standard (McDougall and Roksandic, 1974) for which an age of  $99.738 \pm 0.100$  Ma is adopted (Renne *et al.*, 1998), were loaded into a high-grade aluminium disc. These were wrapped in aluminium foil and placed in a quartz tube, followed by 3 hours of irradiation in the Oregon State TRIGA reactor.

### 5.4.2. Argon gas extraction and analysis

Step-heating of the samples and analysis of the resulting argon isotopes was performed with the new generation multi-collector ARGUS VI mass spectrometer, coupled to a 100 W Photon Machines Fusions 10.6 CO<sub>2</sub> laser at the West Australian Argon Isotope Facility, Perth (Oostingh *et al.*, 2017). This mass spectrometer is equipped with five Faraday detectors as well as an ultra-sensitive compact

discrete dynode (CDD); which is an ion-counting electron multiplier, required to detect the extremely low concentrations of  $^{36}\text{Ar}$  and  $^{38}\text{Ar}$  in these samples.

Approximately 80 - 150 mg of mineral separate was placed as a single layer in a high-grade aluminium disc. Both sample chamber and extraction line were baked for at least 12 h at 120 °C to ensure acceptable ultra-high vacuum (UHV) background levels. Before sample analysis, Faraday detectors were electronically calibrated to normalize the gain of each detector to the others, whereas the CDD was calibrated for its actual yield with a series of four air aliquots. Multiple series of three air aliquots ( $^{40}\text{Ar}/^{36}\text{Ar}$  ratio of  $298.56 \pm 0.31$ ; Lee *et al.*, 2006) from an automated air pipette system was run before, during and after each sample, allowing the calculation of the mass discrimination, which ranged from  $0.990372 \pm 0.03$  ( $1\sigma$ ) to  $0.993761 \pm 0.04$  ( $1\sigma$ ) per Dalton (atomic mass unit). Argon gas aliquots were extracted during 12 to 20 heating steps between 1% and 50% of maximum laser power (maximum power of 65 W). A homogenized 4 mm laser beam was jogged over the sample for one minute to ensure a homogenous temperature gradient between grains for each step. System blanks were measured before and after two incremental heating steps and are around 0 – 0.05 fA for masses 36, 37, 38 and 39 and around 15 – 25 fA for mass 40. Argon isotopes measurements were performed in multi-collector mode, with  $^{40}\text{Ar}$ ,  $^{39}\text{Ar}$  and  $^{37}\text{Ar}$  measured on the Faraday detectors and  $^{36}\text{Ar}$  and  $^{38}\text{Ar}$  alternatively on the CDD during two sequences of peak-hopping for each step with an integration time of 33s. Ten cycles were measured for each step, to optimize the precision of the measurements. Single fusion of the GA1550 biotite or Fish Canyon Tuff sanidine standards in a separate disc allowed the calculation of the J-value for each irradiated sample. We used interference correction factors obtained from prolonged analysis of K-Ca-Cl glass/salts at the Oregon State TRIGA reactor:  $(^{39}\text{Ar}/^{37}\text{Ar})_{\text{Ca}} = (7.60 \pm 0.09) \times 10^{-4}$ ;  $(^{36}\text{Ar}/^{37}\text{Ar})_{\text{Ca}} = (2.70 \pm 0.02) \times 10^{-4}$ ;  $(^{40}\text{Ar}/^{39}\text{Ar})_{\text{K}} = (7.30 \pm 0.90) \times 10^{-4}$ ; and  $(^{38}\text{Ar}/^{39}\text{Ar})_{\text{K}} = (1.24 \pm 0.004) \times 10^{-2}$  (Jourdan and Renne, 2007). Furthermore, we used a value of  $0.00082636 \pm 0.11\%$  (Renne and Norman, 2001) to correct for  $^{37}\text{Ar}(\text{Ca})$  produced in the reactor with a half-life of 35 days, which greatly improves precision on the  $^{37}\text{Ar}/^{36}\text{Ar}$  and  $^{38}\text{Ar}/^{36}\text{Ar}$  ratios as compared to using the more standard value of  $0.000823 \pm 1\%$  (Koppers, 2002).

#### 5.4.3. Data reduction and exposure age calculation

Argon isotope data was regressed using the ArArCALC software (Koppers, 2002). The resulting isotopic abundances corrected for blank, mass fractionation and reactor interference were exported to an *in house* developed Excel spreadsheet to calculate exposure ages. This alternate spreadsheet was developed to work on raw analytical data, with the additional possibility to carry out the interference

corrections offline to make sure no bias was introduced using ArArCALC. Here, the corrected data can be used to construct a cosmochron using the Isoplot algorithm (Ludwig, 2012), by plotting  $[\text{}^{37}\text{ArCa} / (\text{}^{36}\text{Ar}_{\text{atm}} + \text{}^{36}\text{Ar}_{\text{cos}})]$  versus  $[(\text{}^{38}\text{Ar}_{\text{atm}} + \text{}^{38}\text{Ar}_{\text{cos}}) / (\text{}^{36}\text{Ar}_{\text{atm}} + \text{}^{36}\text{Ar}_{\text{cos}})]$  on a bivariate diagram. The slope ( $\text{}^{38}\text{Ar}/\text{}^{37}\text{Ar}$ ) and y-intercept ( $\text{}^{38}\text{Ar}_{\text{atm}}/\text{}^{36}\text{Ar}_{\text{atm}}$ ) of the resulting cosmochron can be used to calculate an exposure age (Levine *et al.*, 2007; Turner *et al.*, 1971) using a modified equation of Hennesy and Turner (1980);

$$\frac{\text{}^{38}\text{Ar}}{\text{Ca}} = \text{slope} * \left[ \frac{1}{1 - \text{intercept} / \left( \frac{\text{}^{38}\text{Ar}}{\text{}^{36}\text{Ar}} \right)_{\text{cos}}} \right] * \alpha * J * 7.012 \times 10^{-3} \quad (1)$$

where  $\alpha$  is the proportionality factor to convert  $\text{}^{38}\text{Ar}/\text{}^{37}\text{Ar}$  into  $\text{}^{38}\text{Ar}/\text{Ca}$  (Cohen *et al.*, 2001), depending on the efficiency of the reactor to convert Ca/K into  $\text{}^{37}\text{Ar}/\text{}^{39}\text{Ar}$  (0.52 for the Oregon TRIGA reactor as measured with Hb3gr; Jourdan and Renne, 2007; Kennedy *et al.*, 2013). J is the irradiation parameter, which ranged between  $0.0000922 \pm 0.0000003$  ( $2\sigma$ ) and  $0.0000931 \pm 0.0000003$  ( $2\sigma$ ) for the pyroxenes and between  $0.0007720 \pm 0.0000010$  ( $2\sigma$ ) and  $0.0007777 \pm 0.0000022$  ( $2\sigma$ ) for the apatite samples. The factor  $7.012 \times 10^{-3}$  incorporates constants of K-decay and unit conversions to make  $\text{}^{38}\text{Ar}/\text{Ca}$  into units of cc STP/g.

$(\text{}^{38}\text{Ar}/\text{}^{36}\text{Ar})_{\text{cos}}$  relates the  $\text{}^{38}\text{Ar}/\text{}^{36}\text{Ar}$  ratio to the cosmogenic component only (Levine *et al.*, 2007).  $\text{}^{36}\text{Ar}_{\text{cos}}$  is both derived from calcium with a production rate [rate at which a specific nuclide is produced from a specific target element in a mineral (units: atoms/g target material/y)] of  $\text{}^{38}\text{Ar}$  produced by calcium [hereafter P38(Ca); Niedermann *et al.*, 2007]] of approximately 69 atoms/g Ca/y (Lal, 1991), but is also naturally generated from  $\beta$ -decay on cosmogenic  $\text{}^{36}\text{Cl}$  (P36(Cl) = 67 atoms/g Cl/y) with a half-life ( $t_{1/2}$ ) of 300,000 yr. This implies that the ratio  $(\text{}^{38}\text{Ar}/\text{}^{36}\text{Ar})_{\text{cos}}$  is time-dependent and ranges from 2.90 for recently exposed samples to 1.47 for samples with  $> 1 \times 10^6$  years exposure (Renne *et al.*, 2001).  $\text{}^{40}\text{Ar}/\text{}^{39}\text{Ar}$  dating on Mt Elephant resulted in an eruption age of  $184 \pm 15$  ( $2\sigma$ ) ka (Oostingh *et al.*, 2017), which results in a  $(\text{}^{38}\text{Ar}/\text{}^{36}\text{Ar})_{\text{cos}}$  ratio of 2.17; calculated using the time dependent production ratio equation of Renne et al (2001). We assign a relative generous absolute error of  $\pm 0.1$  to the calculated  $(\text{}^{38}\text{Ar}/\text{}^{36}\text{Ar})_{\text{cos}}$  ratio (4.6 % for the ratio of 2.17; Levine *et al.*, 2007) to reflect the uncertainties associated with the production rates used in this calculation (Renne *et al.*, 2001). The presumably old southwest Australian apatite samples are thought to be in secular equilibrium with respect to the  $\beta$ -decay reaction on cosmogenic  $\text{}^{36}\text{Cl}$ , and a  $(\text{}^{38}\text{Ar}/\text{}^{36}\text{Ar})_{\text{cos}}$  ratio of 1.47 is taken for these samples.

The resulting  $^{38}\text{Ar}/\text{Ca}$  is then divided by the relevant P38(Ca) scaled to the latitude and elevation of interest to obtain a cosmogenic exposure age

#### 5.4.4. Apatite (U-Th)/He analysis

As published age constraints are limited for the Western Australian granites, we performed (U-Th)/He dating of apatite for all samples to derive a maximum potential Ar exposure age and minimum age for radiogenic Ar retention. Approximately 10 to 15 grains were selected under a binocular stereomicroscope from the 125 – 250  $\mu\text{m}$  size apatite concentrate. He, U, Th and Sm analyses were performed at the GeoHistory laboratory at the John de Laeter Centre of Isotope Research in Perth, Western Australia, using the methods outlined in Danišik *et al.* (2012) and Evans *et al.* (2005). Single apatite grains were loaded in Pt tubes, degassed at  $\sim 960^\circ\text{C}$  under UHV using laser heating, and analyzed for  $^4\text{He}$  by isotope dilution on a Pfeiffer Prisma QMS-200 mass spectrometer. Each gas extraction was followed by a re-extract (Farley, 2002) to ensure complete degassing of the apatite grains. Following degassing, all samples were dissolved and spiked with  $^{235}\text{U}$  and  $^{230}\text{Th}$ . Resulting solutions were analysed by isotope dilution for  $^{232}\text{Th}$  and  $^{238}\text{U}$  and by external calibration for  $^{147}\text{Sm}$  on an Agilent 7500 ICP-MS. The total analytical uncertainty (TAU) was calculated as the square root of the sum of the squares of weighted uncertainties on the U, Th and He abundances and was used to calculate the error on the raw He ages. The raw He ages were corrected for alpha-ejection (Farley *et al.*, 1996) assuming homogeneous distribution of parent nuclides.

#### 5.4.5. ELA-ICP-MS analysis

Selected major (Ca, K) and trace element (Mg, Ti, Fe, Ni, Cl, Th and U) analyses were performed on VIC66 pyroxene and all apatite samples using a Resonetics S-155-LR 193 nm excimer laser ablation system coupled to an Agilent 7700x quadrupole ICP-MS at the GeoHistory laboratory, John de Laeter Centre, Curtin University. As compositions were derived from averaging element abundances of two to four (250  $\mu\text{m}$  diameter) spots per mineral which could potentially include inclusions; we acknowledge that these compositions are indicative only.

### 5.5. Results

#### 5.5.1. Degassing characteristics

##### 5.5.1.1. Irradiated pyroxene

Figure 5.3a shows the degassing pattern,  $^{38}\text{Ar}/^{36}\text{Ar}$  ratios and K/Ca ratios of a typical pyroxene (VIC66); spectra for all other pyroxene samples can be found in Appendix L. Pyroxene samples show a complex, two-step  $^{38}\text{Ar}$  release pattern with low isotopic abundances (Figure 5.3a). The first step of  $^{38}\text{Ar}$  release is closely coupled to high K/Ca ratios; with  $^{38}\text{Ar}$  abundances as high as 0.3 fA for sample VIC66. From around 10% laser power onwards, K/Ca ratios approach zero (0.003 – 0.017)

and  $^{38}\text{Ar}$  gas release is closely coupled with release of  $^{37}\text{Ar}$ . This second stage of  $^{38}\text{Ar}$  gas release is characterized by  $^{38}\text{Ar}/^{36}\text{Ar}$  on or just above the uniform non-cosmogenic terrestrial (UNCT) composition of  $0.18826 \pm 0.00018$  ( $2\sigma$ ; green line in Figure 5.3; Renne *et al.*, 2001).  $^{39}\text{Ar}$  abundances (Appendix J) are much higher than initially expected from these K-poor minerals, but consistent with recent results on dating pyroxene with the  $^{40}\text{Ar}/^{39}\text{Ar}$  technique (Ware *et al.*, 2015). The  $^{39}\text{Ar}$  release pattern closely follows both the pattern and the abundance of the  $^{38}\text{Ar}$  isotope for each sample. Nevertheless, most of the  $^{38}\text{Ar}$  gas released is associated with K/Ca value near zero indicating that the  $^{38}\text{Ar}$  comes from the spallation of  $^{40}\text{Ca}$  and that the  $^{40}\text{K}$  contribution is negligible, especially after ca. 15% of maximum laser power.

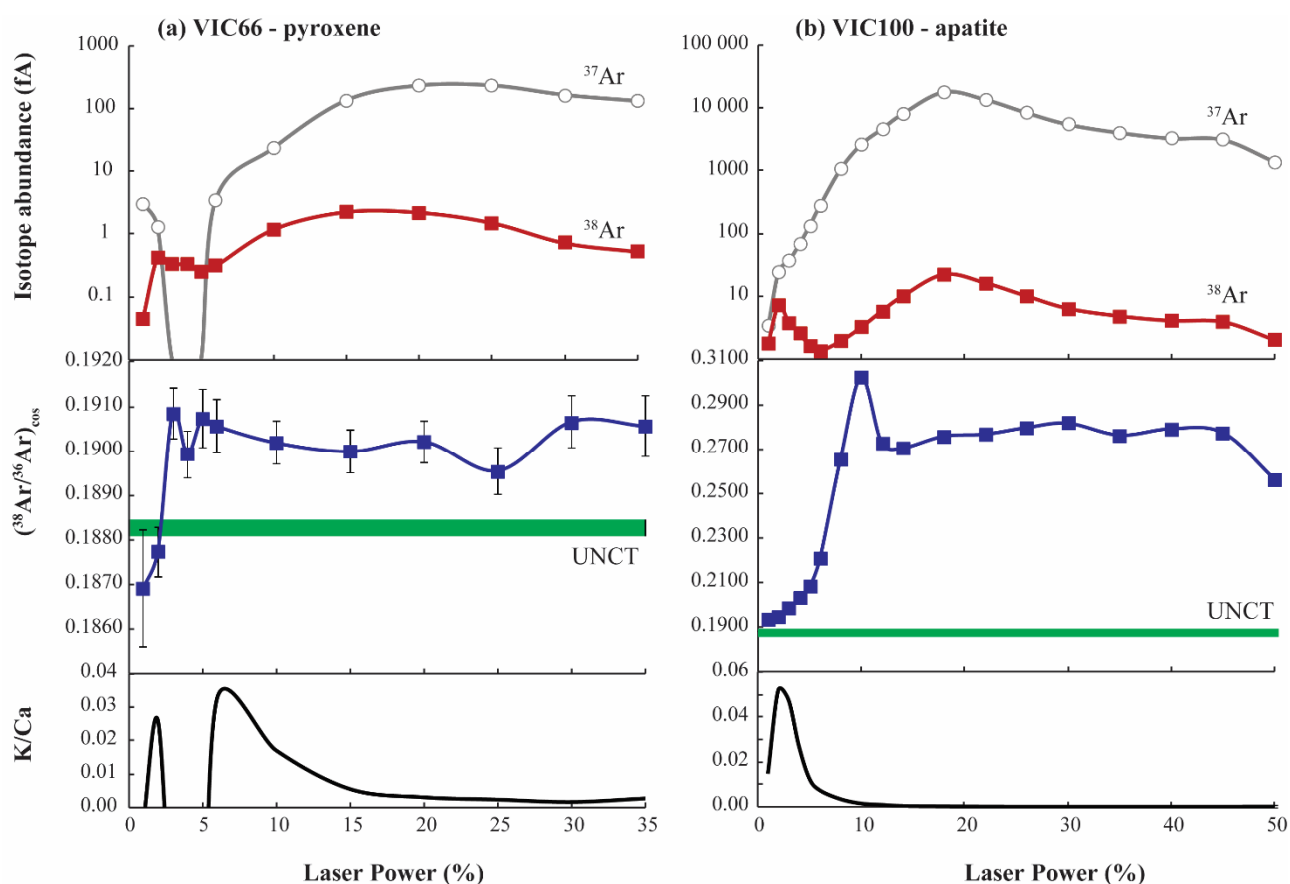


Figure 5.3. Degassing patterns of (a) typical pyroxene and (b) typical apatite. The top diagram displays isotopic abundance (in fA) for  $^{37}\text{Ar}$  (grey line, open circles) and  $^{38}\text{Ar}$  (red line, closed squares). Note the exponential scale and the order of magnitude difference between the  $^{37}\text{Ar}$  and  $^{38}\text{Ar}$  signal. The middle diagram displays the  $^{38}\text{Ar}/^{36}\text{Ar}$  ratio and associated  $2\sigma$  error. Note that the size of the symbols is larger than the error for the apatite. The green line in the  $^{38}\text{Ar}/^{36}\text{Ar}$  graphs represents the UNCT value of  $0.18826 \pm 0.00018$  (Renne *et al.*, 2001). The lower diagram displays the K/Ca ratio calculated after the  $^{39}\text{Ar}/^{37}\text{Ar}$  ratio.

#### 5.5.1.2. Irradiated apatite

Figure 5.3b shows the degassing pattern,  $^{38}\text{Ar}/^{36}\text{Ar}$  ratios and K/Ca ratios of a typical apatite (VIC100); spectra for all other samples can be found in Appendix M, where VIC101B represents a second aliquant of sample VIC101. Apatite shows degassing characteristics similar to those of

pyroxene, but with much higher isotopic abundances (e.g.  $> 17\,000$  fA for  $^{37}\text{Ar}$ ). Again,  $^{38}\text{Ar}$  is released in two major steps; one up to 6% laser power and another larger one from  $\sim 10\%$  laser power onwards. The first step of  $^{38}\text{Ar}$  release (max of 7 fA) is closely linked to relatively high K/Ca ratios (0.01 – 0.05), but is not supported by release of  $^{37}\text{Ar}$ . The  $^{38}\text{Ar}/^{36}\text{Ar}$  ratio associated with this first step of  $^{38}\text{Ar}$  release is relatively low and ranges from 0.1903 (VIC101B) to 0.2336 (VIC103; Appendix K). The second step in  $^{38}\text{Ar}$  release is closely linked to the release of  $^{37}\text{Ar}$  and extremely small K/Ca ratios. The  $^{38}\text{Ar}$  signal is detected well above background values ( $\sim 0.03$  fA) and ranges from 1 – 22 fA for VIC100; 1 – 11 fA for VIC101, 1 – 14 fA for VIC101B; 1 – 10 fA for VIC102 and 1 – 10 fA for VIC103 with 1 sigma errors smaller than 0.2% in most cases (Appendix K). The  $^{38}\text{Ar}/^{36}\text{Ar}$  ratio for the second release step is very high and constant for each sample, showing values up to 0.3021 for sample VIC100 (Figure 5.3b).

## 5.5.2. Cosmochron characteristics

### 5.5.2.1. Irradiated pyroxene

Figure 5.4 shows the cosmochron diagrams for all pyroxene samples, whereas full argon isotope abundances and  $^{38}\text{Ar}/^{36}\text{Ar}$  and  $^{37}\text{Ar}/^{36}\text{Ar}$  ratios can be found in Appendix J. Initial steps of gas release are not reflective of cosmogenic  $^{38}\text{Ar}$  release derived from Ca (no correlation between  $^{37}\text{Ar}$  release and  $^{38}\text{Ar}$  release) but rather from the presence of K (Figure 5.3a), therefore, for the present exercise, the  $^{38}\text{Ar}/^{36}\text{Ar}$  intercept was forced through the atmospheric  $^{38}\text{Ar}/^{36}\text{Ar}$  ratio. Furthermore, outliers (no correlation between  $^{37}\text{Ar}$  release and  $^{38}\text{Ar}$  release) were removed from the data and are represented by a grey colour in the cosmochron diagrams. These typically represent the first few steps of gas release; the contribution of outliers to total gas release for e.g. sample VIC66 is 11%. While these particular pyroxene minerals are perhaps not ideal for accurate dating due to the presence of K-rich inclusions, the approach of removing the first degassing steps associated with high K concentrations and forcing the  $^{38}\text{Ar}/^{36}\text{Ar}$  intercept through the atmospheric value has the merit to allow us to test if any apparent exposure age can be derived from the present dataset. Hence, we can test what age uncertainty could be derived from a similar, but better-behaved, dataset derived from inclusion-free minerals.

Isotopic abundances of  $^{38}\text{Ar}$  and  $^{36}\text{Ar}$  for these young samples are just above the blank level ( $\sim 0.05$  fA); nevertheless 1 sigma absolute errors on the  $^{38}\text{Ar}/^{36}\text{Ar}$  ratio are around 0.30%. The extreme sensitivity of the CDD collector results in statistically significant ( $p\text{-value} > 0.05$ ) cosmochrons for four (VIC63, VIC64, VIC65 and VIC65) out of six samples with slopes ranging from  $1.38\text{E-}5$  to  $2.78\text{E-}5$  (Table 2). An ‘*error-cosmochron*’ with statistically less meaningful correlation ( $p\text{-value} =$

0.02) was obtained for sample VIC61 and exposure ages calculated based on this cosmochron should be taken as indicative only. No cosmochron correlation could be obtained for sample VIC62.

#### 5.5.2.2. Irradiated apatite

Figure 5.5 shows the cosmochrons for all irradiated apatite samples, whereas full argon isotope abundances and  $^{38}\text{Ar}/^{36}\text{Ar}$  and  $^{37}\text{Ar}/^{36}\text{Ar}$  ratios can be found in Appendix K. Again, the incremental heating steps from the first  $^{38}\text{Ar}$  release not linked to  $^{37}\text{Ar}$  release, as well as steps associated with the sudden degassing peak in  $^{37}\text{Ar}$ ,  $^{38}\text{Ar}$  and  $^{39}\text{Ar}$  were excluded from the cosmochron slope calculation and the slope was forced through the atmospheric  $^{38}\text{Ar}/^{36}\text{Ar}$  ratio. All samples are characterized by much higher  $^{37}\text{Ar}/^{36}\text{Ar}$  (e.g. 923 for VIC103) and  $^{38}\text{Ar}/^{36}\text{Ar}$  (e.g. 0.44 for VIC103) ratios than the pyroxene samples; due to higher Ca content and especially the longer irradiation time (3h). Absolute errors ( $1\sigma$ ) on these ratios are around 0.20 – 0.30%. None of the apatite samples yield a statistically significant cosmochron, the resulting ‘error-cosmochrons’ have slope values ranging from 2.58E-4 (VIC101) to 4.98E-4 (VIC100).

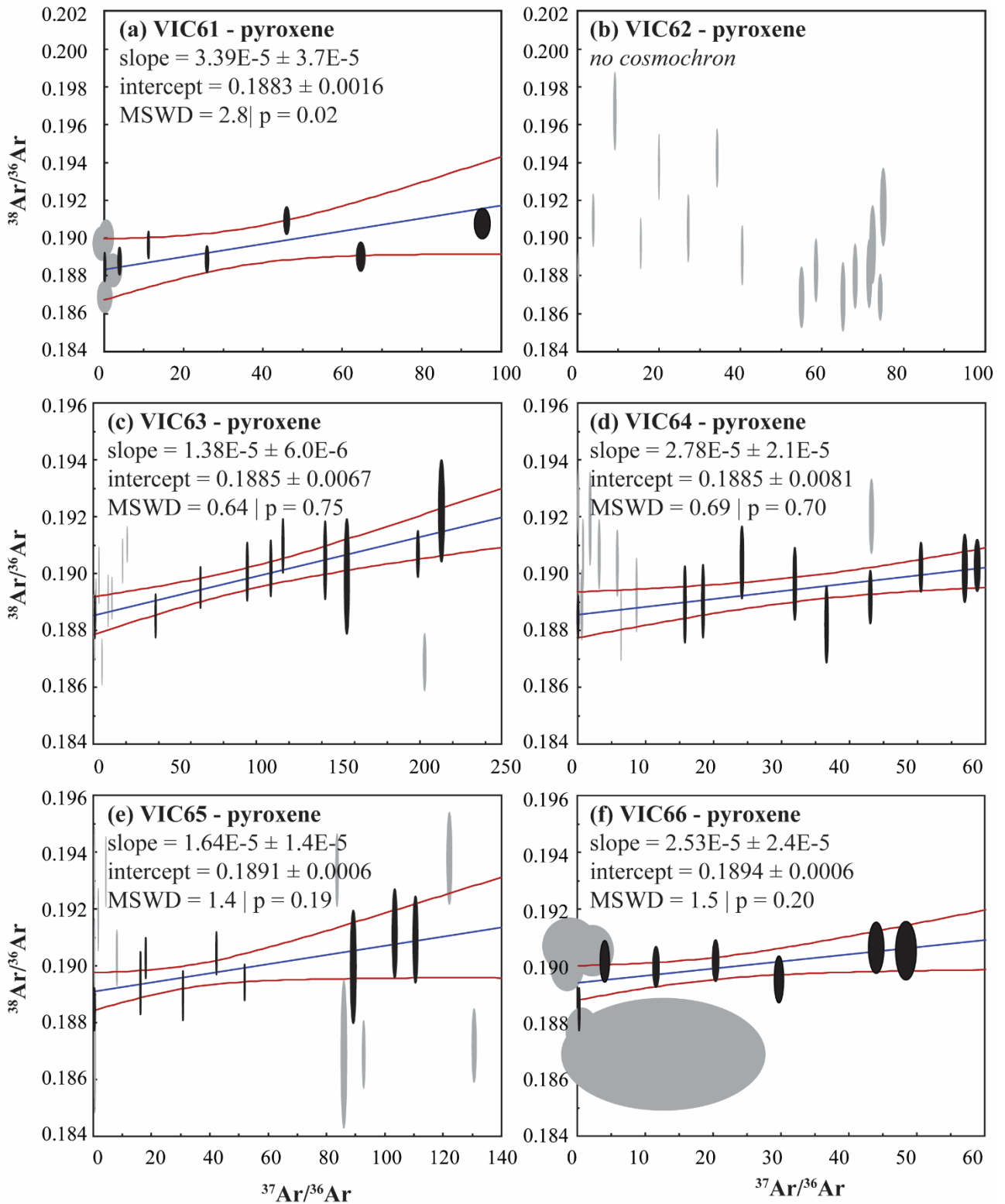


Figure 5.4. Cosmochron diagrams for irradiated pyroxene. Data in grey forms outliers to the main trend and are not used in the construction of the cosmochron.



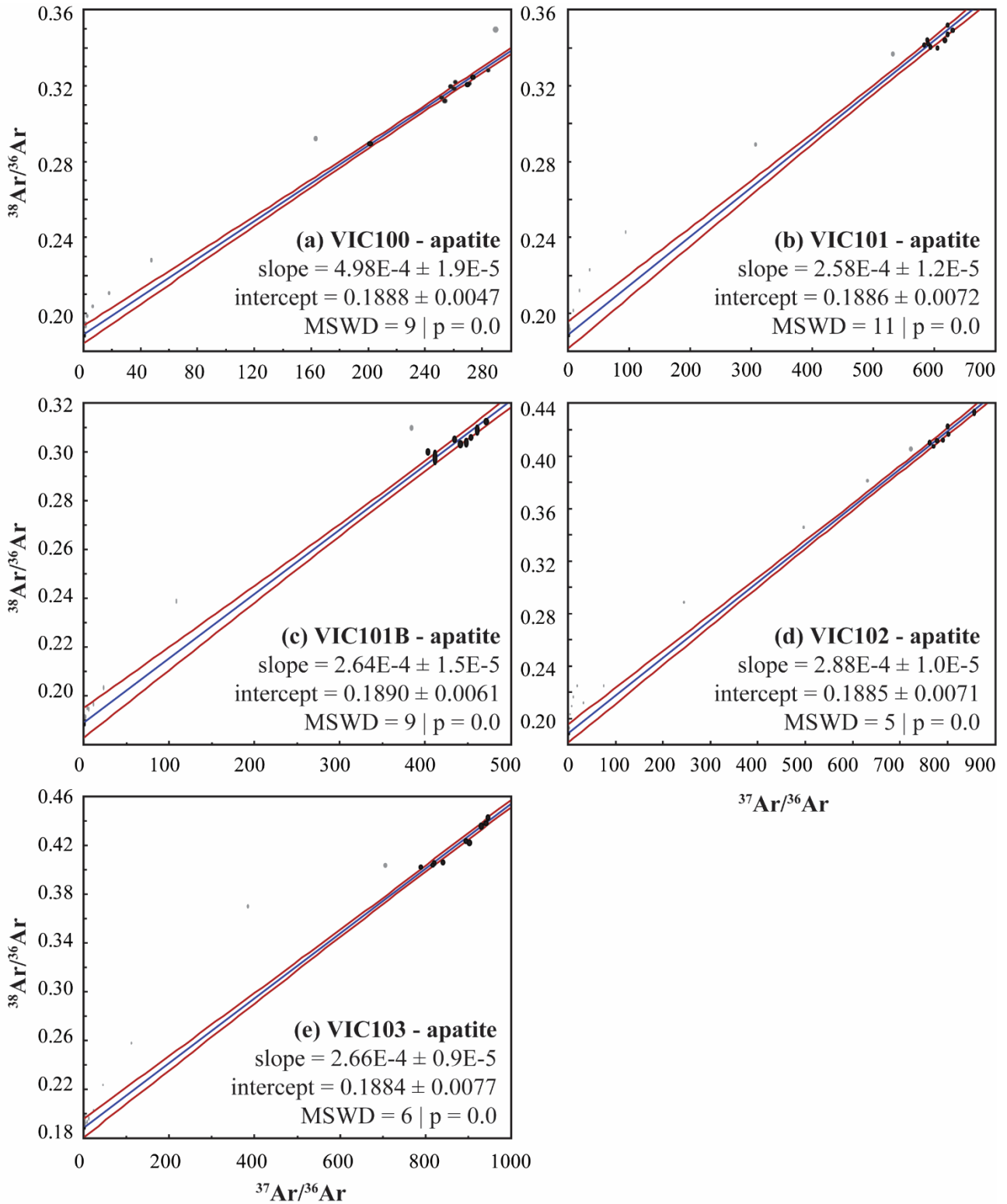


Figure 5.5. Cosmochron diagrams for irradiated apatite. Data in grey forms outliers to the main trend and are not used in the construction of the cosmochron.

### 5.5.3. Apatite (U-Th)/He ages

Mean apatite (U-Th)/He ages of  $378 \pm 28$  Ma ( $1\sigma$ ),  $395 \pm 27$  Ma ( $1\sigma$ ) and  $402 \pm 29$  Ma ( $1\sigma$ ) measured for three granites overlap within  $1\sigma$  error. The mean weighted average age calculated for all aliquots is  $387 \pm 11$  Ma ( $1\sigma$ ) (Table 5.1). This age is interpreted to record the cooling below  $70^\circ\text{C}$  (Farley, 2002) and provides the maximum age for Ar exposure and minimum age for Ar retention.

### 5.5.4. Apatite $^{40}\text{Ar}/^{39}\text{Ar}$ ages.

Surprisingly, we were able to derive apparent age spectra for the apatite samples; showing that these samples contain small, but measurable, amounts of K (Figure 5.6). Although none of these show statistically significant plateau ages; total fusion ages range from  $1155 \pm 17$  Ma (VIC101B;  $2\sigma$ ) to  $1574 \pm 21$  Ma (VIC102;  $2\sigma$ ). These total fusion ages provide an estimate of the potential Ar retention age of these samples.

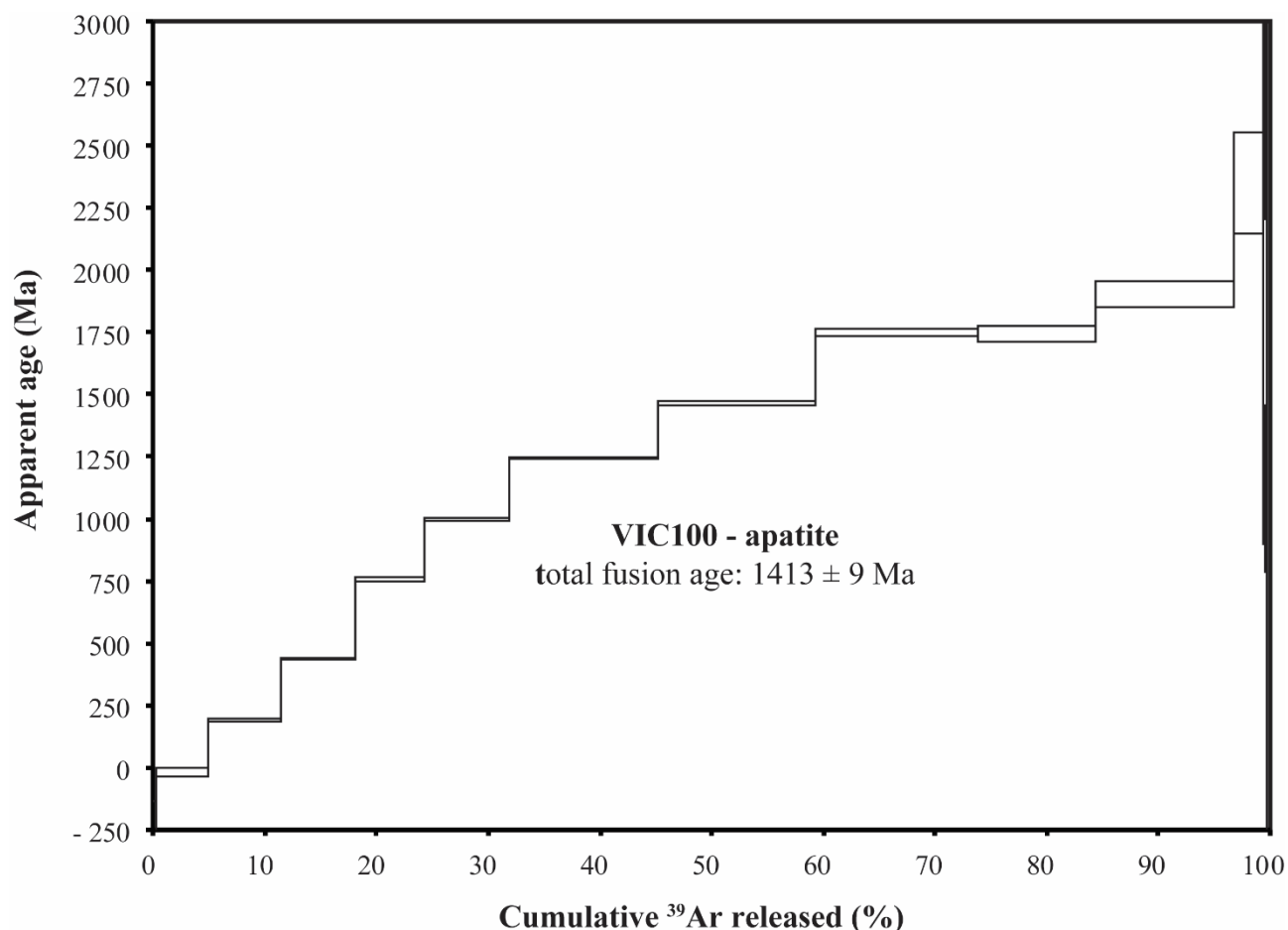


Figure 5.6.  $^{40}\text{Ar}/^{39}\text{Ar}$  apparent age diagram of sample VIC100 – apatite; the total fusion age of this sample is 1.4 Ga. Note that this age does not represent the formation age of this rock in any case; but rather provides an estimate of the integral theoretical duration of  $^{40}\text{Ar}$  (and thus nucleogenic  $^{38}\text{Ar}$ ) retention in the rock since formation.

## 5.6. Discussion

## 5.6.1. Analytical advancement

This study represents the first publication of terrestrial cosmochrons using the  $^{38}\text{Ar}$  isotope system. We have shown that the ARGUSVI mass spectrometer allows measurement of the  $^{38}\text{Ar}/^{36}\text{Ar}$  ratio with a precision up to  $\pm 0.30\%$  for both pyroxene and apatite minerals. Furthermore, we were able to discriminate between atmospheric  $^{38}\text{Ar}/^{36}\text{Ar}$  ratios and cosmogenic  $^{38}\text{Ar}/^{36}\text{Ar}$  ratios on very young pyroxene samples.

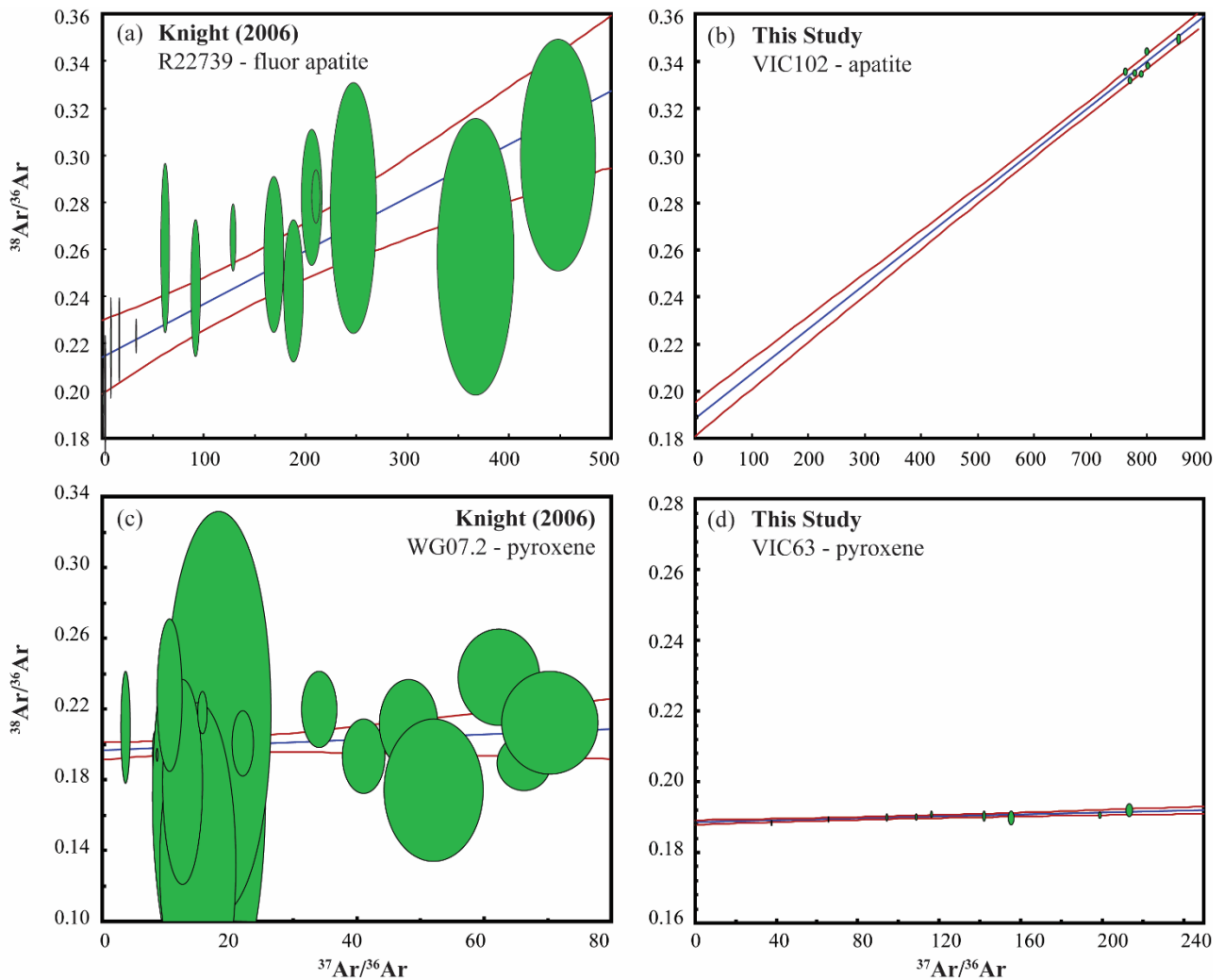


Figure 5.7. Cosmochron comparison diagrams between (a) and meteorite pyroxene samples analysed on the MAP 250-50 mass spectrometer (Kennedy *et al.*, 2013) and (b) and terrestrial pyroxene analysed on the ARGUSVI. The difference in analytical precision is obvious.

To better illustrate the advancement in analytical precision offered by the new generation of multi-collector mass spectrometers to the benefit of the cosmogenic  $^{38}\text{Ar}$  exposure age dating method, cosmochrons between irradiated pyroxene from meteorite material as analysed on the MAP 250-50 mass spectrometer (Kennedy *et al.*, 2013) versus the terrestrial pyroxene analysed on the new

generation mass spectrometer ARGUS VI in this work are shown in Figure 5.7a and Figure 5.7b. We have selected the pyroxene sample with a similar order of magnitude exposure age (ca. 7 Ma) from the Kennedy et al (2013) study. Note however that the vertical scale of these authors' Lake Carnegie pyroxene is more than thirty times as large for displaying reasons; which only further illustrates the advancement in analytical precision. All errors are given at the 1 sigma level in these diagrams. New generation multi-collector mass spectrometers (such as the ARGUS VI) represent a major leap forward in analytical precision; with  $1\sigma$  uncertainty for the MAP 250-50 on the  $^{37}\text{Ar}/^{36}\text{Ar}$  and the  $^{38}\text{Ar}/^{36}\text{Ar}$  ratio about 3% and 8% respectively, as compared with  $1\sigma$  uncertainties on the ARGUS VI for both the  $^{37}\text{Ar}/^{36}\text{Ar}$  and the  $^{38}\text{Ar}/^{36}\text{Ar}$  ratio of around 0.3%.

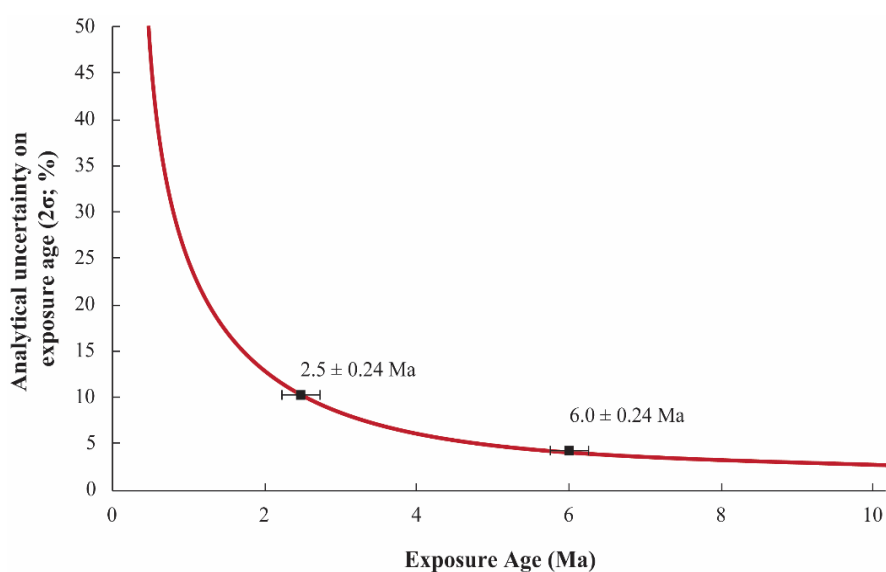


Figure 5.8. Calculated potential analytical uncertainty on the exposure age that can be obtained with the new generation multi-collector mass spectrometers. Indicated two potential ages as discussed in the text.

Using the ARGUS VI' typical  $1\sigma$  absolute error on the  $^{37}\text{Ar}/^{36}\text{Ar}$  and  $^{38}\text{Ar}/^{36}\text{Ar}$  isotopic abundances of 0.1 and 0.0005 respectively, we calculate the absolute age uncertainty that can be achieved with the current analytical power. Here, we have used ArArCALC to regress a cosmochron through 5 data points (Figure 5.8; X and Y of  $^{37}\text{Ar}/^{36}\text{Ar}$  and  $^{38}\text{Ar}/^{36}\text{Ar}$  with associated absolute errors on these ratios

as reported above), which in turn were generated by plotting points along a forced slope that would yield a certain age (e.g. a slope of  $2.5\text{E}-5$  yields an age of 1 Ma). This calculation did not consider the observation that measurements typically become slightly more precise with higher beam signal, however, it will still give a good idea of what can be expected.

It can be seen in Figure 5.8 that an analytical uncertainty of less than 10% ( $2\sigma$ ) can be achieved on samples with expected exposure ages of  $> 2.5$  Ma and less than 5% for ages above 4 Ma. For example, an exposure age of 6.0 Ma should be associated with an uncertainty of  $\pm 0.24$  Ma. Those uncertainties are smaller than the 14% ( $2\sigma$ ) quoted for the analytical uncertainty typically found during  $^{10}\text{Be}$  dating

(Gosse and Phillips, 2001) and show that cosmogenic  $^{38}\text{Ar}$  exposure dating using the new generation mass spectrometers is a valuable new dating tool for rocks exposed over a few Ma.

	Th (ng)	Th uncert. (±, %)	U (ng)	U uncert. (±, %)	Sm (ng)	Sm uncert. (±, %)	He (ncc)	He uncert. (±, %)	TAU (%)	Th/ U	Uncorr. age (Ma)	Uncorr. age uncert. ±1σ (Ma)	Ft	Corr. age (Ma)	Corr. age uncert. ±1σ (Ma)
<b>Mean weighted average age for all aliquots: 387 ± 11 Ma (2σ)</b>															
V100-1	0.522	5.3	0.071	5.4	0.126	0.3	6.956	1.6	4.2	7.25	288.1	12.2	0.78	369.4	24.2
V100-2	0.813	3.8	0.115	3.9	0.141	0.3	9.667	2.0	3.4	7.01	254.7	8.7	0.67	377.7	22.9
V100-3	1.231	5.6	0.250	5.4	0.221	0.3	20.362	2.4	4.6	4.89	303.5	14.0	0.78	387.0	26.4
V100-4	0.532	3.8	0.172	4.0	0.050	0.3	9.832	2.5	3.7	3.08	267.1	10.0	0.81	329.4	20.6
V100-5	0.511	5.3	0.093	5.4	0.130	0.3	8.332	2.2	4.4	5.46	314.2	13.8	0.77	409.1	27.2
V100-6	0.565	3.8	0.121	3.9	0.072	0.3	10.231	2.2	3.5	4.65	324.4	11.3	0.74	439.7	26.8
V100-7	0.836	5.3	0.242	5.4	0.202	0.3	15.607	2.4	4.5	3.42	285.5	12.8	0.71	400.0	26.9
V100-9	1.251	3.8	0.205	3.9	0.198	0.3	17.557	2.5	3.7	6.06	283.5	10.5	0.75	378.9	23.5
V100-11	0.629	5.3	0.153	5.4	0.085	0.4	13.394	1.7	4.2	4.09	356.9	14.9	0.78	457.9	29.8
V100-12	0.698	3.8	0.259	3.9	0.195	0.3	13.599	1.9	3.4	2.68	258.5	8.8	0.74	348.2	21.1
V100-13	0.841	5.3	0.268	5.4	0.265	0.3	17.950	1.5	4.1	3.12	308.9	12.8	0.81	382.0	24.8
V100-14	1.573	3.8	0.373	3.9	0.236	0.3	25.946	1.5	3.1	4.19	281.2	8.8	0.77	363.8	21.5
V100-15	1.806	5.3	0.234	5.4	0.269	0.4	25.199	2.1	4.5	7.68	308.4	13.7	0.79	390.7	26.2
<b>Mean weighted average age: 381 ± 20 Ma (2σ)</b>															
V101-1	0.279	5.3	0.323	5.4	0.234	0.3	14.115	1.7	4.9	0.86	289.8	14.2	0.82	353.2	24.7
V101-2	0.057	3.8	0.116	3.9	0.109	0.3	5.929	1.7	3.9	0.48	360.5	14.1	0.81	444.3	28.2
V101-3	0.097	5.3	0.160	5.4	0.109	0.4	7.736	2.4	5.4	0.61	336.3	18.1	0.78	430.9	31.6

Table 5.1. Apatite (U-Th)/He results. Th, <sup>232</sup>Th; ng, nanogram; U, <sup>238</sup>U; Sm, <sup>147</sup>Sm; He, <sup>4</sup>He in ncc at STP; ncc, nano cubic centimetre; TAU, total analytical uncertainty, Ft, alpha recoil correction factor after Farley et al., 1996. Data in italics is excluded for the calculation of the mean weighted average age.

	Th (ng)	Th uncert. (±, %)	U (ng)	U uncert. (±, %)	Sm (ng)	Sm uncert. (±, %)	He (ncc)	He uncert. (±, %)	TAU (%)	Th/ U	Uncorr. age (Ma)	Uncorr. age uncert. ±1σ (Ma)	Ft	Corr. age (Ma)	Corr. age uncert. ±1σ (Ma)
V101-4	0.072	3.8	0.042	3.9	0.084	0.3	2.390	1.8	3.5	1.72	323.6	11.2	0.81	401.6	24.5
V101-5	0.105	5.3	0.197	5.4	0.111	0.3	8.313	2.4	5.4	0.53	299.2	16.2	0.78	383.4	28.3
V101-6	0.082	3.8	0.098	3.9	0.094	0.4	3.981	2.1	4.0	0.83	271.1	10.8	0.80	338.7	21.6
V101-7	0.154	5.3	0.204	5.4	0.146	0.3	9.275	2.4	5.2	0.75	307.0	16.1	0.80	384.5	27.8
V101-8	0.157	3.8	0.404	4.0	0.191	0.3	15.374	2.2	4.2	0.38	278.1	11.8	0.80	347.9	22.8
V101-9	0.142	5.3	0.270	5.4	0.191	0.4	12.610	1.2	5.0	0.52	329.9	16.5	0.79	416.8	29.5
V101-10	1.374	3.8	0.530	3.9	0.063	0.4	28.976	1.6	3.2	2.57	273.5	8.8	0.77	354.2	21.1
<b>Mean weighted average age: 378 ± 26 Ma (2σ)</b>															
V102-1	0.060	3.8	0.121	3.9	0.066	0.4	4.610	1.5	3.9	0.49	271.5	10.5	0.73	372.6	23.5
V102-2	0.091	5.3	0.346	5.4	0.119	0.3	17.000	2.3	5.6	0.26	366.5	20.6	0.79	466.7	35.1
V102-3	0.159	3.8	0.244	3.9	0.107	0.3	10.898	2.2	4.1	0.65	308.9	12.7	0.80	386.2	25.0
V102-4	0.170	5.3	0.318	5.4	0.147	0.3	14.623	1.7	5.1	0.53	324.9	16.7	0.79	413.4	29.6
V102-5	0.136	3.8	0.249	3.9	0.090	0.4	11.386	1.3	3.8	0.54	322.9	12.1	0.77	419.3	26.2
V102-6	0.108	5.3	0.254	5.4	0.121	0.3	10.064	1.3	5.1	0.42	287.6	14.7	0.80	357.6	25.6
V102-7	0.059	3.8	0.119	3.9	0.061	0.3	7.814	1.3	3.8	0.49	460.7	17.3	0.77	600.4	37.6
V102-8	0.228	5.3	0.154	5.4	0.025	0.3	9.201	1.3	4.4	1.47	353.9	15.7	0.78	455.5	30.5
V102-10	0.078	3.8	0.083	3.9	0.063	0.3	3.843	1.3	3.5	0.94	302.6	10.7	0.76	398.0	24.3
<b>Mean weighted average age: 402 ± 29 Ma (2σ)</b>															
V103-1	0.410	5.3	0.338	5.4	0.137	0.3	16.766	1.5	4.6	1.20	308.3	14.3	0.80	387.2	26.4
V103-2	0.162	3.8	0.086	3.9	0.049	0.4	4.766	1.5	3.3	1.88	308.1	10.2	0.78	395.8	23.7

Table 5.1. Continued.

	Th (ng)	Th uncert. ( $\pm$ , %)	U (ng)	U uncert. ( $\pm$ , %)	Sm (ng)	Sm uncert. ( $\pm$ , %)	He (ncc)	He uncert. ( $\pm$ , %)	TAU (%)	Th/ U	Uncorr. age (Ma)	Uncorr. age uncert. $\pm 1\sigma$ (Ma)	Ft	Corr. age (Ma)	Corr. age uncert. $\pm 1\sigma$ (Ma)
V103-3	0.120	5.3	0.598	5.4	0.302	0.3	26.847	1.4	5.4	0.20	339.7	18.2	0.77	443.3	32.5
V103-4	0.135	3.8	0.182	3.9	0.138	0.3	8.589	1.4	3.7	0.73	319.7	11.7	0.80	400.3	24.8
V103-5	0.158	5.3	0.337	5.4	0.151	0.3	13.449	1.4	5.1	0.47	286.9	14.6	0.78	369.8	26.4
V103-6	0.281	3.8	0.509	3.9	0.249	0.3	21.380	1.5	3.8	0.55	296.2	11.3	0.81	365.6	23.0
V103-7	0.142	5.3	0.280	5.4	0.142	0.4	12.480	1.6	5.1	0.50	316.5	16.3	0.80	396.8	28.5
V103-9	0.121	3.8	0.184	3.9	0.130	0.3	7.619	2.1	4.0	0.65	285.8	11.5	0.80	359.1	23.0
V103-10	0.145	5.3	0.263	5.4	0.140	0.3	12.359	1.4	5.0	0.55	330.4	16.6	0.82	401.0	28.4
V103-11	0.082	3.8	0.106	3.9	0.089	0.3	6.057	1.4	3.6	0.76	380.6	13.8	0.77	496.0	30.7
<b>Mean weighted average age: 395 <math>\pm</math> 27 Ma (2<math>\sigma</math>)</b>															

Table 5.1. Continued



### 5.6.2. Multiple degassing domains

The irradiation technique (Turner, 1971) is absolutely essential to analyse terrestrial minerals, as we observe multiple degassing domains in both samples. The simultaneous release of  $^{36}\text{Ar}$ ,  $^{37}\text{Ar}$ ,  $^{38}\text{Ar}$  and  $^{39}\text{Ar}$  of irradiated samples can discriminate between K-derived  $^{38}\text{Ar}$  and Ca-derived  $^{38}\text{Ar}$  and provide insight in the compositional complexity of these samples. The degassing characteristics of the irradiated pyroxene and apatite samples show two separate stages of  $^{38}\text{Ar}$  release; the first, which is associated with initial peak release of  $^{39}\text{Ar}$  is interpreted as cosmogenic  $^{38}\text{Ar}$  produced from K-rich domains within the crystal structure. We expect that small K-rich phases (either in inclusions or due to K zoning) release their argon gasses during an early stage of incremental heating. However, the second step of simultaneous  $^{38}\text{Ar}$ ,  $^{37}\text{Ar}$  and  $^{39}\text{Ar}$  release is characterized by very small to nil K/Ca ratios in all cases, which means that K-rich domains cannot be the source for the  $^{38}\text{Ar}$  liberated and that this most likely represents cosmogenic  $^{38}\text{Ar}$  produced from calcium ( $^{37}\text{Ar}$ ). A more unlikely possibility is that the  $^{39}\text{Ar}$  signal in these incremental heating steps represents the effect of isobaric interferences on mass 39 in the mass spectrometer. However, recent development in pyroxene  $^{40}\text{Ar}/^{39}\text{Ar}$  dating (Ware *et al.*, 2015) show a similar and yet, systematic decreasing K/Ca ratio though the age spectrum not corresponding with any age variation, thus suggesting that the variation in K/Ca is due to compositional zoning for the pyroxene. Unfortunately, as the first degassing steps are compromised due to the presence of K-rich domains producing  $^{38}\text{Ar}_c$  (K), no true initial  $^{38}\text{Ar}/^{36}\text{Ar}$  value can be confidently obtained for these samples and an intercept value of  $0.1885 \pm 0.0005$  (Levine *et al.*, 2007) is used to calculate all cosmochrons.

### 5.6.3. Pyroxene as a potential cosmogenic exposure dating tool

The exposure ages for all pyroxene samples for which a slope was derived is calculated using equation 5.1 and are reported in Table 5.2 together with all parameters used in the calculation. Scaling factors have been introduced that can be used to calculate the appropriate production rate at specific latitudes and elevations (Dunai, 2000). For the following exercise, we have used a  $P38(\text{Ca})$  of 250 atoms/g/a (high latitudes; sea level), which is within the published range of potential production rates (Niedermann *et al.*, 2007), but we note that much calibration work remains before an accurate production rate value is established.

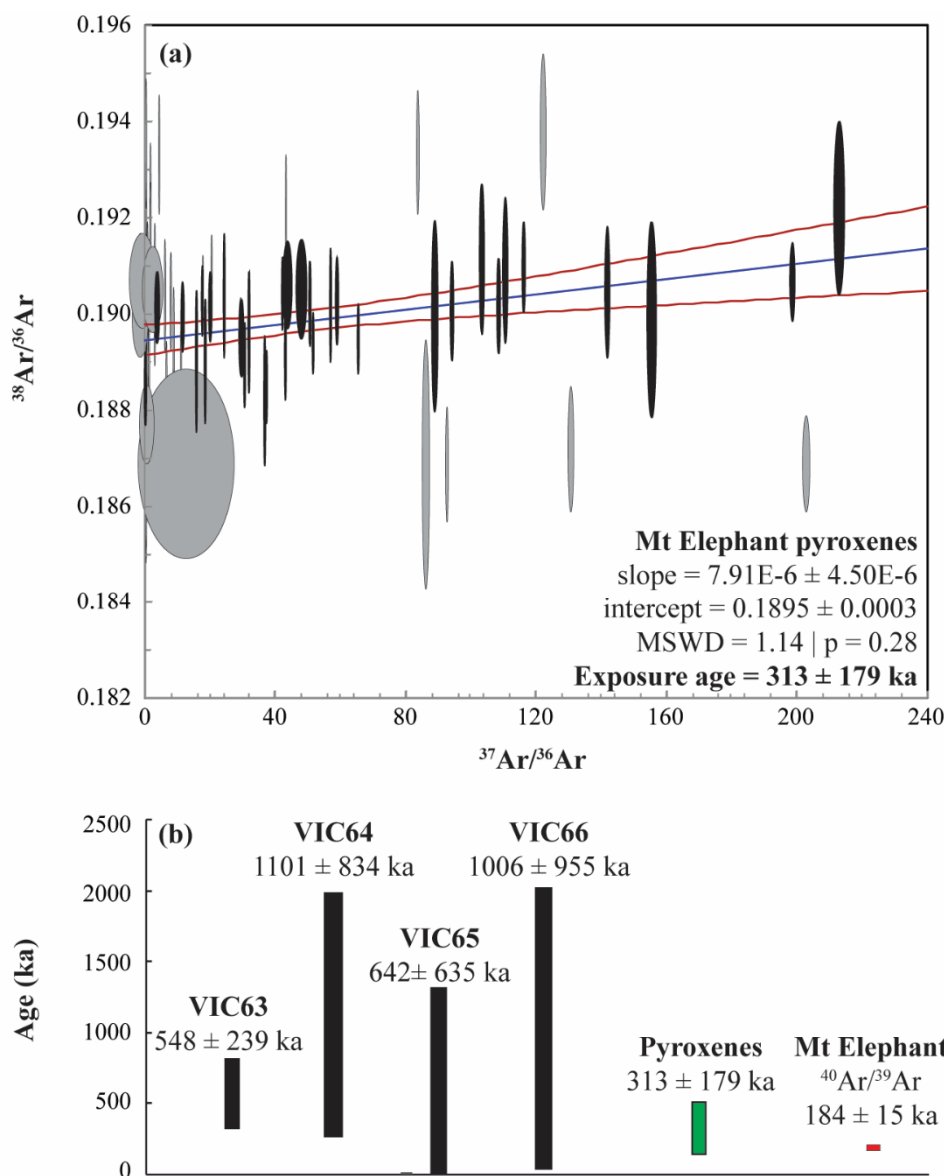


Figure 5.9. (a) Cosmochron diagram for the combined pyroxene samples VIC63, VIC64, VIC65 and VIC66. (b) Age comparison diagram between the individual pyroxene samples, the combined exposure age and the  $^{40}\text{Ar}/^{39}\text{Ar}$  eruption age.

5.6.3.1. Cosmogenic exposure age of Mt Elephant

Individual pyroxene ages range from  $548 \pm 239$  ka to  $1101 \pm 834$  ka and overlap in some cases with the  $^{40}\text{Ar}/^{39}\text{Ar}$  eruption age of  $184 \pm 15$  ka for Mt Elephant (Oostingh *et al.*, 2017) only because of the extremely large errors ( $\pm 100\%$  in some cases). However, combining the data of the four statistically significant cosmochrons (**Error! Reference source not found.**a) results in a total cosmogenic  $^{38}\text{Ar}$  signal significantly higher as compared to a single sample. In this case, we can derive a

more precise apparent age of  $313 \pm 179$  ka; which is far more accurate and precise than the individual ages and still overlaps with the known eruption age (**Error! Reference source not found.**b).

Note that the individual apparent exposure ages appear much older as they are defined by slopes which are skewed to a larger value due to overrepresentation of late degassing steps. This result shows that pyroxene could be a valuable mineral for terrestrial cosmogenic  $^{38}\text{Ar}$  studies. Perhaps not at the young timescales attempted in this study, but rather for a few Ma old surfaces where it would reach a precision better than  $\pm 5\%$  as we have shown above. Furthermore, the results showcase the advantage of the analytical approach used with simultaneous analysis of  $^{36}\text{Ar}$  and  $^{38}\text{Ar}$  on the ultra-

sensitive CDD; which yields statistically meaningful cosmochron slopes even for samples as young as the pyroxenes analysed in this study.

Sample	Latitude (dec degrees)	Longitude (dec degrees)	J-value	Cosmochron characteristics							Exposure Age (1 $\sigma$ )
				Slope	1 sigma	Intercept	1 sigma	MSWD	p		
<b>Southeast Australian pyroxene</b>											
VIC61			0.00009230 $\pm$ 0.00000022	3.39E-05	3.70E-05	0.1883	0.0016	2.80	0.02	<i>1339 <math>\pm</math> 1467 ka</i>	
VIC62			0.00009230 $\pm$ 0.00000022				<i>no cosmochron</i>				
VIC63	-37.956	143.201	0.00009230 $\pm$ 0.00000022	1.38E-05	6.00E-06	0.1885	0.0067	0.64	0.75	<b>548 <math>\pm</math> 239 ka</b>	
VIC64			0.00009230 $\pm$ 0.00000022	2.78E-05	2.10E-05	0.1885	0.0081	0.69	0.70	<b>1101 <math>\pm</math> 834 ka</b>	
VIC65			0.00009230 $\pm$ 0.00000022	1.64E-05	1.40E-05	0.1891	0.0006	1.40	0.19	<b>642 <math>\pm</math> 635 ka</b>	
VIC66			0.00009260 $\pm$ 0.00000016	2.53E-05	2.40E-05	0.1894	0.0006	1.50	0.20	<b>1006 <math>\pm</math> 955 ka</b>	
<b>Combined exposure age: 313 <math>\pm</math> 179 ka (MSWD = 1.14   p = 0.28)</b>											
<b>West Australian apatite</b>											
VIC100	-32.543	118.009	0.0007720 $\pm$ 0.00000010	4.98E-04	1.90E-05	0.1888	0.005	9	0.00	<i>173 <math>\pm</math> 14 Ma</i>	
VIC100 – Cl corrected				3.24E-04	2.00E-05	0.1885	0.005	16	0.00	<i>112 <math>\pm</math> 11 Ma</i>	
VIC101	-32.937	118.507	0.0007720 $\pm$ 0.00000010	2.58E-04	1.20E-05	0.1886	0.007	11	0.00	<i>90 <math>\pm</math> 8 Ma</i>	
VIC100 – Cl corrected				1.61E-04	1.30E-05	0.1884	0.007	21	0.00	<i>56 <math>\pm</math> 6 Ma</i>	
VIC101B	-32.937	118.507	0.0007777 $\pm$ 0.00000022	2.64E-04	1.50E-05	0.1890	0.006	9	0.00	<i>92 <math>\pm</math> 9 Ma</i>	
VIC101B – Cl corrected				1.66E-04	1.00E-05	0.1886	0.004	6	0.00	<i>58 <math>\pm</math> 5 Ma</i>	
VIC102	-32.937	118.507	0.0007777 $\pm$ 0.00000022	2.88E-04	0.95E-05	0.1885	0.071	5	0.00	<i>100 <math>\pm</math> 8 Ma</i>	
VIC102 – Cl corrected				1.80E-04	0.90E-05	0.1884	0.071	10	0.00	<i>60 <math>\pm</math> 10 Ma</i>	
VIC103	-32.553	119.234	0.0007720 $\pm$ 0.00000010	2.66E-04	0.90E-05	0.1884	0.008	6	0.00	<i>92 <math>\pm</math> 8 Ma</i>	
VIC103 – Cl corrected				1.49E-04	0.90E-05	0.1882	0.008	14	0.00	<i>52 <math>\pm</math> 5 Ma</i>	

*Table 5.2. Cosmochron characteristics and resulting exposure ages for all irradiated samples. The ( $^{38}\text{Ar}/^{36}\text{Ar}$ )<sup>cosmogenic</sup> ratio is 1.49 for the apatite samples and 2.17 for the pyroxene samples. The alpha-coefficient is 0.52 for all samples. A P38(Ca) of  $\sim$  250 (high latitude, sea level) was used to calculate all exposure ages. Exposure ages derived from statistically meaningful cosmochrons are indicated in bold, apparent exposure ages are indicated in italics. See text for discussion on the Cl correction on the Cl corrected of the apatite samples.*

#### 5.6.4. Apatite as a potential cosmogenic exposure dating tool

##### 5.6.4.1. Cosmogenic exposure age using irradiated apatite

None of the apatite samples yielded a statistically significant cosmochron correlation, suggesting a problem with this set of samples. Forcing an errorchron through the data to get an idea of the exposure age, results in apparent, yet improbable, exposure ages which are Late Cenozoic in age and range from 90 to 173 Ma (Table 5.2). These apparent exposure ages are most likely largely overestimated, as much more than 10 cm erosion is to be expected on such timescales. We expect that the composition of apatite (Cl-rich) as well as the composition of the host rock (U-rich) are the cause for the overestimated exposure ages, and we will explore this further in the following sections.

##### 5.6.4.2. The effect of reactor-induced $^{38}\text{Ar}(\text{Cl})$

Whereas corrections for reactor-induced argon from K and Ca are relatively straightforward, failure to correct for argon produced from Cl during irradiation could result in a significant overestimated exposure age (Renne *et al.*, 2001).

	VIC100	VIC101	VIC102	VIC103	VIC63
<i>Major target elements (wt%)</i>					
<b>Ca</b>	39.7	39.6	39.5	39.5	15.3
<b>K</b>	<d.l.	<d.l.	<d.l.	<d.l.	0.0006
<i>Minor target elements (ppm)</i>					
<b>Mg</b>	83	20	201	26	688
<b>Ti</b>	179	178	178	178	334
<b>Fe</b>	298	102	751	199	29548
<b>Ni</b>	0.32	0.35	0.39	0.34	5
<b>Cl</b>	471	251	279	304	180
<b>U</b>	28	15	30	32	0.08
<b>Th</b>	154	9	18	21	0.001

Table 5.3. Composition of apatite (VIC100, VIC101, VIC102 and VIC103) and pyroxene (VIC63) samples as derived from averaging two-spot (apatite) and four-spot (pyroxene) ELA-ICP-MS analysis.

It is expected that apatite minerals will suffer more than the pyroxene minerals from this reactor-induced chlorogenic argon, due to their natural Cl-bearing composition, if minimal (Table 5.3); and, - in the case of this experiment - the long irradiation time (3 hours). Natural chlorine consists of two isotopes with relatively large cross sections for thermal neutron capture reactions;  $^{35}\text{Cl}$  (2000 barns) and  $^{37}\text{Cl}$  (20 barns) - which will be followed by  $\beta$ -decay to form  $^{36}\text{ArCl}$  and  $^{38}\text{ArCl}$  respectively. Although production of  $^{36}\text{Cl}$  and  $^{38}\text{Cl}$  from calcium is not significant during irradiation, reactions on potassium are possible via  $^{39}\text{K}(\text{n}, \alpha)^{36}\text{Cl}$  ( $\beta$ -decay to  $^{36}\text{Ar}$  with  $t_{1/2}$  of 300 000 y) and  $^{39}\text{K}(\text{n}, \text{D})^{38}\text{Cl}$

( $\beta$ -decay to  $^{38}\text{Ar}$  with  $t_{1/2}$  of 37 minutes). ELA-ICP-MS spot analysis on the apatite samples shows that potassium contents of these minerals are below detection limits, whereas chlorine contents are significant at 180 – 471 ppm (Table 5.3). We therefore perform a Cl correction on the  $^{38}\text{Ar}$  abundance to account for the natural and reactor-induced  $^{37}\text{Cl}$  ( $n, \gamma$ )  $^{38}\text{Cl} \rightarrow \beta$ -  $^{38}\text{Ar}_{\text{Cl}}$  ( $t_{1/2} = \sim 35$  days) reaction. Here, we have converted the Ca/Cl composition of the sample into  $^{38}\text{Ar}_{\text{Cl}}/^{37}\text{Ar}_{\text{Ca}}$  by using the relative production of  $^{38}\text{Ar}_{\text{Ca}}/^{38}\text{Ar}_{\text{Cl}}$  in the Oregon State TRIGA reactor of 7.4.

Figure 5.10 and Table 5.2 shows a comparison between Cl-corrected data (Figure 5.10b) versus the original uncorrected data (Figure 5.10a) and the resulting difference in apparent exposure age. All other Cl-corrected cosmochrons can be found in Appendix N. Accounting for the reactor-induced  $^{38}\text{Ar}$  contribution from Cl significantly decreases the  $^{38}\text{Ar}/^{36}\text{Ar}$  ratio; although resulting apparent exposure ages are still overestimated; ranging from 52 Ma to 112 Ma. The Cl-correction results in a 35% - 43% correction on the exposure age.

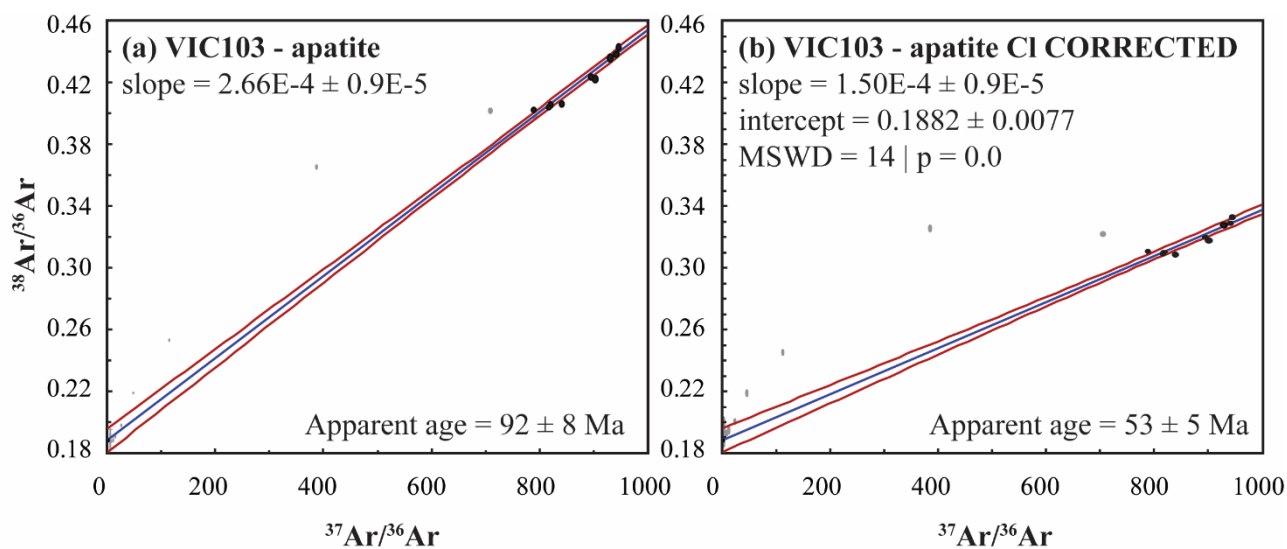


Figure 5.10. Cosmochron diagrams of typical apatite showing the difference in isotopic abundance for (a) the uncorrected data vs (b) natural and reactor-derived Cl-corrected data.

#### 5.6.4.3. Cosmogenic exposure age using unirradiated apatite

If argon produced from Cl during irradiation is indeed responsible for producing most of the  $^{38}\text{Ar}$ , we would expect that the non-irradiated apatite samples VIC100ap\_unirr and VIC102ap\_unirr would yield a correct  $^{38}\text{Ar}/^{36}\text{Ar}$  ratio (corrected for *natural* interferences of Cl content) derived only from the exposure history, while unfortunately not providing any information about the  $^{37}\text{Ar}/^{36}\text{Ar}$  ratio. As a complementary experiment, to test our hypothesis, and since the aliquots analysed have a very similar mass ( $\sim 100$  mg) and were analysed using the same step-heating protocol, we have combined the measured  $^{38}\text{Ar}/^{36}\text{Ar}$  ratios for every step, with the  $^{37}\text{Ar}/^{36}\text{Ar}$  value derived for every step from the

irradiated aliquots of these two samples to construct a cosmochron diagram which should theoretically not be effected by any reactor-induced Cl interferences. In theory, the slope and intercept derived from these cosmochrons should provide us with a more meaningful exposure age; as the slope and intercept are not effected by any unwanted reactor-induced interferences. Of course, no true age could be derived for such an approach, but the value of the slope obtained should return an apparent age not too far from the real exposure age. Figure 5.11 shows the cosmochron diagrams of irradiated samples VIC100ap and VIC102ap and the non-irradiated samples VIC100ap\_unirr and VIC102ap\_unirr having  $^{37}\text{Ar}/^{36}\text{Ar}$  from the same respective irradiated aliquots. It can be seen that the slopes of the cosmochrons are much steeper for the irradiated samples as compared to the non-irradiated samples; hence confirming the effect of reactor-induced  $^{38}\text{Ar}_{\text{Cl}}$  interferences which result in much higher total  $^{38}\text{Ar}$  values. This confirms our reservation towards the old apparent ages derived for these samples.

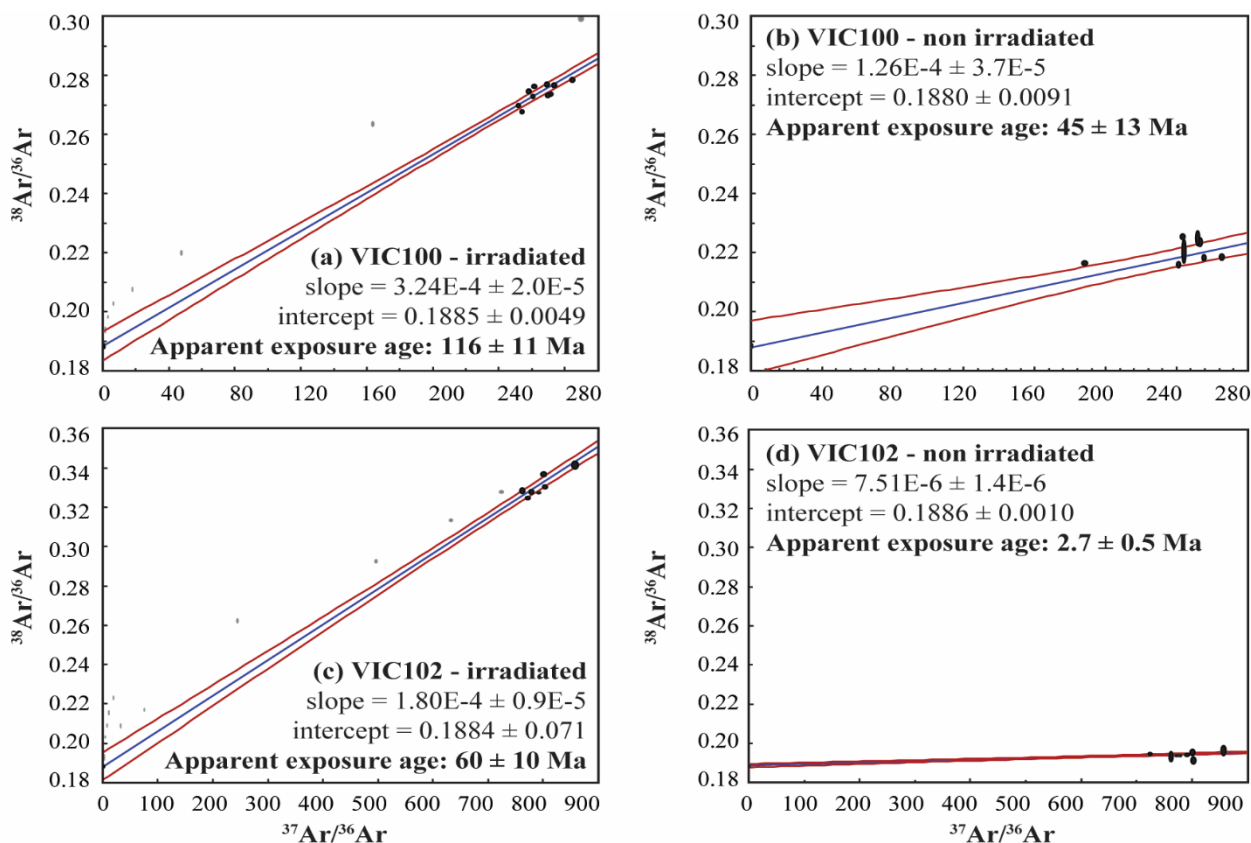


Figure 5.11. Cosmochron diagrams to compare exposure ages derived from irradiated apatite samples and non-irradiated samples with  $^{38}\text{Ar}/^{36}\text{Ar}$  taken from non-irradiated degassing experiment and  $^{37}\text{Ar}/^{36}\text{Ar}$  taken from corresponding irradiated aliquot. It can be seen that the irradiated samples have extremely high  $^{38}\text{Ar}$  values which are most likely derived from reactor-induced chlorogenic interferences. The artificially constructed cosmochron slope of the non-irradiated apatite samples is thought to be more geologically meaningful and a statistically significant ( $p > 0.05$ ) exposure age can be obtained for sample VIC102ap\_unirr at  $2.7 \pm 0.5$  Ma.

In fact, sample VIC102ap\_unirr yields a statistically significant cosmochron and thus a much more plausible exposure age of  $2.7 \pm 0.5$  Ma. We expect that this age is the close to the actual exposure age of the West-Australian granite inselbergs. However, VIC100 persists in returning a very old apparent, yet implausible age of ca. 45 Ma (Figure 5.11) suggesting that other factors than  $^{38}\text{Ar}_{\text{Cl}}$  played a role in the production of  $^{38}\text{Ar}$ .

#### 5.6.4.4. The effect of nucleogenic $^{38}\text{Ar}$

Uranium-rich rocks will have a contribution of nucleogenic argon from  $^{35}\text{Cl}$  ( $\alpha$ , p)  $^{38}\text{Ar}$  and  $^{35}\text{Cl}$  (n,  $\gamma$ )  $^{36}\text{Ar}$  via reactions on target elements fluorine, magnesium, chlorine and potassium by  $\alpha$ -particles derived from natural decay of U and Th and neutrons mainly derived from spontaneous fission of  $^{238}\text{U}$  (Eikenberg *et al.*, 1993). Nucleogenic contributions on both  $^{38}\text{Ar}$  and  $^{36}\text{Ar}$  could therefore be significant in yielding an overestimated exposure age for the apatite samples. The nucleogenic  $^{38}\text{Ar}$  production rate (in cc STP/g/y) is given as (Ballentine and Burnard, 2002);

$$^{38}\text{Ar}_{\text{nucl}} = \{[\text{Cl}](0.76[\text{U}] + 0.104[\text{Th}])\} * 10^{-25} \quad (2)$$

Where [Cl], [U] and [Th] are in ppm. We calculate the contribution to  $^{38}\text{Ar}$  from the various Cl, U and Th concentrations in the samples as ranging from 0.02 to 9.89 atoms/g/y (median value of 1.6 atoms/g target/y). The apatite (U-Th)/He ages of  $\sim 400$  Ma provide a maximum age at which the granite rocks were at the  $\sim 70^\circ\text{C}$  isotherm (Farley, 2002) and thus provide a minimum Ar retention age in apatite. Furthermore, we succeeded in deriving  $^{40}\text{Ar}/^{39}\text{Ar}$  age spectra from the irradiated apatite thanks to the minute amount of potassium present in the crystal. The apparent  $^{40}\text{Ar}/^{39}\text{Ar}$  age spectrum (Figure 5.6), although by no means providing a meaningful formation age, offers another estimate of Ar retention in these rocks. The total fusion error-age of the apatite is  $\sim 1.4$  Ga, which suggests that there is approximately 1.4 Ga worth of  $^{40}\text{Ar}$  still present in the sample. Assuming that all argon isotopes show similar diffusion behaviour, this suggests that there is 1.4 Ga worth of nucleogenic  $^{38}\text{Ar}$  present in the sample as well. Figure 5.12 shows the relative contribution (in percentage) of nucleogenic  $^{38}\text{Ar}$  on the total  $^{38}\text{Ar}$  abundance for various exposure ages, depending on the formation age of the rock. For example; for a 400 Ma old host rock which is exposed over 10 Ma, the nucleogenic contribution to the total  $^{38}\text{Ar}$  abundance is ca. 20%. However, for a 1.4 Ga old host rock which was exposed over 1 Ma; the nucleogenic contribution to the total  $^{38}\text{Ar}$  abundance is more than 90% and will completely overwhelm the cosmogenic  $^{38}\text{Ar}$  abundance, resulting in a strongly overestimated exposure age. Such model curves are in good agreement with the data obtained for sample VIC100. If we assume an approximate exposure age of 2.5 Ma for VIC100 and not 45 Ma,



this would suggest that 94% of the total  $^{38}\text{Ar}$  is of nucleogenic origin, as expected for an Archean basement.

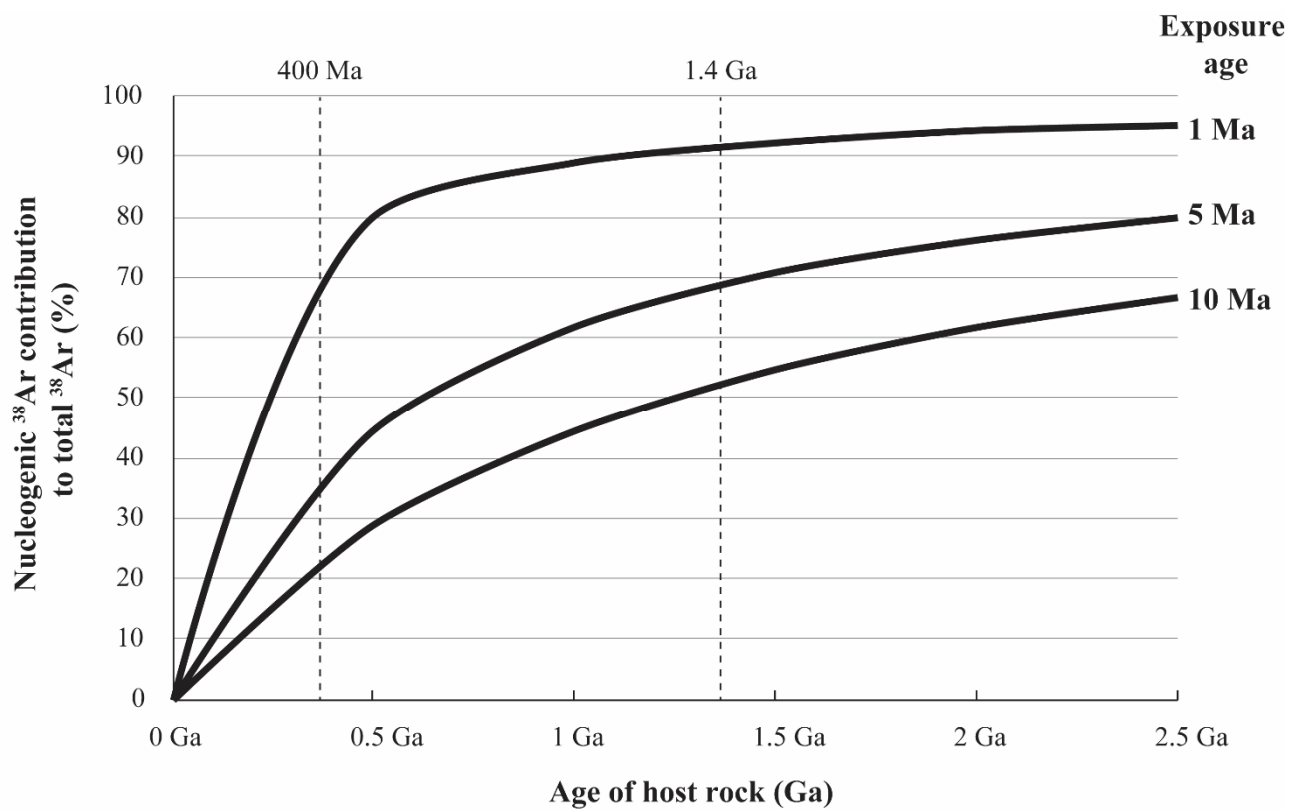


Figure 5.12. Relative contribution of nucleogenic  $^{38}\text{Ar}$  (in %) on the total  $^{38}\text{Ar}$  abundance over a range of potential formation ages of a rock and different exposure ages.

#### 5.6.5. Applicability of cosmogenic $^{38}\text{Ar}$ exposure dating.

As outlined above, pyroxene could be a significant new tool to date the exposure of rocks with exposure ages of a few Ma, where a precision of 5% or less could be achieved. However, we strongly advise against using apatite (in particular from old host rocks) for this objective due to the inevitable presence of Cl in apatite (Sha and Chappell, 1999) and the large effect of reactor-induced and nucleogenic  $^{38}\text{Ar}_{\text{Cl}}$  on the age calculation. Cosmogenic  $^{38}\text{Ar}$  exposure dating of Ca-rich (and eventually K-rich), yet Cl-free, minerals is a valuable addition to the range of existing cosmogenic exposure dating techniques due to various reasons (Renne *et al.*, 2001). As  $^{38}\text{Ar}$  is stable, the applicability extends beyond the time scale of short-living cosmogenic isotope systems, such as  $^{10}\text{Be}$  (< 2.2 Ma),  $^{26}\text{Al}$  (< 1 Ma) and  $^{36}\text{Cl}$  (< 430 ka; Gosse and Phillips, 2001). Furthermore, due to its much larger Van der Waals radius than helium or neon, argon is generally quantitatively retained under environmental conditions (Lippolt and Weigel, 1988). For example, testing the usability of calcite (e.g. Cassata and Renne, 2013), should be high in the list of priorities of developing this technique since this mineral is omnipresent in geological landscape and fault planes. Nevertheless, the most

important task is to accurately determine the P38(Ca) by comparison of well-defined cosmochron-derived  $^{38}\text{Ar}$  exposure ages with ages from other exposure dating techniques (e.g. Niedermann *et al.*, 2007).

### 5.7. Conclusions

Ultra-precise analysis of cosmogenic  $^{36}\text{Ar}$  and  $^{38}\text{Ar}$  abundances in irradiated terrestrial pyroxene and apatite from Australia provides invaluable insight into the argon degassing characteristics of these minerals and the potential for further development of the cosmogenic  $^{38}\text{Ar}$  exposure dating technique. Pyroxene samples from Mt Elephant ( $^{40}\text{Ar}/^{39}\text{Ar}_{\text{groundmass}} = 183 \pm 15$  ka) in Southeast Australia show a complex, two-step  $^{38}\text{Ar}$  degassing behaviour. Four statistically significant cosmochrons were derived. A combined exposure age from all four samples and using a  $^{38}\text{Ar}$  production rate (Ca) of 250 atoms /g Ca/ yr results in a geologically meaningful age of  $313 \pm 179$  ka; which overlaps with the known eruption age. Importantly, even for these young pyroxenes, absolute errors on the  $^{38}\text{Ar}$  and  $^{36}\text{Ar}$  abundances are extremely small ( $\sim 0.30\%$ ) suggesting that a precision of less than  $\pm 5\%$  is achievable for rocks of few million years old. Apatite samples from granite inselbergs in West-Australia [(U-Th)/He and  $^{40}\text{Ar}/^{39}\text{Ar}$  closure age of 400 Ma and 1.4 Ga, respectively] show similar degassing behaviour, although our analyses and modelling show that samples suffer from reactor-produced interferences on  $^{38}\text{Ar}$  as well as a strong nucleogenic  $^{38}\text{Ar}$  contribution and give erroneously old exposure ages.

### 5.8. Acknowledgements

We would like to thank Celia Mayers, Adam Frew and Zdenka Martelli of the West Australian Argon Isotope Facility (Perth), Tanya Jude-Eton of the SelFrag laboratory, Curtin University (Perth) and Brad McDonald of the John de Laeter Centre for Isotope Research (Perth) for their assistance during sample preparation and ELA-ICP-MS analysis. The support of TiGER and the department Applied Geology at Curtin University of Technology is gratefully acknowledged. Dr. Marc Norman is thanked for editorial handling. The manuscript benefitted greatly from the comments of two anonymous reviewers. This research was funded by Australian Research Council Discovery grant DP130100517.

### 5.9. References

- Ballentine, C. J. & Burnard, P. G. (2002). Production, Release and Transport of Noble Gases in the Continental Crust. *Reviews in Mineralogy and Geochemistry* 47, 481–538.
- Bierman, P. R. & Caffee, M. (2002). Cosmogenic exposure and erosion history of Australian bedrock landforms. *Bulletin of the Geological Society of America* 114, 787–803.
- Cassata, W. S. & Renne, P. R. (2013). Kinetics of argon diffusion in calcite. *Chemie der Erde - Geochemistry* 73, 113–115.

Cohen, B. A., Snyder, G. A., Hall, C. M., Taylor, L. A. & Nazarov, M. A. (2001). Argon-40-argon-39 chronology and petrogenesis along the eastern limb of the Moon from Luna 16, 20 and 24 samples. *Meteoritics and Planetary Science* 1366, 1345–1366.

Danišík, M., Štěpančíková, P. & Evans, N. J. (2012). Constraining long-term denudation and faulting history in intraplate regions by multisystem thermochronology: An example of the Sudetic Marginal Fault (Bohemian Massif, central Europe). *Tectonics* 31, 1–19.

Dunai, T. J. (2000). Scaling factors for production rates of in situ production cosmogenic nuclides: a critical reevaluation. *Earth and Planetary Science Letters* 176, 157–169.

Eikenberg, J., Signer, P. & Wieler, R. (1993). U-Xe, U-Kr, and U-Pb systematics for dating uranium minerals and investigations of the production of nucleogenic neon and argon. *Geochimica et Cosmochimica Acta* 57, 1053–1069.

Evans, N. J., Byrne, J. P., Keegan, J. T. & Dotter, L. E. (2005). Determination of Uranium and Thorium in Zircon, Apatite, and Fluorite: Application to Laser (U-Th)/He Thermochronology. *Journal of Analytical Chemistry* 60, 1159–1165.

Farley, K. A. (2002). (U-Th)/He Dating: Techniques, Calibrations, and Applications. *Reviews in Mineralogy and Geochemistry* 47, 819–844.

Farley, K. A., Wolf, R. A. & Silver, L. T. (1996). The effects of long alpha-stopping distances on (U-Th)/He ages. *Geochimica et Cosmochimica Acta* 60, 4223–4229.

Gosse, J. C. & Phillips, F. M. (2001). Terrestrial in situ cosmogenic nuclides: theory and application. *Quaternary Science Reviews* 20, 1475–1560.

Hennesy, J. & Turner, G. (1980).  $^{40}\text{Ar}$ - $^{39}\text{Ar}$  ages and irradiation history of Luna 24 basalts. *Philosophical Transactions of the Royal Society of London. Series A, Mathematical and Physical Sciences*. 297, 27–39.

Jourdan, F. & Renne, P. R. (2007). Age calibration of the Fish Canyon sanidine  $^{40}\text{Ar}/^{39}\text{Ar}$  dating standard using primary K–Ar standards. *Geochimica et Cosmochimica Acta* 71, 387–402.

Jourdan, F., Sharp, W. D. & Renne, P. R. (2012).  $^{40}\text{Ar}/^{39}\text{Ar}$  ages for deep (~3.3 km) samples from the Hawaii Scientific Drilling Project, Mauna Kea volcano, Hawaii. *Geochemistry, Geophysics, Geosystems* 13.

Kaneoka, I. (1980). Rare gas isotopes and mass fractionation; an indicator of gas transport into or from a magma. *Earth and Planetary Science Letters* 48, 284–292.

Kennedy, T., Jourdan, F., Bevan, A. W. R., Mary Gee, M. A. & Frew, A. (2013). Impact history of the HED parent body(ies) clarified by new  $^{40}\text{Ar}/^{39}\text{Ar}$  analyses of four HED meteorites and one anomalous basaltic achondrite. *Geochimica et Cosmochimica Acta*. Elsevier Ltd 115, 162–182.

Knight, K. B. (2006). Argon geochronology: Applied  $^{40}\text{Ar}/^{39}\text{Ar}$  methods to the chronology of large igneous provinces: development of cosmogenic argon methods for terrestrial geochronology. University of California, Berkeley.

Koppers, A. A. P. (2002). ArArCALC - software for  $^{40}\text{Ar}/^{39}\text{Ar}$  age calculations. *Computer and Geosciences* 28, 605–619.

- Lal, D. (1991). Cosmic ray labeling of erosion surfaces: in situ nuclide production rates and erosion models. *Earth and Planetary Science Letters* 104, 424–439.
- Lee, J. B., Marti, K., Severinghaus, J. P., Kawamura, K., Yoo, H. & Kim, J. S. (2006). A redetermination of the isotopic abundances of atmospheric Ar. *Geochimica et Cosmochimica Acta* 70, 4507–4512.
- Levine, J., Renne, P. R. & Muller, R. A. (2007). Solar and cosmogenic argon in dated lunar impact spherules. *Geochimica et Cosmochimica Acta* 71, 1624–1635.
- Lippolt, H. J. & Weigel, E. (1988).  $4\text{He}$  diffusion in  $^{40}\text{Ar}$ -retentive minerals. *Geochimica et Cosmochimica Acta* 52, 1449–1458.
- Ludwig, K. R. (2012). User's Manual for Isoplot 3.75. A Geochronological Toolkit for Microsoft Excel. Berkeley, California.
- Matchan, E. L. & Phillips, D. (2014). High precision multi-collector  $^{40}\text{Ar}/^{39}\text{Ar}$  dating of young basalts: Mount Rouse volcano (SE Australia) revisited. *Quaternary Geochronology*. Elsevier Ltd.
- McDougall, I. & Roksandic, Z. (1974). Total fusion  $^{40}\text{Ar}/^{39}\text{Ar}$  ages using Hifar reactor. *Journal of the Geological Society of Australia*. Taylor & Francis 21, 81–89.
- Merrihue, C. & Turner, G. (1966). Potassium-Argon dating by activation with fast neutrons. *Journal of Geophysical Research* 71, 2852–2857.
- Niedermann, S. (2002). Cosmic-Ray-Produced noble gases in terrestrial rocks: dating tools for surface processes. *Reviews in Mineralogy and Geochemistry* 47, 731–784.
- Niedermann, S., Schaefer, J., Wieler, R. & Naumann, R. (2007). The production rate of cosmogenic  $^{38}\text{Ar}$  from calcium in terrestrial pyroxene. *Earth and Planetary Science Letters* 257, 596–608.
- Oostingh, K. F., Jourdan, F., Matchan, E. L. & Phillips, D. (2017).  $^{40}\text{Ar}/^{39}\text{Ar}$  geochronology reveals rapid change from plume-assisted to stress-dependent volcanism in the Newer Volcanic Province, SE Australia. *Geochemistry, Geophysics, Geosystems* 18, 1065–1089.
- Oostingh, K. F., Jourdan, F., Merle, R. & Chiaradia, M. (2016). Spatio-temporal Geochemical Evolution of the SE Australian Upper Mantle Deciphered from the Sr, Nd and Pb Isotope Compositions of Cenozoic Intraplate Volcanic Rocks. *Journal of Petrology* 57, 1509–1530.
- Price, R. C., Nicholls, I. A. & Gray, C. M. (2003). Cainozoic igneous activity. In: Birch, W. D. (ed.) *Geology of Victoria*. Geological Society of Australia (Victoria Division), 361–375.
- Renne, P. R., Balco, G., Ludwig, K. R., Mundil, R. & Min, K. (2011). Response to the comment by W.H. Schwarz et al. on “Joint determination of  $^{40}\text{K}$  decay constants and  $^{40}\text{Ar}^*/^{40}\text{K}$  for the Fish Canyon sanidine standard, and improved accuracy for  $^{40}\text{Ar}/^{39}\text{Ar}$  geochronology” by P.R. Renne et al. (2010). *Geochimica et Cosmochimica Acta*. Elsevier Ltd 75, 5097–5100.
- Renne, P. R., Farley, K. A., Becker, T. A. & Sharp, W. D. (2001). Terrestrial cosmogenic argon. *Earth and Planetary Science Letters* 188, 435–440.
- Renne, P. R. & Norman, E. B. (2001). Determination of the half-life of  $^{37}\text{Ar}$  by mass spectrometry. *Physical Review C*. American Physical Society 63.

Renne, P. R., Swisher, C. C., Deino, A. L., Karner, D. B., Owens, T. L. & DePaolo, D. J. (1998). Intercalibration of standards, absolute ages and uncertainties in  $^{40}\text{Ar} / ^{39}\text{Ar}$  dating. *Chemical Geology (Isotope Geoscience Section)* 145, 117–152.

Sha, L.-K. & Chappell, B. W. (1999). Apatite chemical composition, determined by electron microprobe and laser-ablation inductively coupled plasma mass spectrometry, as a probe into granite petrogenesis. *Geochimica et Cosmochimica Acta* 63, 3861–3881.

Shuster, D. L. & Cassata, W. S. (2015). Paleotemperatures at the lunar surfaces from open system behavior of cosmogenic  $^{38}\text{Ar}$  and radiogenic  $^{40}\text{Ar}$ . *Geochimica et Cosmochimica Acta*. Elsevier Ltd 155, 154–171.

Turner, G. (1971). Ar-40-Ar-39 ages from the lunar maria. *Earth and Planetary Science Letters* 11, 169–191.

Turner, G., Huneke, J. C., Podosek, F. A. & Wasserburg, G. J. (1971).  $^{40}\text{Ar}$ - $^{39}\text{Ar}$  ages and cosmic ray exposure of Apollo-14 samples. *Earth and Planetary Science Letters* 12, 19–35.

Twidale, C. R. & Bourne, J. A. (1998). Origin and age of bornhardts, Southwest Western Australia. *Australian Journal of Earth Sciences* 45, 903–914.

Ware, B. D., Jourdan, F. & Vinnicombe, K. (2015). High Precision  $^{40}\text{Ar}/^{39}\text{Ar}$  Geochronology of Large Igneous Provinces: The Tasmanian Dolerites of the Ferrar LIP. *Goldschmidt Abstracts* 3360.

## Chapter 6 (U-Th)/He dating of olivine phenocrysts in the K-rich Ellendale olivine lamproite, Western Australia<sup>4</sup>

### 6.1. Abstract

We present a new olivine (U-Th)/He dating approach and apply it to phenocrysts derived from the Ellendale E9 lamproite deposit (Western Australia) using precise  $^{40}\text{Ar}/^{39}\text{Ar}$  geochronology to calibrate the accuracy of olivine (U-Th)/He ages. Obtaining precise and accurate measures of low abundances of U, Th and He in olivine has been a limiting factor in previous studies and was resolved here by analysing large quantities of olivine in the range of 1.3 – 5.7 mg in each dated aliquot. Our method employs careful handpicking, air abrasion and crushing techniques (to assure removal of trapped He from the phenocrysts), followed by repeated heating (re-extracts) in a furnace to verify complete He extraction, and He measurements by isotope dilution. Parent isotope abundances were determined by isotope dilution using inductively coupled mass spectrometry and total acid dissolution in pressure digestion vessels. Fresh olivine phenocrysts yielded three (U-Th)/He ages of  $18.7 \pm 5.2$  Ma,  $18.7 \pm 5.6$  Ma and  $34 \pm 13$  Ma; equivalent to phlogopite  $^{40}\text{Ar}/^{39}\text{Ar}$  ages within uncertainty [ $22.37 \pm 0.03$  Ma ( $2\sigma$ ),  $22.40 \pm 0.03$  Ma ( $2\sigma$ ) and  $22.42 \pm 0.04$  Ma ( $2\sigma$ )]. Several additional aliquots yielded too-old ages (ranging from  $53.3 \pm 5.0$  Ma to  $39.8 \pm 3.4$  Ma) which are explained by the loss of parental isotope during sample processing, either due to incomplete recovery of all sample material after degassing or due to sample volatilization after too many heating cycles. The results obtained in this study are promising and show that (U-Th)/He dating of olivine phenocrysts could be a viable new geochronology technique.

---

<sup>4</sup> This Chapter was submitted as a paper to the Australian Journal of Earth Sciences on December 11, 2016 and is currently under review.

## 6.2. Introduction

High analytical sensitivity for U and Th concentrations and low background levels of ‘excess’ He (Farley, 2002) suggest that (U-Th)/He geochronology could be a promising alternative when conventional geochronology methods are unavailable, due to, for example; the absence of minerals suitable for dating, incomplete degassing behaviour of samples and/or the presence of altered phases. Successful application of the (U-Th)/He geochronology and thermochronology technique has been demonstrated on apatite (House et al., 1998; Zeitler et al., 1987), zircon (Danišik *et al.*, 2012a; McInnes *et al.*, 2009), hematite (Danišik et al., 2013), magnetite (Blackburn et al., 2007), titanite (Reiners and Farley, 1999), fluorite (Evans et al., 2005b; Pi et al., 2005) and garnet (Aciego et al., 2003; Dunai and Roselieb, 1996). Recent work has shown that (U-Th)/He geochronology has the potential to be applied on common volcanic phenocrysts such as olivine, with (U-Th)/He ages of olivine phenocrysts similar to  $^{40}\text{Ar}/^{39}\text{Ar}$  ages of Box Canyon basalts (Aciego et al., 2007) and the basaltic sequence on Hawaii (Aciego et al., 2010). Nevertheless, research towards routine application of the (U-Th)/He dating technique on olivine has been limited to these two studies only, which suffered from analytical complexity and an inability to measure precise He abundances. Here, we investigate the applicability of (U-Th)/He geochronology on olivine from the Western Australian Ellendale E9 olivine lamproite deposit (Jaques et al., 1986), using an extraction line customized for He dating, and calibrating of the (U-Th)/He ages against high-precision  $^{40}\text{Ar}/^{39}\text{Ar}$  ages from co-genetic phlogopite.

### 6.2.1. Theoretical background

#### 6.2.1.1. Helium

Radiogenic  $^4\text{He}$  is produced both by radioactive decay of parent isotopes  $^{238}\text{U}$ ,  $^{235}\text{U}$ ,  $^{232}\text{Th}$  as well as a negligible amount derived from  $\alpha$ -decay of  $^{147}\text{Sm}$ . For samples  $>350$  ka, secular equilibrium of all daughter products in the decay chain can be assumed and the He age can be obtained from solving for  $t$  (time in year) in the He ingrowth equation:

$$\text{He} = 8 * ^{238}\text{U}(e^{\lambda_{238}t} - 1) + 7 * \left(\frac{^{238}\text{U}}{137.88}\right) (e^{\lambda_{235}t} - 1) + 6 * ^{232}\text{Th}(e^{\lambda_{232}t} - 1) \quad (1)$$

where  $\lambda$  is the decay constant ( $\lambda_{238} = 1.551 \times 10^{-10} \text{ year}^{-1}$ ,  $\lambda_{235} = 9.849 \times 10^{-10} \text{ year}^{-1}$ ,  $\lambda_{232} = 4.948 \times 10^{-11} \text{ year}^{-1}$ ), the coefficients the multiple  $\alpha$  particles emitted and the ratio (1/137.88) the current  $^{235}\text{U}/^{238}\text{U}$  ratio (Mamyrin and Tolstikhin, 1984). To calculate a meaningful age using this equation, there are several assumptions to bear in mind; 1) initial  $^4\text{He}$  is absent from the sample, 2) the sample is in secular equilibrium with respect to the daughters in the decay chain; 3) information about the retentive qualities for He of the mineral being dated is known.

The total amount of  $^4\text{He}$  in an olivine phenocryst is potentially derived from three different sources: 1) radiogenic  $^4\text{He}$  ( $^4\text{He}_{\text{rad}}$ ) produced by decay, 2) cosmogenic  $^4\text{He}$  ( $^4\text{He}_{\text{cos}}$ ) produced by exposure of the sample to cosmic rays, and 3) initial  $^4\text{He}$  ( $^4\text{He}_{\text{init}}$ ) derived from incomplete degassing of the sample upon eruption. Therefore, to derive a meaningful (U-Th)/He age, it is of paramount importance to avoid  $^4\text{He}_{\text{cos}}$  and  $^4\text{He}_{\text{init}}$  during analyses. Cosmogenic  $^4\text{He}$  can be avoided by taking samples from depth, well below the penetration depth of cosmic rays (up to  $10^6 \text{ g cm}^{-2}$ , corresponding to an approximate depth of  $\sim 10 \text{ cm}$  (Masarik and Reedy, 1995). However, removal of  $^4\text{He}_{\text{init}}$  can be more challenging and requires careful crushing of the sample to liberate  $^4\text{He}_{\text{init}}$  from fluid inclusions (Kurz, 1986), while also preserving  $^4\text{He}_{\text{rad}}$  present in the matrix. It has been shown that in vacuo crushing of olivine and pyroxene phenocrysts quantitatively retains the cosmogenic and nucleogenic/radiogenic  $^3\text{He}$  and  $^4\text{He}$ , providing the size fraction is  $>10 \mu\text{m}$  and temperature during crushing is kept to a minimum ( $<300^\circ\text{C}$ ; Blard et al., 2008). Ignoring the presence of residual  $^3\text{He}$  and  $^4\text{He}$  from atmospheric and/or magmatic sources resulting from under-crushing of the sample will result in overestimated ages. Crushed samples can be analysed and corrected for the presence of  $^4\text{He}_{\text{init}}$  by incorporating a low temperature (e.g.  $300^\circ\text{C}$ ) gas extraction step, where any gas released represents  $^4\text{He}_{\text{init}}$  derived from fluid inclusions.

It has been shown that He is quantitatively retained within the olivine and pyroxene mineral structure at surface temperatures (Aciego et al., 2003, 2007; Niedermann, 2002). However, slowly cooled samples might have undergone He diffusion. For olivine at low temperatures ( $150^\circ\text{C} - 600^\circ\text{C}$ ) it has been shown that He diffusion obeys the standard Arrhenius relationship of diffusion, with very low diffusivities (approximately  $1 \times 10^{-22} \text{ cm}^2/\text{s}$ ) at environmental temperatures (activation energy [ $E_a$ ] =  $25 \pm 4 \text{ kcal/mole}$ ; Trull et al., 1991). At mantle temperatures ( $\sim 1200^\circ\text{C} - 1350^\circ\text{C}$ ), diffusion of He in olivine is relatively fast at  $2.2 \times 10^{-8} \text{ cm}^2/\text{s}$  ( $E_a = 120 \pm 30 \text{ kcal/mole}$ ; Hart, 1984) to  $5.3 \times 10^{-9} \text{ cm}^2/\text{s}$  ( $E_a = 100 \pm 4.8 \text{ kcal/mole}$ ; Trull and Kurz, 1993), which suggest that phenocrysts are readily degassed from any magmatic He. However, the presence of trapped magmatic He in samples (Aciego et al., 2007, 2010), released during in vacuo crushing, suggests that some magmatic He is retained in phenocrysts forming at magmatic temperatures. Using the diffusion parameters of Hart (1984) for the grain sizes used in this study ( $\sim 300 \mu\text{m}$ ) and the expected fast cooling rate of  $10^7^\circ\text{C}/\text{Ma}$  for the small ( $\sim 50 \text{ m}$ ; Jaques et al., 1986) lamproite intrusion at Ellendale, the closing temperature for He in olivine is about  $1000 - 1100^\circ\text{C}$ . It has been shown that  $\text{CO}_2$ -rich and  $\text{H}_2\text{O}$ -rich peridotite melts have solidus temperatures below  $1000^\circ\text{C}$  between  $20 - 30 \text{ GPa}$  (Foley et al., 2009), which implies that trapped



magmatic He will be retained in olivine phenocrysts during formation of such rocks. Therefore, removal of this  ${}^4\text{He}_{\text{init}}$  before degassing is of paramount importance for accurate age determination.

#### 6.2.1.2. Uranium and thorium

Uranium and thorium concentrations of individual olivine phenocrysts from single basalt flows typically show a wide range between 0.002 and 400 parts per million (ppm) for U and 0.005 and 445 ppm for Th (Blard and Farley, 2008), stressing the importance of determining parental U and Th isotope concentrations on the exact same aliquot of olivine used for He extraction. Furthermore, U and Th are commonly heterogeneously distributed in the phenocryst, and concentrations are usually much higher than that expected on the basis of partition coefficients (Beattie, 1993), probably due to the presence of micro-inclusions of U and Th rich phases.

### 6.3. Sample description<sup>5</sup>

In lamproitic rocks the partition coefficient for U (and other incompatible elements) is generally high ( $K_d = 0.0012$ ) for olivine phenocrysts, relative to less alkaline rocks ( $K_d = 0.0001$ ; McKenzie and O’Nions, 1991) due to a favourably larger M2 site (Foley and Jenner, 2004). Therefore, these rocks are ideal candidates for the development of more accurate (U-Th)/He dating techniques. However, the outer 20  $\mu\text{m}$  of the olivine phenocryst can be subjected to implantation of alpha particles from more U-rich neighbours in the groundmass (e.g. leucite:  $K_d = 0.005$ ; Farley et al., 2002; Foley and Jenner, 2004; Ziegler, 1977). This effect can be corrected for, either using a quantitative model to calculate the correction factor ( $F_T$ ) based on the grain size and geometry (Farley et al., 1996), or by physically abrading the outer 20  $\mu\text{m}$  of the sample (Min et al., 2006). Min et al. (2006) have shown that physical removal of the outer 20  $\mu\text{m}$  of sufficiently large grains corresponds to an alpha-implantation correction factor  $F_T$  (Farley et al., 1996) approaching unity.

We have sampled an Olivine-Clinopyroxene-Phlogopite lamproite from the Ellendale diamondiferous lamproite field in the Kimberley region of Western Australia (hereafter sample E9; Figure 6.1; Jaques et al., 1986). Geochemical data suggests that these rocks were derived from an extremely enriched mantle (McCulloch et al., 1983) that underwent a three-stage enrichment evolution (Fraser et al., 1985). Although the distribution of lamproite pipes in Western Australia appears strongly dependent on the presence of major crustal structures (Jaques and Milligan, 2004); their ultimate magmatic provenance remains enigmatic. Geochronology has shown that these rocks are Mesozoic, with combined whole rock and phlogopite Rb-Sr dating showing ages around 24 Ma,

---

<sup>5</sup> We have performed multi-mineral  ${}^{40}\text{Ar}/{}^{39}\text{Ar}$  dating on two other lamproites from Spain and Serbia as well, but as these did not yield olivine for (U-Th)/He dating they were not included in the manuscript. The data and interpretation can be found in Appendix N.

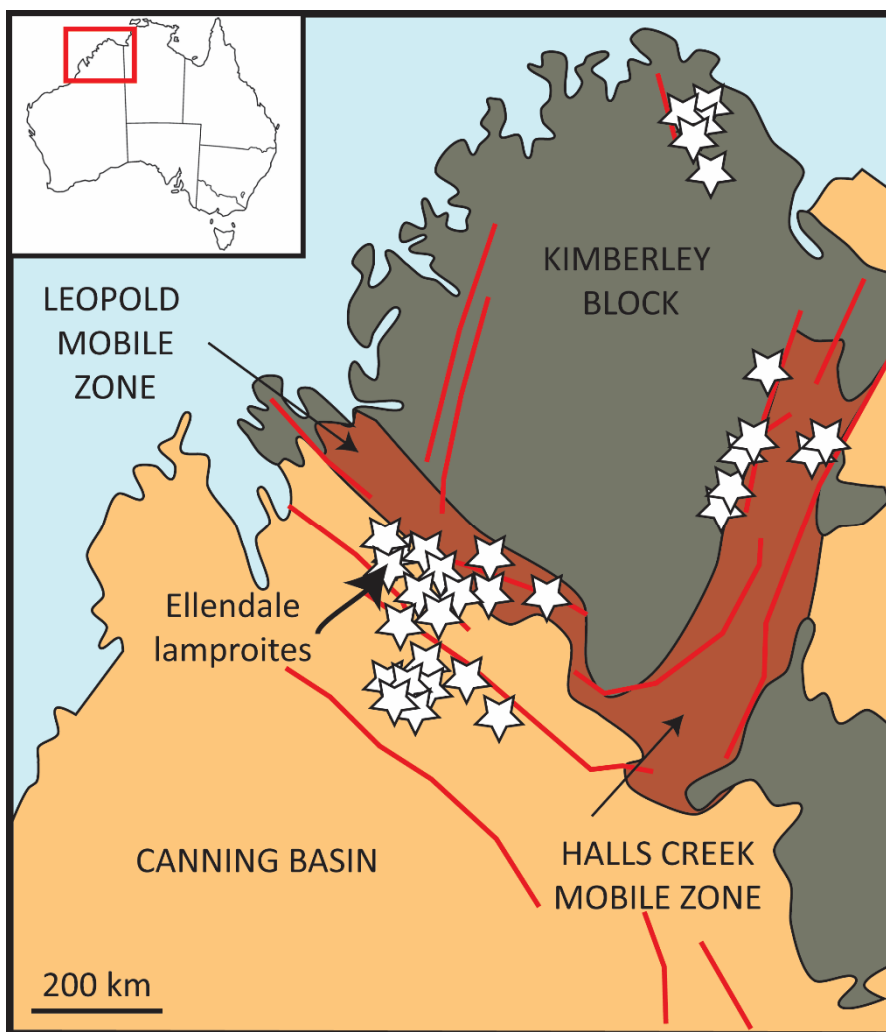


Figure 6.1. Simplified location map of the Ellendale lamproite field after Jaques et al (1986). Major geological units are distinguished by different colours. Major faults are indicated by red lines. Lamproite deposits are indicated by a star.

and phlogopite K-Ar dating showing an age of  $22.0 \pm 0.6$  Ma for closely located Mt Percy (Wellman, 1973). More recent (U-Th)/He dating of zircon from Ellendale confirms Mesozoic emplacement with an age of  $20.6 \pm 2.8$  Ma and a maximum age of ca. 22 Ma derived from a  $^{40}\text{Ar}/^{39}\text{Ar}$  mini-plateau (Evans et al., 2012). Thin section analysis (Figure 6.2) shows that E9 has a very fine grained to glassy matrix with abundant perovskite and fresh phlogopite microcrysts present, whereas slightly altered phlogopite is also present as macrocrysts together with slightly serpentinized olivine. Two generations of

olivine are present; the fraction 300 – 400  $\mu\text{m}$  selected for this study is the second-generation of olivine phenocrysts thought to represent lamproite compositions (Sobolev et al., 1989).

#### 6.4. Analytical methodology

Approximately 3 kg of lamproite material was disaggregated using the high voltage pulse power fragmentation SelFrag™ instrument. This process leaves all mineral phases intact; which was required to yield adequate amounts of olivine for (U-Th)/He analyses and identifiable K-rich phases for  $^{40}\text{Ar}/^{39}\text{Ar}$  geochronology.

#### 6.4.1. $^{40}\text{Ar}/^{39}\text{Ar}$ geochronology

Disaggregated sample material was sieved to multiple fractions and washed. Phlogopite was extracted using a series of magnetic and density separations, followed by handpicking using a binocular stereomicroscope, avoiding altered grains as well as grains containing inclusions. Mineral separates were leached for 5 minutes with methanol and dilute HF (2N) followed by duplicate DI washes to remove any silicate phases, loaded into aluminium discs wrapped with aluminium foil and placed in quartz tubes along with the fully inter-calibrated flux monitor Fish Canyon Tuff sanidine ( $28.294 \pm 0.036$  Ma,  $1\sigma$ ; Renne et al., 2011) and irradiated for 3 hours in the axial position at the Cadmium-Lined In-Core Irradiation Tube (Cd shielding to avoid nuclear interference reactions) at the Oregon State TRIGA reactor, USA.

$^{40}\text{Ar}/^{39}\text{Ar}$  step-heating analyses were performed with the high precision, new generation, multi-collector mass spectrometer ARGUSVI from Thermofisher© at the West Australian Argon Isotope Facility, John de Laeter Center, Curtin University, Perth. Argon isotopes were released from approximately 5 mg of sample material in 26 steps of increasing temperature using a Photon Fusions 10.6 CO<sub>2</sub> laser operating between 1 and 50% laser power (max power of 60 W). Resulting gases were purified using a SAES GP50 getter and two AP10 SAES getters as well as a polycold electrical cryocooler condensation trap, and analysed on the ARGUSVI mass spectrometer with  $^{37}\text{Ar}$ ,  $^{38}\text{Ar}$ ,  $^{39}\text{Ar}$  and  $^{40}\text{Ar}$  analysed on four Faraday detectors and  $^{36}\text{Ar}$  on the ultra-sensitive ion counting electron multiplier. A more complete description of the extraction line and ARGUSVI mass spectrometer can be found in Oostingh et al. (2016).

Argon isotope results were corrected for system blanks, mass discrimination, radioactive decay and reactor-induced interference reactions. System blanks proved to be around 11 fA for  $^{40}\text{Ar}$  as compared to > 150 fA for a typical analysis and were measured every fourth sample. Mass discrimination was closely monitored via a series of air shots before and after each step-heating experiment assuming an atmospheric  $^{40}\text{Ar}/^{36}\text{Ar}$  ratio of  $298.56 \pm 0.31$  (Lee et al., 2006) and ranged from  $0.992294 \pm 0.0003$  (0.03%;  $1\sigma$ ) to  $0.993432 \pm 0.0008$  (0.08%;  $1\sigma$ ). The J-value of  $0.0008266 \pm 0.00000029$  (0.035%;  $1\sigma$ ) for all specific levels was calculated by averaging the mean ( $^{40}\text{Ar}^*/^{39}\text{Ar}$ ) ratios from total fusion analysis of four aliquots of FC sanidine bracketing the samples. We used correction factors obtained from prolonged analysis of K-Ca-Cl glass/salts at the Oregon State TRIGA reactor:  $(^{39}\text{Ar}/^{37}\text{Ar})_{\text{Ca}} = (7.60 \pm 0.09) \times 10^{-4}$ ;  $(^{36}\text{Ar}/^{37}\text{Ar})_{\text{Ca}} = (2.70 \pm 0.02) \times 10^{-4}$ ;  $(^{40}\text{Ar}/^{39}\text{Ar})_{\text{K}} = (7.30 \pm 0.90) \times 10^{-4}$ ; and  $(^{38}\text{Ar}/^{39}\text{Ar})_{\text{K}} = (1.24 \pm 0.004) \times 10^{-2}$  (Jourdan and Renne, 2007).

The ArArCALC algorithm (Koppers, 2002) was used for data regression and age calculation. We define statistically significant plateau ages as including > 70 % of released  $^{39}\text{Ar}$  from at least 3 subsequent steps with  $^{40}\text{Ar}/^{39}\text{Ar}$  ratios within error of the  $2\sigma$  confidence level (McDougall and Harrison, 1999) and correlations satisfying a probability of fit ( $p$ ) based on the  $\chi^2$ -test distribution of more than 5% (Jourdan *et al.*, 2009a). Ages were calculated relative to the FC sanidine age of  $28.294 \pm 0.036$  Ma (Renne *et al.*, 2011) using the decay constants of Renne *et al.* (2011) and the atmospheric argon composition of Lee *et al.* (2006). Uncertainties were calculated using error propagation of uncertainties associated with the mean and plateau ages and J-value and are reported at the  $2\sigma$  or 95% confidence level.

#### 6.4.2. (U-Th)/He geochronology

Disaggregated material from sample E9 was sieved to the fraction 300 – 400  $\mu\text{m}$ , which optically contained the freshest olivine. Subsequent magnetic and density separation ensured almost perfect separation of olivine phenocrysts and host rock material, however, we carefully handpicked fresh olivine to avoid altered (serpentinized) phenocrysts or phenocrysts with inclusions. The handpicked olivine was air-abraded for 3 days, using pyrite as shock-absorber, to remove the outer 20  $\mu\text{m}$  of the grains in order to overcome errors resulting from alpha-implantation of the olivine from the groundmass (Aciego *et al.*, 2007; Blackburn *et al.*, 2007; Farley, 2002; Min *et al.*, 2006). Resulting abraded grains were thoroughly washed with alternating acetone, ethanol and DI in a sonic bath to remove adhering pyrite powder. Following the approach of Blard *et al.* (2008), abraded grains were carefully crushed with an agate mortar and pestle to release  $^4\text{He}_{\text{init}}$  from fluid inclusions, while retaining  $^4\text{He}_{\text{rad}}$  in the matrix. The resulting crushed fraction was sieved to 53 – 100  $\mu\text{m}$  and various weights (1.3 – 5.7 mg; Table 2) were loaded in degassed Nb crucibles for He extraction.

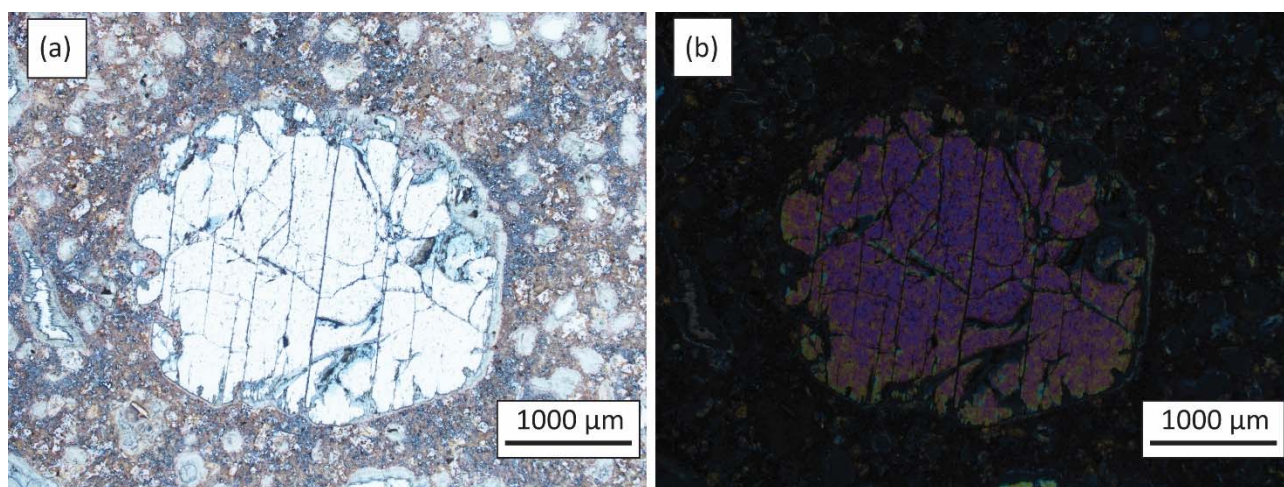


Figure 6.2. Thin section images of an olivine phenocryst in the Ellendale E9 sample. (a) Plane polarized light and (b) cross polarized light.

Helium analysis was performed on an Alphachron™ instrument at the GeoHistory laboratory, John de Laeter Centre, Curtin University, Perth. This instrument consists of an UHV extraction line (150 cc) containing two SAES getters to purify gases; one operating at high temperature (350 °C) and one operating at room temperature (18 °C).  $^4\text{He}_{\text{rad}}$  abundances were analysed by means of isotope dilution on a Pfeiffer Prisma QMS-200 mass spectrometer, by spiking the standard/sample  $^4\text{He}$  gas with a standard aliquot of  $^3\text{He}$  and determining the resultant  $^4\text{He}/^3\text{He}$  isotopic ratio. Typical long-term instrumental blank is approximately 0.005 ncc. The low temperature blank of the extraction line ranged from 0.000025 – 0.000418 ncc  $^4\text{He}$ , whereas the procedural hot blanks at 300° C and 1300° C ranged from 0.001826 to 0.004228 ncc  $^4\text{He}$  and from 0.007597 to 0.010160 ncc  $^4\text{He}$  respectively. Gases were extracted in three temperature steps, using an externally heated tube furnace to heat individual Nb crucibles located in an Inconel® sample tube. The first step consisted of raising the temperature to 300° C for 15 mins to release any adsorbed He, the second step consisted of raising the temperature to 1300° C for 150 mins to liberate all He from the matrix. This was followed by the re-extract step at 1300° C for 150 mins to ensure all He was released. Crucibles were retrieved after total gas extraction and sample material removed for U and Th isotope analyses.

U and Th isotope analyses were performed using isotope dilution inductively coupled plasma mass spectrometry following methods outlined in Evans et al. (2005). To facilitate dissolution of the olivine, samples were split in aliquots of 0.5 mg each and placed in 0.35 mL Savillex micro-vials with 350  $\mu\text{L}$  of concentrated HF and 50  $\mu\text{L}$  of a mixed 15 ng/mL  $^{235}\text{U}$  –  $^{230}\text{Th}$  spike (7M  $\text{HNO}_3$ ). Nine aliquots, a blank and a spiked standard were added to a single Parr pressure dissolution vessel, which was heated to 240° C for 36 hours. Samples were taken to incipient dryness and re-bombed with hydrochloric acid to remove fluoride salts. The final solution was taken up in 900  $\mu\text{L}$  of MilliQ  $\text{H}_2\text{O}$  and analysed for U and Th isotopes on an Agilent 7500 quadrupole inductively coupled plasma mass spectrometer at TSW Analytical, Perth. Accurate U and Th isotopic abundances were acquired by means of isotope dilution, using a spike with  $[^{235}\text{U}] = 15.6 \pm 0.6$  ppb,  $[^{230}\text{Th}] = 5.8 \pm 0.2$  ppb,  $^{230}\text{Th}/^{232}\text{Th} = 0.2119 \pm 0.0007$  and  $^{235}\text{U}/^{238}\text{U} = 0.5922 \pm 0.0019$ . The resulting absolute errors on U and Th concentrations after recombining the 0.5 mg aliquots for each sample range from 13.22 % - 16.16 % ( $1\sigma$ ) and 13.79 % - 25.91 % ( $1\sigma$ ) respectively.

## 6.5. Results

### 6.5.1. $^{40}\text{Ar}/^{39}\text{Ar}$ geochronology

Table 6.1 provides a summary of the  $^{40}\text{Ar}/^{39}\text{Ar}$  geochronology results, whereas corresponding apparent age plateaus can be found in Figure 6.3. Full step-heating results can be found in Appendix

M. All plateau ages reported in this paper are inverse isochron  $^{40}\text{Ar}/^{36}\text{Ar}$  intercept corrected (see Oostingh et al., 2016 for a discussion on this approach). The three aliquots of phlogopite that were analysed for sample E9 all yield statistically significant plateau ages (probability of fit (P) based on the  $\chi^2$  test distribution of at least 0.05; Jourdan et al., 2009), from which a weighted mean average age of  $22.39 \pm 0.02$  Ma could be calculated.

Sample	Mineral	Plateau characteristics				Inverse Isochron characteristics				
		Plateau age (Ma, $\pm 2\sigma$ )	Total $^{39}\text{Ar}$ released (%)	MSWD	P	Inverse Isochron age (Ma, $\pm 2\sigma$ )	n	$^{40}\text{Ar}/^{36}\text{Ar}$ intercept ( $\pm 2\sigma$ )	MSWD	P
E9	phlogopite	22.37 $\pm$ 0.03	99	1.11	0.33	22.37 $\pm$ 0.03	20	285.1 $\pm$ 1.9	1.24	0.22
	phlogopite	22.40 $\pm$ 0.03	96	0.93	0.54	22.43 $\pm$ 0.05	20	292 $\pm$ 11	0.89	0.59
	phlogopite	22.42 $\pm$ 0.04	97	1.16	0.29	22.40 $\pm$ 0.07	19	303 $\pm$ 15	1.19	0.27

**weighted mean age for E9: 22.39  $\pm$  0.02 Ma**

*Table 6.1. Summary of  $^{40}\text{Ar}/^{39}\text{Ar}$  results of three phlogopite aliquots for Ellendale E9.*

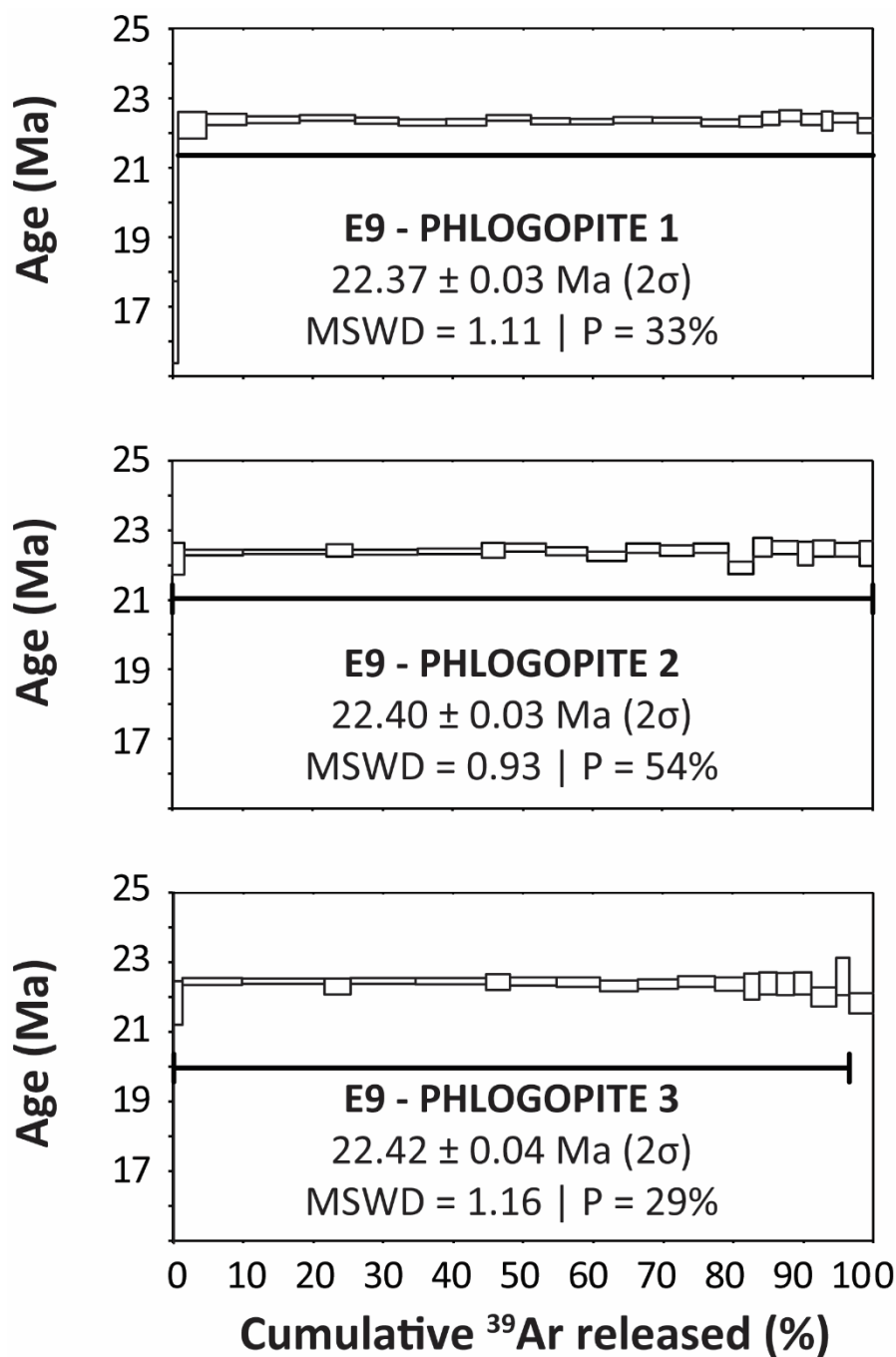


Figure 6.3. Age spectra of the three E9 phlogopite aliquots. The size of the error box represents a  $2\sigma$  uncertainty on the apparent age.

extraction step. As absolute errors of the He abundances range from 0.7 % – 1.6 % ( $1\sigma$ ), the relatively large uncertainty of the calculated (U-Th)/He age ( $>10\%$ ) is mainly caused by the propagated uncertainties in calculation of U and Th concentrations.

### 6.5.2. (U-Th)/He geochronology

Table 6.2 provides an overview of the He degassing characteristics for each heating step, as well as the U, Th and Sm concentrations of each degassed olivine aliquot and resulting (U-Th)/He ages. Samarium is not present in high enough abundances to significantly impact the age calculation. Secular equilibrium between U and

Th decay series is assumed, as samples are expected to be  $> 1 \text{ Ma}$  old. Ages range from  $53.3 \pm 5.0 \text{ Ma}$  to  $18.7 \pm 2.6 \text{ Ma}$  for the six different aliquots. The degassing step at  $300^\circ\text{C}$  yields insignificant amounts of  $^4\text{He}_{\text{init}}$  for each sample and  $^4\text{He}$  released during re-extract steps is less than 10% of the main



Sample	Weight (mg)	Degassing step	<sup>4</sup> He (ncc)	<sup>238</sup> U (ng, 1σ)	<sup>232</sup> Th (ng, 1σ)	<sup>147</sup> Sm (ng, 1σ)	(U-Th)/He age (2σ)
E9 #61	1.3	<b><u>Total <sup>4</sup>He (ncc) = 0.180 ± 0.002</u></b>					
		300°C	0.001	0.022 ± 0.001	0.028 ± 0.002	< d.l.	53.3 ± 5.0 Ma
		1300°C	0.175				
E9 #9	1.8	1300°C Re-extract	0.004				
		<b><u>Total <sup>4</sup>He (ncc) = 0.203 ± 0.002</u></b>		0.031 ± 0.002	0.045 ± 0.002	< d.l.	39.8 ± 3.4 Ma
		300°C	0.001				
E9 #4	4.2	1300°C	0.203				
		<b><u>Total <sup>4</sup>He (ncc) = 0.465 ± 0.005</u></b>		0.060 ± 0.003	0.145 ± 0.007	< d.l.	40.5 ± 9.2 Ma
		300°C	< d.l.				
		1300°C	0.439				
E9 #5	4.3	1300°C Re-extract	0.026				
		1300°C Re-extract 2	< d.l.				
		<b><u>Total <sup>4</sup>He (ncc) = 0.580 ± 0.004</u></b>		0.099 ± 0.007	0.172 ± 0.008	< d.l.	34 ± 13 Ma
		300°C	0.002				
E9 #55	4.7	1300°C	0.541				
		1300°C Re-extract	0.039				
		<b><u>Total <sup>4</sup>He (ncc) = 0.625 ± 0.004</u></b>		0.184 ± 0.010	0.380 ± 0.018	< d.l.	18.7 ± 5.6 Ma
E9 #91	5.7	300°C	0.001				
		1300°C	0.554				
		1300°C Re-extract	0.070				
		<b><u>Total <sup>4</sup>He (ncc) = 0.695 ± 0.006</u></b>		0.189 ± 0.010	0.490 ± 0.023	< d.l.	18.7 ± 5.2 Ma
		300°C	< d.l.				
		1300°C	0.645				
		1300°C Re-extract	0.049				

Table 6.2. (U-Th)/He degassing summary (all blank subtracted) and resulting ages.

## 6.6. Discussion

6.6.1.  $^{40}\text{Ar}/^{39}\text{Ar}$  versus (U-Th)/He dating

The ultra-precise  $^{40}\text{Ar}/^{39}\text{Ar}$  age of  $22.39 \pm 0.02$  Ma obtained for the three phlogopite aliquots confirms the Mesozoic emplacement of the Ellendale suite. Furthermore, the precise age shows the advantage in using new generation multi-collected mass spectrometers such as the ARGUSVI when analysing K-rich minerals. Our approach also shows the importance of adopting strict sample selection protocols, as careful handpicking of the unaltered small-size fraction of phlogopite yields an accurate eruption age, whereas previous  $^{40}\text{Ar}/^{39}\text{Ar}$  analysis of the slightly altered but significantly larger size fraction only yielded a maximum age (Evans et al., 2012).

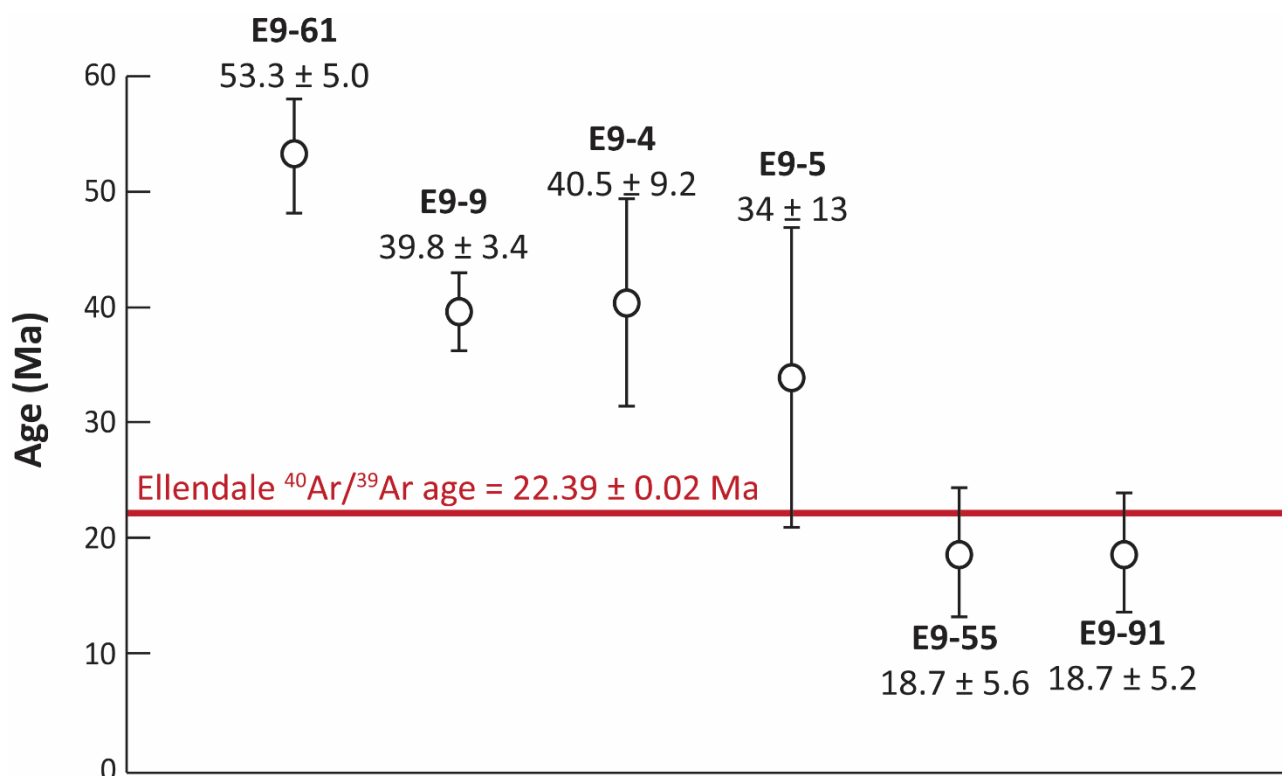


Figure 6.4. Age comparison between (U-Th)/He ages of six olivine aliquots and the ultra-precise weighted mean  $^{40}\text{Ar}/^{39}\text{Ar}$  age of the three phlogopite aliquots of sample Ellendale E9. All errors are  $2\sigma$ .

Three of the six olivine aliquots overlap within  $2\sigma$  error with the mean weighted phlogopite  $^{40}\text{Ar}/^{39}\text{Ar}$  age of  $22.39 \pm 0.02$  Ma (Figure 6.4), although age precision (38% error) on the E9-5 sample is poor due to a large uncertainty in the determination of the U concentration of this sample (25%). The three aliquots with the smallest amount of sample material yield ages that are much older than expected; 53 Ma (E9-61; 1.3 mg), 40 Ma (E9-9; 1.8 mg) and 41 Ma (E9-4; 4.2 mg). Here, we will discuss the potential causes of these overestimated ages; presence of excess daughter ( $^4\text{He}$ ) or loss of parent (U and/or Th).

### 6.6.1.1. Excess helium?

As mentioned above, olivine phenocrysts contain multiple reservoirs of helium. Trapped  $^4\text{He}_{\text{init}}$ , could either be present in fluid inclusions with magmatic composition or derived from alpha-implantation in the outer 20  $\mu\text{m}$  of the olivine from U and Th rich groundmass. Furthermore, radiogenic  $^4\text{He}_{\text{rad}}$  will be present from decay reactions of parent isotopes U and Th. Cosmogenically produced  $^3\text{He}_{\text{cos}}$  is considered insignificant for these samples, as the Ellendale olivine lamproite sample was taken from a recently exposed quarry (Evans et al., 2012). Following the recommendation of Aciego et al. (2007), we performed air abrasion as well as crushing techniques to remove the effects of alpha-implantation/diffusion and liberate trapped  $^4\text{He}_{\text{init}}$  from fluid inclusions. It has been shown that radiogenic  $^4\text{He}_{\text{rad}}$  is quantitatively retained in olivine phenocrysts during crushing, as long as the temperature during crushing is kept to a minimum (Blard et al., 2008). Under-crushing of the sample could prove to be a potential risk, which would result in an overestimated (U-Th)/He age. However, as all low temperature (300°C) gas extraction steps yielded  $^4\text{He}_{\text{init}}$  either below experimental blank levels or at concentrations <1% of those obtained during the main heating step, we conclude that we have successfully removed excess He from fluid inclusions.

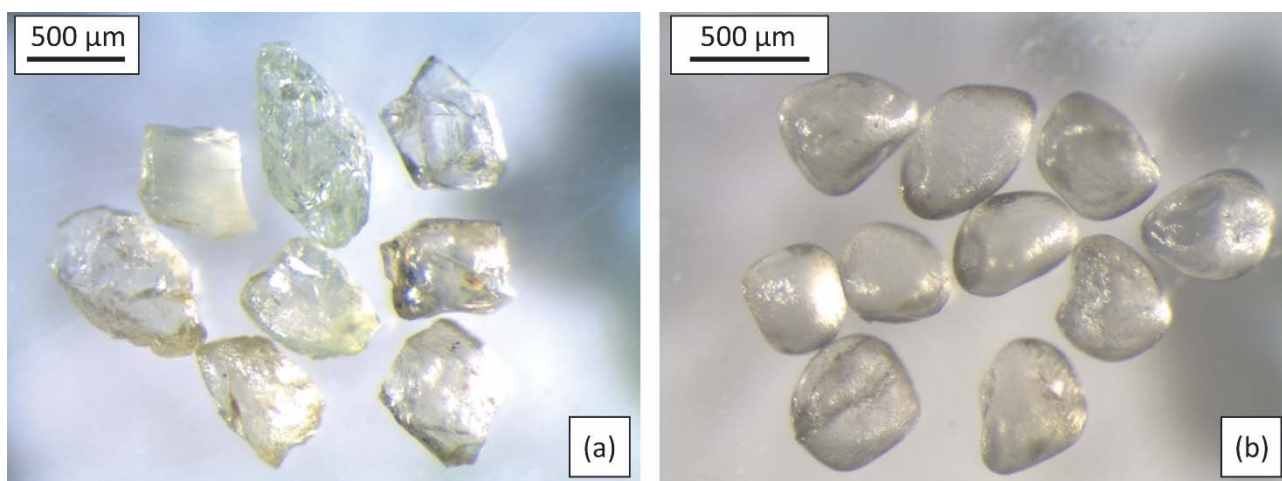


Figure 6.5. Ellendale E9 olivine phenocrysts (a) before and (b) after three days of air abrasion used to remove the outer edge of 20  $\mu\text{m}$  from the grains to overcome  $\alpha$ -implantation effects from the U and Th rich lamproite groundmass.

It is possible, however, that we did not completely remove the outer 20  $\mu\text{m}$  layer during air abrasion. As the lamproite groundmass is expected to be much more enriched in U and Th than the olivine phenocrysts (e.g. 0.1 - 4.8 ppm U for lamproite glass versus < 0.005 ppm U for olivine in the Gausberg lamproites; Foley and Jenner, 2004; Zanetti et al., 2004), incomplete removal of the outer layer could result in overestimated ages due to net alpha-implantation into the grains. Unfortunately, it was not possible to do a volume approximation calculation (Aciego et al., 2007) to verify the amount of material removed, as some grains were completely pulverized during air abrasion. We

have used visual techniques instead (Figure 6.5). However, as all samples have undergone the same air abrasion procedure, it would be expected that incomplete removal of the outer layer would result in overestimated ages for each sample aliquot. This is clearly not the case, as three out of six aliquots provide geologically meaningful (U-Th/He) ages; we therefore conclude that we have successfully removed any alpha-implantation effects from the grains during air abrasion.

#### 6.6.1.2. Uranium and/or thorium loss?

A more likely cause of the three overestimated ages is the partial loss of parent isotopes during sample preparation and/or analysis. It was challenging to fully recover all the gas-extracted olivine for all samples except E9-55 and E9-91 (largest by mass) so it is conceivable that some of the material from which He was recovered, did not have their full complement of U and Th due to loss during sample recovery (i.e., transfer of grains from Nb microvials to dissolution vessels). We recommend a minimum sample weight of 4.7 mg when using similar crucibles, as we observed that no sample material was optically visible after removal following gas extraction in the two crucibles with largest sample mass.

It has been suggested that volatilization of U and Th might play an important role during high-temperature gas extraction (Danišik et al., 2013). Our initial experimental set-up (where four samples are dropped into the furnace sequentially), causes the samples that are analysed first to be exposed to extraction and re-extraction steps at 1300°C for more than eight times as subsequent samples drop and are heated. For example, sample E9-4 (41 Ma) was heated for four cycles, samples E9-9 (40 Ma) and E9-5 (34 Ma) were heated for three cycles, samples E9-61 (53 Ma) and E9-55 (19 Ma) were heated for two cycles, and E9-91 (19 Ma) was only exposed to a single heating cycle. We suspect that U and Th volatilization could be an additional source of overestimated ages to that derived from incomplete sample removal. Hence, we would recommend subjecting each sample to a single gas extraction and heating schedule only and we propose that too-old ages were obtained on samples that lost U and Th during excess heating for He extraction. More experimental work is required to quantify the effect of potential U and Th volatilization from olivine phenocrysts exposed to multiple heating schedules.

#### 6.6.2. Future implications

In contrast to earlier work on (U-Th)/He dating of olivine phenocrysts which suggested limitations around accurate He determinations (Aciego et al., 2007), the methodology outlined here yielded relatively precise He analysis (ca 1%) and less precise U and Th analyses (ca 15% and 25%). Resulting (U-Th)/He ages show errors around 10% which is much higher than 3 – 5% errors generally

encountered using (U-Th)/He dating of apatite and zircon (McInnes et al., 2009; Zeitler et al., 1987). The dissolution method employed by Aciego et al (2007) utilized up to 1 g of olivine for U and Th analysis as compared to the 0.5 mg aliquots used in this study, resulting in absolute errors of ca. 1% for Th and ca. 0.5% for U. Importantly, we show that He determination using isotope dilution on the Alphachron™ instrument yields accurate He concentrations with extremely small errors, even on small sample sizes (< 5.7 mg). This study shows that (U-Th)/He dating of olivine phenocrysts using the simple analytical methodology outlined above may provide meaningful geological ages in cases when traditional geochronology techniques are not applicable. However, more research is required to investigate the potential effects of U and Th volatilization and to find the optimum sample weight that ensures both full retrieval of sample material and easy digestion of degassed sample.

### 6.7. Conclusion

This study provides a detailed analytical methodology for (U-Th)/He dating on olivine phenocrysts. We have obtained (U-Th)/He ages ranging from  $53.3 \pm 5.0$  Ma to  $18.7 \pm 2.6$  Ma for six olivine separates from the Ellendale E9 lamproite (Western Australia). Three of these ages statistically overlap with a newly acquired  $^{40}\text{Ar}/^{39}\text{Ar}$  age of  $22.39 \pm 0.02$  Ma for phlogopite in this lamproite. Overestimated ages can be explained by parental isotope loss either due to incomplete crystal recovery after degassing or U and Th volatilization during multiple heating cycles. The low precision of the (U-Th)/He ages can be explained by relative large errors during U and Th analysis, due to small sample sizes. Degassing characteristics as well as the (U-Th)/He ages show that we have successfully removed trapped, magmatic  $^4\text{He}_{\text{init}}$  as well as implanted He from the olivine grains by employing a combination of careful handpicking, air abrasion and crushing techniques before gas extraction. Therefore, (U-Th)/He dating of olivine phenocrysts shows potential as a new geochronology technique.

### 6.8. Acknowledgements

Celia Mayers, Zdenka Martelli and Adam Frew of WAAIF are thanked for their aid during sample preparation for  $^{40}\text{Ar}/^{39}\text{Ar}$  analysis. Dr Lynton Jaques (Australian National University) and Dr Dejan Prelevic (University of Mainz) are thanked for their contribution of sample material. The support of TiGER and the department Applied Geology at Curtin University of Technology is gratefully acknowledged. We would like to thank Chris May and Cameron Scadding at TSW Analytical for assistance with mass spectrometry. This research was funded by Australian Research Council Discovery grant DP130100517.

## 6.9. References

- Aciego, S., Kennedy, B. M., DePaolo, D. J., Christensen, J. N. & Hutcheon, I. (2003). U-Th/He age of phenocrystic garnet from the 79 AD eruption of Mt. Vesuvius. *Earth and Planetary Science Letters* 216, 209–219.
- Aciego, S. M., DePaolo, D. J., Kennedy, B. M., Lamb, M. P., Sims, K. W. W. & Dietrich, W. E. (2007). Combining [3He] cosmogenic dating with U–Th/He eruption ages using olivine in basalt. *Earth and Planetary Science Letters* 254, 288–302.
- Aciego, S. M., Jourdan, F., DePaolo, D. J., Kennedy, B. M., Renne, P. R. & Sims, K. W. W. (2010). Combined U–Th/He and  $^{40}\text{Ar}/^{39}\text{Ar}$  geochronology of post-shield lavas from the Mauna Kea and Kohala volcanoes, Hawaii. *Geochimica et Cosmochimica Acta*. Elsevier Ltd 74, 1620–1635.
- Beattie, P. (1993). The generation of uranium series disequilibria by partial melting of spinel peridotite: constraints from partitioning studies. *Earth and Planetary Science Letters* 117, 379–391.
- Blackburn, T. J., Stockli, D. F. & Walker, J. D. (2007). Magnetite (U-Th)/He dating and its application to the geochronology of intermediate to mafic volcanic rocks. *Earth and Planetary Science Letters* 259, 360–371.
- Blard, P.-H. & Farley, K. A. (2008). The influence of radiogenic  $^4\text{He}$  on cosmogenic  $^3\text{He}$  determinations in volcanic olivine and pyroxene. *Earth and Planetary Science Letters*. Elsevier B.V. 276, 20–29.
- Blard, P.-H., Puchol, N. & Farley, K. A. (2008). Constraints on the loss of matrix-sited helium during vacuum crushing of mafic phenocrysts. *Geochimica et Cosmochimica Acta* 72, 3788–3803.
- Danišík, M., Evans, N. J., Ramanaidou, E. R., McDonald, B. J., Mayers, C. & McInnes, B. I. A. (2013). (U-Th)/He chronology of the Robe River channel iron deposits, Hamersley Province, Western Australia. *Chemical Geology* 354, 150–162.
- Danišík, M., Shane, P., Schmitt, A. K., Hogg, A., Santos, G. M., Storm, S., Evans, N. J., Fifield, L. K. & Lindsay, J. M. (2012). Re-anchoring the late Pleistocene tephrochronology of New Zealand based on concordant radiocarbon ages and combined  $^{238}\text{U}/^{230}\text{Th}$  disequilibrium and (U–Th)/He zircon ages. *Earth and Planetary Science Letters* 349–350, 240–250.
- Dunai, T. J. & Roselieb, K. (1996). Sorption and diffusion of helium in garnet: implications for volatile tracing and dating. *Earth and Planetary Science Letters*. JOUR. 139, 411–421.

- Evans, N. J., Byrne, J. P., Keegan, J. T. & Dotter, L. E. (2005a). Determination of Uranium and Thorium in Zircon, Apatite, and Fluorite: Application to Laser (U-Th)/He Thermochronology. *Journal of Analytical Chemistry* 60, 1159–1165.
- Evans, N. J., McInnes, B. I. A., McDonald, B. J., Danišik, M., Jourdan, F., Mayers, C., Thern, E. & Corbett, D. (2012). Emplacement age and thermal footprint of the diamondiferous Ellendale E9 lamproite pipe, Western Australia. *Mineralium Deposita* 48, 413–421.
- Evans, N. J., Wilson, N. S. F., Cline, J. S., McInnes, B. I. A. & Byrne, J. (2005b). Fluorite (U-Th)/He thermochronology: Constraints on the low temperature history of Yucca Mountain, Nevada. *Applied Geochemistry*. JOUR. 20, 1099–1105.
- Farley, K. A. (2002). (U-Th)/He Dating: Techniques, Calibrations, and Applications. *Reviews in Mineralogy and Geochemistry* 47, 819–844.
- Farley, K. A., Kohn, B. P. & Pillans, B. (2002). The effects of secular disequilibrium on (U-Th)/He systematics and dating of Quaternary volcanic zircon and apatite. *Earth and Planetary Science Letters* 201, 117–125.
- Farley, K. A., Wolf, R. A. & Silver, L. T. (1996). The effects of long alpha-stopping distances on (U-Th)/He ages. *Geochimica et Cosmochimica Acta* 60, 4223–4229.
- Foley, S. F. & Jenner, G. A. (2004). Trace element partitioning in lamproitic magmas—the Gaussberg olivine leucitite. *Lithos* 75, 19–38.
- Foley, S. F., Yaxley, G. M., Rosenthal, A., Buhre, S., Kiseeva, E. S., Rapp, R. P. & Jacob, D. E. (2009). The composition of near-solidus melts of peridotite in the presence of CO<sub>2</sub> and H<sub>2</sub>O between 40 and 60 kbar. *Lithos*. Elsevier B.V. 112, 274–283.
- Fraser, K. J., Hawkesworth, C. J., Erlank, A. J., Mitchell, R. H. & Scott-Smith, B. H. (1985). Sr, Nd and Pb isotope and minor element geochemistry of lamproites and kimberlites. *Earth and Planetary Science Letters* 76, 57–70.
- Hart, S. R. (1984). He diffusion in olivine. *Earth and Planetary Science Letters* 70, 297–302.
- House, M. A., Wernicke, B. P. & Farley, K. A. (1998). Dating topography of the Sierra Nevada, California, using apatite (U-Th)/He ages. *Nature*. JOUR. 396, 66–69.

- Jaques, A. L., Lewis, J. D. & Smith, C. B. (1986). The West Kimberley Province. In: Smith, C. B. (ed.) The kimberlites and lamproites of Western Australia. Geological Survey of Western Australia, 71–125.
- Jaques, A. L. & Milligan, P. R. (2004). Patterns and controls on the distribution of diamondiferous intrusions in Australia. *Lithos* 77, 783–802.
- Jourdan, F. & Renne, P. R. (2007). Age calibration of the Fish Canyon sanidine  $^{40}\text{Ar}/^{39}\text{Ar}$  dating standard using primary K–Ar standards. *Geochimica et Cosmochimica Acta* 71, 387–402.
- Jourdan, F., Renne, P. R. & Reimold, W. U. (2009). An appraisal of the ages of terrestrial impact structures. *Earth and Planetary Science Letters* 286, 1–13.
- Koppers, A. A. P. (2002). ArArCALC - software for  $^{40}\text{Ar}/^{39}\text{Ar}$  age calculations. *Computer and Geosciences* 28, 605–619.
- Kurz, M. D. (1986). Cosmogenic helium in a terrestrial igneous rock. *Nature* 320, 435–439.
- Lee, J. B., Marti, K., Severinghaus, J. P., Kawamura, K., Yoo, H. & Kim, J. S. (2006). A redetermination of the isotopic abundances of atmospheric Ar. *Geochimica et Cosmochimica Acta* 70, 4507–4512.
- Mamyrin, B. A. & Tolstikhin, I. N. (1984). Helium isotopes in nature. Elsevier.
- Masarik, J. & Reedy, R. C. (1995). Terrestrial cosmogenic-nuclide production systematics calculated from numerical simulations. *Earth and Planetary Science Letters* 136, 381–395.
- McCulloch, M. T., Jaques, A. L., Nelson, D. R. & Lewis, J. D. (1983). Nd and Sr isotopes in kimberlites and lamproites from Western Australia; an enriched mantle origin. *Nature Letters* 302.
- McDougall, I. & Harrison, T. M. (1999). Geochronology and thermochronology by the  $^{40}\text{Ar}/^{39}\text{Ar}$  method. Oxford University Press.
- McInnes, B. I. A., Evans, N. J., McDonald, B. J., Kinny, P. D. & Jakimowicz, J. (2009). Zircon U–Th–Pb–He double dating of the Merlin kimberlite field, Northern Territory, Australia. *Lithos*. Elsevier B.V. 112, 592–599.
- McKenzie, D. & O’Nions, R. K. (1991). Partial Melt Distributions from Inversion of Rare Earth Element Concentrations. *Journal of Petrology* 32, 1021–1091.



- Min, K., Reiners, P. W., Wolff, J. A., Mundil, R. & Winters, R. L. (2006). (U-Th)/He dating of volcanic phenocrysts with high-U-Th inclusions, Jemez Volcanic Field, New Mexico. *Chemical Geology* 227, 223–235.
- Niedermann, S. (2002). Cosmic-Ray-Produced noble gases in terrestrial rocks: dating tools for surface processes. *Reviews in Mineralogy and Geochemistry* 47, 731–784.
- Oostingh, K. F., Jourdan, F., Matchan, E. L. & Phillips, D. (2017).  $^{40}\text{Ar}/^{39}\text{Ar}$  geochronology reveals rapid change from plume-assisted to stress-dependent volcanism in the Newer Volcanic Province, SE Australia. *Geochemistry, Geophysics, Geosystems* 18, 1065–1089.
- Pi, T., Solé, J. & Taran, Y. (2005). (U-Th)/He dating of fluorite: application to the La Azul fluorite deposit in the Taxco mining district, Mexico. *Mineralium Deposita. JOUR.* 39, 976–982.
- Reiners, P. W. & Farley, K. A. (1999). Helium diffusion and (U-Th)/He thermochronometry of titanite. *Geochimica et Cosmochimica Acta. JOUR.* 63, 3845–3859.
- Renne, P. R., Balco, G., Ludwig, K. R., Mundil, R. & Min, K. (2011). Response to the comment by W.H. Schwarz et al. on “Joint determination of  $^{40}\text{K}$  decay constants and  $^{40}\text{Ar}^*/^{40}\text{K}$  for the Fish Canyon sanidine standard, and improved accuracy for  $^{40}\text{Ar}/^{39}\text{Ar}$  geochronology” by P.R. Renne et al. (2010). *Geochimica et Cosmochimica Acta. Elsevier Ltd* 75, 5097–5100.
- Renne, P. R., Swisher, C. C., Deino, A. L., Karner, D. B., Owens, T. L. & DePaolo, D. J. (1998). Intercalibration of standards, absolute ages and uncertainties in  $^{40}\text{Ar}/^{39}\text{Ar}$  dating. *Chemical Geology (Isotope Geoscience Section)* 145, 117–152.
- Sobolev, A. V., Sobolev, N. V., Smith, C. B. & Dubessy, J. (1989). Fluid and melt compositions in lamproites and kimberlites based on the study of inclusions in olivine. In: Ross, J. (ed.) 4th International Kimberlite Conference. Geological Society of Australia Special Publication 23, 220–241.
- Trull, T. W. & Kurz, M. D. (1993). Experimental measurements of  $^3\text{He}$  and  $^4\text{He}$  mobility in olivine and clinopyroxene at magmatic temperatures. *Geochimica et Cosmochimica Acta* 57, 1313–1324.
- Trull, T. W., Kurz, M. D. & Jenkins, W. J. (1991). Diffusion of cosmogenic  $^3\text{He}$  in olivine and quartz: implications for surface exposure dating. *Earth and Planetary Science Letters* 103, 241–256.
- Wellman, P. (1973). Early Miocene potassium-argon age for the Fitzroy Lamproites of Western Australia. *Journal of the Geological Society of Australia* 19, 471–474.

Zanetti, A., Tiepolo, M., Oberti, R. & Vannucci, R. (2004). Trace-element partitioning in olivine: Modelling of a complete data set from a synthetic hydrous basanite melt. *Lithos* 75, 39–54.

Zeitler, P. K., Herczeg, A. L., McDougall, I. & Honda, M. (1987). U-Th-He dating of apatite: A potential thermochronometer. *Geochimica et Cosmochimica Acta. JOUR.* 51, 2865–2868.

Ziegler, J. F. (1977). *Helium: stopping powers and ranges in all elemental matter*. New York: Pergamon Press.

## Chapter 7 THESIS CONCLUSIONS

The research discussed in this thesis demonstrates how the availability of accurate age data is critical to understand the geological development of igneous provinces; both by enabling an integrated geochemical and geochronological study towards the cause of volcanism in the Newer Volcanic Province (NVP), SE Australia, as well as by allowing development of new geochronology techniques that will further enhance our understanding of the timescales of igneous and land surface processes. As outlined in Chapter 2; the exact magmatic provenance of the NVP remained enigmatic due to a lack of high-resolution age data. Most of the available data were K-Ar ages; which will only represent geological meaningful ages if samples are unaltered, sample splits for Ar and K analyses are homogenous and the composition of trapped Ar is atmospheric. Furthermore, no attempts were yet made in the literature to interpret the available geochronology in a wider geological context.

New major and trace element as well as Sr, Nd and Pb isotope data on the youngest expression of volcanism in the NVP, which comprises the scoria cones, lava shields and maars of the Newer Cones series, is interpreted in Chapter 3. Here, new geochemical data of the < 1 Ma Newer Cones series is combined with published data on three older volcanic series in the NVP: the lava fields of the ca. 1 – 5 Ma Newer Plains series, the mafic rocks of the ca. 7 Ma Euroa Volcanics series and the central volcanoes of the ca. 95 – 67 Ma Older Volcanics series. It is shown that the geochemical composition of the mantle source and the geodynamic processes driving volcanism dramatically changed over time; caused by melting of various mantle components during the process of edge driven convection of mantle material assisted by shear driven upwelling of magma. It is shown that the Older Volcanics igneous products have geochemical compositions that can be interpreted as being derived from melting a mixture of 10% carbonatite metasomatised vein material of the sub-continental lithospheric mantle during decompression melting with Indian mid ocean ridge basalt. Pb and Nd isotope data shows that the Euroa Volcanics are derived from a magma source with a composition changing from that of the Older Volcanics to that of the Newer Cones. These latter rocks are most likely derived from a more and more depleted source during ongoing thermal erosion; as it is shown that their geochemical composition reflects small degrees (5 – 10%) of partial melting of a depleted, anhydrous, Indian MORB type spinel lherzolite and enriched, hydrous spinel lherzolite metasomatised by alkaline melts. It is furthermore shown that the geochemical composition of the Newer Plains reflects up to 5% crustal contamination.

In Chapter 4 a geochronological framework is presented to further interpret part of the geodynamic processes described in Chapter 3, where 5 new ultra-precise  $^{40}\text{Ar}/^{39}\text{Ar}$  ages of the Newer Plains and over 20 new, ultra-precise  $^{40}\text{Ar}/^{39}\text{Ar}$  ages of the Newer Cones are given. It is shown that ages ranging from 3.8 – 4.3 Ma for Newer Plains samples vertically distributed in two boreholes indicate that the rate of volcanism was higher < 4 Ma, after which it declined throughout the NVP. This is interpreted as the effect of added thermal input to the existing process of edge driven convection by the migration of the Cosgrove track mantle plume along the NVP at that time. Spatial analysis of the distribution of volcanic centres was performed to better interpret the ages of the Newer Cones; which range from 1.9 Ma to 40 ka and show an apparent age trend in the onset of volcanism from east to west throughout the NVP. It is shown that the distribution of the scoria cones, lava shields and maars of the Newer Cones is strongly dependent on the location of underlying basement faults; especially those structures which represent the northerly extension of the major Tasman Fault Zone south of the NVP. Hence, it is suggested in Chapter 4 that the migration of stress caused by sinistral movement along the Tasman Fault Zone was accommodated from east to west throughout the NVP over time; assisting the existing process of edge driven convection with shear driven upwelling by opening existing basement faults facilitating magma ascent.

The Ar isotope system is not only suitable for conventional geochronology, but as  $^{38}\text{Ar}$  is formed by cosmogenic spallation reactions on Ca and K; it promises to be a valuable dating tool to constrain the timescales of land surface processes as well. However, the application of cosmogenic  $^{38}\text{Ar}$  dating on terrestrial rocks is still in its infancy; and Chapter 5 explores the potential of this technique in more detail. Here, four strategically sampled and irradiated pyroxene samples from Mt Elephant in the NVP, SE Australia, yield statistically significant cosmochrons; and a combined geologically meaningful age of  $313 \pm 179$  ka which overlaps with the known eruption age of  $183 \pm 15$  ka. Hence; pyroxene minerals with exposure ages of a few Ma have strong potential as a new dating tool, especially as we show that the current analytical precision that can be achieved with the new generation multi-collector ARGUS VI mass spectrometer on such timescales is better than 5%. However, strategically sampled and irradiated apatite minerals from granite batholiths in West Australia show less potential as a new cosmogenic  $^{38}\text{Ar}$  dating tool; as these suffer from strong natural and reactor-induced Cl contributions on the  $^{38}\text{Ar}$  abundance as well as nucleogenic contributions from high U and Th concentrations in the host rock.

In some cases, the application of conventional geochronology techniques (such as  $^{40}\text{Ar}/^{39}\text{Ar}$ ) is problematic, due to e.g. the alteration of phases, or the absence of suitable phases for dating.

Therefore, new geochronology techniques need to be developed to enable the construction of a geochronological framework for all geological systems. Chapter 6 presents the results of the further development of the (U-Th)/He dating technique on olivine phenocrysts; which are omnipresent in many rocks, relatively resistant to weathering and quantitatively retain He for long periods of time at Earth surface temperatures. The existing methodology was deemed too complex and suffered from ultra-low U and Th abundances in olivine. Here, olivine phenocrysts from K, U and Th-rich Ellendale E9 (West Australia) lamproite yielded three (U-Th)/He ages ranging from  $53.3 \pm 5.0$  Ma to  $18.7 \pm 2.6$  Ma; of which three statistically overlapped with the ultra-precise phlogopite  $^{40}\text{Ar}/^{39}\text{Ar}$  age of  $22.39 \pm 0.02$  Ma obtained during this study. It is proposed that the other three, overestimated (U-Th)/He ages are most likely the result of either sample loss during sample retrieval after degassing or due to volatilization of U and Th during multiple heating steps.

In general; this thesis provides an example of how more accurate geochronology techniques can help to better understand and interpret igneous processes on Earth. It furthermore shows how the analytical precision that can be obtained with the new generation mass spectrometers aids in the development of new geochronology techniques: cosmogenic  $^{38}\text{Ar}$  dating of terrestrial rocks and (U-Th)/He dating of olivine phenocrysts.

## Chapter 8 BIBLIOGRAPHY

- Aciego, S., Kennedy, B. M., DePaolo, D. J., Christensen, J. N. & Hutcheon, I. (2003). U-Th/He age of phenocrystic garnet from the 79 AD eruption of Mt. Vesuvius. *Earth and Planetary Science Letters* **216**, 209–219.
- Aciego, S. M., DePaolo, D. J., Kennedy, B. M., Lamb, M. P., Sims, K. W. W. & Dietrich, W. E. (2007). Combining [3He] cosmogenic dating with U–Th/He eruption ages using olivine in basalt. *Earth and Planetary Science Letters* **254**, 288–302.
- Aciego, S. M., Jourdan, F., DePaolo, D. J., Kennedy, B. M., Renne, P. R. & Sims, K. W. W. (2010). Combined U–Th/He and  $^{40}\text{Ar}/^{39}\text{Ar}$  geochronology of post-shield lavas from the Mauna Kea and Kohala volcanoes, Hawaii. *Geochimica et Cosmochimica Acta*. Elsevier Ltd **74**, 1620–1635.
- Ahluwalia, H. S. (2003). Solar wind modulation of galactic cosmic rays. *Geophysical Research Letters* **30**, 1133.
- Aivazpourporgou, S., Thiel, S., Hayman, P. C., Moresi, L. N. & Heinson, G. (2015). Decompression melting driving intraplate volcanism in Australia: Evidence from magnetotelluric sounding. *Geophysical Research Letters* **42**, 1–9.
- Aziz-ur-Rahman & McDougall, I. (1972). Potassium-Argon ages on the Newer Volcanics of Victoria. *Proceedings of the Royal Society of Victoria* **85**.
- Baker, J., Peate, D., Waight, T. & Meyzen, C. (2004). Pb isotopic analysis of standards and samples using a  $^{207}\text{Pb}$ - $^{204}\text{Pb}$  double spike and thallium to correct for mass bias with a double-focusing MC-ICPMS. *Chemical Geology* **211**, 275–303.
- Ballentine, C. J. & Burnard, P. G. (2002). Production, Release and Transport of Noble Gases in the Continental Crust. *Reviews in Mineralogy and Geochemistry* **47**, 481–538.
- Beattie, P. (1993). The generation of uranium series disequilibria by partial melting of spinel peridotite: constraints from partitioning studies. *Earth and Planetary Science Letters* **117**, 379–391.
- Beggan, C. & Hamilton, C. W. (2010). New image processing software for analyzing object size-frequency distributions, geometry, orientation, and spatial distribution. *Computers and Geosciences* **36**, 539–549.

- Bergman, S. C. (1987). Lamproites and other potassium-rich igneous rocks: a review of their occurrence, mineralogy and geochemistry. *Geological Society, London, Special Publications* **30**, 103–190.
- Bierman, P. R. & Caffee, M. (2002). Cosmogenic exposure and erosion history of Australian bedrock landforms. *Bulletin of the Geological Society of America* **114**, 787–803.
- Bishop, M. A. (2007). Point pattern analysis of eruption points for the Mount Gambier volcanic sub-province: A quantitative geographical approach to the understanding of volcano distribution. *Area* **39**, 230–241.
- Blackburn, G., Allison, G. B. & Leaney, F. W. J. (1982). Further evidence on the age of tuff at Mt Gambier, South Australia. *Transactions of the Royal Society of South Australia* **106**, 163–167.
- Blackburn, T. J., Stockli, D. F. & Walker, J. D. (2007). Magnetite (U-Th)/He dating and its application to the geochronology of intermediate to mafic volcanic rocks. *Earth and Planetary Science Letters* **259**, 360–371.
- Blard, P.-H. & Farley, K. A. (2008). The influence of radiogenic  $^4\text{He}$  on cosmogenic  $^3\text{He}$  determinations in volcanic olivine and pyroxene. *Earth and Planetary Science Letters*. Elsevier B.V. **276**, 20–29.
- Blard, P.-H., Puchol, N. & Farley, K. A. (2008). Constraints on the loss of matrix-sited helium during vacuum crushing of mafic phenocrysts. *Geochimica et Cosmochimica Acta* **72**, 3788–3803.
- Bohrson, W. A. & Spera, F. J. (2001). Energy-Constrained Open-System Magmatic Processes II : Application of Energy- Constrained Assimilation – Fractional Crystallization (EC-AFC) Model to Magmatic Systems. *Journal of Petrology* **42**, 1019–1041.
- Boyce, J. (2013). The Newer Volcanics Province of southeastern Australia: a new classification scheme and distribution map for eruption centres. *Australian Journal of Earth Sciences* **60**, 449–462.
- Boyce, J. A., Nicholls, I. A., Keays, R. R. & Hayman, P. C. (2015). Composition and volatile contents of parental magmas of Mt. Rouse, a polymagmatic volcano in the Newer Volcanics intraplate basaltic province, SE Australia. *Contributions to Mineralogy and Petrology* **169**, 1–21.
- Boyce, J., Keays, R. R., Nicholls, I. A. & Hayman, P. (2014). Eruption centres of the Hamilton area of the Newer Volcanics Province, Victoria, Australia: pinpointing volcanoes from a multifaceted

- approach to landform mapping. *Australian Journal of Earth Sciences* 1–20.
- Brenna, M., Cronin, S. J., Smith, I. E. M., Sohn, Y. K. & Németh, K. (2010). Mechanisms driving polymagmatic activity at a monogenetic volcano, Udo, Jeju Island, South Korea. *Contributions to Mineralogy and Petrology* **160**, 931–950.
- Brook, E. J., Brown, E. T., Kurz, M. D., Ackert Jr, R. P., Raisbeck, G. M. & Yiou, F. (1995). Constraints on Age, Erosion, and Uplift of Neogene Glacial Deposits in the Transantarctic Mountains Determined From in-Situ Cosmogenic Be-10 and Al-26. *Geology* **23**, 1063–1066.
- Carslaw, K. S., Harrison, R. G. & Kirkby, J. (2002). Cosmic Rays, Clouds, and Climate. *Science* **298**, 1732–1737.
- Cartwright, I., Weaver, T., Tweed, S., Ahearne, D., Cooper, M., Czapnik, K. & Tranter, J. (2002). Stable isotope geochemistry of cold CO<sub>2</sub>-bearing mineral spring waters, Daylesford, Victoria, Australia: Sources of gas and water and links with waning volcanism. *Chemical Geology* **185**, 71–91.
- Cassata, W. S. & Renne, P. R. (2013). Kinetics of argon diffusion in calcite. *Chemie der Erde - Geochemistry* **73**, 113–115.
- Cayley, R. A. *et al.* (2011). Crustal architecture of central Victoria: results from the 2006 deep crustal reflection seismic survey. *Australian Journal of Earth Sciences* **58**, 113–156.
- Cayley, R. A. (2011). Exotic crustal block accretion to the eastern Gondwanaland margin in the Late Cambrian-Tasmania, the Selwyn Block, and implications for the Cambrian-Silurian evolution of the Ross, Delamerian, and Lachlan orogens. *Gondwana Research*. Elsevier B.V. **19**, 628–649.
- Cebriá, J. M., Martín-Escorza, C., López-Ruiz, J., Morán-Zenteno, D. J. & Martiny, B. M. (2011). Numerical recognition of alignments in monogenetic volcanic areas: Examples from the Michoacán-Guanajuato Volcanic Field in Mexico and Calatrava in Spain. *Journal of Volcanology and Geothermal Research*. Elsevier B.V. **201**, 73–82.
- Chiaradia, M., Muntener, O. & Beate, B. (2011). Enriched Basaltic Andesites from Mid-crustal Fractional Crystallization, Recharge, and Assimilation (Pilavo Volcano, Western Cordillera of Ecuador). *Journal of Petrology* **52**, 1107–1141.
- Clark, P. J. & Evans, F. C. (1954). Distance to Nearest Neighbor as a Measure of Spatial Relationships



- in Populations. *Ecology* **35**, 445–453.
- Cloetingh, S., Ziegler, P. A., Beekman, F., Andriessen, P. A. M., Hardebol, N. & Dezes, P. (2005). Intraplate deformation and 3D rheological structure of the Rhine Rift System and adjacent areas of the northern Alpine foreland. *International Journal of Earth Sciences* **94**, 758–778.
- Cohen, B. A., Snyder, G. A., Hall, C. M., Taylor, L. A. & Nazarov, M. A. (2001). Argon-40-argon-39 chronology and petrogenesis along the eastern limb of the Moon from Luna 16, 20 and 24 samples. *Meteoritics and Planetary Science* **1366**, 1345–1366.
- Cohen, B. E. (2007). High-Resolution  $^{40}\text{Ar}/^{39}\text{Ar}$  geochronology of intraplate volcanism in eastern Australia. University of Queensland.
- Compston, W. & Pidgeon, R. T. (1986). Jack Hills, evidence of more very old detrital zircons in Western Australia. *Nature* **321**, 766–769.
- Conrad, C. P., Bianco, T. A., Smith, E. I. & Wessel, P. (2011). Patterns of intraplate volcanism controlled by asthenospheric shear. *Nature Geoscience*. Nature Publishing Group **4**, 317–321.
- Conrad, C. P., Wu, B., Smith, E. I., Bianco, T. A. & Tibbetts, A. (2010). Shear-driven upwelling induced by lateral viscosity variations and asthenospheric shear: A mechanism for intraplate volcanism. *Physics of the Earth and Planetary Interiors* **178**, 162–175.
- Crowley, G. M. & Kershaw, A. P. (1994). Late Quaternary environmental change and human impact around Lake Bolac, Western Victoria, Australia. *Journal of Quaternary Science* **9**, 367–377.
- Cvetković, V., Prelević, D., Downes, H., Jovanović, M., Vaselli, O. & Pécskay, Z. (2004). Origin and geodynamic significance of Tertiary postcollisional basaltic magmatism in Serbia (central Balkan Peninsula). *Lithos* **73**, 161–186.
- Danišík, M., Evans, N. J., Ramanaidou, E. R., McDonald, B. J., Mayers, C. & McInnes, B. I. A. (2013). (U-Th)/He chronology of the Robe River channel iron deposits, Hamersley Province, Western Australia. *Chemical Geology* **354**, 150–162.
- Danišík, M., Shane, P., Schmitt, A. K., Hogg, A., Santos, G. M., Storm, S., Evans, N. J., Fifield, L. K. & Lindsay, J. M. (2012a). Re-anchoring the late Pleistocene tephrochronology of New Zealand based on concordant radiocarbon ages and combined  $^{238}\text{U}/^{230}\text{Th}$  disequilibrium and (U-Th)/He zircon ages. *Earth and Planetary Science Letters* **349–350**, 240–250.
- Danišík, M., Štěpančíková, P. & Evans, N. J. (2012b). Constraining long-term denudation and

- faulting history in intraplate regions by multisystem thermochronology: An example of the Sudetic Marginal Fault (Bohemian Massif, central Europe). *Tectonics* **31**, 1–19.
- Davies, D. R. & Rawlinson, N. (2014). On the origin of recent intraplate volcanism in Australia. *Geology* 1–4.
- Davies, D. R., Rawlinson, N., Iaffaldano, G. & Campbell, I. H. (2015). Lithospheric controls on magma composition along Earth's longest continental hotspot track. *Nature*.
- Day, R. A. (1983). *Petrology and Geochemistry of the Older Volcanics, Victoria: distribution, characterization, and petrogenesis*. Monash University, Clayton, Victoria.
- Day, R. A. (1989). East Australian Volcanic Geology; Victoria and South Australia. In: Johnson, R. W. (ed.) *Intraplate volcanism of Eastern Australia and New Zealand*. Australian Academy of Science, 132–142.
- Demidjuk, Z., Turner, S., Sandiford, M., George, R., Foden, J. & Etheridge, M. (2007). U-series isotope and geodynamic constraints on mantle melting processes beneath the Newer Volcanic Province in South Australia. *Earth and Planetary Science Letters* **261**, 517–533.
- Dep, L., Elmore, D., Fabryka-Martin, J., Masarik, J. & Reedy, R. C. (1994). Production rate systematics of in-situ-produced cosmogenic nuclides in terrestrial rocks: Monte Carlo approach of investigating  $^{35}\text{Cl}$  ( $n, \gamma$ )  $^{36}\text{Cl}$ . *Nuclear Instruments and Methods in Physics Research Section B: Beam Interactions with Materials and Atoms* **92**, 321–325.
- Dickinson, J. A., Wallace, M. W., Holdgate, G. R., Gallagher, S. J. & Thomas, L. (2002). Origin and Timing of the Miocene-Pliocene Unconformity in Southeast Australia. *Journal of Sedimentary Research* **72**, 288–303.
- Duggen, S. (2005). Post-Collisional Transition from Subduction- to Intraplate-type Magmatism in the Westernmost Mediterranean: Evidence for Continental-Edge Delamination of Subcontinental Lithosphere. *Journal of Petrology* **46**, 1155–1201.
- Dunai, T. J. (2000). Scaling factors for production rates of in situ production cosmogenic nuclides: a critical reevaluation. *Earth and Planetary Science Letters* **176**, 157–169.
- Dunai, T. J. (2010). *Cosmogenic Nuclides, Principles, Concepts and Applications in the Earth Surface Sciences*. Cambridge University Press.
- Dunai, T. J. & Roselieb, K. (1996). Sorption and diffusion of helium in garnet: implications for

- volatile tracing and dating. *Earth and Planetary Science Letters* **139**, 411–421.
- Edney, P. A., Kershaw, A. P. & De Deckker, P. (1990). A late Pleistocene and Holocene vegetation and environmental record from Lake Wangoom, Western Plains of Victoria, Australia. *Palaeogeography, Palaeoclimatology, Palaeoecology* **80**, 325–343.
- Eikenberg, J., Signer, P. & Wieler, R. (1993). U-Xe, U-Kr, and U-Pb systematics for dating uranium minerals and investigations of the production of nucleogenic neon and argon. *Geochimica et Cosmochimica Acta* **57**, 1053–1069.
- Ellis, D. J. (1976). High pressure cognate inclusions in the Newer Volcanics of Victoria. *Contributions to Mineralogy and Petrology* **58**, 149–180.
- Evans, N. J., Byrne, J. P., Keegan, J. T. & Dotter, L. E. (2005a). Determination of Uranium and Thorium in Zircon, Apatite, and Fluorite: Application to Laser (U-Th)/He Thermochronology. *Journal of Analytical Chemistry* **60**, 1159–1165.
- Evans, N. J., McInnes, B. I. A., McDonald, B. J., Danišik, M., Jourdan, F., Mayers, C., Thern, E. & Corbett, D. (2012). Emplacement age and thermal footprint of the diamondiferous Ellendale E9 lamproite pipe, Western Australia. *Mineralium Deposita* **48**, 413–421.
- Evans, N. J., Wilson, N. S. F., Cline, J. S., McInnes, B. I. A. & Byrne, J. (2005b). Fluorite (U-Th)/He thermochronology: Constraints on the low temperature history of Yucca Mountain, Nevada. *Applied Geochemistry* **20**, 1099–1105.
- Ewart, A. (2004). Petrology and Geochemistry of Early Cretaceous Bimodal Continental Flood Volcanism of the NW Etendeka, Namibia. Part 1: Introduction, Mafic Lavas and Re-evaluation of Mantle Source Components. *Journal of Petrology* **45**, 59–105.
- Farley, K. A. (2002). (U-Th)/He Dating: Techniques, Calibrations, and Applications. *Reviews in Mineralogy and Geochemistry* **47**, 819–844.
- Farley, K. A., Kohn, B. P. & Pillans, B. (2002). The effects of secular disequilibrium on (U-Th)/He systematics and dating of Quaternary volcanic zircon and apatite. *Earth and Planetary Science Letters* **201**, 117–125.
- Farley, K. A., Wolf, R. A. & Silver, L. T. (1996). The effects of long alpha-stopping distances on (U-Th)/He ages. *Geochimica et Cosmochimica Acta* **60**, 4223–4229.
- Fishwick, S., Heintz, M., Kennett, B. L. N., Reading, A. M. & Yoshizawa, K. (2008). Steps in

- lithospheric thickness within eastern Australia, evidence from surface wave tomography. *Tectonics* **27**, 1–17.
- Foden, J., Song, S. H., Turner, S., Elburg, M., Smith, P. B., Van der Steldt, B. & Van Penglis, D. (2002). Geochemical evolution of lithospheric mantle beneath S.E. South Australia. *Chemical Geology* **182**, 663–696.
- Foley, S. F. & Jenner, G. A. (2004). Trace element partitioning in lamproitic magmas-the Gausberg olivine leucitite. *Lithos* **75**, 19–38.
- Foley, S. F. & Peccerillo, A. (1992). Potassic and ultrapotassic magmas and their origin. *Lithos* **28**, 181–185.
- Foley, S. F., Yaxley, G. M., Rosenthal, A., Buhre, S., Kiseeva, E. S., Rapp, R. P. & Jacob, D. E. (2009). The composition of near-solidus melts of peridotite in the presence of CO<sub>2</sub> and H<sub>2</sub>O between 40 and 60 kbar. *Lithos*. Elsevier B.V. **112**, 274–283.
- Fraser, K. J., Hawkesworth, C. J., Erlank, A. J., Mitchell, R. H. & Scott-Smith, B. H. (1985). Sr, Nd and Pb isotope and minor element geochemistry of lamproites and kimberlites. *Earth and Planetary Science Letters* **76**, 57–70.
- Frey, F. A. & Green, D. H. (1974). The mineralogy, geochemistry and origin of lherzolite inclusions in Victorian basanites. *Geochimica et Cosmochimica Acta* **38**, 1023–1059.
- Frey, F. A., Green, D. H. & Roy, S. D. (1978). Integrated Models of Basalt Petrogenesis: A Study of Quartz Tholeiites to Olivine Melilitites from South Eastern Australia Utilizing Geochemical and Experimental Petrological Data. *Journal of Petrology* **19**, 463–513.
- Garner, E. L., Murphy, J., Gramlich, J. W., Paulsen, P. J. & Barnes, I. L. (1975). Absolute isotopic abundance ratios and atomic weight of a reference sample of potassium. *Journal of Research of the National Institute of Standards and Technology* **79A**, 713–725.
- Ghiorso, M. S. & Sack, R. O. (1995). Chemical mass transfer in magmatic processes IV. A revised and internally consistent thermodynamic model for the interpolation and extrapolation of liquid-solid equilibria in magmatic systems at elevated temperatures and pressures. *Contributions to Mineralogy and Petrology* **119**, 197–212.
- Gibson, G. M., Totterdell, J. M., White, L. T., Mitchell, C. H., Stacey, A. R., Morse, M. P. & Whitaker, A. (2013). Pre-existing basement structure and its influence on continental rifting and

- fracture zone development along Australia's southern rifted margin. *Journal of the Geological Society* **170**, 365–377.
- Gillen, D., Honda, M., Chivas, A. R., Yatsevich, I., Patterson, D. B. & Carr, P. F. (2010). Cosmogenic  $^{21}\text{Ne}$  exposure dating of young basaltic lava flows from the Newer Volcanic Province, western Victoria, Australia. *Quaternary Geochronology*. Elsevier Ltd **5**, 1–9.
- Gosse, J. C. & Phillips, F. M. (2001). Terrestrial in situ cosmogenic nuclides: theory and application. *Quaternary Science Reviews* **20**, 1475–1560.
- Graeber, F. M., Houseman, G. A. & Greenhalgh, S. A. (2002). Regional teleseismic tomography of the western Lachlan Orogen and the Newer Volcanic Province, southeast Australia. *Geophysical Journal International* **149**, 249–266.
- Gray, C. M. & McDougall, I. (2009). K-Ar geochronology of basalt petrogenesis, Newer Volcanic Province, Victoria. *Australian Journal of Earth Sciences* **56**, 245–258.
- Gray, D. R. *et al.* (2003). Structure, metamorphism, geochronology and tectonics of Palaeozoic rocks - interpreting a complex, long-lived orogenic system. In: Birch, W. D. (ed.) *Geology of Victoria*. Geological Society of Australia, 15–71.
- Griffin, W. L., O'Reilly, S. Y. & Stabel, A. (1988). Mantle metasomatism beneath western Victoria, Australia : II . Isotopic geochemistry. *Geochimica et Cosmochimica Acta* **52**, 449–459.
- Gurnis, M., Müller, R. D. & Moresi, L. N. (1998). Cretaceous Vertical Motion of Australia and the Australian Antarctic Discordance. *Science* **279**, 1499 LP-1504.
- Handler, M. R., Bennett, V. C. & Esat, T. M. (1997). The persistence of off-cratonic lithospheric mantle: Os isotopic systematics of variably metasomatised southeast Australian xenoliths. *Earth and Planetary Science Letters* **151**, 61–75.
- Hare, A. G., Cas, R. A. F., Musgrave, R. & Phillips, D. (2005a). Magnetic and chemical stratigraphy for the Werribee Plains basaltic lava flow-field, Newer Volcanics Province, southeast Australia: implications for eruption frequency. *Australian Journal of Earth Sciences* **52**, 41–57.
- Hare, A. G., Cas, R. A. F., Musgrave, R. & Phillips, D. (2005b). Magnetic and chemical stratigraphy for the Werribee Plains basaltic lava flow-field, Newer Volcanics Province, southeast Australia: implications for eruption frequency. *Australian Journal of Earth Sciences* **52**, 41–57.
- Harle, K. J. (1997). Late Quaternary vegetation and climate change in southeastern Australia:

- palynological evidence from marine core E55-6. *Paleogeography, Paleoclimatology, Paleoecology* **131**, 465–483.
- Harle, K. J., Heijnis, H., Chisari, R., Kershaw, a. P., Zoppi, U. & Jacobsen, G. (2002). A chronology for the long pollen record from Lake Wangoom, western Victoria (Australia) as derived from uranium/thorium disequilibrium dating. *Journal of Quaternary Science* **17**, 707–720.
- Hart, S. R. (1984). He diffusion in olivine. *Earth and Planetary Science Letters* **70**, 297–302.
- Hennesy, J. & Turner, G. (1980).  $^{40}\text{Ar}$ - $^{39}\text{Ar}$  ages and irradiation history of Luna 24 basalts. *Philosophical Transactions of the Royal Society of London. Series A, Mathematical and Physical Sciences.* **297**, 27–39.
- Hillis, R. R., Sandiford, M., Reynolds, S. D. & Quigley, M. C. (2008). Present-day stresses, seismicity and Neogene-to-Recent tectonics of Australia's "passive" margins: intraplate deformation controlled by plate boundary forces. In: Johnson, H., Dore, A. G., Gatliff, R. W., Holdsworth, R., Lundin, E. R. & Ritchie, J. D. (eds) *Geological Society, London, Special Publications*. The Geological Society of London, 71–90.
- Hofmann, A. W., Jochum, K. P., Seufert, M. & White, W. M. (1986). Nb and Pb in oceanic basalts: new constraints on mantle evolution. *Earth and Planetary Science Letters* **79**, 33–45.
- Holcombe, R. (2010). GEOrient - structural geology software. .
- Holt, S. J., Holford, S. P. & Foden, J. (2013). New insights into the magmatic plumbing system of the South Australian Quaternary Basalt province from 3D seismic and geochemical data. *Australian Journal of Earth Sciences* **60**, 797–817.
- House, M. A., Wernicke, B. P. & Farley, K. A. (1998). Dating topography of the Sierra Nevada, California, using apatite (U-Th)/He ages. *Nature* **396**, 66–69.
- Irvine, T. N. & Baragar, W. R. A. (1971). A Guide to the Chemical Classification of the Common Volcanic Rocks. *Canadian Journal of Earth Sciences* **8**, 523–548.
- Irving, A. J. & Green, D. H. (1976). Geochemistry and petrogenesis of the newer basalts of Victoria and South Australia. *Journal of the Geological Society of Australia: An International Geoscience Journal of the Geological Society of Australia* **23**, 45–66.
- Jaques, A. L., Lewis, J. D. & Smith, C. B. (1986). The West Kimberley Province. In: Smith, C. B. (ed.) *The kimberlites and lamproites of Western Australia*. Geological Survey of Western

Australia, 71–125.

- Jaques, A. L. & Milligan, P. R. (2004). Patterns and controls on the distribution of diamondiferous intrusions in Australia. *Lithos* **77**, 783–802.
- Jourdan, F., Féraud, G., Bertrand, H. & Watkeys, M. K. (2007). From flood basalts to the inception of oceanization: Example from the  $^{40}\text{Ar}/^{39}\text{Ar}$  high-resolution picture of the Karoo large igneous province. *Geochemistry, Geophysics, Geosystems* **8**.
- Jourdan, F. & Renne, P. R. (2007). Age calibration of the Fish Canyon sanidine  $^{40}\text{Ar}/^{39}\text{Ar}$  dating standard using primary K–Ar standards. *Geochimica et Cosmochimica Acta* **71**, 387–402.
- Jourdan, F. & Renne, P. R. (2014). Neutron-induced  $^{37}\text{Ar}$  recoil ejection in Ca-rich minerals and implications for  $^{40}\text{Ar}/^{39}\text{Ar}$  dating. *Geological Society, London, Special Publications* **378**, 33–52.
- Jourdan, F., Renne, P. R. & Reimold, W. U. (2009a). An appraisal of the ages of terrestrial impact structures. *Earth and Planetary Science Letters* **286**, 1–13.
- Jourdan, F., Renne, P. R. & Reimold, W. U. (2009b). An appraisal of the ages of terrestrial impact structures. *Earth and Planetary Science Letters*. Elsevier B.V. **286**, 1–13.
- Jourdan, F., Sharp, W. D. & Renne, P. R. (2012).  $^{40}\text{Ar}/^{39}\text{Ar}$  ages for deep (~3.3 km) samples from the Hawaii Scientific Drilling Project, Mauna Kea volcano, Hawaii. *Geochemistry, Geophysics, Geosystems* **13**.
- Kaislaniemi, L. & Van Hunen, J. (2014). Dynamics of lithosphere thinning and mantle melting by edge-driven convection; application to the Moroccan Atlas mountains. *Geochemistry, Geophysics, Geosystems* **15**, 3175–3189.
- Kaneoka, I. (1980). Rare gas isotopes and mass fractionation; an indicator of gas transport into or from a magma. *Earth and Planetary Science Letters* **48**, 284–292.
- Kelley, S. P. (2002). Excess argon in K–Ar and Ar–Ar geochronology. *Chemical Geology* **188**, 1–22.
- Kennedy, T., Jourdan, F., Bevan, A. W. R., Mary Gee, M. A. & Frew, A. (2013). Impact history of the HED parent body(ies) clarified by new  $^{40}\text{Ar}/^{39}\text{Ar}$  analyses of four HED meteorites and one anomalous basaltic achondrite. *Geochimica et Cosmochimica Acta*. Elsevier Ltd **115**, 162–182.

- King, S. D. & Anderson, D. L. (1998). Edge-driven convection. *Earth and Planetary Science Letters* **160**, 289–296.
- Knesel, K. M., Cohen, B. E., Vasconcelos, P. M. & Thiede, D. S. (2008). Rapid change in drift of the Australian plate records collision with Ontong Java plateau. *Nature* **454**, 754–7.
- Knight, K. B. (2006). Argon geochronology. University of California.
- Kohn, B. P., Gleadow, A. J. W., Brown, R. W., Gallagher, K., O’Sullivan, P. B. & Foster, D. A. (2002). Shaping the Australian crust over the last 300 million years: Insights from fission track thermotectonic imaging and denudation studies of key terranes. *Australian Journal of Earth Sciences* **49**, 697–717.
- Koppers, A. A. P. (2002). ArArCALC - software for  $^{40}\text{Ar}/^{39}\text{Ar}$  age calculations. *Computer and Geosciences* **28**, 605–619.
- Kuiper, Y. (2002). The interpretation of inverse isochron diagrams in  $^{40}\text{Ar}/^{39}\text{Ar}$  geochronology. *Earth and Planetary Science Letters* **203**, 499–506.
- Kurz, M. D. (1986). Cosmogenic helium in a terrestrial igneous rock. *Nature* **320**, 435–439.
- Lal, D. (1991). Cosmic ray labeling of erosion surfaces: in situ nuclide production rates and erosion models. *Earth and Planetary Science Letters* **104**, 424–439.
- Lal, D. & Peters, B. (1967). Cosmic Ray Produced Radioactivity on the Earth. In: Sitte, K. (ed.) *Kosmische Strahlung II / Cosmic Rays II*. Berlin, Heidelberg: Springer Berlin Heidelberg, 551–612.
- Lavielle, B., Marti, K., Jeannot, J., Nishiizumi, K. & Caffee, M. W. (1999). The  $^{36}\text{Cl}$  –  $^{36}\text{Ar}$  –  $^{40}\text{K}$  –  $^{41}\text{K}$  records and cosmic ray production rates in iron meteorites. *Earth and Planetary Science Letters* **170**, 93–104.
- Le Bas, M. J., Le Maitre, R. W., Streckeisen, A. & Zanettin, B. (1986). A chemical classification of volcanic rocks based on the total alkali vs. silica diagram. *Journal of Petrology* **27**, 745–750.
- Le Corvec, N., Bebbington, M. S., Lindsay, J. M. & McGee, L. E. (2013a). Age, distance, and geochemical evolution within a monogenetic volcanic field: Analyzing patterns in the Auckland Volcanic Field eruption sequence. *Geochemistry, Geophysics, Geosystems* **14**, 3648–3665.
- Le Corvec, N., Spörli, K. B., Rowland, J. & Lindsay, J. M. (2013b). Spatial distribution and



- alignments of volcanic centers: Clues to the formation of monogenetic volcanic fields. *Earth-Science Reviews*. Elsevier B.V. **124**, 96–114.
- Lee, J. B., Marti, K., Severinghaus, J. P., Kawamura, K., Yoo, H. & Kim, J. S. (2006). A redetermination of the isotopic abundances of atmospheric Ar. *Geochimica et Cosmochimica Acta* **70**, 4507–4512.
- Lesti, C., Giordano, G., Salvini, F. & Cas, R. A. F. (2008). Volcano tectonic setting of the intraplate, Pliocene-Holocene, Newer Volcanic Province (southeast Australia): Role of crustal fracture zones. *Journal of Geophysical Research* **113**.
- Levine, J., Renne, P. R. & Muller, R. A. (2007). Solar and cosmogenic argon in dated lunar impact spherules. *Geochimica et Cosmochimica Acta* **71**, 1624–1635.
- Lippolt, H. J. & Weigel, E. (1988).  $^4\text{He}$  diffusion in  $^{40}\text{Ar}$ -retentive minerals. *Geochimica et Cosmochimica Acta* **52**, 1449–1458.
- Ludwig, K. R. (2012). *User's Manual for Isoplot 3.75. A Geochronological Toolkit for Microsoft Excel*. Berkeley, California.
- Mamyrin, B. A. & Tolstikhin, I. N. (1984). *Helium isotopes in nature*. Elsevier.
- Mark, D. F., Stuart, F. M. & de Podesta, M. (2011). New high-precision measurements of the isotopic composition of atmospheric argon. *Geochimica et Cosmochimica Acta* **75**, 7494–7501.
- Masarik, J. & Beer, J. (1999). Simulation of particle fluxes and cosmogenic nuclide production in the earth atmosphere. *Journal of Geophysical Research* **104**, 12099–12111.
- Masarik, J. & Beer, J. (2009). An updated simulation of particle fluxes and cosmogenic nuclide production in the Earth's atmosphere. *Journal of Geophysical Research: Atmospheres* **114**, 1–9.
- Masarik, J., Emrich, P., Povinec, P. & Tokar, S. (1986). Monte Carlo simulation of cosmogenic nuclide production. *Nuclear Instruments and Methods in Physics Research* **B17**, 483–489.
- Masarik, J. & Reedy, R. C. (1995). Terrestrial cosmogenic-nuclide production systematics calculated from numerical simulations. *Earth and Planetary Science Letters* **136**, 381–395.
- Matchan, E. L., Joyce, E. B. & Phillips, D. (2016). A new  $^{40}\text{Ar}/^{39}\text{Ar}$  eruption age for the Mount Widderin volcano, Newer Volcanic Province, Australia, with implications for eruption

- frequency in the region. *Australian Journal of Earth Sciences* **99**, 1–12.
- Matchan, E. L. & Phillips, D. (2011). New  $^{40}\text{Ar}/^{39}\text{Ar}$  ages for selected young (<1 Ma) basalt flows of the Newer Volcanic Province, southeastern Australia. *Quaternary Geochronology*. Elsevier B.V **6**, 356–368.
- Matchan, E. L. & Phillips, D. (2014). High precision multi-collector  $^{40}\text{Ar}/^{39}\text{Ar}$  dating of young basalts: Mount Rouse volcano (SE Australia) revisited. *Quaternary Geochronology*. Elsevier Ltd.
- Matchan, E. L., Phillips, D., Jourdan, F. & Oostingh, K. F. (n.d.). New insights into earliest Aboriginal presence in SE Australia from high-precision  $^{40}\text{Ar}/^{39}\text{Ar}$  dating of young volcanic eruptions. *Nature Letters*.
- Mazzarini, F. (2004). Volcanic vent self-similar clustering and crustal thickness in the northern Main Ethiopian Rift. *Geophysical Research Letters* **31**, 1–4.
- McBride, J. S., Lambert, D. D., Nicholls, I. A. & Price, R. C. (2001). Osmium Isotopic Evidence for Crust – Mantle Interaction in the Genesis of Continental Intraplate Basalts from the Newer Volcanics Province, Southeastern Australia. *Journal of Petrology* **42**, 1197–1218.
- McCulloch, M. T., Jaques, A. L., Nelson, D. R. & Lewis, J. D. (1983). Nd and Sr isotopes in kimberlites and lamproites from Western Australia; an enriched mantle origin. *Nature Letters* **302**.
- McDonough, W. F. & McCulloch, M. T. (1987). The southeast Australian lithospheric mantle: isotopic and geochemical constraints on its growth and evolution. *Earth and Planetary Science Letters* **86**, 327–340.
- McDonough, W. F., McCulloch, M. T. & Sun, S. S. (1985). Isotopic and geochemical systematics in Tertiary-Recent basalts from southeastern Australia and implications for the evolution of the sub-continental lithosphere. *Geochimica et Cosmochimica Acta* **49**, 2051–2067.
- McDougall, I., Allsopp, H. L. & Chamalaun, F. H. (1966). Isotopic dating of the newer volcanics of Victoria, Australia, and geomagnetic polarity epochs. *Journal of Geophysical Research* **71**, 6107–6118.
- McDougall, I. & Harrison, T. M. (1999). *Geochronology and thermochronology by the  $^{40}\text{Ar}/^{39}\text{Ar}$  method*. Oxford University Press.

- McDougall, I. & Roksandic, Z. (1974). Total fusion  $^{40}\text{Ar}/^{39}\text{Ar}$  ages using Hifar reactor. *Journal of the Geological Society of Australia*. Taylor & Francis **21**, 81–89.
- McGee, L. E., Beier, C., Smith, I. E. M. & Turner, S. P. (2011). Dynamics of melting beneath a small-scale basaltic system: A U-Th-Ra study from Rangitoto volcano, Auckland volcanic field, New Zealand. *Contributions to Mineralogy and Petrology* **162**, 547–563.
- McGee, L. E., Smith, I. E. M., Millet, M. A., Handley, H. K. & Lindsay, J. M. (2013). Asthenospheric control of melting processes in a monogenetic basaltic system: A case study of the Auckland volcanic field, New Zealand. *Journal of Petrology* **54**, 2125–2153.
- McInnes, B. I. A., Evans, N. J., McDonald, B. J., Kinny, P. D. & Jakimowicz, J. (2009). Zircon U–Th–Pb–He double dating of the Merlin kimberlite field, Northern Territory, Australia. *Lithos*. Elsevier B.V. **112**, 592–599.
- McKenzie, D. & O’Nions, R. K. (1991). Partial Melt Distributions from Inversion of Rare Earth Element Concentrations. *Journal of Petrology* **32**, 1021–1091.
- Merrihue, C. & Turner, G. (1966). Potassium-Argon dating by activation with fast neutrons. *Journal of Geophysical Research* **71**, 2852–2857.
- Min, K., Reiners, P. W., Wolff, J. A., Mundil, R. & Winters, R. L. (2006). (U-Th)/He dating of volcanic phenocrysts with high-U-Th inclusions, Jemez Volcanic Field, New Mexico. *Chemical Geology* **227**, 223–235.
- Mitchell, R. H. & Bergman, S. C. (1991). *Petrology of Lamproites*. Plenum Press, New York.
- Mohr, P. A. & Wood, C. A. (1976). Volcano spacings and lithospheric attenuation in the Eastern Rift of Africa. *Earth and Planetary Science Letters* **33**, 126–144.
- Mooney, S. (1997). A fine-resolution palaeoclimatic reconstruction of the last 2000 years, from Lake Keilambete, southeastern Australia. *The Holocene* **7**, 139–149.
- Morgan, L. E., Renne, P. R., Taylor, R. E. & WoldeGabriel, G. (2009). Archaeological age constraints from extrusion ages of obsidian: Examples from the Middle Awash, Ethiopia. *Quaternary Geochronology*. Elsevier Ltd **4**, 193–203.
- Morgan, W. J. (1972). Deep mantle convection plumes and plate motions. *The American Association of Petroleum Geologist Bulletin* **2**, 203–213.

- Nelson, D. R., McCulloch, M. T. & Sun, S. S. (1986). The origins of ultrapotassic rocks as inferred from Sr, Nd and Pb isotopes. *Geochimica et Cosmochimica Acta* **50**, 231–245.
- Niedermann, S. (2002). Cosmic-Ray-Produced noble gases in terrestrial rocks: dating tools for surface processes. *Reviews in Mineralogy and Geochemistry* **47**, 731–784.
- Niedermann, S., Schaefer, J., Wieler, R. & Naumann, R. (2007). The production rate of cosmogenic  $^{38}\text{Ar}$  from calcium in terrestrial pyroxene. *Earth and Planetary Science Letters* **257**, 596–608.
- O'Reilly, S. Y. & Griffin, W. L. (1984). Sr isotopic heterogeneity in primitive basaltic rocks, southeastern Australia: correlation with mantle metasomatism. *Contributions to Mineralogy and Petrology* **87**, 220–230.
- O'Reilly, S. Y. & Griffin, W. L. (1988). Mantle metasomatism beneath western Victoria, Australia: I. Metasomatic processes in Cr-diopside lherzolites. *Geochimica et Cosmochimica Acta* **52**, 433–447.
- O'Reilly, S. Y. & Zhang, M. (1995). Geochemical characteristics of lava-field basalts from eastern Australia and inferred sources: connections with the subcontinental lithospheric mantle? *Contributions to Mineralogy and Petrology* **121**, 148–170.
- Onstott, T. C., Miller, M. L., Ewing, R. C., Arnold, G. W. & Walsh, D. S. (1995). Recoil refinements: Implications for the  $^{40}\text{Ar}/^{39}\text{Ar}$  dating technique. *Geochimica et Cosmochimica Acta* **59**, 1821–1834.
- Oostingh, K. F., Jourdan, F., Matchan, E. L. & Phillips, D. (2017).  $^{40}\text{Ar}/^{39}\text{Ar}$  geochronology reveals rapid change from plume-assisted to stress-dependent volcanism in the Newer Volcanic Province, SE Australia. *Geochemistry, Geophysics, Geosystems* **18**, 1065–1089.
- Oostingh, K. F., Jourdan, F., Merle, R. & Chiaradia, M. (2016). Spatio-temporal Geochemical Evolution of the SE Australian Upper Mantle Deciphered from the Sr, Nd and Pb Isotope Compositions of Cenozoic Intraplate Volcanic Rocks. *Journal of Petrology* **57**, 1509–1530.
- Oostingh, K. F., Jourdan, F., Phillips, D. & Matchan, E. L. (2015). Ultra-precise  $^{40}\text{Ar}/^{39}\text{Ar}$  geochronology and  $^{38}\text{Ar}$  exposure dating on young basalts from the Newer Volcanic Province, Australia. *Goldschmidt 2015 Conference Abstracts*.
- Patterson, C. (1956). Age of meteorites and the earth. *Geochimica et Cosmochimica Acta*. Pergamon **10**, 230–237.

- Paul, B., Hergt, J. M. & Woodhead, J. D. (2005). Mantle heterogeneity beneath the Cenozoic volcanic provinces of central Victoria inferred from trace-element and Sr, Nd, Pb and Hf isotope data. *Australian Journal of Earth Sciences* **52**, 243–260.
- Paulsen, T. S. & Wilson, T. J. (2010). New criteria for systematic mapping and reliability assessment of monogenetic volcanic vent alignments and elongate volcanic vents for crustal stress analyses. *Tectonophysics*. Elsevier B.V. **482**, 16–28.
- Peucker-Ehrenbrink, B. & Jahn, B. (2001). Rhenium-osmium isotope systematics and platinum group element concentrations: Loess and the upper continental crust. *Geochemistry Geophysics Geosystems* **2**.
- Phillips, D. & Matchan, E. L. (2013). Ultra-high precision  $^{40}\text{Ar}/^{39}\text{Ar}$  ages for Fish Canyon Tuff and Alder Creek Rhyolite sanidine: New dating standards required? *Geochimica et Cosmochimica Acta*. Elsevier Ltd **121**, 229–239.
- Pi, T., Solé, J. & Taran, Y. (2005). (U–Th)/He dating of fluorite: application to the La Azul fluor spar deposit in the Taxco mining district, Mexico. *Mineralium Deposita* **39**, 976–982.
- Powell, W., Zhang, M., O'Reilly, S. Y. & Tiepolo, M. (2004). Mantle amphibole trace-element and isotopic signatures trace multiple metasomatic episodes in lithospheric mantle, western Victoria, Australia. *Lithos* **75**, 141–171.
- Prelević, D. (2005). Tertiary Ultrapotassic Volcanism in Serbia: Constraints on Petrogenesis and Mantle Source Characteristics. *Journal of Petrology* **46**, 1443–1487.
- Prelević, D., Foley, S. F., Romer, R. L. & Conticelli, S. (2008). Mediterranean Tertiary lamproites derived from multiple source components in postcollisional geodynamics. *Geochimica et Cosmochimica Acta* **72**, 2125–2156.
- Prelević, D., Stracke, A., Foley, S. F., Romer, R. L. & Conticelli, S. (2010). Hf isotope compositions of Mediterranean lamproites: Mixing of melts from asthenosphere and crustally contaminated mantle lithosphere. *Lithos* **119**, 297–312.
- Price, R. C., Gray, C. M. & Frey, F. A. (1997). Strontium isotopic and trace element heterogeneity in the plains basalts of the Newer Volcanic Province, Victoria, Australia. *Geochimica et Cosmochimica Acta* **61**, 171–192.
- Price, R. C., Nicholls, I. A. & Day, A. (2014). Lithospheric influences on magma compositions of

- late Mesozoic and Cenozoic intraplate basalts (the Older Volcanics) of Victoria, south-eastern Australia. *Lithos*. Elsevier B.V. **206–207**, 179–200.
- Price, R. C., Nicholls, I. A. & Gray, C. M. (2003). Cainozoic igneous activity. In: Birch, W. D. (ed.) *Geology of Victoria*. Geological Society of Australia (Victoria Division), 361–375.
- Rawlinson, N., Kennett, B. L. N., Salmon, M. & Glen, R. A. (2015a). Origin of Lateral Heterogeneities in the Upper Mantle Beneath South-east Australia from Seismic Tomography. In: Khan, A. & Deschamps, F. (eds) *The Earth's Heterogeneous Mantle*. Springer Geophysics, 47–78.
- Rawlinson, N., Pilia, S., Young, M., Salmon, M. & Yang, Y. (2015b). Crust and upper mantle structure beneath southeast Australia from ambient noise and teleseismic tomography. *Tectonophysics*. Elsevier B.V.
- Rehkamper, M. & Hofmann, A. W. (1997). Recycled ocean crust and sediment in Indian Ocean MORB. *Earth and Planetary Science Letters* **147**, 93–106.
- Reiners, P. W. & Farley, K. A. (1999). Helium diffusion and (U–Th)/He thermochronometry of titanite. *Geochimica et Cosmochimica Acta* **63**, 3845–3859.
- Renne, P. R., Balco, G., Ludwig, K. R., Mundil, R. & Min, K. (2011). Response to the comment by W.H. Schwarz et al. on “Joint determination of 40K decay constants and 40Ar\*/40K for the Fish Canyon sanidine standard, and improved accuracy for 40Ar/39Ar geochronology” by P.R. Renne et al. (2010). *Geochimica et Cosmochimica Acta*. Elsevier Ltd **75**, 5097–5100.
- Renne, P. R., Cassata, W. S. & Morgan, L. E. (2009). The isotopic composition of atmospheric argon and 40Ar/39Ar geochronology: Time for a change? *Quaternary Geochronology* **4**, 288–298.
- Renne, P. R., Farley, K. A., Becker, T. A. & Sharp, W. D. (2001). Terrestrial cosmogenic argon. *Earth and Planetary Science Letters* **188**, 435–440.
- Renne, P. R., Knight, K. B., Nomade, S., Leung, K. N. & Lou, T. P. (2005). Application of deuterium-deuterium (D-D) fusion neutrons to 40Ar/39Ar geochronology. *Applied Radiation and Isotopes* **62**, 25–32.
- Renne, P. R., Mundil, R., Balco, G., Min, K. & Ludwig, K. R. (2010). Joint determination of 40K decay constants and 40Ar\*/40K for the Fish Canyon sanidine standard, and improved accuracy for 40Ar/39Ar geochronology. *Geochimica et Cosmochimica Acta* **74**, 5349–5367.

- Renne, P. R. & Norman, E. B. (2001). Determination of the half-life of  $^{37}\text{Ar}$  by mass spectrometry. *Physical Review C*. American Physical Society **63**.
- Renne, P. R., Swisher, C. C., Deino, A. L., Karner, D. B., Owens, T. L. & DePaolo, D. J. (1998). Intercalibration of standards, absolute ages and uncertainties in  $^{40}\text{Ar} / ^{39}\text{Ar}$  dating. *Chemical Geology (Isotope Geoscience Section)* **145**, 117–152.
- Roddick, J. C. (1978). The application of isochron diagrams in  $^{40}\text{Ar}/^{39}\text{Ar}$  dating: a discussion. *Earth and Planetary Science Letters* **41**, 233–244.
- Rosengren, N. (1994). *Eruption points of the Newer Volcanics Province - an inventory and evaluation of scientific significance*. Melbourne.
- Sandiford, M. (2003). Neotectonics of southeastern Australia; linking Quaternary faulting record with seismicity and in situ stress. *Geological Society of Australia Special Publication* **22**, 101–113.
- Sandiford, M. (2007). The tilting continent: A new constraint on the dynamic topographic field from Australia. *Earth and Planetary Science Letters* **261**, 152–163.
- Sandiford, M., Wallace, M. & Coblenz, D. D. (2004). Origin of the in situ stress field in south-eastern Australia. *Basin Research* **16**, 325–338.
- Sella, G. F., Dixon, T. H. & Mao, A. (2002). REVEL: A model for Recent plate velocities from space geodesy. *Journal of Geophysical Research* **107**.
- Sha, L.-K. & Chappell, B. W. (1999). Apatite chemical composition, determined by electron microprobe and laser-ablation inductively coupled plasma mass spectrometry, as a probe into granite petrogenesis. *Geochimica et Cosmochimica Acta* **63**, 3861–3881.
- Shaw, D. M. (1970). Trace element fractionation during anatexis. *Geochimica et Cosmochimica Acta* **34**, 237–243.
- Shuster, D. L. & Cassata, W. S. (2015). Paleotemperatures at the lunar surfaces from open system behavior of cosmogenic  $^{38}\text{Ar}$  and radiogenic  $^{40}\text{Ar}$ . *Geochimica et Cosmochimica Acta*. Elsevier Ltd **155**, 154–171.
- Singleton, O. P. & Joyce, E. B. (1970). *Catalogue of the post-Miocene volcanoes of Victoria, Australia. Prepared for the IAVCEI Catalogue of post-Miocene Volcanoes of the World.* .
- Singleton, O. P., McDougall, I. & Mallett, C. W. (1976). The Pliocene-Pleistocene boundary in

- Southeastern Australia. *Journal of the Geological Society of Australia*. Taylor & Francis **23**, 299–311.
- Smith, B. W. & Prescott, J. R. (1987). Thermoluminescence dating of the eruption at Mt Schank, South Australia. *Australian Journal of Earth Sciences* **34**, 335–342.
- Sobolev, A. V., Sobolev, N. V., Smith, C. B. & Dubessy, J. (1989). Fluid and melt compositions in lamproites and kimberlites based on the study of inclusions in olivine. In: Ross, J. (ed.) *4th International Kimberlite Conference*. Geological Society of Australia Special Publication 23, 220–241.
- Spera, F. J. (2001). Energy-Constrained Open-System Magmatic Processes I: General Model and Energy-Constrained Assimilation and Fractional Crystallization (EC-AFC) Formulation. *Journal of Petrology* **42**, 999–1018.
- Stolz, A. J. & Davies, G. R. (1988). Chemical and isotopic evidence from spinel lherzolite xenoliths from episodic metasomatism of the upper mantle beneath southeastern Australia. *Journal of Petrology Spec. Vol.*, 303–330.
- Stone, J., Peterson, J. A., Fifield, L. K. & Cresswell, R. G. (1997). Cosmogenic Chlorine-36 exposure ages for two basalt flows in the Newer Volcanics Province, Western Victoria. *Proceedings of the Royal Society of Victoria* **109**, 121–131.
- Stracke, A., Bizimis, M. & Salters, V. J. M. (2003). Recycling oceanic crust: Quantitative constraints. *Geochemistry, Geophysics, Geosystems* **4**.
- Sun, S. S. & McDonough, W. F. (1989). Chemical and isotopic systematics of oceanic basalts: implications for mantle composition and processes. *Geological Society, London, Special Publications* **42**, 313–345.
- Sutherland, F. L., Graham, I. T., Hollis, J. D., Meffre, S., Zwingmann, H., Jourdan, F. & Pogson, R. E. (2014). Multiple felsic events within post-10 Ma volcanism, Southeast Australia: inputs in appraising proposed magmatic models. *Australian Journal of Earth Sciences*. Taylor & Francis **61**, 241–267.
- Tainton, K. M. & McKenzie, D. (1994). The Generation of Kimberlites, Lamproites, and their Source Rocks. *Journal of Petrology* **35**, 787–817.
- Tanaka, T., Togashi, S., Kamioka, H., Amakawa, H., Kagami, H. & Hamamoto, T. (2000). JNdi-1: a



- neodymium isotopic reference in consistency with LaJolla neodymium. *Chemical Geology* **168**, 279–281.
- Taylor, S. R. & McLennan, S. M. (1995). The geochemical evolution of the continental crust. *Reviews of Geophysics* **33**, 241–265.
- Tedford, R. H., Banks, M. R., Kemp, N. R., McDougall, I. A. & Sutherland, F. L. (1975). Recognition of the oldest known fossil marsupials from Australia. *Nature* **255**, 141–142.
- Thomson, W. (1899). The age of the Earth as an abode fitted for life. *Journal of the Transactions of the Victoria Institute* **31**, 11–38.
- Trull, T. W. & Kurz, M. D. (1993). Experimental measurements of  $^3\text{He}$  and  $^4\text{He}$  mobility in olivine and clinopyroxene at magmatic temperatures. *Geochimica et Cosmochimica Acta* **57**, 1313–1324.
- Trull, T. W., Kurz, M. D. & Jenkins, W. J. (1991). Diffusion of cosmogenic  $^3\text{He}$  in olivine and quartz : implications for surface exposure dating. *Earth and Planetary Science Letters* **103**, 241–256.
- Turner, G. (1971). Ar-40-Ar-39 ages from the lunar maria. *Earth and Planetary Science Letters* **11**, 169–191.
- Turner, G., Huneke, J. C., Podosek, F. A. & Wasserburg, G. J. (1971).  $^{40}\text{Ar}$ - $^{39}\text{Ar}$  ages and cosmic ray exposure of Apollo-14 samples. *Earth and Planetary Science Letters* **12**, 19–35.
- Twidale, C. R. & Bourne, J. A. (1998). Origin and age of bornhardts, Southwest Western Australia. *Australian Journal of Earth Sciences* **45**, 903–914.
- Van Otterloo, J., Cas, R. A. F. & Sheard, M. J. (2013). Eruption processes and deposit characteristics at the monogenetic Mt. Gambier Volcanic Complex, SE Australia: implications for alternating magmatic and phreatomagmatic activity. *Bulletin of Volcanology* **75**, 1–21.
- Van Otterloo, J., Raveggi, M., Cas, R. A. F. & Maas, R. (2014). Polymagmatic Activity at the Monogenetic Mt Gambier Volcanic Complex in the Newer Volcanics Province, SE Australia: New Insights into the Occurrence of Intraplate Volcanic Activity in Australia. *Journal of Petrology* **55**, 1317–1351.
- Vasconcelos, P. M., Knesel, K. M., Cohen, B. E. & Heim, J. A. (2008). Geochronology of the Australian Cenozoic: a history of tectonic and igneous activity, weathering, erosion, and sedimentation. *Australian Journal of Earth Sciences* **55**, 865–914.

- Veevers, J. J. (1986). Breakup of Australia and Antarctica estimated as mid-Cretaceous ( $95 \pm 5$  Ma) from magnetic and seismic data at the continental margin. *Earth and Planetary Science Letters* **77**, 91–99.
- Venturelli, G., Capedri, S., Battistini, G. D. I., Crawford, A. J., Kogarko, L. N. & Celestini, S. (1984). The ultrapotassic rocks from southeastern Spain. *Lithos* **17**, 37–54.
- Verati, C. & Jourdan, F. (2014). Modelling effect of sericitization of plagioclase on the  $40\text{K}/40\text{Ar}$  and  $40\text{Ar}/39\text{Ar}$  chronometers: implication for dating basaltic rocks and mineral deposits. *Geological Society, London, Special Publications* **378**, 155–174.
- Vogel, D. C. & Keays, R. R. (1997). The petrogenesis and platinum-group element geochemistry of the Newer Volcanic Province, Victoria, Australia. *Chemical Geology* **136**, 181–204.
- Vogt, P. R. (1974). Volcano spacing, fractures, and thickness of the lithosphere. *Earth and Planetary Science Letters* **21**, 235–252.
- Vollmer, R. (1976). Rb-Sr and U-Th-Pb systematics of alkaline rocks: the alkaline rocks from Italy. *Geochimica et Cosmochimica Acta* **40**, 283–295.
- Ware, B. D., Jourdan, F. & Vinnicombe, K. (2015). High Precision  $40\text{Ar}/39\text{Ar}$  Geochronology of Large Igneous Provinces: The Tasmanian Dolerites of the Ferrar LIP. *Goldschmidt Abstracts* 3360.
- Wellman, P. (1973). Early Miocene potassium-argon age for the Fitzroy Lamproites of Western Australia. *Journal of the Geological Society of Australia* **19**, 471–474.
- Wellman, P. (1974). Potassium-argon ages on the Cainozoic Volcanic rocks of Eastern Victoria, Australia. *Journal of the Geological Society of Australia* **21**, 359–376.
- Wellman, P. & McDougall, I. (1974). Cainozoic igneous activity in eastern Australia. *Tectonophysics* **23**, 49–65.
- Wilkins, D., Gouramanis, C., De Deckker, P., Fifield, L. K. & Olley, J. M. (2013). Holocene lake-level fluctuations in Lakes Keilambete and Gnotuk, southwestern Victoria, Australia. *The Holocene* **23**, 784–795.
- Woolley, A. R., Bergman, S. C., Edgar, A. D., Le Bas, M. J., Mitchell, R. H., Rock, N. M. S. & Scott-Smith, B. H. (1996). Classification of Lamprophyres, Lamproites, Kimberlites, and the Kalsilitic, Melilitic, and Leucitic rocks. *The Canadian Mineralogist* **34**, 175–186.

- Yaxley, G. M., Crawford, A. J. & Green, D. H. (1991). Evidence for carbonatite metasomatism in spinel peridotite xenoliths from western Victoria, Australia. *Earth and Planetary Science Letters* **107**, 305–317.
- Yaxley, G. M., Kamenetsky, V. S., Green, D. H. & Falloon, T. J. (1997). Glasses in mantle xenoliths from western Victoria, Australia, and their relevance to mantle processes. *Earth and Planetary Science Letters* **148**, 433–446.
- Zanetti, A., Tiepolo, M., Oberti, R. & Vannucci, R. (2004). Trace-element partitioning in olivine: Modelling of a complete data set from a synthetic hydrous basanite melt. *Lithos* **75**, 39–54.
- Zeitler, P. K., Herczeg, A. L., McDougall, I. & Honda, M. (1987). U-Th-He dating of apatite: A potential thermochronometer. *Geochimica et Cosmochimica Acta* **51**, 2865–2868.
- Zhang, M., O'Reilly, S. Y. & Chen, D. (1999). Location of Pacific and Indian mid-ocean ridge-type mantle in two time slices: Evidence from Pb, Sr, and Nd isotopes for Cenozoic Australian basalts. *Geology* **27**, 39.
- Ziegler, J. F. (1977). *Helium: stopping powers and ranges in all elemental matter*. New York: Pergamon Press.
- Zindler, A. & Hart, S. R. (1986). Chemical geodynamics. *Annual review of earth and planetary sciences* **14**, 493–571.

Every reasonable effort has been made to acknowledge the owners of copyright material. I would be pleased to hear from any copyright owner who has been omitted or incorrectly acknowledged

## APPENDIX A. FIRST AUTHOR JOURNAL PUBLICATIONS

This Appendix presents the published papers (reprinted with permission from Oxford University Press [Journal of Petrology] and John Wiley and Sons [Geochemistry, Geophysics, Geosystems]):

Oostingh, K. F., Jourdan, F., Merle, R. & Chiaradia, M. (2016). Spatio-temporal Geochemical Evolution of the SE Australian Upper Mantle Deciphered from the Sr, Nd and Pb Isotope Compositions of Cenozoic Intraplate Volcanic Rocks. *Journal of Petrology* **57**, 1509–1530.

Oostingh, K. F., Jourdan, F., Matchan, E. L. & Phillips, D. (2017).  $^{40}\text{Ar}/^{39}\text{Ar}$  geochronology reveals rapid change from plume-assisted to stress-dependent volcanism in the Newer Volcanic Province, SE Australia. *Geochemistry, Geophysics, Geosystems* **18**, 1065–1089.

Furthermore, the Appendix presents all Statement of Authorship forms for all other submitted papers.


# Statement of Authorship


Title of Paper	Spatio-temporal geochemical evolution of the SE Australian upper mantle deciphered from Sr, Nd and Pb isotopes of Cainozoic intraplate volcanics.		
Publication Status	<input type="radio"/> Published <input type="radio"/> Submitted for Publication	<input checked="" type="radio"/> Published <input type="radio"/> Accepted for Publication <input type="radio"/> Publication Style	
Publication Details	Oostingh, K. F., Jourdan, F., Merle, R. & Chiaradia, M. (2016). Spatio-temporal Geochemical Evolution of the SE Australian Upper Mantle Deciphered from the Sr, Nd and Pb Isotope Compositions of Cenozoic Intraplate Volcanic Rocks. <i>Journal of Petrology</i> 57, 1509–1530.		


## Author Contributions

By signing the Statement of Authorship, each author certifies that their stated contribution to the publication is accurate and that permission is granted for the publication to be included in the candidate's thesis.

Name of Principal Author (Candidate)	Korien Oostingh		
Contribution to the Paper	Korien Oostingh was responsible for the majority of data collection, interpretation of results and the drafting of the document.		
Overall percentage (%)	65		
Signature	<i>Korien Oostingh</i>	Date	21/12/2016

Name of Co-Author	Fred Jourdan		
Contribution to the Paper	Fred Jourdan is the principal supervisor and assisted with the drafting of the manuscript and the interpretation of the results.		
Overall percentage (%)	20		
Signature		Date	21/12/2016

Name of Co-Author	Renaud Merle		
Contribution to the Paper	Renaud Merle assisted with the interpretation of the results.		
Overall percentage (%)	10		
Signature		Date	21/12/2016

Name of Co-Author	Massimo Chiaradia		
Contribution to the Paper	Massimo Chiaradia was responsible for the Sr, Nd and Pb isotope analysis		
Overall percentage (%)	5		
Signature		Date	21/12/2016

19218216

RightsLink Printable License

**OXFORD UNIVERSITY PRESS LICENSE  
TERMS AND CONDITIONS**

Dec 21, 2016

This Agreement between Korien Oostingh ("You") and Oxford University Press ("Oxford University Press") consists of your license details and the terms and conditions provided by Oxford University Press and Copyright Clearance Center.

<b>License Number</b>	4004010081292
<b>License date</b>	Dec 08, 2016
<b>Licensed content publisher</b>	Oxford University Press
<b>Licensed content publication</b>	Journal of Petrology
<b>Licensed content title</b>	Spatio-temporal Geochemical Evolution of the SE Australian Upper Mantle Dedphered from the Sr, Nd and Pb Isotope Compositions of Cenozoic Intraplate Volcanic Rocks
<b>Licensed content author</b>	K. F. Oostingh, F. Jourdan, R. Merle, M. Chiaradia
<b>Licensed content date</b>	August 1, 2016
<b>Type of Use</b>	Thesis/Dissertation
<b>Institution name</b>	
<b>Title of your work</b>	Ultra-Precise <sup>40</sup> Ar/ <sup>39</sup> Ar Geochronology; Development of <sup>38</sup> Ar Cosmogenic Exposure and Olivine (U-Th)/He Dating Techniques; and Dedphering the Geochemical Evolution of the Newer Volcanic Province, SE Australia.
<b>Publisher of your work</b>	n/a
<b>Expected publication date</b>	Jan 2017
<b>Permissions cost</b>	0.00 USD
<b>Value added tax</b>	0.00 USD
<b>Total</b>	0.00 USD
<b>Requestor Location</b>	Korien Oostingh Kent St  Perth, WA 6845 Australia Attr: Korien Oostingh
<b>Publisher Tax ID</b>	GB125506730
<b>Billing Type</b>	Invoice
<b>Billing Address</b>	Korien Oostingh Kent St  Perth, Australia 6845 Attr: Korien Oostingh
<b>Total</b>	0.00 USD
<b>Terms and Conditions</b>	

**STANDARD TERMS AND CONDITIONS FOR REPRODUCTION OF MATERIAL  
FROM AN OXFORD UNIVERSITY PRESS JOURNAL**

1. Use of the material is restricted to the type of use specified in your order details.
2. This permission covers the use of the material in the English language in the following territory: world. If you have requested additional permission to translate this material, the

<http://www.copyright.com/CustomerAdmin/PLF.jsp?ref=1c2b6c2-068a-42b-ea8e-d6f2b8828b>

v2

12212016

RightsLink Printable License

terms and conditions of this reuse will be set out in clause 12.

3. This permission is limited to the particular use authorized in (1) above and does not allow you to sanction its use elsewhere in any other format other than specified above, nor does it apply to quotations, images, artistic works etc that have been reproduced from other sources which may be part of the material to be used.

4. No alteration, omission or addition is made to the material without our written consent. Permission must be re-cleared with Oxford University Press if/when you decide to reprint.

5. The following credit line appears wherever the material is used: author, title, journal, year, volume, issue number, pagination, by permission of Oxford University Press or the sponsoring society if the journal is a society journal. Where a journal is being published on behalf of a learned society, the details of that society must be included in the credit line.

6. For the reproduction of a full article from an Oxford University Press journal for whatever purpose, the corresponding author of the material concerned should be informed of the proposed use. Contact details for the corresponding authors of all Oxford University Press journal contact can be found alongside either the abstract or full text of the article concerned, accessible from [www.oxfordjournals.org](http://www.oxfordjournals.org). Should there be a problem clearing these rights, please contact [journals.permissions@oup.com](mailto:journals.permissions@oup.com)

7. If the credit line or acknowledgement in our publication indicates that any of the figures, images or photos was reproduced, drawn or modified from an earlier source it will be necessary for you to clear this permission with the original publisher as well. If this permission has not been obtained, please note that this material cannot be included in your publication/photocopies.

8. While you may exercise the rights licensed immediately upon issuance of the license at the end of the licensing process for the transaction, provided that you have disclosed complete and accurate details of your proposed use, no license is finally effective unless and until full payment is received from you (either by Oxford University Press or by Copyright Clearance Center (CCC)) as provided in CCC's Billing and Payment terms and conditions. If full payment is not received on a timely basis, then any license preliminarily granted shall be deemed automatically revoked and shall be void as if never granted. Further, in the event that you breach any of these terms and conditions or any of CCC's Billing and Payment terms and conditions, the license is automatically revoked and shall be void as if never granted. Use of materials as described in a revoked license, as well as any use of the materials beyond the scope of an unrevoked license, may constitute copyright infringement and Oxford University Press reserves the right to take any and all action to protect its copyright in the materials.

9. This license is personal to you and may not be sublicensed, assigned or transferred by you to any other person without Oxford University Press's written permission.

10. Oxford University Press reserves all rights not specifically granted in the combination of (i) the license details provided by you and accepted in the course of this licensing transaction, (ii) these terms and conditions and (iii) CCC's Billing and Payment terms and conditions.

11. You hereby indemnify and agree to hold harmless Oxford University Press and CCC, and their respective officers, directors, employes and agents, from and against any and all claims arising out of your use of the licensed material other than as specifically authorized pursuant to this license.

12. Other Terms and Conditions:

v1.4

Questions? [customerscare@copyright.com](mailto:customerscare@copyright.com) or +1-855-238-3415 (toll free in the US) or +1-978-646-2777.



## Spatio-temporal Geochemical Evolution of the SE Australian Upper Mantle Deciphered from the Sr, Nd and Pb Isotope Compositions of Cenozoic Intraplate Volcanic Rocks

K. F. Oostingh<sup>1\*</sup>, F. Jourdan<sup>1</sup>, R. Merle<sup>2</sup> and M. Chiaradia<sup>3</sup>

<sup>1</sup>Department of Applied Geology and JdL Centre, Curtin University, Perth, WA 6845, Australia; <sup>2</sup>Research School of Earth Sciences, The Australian National University, Canberra, ACT 0200, Australia and <sup>3</sup>Section des Sciences de la Terre, University of Geneva, 13 Rue de Maraichers, 12011, Geneva, Switzerland

\*Corresponding author. Present address: Department of Applied Geology, Curtin University, GPO Box U1987, Perth, WA 6845, Australia. E-mail: k.oostingh@postgrad.curtin.edu.au

Received October 15, 2015; Accepted July 28, 2016

### ABSTRACT

Intraplate basaltic volcanic rocks ranging in age from Late Cretaceous to Holocene are distributed across southeastern Australia in Victoria and eastern South Australia. They comprise four provinces differentiated on the basis of age and spatial distribution. The youngest of these (<4.6 Ma) is the Newer Volcanic Province (NVP), which incorporates lava flows, scoria cones and maars, distributed across western and central Victoria into South Australia. The oldest eruptive rocks belong to the 95–19 Ma Older Volcanic Province, which comprises basaltic lava flows and shallow intrusions distributed across eastern and central Victoria. When examined within the broader framework of geochemical data available for Cretaceous to Cenozoic intraplate volcanism in southeastern Australia, new major, minor and trace element and Sr, Nd and Pb isotope analyses of volcanic rocks from the NVP suggest that their parental magmas originated from a distinctively different mantle source compared with that of the Older Volcanics. We propose that the magmas represented by the Older Volcanics originated from low degrees of partial melting of a mixed source of Indian mid-ocean ridge basalt (MORB)-source mantle and calcio-carbonatite metasomatized sub-continental lithospheric mantle (SCLM), followed by up to 20% fractional crystallization. The magmas of the youngest (<500 ka) suite of the NVP (the Newer Cones) were generated by up to 13% partial melting of a garnet-rich source, followed by similar degrees of fractional crystallization. We also suggest that the temporally intermediate Euroa Volcanics (~7 Ma) reflect chemical evolution from the source of the Older Volcanics to that of the Newer Cones. Furthermore, energy-constrained recharge, assimilation and fractional crystallization (EC-RA<sub>FC</sub>) modelling suggests that the Sr isotope signature of the ~4.6–1 Ma Newer Plains component of the NVP can be explained by up to 5% upper crustal assimilation. On the basis of these results and data from the literature for mantle xenoliths, we propose a geodynamic model involving decompression melting of metasomatized veins at the base of the SCLM generating the Older Volcanics and modifying the ambient asthenosphere of Indian MORB isotope character. This was followed by thermal erosion and entrainment of the resulting depleted SCLM into the modified Indian MORB-source asthenospheric mantle, generating the Newer Cones. Such a model is in agreement with recent geophysical observations in the area suggesting edge-driven convection with shear-driven upwelling as a potential geodynamic model resulting in temporal upwelling in the region.

**Key words:** Newer Volcanic Province; SE Australia; basalt; intraplate volcanism

## INTRODUCTION

Cainozoic intraplate volcanism in SE Australia was initiated during the breakup of Gondwana and subsequent rapid northward rifting of the Australian plate from 40 Ma onward (Veevers, 1986). In Victoria and South Australia, volcanism is represented by the 95–19 Ma Older Volcanics and the eruptive products of the Newer Volcanic Province (NVP; Fig. 1), comprising the 4.5–1 Ma Newer Plains and the <1 Ma Newer Cones. A 10–5 Ma volcanic field of similar age to the largely felsic rocks of the Macedon–Trentham volcanic province (Price *et al.*, 2003) and with spatial affinities to both the westernmost Older Volcanics and the easternmost Newer Volcanics is located near the town of Euroa (Fig. 1; hereafter referred to as the Euroa Volcanics after Paul *et al.* (2005)). The NVP is subdivided into two distinct regions based on geomorphology: the Central Highlands and Western Plains (Fig. 1). The presence of hot springs (Cartwright *et al.*, 2002) suggests that the province is still active. Nevertheless, the source and provenance of the Older Volcanics, the Newer Plains and Newer Cones basalts are still a matter of debate (O'Reilly & Zhang, 1995; Price *et al.*, 1997, 2014; Zhang *et al.*, 1999; Demidjuk *et al.*, 2007). Enriched geochemical signatures for the Newer Plains eruptive rocks, which have spatially variable Sr isotope compositions corresponding to the location of both the Moyston Fault and the Selwyn Block (Fig. 1), led Price *et al.* (1997, 2014) to suggest that the lithosphere had an important control on the observed geochemical variation within the series. It is now well established that the region is underlain by a complex Palaeozoic basement (Cayley *et al.*, 2011) as well as metasomatized and heterogeneous sub-continental lithospheric mantle (SCLM) (Griffin *et al.*, 1988; O'Reilly & Griffin, 1988; Stolz & Davies, 1988; Yaxley *et al.*, 1991; Handler *et al.*, 1997). Pb isotope systematics may be able to resolve mantle source variations at much higher resolution than Sr and Nd isotope and trace element systematics (e.g. Ewart, 2004); however, Pb isotope data are available only for basalts of the Older Volcanics (Price *et al.*, 2014), the suite of volcanic rocks around the town of Euroa (Paul *et al.*, 2005) and two eruption centres of the Newer Cones—Mt Rouse (Boyce *et al.*, 2015) and Mt Gambier (Van Otterloo *et al.*, 2014). However, single eruptions typically represent discrete and compositionally distinct magma batches, resulting in considerable geochemical variation within and between eruption centres, stressing the need for larger scale geochemical investigations to understand the processes involved in monogenetic volcanism (McGee *et al.*, 2013). Here, we present new major and trace element and Pb, Sr and Nd isotope data for 11 volcanic centres, and their associated flows, of the Newer Cones, which, with a relatively young age span from around 500 000 to 5000 years (Blackburn *et al.*, 1982; Matchan & Phillips, 2011, 2014), represent a proxy for the current geochemical composition of the mantle beneath SE Australia. Recent ultra-precise

$^{40}\text{Ar}/^{39}\text{Ar}$  age dating of these samples confirms their young age, and exemplifies the major age difference between the ~4 Ma Newer Plains (Gray & McDougall, 2008) and the <500 ka Newer Cones in the NVP (Oostingh *et al.*, 2015). Combined data from the Older Volcanics, Euroa Volcanics and the Newer Plains and Newer Cones allow us to resolve spatial and temporal source variations and differences in magmatic processes to elucidate the origin of SE Australian Cenozoic magmatism.

## OVERVIEW OF CENOZOIC MAGMATISM IN SE AUSTRALIA

### Older Volcanics

Day (1983, 1989) subdivided the limited outcrops of the Older Volcanics (Fig. 1b) into 15 separate fields on the basis of their major and trace element compositions and outcrop distribution. There is a continuum of compositions from nephelinitic to quartz-tholeiitic basalt, showing no spatial and temporal correlation between basalt type and location or age. Even though K–Ar dating suggests that volcanism was almost continuous from 95 to 19 Ma (Wellman, 1974), single volcanic fields show a more restricted age range, leading Day (1983, 1989) to subdivide the Older Volcanics into four groups: Group 1 (95–55 Ma), Group 2 (59–38 Ma), Group 3 (44–31 Ma) and Group 4 (29–19 Ma). Recently published major and trace element and Sr, Nd and Pb isotope data (Price *et al.*, 2014) suggest that the Older Volcanics were derived from a three-component source involving depleted mantle (DM) and enriched (EMI and EMII) mantle components. Enrichment in incompatible trace elements and light rare earth elements (LREE) over heavy rare earth elements (HREE) in the Older Volcanics can be explained by partial melting of a heterogeneous mantle source followed by limited fractional crystallization and minor crustal assimilation (Price *et al.*, 2014). Price *et al.* also recognized two groups of high Mg-number samples that exhibit subtle variations in their trace element characteristics, potentially derived from depleted mantle mixing with different metasomatized components (either 2–3% EMI or 1% calcio-carbonatite).

### Euroa Volcanics

The Euroa region represents a key location, as it has spatial affinities with both the Older Volcanics and Newer Plains and Newer Cones basalts, as well as the small felsic flows, domes, plugs and spines of the Macedon–Trentham region (Paul *et al.*, 2005; Fig. 1b) and is located on a north–south trend of more felsic magmatism (8–5 Ma; Wellman & McDougall, 1974). These more evolved rocks (mugearite to trachyte) have been previously interpreted as the southernmost extent of the New South Wales leucite suite, a north–south-trending linear chain of volcanic centres proposed as a trace of hotspot volcanism (Nelson *et al.*, 1986; Davies

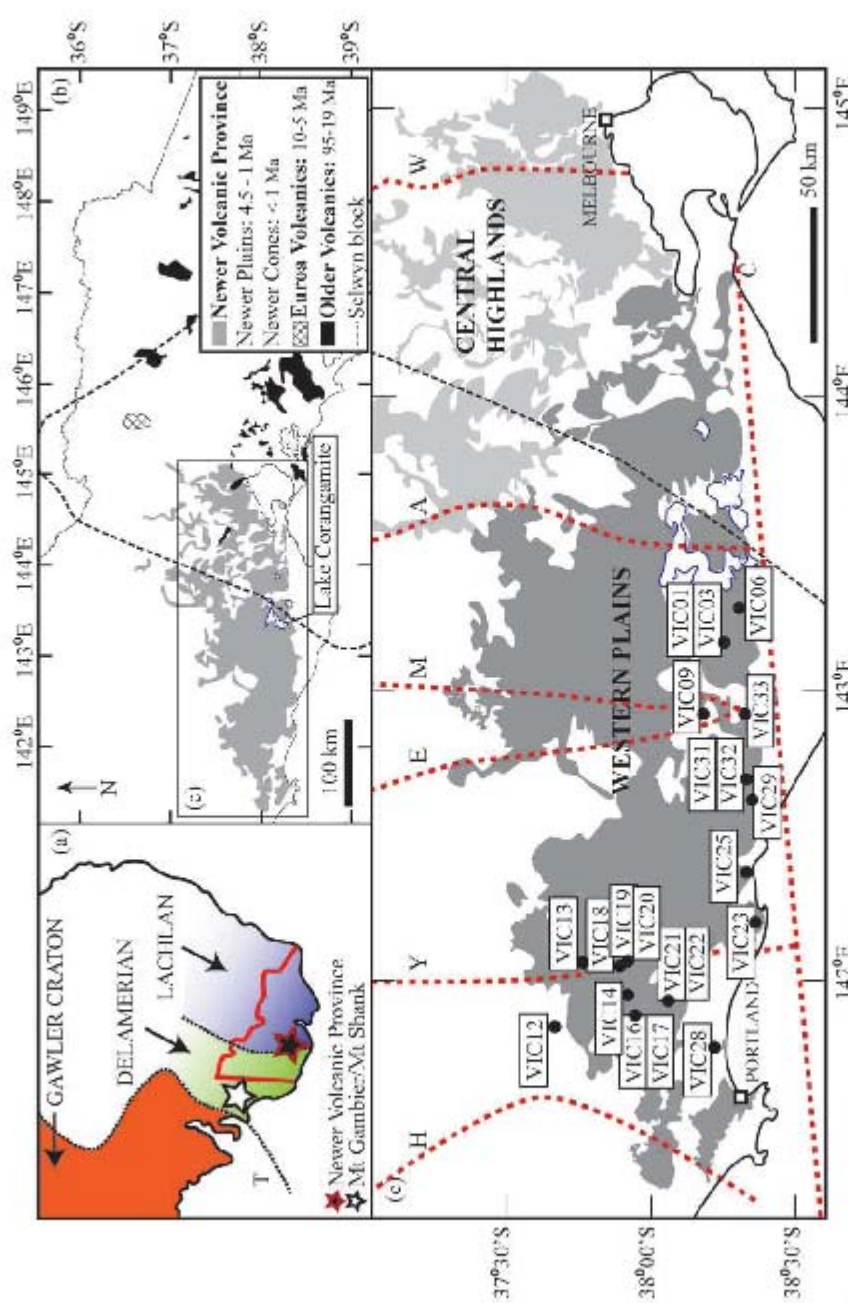


Fig. 1. (a) Location of the Newer Volcanic Province in Victoria and its youngest expression (Mt Gambier and Mt Shank) in South Australia. The Tasman Line (T), the Gawler Craton, as well as the Delamerian and Lachlan fold belts are indicated. (b) Enlarged section of (a) indicating the approximate extent of the Newer Volcanic Province in grey; the 4.5–1 Ma Newer Plains are located stratigraphically below the <1 Ma Newer Cones. The 10–5 Ma Euroa Volcanics are indicated by cross-hatching. The 95–19 Ma Older Volcanics are indicated in black. The dashed line represents the approximate outline of the Selwyn Block at depth (Cayley *et al.*, 2011). (c) Simplified outcrop of the volumetrically dominant Western Plains sub-province indicated in dark grey and location of samples. Indicated in light grey is the Central Highlands sub-province; this is an area of slightly older volcanism (Azizur-Rahman & McDougall, 1972). The black dashed line represents the approximate westmost outline of the Selwyn block at depth. Major faults are indicated by dashed red lines: C, Colac lineament; H, Hummocks fault; Y, Yarramyllip fault; E, Escondido fault; M, Moyston fault; A, Avoca fault; W, Mt William fault.

Downloaded from <http://petrology.oxfordjournals.org/> by guest on October 19, 2016

*et al.*, 2015). However, work by Paul *et al.* (2005) revealed that the geochemical characteristics of the Euroa Volcanics are distinct from the New South Wales leucites, questioning the extension of potential hotspot-related extrusive rocks into Victoria. Geochemical similarities of the Euroa Volcanics to both the Older Volcanics and Newer Plains and Newer Cones basalt suites (Price *et al.*, 2014) suggest a common source. Their age range and location provide an additional constraint on the temporal and spatial variability of this source and magmatic processes.

#### Newer Volcanics

The youngest expressions of intraplate volcanism are the <4.6 Ma (McDougall *et al.*, 1966; Aziz-ur-Rahman & McDougall, 1972; Gray & McDougall, 2009) alkaline basaltic volcanic products of the Newer Plains and Newer Cones series in the NVP (Fig. 1a and b) covering around 15 000–20 000 km<sup>2</sup> of Victoria and South Australia (Price *et al.*, 2003; Boyce, 2013) and comprising more than 704 eruption points from >416 volcanic centres (Boyce, 2013). In the Central Highlands sub-province, scoria cones and lava shield volcanoes have produced valley flows and small lava plains. In the volumetrically dominant Western Plains sub-province, thin, ~4–6–1 Ma lava flows (Gray & McDougall, 2009; termed the Newer Plains) cover a basement of Palaeozoic sediments and granite, whereas a younger (<10–300 ka; Aziz-ur-Rahman & McDougall, 1972) volcanic phase is characterized by small (<100 m high) scoria cones, maars and lava shields with associated flows (termed the Newer Cones; Price *et al.*, 2003). These Newer Cones eruptive rocks are alkalic in composition and have strong incompatible element enrichment, whereas the underlying Newer Plains eruptive rocks comprise less enriched transitional to tholeiitic rock types (Price *et al.*, 2003).

#### GEOLOGICAL SETTING AND SAMPLE DESCRIPTIONS

The NVP is restricted between 141 and 145°E and 37 and 38.5°S, and is underlain by a complex Palaeozoic basement consisting of a series of eastward younging, stacked fold belts of deformed and metamorphosed rocks of the Delamerian and Lachlan orogenies, occurring east of the Tasman Line, which subdivides the Palaeozoic basement from the Proterozoic Gawler Craton (Fig. 1a). An important structural domain is the early Ordovician continental crust of the inferred Selwyn basement block within the southern Lachlan Orogen (Cayley *et al.*, 2011), which underlies most of the Older Volcanics, but is absent from the basement below our samples of the Newer Volcanics of the Western Plains that were sampled west of Lake Corangamite (Fig. 1b).

We focused our sampling efforts on the volumetrically dominant Western Plains sub-province in the NVP, targeting the young Newer Cones. Although extensive

literature data are available on the petrology and major and trace element geochemistry of these Newer Cones (see Price *et al.*, 2003, and references therein), isotope data are scarce. A recent study by Price *et al.* (2014), as well as work by Paul *et al.* (2005), reported isotope data for the Older Volcanics, Newer Plains and Euroa Volcanics. This highlights the need for an updated dataset for the Newer Cones to expand the current isotope geochemical database available for localized volcanic centres (Van Otterloo *et al.*, 2014; Boyce *et al.*, 2015). We targeted young scoria cones and lava shields and their flows at Mt Leura (VIC03), Mt Pomdon (VIC06), Mt Noorat (VIC09), Mt Pierrepoint (VIC13), Mt Napier (VIC18, VIC19 and VIC20) and its Harman flow (VIC14, VIC16 and VIC17), the flow from Mt Rouse (VIC23), the Tower Hill complex (VIC25), Mt Eccles (VIC21 and VIC22) and its Tyrendarra flow (VIC28) and Staughton Hill (VIC33), as well as a smaller, as yet unnamed cone GEOVIC ME-2 (Boyce, 2013; VIC31 and VIC32) which we will refer to subsequently as Mt Boomerang, and the flow at Hopkins Falls that cannot be linked to a clear eruptive centre (VIC29). Samples are typically dark grey, cryptocrystalline basalt with fresh plagioclase laths and fresh olivine visible in hand specimen and minor vesicularity; in the case of flows, vesicles are commonly aligned. Samples VIC19 and VIC22 represent scoriae samples with a very fine, glassy groundmass, whereas VIC25 represents a volcanic bomb within tuff layers at the Tower Hill complex. Mantle xenoliths (centimetre-scale) are present in samples VIC03, VIC09 and VIC31 and VIC32 and olivine glomerocrysts occur in samples VIC29 and VIC33. All samples are devoid of any alteration in thin section. The principal mineral phases observed are phenocrysts of olivine, plagioclase and clinopyroxene in groundmass containing laths of plagioclase and Fe-Ti oxides.

#### METHODS

Samples were pulverized in an agate pestle and mortar. The major, minor and trace element contents of 20 samples were analysed for major elements at Intertek Genalysis Laboratories, Perth, using X-ray fluorescence (XRF), followed by standard dissolution techniques and analysis of solutions for trace elements by inductively coupled plasma mass spectrometry (ICP-MS). Internal standards SARM1 and SY-4 were used for the major elements and SY-4, OREAS25a, OREAS25b and GBW07105 for the trace elements. All major (XRF) and trace element (ICP-MS) analyses have an internal and external precision better than 5% at the 95% confidence level (2 $\sigma$ ), except for V and Zr, which show precision >5% (2 $\sigma$ ) for the standards reported.

Strontium, Nd and Pb isotopes were analysed on a subset of nine samples at the Department of Earth Sciences (University of Geneva, Switzerland) using the method described by Chiaradia *et al.* (2011) and a Thermo Neptune PLUS multi-collector ICP-MS system in

Table 1: Major (wt %) and trace element (ppm) analyses of Newer Volcanic Province basalts

Location:	VIC03 Mt Laura	VIC06 Mt Pomdon	VIC09 Mt Noorat	VIC12 Wannon Falls	VIC13 Mt Pierre- point	VIC14 Harman flow	VIC16 Harman flow	VIC17 Harman flow	VIC18 Mt Napier	VIC19 Mt Napier
Lat. (°):	-38.25	-38.30	-38.18	-37.67	-37.77	-37.92	-37.94	-37.94	-37.89	-37.89
Long. (°):	143.16	143.28	142.92	141.84	142.06	141.95	141.88	141.88	142.05	142.05
<b>Major elements (wt %)</b>										
SiO <sub>2</sub>	44.06	50.68	46.87	49.57	51.19	48.62	48.54	48.88	50.02	50.47
Al <sub>2</sub> O <sub>3</sub>	12.86	13.97	14.11	14.45	14.21	14.50	13.78	13.57	15.28	15.42
TiO <sub>2</sub>	3.22	2.13	2.76	1.88	1.83	1.82	2.09	2.03	2.34	2.32
Fe <sub>2</sub> O <sub>3</sub>	14.37	12.23	13.20	11.65	11.53	12.23	12.29	12.16	11.71	11.46
MnO	0.17	0.16	0.17	0.15	0.15	0.15	0.16	0.16	0.15	0.15
MgO	9.72	8.05	7.45	9.27	8.07	7.76	9.94	10.21	6.75	6.46
CaO	8.34	8.46	7.37	8.40	8.41	8.66	8.98	8.98	8.29	8.45
Na <sub>2</sub> O	4.37	3.48	4.96	3.51	3.45	3.45	3.21	3.30	4.09	3.91
K <sub>2</sub> O	2.26	1.16	2.76	1.16	0.92	0.92	1.08	1.13	1.39	1.39
Cr <sub>2</sub> O <sub>3</sub>	0.04	0.04	0.03	0.04	0.05	0.04	0.05	0.05	0.02	0.02
P <sub>2</sub> O <sub>5</sub>	1.29	0.44	1.02	0.41	0.33	0.33	0.45	0.43	0.50	0.43
LOI	-0.69	-0.59	-0.83	-0.35	0.02	0.25	-0.34	-0.65	-0.52	-0.44
Total	100.10	100.30	100.00	100.18	100.19	99.77	100.28	100.30	100.06	100.09
Mg-no.	61	61	57	65	62	60	65	66	57	57
<b>Trace elements (ppm)</b>										
Rb	51.1	27.6	48.4	19.8	17.9	14.8	14.7	20.6	28.0	25.7
Ba	590.4	240.8	567.9	296.6	267.8	258.1	307.6	303.4	342.2	368.6
Th	6.4	3.1	7.1	2.8	2.2	2.1	2.8	2.8	3.0	3.2
Nb	78.2	28.8	77.8	31.7	25.2	23.5	30.2	29.2	34.3	34.2
Sr	1044.3	477.0	1095.6	670.4	466.5	475.1	529.9	536.5	609.9	627.4
Hf	7.9	4.6	9.0	4.1	3.6	3.3	3.7	3.6	4.3	4.6
Zr	311	166	363	154	138	124	142	135	169	176
Y	26.2	21.6	23.4	19.9	20.6	19.8	19.1	19.1	21.4	21.9
Pb	5.3	2.8	6.7	2.1	2.7	1.9	2.1	3.4	2.3	2.7
Ta	4.7	1.7	5.2	1.9	1.5	1.5	1.8	1.7	2.1	2.1
U	1.8	0.9	2.0	0.6	0.5	0.1	0.7	0.6	0.7	0.8
Sc	13.0	18.0	11.0	19.0	18.0	18.0	19.0	18.0	15.0	16.0
V	197	185	161	180	153	171	192	188	192	191
Cr	236	245	176	285	308	296	293	304	101	103
Co	63.5	49.1	49.4	53.7	51.5	55.7	55.0	56.5	43.4	62.1
Ni	230.8	149.0	157.1	195.2	209.0	214.4	216.6	224.1	109.0	101.8
La	65.0	23.3	59.6	22.5	18.1	17.8	21.3	22.1	25.0	25.6
Ce	133.8	49.0	117.7	44.8	37.3	35.7	45.1	44.0	49.9	50.7
Pr	15.5	6.2	14.2	5.5	4.8	4.5	5.6	5.4	6.3	6.2
Nd	62.9	26.0	54.7	23.5	20.5	18.9	24.0	23.0	25.5	27.3
Sm	12.0	6.1	10.7	5.3	5.0	4.7	5.3	5.3	5.8	5.9
Eu	4.1	2.0	3.5	1.8	1.7	1.7	1.9	1.8	2.1	2.1
Gd	10.3	6.0	9.5	5.1	5.2	5.2	5.5	5.3	6.1	6.0
Tb	1.3	0.9	1.3	0.8	0.8	0.7	0.8	0.8	0.8	0.9
Dy	6.5	4.9	5.8	4.1	4.2	4.2	4.2	4.1	4.5	4.7
Ho	1.1	0.8	1.0	0.7	0.8	0.8	0.8	0.7	0.8	0.8
Er	2.4	2.3	2.2	2.0	2.0	2.0	1.9	1.9	2.1	2.1
Tm	0.3	0.3	0.3	0.2	0.2	0.3	0.2	0.2	0.3	0.3
Yb	1.6	1.7	1.3	1.3	1.4	1.5	1.6	1.6	1.6	1.6
Lu	0.2	0.2	0.2	0.2	0.2	0.2	0.2	0.2	0.2	0.2

(continued)

static mode. Ratios used for internal fractionation were  $^{88}\text{Sr}/^{87}\text{Sr}=8.375209$  for  $^{87}\text{Sr}/^{86}\text{Sr}$ ,  $^{146}\text{Nd}/^{144}\text{Nd}=0.7219$  for  $^{143}\text{Nd}/^{144}\text{Nd}$  and  $^{202}\text{Tl}/^{203}\text{Tl}=0.418922$  for the three Pb isotope ratios (a Tl standard solution was added to the sample). The  $^{144}\text{Sm}$  interference on  $^{144}\text{Nd}$  was monitored on mass  $^{147}\text{Sm}$  and corrected by using a  $^{144}\text{Sm}/^{147}\text{Sm}$  value of 0.206700, and  $^{204}\text{Hg}$  interference on  $^{204}\text{Pb}$  was corrected by monitoring  $^{202}\text{Hg}$ . External standards used were SRM987 ( $^{87}\text{Sr}/^{86}\text{Sr}=0.710248$ , long-term external reproducibility 10 ppm), JNd-1 ( $^{143}\text{Nd}/^{144}\text{Nd}=0.512115$  (Tanaka *et al.*, 2000), long-term external reproducibility 10 ppm), and SRM981 (Baker *et al.*, 2004) for Pb (long-term external reproducibility of

0.0048% for  $^{206}\text{Pb}/^{204}\text{Pb}$ , 0.0049% for  $^{207}\text{Pb}/^{204}\text{Pb}$  and 0.0062% for  $^{208}\text{Pb}/^{204}\text{Pb}$ ). Based on the systematic discrepancy between the measured and accepted Sr, Nd and Pb isotope ratios for the above standards, sample values were further corrected for external fractionation by a value of -0.039%, +0.047% and +0.5% a.m.u., respectively.

## RESULTS

All our new analyses of Newer Cones samples have loss on ignition (LOI) < 2 wt % (Table 1). Major element data have been normalized to 100% on a volatile-free

Table 1: Continued

Location:	VIC20 Mt Napier	VIC21 Mt Eccles	VIC22 Mt Eccles	VIC23 Mt Rouse flow	VIC25 Tower Hill	VIC28 Tyrendarra flow	VIC29 Hopkins Falls	VIC31 GEOVIC ME-2	VIC32 GEOVIC ME-2	VIC33 Stoughton Hill
Lat. (°):	-37.92	-38.06	-38.06	-38.36	-38.33	-38.22	-38.35	-38.33	-38.33	-38.32
Long. (°):	142.07	141.93	141.93	142.20	142.37	141.77	142.62	142.69	142.69	142.92
<b>Major elements (wt %)</b>										
SiO <sub>2</sub>	49.93	46.16	46.87	48.11	46.44	48.20	46.70	45.47	45.56	46.51
Al <sub>2</sub> O <sub>3</sub>	14.64	14.09	13.35	14.15	13.78	14.11	13.19	13.19	13.18	12.88
TiO <sub>2</sub>	2.24	2.60	2.36	2.29	2.46	2.22	2.45	2.81	2.76	2.40
Fe <sub>2</sub> O <sub>3</sub>	11.73	12.91	13.20	12.80	13.05	12.99	13.18	12.99	12.77	13.37
MnO	0.15	0.17	0.17	0.16	0.17	0.17	0.17	0.17	0.16	0.17
MgO	7.84	7.92	10.10	8.87	8.86	8.68	11.01	10.60	10.48	11.12
CaO	8.58	9.66	9.19	9.03	8.79	8.75	9.05	9.01	9.16	9.05
Na <sub>2</sub> O	3.78	3.69	3.27	3.43	4.07	3.69	3.32	3.45	3.44	3.05
K <sub>2</sub> O	1.34	1.62	1.44	1.15	2.17	1.51	1.37	1.77	1.77	1.33
Cr <sub>2</sub> O <sub>3</sub>	0.03	0.04	0.05	0.04	0.03	0.04	0.05	0.04	0.05	0.05
P <sub>2</sub> O <sub>5</sub>	0.48	0.85	0.61	0.45	0.82	0.58	0.58	0.62	0.62	0.57
BaO	0.05	0.05	0.04	0.04	0.06	0.05	0.05	0.05	0.05	0.04
SO <sub>3</sub>	0.01	0.04	0.07	0.01	0.05	0.02	0.01	0.02	0.03	0.01
LOI	-0.74	0.32	-0.61	-0.43	-0.52	-0.74	-0.87	-0.11	0.07	-0.47
Total	100.06	100.11	100.11	100.10	100.24	100.25	100.25	100.08	100.10	100.09
Mg-no.	61	59	64	62	61	66	66	66	66	66
<b>Trace elements (ppm)</b>										
Rb	26.5	31.8	27.5	21.9	44.8	30.9	25.4	33.6	35.3	23.9
Ba	350.1	457.2	350.3	278.2	518.5	390.6	354.9	411.8	399.8	344.9
Th	2.9	4.2	3.2	2.8	5.3	3.7	3.0	4.3	4.6	2.7
Nb	33.0	56.1	39.0	32.7	61.7	45.6	38.4	51.8	52.3	37.1
Sr	578.1	969.0	661.2	582.6	876.4	670.8	677.8	709.3	717.7	587.7
Hf	4.2	5.4	4.3	4.4	7.3	5.2	4.5	5.7	6.0	4.5
Zr	160	228	169	173	279	202	168	224	225	171
Y	20.7	25.6	20.6	21.0	25.5	23.0	20.9	21.6	21.9	21.3
Pb	2.5	2.8	2.3	2.2	4.0	2.9	3.1	2.8	3.1	1.6
Ta	2.1	3.3	2.3	2.1	3.9	2.8	2.4	3.5	3.4	2.3
U	0.8	1.3	0.9	0.8	1.5	0.9	0.9	1.1	1.3	0.7
Sc	17.0	19.0	18.0	20.0	17.0	18.0	19.0	18.0	19.0	19.0
V	191	219	203	200	194	189	208	221	231	204
Cr	171	242	282	273	205	238	311	281	295	367
Co	48.6	49.1	60.2	55.9	53.1	49.8	62.2	63.3	60.5	64.4
Ni	137.9	136.9	228.8	175.7	174.1	166.3	245.6	231.8	213.9	276.7
La	24.6	43.2	29.4	24.5	47.8	33.5	29.2	36.9	37.1	27.3
Ce	49.4	86.4	59.2	50.8	96.6	66.8	60.7	73.5	74.0	56.0
Pr	6.2	10.2	7.2	6.3	11.5	8.1	7.6	8.9	8.8	7.1
Nd	26.3	43.2	30.5	26.2	46.0	32.9	31.4	35.2	36.6	29.1
Sm	5.8	8.6	6.6	5.8	8.8	6.7	6.6	7.3	7.4	6.3
Eu	2.1	2.9	2.3	2.0	3.0	2.4	2.3	2.4	2.5	2.3
Gd	5.7	8.6	6.4	5.7	7.9	7.0	6.4	7.2	6.9	6.4
Tb	0.8	1.1	0.9	0.8	1.1	0.9	0.9	0.9	0.9	0.9
Dy	4.5	5.6	4.8	4.5	5.7	4.9	4.6	5.0	4.9	4.7
Ho	0.8	1.0	0.8	0.8	1.0	0.9	0.8	0.9	0.9	0.8
Er	2.1	2.3	2.1	2.0	2.4	2.2	2.0	2.2	2.2	2.0
Tm	0.2	0.3	0.2	0.2	0.3	0.3	0.2	0.3	0.3	0.2
Yb	1.5	1.7	1.5	1.7	1.6	1.8	1.2	1.5	1.5	1.4
Lu	0.2	0.2	0.2	0.2	0.2	0.2	0.2	0.2	0.2	0.2

Downloaded from <http://petrology.oxfordjournals.org/> by guest on October 19, 2016

basis, reported in Supplementary Data Table A1 (major and trace elements); isotopic data are reported in Supplementary Data Table A2 (Sr, Nd and Pb isotopes) (supplementary data are available for downloading at <http://www.petrology.oxfordjournals.org/>). For comparison, we have also used whole-rock major and trace element data from the GEOROC database and data from Price *et al.* (2014), Van Otterloo *et al.* (2014) and Boyce *et al.* (2015) for the Cretaceous and Cenozoic intraplate volcanic rocks of southeastern Australia. We have not used data for altered samples with LOI > 3 wt % or without LOI recorded as the quality of the data cannot be assessed.

### Major elements

On a total alkalis-silica (TAS) diagram (Fig. 2; Le Bas *et al.*, 1986), the data obtained from this study overlap with published data for the Newer Cones, with all samples except VIC06, VIC13 and VIC14 plotting above the alkaline-sub-alkaline division line of Irvine & Baragar (1971). Seventeen Newer Cones samples plot within the basalt and trachybasalt fields, with three samples (VIC03, VIC09 and VIC25) classifying as basaltite based on CIPW norm calculation. Data for sample VIC09 (SiO<sub>2</sub> 47.1 wt % and total alkalis 7.8 wt %) overlap with those previously published for Mt Gambier and Mt Shank



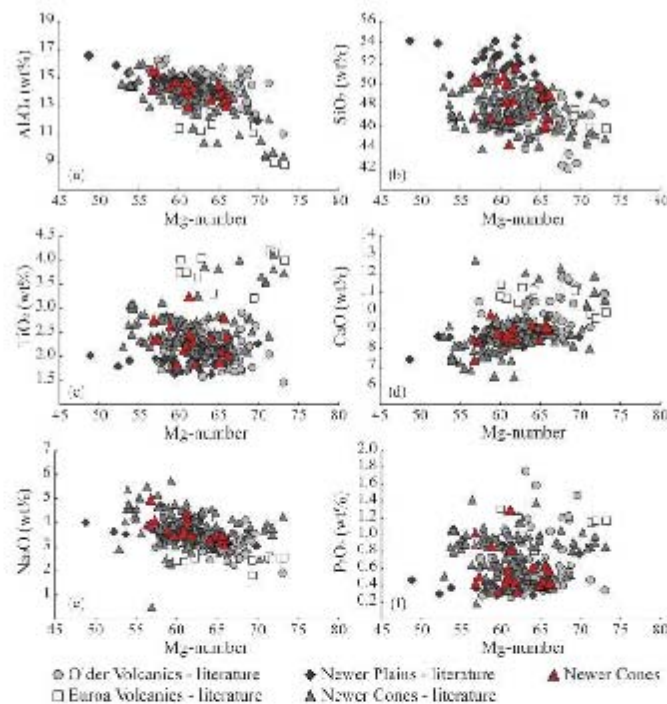


Fig. 3. Major element variation diagrams, all data normalized to 100% on a volatile-free basis. Mg-number calculated as the atomic ratio of  $[100\text{Mg}/(\text{Mg} + 0.85\text{Fe}_{\text{ox}})]$ . Data sources as in Fig. 2.

measured values, with differences ranging between 0.00012% and 0.00001% from the analysed isotope composition. The samples define a relatively narrow range of  $(^{87}\text{Sr}/^{86}\text{Sr})_i$  from 0.70387 for VIC03 to 0.70424 for VIC25 (Table 2) for a wide range of Mg-numbers (Fig. 7), as well as a narrow range in  $(^{143}\text{Nd}/^{144}\text{Nd})_i$  ranging from 0.51281 to 0.51286. When plotted on a  $(^{87}\text{Sr}/^{86}\text{Sr})_i$  vs  $(^{143}\text{Nd}/^{144}\text{Nd})_i$  diagram, all samples are located within the mantle array (Fig. 8a), trending towards Bulk Silicate Earth (BSE; Zindler & Hart, 1986). Our samples show high  $(^{207}\text{Pb}/^{204}\text{Pb})_i$  and  $(^{208}\text{Pb}/^{204}\text{Pb})_i$  for a given  $(^{206}\text{Pb}/^{204}\text{Pb})_i$ , ranging from 15.5472 to 15.6112 and from 38.7402 to 38.7449, respectively;  $(^{208}\text{Pb}/^{204}\text{Pb})_i$  shows a narrow spread over a wide range of Mg-number values, whereas  $(^{207}\text{Pb}/^{204}\text{Pb})_i$  and  $(^{206}\text{Pb}/^{204}\text{Pb})_i$  show similar trends but are slightly more scattered (Fig. 7). When plotted on  $(^{206}\text{Pb}/^{204}\text{Pb})_i$  vs  $(^{207}\text{Pb}/^{204}\text{Pb})_i$  and  $(^{206}\text{Pb}/^{204}\text{Pb})_i$  vs  $(^{208}\text{Pb}/^{204}\text{Pb})_i$  diagrams, most of the samples plot above and parallel to the Northern Hemisphere Reference Line (NHRL; Fig. 8b and c). When plotted on a  $(^{207}\text{Pb}/^{204}\text{Pb})_i$  vs  $(^{143}\text{Nd}/^{144}\text{Nd})_i$  diagram (Fig. 8d) it can be seen that the Newer Cones trend

towards the HIMU mantle end-member, whereas the Older Volcanics trend towards EMIL.

## DISCUSSION

### Geochemical comparison between the Newer Cones and the Older Volcanics, Euroa Volcanics and Newer Plains

#### Major and trace elements

The Newer Cones data overlap with those for the Older Volcanics and Euroa Volcanics in the alkaline field of the TAS diagram, whereas the Newer Plains show a more sub-alkaline geochemical composition (Fig. 2). All series show a wide range in major element compositions; in particular, a negative correlation between  $\text{Al}_2\text{O}_3$  or  $\text{Na}_2\text{O}$  and  $\text{MgO}$  content and a slight positive correlation between  $\text{CaO}$  and Mg-number that indicates fractional crystallization of olivine and clinopyroxene without plagioclase (Fig. 3). Similar trends are observed for the Newer Cones, Newer Plains and the Older Volcanics. The Euroa Volcanics are distinct from the



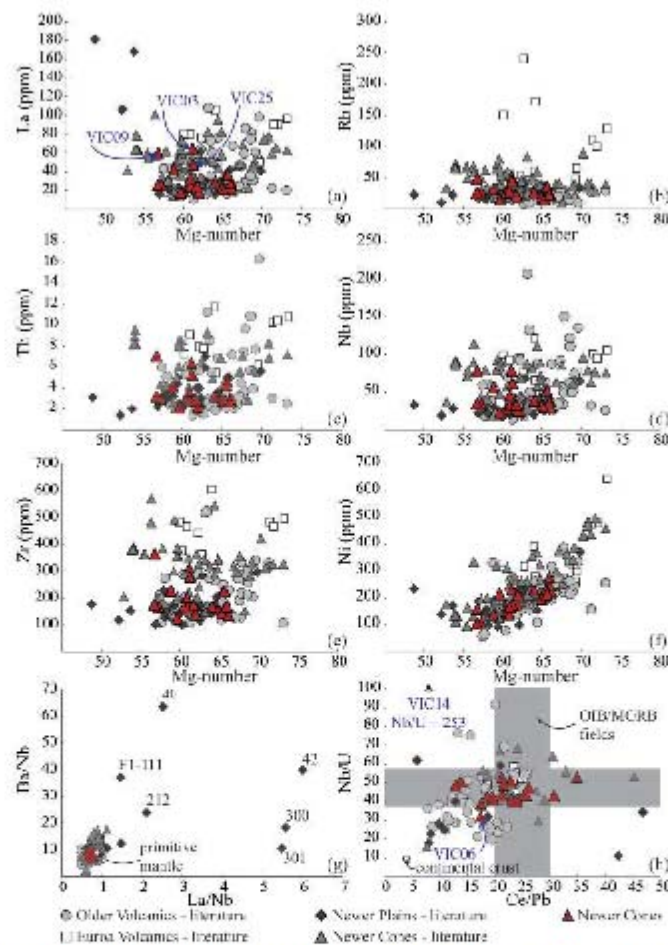


**Fig. 4.** (a–f) Trace element plots vs Mg-number for all series; data sources as in Fig. 2. Basaltic samples VIC03, VIC09 and VIC25 are indicated in (a); (g): La/Nb vs Ba/Nb; the Primitive Mantle value is from Sun & McDonough (1989). Samples F1-111, 40, 42, 212, 300 and 301 (Price *et al.*, 1997) are indicated. (h) Ce/Pb vs Nb/U after Hofmann *et al.* (1998); the gray field represents the Ce/Pb ( $25 \pm 5$ ) and Nb/U ( $47 \pm 10$ ) ratios in both ocean island basalt (OIB) and mid-ocean ridge basalt (MORB); average continental crust is indicated (Nb/U = 10; Ce/Pb = 4; Taylor & McLennan, 1995).

other groups, having lower  $Al_2O_3$  and  $Na_2O$  and higher MgO,  $TiO_2$  and CaO contents similar to those of the Newer Cones in South Australia (Fig. 3).

Compared with the Newer Cones, the Euroa Volcanics are enriched in highly and moderately incompatible trace elements, with Rb contents up to ~240 ppm and Zr up to ~605 ppm. Whereas the Newer Plains generally show a restricted range in Mg-number and trace element composition, except for some outliers, the Older Volcanics display constant variation with Mg-numbers of 57–73 and a wide spread in trace

element concentrations (Th 1.4–16.1 ppm, Zr 105–523 ppm, Nb 20–208 ppm), except for their narrow range of Rb concentrations of around 25 ppm (Fig. 4). Six Newer Plains samples (40, 42, 212, 300, 300 and F1-111; Price *et al.*, 1997) show extreme La/Nb enrichment of 1.5–6, with four of those (40, 42, 212 and F1-111) also having high Ba/Nb ratios of 23.95–63.58, suggestive of fluid metasomatism of their source (Price *et al.*, 1997). The other series show a gradual trend, with the Older Volcanics having the lowest La/Nb and Ba/Nb ratios (~0.5 and ~6 respectively; Fig. 4g), whereas the Euroa

Volcanics overlap with our Newer Cones data having La/Nb of ~0.7 and Ba/Nb of ~8, followed by the Newer Plains, which show the most extreme enrichment. All groups show enrichment in Ni (Fig. 4f) with increasing Mg-number. A major part of the Newer Plains as well as some of the Older Volcanics trend towards the average continental crust value (Taylor & McLennan, 1995) on a Ce/Pb vs Nb/U diagram (Fig. 4h), suggestive of crustal contamination. The Older Volcanics and the Euroa

Volcanics have very similar OIB-type trace element characteristics, with negative Pb and positive Nb anomalies (Fig. 5). These anomalies are absent in some of the Newer Plains basalts, which instead show a positive U anomaly for some samples. Figure 6 shows that the Older Volcanics and Newer Plains have C1 chondrite-normalized REE patterns similar to those of the Newer Cones, whereas the Euroa Volcanics are characterized by greater LREE enrichment.

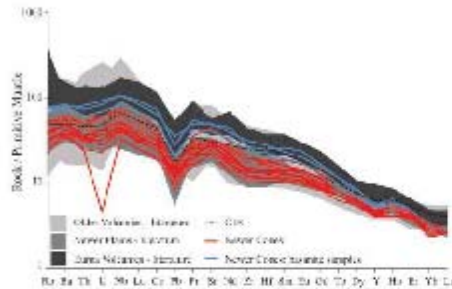


Fig. 5. Primitive mantle normalized trace element patterns for the Newer Cones compared with the Older Volcanics. Typical ocean island basalt (OIB; Sun & McDonough, 1989) is indicated with a black dashed line. Basaltic samples VIC03, VIC09 and VIC25 indicated are indicated by blue lines. Data sources as in Fig. 2.

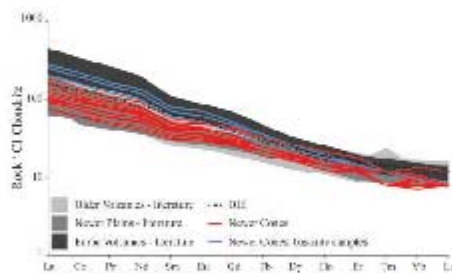


Fig. 6. Rare earth element (REE) C1 chondrite (Sun & McDonough, 1989) normalized patterns. Typical ocean island basalt (OIB; Sun & McDonough, 1989) is indicated with a black dashed line. Basaltic samples VIC03, VIC09 and VIC25 are indicated by blue lines. Data sources as in Fig. 2.

**Sr, Nd and Pb isotopes**

Strontium and Nd isotope data for the Newer Cones overlap with published data (Fig. 7a and b). Our Pb isotope data overlap with the recently published data for Mt Rouse (Boyce *et al.*, 2015), a volcanic centre of the Newer Cones field. However, Pb isotope data for Mt Gambier show slightly higher values (Van Otterloo *et al.*, 2014). Thus far, isotope data for the Newer Plains have been limited to (<sup>87</sup>Sr/<sup>86</sup>Sr) only (Price *et al.*, 1997); these show higher isotopic ratios compared with the other series for a wide range in Mg-number (Fig. 7a). Our Newer Cones data generally show a narrower range in Sr, Nd and Pb isotope compositions compared with those of the Older Volcanics and Euroa Volcanics (Fig. 7a–d). These latter two series show more scatter than our new data but none of the series displays an obvious trend in Mg-number vs initial isotopic ratio plots (Fig. 7a–d). As observed by Price *et al.* (2014), all series overlap the mantle array in a (<sup>87</sup>Sr/<sup>86</sup>Sr) vs (<sup>143</sup>Nd/<sup>144</sup>Nd) isotope diagram, with the Older Volcanics defining a steeper slope (Fig. 8a). There is no obvious correlation between trace element signature and isotope variation, as the difference in Sr–Nd isotope trends for the Older Volcanics is independent of Ca/Pb and Nb/U ratio, as are the high Sr isotope ratios for the Newer Plains. Pb isotope data for our samples display a parallel trend to the NHRL that is also observed for the Older Volcanics and Euroa Volcanics (Fig. 8b and c). A (<sup>207</sup>Pb/<sup>204</sup>Pb) vs (<sup>143</sup>Nd/<sup>144</sup>Nd) diagram (Fig. 8d) shows that data for the Older Volcanics, Euroa Volcanics and Newer Cones trend towards mantle xenoliths of different isotopic composition (Stolz & Davies, 1988), indicative of a heterogeneous source.

**Petrogenesis**

*Partial melting*

Distinct isotope and trace element compositions differentiate the Older Volcanics from the Euroa Volcanics

Table 2. Sr–Nd–Pb isotope data for the Newer Cones

	Sr (ppm)	Nd (ppm)	Pb (ppm)	<sup>87</sup> Sr/ <sup>86</sup> Sr	2σ	<sup>143</sup> Nd/ <sup>144</sup> Nd	2σ	<sup>208</sup> Pb/ <sup>204</sup> Pb	2σ	<sup>207</sup> Pb/ <sup>204</sup> Pb	2σ	<sup>206</sup> Pb/ <sup>204</sup> Pb	2σ
VC03	1044.3	62.90	5.3	0.70387	1.59E–05	0.51284	5.95E–06	18.8333	2.67E–02	15.6112	1.23E–03	38.6758	3.13E–02
VC06	477.0	26.00	2.8	0.70455	1.88E–05	0.51278	7.32E–06	18.7927	2.54E–02	15.6359	1.17E–02	38.8884	2.88E–02
VC09	1095.6	54.70	6.7	0.70394	1.44E–05	0.51284	6.10E–06	18.7441	2.35E–02	15.5909	1.08E–03	38.7035	2.75E–02
VC16	529.9	24.00	2.1	0.70396	5.12E–06	0.51283	3.91E–06	18.5334	1.48E–04	15.6019	6.82E–06	38.6134	1.95E–04
VC17	536.5	23.00	3.4	0.70401	8.25E–06	0.51283	4.75E–06	18.4525	9.09E–05	15.5472	4.19E–06	38.4706	1.40E–04
VC18	69.9	25.50	2.3	0.70390	1.49E–05	0.51283	7.09E–06	18.5041	2.38E–02	15.5876	1.10E–03	38.5615	3.36E–02
VC21	959.0	43.20	2.8	0.70392	6.93E–06	0.51286	3.99E–06	18.5346	2.34E–04	15.5952	1.08E–05	38.5757	2.49E–04
VC25	876.4	46.00	4.0	0.70424	2.35E–06	0.51281	8.45E–07	18.6453	4.17E–05	15.5846	1.92E–04	38.7449	4.86E–03
VC29	677.8	31.40	3.1	0.70388	1.16E–06	0.51284	9.58E–07	18.6072	2.17E–05	15.5705	1.00E–04	38.6349	2.39E–03

Downloaded from <http://jpetrology.oxfordjournals.org/> by guest on October 19, 2016

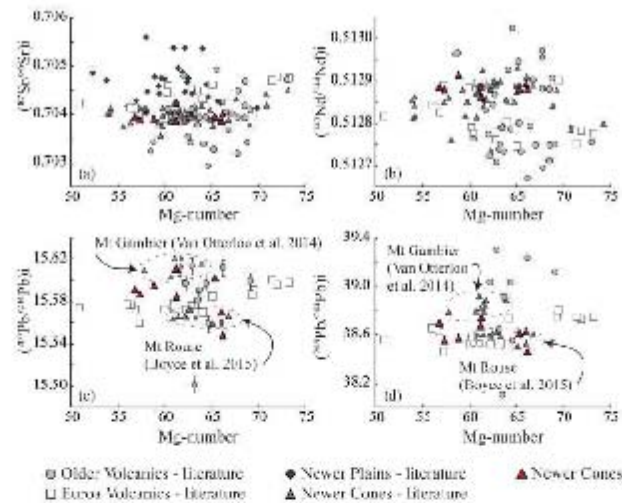


**Fig. 7.**  $^{87}\text{Sr}/^{86}\text{Sr}$ ,  $^{143}\text{Nd}/^{144}\text{Nd}$ ,  $^{207}\text{Pb}/^{204}\text{Pb}$  and  $^{208}\text{Pb}/^{204}\text{Pb}$  vs Mg-number [atomic ratio of  $100\text{Mg}/(\text{Mg} + 0.85\text{Fe}_{\text{total}})$ ]. All isotope data are corrected to initial values; Newer Cones 500–41 ka, Newer Plains 4–6–1 Ma, Euroa Volcanics 7 Ma; Older Volcanics 95–19 Ma. Error bars ( $2\sigma$ ) are indicated in (c), but are smaller than the symbols for the  $^{87}\text{Sr}/^{86}\text{Sr}$ ,  $^{143}\text{Nd}/^{144}\text{Nd}$  and  $^{207}\text{Pb}/^{204}\text{Pb}$  isotope data. Published Pb isotope data for the Newer Cones are limited to recent studies of Mt Rouse (Boyce *et al.*, 2015) and Mt Gambier (Van Otterloo *et al.*, 2014); the respective fields are indicated in (c) and (d). No major element data are available for the basalts analysed for Pb isotope composition by Cooper & Green (1969). Other data sources are as in Fig. 2.

and the Newer Cones and Newer Plains series, as illustrated by the different trends between the series on bivariate REE ratio diagrams (Fig. 9a and b). Whereas the Euroa Volcanics and Newer Cones and Newer Plains show a narrow range in LREE/MREE [(La/Sm) $_{\text{C1}}$  of 2.5–5] and high MREE/HREE [(Sm/Yb) $_{\text{C1}}$  of 3–9.5], the Older Volcanics show a slightly wider range in LREE/MREE [(La/Sm) $_{\text{C1}}$  of 2.5–6] and lower MREE/HREE [(Sm/Yb) $_{\text{C1}}$  of 2–6] values. Trace element behaviour in all series is independent of Mg-number variations (Fig. 4) and therefore the observed trends cannot be explained by either fractional crystallization or crustal contamination processes. On the contrary, the different trends observed among the Cretaceous and Cenozoic intraplate basalts of southeastern Australia are most probably caused by subtle variations in the melting modalities of their respective sources.

To test the melting conditions we have used the standard equation from Shaw (1970), which describes trace element distribution during partial melting. The model was applied only to samples with less than 5% fractional crystallization. A wide range of published trace element concentrations for peridotite xenoliths from the NVP (Frey & Green, 1974; O'Reilly & Griffin, 1984; Yaxley *et al.*, 1997; Foden *et al.*, 2002) was used to constrain the composition of the potential initial source.

We found that the trace element distribution patterns of the Newer Cones, Newer Plains and Euroa Volcanics are best represented by up to ~15% batch melting of a hydrous, garnet-bearing lherzolite source with a modal composition of 57 wt % olivine, 25 wt % orthopyroxene, 11 wt % clinopyroxene, 6 wt % amphibole and 2 wt % garnet (La 0.26 ppm, La/Yb 15, La/Sm 2). However, the Older Volcanics are better represented by smaller degrees (5–10%) of batch melting of a hydrous, spinel-bearing lherzolite source with a modal composition of 55 wt % olivine, 25 wt % orthopyroxene, 11 wt % clinopyroxene, 8 wt % amphibole and 1 wt % spinel (La 0.35 ppm, La/Yb 15, La/Sm 1; Fig. 9a and b). These results indicate that over time, the mantle source beneath SE Australia became more enriched in MREE, and that degrees of partial melting, as well as depth of melting, slightly increased. These degrees of partial melting are slightly higher than those suggested for different intraplate volcanic centres in similar settings, such as, for example, 5–7% for lava shields of the Jeju Island volcanic field, South Korea (Brenna *et al.*, 2010) and 2–3% for alkaline basalts in the Auckland Volcanic field (McGee *et al.*, 2011). It is important to note that for this modelling we have assumed that the source region is predominantly homogeneous; however, trends in isotope variation diagrams are an indication that source

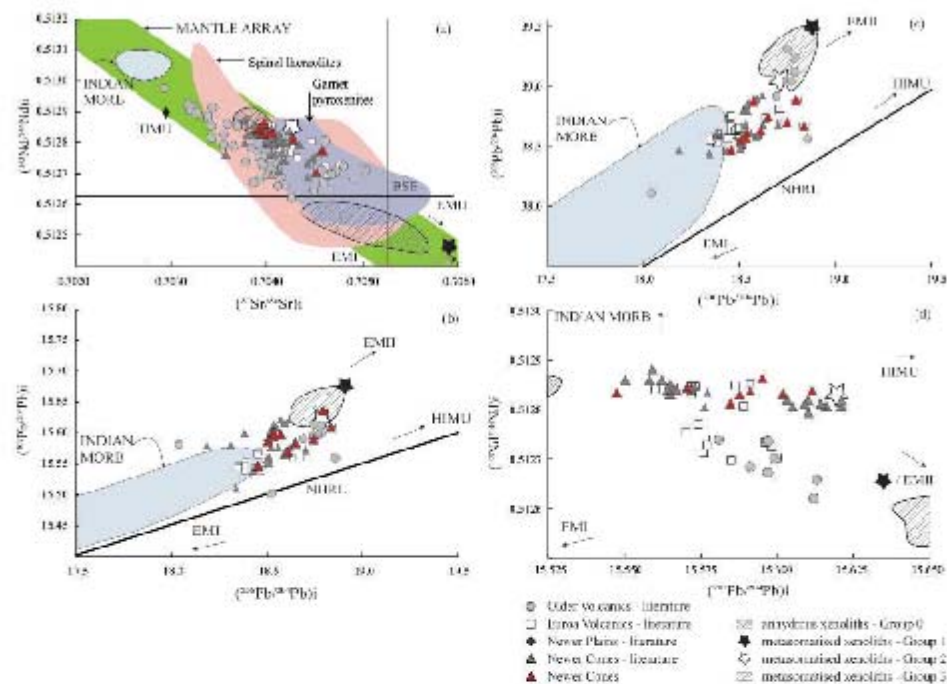


**Fig. 8.** (a)  $(^{87}\text{Sr}/^{86}\text{Sr})_i$  vs  $(^{143}\text{Nd}/^{144}\text{Nd})_i$ , showing the mantle array in green and approximate locations of mantle end-members. Indicated are fields for Newer Volcanic Province spinel ilmenite (pink) and garnet pyroxenite (purple) xenoliths (McDonough *et al.*, 1986; Griffin *et al.*, 1988; O'Reilly & Griffin, 1988; Yaxley *et al.*, 1991; Powell *et al.*, 2004) as well as Group 0 anhydrous xenoliths (cross-hatched), Group 1  $\text{CO}_2$  fluid metasomatized (black star), Group 2 alkaline melt metasomatized (white star) and Group 3 carbonatite metasomatized xenoliths (diagonal lines) after Stolz & Davies (1988). NHRL, Northern Hemisphere Reference Line. Newer Cones literature data are from Cooper & Green (1969), Stolz & Davies (1988), Van Otterloo *et al.* (2014) and Boyce *et al.* (2015). (b)  $(^{207}\text{Pb}/^{204}\text{Pb})_i$  vs  $(^{206}\text{Pb}/^{204}\text{Pb})_i$ , indicating fields for xenoliths after Stolz & Davies (1988). (c)  $(^{207}\text{Pb}/^{204}\text{Pb})_i$  vs  $(^{206}\text{Pb}/^{204}\text{Pb})_i$ , and (d)  $(^{207}\text{Pb}/^{204}\text{Pb})_i$  vs  $(^{143}\text{Nd}/^{144}\text{Nd})_i$  showing the isotopic variation in the Older Volcanics, Euroa Volcanics and Newer Cones, as well as the isotope composition of various mantle end-members: enriched mantle I (EMI), enriched mantle II (EMII) and UIMU (High- $\mu$ ; high  $^{238}\text{U}/^{235}\text{U}$ ) (Stracke *et al.*, 2006), and the isotope compositions of the various groups of mantle xenoliths from Stolz & Davies (1988). Other data sources as in Fig. 2.

heterogeneity could have played an important role in the petrogenesis of the southeastern Australian intra-plate basalts. Therefore, the degrees of partial melting found for all series most probably indicate maximum values.

#### Fractional crystallization

Covariation on major element variation diagrams as well as subparallel REE patterns on chondrite (C1) normalized REE diagrams suggest that all series might have undergone some fractional crystallization. We used the MELTS algorithm (Ghiorso & Sack, 1995) to test this hypothesis for the Newer Cones sample suite and to quantify further the extent of fractional crystallization for all series. We have used model parameters for isobaric cooling at low pressure (1 kbar) from 1200 to 800°C ( $f\text{O}_2 = \text{QFM}$  (quartz-fayalite-magnetite)) using

our least differentiated sample VC33 (MgO = 11.2 wt%; Ni = 277 ppm, Cr = 367 ppm) as starting composition. Figure 10a shows that the magmas represented by the Newer Cones basalts could have been generated by up to 20% fractional crystallization of olivine and clinopyroxene. This process led the remaining liquid to be progressively enriched in  $\text{Al}_2\text{O}_3$ . A few other Newer Cones samples previously studied have probably undergone similar amounts of fractional crystallization, but were potentially generated from a more primitive initial composition. The Older Volcanics as well as the Newer Plains show similar trends to the Newer Cones on MgO vs  $\text{Al}_2\text{O}_3$  diagrams, and these can also be explained by up to 20% fractional crystallization using physical conditions similar to those applicable to the Newer Cones (isobaric cooling at low pressure (1 kbar) from 1200 to 800°C,  $f\text{O}_2 = \text{QFM}$ ). The Euroa Volcanics show a different trend, possibly because of plagioclase crystallization in

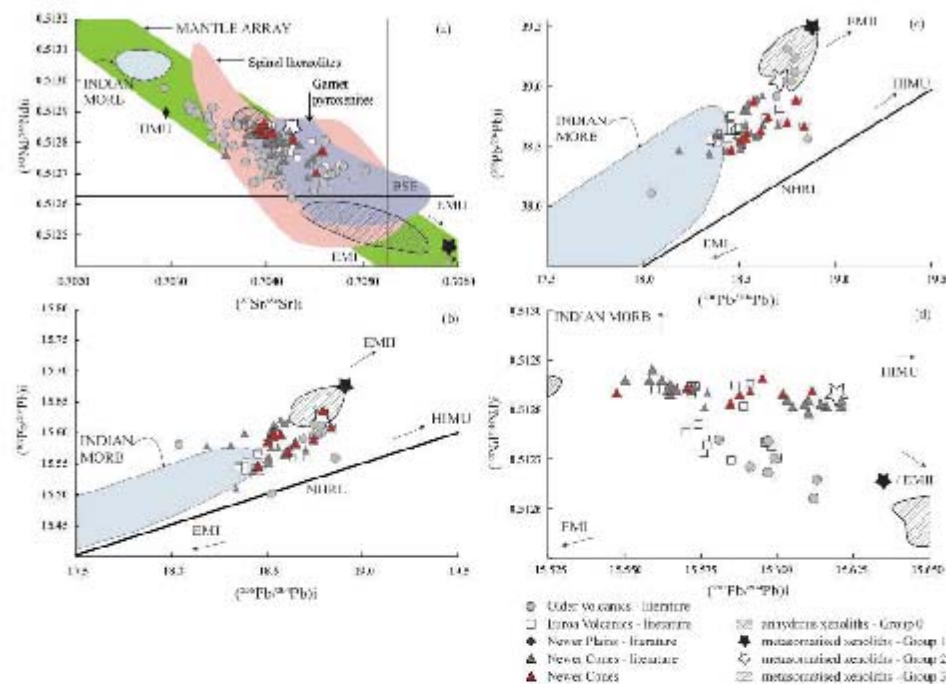


**Fig. 8.** (a)  $(^{87}\text{Sr}/^{86}\text{Sr})_i$  vs  $(^{143}\text{Nd}/^{144}\text{Nd})_i$ , showing the mantle array in green and approximate locations of mantle end-members. Indicated are fields for Newer Volcanic Province spinel ilmenite (pink) and garnet pyroxenite (purple) xenoliths (McDonough *et al.*, 1986; Griffin *et al.*, 1988; O'Reilly & Griffin, 1988; Yaxley *et al.*, 1991; Powell *et al.*, 2004) as well as Group 0 anhydrous xenoliths (cross-hatched), Group 1  $\text{CO}_2$  fluid metasomatized (black star), Group 2 alkaline melt metasomatized (white star) and Group 3 carbonatite metasomatized xenoliths (diagonal lines) after Stolz & Davies (1988). NHRL, Northern Hemisphere Reference Line. Newer Cones literature data are from Cooper & Green (1969), Stolz & Davies (1988), Van Otterloo *et al.* (2014) and Boyce *et al.* (2015). (b)  $(^{207}\text{Pb}/^{204}\text{Pb})_i$  vs  $(^{206}\text{Pb}/^{204}\text{Pb})_i$ , indicating fields for xenoliths after Stolz & Davies (1988). NHRL, Northern Hemisphere Reference Line. Newer Cones literature data are from Cooper & Green (1969), Stolz & Davies (1988), Van Otterloo *et al.* (2014) and Boyce *et al.* (2015). (c)  $(^{207}\text{Pb}/^{204}\text{Pb})_i$  vs  $(^{206}\text{Pb}/^{204}\text{Pb})_i$ , and (d)  $(^{207}\text{Pb}/^{204}\text{Pb})_i$  vs  $(^{143}\text{Nd}/^{144}\text{Nd})_i$  showing the isotopic variation in the Older Volcanics, Euro Volcanics and Newer Cones, as well as the isotope composition of various mantle end-members: enriched mantle I (EMI), enriched mantle II (EMII) and UIMU (High- $\mu$ ; high  $^{238}\text{U}/^{235}\text{U}$ ) (Stracke *et al.*, 2006), and the isotope compositions of the various groups of mantle xenoliths from Stolz & Davies (1988). Other data sources as in Fig. 2.

heterogeneity could have played an important role in the petrogenesis of the southeastern Australian intra-plate basalts. Therefore, the degrees of partial melting found for all series most probably indicate maximum values.

#### Fractional crystallization

Covariation on major element variation diagrams as well as subparallel REE patterns on chondrite (C1) normalized REE diagrams suggest that all series might have undergone some fractional crystallization. We used the MELTS algorithm (Ghiorso & Sack, 1995) to test this hypothesis for the Newer Cones sample suite and to quantify further the extent of fractional crystallization for all series. We have used model parameters for isobaric cooling at low pressure (1 kbar) from 1200 to 800°C ( $f\text{O}_2 = \text{QFM}$  (quartz-fayalite-magnetite)) using

our least differentiated sample VC33 (MgO = 11.2 wt%; Ni = 277 ppm, Cr = 367 ppm) as starting composition. Figure 10a shows that the magmas represented by the Newer Cones basalts could have been generated by up to 20% fractional crystallization of olivine and clinopyroxene. This process led the remaining liquid to be progressively enriched in  $\text{Al}_2\text{O}_3$ . A few other Newer Cones samples previously studied have probably undergone similar amounts of fractional crystallization, but were potentially generated from a more primitive initial composition. The Older Volcanics as well as the Newer Plains show similar trends to the Newer Cones on MgO vs  $\text{Al}_2\text{O}_3$  diagrams, and these can also be explained by up to 20% fractional crystallization using physical conditions similar to those applicable to the Newer Cones (isobaric cooling at low pressure (1 kbar) from 1200 to 800°C,  $f\text{O}_2 = \text{QFM}$ ). The Euro Volcanics show a different trend, possibly because of plagioclase crystallization in

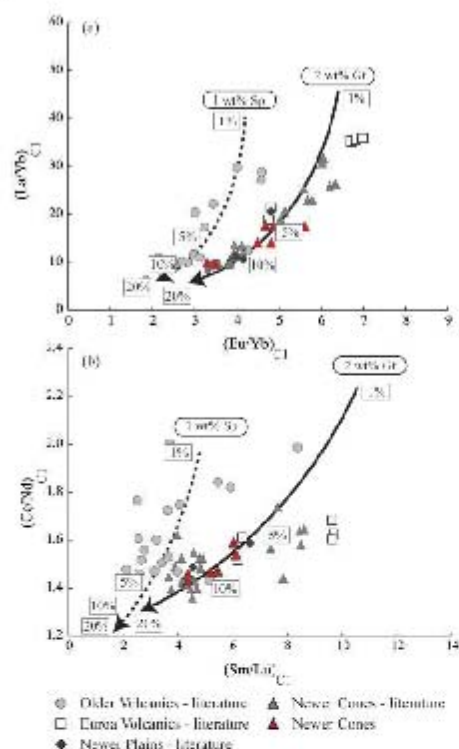


**Fig. 9.** Models for trace element fractionation during non-modal partial melting of Newer Volcanic Province xenolith compositions (Griffin *et al.*, 1988; Stolz & Davies, 1988; Yaxley *et al.*, 1991) with either added garnet (continuous line) or added spinel (dashed line), using the equation from Shaw (1970). Only basalt samples are plotted for which less than 5% fractional crystallization is inferred. Compositions are normalized to chondrite after Sun & McDonough (1989). Trace element distribution coefficients are from McKenzie & O'Nions (1983). Starting modal composition: continuous line: 56 wt % olivine, 25 wt % orthopyroxene, 11 wt % clinopyroxene, 2 wt % garnet, 6 wt % amphibole and La/Yb = 11; dashed line: 56 wt % olivine, 25 wt % orthopyroxene, 11 wt % clinopyroxene, 1 wt % spinel, 7 wt % amphibole and La/Yb = 15. Melting mode modified from Walter (1998): ol 0.08, cpx -0.19, cpx 0.81, gt 0.15 and sp 0.15. Data sources as in Fig. 2. Numbers in rectangles indicate per cent melting.

the more evolved melts. These rocks have high MgO contents; however, olivine compositions are in good agreement with olivine that crystallizes in equilibrium with liquids having compositions similar to the bulk-rock analyses of these rocks, indicating that these rocks are unlikely to be cumulates (Paul *et al.*, 2005). MELTS modelling is compatible with these rocks being formed in a slightly more oxidizing environment ( $fO_2 = QFM + 2$ ) using melting conditions similar to those applied in other cases (isobaric at 1 kbar, 1200–800°C). However,

deviation from the modelled fractionation trend for some Euroa samples suggests that these results are indicative only. Paul *et al.* (2005) reported the presence of leucite in some of the most primitive samples, which could indicate derivation of the Euroa Volcanics from a more enriched mantle source, or the generation of undersaturated melts by a lower degree of melting.

#### Crustal contamination

The basement below South Australia and Victoria is complex in both structure and stratigraphy, containing fragments of Neoproterozoic continental crust incorporated into eastward younging Palaeozoic subduction-accretionary wedges. Furthermore, it includes Cambrian–Ordovician boninitic and MORB-type tholeiitic volcanic rocks as well as deep-ocean sedimentary rocks and arc-related volcanic rocks (Cayley *et al.*, 2011). McBride *et al.* (2001) suggested on the basis of osmium isotopes that the Newer Plains ( $^{187}\text{Os}/^{188}\text{Os}$  0.18096 ± 52 to 0.4456 ± 22) basalts might have been crustally contaminated [upper continental crust having much higher  $^{37}\text{Sr}/^{86}\text{Sr}$  of *c.* 1.4 based on a  $^{187}\text{Re}/^{188}\text{Os}$  isotope ratio of 34.4; Peucker-Ehrenbrink & Jahn (2001)], in contrast to the Newer Cones, which display  $^{187}\text{Os}/^{188}\text{Os}$  ratios compatible with a derivation from an uncontaminated OIB-like mantle source ( $^{187}\text{Os}/^{188}\text{Os}$  of 0.13423 ± 33 and 0.13677 ± 37). A narrow range of ( $^{87}\text{Sr}/^{86}\text{Sr}$ )<sub>i</sub> compositions over a wide range of Mg-numbers (73–54) and Ce/Pb and Nb/U ratios similar to those for OIB and MORB (Fig. 4) show that most of the Newer Cones and Euroa Volcanics are indeed unlikely to have been affected by crustal contamination. On the other hand, negative covariation between Sr isotopes and bulk-rock Sr element concentration, as well as non-OIB or MORB-like Ce/Pb and Nb/U ratios (Hofmann *et al.*, 1986) for the Older Volcanics, Newer Plains and one Newer Cones sample (VIC06), suggests that contamination by upper or lower continental crust might have affected at least some of these basalts. We have used the energy-constrained recharge, assimilation and fractional crystallization (EC-R<sub>A</sub>-FC) algorithm (Bohrson & Spera, 2001; Spera, 2001) to investigate the possible extent of crustal assimilation in these potentially contaminated rocks. Owing to the complexity of the crust as outlined above, we have used data for average upper and lower continental crust (Taylor & McLennan, 1995) instead of detailed compositions for each structural zone. Table 3 provides the thermal and compositional input parameters used for the modelling. The Newer Cones do not show any correlation between Sr and ( $^{87}\text{Sr}/^{86}\text{Sr}$ )<sub>i</sub> other than that expected of fractional crystallization, suggesting that crustal contamination was either absent or well below 1% (Fig. 11a). The Euroa Volcanics show a similar narrow range in Sr isotope composition over a wide range of Sr concentrations. Covariation in Sr isotope composition vs Sr concentration is also absent for the Older Volcanics. However, ( $^{87}\text{Sr}/^{86}\text{Sr}$ )<sub>i</sub> values for the Newer

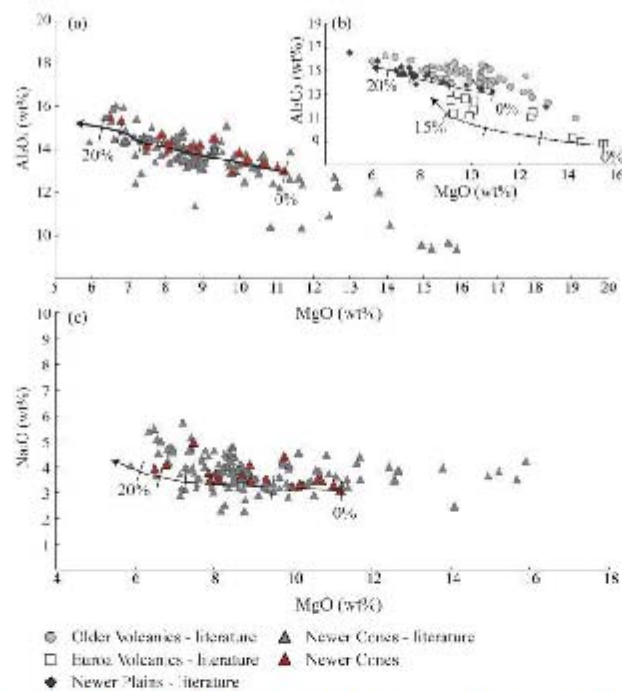


**Fig. 10.** MELTS (Ghiorso & Sack, 1995) modelling results for (a) and (c) the Newer Cones and (b) the Older Volcanics, Euroa Volcanics and Newer Plains. Data sources as in Fig. 2. Continuous lines represent isobaric (1 kbar) cooling (from 1200 to 800°C) of a dry magma,  $fO_2 = QFM + 1$ ; dashed line represents isobaric (1 kbar) cooling (from 1200 to 800°C) of a dry magma,  $fO_2 = QFM + 2$ . Tick marks represent 5% steps.

Plains increase with decreasing Sr concentration, which can be satisfactorily modelled by up to 5% assimilation of average upper continental crust using the most primitive composition among these basalts (Fig. 11b). Whereas the majority of the Newer Plains Sr isotope compositions are suggestive of crustal assimilation, with high Sr initial ratios, most of the Older Volcanics, Euroa Volcanics and the majority of the Newer Cones appear to be uncontaminated, as noted above. Their initial Sr, Nd and Pb isotope ratios probably reflect their mantle source characteristics. Whereas a slightly low Nb/U ratio for VIC06 is suggestive of significant crustal contamination, depletion in U for VIC14 is indicative of potential fluid interaction and thus alteration; these samples are therefore omitted from the following discussion.

#### Mantle source compositions

##### Identifying potential mantle end-members

Even though agreement exists over the involvement of partial melting and open (assimilation) and closed (fractional crystallization) processes contributing to the

geochemical characteristics of the basalts of the Older Volcanics, Euroa Volcanics, Newer Plains and Newer Cones, the possible contribution of the lithosphere and asthenosphere in terms of mantle sources remains contentious. Whereas some researchers favour partial melting of the asthenosphere, either of homogeneous composition (Paul *et al.*, 2005) or changing over time (Zhang *et al.*, 1999), others argue for melting of the lithospheric mantle and entrainment of this melt into the convecting asthenosphere (Price *et al.*, 1997, 2014).

The southeastern Australian lithospheric mantle has been extensively sampled by exhumed spinel lherzolite and garnet pyroxenite xenoliths, which have undergone up to three metasomatic events, as represented in the xenolith suites of many of the Newer Cones (McDonough & McCulloch, 1987; Griffin *et al.*, 1988; O'Reilly & Griffin, 1988; Stolz & Davies, 1988; Yaxley *et al.*, 1991; Powell *et al.*, 2004). On a ( $^{87}\text{Sr}/^{86}\text{Sr}$ )<sub>i</sub> vs ( $^{143}\text{Nd}/^{144}\text{Nd}$ )<sub>i</sub> isotope diagram (Fig. 8a) the Newer Cones and the Euroa Volcanics overlap the isotope compositions of SE Australian spinel lherzolites and garnet pyroxenites. Some samples of the Older Volcanics have less radiogenic ( $^{87}\text{Sr}/^{86}\text{Sr}$ )<sub>i</sub>

**Table 3:** Input parameters for EC-RA<sub>x</sub>FC modelling, thermal parameters, and standard upper and lower crustal composition after Bohlen & Spera (2001)

	Thermal parameters			
	Upper crust	Lower crust		
Magma liquidus temperature, $T_{lm}$	1280°C	1320°C	Crystallization enthalpy, $\Delta h_{cr}$ ( $J\ kg^{-1}$ ) [Q15]	396000
Magma initial temperature, $T_m^0$	1280°C	1320°C	Isobaric specific heat of magma, $C_{p,m}$ ( $J\ kg^{-1}\ K^{-1}$ )	1484
Assimilant liquidus temperature, $T_{la}$	1000°C	1100°C	Fusion enthalpy, $\Delta h_{fus}$ ( $J\ kg^{-1}$ )	270000
Assimilant initial temperature, $T_a^0$	300°C	600°C	Isobaric specific heat of assimilant, $C_{p,a}$ ( $J\ kg^{-1}\ K^{-1}$ )	1370
Solidus temperature, $T_s$	900°C	960°C		
Equilibrium temperature, $T_{eq}$	980°C	980°C		
	Compositional parameters			
	Newer Cones		Newer Plains	
	Upper crust Sr	Lower crust Sr	Upper crust Sr	Lower crust Sr
Magma initial concentration (ppm), $C_m^0$	1095.6	1095.6	718	718
Magma isotope ratio, $c_m$	0.70394	0.70394	0.70415	0.70415
Magma trace element distribution coefficient, $D_m$	1.5	1.5	1.5	1.5
Enthalpy of trace element distribution reaction, $\Delta H_m$	—	—	—	—
Assimilant initial concentration (ppm), $C_a^0$	350	230	350	230
Assimilant isotope ratio, $c_a$	0.722	0.7100	0.722	0.7100
Assimilant trace element distribution coefficient, $D_a$	1.5	0.05	1.5	0.05
Enthalpy of trace element distribution reaction, $\Delta H_a$	—	—	—	—

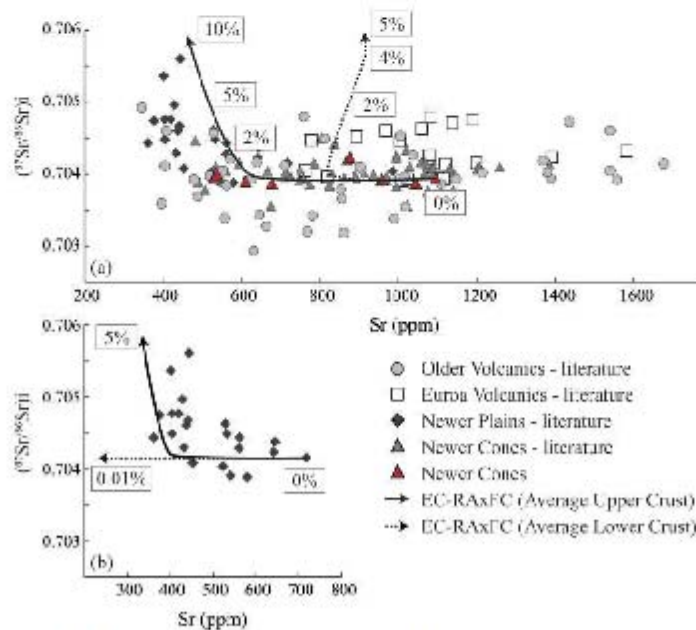


**Fig. 11.** (a) Sr (ppm) vs  $^{87}Sr/^{86}Sr$  for all Newer Cones samples showing EC-RA<sub>x</sub>FC modelling using input parameters as in Table 3. (b) Enlarged section of (a) showing EC-RA<sub>x</sub>FC modelling results for the Newer Plains (Price *et al.*, 1997, 2014) using input parameters as in Table 3. The continuous and dashed lines represent assimilation and fractional crystallization of average upper and lower crust (Taylor & McLennan, 1996), respectively.

Downloaded from <http://petrology.oxfordjournals.org/> by guest on October 19, 2016



compositions trending toward Indian MORB compositions (Fig. 8a). This suggests that a mantle source such as Indian MORB-source asthenosphere may be considered as one of the end-members for these rocks, which is in agreement with our trace element modelling.

As far as we are aware, only Stolz & Davies (1988) have presented Pb isotope data for the xenoliths of the NVP; these have heterogeneous Pb isotope compositions, which are representative of the lithospheric mantle beneath the region. Stolz & Davies subdivided spinel lherzolites from Mount Gnotuk and Lake Bullenmerri into four suites based on their trace element and isotope compositions: Group 0: depleted, anhydrous xenoliths with Pb isotope composition similar to isotopically distinct Indian MORB (Rehkamper & Hofmann, 1997); Group 1: enriched, anhydrous xenoliths, probably metasomatized by CO<sub>2</sub>-rich fluids, with Pb isotope compositions trending towards EMI; Group 2: hydrous xenoliths probably metasomatized by interaction between alkaline magmas and the source of the depleted anhydrous xenoliths (Group 0) with Pb isotope compositions similar to Group 3, but having lower Sr isotope and higher Nd isotope compositions respectively; Group 3: hydrous xenoliths metasomatized subsequently by fluids originating from deeper levels in the mantle with Pb isotope composition similar to Group 2, but having higher Sr isotope and lower Nd isotope compositions (Stolz & Davies, 1988). The metasomatic agent for this last group is suspected to be calcio-carbonatite fluid (Stolz & Davies, 1988); the Sr–Nd isotope compositions of this group overlap with those of Group B of Powell *et al.* (2004), which are interpreted to have undergone carbonatite metasomatism. Price *et al.* (2014) also indicated the potential for 1% calcio-carbonatite fluid to have been added to depleted mantle to generate the range of Older Volcanics with distinctive negative K anomalies.

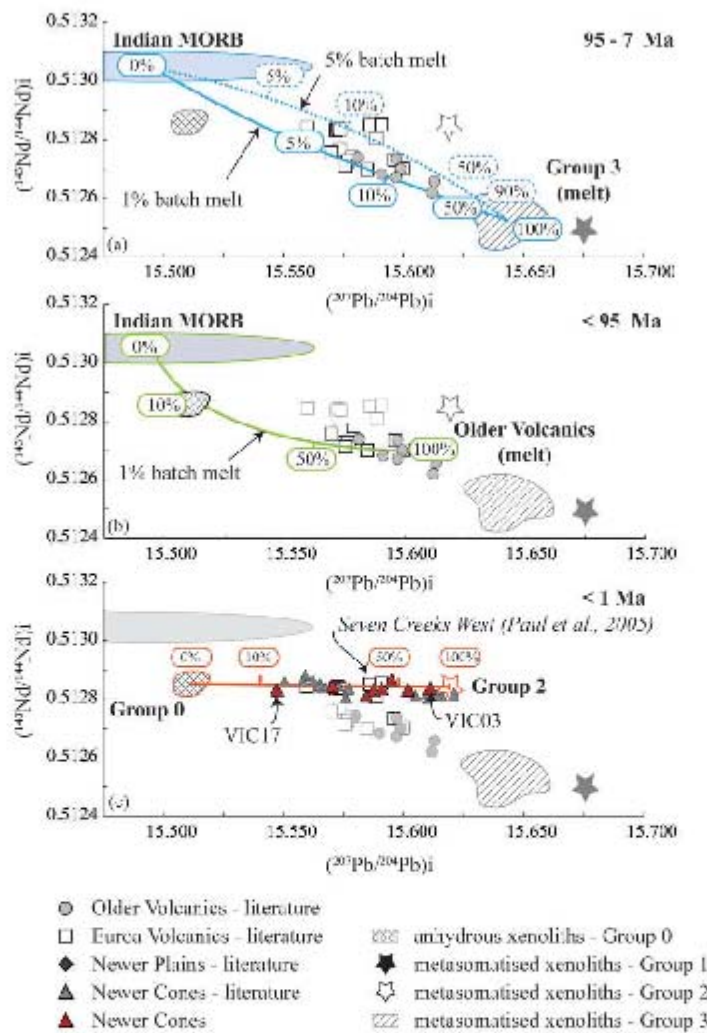
The difference between the three basalt groups is expressed in a (<sup>207</sup>Pb/<sup>204</sup>Pb)<sub>i</sub> vs (<sup>143</sup>Nd/<sup>144</sup>Nd)<sub>i</sub> diagram, where there is a clear distinction between the trends of the Newer Cones, Euroa Volcanics and Older Volcanics (Fig. 12). As a consequence, we propose that the isotopic compositions of the Older Volcanics and part of the Euroa Volcanics can be explained by binary mixing between a mantle source similar to the depleted asthenospheric source of Indian MORB and metasomatized lithospheric mantle represented by the Group 3 xenoliths. In contrast, the isotopic signature of the Newer Cones is more consistent with binary mixing between mantle sources similar to the Group 0 and Group 2 xenoliths. We modelled this mixing using the equation of Vollmer (1976).

Figure 12a (blue lines) shows that the range of Older Volcanics isotope compositions can be generated by mixing of Indian MORB-source mantle (<sup>143</sup>Nd/<sup>144</sup>Nd = 0.51303, <sup>207</sup>Pb/<sup>204</sup>Pb = 15.486 [based on the average composition of Indian MORB reported by Stracke *et al.* (2003)], [Nd] = 9 ppm and [Pb] = 0.6 ppm (Sun & McDonough, 1989) and a small-degree partial melt

derived from the protolith of the Group 3 xenoliths (<sup>143</sup>Nd/<sup>144</sup>Nd = 0.512523, <sup>207</sup>Pb/<sup>204</sup>Pb = 15.6424; Stolz & Davies, 1988). Trace element concentrations used for mixing modelling of the Group 3 xenoliths were [Nd] = 167.78 ppm and [Pb] = 13.68 ppm and Nd = 85.24 ppm and Pb = 3.17 ppm derived from calculations based on 1% and 5% batch melting, respectively, of the most primitive Group 3 xenolith (MgO = 41.02 wt %, [Ni] = 2072 ppm, [Cr] = 5967 ppm; Stolz & Davies, 1988). It is shown that the Older Volcanics with low <sup>143</sup>Nd/<sup>144</sup>Nd for a given <sup>207</sup>Pb/<sup>204</sup>Pb can be derived from a source comprising Indian MORB-source mantle to which 5–10% of small-degree Group 3 melts are added (1% partial melting of the original peridotite), whereas the Older Volcanics with slightly higher <sup>143</sup>Nd/<sup>144</sup>Nd for a given <sup>207</sup>Pb/<sup>204</sup>Pb are more probably derived from a source resulting from mixing of Indian MORB-source mantle and up to 40% Group 3 melt (5% partial melting). The Group 0 depleted, anhydrous xenoliths of Stolz & Davies (1988) have Pb isotope compositions similar to Indian MORB, but have slightly higher and lower Sr and Nd isotope compositions, respectively. We propose that subsequent interaction of Indian MORB-source mantle with the alkaline melts that generated the Older Volcanics could have generated the protolith of the Group 0 xenoliths. Mixing between the most primitive of the Older Volcanics [(<sup>143</sup>Nd/<sup>144</sup>Nd)<sub>i</sub> = 0.5127, (<sup>207</sup>Pb/<sup>204</sup>Pb)<sub>i</sub> = 15.599, Mg-number = 69 (Price *et al.*, 2014)] and Indian MORB-source mantle, with the composition given above, shows that adding c. 10% alkaline melt to Indian MORB-source mantle lowers the Nd isotope composition towards that of the Group 0 xenoliths (Fig. 12b, green line).

The Newer Cones, however, show contrasting behaviour with a very narrow range in Nd isotope composition for a given (<sup>207</sup>Pb/<sup>204</sup>Pb)<sub>i</sub>, forming a trend between the Group 0 and Group 2 xenoliths. Mixing between Group 0 (<sup>143</sup>Nd/<sup>144</sup>Nd = 0.51265, <sup>207</sup>Pb/<sup>204</sup>Pb = 15.507, [Nd] = 1.36 ppm and [Pb] = 0.019 ppm) and Group 2 (<sup>143</sup>Nd/<sup>144</sup>Nd = 0.512841, <sup>207</sup>Pb/<sup>204</sup>Pb = 15.619, [Nd] = 4.86 ppm and [Pb] = 0.059 ppm; Stolz & Davies, 1988) sources shows that VIC17 can be generated by only 10% addition of Group 2 into the depleted anhydrous mantle, whereas VIC03 requires a greater amount of mixing (~80% of Group 2; Fig. 12c). There is no direct evidence that carbonatite metasomatized xenoliths (Group 3) have had much influence in the generation of the Newer Cones basalts.

The Euroa Volcanics are divided into two groups of which the majority approximately follow the trend of the Older Volcanics (Fig. 12a), whereas the data for samples from Seven Creeks West (Paul *et al.*, 2005) overlap with our data on the Newer Cones (Fig. 12c). It would be interesting to determine the age of the samples from the Seven Creeks, as an old age would imply that they originated from the same process as the Older Volcanics, as described above, whereas ages similar to the Newer Cones would indicate that they were derived by melting of mixed Group 0 and Group 2 lithospheric mantle sources.



Downloaded from <http://jpetrology.oxfordjournals.org/> by guest on October 19, 2016

**Fig. 12.**  $(^{207}\text{Pb}/^{204}\text{Pb})_i$  vs  $(^{143}\text{Nd}/^{144}\text{Nd})_i$  for samples interpreted to represent magmas unaffected by crustal assimilation showing: (a) calculated mixing line (Vollmer, 1976) between Indian MORB-source mantle and melts derived by 1% (blue continuous line) and 5% (blue dashed line) partial melting of Group 3 xenoliths; (b) calculated mixing line between Indian MORB-source mantle and the most primitive sample (Mg-number = 67) of the Older Volcanics (green continuous line); (c) calculated mixing line between Group 0 and Group 2 xenoliths. It should be noted that the Euroa Volcanics plot in two groups. The Seven Creek West samples (Paul *et al.*, 2005) are indicated.

In summary, whereas the 95–19 Ma Older Volcanics as well as part of the Euroa Volcanics have isotopic compositions indicating basalt generation from a source with isotope characteristics similar to that of a

mixture between Indian MORB-source mantle and small-degree partial melts of the protolith of Group 3 (carbonatite metasomatized) xenoliths, the <1 Ma Newer Plains and perhaps the remainder of the Euroa

Volcanics show that basalt generation can be explained entirely by melting of a distinctively different suite of source materials comprising modified Indian MORB-source mantle (Group 0) and alkaline melt metasomatized xenoliths (Group 2). Our model compares well with, and is an extension of, the model of Price *et al.* (2014), who suggested mixing of 1% calcio-carbonatite fluid to the depleted mantle to generate the geochemical signature of the Older Volcanics.

### Geodynamics

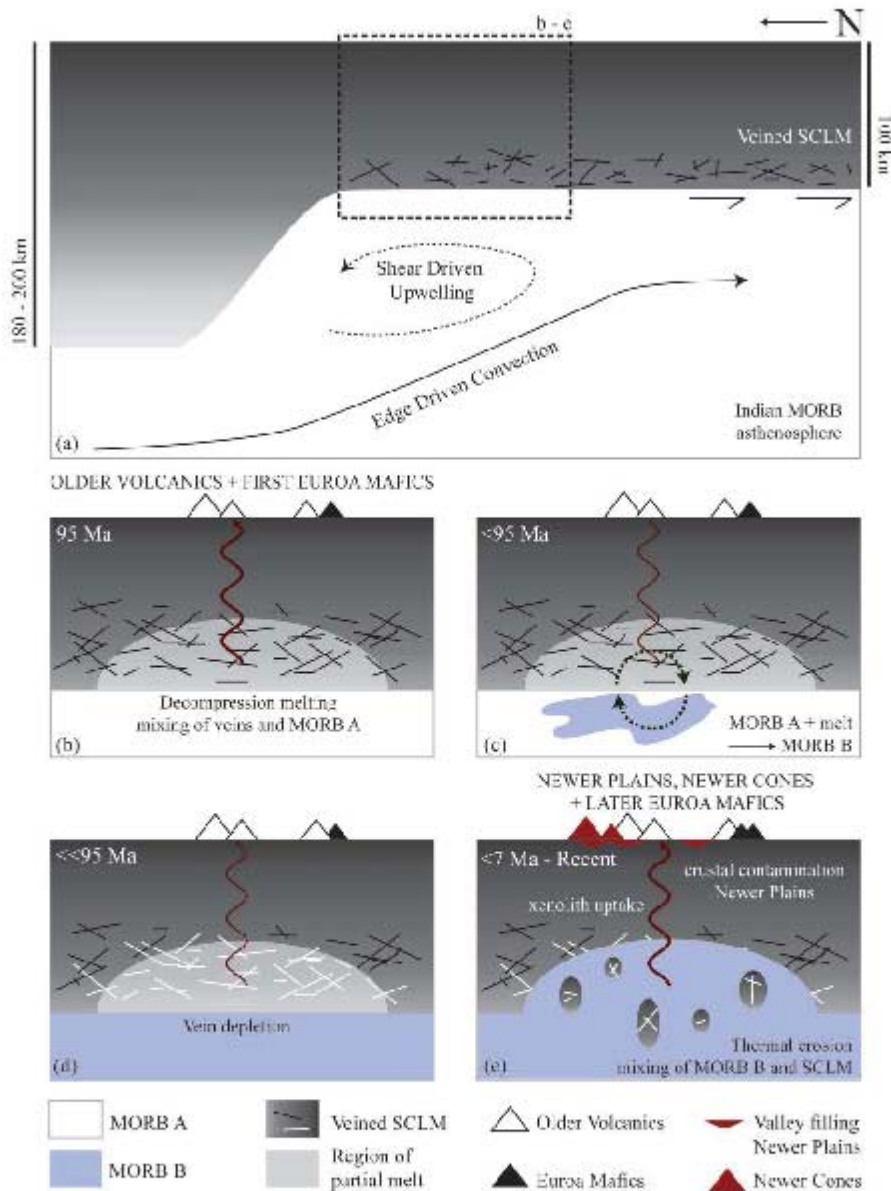
A recent teleseismic tomography study (Davies & Rawlinson, 2014), based on variations in P-wave velocity, has revealed the presence of a low-velocity anomaly in the upper mantle that spatially corresponds to the surface extent of the NVP. Such an anomaly is indicative of the presence of elevated temperatures (mantle plume) and/or a region of partial melt in the upper mantle (Davies & Rawlinson, 2014), the latter hypothesis being preferred owing to the limited topographic response in the region (Demidjuk *et al.*, 2007). The existence of U/Th disequilibria showing a  $^{230}\text{Th}$  excess of 12–57% (Demidjuk *et al.*, 2007) is suggestive of dynamic melting in the upwelling upper asthenosphere rather than static batch melting within the lithosphere, an interpretation that is supported by magnetotelluric sounding that provides evidence for decompression melting in the upper asthenosphere (Aivazpourporgou *et al.*, 2015). It is thought that this upwelling is triggered by three-dimensional (3D) thickness variations in the lithosphere causing edge-driven convection (King & Anderson, 1998). Rapid plate movement from 40 Ma onwards, after the separation of Antarctica and Australia (Veevers, 1986), resulted in a fast, northward plate movement of  $6.5\text{ cm a}^{-1}$  (Sela *et al.*, 2002). As this plate movement is perpendicular to a step in lithospheric thickness (Demidjuk *et al.*, 2007) and plate movement is  $>1\text{ cm a}^{-1}$ , edge-driven convection with shear resulting in upwelling is postulated to be the geodynamic cause of the NVP magmatism (Conrad *et al.*, 2011). Convection cell sizes of the order of 150–200 km may form during edge-driven convection (King & Anderson, 1998), which is comparable with the spatial extent of volcanism in SE Australia. Recent edge-driven convection modelling for the Moroccan Cenozoic volcanic province (Kaislaniemi & Van Hunen, 2014) shows that upwelling mantle (1) facilitates decompression melting, removing any hydrous mantle components, and (2) erodes the bottom of the mantle lithosphere, entraining the residual depleted lithosphere. Furthermore, that study found that edge-driven convection with shear produces convection rolls with axes perpendicular to lithosphere thickness steps. The complex lithosphere configuration beneath Victoria, with a stacked alternation of continental (Delamerian) and continental and oceanic (Lachlan) crust, as well as a locally constrained continental section of the Selwyn block within the Lachlan fold belt, potentially generates a complex 3D configuration of convection rolls, capable of

variably focusing the loci of upwelling and associated magmatism in the region.

Figure 13a shows a schematic representation of our interpretation of the processes leading to the genesis of the Older Volcanics, Euroa Volcanics, Newer Plains and Newer Cones magmatism. Using the different xenolith groups as proxies for larger scale mantle components [Group 0 = modified Indian MORB-source mantle ('MORB-B'); Group 2 = depleted SCLM; Group 1 and Group 3 = veined SCLM] we can deduce the spatial and temporal variations in the composition of the mantle beneath SE Australia. We suggest that at the time of earliest basalt generation (Fig. 13b) the mantle beneath Victoria consisted of an Indian MORB-source asthenosphere (MORB-A) and a veined, Group 3-type SCLM (O'Reilly & Griffin, 1988). Such veins can have solidus temperatures up to 200°C lower than their surrounding wall-rocks (Foden *et al.*, 2002) and will melt first during decompression melting at the base of the lithosphere. Mixing of melts of these veins with upwelling Indian MORB-source mantle potentially resulted in the distinct  $(\text{Sm}/\text{Yb})_{\text{CL}}$ ,  $(\text{Eu}/\text{Yb})_{\text{CL}}$  and Pb and Nd isotope signatures of the Older Volcanics and part of the Euroa Volcanics. Prolonged periods of decompression melting could have caused minor modification of the Indian MORB-source asthenosphere (MORB-B) owing to mixing of alkaline melts with this source as evidenced by the Group 0 xenolith compositions (Stolz & Davies, 1988; Figs 12b and 13c). Furthermore, continuing vein melting in the region of decompression melting would have purged the SCLM of enriched Group 3 veins, leaving a more depleted residual SCLM (Fig. 13d). As upwelling continued (Fig. 13e), thermal erosion of the depleted residual SCLM potentially resulted in lithosphere delamination and mixing of this depleted SCLM with modified Indian MORB-source asthenosphere; which in turn was the source of the basalts of the Newer Plains and Newer Cones. High degrees of partial melting following lithosphere delamination could have resulted in the volumetrically dominant, tholeiitic Newer Plains magmas. As the Newer Plains magmatic rocks are relatively depleted in incompatible elements compared with the Newer Cones, crustal contamination would have affected their isotope and trace element compositions more than the compositions of the Newer Cones. Both of these slightly deeper melts might have incorporated shallow, enriched, metasomatized xenoliths of all groups that were unaffected by decompression melting *en route* to the surface, as indicated by the presence of abundant, compositionally variable mantle xenoliths within the Newer Cones. Such a model is in agreement with recent geophysical observations in the province as well as with the wide range of pressures calculated for both Older Volcanics and Newer Cones basalt generation (1.5–4.5 GPa; Price *et al.*, 2014).

### CONCLUSIONS

New major and trace element and Sr, Nd and Pb isotope data for the youngest expression of Cretaceous to



Downloaded from <http://jpetrology.oxfordjournals.org/> by guest on October 19, 2016

**Fig. 13.** (a) Interpreted temporal geodynamic evolution of the mantle below SE Australia (after Kaisaniemi & Van Hunen, 2014). Thickness to the base of the lithosphere after Davies & Rawlinson (2014). (b) Enlarged section. Decompression melting at the base of the lithosphere results in preferential melting of metasomatized veins and mixing of the resultant enriched partial melts with Indian MORB-source mantle (MORB-A) thereby generating the magmas parental to the Older Volcanics. (c) Mixing of MORB-A with the alkaline melts represented by the Older Volcanics results in a slightly modified Indian MORB-source mantle (MORB-B). (d) Prolonged periods of melting will deplete the SCLM of calcio-carbonate metasomatized veins. (e) Continued edge-driven convection with shear causes thermal erosion of the base of the lithosphere, incorporating depleted SCLM within MORB-B. The resultant melts have the potential to incorporate enriched vein material from the SCLM en route to the surface.

Cenozoic volcanism in SE Australia suggest spatial and long-term temporal geochemical and geodynamic variations within the mantle below. We find that basalts of the <1 Ma Newer Cones were generated by c. 5–10% partial melting of a garnet-spinel mantle source, the composition of which can be represented as a mixture of depleted, anhydrous, Indian MORB-source spinel lherzolite and enriched, hydrous spinel lherzolite metasomatized by alkaline melts. The resulting melts evolved by fractional crystallization. According to our modelling, up to 20% crystallization is required to reach the composition of the analysed samples. EC-RA<sub>1</sub>FC modelling shows that the Newer Cones magmas were not affected by crustal assimilation processes. Conversely, the enriched trace element and isotope signatures of the <4.6 Ma Newer Plains magmatic rocks can be modelled by up to 5% assimilation of average upper crust. The ~7 Ma Euroa Volcanics represent basaltic magmas generated by similar degrees of partial melting (10%) but slightly smaller amounts of fractional crystallization (15%). Their Pb and Nd isotope compositions suggest a heterogeneous source, which we interpret to reflect a progressive temporal change from the source of the Older Volcanics to the source of the Newer Cones. The 95–19 Ma Older Volcanics have trace element and Sr–Nd–Pb isotope signatures that are distinct from those of the other series; their source can be modelled by adding c. 10% melt derived by small degrees of partial melting of carbonatite metasomatized vein material to a composition similar to that of Indian MORB-source mantle. We suggest that the temporal variation in the mantle source can be explained by a geodynamical model of edge-driven convection with shear. The primary magmas of the Older Volcanics were formed by decompression melting that favoured the partial melting of hydrous, carbonatite metasomatized mantle veins. Subsequent thermal erosion and entrainment of the depleted SCLM in the locally slightly enriched upper asthenosphere resulted in the generation of the Euroa Volcanics, Newer Plains and Newer Cones.

#### ACKNOWLEDGEMENTS

Professor David Phillips and Dr Erin Matchan of the University of Melbourne and David Taylor of the Geological Survey of Victoria are thanked for their assistance in the field. Michèle Senn (University of Geneva) is thanked for performing the column chemistry for the Sr, Nd and Pb isotope analyses. Richard Price (University of Waikato), Lucy McGee (Universidad de Chile) and an anonymous reviewer provided constructive reviews, and Richard Price and Marjorie Wilson are thanked for editorial handling. The support of TIGER and the Department of Applied Geology at Curtin University of Technology is gratefully acknowledged.

#### FUNDING

This research was funded by Australian Research Council Discovery grant DP130100517.

#### SUPPLEMENTARY DATA

Supplementary data for this paper are available at *Journal of Petrology* online.

#### REFERENCES

- Aivazpourporgou, S., Thiel, S., Hayman, P. C., Moresi, L. N. & Heinson, G. (2015). Decompression melting driving intraplate volcanism in Australia: Evidence from magnetotelluric sounding. *Geophysical Research Letters* **42**, 1–9.
- Aziz-ur-Rahman & McDougall, I. (1972). Potassium-argon ages on the Newer Volcanics of Victoria. *Proceedings of the Royal Society of Victoria* **85**, 61–69.
- Baker, J., Peato, D., Waight, T. & Meyzer, C. (2004). Pb isotopic analysis of standards and samples using a <sup>207</sup>Pb–<sup>204</sup>Pb double spike and thallium to correct for mass bias with a double-focusing MC-ICPMS. *Chemical Geology* **211**, 275–303.
- Blackburn, G., Allison, G. B. & Leaney, F. W. J. (1982). Further evidence on the age of tuff at Mt Gambier, South Australia. *Transactions of the Royal Society of South Australia* **106**, 163–167.
- Bohrson, W. A. & Spera, F. J. (2001). Energy-constrained open-system magmatic processes II: Application of energy-constrained assimilation-fractional crystallization (EC-AFC) model to magmatic systems. *Journal of Petrology* **42**, 1019–1041.
- Boyce, J. (2013). The Newer Volcanics Province of southeastern Australia: a new classification scheme and distribution map for eruption centres. *Australian Journal of Earth Sciences* **60**, 449–462.
- Boyce, J. A., Nicholls, I. A., Keays, R. R. & Hayman, P. C. (2015). Composition and volatile contents of parental magmas of Mt. Rouse, a polymagmatic volcano in the Newer Volcanics intraplate basaltic province, SE Australia. *Contributions to Mineralogy and Petrology* **169**, 1–21.
- Brenna, M., Cronin, S. J., Smith, I. E. M., Sohn, Y. K. & Németh, K. (2010). Mechanisms driving polymagmatic activity at a monogenetic volcano, Udo, Jeju Island, South Korea. *Contributions to Mineralogy and Petrology* **160**, 931–950.
- Cartwright, I., Weaver, T., Tweed, S., Ahasme, D., Cooper, M., Czupnik, K. & Tranter, J. (2002). Stable isotope geochemistry of cold CO<sub>2</sub>-bearing mineral spring waters, Daylesford, Victoria, Australia: Sources of gas and water and links with waning volcanism. *Chemical Geology* **185**, 71–91.
- Cayley, R. A., Korsch, K. J., Moore, D. H. et al. (2011). Crustal architecture of central Victoria: results from the 2006 deep crustal reflection seismic survey. *Australian Journal of Earth Sciences* **58**, 113–156.
- Chiaradia, M., Muntaner, O. & Beate, B. (2011). Enriched basaltic andesites from mid-crustal fractional crystallization, recharge, and assimilation (Pilavo Volcano, Western Cordillera of Ecuador). *Journal of Petrology* **52**, 1107–1141.
- Conrad, C. P., Bianco, T. A., Smith, E. I. & Wessel, P. (2011). Patterns of intraplate volcanism controlled by asthenospheric shear. *Nature Geoscience* **4**, 317–321.
- Cooper, J. A. & Green, D. H. (1969). Lead isotope measurements on lherzolite inclusions and host basanites from Western Victoria, Australia. *Earth and Planetary Science Letters* **6**, 69–76.
- Davies, D. R. & Rawlinson, N. (2014). On the origin of recent intraplate volcanism in Australia. *Geology* **42**, 1–4.
- Davies, D. R., Rawlinson, N., Iaffaldano, G. & Campbell, I. H. (2015). Lithospheric controls on magma composition along Earth's longest continental hotspot track. *Nature* **525**, 511–514.

- Day, R. A. (1983). Petrology and geochemistry of the Older Volcanics, Victoria: distribution, characterization, and petrogenesis. Monash University, PhD thesis, Department of Earth Sciences.
- Day, R. A. (1989). East Australia volcanic geology, Victoria and South Australia. In: Johnson, R. W. (ed.) *Intraplate Volcanism of Eastern Australia and New Zealand*. Australian Academy of Science, pp. 132–142.
- Demidjuk, Z., Turner, S., Sandiford, M., George, R., Foden, J. & Etheridge, M. (2007). U-series isotope and geodynamic constraints on mantle melting processes beneath the Newer Volcanic Province in South Australia. *Earth and Planetary Science Letters* 261, 517–533.
- Ellis, D. J. (1976). High pressure cognate inclusions in the Newer Volcanics of Victoria. *Contributions to Mineralogy and Petrology* 58, 149–180.
- Ewart, A. (2004). Petrology and geochemistry of Early Cretaceous bimodal continental flood volcanism of the NW Etendeka, Namibia. Part 1: Introduction, mafic lavas and re-evaluation of mantle source components. *Journal of Petrology* 45, 59–105.
- Foden, J., Song, S. H., Turner, S., Elburg, M., Smith, P. B., Van der Steldt, B. & Van Panglis, D. (2002). Geochemical evolution of lithospheric mantle beneath S.E. South Australia. *Chemical Geology* 182, 663–696.
- Frey, F. A. & Green, D. H. (1974). The mineralogy, geochemistry and origin of ilherzolite inclusions in Victorian basanites. *Geochimica et Cosmochimica Acta* 38, 1023–1059.
- Frey, F. A., Green, D. H. & Roy, S. D. (1978). Integrated models of basalt petrogenesis: a study of quartz tholeiites to olivine melilitites from south eastern Australia utilizing geochemical and experimental petrological data. *Journal of Petrology* 19, 463–613.
- Ghiorso, M. S. & Sack, R. O. (1995). Chemical mass transfer in magmatic processes IV. A revised and internally consistent thermodynamic model for the interpolation and extrapolation of liquid–solid equilibria in magmatic systems at elevated temperatures and pressures. *Contributions to Mineralogy and Petrology* 119, 197–212.
- Gray, C. M. & McDougall, I. (2009). K–Ar geochronology of basalt petrogenesis, Newer Volcanic Province, Victoria. *Australian Journal of Earth Sciences* 56, 245–258.
- Griffin, W. L., O'Reilly, S. Y. & Stabel, A. (1988). Mantle metasomatism beneath western Victoria, Australia: II. Isotopic geochemistry. *Geochimica et Cosmochimica Acta* 52, 449–459.
- Handler, M. R., Bennett, V. C. & Esat, T. M. (1997). The persistence of off-cratonic lithospheric mantle: Os isotopic systematics of variably metasomatised southeast Australian xenoliths. *Earth and Planetary Science Letters* 151, 61–75.
- Hofmann, A. W., Jochum, K. P., Seufert, M. & White, W. M. (1986). Nb and Pb in oceanic basalts: new constraints on mantle evolution. *Earth and Planetary Science Letters* 79, 33–45.
- Irvine, T. N. & Baragar, W. R. A. (1971). A guide to the chemical classification of the common volcanic rocks. *Canadian Journal of Earth Sciences* 8, 523–548.
- Kaislaniemi, L. & Van Hunen, J. (2014). Dynamics of lithosphere thinning and mantle melting by edge-driven convection; application to the Moroccan Atlas mountains. *Geochemistry, Geophysics, Geosystems* 15, 3175–3189.
- King, S. D. & Anderson, D. L. (1998). Edge-driven convection. *Earth and Planetary Science Letters* 160, 289–296.
- Le Bas, M. J., La Maitre, R. W., Streckeisen, A. & Zanettin, B. (1986). A chemical classification of volcanic rocks based on the total alkali vs. silica diagram. *Journal of Petrology* 27, 745–750.
- Matchan, E. L. & Phillips, D. (2011). New  $^{40}\text{Ar}/^{39}\text{Ar}$  gas for selected young (<1Ma) basalt flows of the Newer Volcanic Province, southeastern Australia. *Quaternary Geochronology* 6, 356–368.
- Matchan, E. L. & Phillips, D. (2014). High precision multi-collector  $^{40}\text{Ar}/^{39}\text{Ar}$  dating of young basalts: Mount Rouse volcano (SE Australia) revisited. *Quaternary Geochronology* 22, 57–64.
- McBride, J. S., Lambert, D. D., Nicholls, I. A. & Price, R. C. (2001). Osmium isotopic evidence for crust–mantle interaction in the genesis of continental intraplate basalts from the Newer Volcanics Province, southeastern Australia. *Journal of Petrology* 42, 1197–1218.
- McDonough, W. F. & McCulloch, M. T. (1987). The southeast Australian lithospheric mantle: isotopic and geochemical constraints on its growth and evolution. *Earth and Planetary Science Letters* 86, 327–340.
- McDonough, W. F., McCulloch, M. T. & Sun, S. S. (1985). Isotopic and geochemical systematics in Tertiary–Recent basalts from southeastern Australia and implications for the evolution of the sub-continental lithosphere. *Geochimica et Cosmochimica Acta* 49, 2051–2067.
- McDougall, I., Allsopp, H. L. & Chamalaun, F. H. (1966). Isotopic dating of the newer volcanics of Victoria, Australia, and geomagnetic polarity epochs. *Journal of Geophysical Research* 71, 6107–6118.
- McGee, L. E., Beier, C., Smith, I. E. M. & Turner, S. P. (2011). Dynamics of melting beneath a small-scale basaltic system: A U–Th–Ra study from Rangitoto volcano, Auckland volcanic field, New Zealand. *Contributions to Mineralogy and Petrology* 162, 547–563.
- McGee, L. E., Smith, I. E. M., Millet, M. A., Handley, H. K. & Lindsay, J. M. (2013). Asthenospheric control of melting processes in a monogenetic basaltic system: A case study of the Auckland volcanic field, New Zealand. *Journal of Petrology* 54, 2125–2153.
- McKenzie, D. & O'Nions, R. K. (1983). Mantle reservoirs and ocean island basalts. *Nature* 301, 229–231.
- Nelson, D. R., McCulloch, M. T. & Sun, S. S. (1986). The origins of ultrapotassic rocks as inferred from Sr, Nd and Pb isotopes. *Geochimica et Cosmochimica Acta* 50, 231–245.
- Oostingh, K. F., Jourdan, F., Phillips, D. & Matchan, E. L. (2015). Ultra-precise  $^{40}\text{Ar}/^{39}\text{Ar}$  geochronology and  $^{39}\text{Ar}$  exposure dating on young basalts from the Newer Volcanic Province, Australia. *Goldschmidt 2015 Conference Abstracts*. Goldschmidt Conference Abstracts, 2351.
- O'Reilly, S. Y. & Griffin, W. L. (1984). Sr isotopic heterogeneity in primitive basaltic rocks, southeastern Australia: correlation with mantle metasomatism. *Contributions to Mineralogy and Petrology* 87, 220–230.
- O'Reilly, S. Y. & Griffin, W. L. (1988). Mantle metasomatism beneath western Victoria, Australia: I. Metasomatic processes in Cr-diopside ilherzolites. *Geochimica et Cosmochimica Acta* 52, 433–447.
- O'Reilly, S. Y. & Zhang, M. (1995). Geochemical characteristics of lava-field basalts from eastern Australia and inferred sources: connections with the subcontinental lithospheric mantle? *Contributions to Mineralogy and Petrology* 121, 148–170.
- Paul, B., Hergt, J. M. & Woodhead, J. D. (2005). Mantle heterogeneity beneath the Cenozoic volcanic provinces of central Victoria inferred from trace-element and Sr, Nd, Pb and Hf isotope data. *Australian Journal of Earth Sciences* 52, 243–260.
- Peuclet-Ehrenbrink, B. & Jahn, B. (2001). Rhenium–osmium isotope systematics and platinum group element concentrations: Loess and the upper continental crust. *Geochemistry, Geophysics, Geosystems* 2. DOI: 10.1029/2001GC000172.


- Powell, W., Zhang, M., O'Reilly, S. Y. & Tiepolo, M. (2004). Mantle amphibole trace-element and isotopic signatures trace multiple metasomatic episodes in lithospheric mantle, western Victoria, Australia. *Lithos* **75**, 141–171.
- Price, R. C., Gray, C. M. & Frey, F. A. (1997). Strontium isotopic and trace element heterogeneity in the plains basalts of the Newer Volcanic Province, Victoria, Australia. *Geochimica et Cosmochimica Acta* **61**, 171–192.
- Price, R. C., Nicholls, I. A. & Gray, C. M. (2003). Cainozoic igneous activity. In Bird, W. D. (ed.) *Geology of Victoria*. Geological Society of Australia Special Publication 23. Geological Society of Australia (Victoria Division), pp. 361–375.
- Price, R. C., Nicholls, I. A. & Day, A. (2014). Lithospheric influences on magma compositions of late Mesozoic and Cenozoic intraplate basalts (the Older Volcanics) of Victoria, south-eastern Australia. *Lithos* **206–207**, 179–200.
- Rehkamper, M. & Hofmann, A. W. (1997). Recycled ocean crust and sediment in Indian Ocean MORB. *Earth and Planetary Science Letters* **147**, 93–106.
- Sella, G. F., Dixon, T. H. & Mao, A. (2002). REVEL: A model for recent plate velocities from space geodesy. *Journal of Geophysical Research* **107**. DOI: 10.1029/2000JB000033.
- Shaw, D. M. (1970). Trace element fractionation during anatexis. *Geochimica et Cosmochimica Acta* **34**, 237–243.
- Spera, F. J. (2001). Energy-constrained open-system magmatic processes I: General model and energy-constrained assimilation and fractional crystallization (EC-AFC) formulation. *Journal of Petrology* **42**, 999–1018.
- Stolz, A. J. & Davies, G. R. (1988). Chemical and isotopic evidence from spinel lherzolite xenoliths for episodic metasomatism of the upper mantle beneath southeastern Australia. *Journal of Petrology, Special Volume*, 303–330.
- Stracka, A., Bizimis, M. & Salters, V. J. M. (2003). Recycling oceanic crust: Quantitative constraints. *Geochemistry, Geophysics, Geosystems* **4**. DOI: 10.1029/2001GC000223.
- Stracka, A., Hofmann, A. W. & Hart, S. R. (2005). FOZO, HIMU, and the rest of the mantle zoo. *Geochemistry, Geophysics, Geosystems* **6**. DOI: 10.1029/2004GC000824.
- Sun, S. S. & McDonough, W. F. (1989). Chemical and isotopic systematics of oceanic basalts: implications for mantle composition and processes. In: Saunders, A. D. & Norry, M. J. (eds) *Magmaism in the Ocean Basins*. Geological Society, London, *Special Publications* **42**, 313–345.
- Tanaka, T., Togashi, S., Kamioka, H., Amakawa, H., Kagami, H. & Hamamoto, T. (2000). JNd-1: a neodymium isotopic reference in consistency with LaJolla neodymium. *Chemical Geology* **168**, 279–281.
- Taylor, S. R. & McLennan, S. M. (1995). The geochemical evolution of the continental crust. *Reviews of Geophysics* **33**, 241–265.
- Van Otterloo, J., Ravaggi, M., Cas, R. A. F. & Maas, R. (2014). Polymagmatic activity at the monogenetic Mt Gambier volcanic complex in the Newer Volcanics Province, SE Australia: new insights into the occurrence of intraplate volcanic activity in Australia. *Journal of Petrology* **55**, 1317–1351.
- Veevers, J. J. (1986). Breakup of Australia and Antarctica estimated as mid-Cretaceous (95 ± 5 Ma) from magnetic and seismic data at the continental margin. *Earth and Planetary Science Letters* **77**, 91–99.
- Vogel, D. C. & Keays, R. R. (1997). The petrogenesis and platinum-group element geochemistry of the Newer Volcanic Province, Victoria, Australia. *Chemical Geology* **136**, 181–204.
- Vollmer, R. (1976). Rb-Sr and U-Th-Pb systematics of alkaline rocks: the alkaline rocks from Italy. *Geochimica et Cosmochimica Acta* **40**, 283–295.
- Walter, M. J. (1998). Melting of garnet peridotite and the origin of komatiite and depleted lithosphere. *Journal of Petrology* **39**, 29–60.
- Wellman, P. (1974). Potassium-argon ages on the Cainozoic volcanic rocks of Eastern Victoria, Australia. *Journal of the Geological Society of Australia* **21**, 359–376.
- Wellman, P. & McDougall, I. (1974). Cainozoic igneous activity in eastern Australia. *Tectonophysics* **23**, 49–65.
- Yaxley, G. M., Crawford, A. J. & Green, D. H. (1991). Evidence for carbonate metasomatism in spinel peridotite xenoliths from western Victoria, Australia. *Earth and Planetary Science Letters* **107**, 305–317.
- Yaxley, G. M., Kamenetsky, V. S., Green, D. H. & Falloon, T. J. (1997). Glasses in mantle xenoliths from western Victoria, Australia, and their relevance to mantle processes. *Earth and Planetary Science Letters* **148**, 433–446.
- Zheng, M., O'Reilly, S. Y. & Chen, D. (1999). Location of Pacific and Indian mid-ocean ridge-type mantle in two time slices: Evidence from Pb, Sr, and Nd isotopes for Cenozoic Australian basalts. *Geology* **27**, 39.
- Zindler, A. & Hart, S. R. (1986). Chemical geodynamics. *Annual Review of Earth and Planetary Sciences* **14**, 493–571.


# Statement of Authorship


Title of Paper	$^{40}\text{Ar}/^{39}\text{Ar}$ geochronology reveals rapid change from plume-assisted to stress-dependent volcanism in the Newer Volcanic Province, SE Australia.		
Publication Status	<input checked="" type="radio"/> Published	<input type="radio"/> Accepted for Publication	
	<input type="radio"/> Submitted for Publication	<input type="radio"/> Publication Style	
Publication Details	Oostingh, K. F., Jourdan, F., Matchan, E. L. & Phillips, D. (2017). $^{40}\text{Ar}/^{39}\text{Ar}$ geochronology reveals rapid change from plume-assisted to stress-dependent volcanism in the Newer Volcanic Province, SE Australia. <i>Geochemistry, Geophysics, Geosystems</i> ; 18, 1065 - 1089		

## Author Contributions

By signing the Statement of Authorship, each author certifies that their stated contribution to the publication is accurate and that permission is granted for the publication to be included in the candidate's thesis.

Name of Principal Author (Candidate)	Korien Oostingh		
Contribution to the Paper	Korien Oostingh produced the majority of the data and did most of the drafting of the manuscript and the interpretation of the results.		
Overall percentage (%)	70		
Signature		Date	21/12/2016

Name of Co-Author	Fred Jourdan		
Contribution to the Paper	Fred Jourdan is principal supervisor and assisted with the experiments, the drafting of the document and the interpretation of the results.		
Overall percentage (%)	20		
Signature		Date	21/12/2016

Name of Co-Author	Erin Matchan		
Contribution to the Paper	Erin Matchan assisted with the drafting of the document and the interpretation of the results.		
Overall percentage (%)	5		
Signature		Date	21/12/2016



Name of Co-Author	David Phillips		
Contribution to the Paper	David Phillips assisted with the interpretation of the results.		
Overall percentage (%)	5		
Signature	<i>D Phillips</i>	Date	21/12/2016

07/02/17

RightsLink Printable License

**JOHN WILEY AND SONS LICENSE  
TERMS AND CONDITIONS**

May 15, 2017

This Agreement between Korien Oostingh ("You") and John Wiley and Sons ("John Wiley and Sons") consists of your license details and the terms and conditions provided by John Wiley and Sons and Copyright Clearance Center.

License Number	4083401462380
License data	
Licensed Content Publisher	John Wiley and Sons
Licensed Content Publication	Geochemistry, Geophysics, Geosystems
Licensed Content Title	40Ar/39Ar geochronology reveals rapid change from plume-assisted to stress-dependent volcanism in the Newer Volcanic Province, SE Australia
Licensed Content Author	K. F. Oostingh, F. Jourdan, E. L. Matchan, D. Phillips
Licensed Content Date	Mar 21, 2017
Licensed Content Pages	1
Type of use	Dissertation/Thesis
Requestor type	Author of this Wiley article
Format	Electronic
Portion	Full article
Will you be translating?	No
Title of your thesis / dissertation	Ultra-Precise 40Ar/39Ar Geochronology; Development of 38Ar Cosmogenic Exposure and Olivine (U-Th)/He Dating Techniques; and Deciphering the Geochemical Evolution of the Newer Volcanic Province, SE Australia.
Expected completion date	Jan 2017
Expected size (number of pages)	250
Requestor Location	Korien Oostingh Kent St  Perth, WA 6845 Australia Attn: Korien Oostingh
Publisher Tax ID	EU826007151
Billing Type	Invoice
Billing Address	Korien Oostingh Kent St  Perth, Australia 6845 Attn: Korien Oostingh
Total	0.00 USD

**Terms and Conditions****TERMS AND CONDITIONS**

This copyrighted material is owned by or exclusively licensed to John Wiley & Sons, Inc. or one of its group companies (each a "Wiley Company") or handled on behalf of a society with which a Wiley Company has exclusive publishing rights in relation to a particular work

<https://r1100.copyright.com/CustomAdmin/PLF.jsp?m#0606554-4016-40e7-40e0-442e03702020>

145

07/02/17

RightsLink Printable License

(collectively "WILEY"). By clicking "accept" in connection with completing this licensing transaction, you agree that the following terms and conditions apply to this transaction (along with the billing and payment terms and conditions established by the Copyright Clearance Center Inc., ("CCC's Billing and Payment terms and conditions"), at the time that you opened your RightsLink account (these are available at any time at <http://myaccount.copyright.com>).

#### Terms and Conditions

- The materials you have requested permission to reproduce or reuse (the "Wiley Materials") are protected by copyright.
- You are hereby granted a personal, non-exclusive, non-sub licensable (on a stand-alone basis), non-transferable, worldwide, limited license to reproduce the Wiley Materials for the purpose specified in the licensing process. This license, and any CONTENT (PDF or image file) purchased as part of your order, is for a one-time use only and limited to any maximum distribution number specified in the license. The first instance of republication or reuse granted by this license must be completed within two years of the date of the grant of this license (although copies prepared before the end date may be distributed thereafter). The Wiley Materials shall not be used in any other manner or for any other purpose, beyond what is granted in the license. Permission is granted subject to an appropriate acknowledgement given to the author, title of the material/book/journal and the publisher. You shall also duplicate the copyright notice that appears in the Wiley publication in your use of the Wiley Material. Permission is also granted on the understanding that nowhere in the text is a previously published source acknowledged for all or part of this Wiley Material. Any third party content is expressly excluded from this permission.
- With respect to the Wiley Materials, all rights are reserved. Except as expressly granted by the terms of the license, no part of the Wiley Materials may be copied, modified, adapted (except for minor reformatting required by the new Publication), translated, reproduced, transferred or distributed, in any form or by any means, and no derivative works may be made based on the Wiley Materials without the prior permission of the respective copyright owner. For STM Signatory Publishers clearing permission under the terms of the [STM Permissions Guidelines](#) only, the terms of the license are extended to include subsequent editions and for editions in other languages, provided such editions are for the work as a whole in situ and does not involve the separate exploitation of the permitted figures or extracts. You may not alter, remove or suppress in any manner any copyright, trademark or other notices displayed by the Wiley Materials. You may not license, rent, sell, loan, lease, pledge, offer as security, transfer or assign the Wiley Materials on a stand-alone basis, or any of the rights granted to you hereunder to any other person.
- The Wiley Materials and all of the intellectual property rights therein shall at all times remain the exclusive property of John Wiley & Sons Inc, the Wiley Companies, or their respective licensors, and your interest therein is only that of having possession of and the right to reproduce the Wiley Materials pursuant to Section 2 herein during the continuance of this Agreement. You agree that you own no right, title or interest in or to the Wiley Materials or any of the intellectual property rights therein. You shall have no rights hereunder other than the license as provided for above in Section 2. No right, license or interest to any trademark, trade name, service mark or other branding ("Marks") of WILEY or its licensors is granted hereunder, and you agree that you shall not assert any such right, license or interest with respect thereto.
- NEITHER WILEY NOR ITS LICENSORS MAKES ANY WARRANTY OR REPRESENTATION OF ANY KIND TO YOU OR ANY THIRD PARTY, EXPRESS, IMPLIED OR STATUTORY, WITH RESPECT TO THE MATERIALS OR THE ACCURACY OF ANY INFORMATION CONTAINED IN THE

<https://rightslink.copyright.com/CustomerAdmin/PLF.jsp?m#00005514-0010-40e7-80e0-402a03702020>

265

8/18/2017

RightsLink Printable License

**MATERIALS, INCLUDING, WITHOUT LIMITATION, ANY IMPLIED WARRANTY OF MERCHANTABILITY, ACCURACY, SATISFACTORY QUALITY, FITNESS FOR A PARTICULAR PURPOSE, USABILITY, INTEGRATION OR NON-INFRINGEMENT AND ALL SUCH WARRANTIES ARE HEREBY EXCLUDED BY WILEY AND ITS LICENSORS AND WAIVED BY YOU.**

- **WILEY shall have the right to terminate this Agreement immediately upon breach of this Agreement by you.**
- **You shall indemnify, defend and hold harmless WILEY, its Licensors and their respective directors, officers, agents and employees, from and against any actual or threatened claims, demands, causes of action or proceedings arising from any breach of this Agreement by you.**
- **IN NO EVENT SHALL WILEY OR ITS LICENSORS BE LIABLE TO YOU OR ANY OTHER PARTY OR ANY OTHER PERSON OR ENTITY FOR ANY SPECIAL, CONSEQUENTIAL, INCIDENTAL, INDIRECT, EXEMPLARY OR PUNITIVE DAMAGES, HOWEVER CAUSED, ARISING OUT OF OR IN CONNECTION WITH THE DOWNLOADING, PROVISIONING, VIEWING OR USE OF THE MATERIALS REGARDLESS OF THE FORM OF ACTION, WHETHER FOR BREACH OF CONTRACT, BREACH OF WARRANTY, TORT, NEGLIGENCE, INFRINGEMENT OR OTHERWISE (INCLUDING, WITHOUT LIMITATION, DAMAGES BASED ON LOSS OF PROFITS, DATA, FILES, USE, BUSINESS OPPORTUNITY OR CLAIMS OF THIRD PARTIES), AND WHETHER OR NOT THE PARTY HAS BEEN ADVISED OF THE POSSIBILITY OF SUCH DAMAGES. THIS LIMITATION SHALL APPLY NOTWITHSTANDING ANY FAILURE OF ESSENTIAL PURPOSE OF ANY LIMITED REMEDY PROVIDED HEREIN.**
- **Should any provision of this Agreement be held by a court of competent jurisdiction to be illegal, invalid, or unenforceable, that provision shall be deemed amended to achieve as nearly as possible the same economic effect as the original provision, and the legality, validity and enforceability of the remaining provisions of this Agreement shall not be affected or impaired thereby.**
- **The failure of either party to enforce any term or condition of this Agreement shall not constitute a waiver of either party's right to enforce each and every term and condition of this Agreement. No breach under this agreement shall be deemed waived or excused by either party unless such waiver or consent is in writing signed by the party granting such waiver or consent. The waiver by or consent of a party in a breach of any provision of this Agreement shall not operate or be construed as a waiver of or consent to any other or subsequent breach by such other party.**
- **This Agreement may not be assigned (including by operation of law or otherwise) by you without WILEY's prior written consent.**
- **Any fee required for this permission shall be non-refundable after thirty (30) days from receipt by the CCC.**
- **These terms and conditions together with CCC's Billing and Payment terms and conditions (which are incorporated herein) form the entire agreement between you and WILEY concerning this licensing transaction and (in the absence of fraud) supersedes all prior agreements and representations of the parties, oral or written. This Agreement may not be amended except in writing signed by both parties. This Agreement shall be binding upon and issue to the benefit of the parties' successors, legal representatives, and authorized assigns.**

<https://r1100.copyright.com/CustomAdmin/PLF.jsp?m#06065514-401e-40e7-4ba0-442a037b2b23>

265

07/02/17

RightsLink Printink License

- In the event of any conflict between your obligations established by these terms and conditions and those established by CCC's Billing and Payment terms and conditions, these terms and conditions shall prevail.
- WILEY expressly reserves all rights not specifically granted in the combination of (i) the license details provided by you and accepted in the course of this licensing transaction, (ii) these terms and conditions and (iii) CCC's Billing and Payment terms and conditions.
- This Agreement will be void if the Type of Use, Format, Circulation, or Requestor Type was misrepresented during the licensing process.
- This Agreement shall be governed by and construed in accordance with the laws of the State of New York, USA, without regards to such state's conflict of law rules. Any legal action, suit or proceeding arising out of or relating to these Terms and Conditions or the breach thereof shall be instituted in a court of competent jurisdiction in New York County in the State of New York in the United States of America and each party hereby consents and submits to the personal jurisdiction of such court, waives any objection to venue in such court and consents to service of process by registered or certified mail, return receipt requested, at the last known address of such party.

#### WILEY OPEN ACCESS TERMS AND CONDITIONS

Wiley Publishes Open Access Articles in fully Open Access Journals and in Subscription journals offering Online Open. Although most of the fully Open Access journals publish open access articles under the terms of the Creative Commons Attribution (CC BY) License only, the subscription journals and a few of the Open Access Journals offer a choice of Creative Commons Licenses. The license type is clearly identified on the article.

##### The Creative Commons Attribution License

The [Creative Commons Attribution License \(CC-BY\)](#) allows users to copy, distribute and transmit an article, adapt the article and make commercial use of the article. The CC-BY license permits commercial and non-

##### Creative Commons Attribution Non-Commercial License

The [Creative Commons Attribution Non-Commercial \(CC-BY-NC\) License](#) permits use, distribution and reproduction in any medium, provided the original work is properly cited and is not used for commercial purposes. (see below)

##### Creative Commons Attribution-Non-Commercial-NoDerivs License

The [Creative Commons Attribution Non-Commercial-NoDerivs License \(CC-BY-NC-ND\)](#) permits use, distribution and reproduction in any medium, provided the original work is properly cited, is not used for commercial purposes and no modifications or adaptations are made. (see below)

##### Use by commercial "for-profit" organizations

Use of Wiley Open Access articles for commercial, promotional, or marketing purposes requires further explicit permission from Wiley and will be subject to a fee.

Further details can be found on Wiley Online Library

<http://olabout.wiley.com/WileyCDA/Section/id-410895.html>

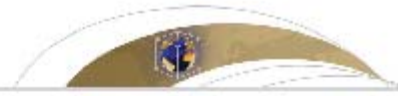
#### Other Terms and Conditions:

v1.10 Last updated September 2015

Questions? [customerscare@copyright.com](mailto:customerscare@copyright.com) or +1-855-239-3415 (toll free in the US) or +1-878-848-2777.

<https://r100.copyright.com/CustomerAdmin/PLF.jsp?m#0006514-016-40e7-0000-402a03702020>

46



## Geochemistry, Geophysics, Geosystems

## RESEARCH ARTICLE

10.1002/2016GC006601

## Key Points:

- Varying production rates of >4 Ma volcanism in SE Australia suggest an interplay between edge-driven convection and the Cosgrove mantle plume
- Volcanism in the Newer Volcanic Province shows a strong spatial dependence on preexisting basement structures
- $^{40}\text{Ar}/^{39}\text{Ar}$  ages of <1 Ma volcanoes show a diffuse age trend from east to west, proposed to be caused by migrating stress across SE Australia

## Supporting Information:

- Supporting Information S1
- Data Set S1

## Correspondence to:

K. Oostingh,  
k.oostingh@postgrad.curtin.edu.au

## Citation:

Oostingh, K. F., Jourdan, E. L., Matchan, and D. Phillips (2017),  $^{40}\text{Ar}/^{39}\text{Ar}$  geochronology reveals rapid change from plume-assisted to stress-dependent volcanism in the Newer Volcanic Province, SE Australia, *Geochim. Geophys. Geost.*, 16, 1065–1089, doi:10.1002/2016GC006601.

Received 22 AUG 2016

Accepted 17 FEB 2017

Accepted article online 21 FEB 2017

Published online 21 MAR 2017

© 2017. American Geophysical Union.  
All Rights Reserved.

## $^{40}\text{Ar}/^{39}\text{Ar}$ geochronology reveals rapid change from plume-assisted to stress-dependent volcanism in the Newer Volcanic Province, SE Australia

K. F. Oostingh<sup>1</sup>, F. Jourdan<sup>1</sup>, E. L. Matchan<sup>2</sup>, and D. Phillips<sup>2</sup>

<sup>1</sup>Western Australian Argon Isotope Facility, Department of Applied Geology, JdL Centre, Curtin University, Perth, Western Australia, Australia, <sup>2</sup>School of Earth Sciences, University of Melbourne, Melbourne, Victoria Australia

**Abstract** Here we present  $^{40}\text{Ar}/^{39}\text{Ar}$  ages of volcanic features in the Cenozoic intraplate Newer Volcanic Province in southeast Australia. The <5 Ma volcanic products in the Newer Volcanic Province can be subdivided into tholeiitic, valley-filling Newer Plains basalts, and alkaline scoria cones, lava shields, and maars of the Newer Cones series. Plateau ages range from  $3.76 \pm 0.01$  to  $4.32 \pm 0.03$  Ma (2 $\sigma$ ; all sources of uncertainties included) for the Newer Plains series, with production rates of volcanism decreasing post 4 Ma. We suggest that magmatism is related to the complex interplay of magma upwelling due to edge-driven convection and the Cosgrove track mantle plume located in the northeast of the province at 6.5–5 Ma. Plateau ages range from  $1290 \pm 20$  to  $41.1 \pm 2.2$  ka (2 $\sigma$ ) for the Newer Cones series, with a diffuse age progression in the onset of volcanism for these features from east to west. Analyses of the distribution and geomorphology of these volcanic features indicates a strong control of basement faults on volcanism, reflected in alignment of volcanic features along Paleozoic north-south oriented basement faults in the east and Cretaceous northwest-southeast oriented extensional features in the west. This age progression can be explained by a westerly migration of stress derived from the left-lateral strike-slip Tasman Fracture Zone. This suggests that the general mechanism of volcanism changed from upwelling due to plume-assisted edge-driven convection prior to ~4 Ma to stress-dependent upwelling at around 1.3 Ma.

## 1. Introduction

The Newer Volcanic Province (NVP) [Price *et al.*, 2003] is a relatively small, intraplate volcanic province which covers an area of around 19,000 km<sup>2</sup> [Boyce, 2013] with basaltic rocks in the densely populated area west of Melbourne in south eastern Australia (141°E–145°E and 37°S–38.5°S; Figure 1a). It is subdivided into three zones; the Central Highlands subprovince, the Western Plains subprovince, and the Mt. Gambler region in South Australia (Figure 1a). There are two geomorphological and geochemical distinct types of Cenozoic volcanism in the area: older (> 1 Ma) [Gray and McDougall, 2009] valley-filling Newer Plains basalts, as well as the younger Newer Cones series, comprising maars, scoria cones, lava shields, and the Ir associated flows.

The NVP is considered dormant on the basis of  $\delta^{13}\text{C}$  value of CO<sub>2</sub> gas found in mineral waters in the area [Cartwright *et al.*, 2002], with the last volcano, Mt Schank in the Gambler region (Figure 1a), erupting ~5 ka ago, based on thermoluminescence dating of quartz from a beach deposit overlain by the Mt Schank lava flow [Smith and Prescott, 1987]. Therefore, it is of paramount importance to have reliable age data available to better understand the distribution and timeframe of volcanism in the NVP. Furthermore, age data can provide a geochronological framework for regional climate reconstructions based on lake [e.g., Mooney, 1997; Harle *et al.*, 2002; Wilkins *et al.*, 2013] and swamp [Crowley and Kershaw, 1994] sediments that formed as a result of disrupted drainage pathways by basalt flows. Accurate ages can also be used to constrain the geodynamic origin of the province, which is still a matter of debate [Demidjuk *et al.*, 2007; Davies and Rawlinson, 2014; Price *et al.*, 2014; Oostingh *et al.*, 2016], and to test if any spatiotemporal migration of the main lobe of volcanism occurred within the NVP.

Currently, the majority of available geochronological data in the NVP were either derived by K-Ar dating ( $N = 147$ ) [e.g., Aziz-ur-Rahman and McDougall, 1972; Gray and McDougall, 2009; McDougall *et al.*, 1966; Singleton *et al.*, 1976] and a few cosmogenic exposure ( $^{21}\text{Ne}$  and  $^{10}\text{Be}$ ;  $n = 6$ ) [Stone *et al.*, 1997; Gillen *et al.*, 2010] and  $^{40}\text{Ar}/^{39}\text{Ar}$  ages ( $n = 9$ ) [Hare *et al.*, 2005a; Matchan and Phillips, 2014, 2011; Matchan *et al.*, 2016]

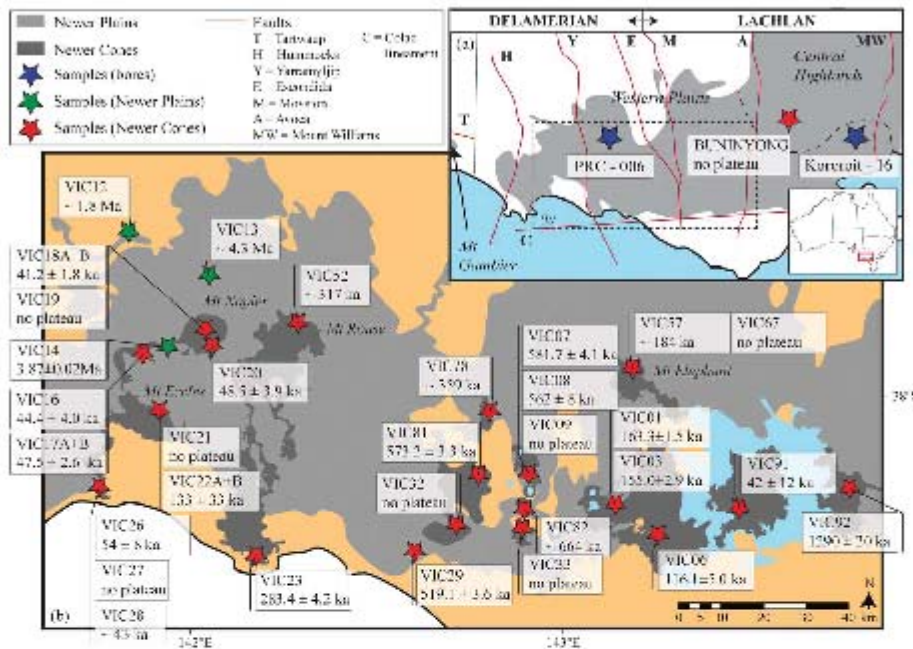


**Figure 1.** Map of the Newer Volcanic Province and sample locations. (a) Approximate extent of the Newer Volcanic Province, indicating subprovinces Central Highlands, Western Plains, and Mt. Gambier. Also indicated are major structural elements (red line): T = Tarweap fault, H = Hummocks fault, Y = Yama myijup fault, E = Econdidala fault, M = Moyston fault, A = Arcoia fault, MW = Mount Williams fault, and C = Colac lineament. (b) Enlarged section of Figure 1a showing the approximate outcrop of Newer Plains in light grey and some relevant Newer Cone flows in dark grey. Also indicated are sample locations (exact coordinates can be found in Tables 1 and 2) and the resulting  $^{40}\text{Ar}/^{39}\text{Ar}$  ages ( $\pm 2\sigma$ ).

(for a review on available geochronology see Vasconcelos et al. [2008]). K-Ar dating suggests continuous volcanism throughout the NVP from ~4.6 Ma to present. These data suggest that three volumetrically dominant stages can be resolved: 4.6–3.0 Ma, dominated by tholeiitic eruptions; 3.0–1.8 Ma, ranging from transitional Hawaiites to basaltic Icelandites and 1.8 Ma–present, with volcanism becoming more alkalic [Price et al., 2003, 1997]. Whereas cosmogenic exposure dating provides minimum ages only due to potential erosion and shielding [Gosse and Phillips, 2001], K-Ar dating will only provide reliable eruption ages if the samples are completely unaltered; sample splits for K and Ar analysis are homogenous; and if the initial trapped  $^{40}\text{Ar}/^{36}\text{Ar}$  ratio is within the range of the air value ( $298.56 \pm 0.31$ ; as measured by Lee et al. [2006] and independently confirmed by Mark et al. [2011]). As we will demonstrate in this study, both assumptions are often erroneous for the NVP basalts, raising questions about the reliability of the existing age data.

$^{40}\text{Ar}/^{39}\text{Ar}$  geochronology is currently widely accepted as an accurate dating technique for a wide variety of geological samples [McDougall and Harrison, 1999]. New generation mass spectrometers such as the multi-collector ARGUS VI equipped with five ultrasensitive Faraday collectors and one ion-counting compact discrete dynode (CDD) have been shown to increase accuracy and precision of analyses of young basalt; due to improved knowledge of the trapped  $^{40}\text{Ar}/^{36}\text{Ar}$  ratio, while decreasing required sample quantities and the time of sample preparation and analysis [Matchan et al., 2016; Matchan and Phillips, 2014]. In this work, we present 19 new  $^{40}\text{Ar}/^{39}\text{Ar}$  ages from 16 individual eruptive centers and associated flows of the Newer Cones series, as well as four new ages from the Newer Plains basalts found in the Western Plains subprovince of the NVP. Furthermore, we evaluate the distribution and spatial characteristics of eruptive centers in the NVP to assess potential relationships between location, geochemistry and eruption age.

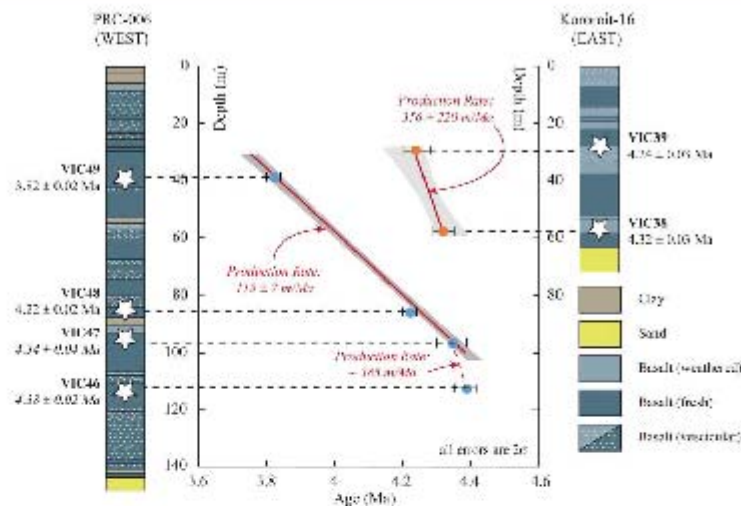


**Figure 2.** Stratigraphic logs of boreholes PRC-006 and Kororoit-16, indicating the depth of samples and their associated  $^{40}\text{Ar}/^{39}\text{Ar}$  age ( $2\sigma$  errors). These ages were used to calculate production rates (thick red lines; m/Ma) and associated  $2\sigma$  errors (grey outlines) using IsoPlot [Lafwig, 2012]. The production rate of VIC46 and VIC47 is apparent only due to poor correlation in isoplot between two closely located points.

## 2. Geological Setting and Sample Description

The onset of predominantly basaltic volcanism in southeast Australia is associated with rifting due to break-up of Australia and Antarctica from Gondwana in the Late Jurassic, and occurred intermittently from 190 Ma onward with the youngest expression of volcanism in the NVP representing a volumetric peak ranging from  $\sim 4.6$  Ma to  $\sim 5$  ka [Blackburn *et al.*, 1982; Price *et al.*, 2003]. The geodynamic model of edge-driven convection [King and Anderson, 1998] accompanied by shear-driven upwelling [Conrad *et al.*, 2010] due to fast northward plate motions of the Australian plate [Sella *et al.*, 2002] (6 cm/yr) and complex 3-D lithospheric thickness variations [Fishwick *et al.*, 2008; Davies and Rawlinson, 2014; Rawlinson *et al.*, 2015a] has been proposed to explain the occurrence of volcanism in southeast Australia [Demidjuk *et al.*, 2007; Price *et al.*, 2014; Oostingh *et al.*, 2016].

Volcanic products are underlain by a complex Paleozoic basement consisting of a series of eastward younging stacked fold belts of deformed and metamorphosed rocks of the Delamerian orogeny (Cambrian to Ordovician) and Lachlan orogeny (Late Ordovician to Carboniferous) as well as rift-related late Mesozoic-Cenozoic sedimentary basins [Gray *et al.*, 2003]. A major lithospheric structure in the region is the north-south trending Moyston Fault Zone, which forms the boundary between the early Paleozoic Delamerian orogeny in the east and the Lachlan orogeny in the west (Figure 1a) [Graeber *et al.*, 2002]. Other major structures are the roughly north-south trending fault zones bordering the major structural divisions within the Delamerian and Lachlan fold belts: the Hummocks and Yarramyllup faults within the Delamerian orogeny, the Avoca fault between the Stawell and Bendigo Zones, and the Mt. William fault between the Bendigo and Melbourne Zones (Figure 1a; see Figure 7 for main structural zones) [Gray *et al.*, 2003]. Sediments of the east-west trending Otway basin underlie the NVP basalts in the South, in which Late Cretaceous extension resulted in west north west-east south east trending structures such as the Tartwaup fault system [Lesti *et al.*, 2008]. The east-west striking Colac lineament marks the southern extent of the NVP volcanics (Figure 1a). The area is currently in a slight compressional stress regime ( $S_{\text{max}}$  oriented N150°) which followed a period of inversion tectonics during the Pliocene and Quaternary [Dickinson *et al.*, 2002; Sandford, 2003; Sandford *et al.*, 2004].



**Table 1.** Summary of  $^{40}\text{Ar}/^{39}\text{Ar}$  Results for the Newer Plains Basalts<sup>a</sup>

Sample Characteristics				Plateau Characteristics				Inverse Isochron Characteristics					
Unit	Sample Number	Mineral	X (Decimal Degree)	Y (Decimal Degree)	Plateau Age (Ma, $\pm 2\sigma$ )	Total $^{39}\text{Ar}$ Released (%)	MSWD	P	Inverse Isochron Age (Ma, $\pm 2\sigma$ )	n	$^{40}\text{Ar}/^{39}\text{Ar}$ Intercept ( $\pm 2\sigma$ )	MSWD	P
Wannon Falls	WC2	GM	141.84097	-37.67492	1.83 $\pm$ 0.01	56	1.09	0.37	1.84 $\pm$ 0.02	9	297.7 $\pm$ 1.1	1.54	0.15
Mt Pierrepont	VIC3	GM	142.06000	-37.77000	No plateau age <sup>b</sup>				No isochron age		293.8 $\pm$ 0.5	3.92	0.00
Napier area old flow	VIC4	GM	141.94814	-37.92333	3.87 $\pm$ 0.02	67	0.95	0.48	3.87 $\pm$ 0.02	9	296.6 $\pm$ 1.0	1.64	0.12
Kororoit-16	VIC8	GM	144.38	-37.44	4.32 $\pm$ 0.03	89	0.54	0.94	4.32 $\pm$ 0.03	17	290.7 $\pm$ 1.5	0.77	0.72
	VIC9	GM	144.38	-37.44	4.34 $\pm$ 0.03	100	0.96	0.51	4.34 $\pm$ 0.03	21	297.1 $\pm$ 0.6	1.17	0.38
PRC-6	VC6	GM	142.339	-37.823	4.38 $\pm$ 0.02	51	0.94	0.46	4.38 $\pm$ 0.03	6	296.5 $\pm$ 3.0	2.11	0.08
	VC7	GM	142.339	-37.823	4.34 $\pm$ 0.04	59	0.35	0.78	4.36 $\pm$ 0.15	11	292 $\pm$ 16	0.76	0.45
	VIC8	GM	142.339	-37.823	4.22 $\pm$ 0.02	87	0.64	0.82	4.23 $\pm$ 0.02	14	313.5 $\pm$ 4.5	1.33	0.19
	VIC9	GM	142.339	-37.823	3.82 $\pm$ 0.02	78	0.61	0.83	3.82 $\pm$ 0.02	13	309.9 $\pm$ 4.9	1.49	0.13

<sup>a</sup>Data in *italics* are derived from mini-plateaus (50–70%  $^{39}\text{Ar}$  released) and are considered minimum ages only. Bold font represents statistically significant plateau ages, whereas data in *italics* represent mini-plateaus. GM = groundmass.

<sup>b</sup>No plateau age is calculated, as the correlation of the inverse isochron diagram is statistically not significant ( $p < 0.05$ ) and the ratio  $^{40}\text{Ar}/^{39}\text{Ar}$  cannot be used to derive a corrected plateau age. The total  $^{39}\text{Ar}$  released value applies for both the plateau and inverse isochron calculations.

Previous dating efforts [McDougall *et al.*, 1966; Aziz-ur-Rahman and McDougall, 1972; Gray and McDougall, 2009] concentrated on the valley-filling Newer Plains basalts, as  $<1$  Ma low-K tholeiitic rocks were typically difficult to date with the previous generations of instruments. We sampled nine Newer Plains basalts (Figures 1 and 2) for  $^{40}\text{Ar}/^{39}\text{Ar}$  dating. WC12 was sampled from a supposedly older flow at Wannon Falls, whereas VIC13 represents a tholeiitic bomb of underlying Newer Plains within the scoria cone of Mt Pierrepont (Figure 1b). VIC14 was sampled from a quarry excavating basalt located stratigraphically below the young flows of Mt Napier (Figure 1b). We have sampled fresh mafic rocks from the Kororoit 16 well (see Figure 1a for location) at two different depth intervals: 60 m (VIC8) and 30 m (VIC9) as well as from PRC-6 (see Figure 1a for location) at four different depth intervals: 112 m (VC46), 97 m (VC47), 86 m (VC48), and 39 m (VC49) to determine the eruption rates of the Newer Plains basalts (Figure 2). We focused the remainder of our sampling efforts on the stratigraphically younger scoria cones and lava shield volcanoes as well as associated lava flows (Newer Cones series) and a single maar (VIC2; Terang maar). We sampled a wide range of volcanic features in the volumetrically dominant Western Plains subprovince, aiming for a wide longitudinal range in sample locations. A total of 29 samples were collected from 16 individual cones and their flows (Figures 1a and 1b and Tables 1 and 2). In all cases, it was possible to sample fresh rock from either recently exposed outcrops in quarries and road cuts, or from at least 0.5 m depth to avoid both the effects of cosmogenic exposure and production of  $^{39}\text{Ar}$ , as well as alteration on flow surfaces. Samples VIC6, VC26, VIC7, and VIC28 were taken at the same location—but deeper levels—of the Gillen *et al.* [2010] and Stone *et al.* [1997] cosmogenic exposure dating sites. Most rocks are represented by dark grey, cryptocrystalline basalt with slight to moderate vesicularity, often directional in the case of flows. Thin section analysis shows that samples are generally unaltered (Figure 3), having glassy to fine grained groundmass containing plagioclase laths and Fe-Ti oxides. The Newer Cones are characterized by the presence of unaltered plagioclase, olivine and clinopyroxene phenocrysts, whereas a few of the older Newer Plains samples show minor alteration indicated by slight iddingsitization of olivine as well as occasional zeolite infill of vesicles.

### 3. Methods

#### 3.1. $^{40}\text{Ar}/^{39}\text{Ar}$ Geochronology

##### 3.1.1. Sample Preparation and Irradiation

All samples were crushed to centimeter scale using a hydraulic press, after which fresh separates were further crushed to several hundred  $\mu\text{m}$  in size in a Tungsten-Carbide ring mill. The resulting crushate was sieved to yield the fraction of interest (355–500  $\mu\text{m}$ ) and washed multiple times with Deionized water in a sonic bath. Approximately 200–500 mg of groundmass grains was handpicked for each sample using a binocular stereomicroscope; which is a quantity that allows for replicate analysis following irradiation. Glassy scoria was handpicked for sample VIC22B. Separates were leached with methanol and diluted HF (2N) for 5 min, followed by duplicate DI washes to remove any silicate phases, and loaded into aluminum discs wrapped in aluminum foil. These discs were stacked together and placed in quartz tubes along with the

**Table 2. Summary of <sup>40</sup>Ar/<sup>39</sup>Ar Results for the Newer Caves Basalts\***

Unit	Sample Characteristics			Plateau Characteristics			Inverse Isochron Characteristics					
	Sample Number	Mineral	X (Decimal Degrees)	Y (Decimal Degrees)	Age (ka ± 2σ)	Total <sup>39</sup> Ar Released (%)	MOWD	P	Inverse Isochron Age (ka ± 2σ)	n	MOWD	P
Mt Barinyong Mt Laram	BUNYG	GM	143.023016	-37.05324	No plateau age <sup>b</sup>	80	0.42	0.99	No isochron age	23	4.01	0.00
	VC01	GM	143.163016	-38.24700	163.3 ± 1.5	80	0.42	0.99	163.2 ± 2.8	23	303.9 ± 4.7	4.01
	VC03	GM	143.163016	-38.24700	155.0 ± 2.9	88	1.35	0.20	160 ± 8	11	293.9 ± 0.7	0.46
	VC06	GM	143.201111	-38.30250	176.1 ± 3.0	99	0.98	0.47	116 ± 11	18	297.3 ± 2.1	1.44
	VC07	GM	142.92392	-38.18039	581.7 ± 4.3	82	0.66	0.80	578 ± 7	14	294.6 ± 0.8	1.40
	VC08	GM	142.92392	-38.18039	542.2 ± 8	90	0.36	0.99	573 ± 15	17	294.9 ± 0.4	0.54
	VC09	GM	142.92392	-38.18039	No plateau age	85	0.48	0.94	No isochron age	14	293.8 ± 1.6	2.87
	VC16	GM	141.85431	-37.03936	46.4 ± 4.0	85	0.48	0.94	44 ± 5	14	296.7 ± 0.6	0.58
Mt Napier	VC17A	GM	141.88369	-37.03881	47.2 ± 3.6	86	1.10	0.16	46.2 ± 5.0	12	295.2 ± 0.6	1.45
	VC17B	GM	141.88369	-37.03881	47.9 ± 3.9	100	1.09	0.16	48 ± 6	16	295.9 ± 0.9	1.48
	Weighted mean age for VC17: 47.2 ± 2.6 ka											
	VC18A	GM	142.05003	-37.08778	41.1 ± 2.2	100	1.21	0.24	41.2 ± 3.1	20	296.1 ± 0.3	1.46
	VC18B	GM	142.05003	-37.08778	41.6 ± 4.3	99	0.58	0.92	41 ± 6	19	295.8 ± 0.4	0.69
	VC19	GM	142.05003	-37.08778	No plateau age	100	0.52	0.95	No isochron age	19	293.9 ± 0.6	1.67
	VC20	GM	142.06866	-37.91997	46.5 ± 3.9	100	0.52	0.95	49 ± 6	19	294.6 ± 0.4	0.61
	VC21	GM	141.93000	-38.09000	No age plateau	98	0.57	0.92	No inverse isochron	18	295.2 ± 0.9	0.88
Mt Eccles	VC22A	GM	141.92786	-38.06131	128 ± 33	80	0.63	0.77	123 ± 45	10	296.9 ± 1.8	0.66
	VC22B	GLA55	141.92786	-38.06131	224 ± 149	80	0.63	0.77	221 ± 143	10	296.9 ± 1.8	0.66
	Weighted mean age for VC22: 133 ± 33 ka											
	VC26	GM	141.26972	-38.21994	54 ± 8	90	0.30	0.99	52 ± 10	12	294.3 ± 0.6	0.42
	VC27	GM	141.26972	-38.21994	No plateau age	67	0.80	0.64	No isochron age	12	292.8 ± 2.1	2.67
	VC28	GM	141.26972	-38.21994	43.7 ± 3.1	67	0.80	0.64	42.3 ± 3.0	12	295.8 ± 0.5	1.55
	VC29	GM	142.19706	-38.36219	388.4 ± 4.2	94	0.38	0.66	384 ± 6	18	295.3 ± 0.3	1.03
	VC32	GM	142.37170	-38.09817	317 ± 7	89	0.16	0.95	316 ± 6	9	295.7 ± 3.9	0.83
Hopkins Falls Two Sisters Terang Maar Alvie Mt Gillbrand	VC33	GM	142.61806	-38.34986	579.1 ± 3.6	90	1.21	0.19	573.9 ± 4.2	9	300.0 ± 1.9	1.09
	VC35	GM	142.91610	-38.31806	No plateau age	64	0.53	0.87	No isochron age	11	298.9 ± 1.1	1.77
	VC37	GM	143.19924	-37.96948	184 ± 15	57	0.85	0.53	184 ± 11	7	350 ± 26	0.94
	VC38	GM	142.81717	-38.05885	339 ± 2	100	0.60	0.91	302 ± 11	19	295.1 ± 0.4	0.88
	VC39	GM	142.79232	-38.18852	573.2 ± 3.3	100	0.60	0.91	573.3 ± 4.0	19	295.1 ± 0.4	0.88
	VC40	GM	142.91565	-38.25012	644 ± 5	51	0.55	0.86	644 ± 7	11	314.2 ± 2.3	1.62
	VC41	GM	143.50315	-38.20743	42 ± 12	92	0.43	0.97	43 ± 15	16	297.0 ± 0.8	1.41
	VC42	GM	143.50315	-38.20743	139.6 ± 2.0	88	0.59	0.87	129.9 ± 4.0	15	293.7 ± 0.8	1.04

\*Data in italics are derived from triplicate analyses (50%–70% <sup>39</sup>Ar release) and are considered minimum ages only. Mt Barinyong is the only volcano analyzed which is located in the Central Highlands subprovince. All other samples are derived from the Western Plains subprovince. GM = groundmass.  
<sup>b</sup>No plateau age is calculated, as the correlation of the inverse isochron diagram is statistically not significant (p < 0.05) and the ratio <sup>40</sup>Ar/<sup>39</sup>Ar cannot be used to derive a corrected plateau age.  
<sup>c</sup>The data does not show any correlation. The total <sup>39</sup>Ar released value applies for both the plateau and inverse isochron calculations.

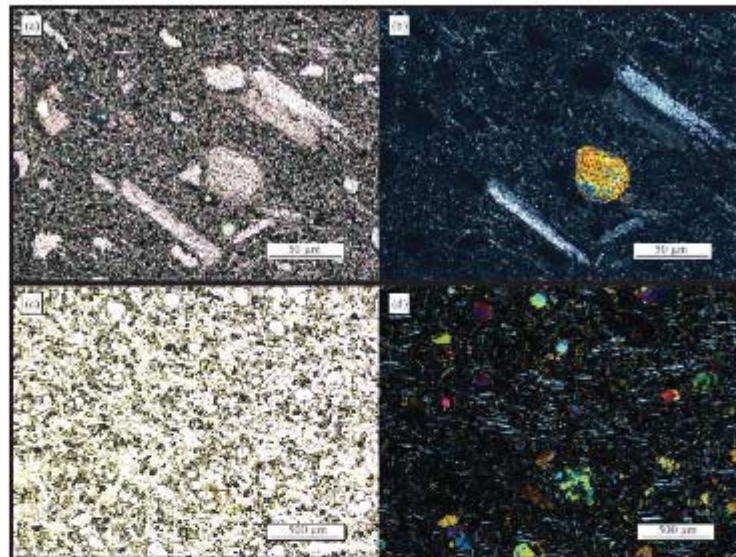


**Figure 3.** (a) Plane polarized and (b) cross-polarized image of VC18 (Newer Conian basalt). (c) Plane polarized and (d) cross-polarized image of VC48 (Newer Plains basalt).

fully intercalibrated flux monitor Fish Canyon Tuff sandline for which an age of  $28,294 \pm 0.036$  Ma is adopted [Renne *et al.*, 2011]. Samples were irradiated for 20 min at the Cadmium-Lined In-Core Irradiation Tube (Cd shielded to minimize undesirable nuclear interference reactions) at the Oregon State TRIGA reactor, USA.

### 3.1.2. Gas Extraction and Analysis

$^{40}\text{Ar}/^{39}\text{Ar}$  step-heating analyses were performed with the ultrahigh precision new generation multicollector mass spectrometer ARGUSM from ThermoFisher® [Phillips and Matchan, 2013] at the West Australian Argon Isotope Facility, Curtin University, Perth. Approximately 100–150 mg of five irradiated groundmass separates was placed as a single layer in a custom-made high-grade aluminum sample disk and loaded into the sample chamber connected to a custom-built, extra low volume (240 cm<sup>3</sup>), stainless steel gas extraction line coupled to the low volume (600 cm<sup>3</sup>) ARGUSVI mass spectrometer. The ARGUSVI contains 5 Faraday detectors and a CDD (compact discrete dynode) ion-counting electron multiplier, which allows for simultaneous analysis of all five Argon isotopes [Matchan and Phillips, 2014]. The sample and extraction line were baked at 120° C for at least 12 h to reach acceptable ultrahigh vacuum (UHV) background levels. Each sample was step heated with a 100 W Photon Machines Fusions 10.6 CO<sub>2</sub> laser using a homogenized 4 mm beam between 3 and 40% laser power (maximum power of 55 W), whereas standards were fused in a single step. The beam was jogged over the sample for approximately 1 min to homogenize the temperature gradient between grains.

Resulting gases were purified using a polycold electrical cryocooler, a liquid nitrogen condensation trap, a SAES GP50 getter operating at 450°C, a AP10 SAES getter operating at 450°C and a AP10 SAES getter operating at room temperature. The purified gases were analyzed in static mode on the ARGUSM mass spectrometer. Measurements were performed in multicollector mode with  $^{37}\text{Ar}$ ,  $^{38}\text{Ar}$ ,  $^{39}\text{Ar}$ , and  $^{40}\text{Ar}$  analyzed on four Faraday detectors and  $^{36}\text{Ar}$  analyzed on the CDD. The relative abundance of each mass was simultaneously measured during 10 cycles of 33 s integration time for each mass. These Faraday detectors incorporate high gain amplifier circuits that allow for gains of  $10^{12}$  Ω resistors on mass 40, 38, and 37 and  $10^{13}$  Ω on mass 39, as well as a high dynamic range due to an improved measurement range of 50,000 fA. The CDD

has an ion-counting efficiency of >95% relative to the Faraday cup set to mass 40, with inherent noise levels lower than 10 counts per minute (cpm). Half of the experiments were run with  $10^{12}$   $\Omega$  resistors for all masses, whereas the other half was run with a  $10^{13}$   $\Omega$  resistor for mass 39. Faraday detectors are routinely calibrated each day to correct for slight offsets in the peak for each isotopic mass either by exposure to a standard electrical current (in case of  $10^{12}$   $\Omega$  resistors for all masses), or with a 2900 fA air shot (in case of  $10^{13}$   $\Omega$  resistor for mass 39), whereas the CDD is calibrated each day for its actual yield by running a series of four air aliquots.

Argon isotope results are corrected for system blanks, mass discrimination, radioactive decay and reactor-induced interference reactions. System blanks were measured every fourth sample. Mass discrimination was closely monitored via an automated air pipette system before and after each step-heating experiment assuming an atmospheric  $^{40}\text{Ar}/^{36}\text{Ar}$  ratio of  $298.56 \pm 0.31$  [Lee *et al.*, 2006; Mark *et al.*, 2011]. The J-value for all specific levels was calculated by averaging the mean ( $^{40}\text{Ar}/^{39}\text{Ar}$ ) ratios from total fusion analysis of four aliquots of FC sandline bracketing the sample. Mass discrimination and J-values ranged from  $0.992121 \pm 0.00019$  to  $0.996254 \pm 0.00019$  per Dalton (atomic mass unit) and  $0.0000932 \pm 0.0000002$  (0.205%) to  $0.0000972 \pm 0.0000004$  (0.375%), respectively. We used correction factors obtained from prolonged analysis of K-Ca-O glass/balts at the Oregon State TRIGA reactor: ( $^{39}\text{Ar}/^{37}\text{Ar}$ )<sub>Ca</sub> =  $(7.60 \pm 0.09) \times 10^{-4}$ ; ( $^{36}\text{Ar}/^{37}\text{Ar}$ )<sub>Ca</sub> =  $(2.70 \pm 0.02) \times 10^{-4}$ ; ( $^{40}\text{Ar}/^{39}\text{Ar}$ )<sub>K</sub> =  $(7.30 \pm 0.90) \times 10^{-4}$ ; and ( $^{39}\text{Ar}/^{39}\text{Ar}$ )<sub>K</sub> =  $(1.24 \pm 0.004) \times 10^{-2}$  [Jourdan and Renne, 2007].

Data regression and age calculation was performed using the ArArCALC algorithm [Koppers, 2002]. Plateau ages are defined as including >70% of released  $^{39}\text{Ar}$  from at least three subsequent steps with  $^{40}\text{Ar}/^{39}\text{Ar}$  ratios within error of the 2 $\sigma$  confidence level and satisfying a probability of fit (P) based on the  $\chi^2$  test distribution of at least 0.05 (see for a description Jourdan *et al.*, [2009]). Plateau ages were calculated using the optimization model of Renne *et al.* [2010] and the standard ages (Fish Canyon sandline:  $28.294 \pm 0.036$  Ma) and decay constants of Renne *et al.* [2011] as well as the atmospheric argon composition of Lee *et al.* [2006] using the mean of all the plateau steps, each weighted by the inverse variance of their individual analytical error. Uncertainties were calculated using error propagation of uncertainties associated with the mean and plateau ages and J-value and are reported at the 2 $\sigma$  confidence level.

All ages reported in the text correspond to plateau ages corrected for deviations from the atmospheric  $^{40}\text{Ar}/^{36}\text{Ar}$  ratio of Lee *et al.* [2006]. Typically, plateau age calculations for young volcanic rocks involve correction of the  $^{40}\text{Ar}$  contribution from atmosphere using these authors'  $^{40}\text{Ar}/^{36}\text{Ar}$  value of 298.56, assuming that the initial trapped ratio has an atmospheric composition. Multiple measurements of the NVP basalts showed that this assumption is not always valid, with ratios both above and below the atmospheric  $^{40}\text{Ar}/^{36}\text{Ar}$  values, respectively, indicating excess argon or air fractionation during cooling or potential isobaric interferences on mass 36. In addition, the standard plateau age calculation does not propagate the uncertainty of the measurement of this trapped ratio, thus likely underestimating the true age uncertainty. Therefore, the inverse isochron ( $^{40}\text{Ar}/^{39}\text{Ar}$  versus  $^{40}\text{Ar}/^{36}\text{Ar}$ ) age, which accounts for both the trapped ratio value and its uncertainty, provides a more accurate representation of the crystallization age of the rock. However, most publications on young volcanics, including each publication on the Newer Volcanic Province, only provide (mode) plateau ages [Hae *et al.*, 2005a; Matchan *et al.*, 2016; Matchan and Phillips, 2014, 2011]. In this study, in addition to providing inverse isochron ages, we use the  $^{40}\text{Ar}/^{36}\text{Ar}$  value and its uncertainty as measured by the inverse isochron, to correct for the true value of the trapped ratio. Note that this approach tends to yield better  $\chi^2$  statistics due to larger errors on each step, but as only inverse isochron  $^{40}\text{Ar}/^{36}\text{Ar}$  values derived from an isochron fit with probability of fit (p) > 5% were taken for the correction, we avoided having plateau ages calculated from statistically insignificant inverse isochrons. In cases where the p value of the inverse isochron was lower than 5%, no plateau age was calculated. The uncertainty of the trapped ratio value is then propagated in the final age uncertainty, which is therefore generally larger than the uncertainty derived from using the standard plateau age model, but smaller than the uncertainty derived from using the inverse isochron. In the text and discussion, we choose to report the corrected plateau ages, as this allows an easier comparison in terms of uncertainty with published ages, all calculated using the standard plateau approach, but is statistically more accurate considering the fact that most studies do not propagate the uncertainty of the trapped ratio in their calculation. In addition, the plateau representation allows ready assessment of the amount of gas included in the age calculation. Both the inverse isochron and corrected-plateau ages are given in Table 1 and Figure 5 for the Newer Plains and Table 2 and Figure 6 for the Newer Cones.

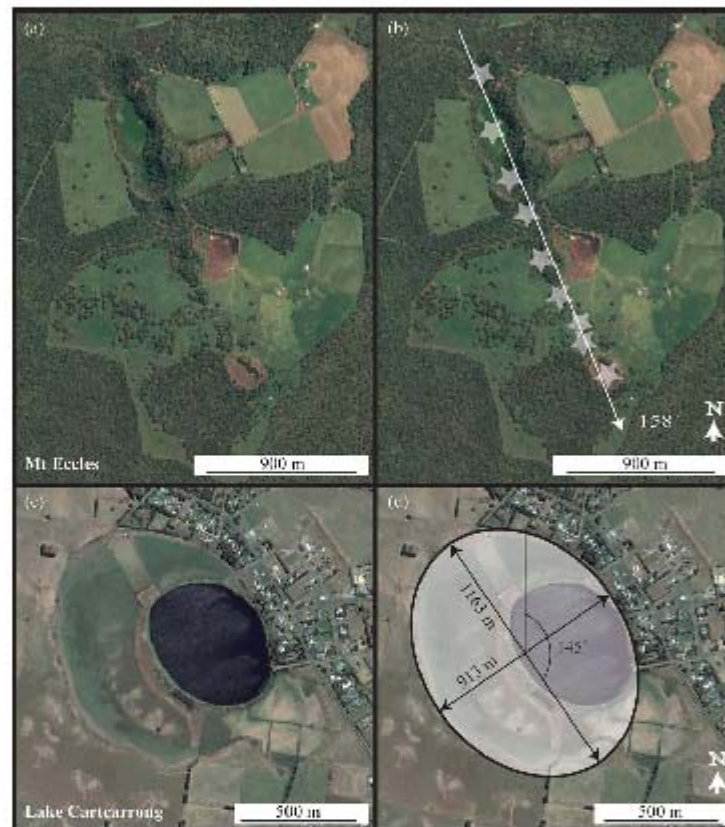


**Figure 4.** Examples of volcanic alignment and geomorphology interpretations. (a) Satellite image of Mt Eccles and (b) interpreted alignment direction. (c) Satellite image of Lake Cartcarrong (maar) and (d) interpreted elongation of the maar structure with preferred orientation.

### 3.2. Spatial Analyses of the Newer Cones

#### 3.2.1. Regional Analysis

We used the database of Boyce [2013] in which 416 individual volcanic centers are recorded with 704 eruption points. These authors merged the database of Geoscience Victoria with existing databases [Singleton and Joyce, 1970; Rosengren, 1994] using both Google Earth and the Department of Primary Industries Seamless Geology ArcGIS layers to identify volcanic features. In contrast to previously used databases for volcanic alignment analysis solely based on satellite imagery [e.g., Lestl et al., 2008], a large amount of the volcanic centers proposed by Boyce [2013] has been confirmed by ground truthing. For the regional-scale density analysis, we used the projected XY coordinates of the 416 individual centers as to not overrepresent volcanic centers with multiple eruption points.

Population density analysis of the entire NVP was performed using the Euclidean nearest neighbor point pattern analysis incorporated in the spatial analyst tool pack of the ArcGIS-ArcMap 10.3.1 software suite using a circular area around each point with radius of 25 km to visualize regional-scale patterns and an

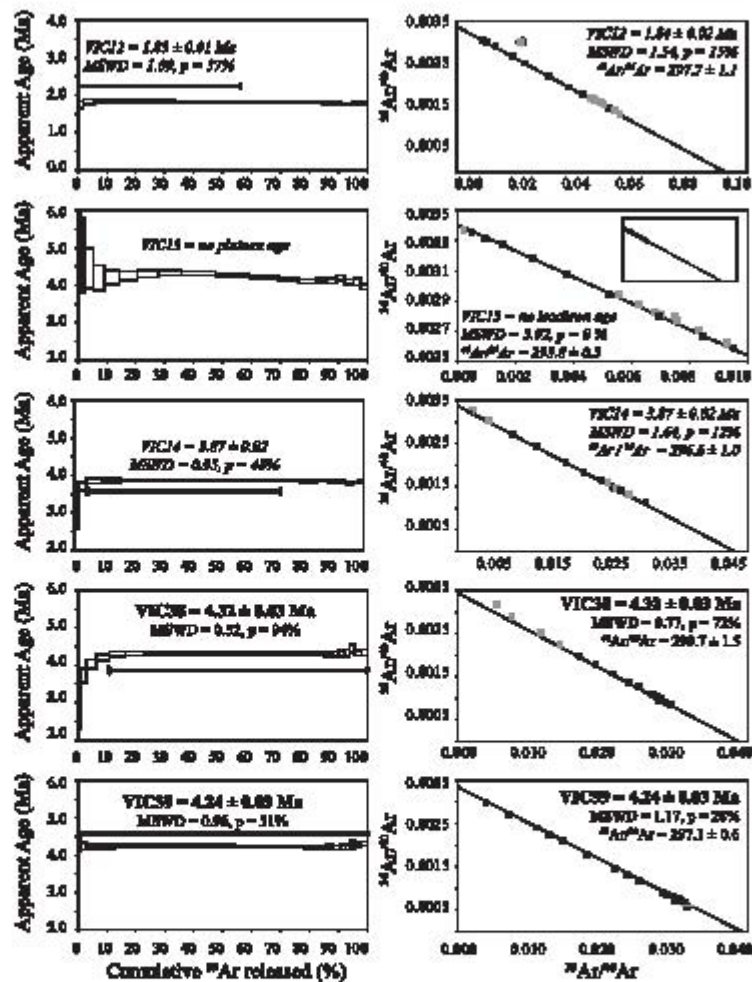


Figure 5. Summary of Newer Plains step-heating analysis; apparent age plateaus and inverse isochron diagrams. Plateau ages (bold) are inverse isochron intercept (<sup>37</sup>Ar/<sup>39</sup>Ar) corrected. Miniplateaus (50–70% cumulative <sup>39</sup>Ar) are indicated in italics. All ages are reported with 2σ uncertainty. The material analyzed was groundmass for all samples.

output cell size corresponding to the approximate areal extent of volcanic features which are typically 1–12 km in diameter [Hare et al., 2005b]. Four clusters (see sections 4.2 and 5.4 and Figure 7) were visually identified.

**3.2.2. Cluster Analysis**

We performed quantitative point pattern analysis of the four high volcanic density clusters visually identified using the Geological Image Analysis Software suite (GIAS) [Beggan and Hamilton, 2010]. This MATLAB operated script allows automated sample size-dependent nearest neighbor (NN) point pattern analysis to

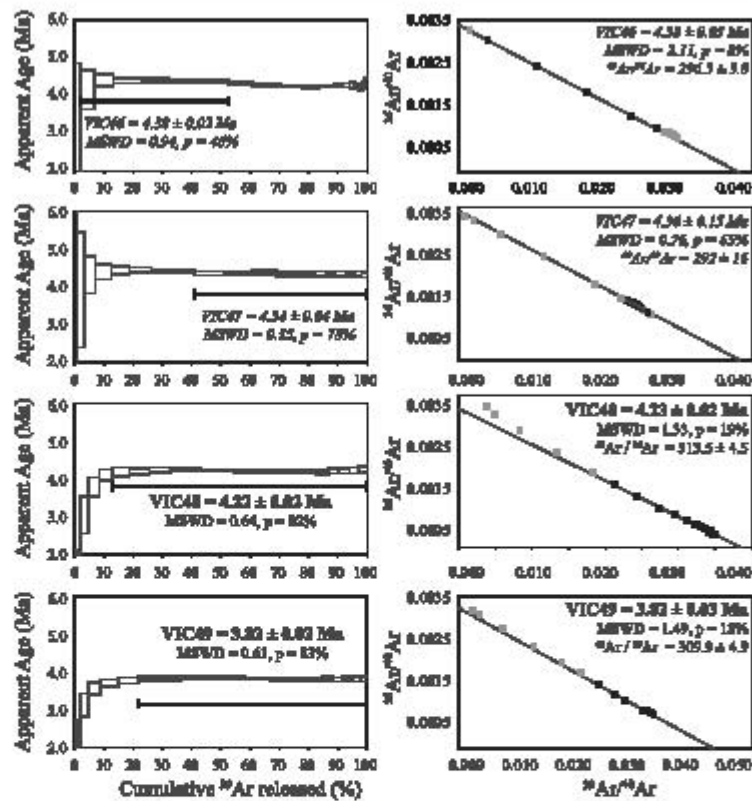
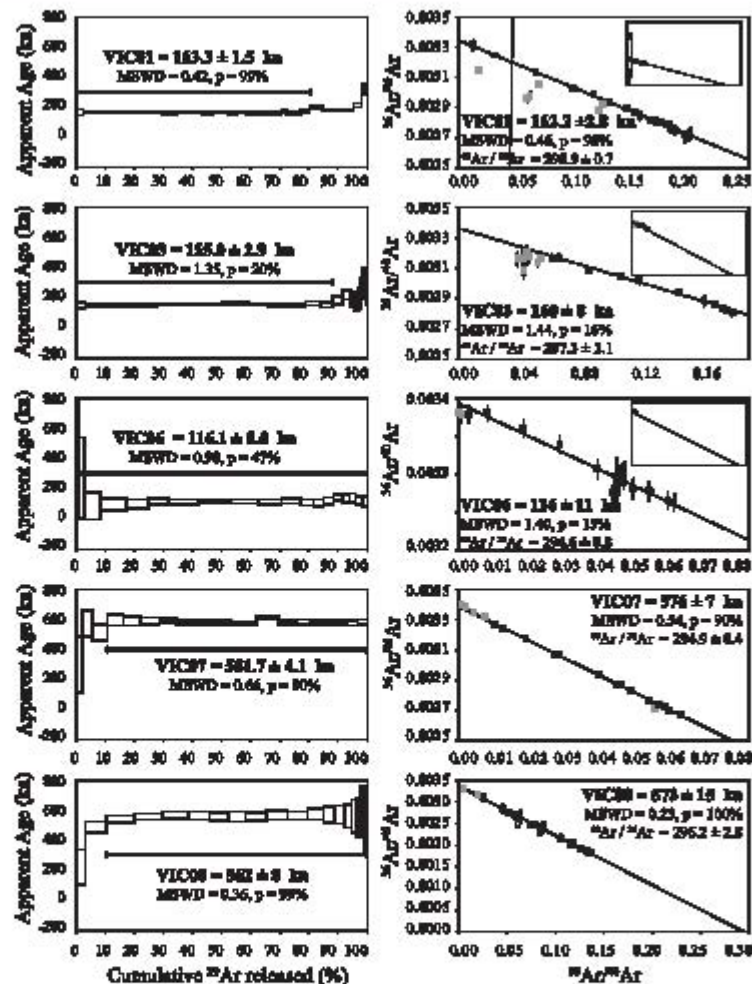


Figure 5. (continued)

quantify the degree of randomness between the points using parameters  $R$  and  $c$  [Beggan and Hamilton, 2010]. Parameter  $R$  is calculated as the ratio between the actual mean NN distance ( $\bar{r}_s$ ) and the expected mean NN distance ( $r_e$ ). The expected mean NN distance  $r_e$  is dependent on the input population density,  $\rho_0$ , given as the number of objects  $N$  divided over the area  $A$  of the feature field. The expected standard error of the Poisson distribution,  $\sigma_s$ , is given as  $[0.26136/\sqrt{(N \times \rho_0)}]$ . Parameter  $c$  is calculated as  $(\bar{r}_s - r_e)/\sigma_s$  [Clark and Evans, 1954]. An ideal set of random Poisson distributed volcanic centers would have an  $R$  value of 1 and a  $c$  value of 0, whereas values of  $R < 1$  or  $R > 1$  would respectively indicate that volcanoes are more closely spaced or more randomly distributed than expected.

### 3.2.3. Alignment Analysis

To test the dependence on geological structure for the volcanic centers within clusters, information of the shape of each volcanic vent is as useful as information about its location [Paulsen and Wilson, 2010]. We used both visual [e.g., Lesti et al., 2008] as well as automated [e.g., Cebrı et al., 2011] techniques to identify potential alignments between volcanic centers and assess the shape of individual volcanoes. For the visual interpretation of volcanic shapes, we printed satellite imagery of each center on a large format to find shapes pointing toward underlying structures, such as elongated cones, clefted crests and aligned eruption points (Figure 4) [Paulsen and Wilson, 2010]. Using a grading scheme (1 = direct observation of elongation/cleft from complete



**Figure 6.** Summary of Newer Corals at ep-heating analysis: apparent age plateau and inverse isochron diagrams. Plateau ages (bold) and inverse isochron intercept ( $^{36}\text{Ar}/^{39}\text{Ar}$ ) corrected. Mini-plateaus (50–70% cumulative  $^{222}\text{Rn}$ ) are indicated in italics. All ages are reported to a 2 $\sigma$  uncertainty. Groundmass was analyzed for all samples except VIC02B (glass).

outcrop, 2 = direct observation of elongation/defl from incomplete outcrop, 3 = elongation derived from topography, 4 = elongation derived from surrounding structure(s) as well as a ratio larger than 1.2 for the elliptical maximum and minimum axis, we derived elongation information with associated azimuth direction on a number of volcanic centers within each cluster. GEOrient software [Halcombe, 2010] was used to plot azimuth directions of alignments, were we chose to only use azimuths derived from grade 1 and grade 2 observations.

A fully automated analysis of small-scale alignments within each duster can be achieved by using the MATLAB script developed by Le Corvec et al. based on two-point azimuth point pattern analysis [Le Corvec et al.,



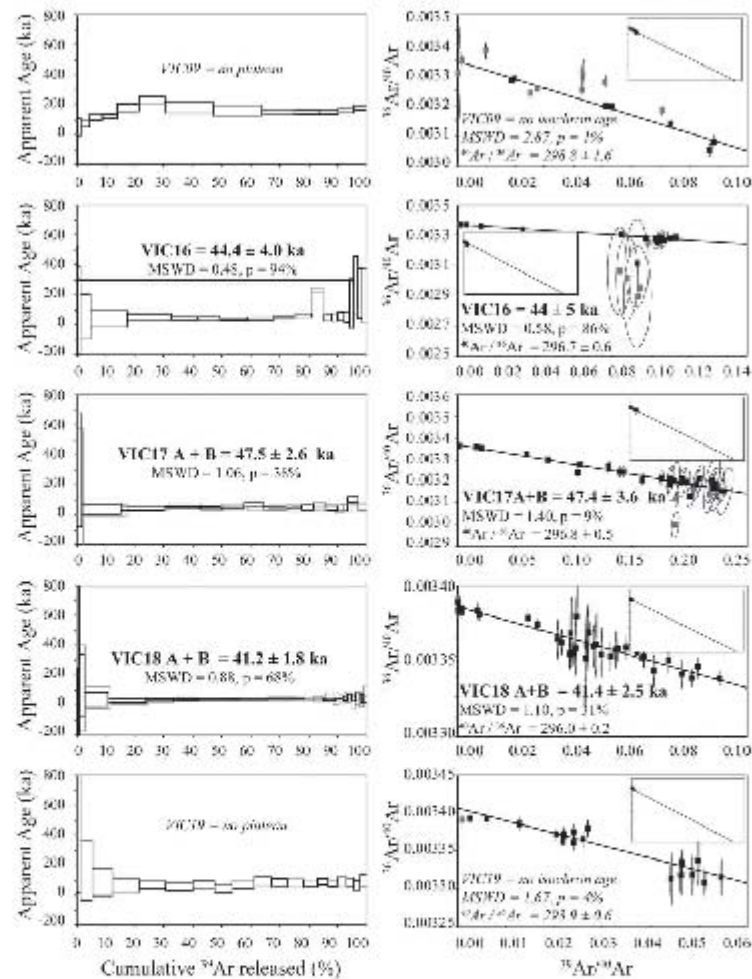


Figure 6. (continued)

2013a, 2013b). We investigated potential alignments between more than three eruption points, allowing a width tolerance of 100–200 m, as this is a typical surface expression of the scale of crustal faults at depth. Furthermore, we used an individual length tolerance for the maximum distance allowed between volcanic centers along a single alignment, based on the relation between density of the volcanic field (as derived from the GIAS analysis) and the minimum number of resulting artifacts which for which we used the relation:  $-2527 \times \ln(x) - 36895$  ( $x$ : population density) [Le Corvec et al., 2013a]. GEORIENT software [Holcombe, 2010] was used to plot azimuth directions of alignments using bins of  $10^\circ$ .

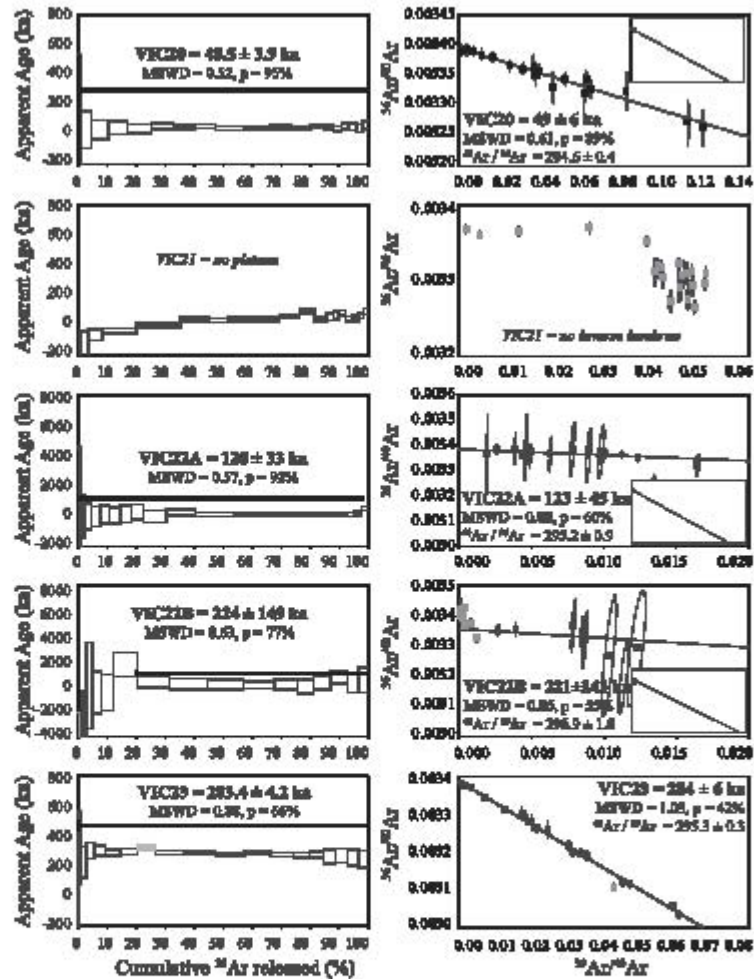


Figure 6. (continued)

#### 4. Results

##### 4.1. $^{40}\text{Ar}/^{39}\text{Ar}$ Geochronology

###### 4.1.1. Newer Plains Basalts

We were able to derive statistically significant ages for four of the nine Newer Plains samples (Figures 1a, 2, and 5 and Table 1) with plateau ages ranging from  $3.82 \pm 0.02$  Ma (VIC49) to  $4.32 \pm 0.03$  Ma (VIC38).

The Newer Plains samples yielded  $^{40}\text{Ar}/^{39}\text{Ar}$  trapped ratios ranging from  $290.7 \pm 1.5$  to  $313.5 \pm 4.5$ , relative to the atmospheric ratio of  $298.56 \pm 0.31$  [Lee et al., 2006]. Samples VIC12, VIC14, VIC46, and VIC47 only

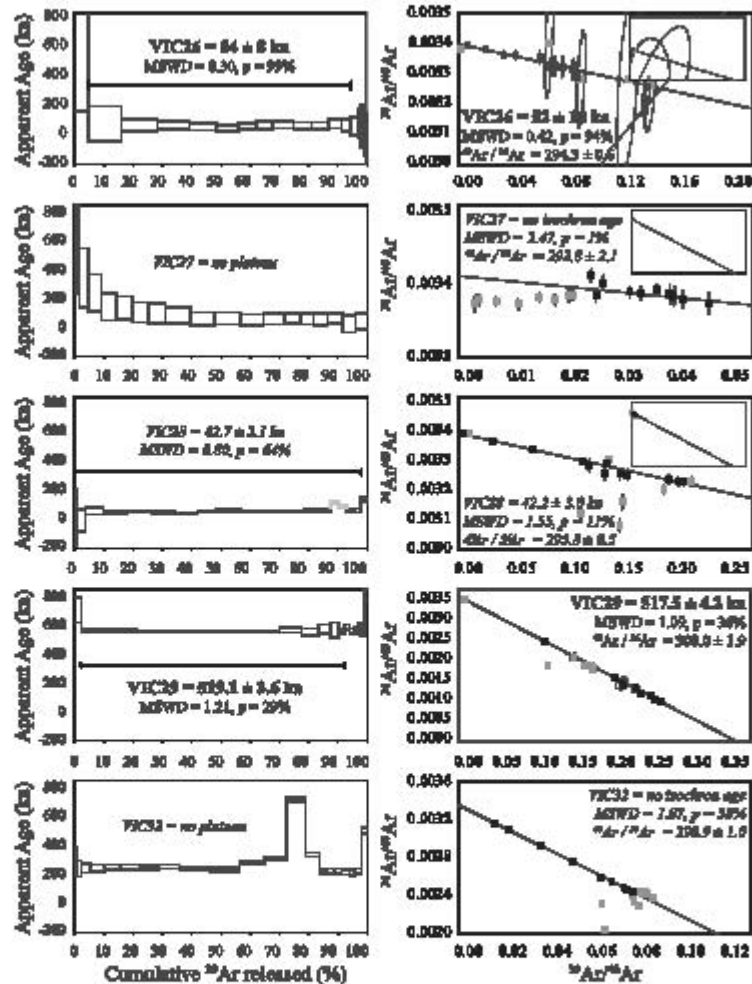


Figure 6. (continued)

yielded a miniplateau (50–70% cumulative <sup>39</sup>Ar) [Jourdan et al., 2007]. Miniplateau ages are less robust than their plateau counterparts and should be treated with caution. They might indicate the true crystallization age, but can also represent maximum or minimum age values, arguably in most cases, not too far from the crystallization age. No age could be calculated for VIC13 as the probability of fit for the inverse isochron was lower than 5%. Figure 5 shows a summary of the apparent age spectra and inverse isochron diagrams for the Newer Plains basalts. Full step-heating analyses as well as all age and isochron spectra can be found in the supporting information data set (red tabs) and supporting information Figure S1, respectively.

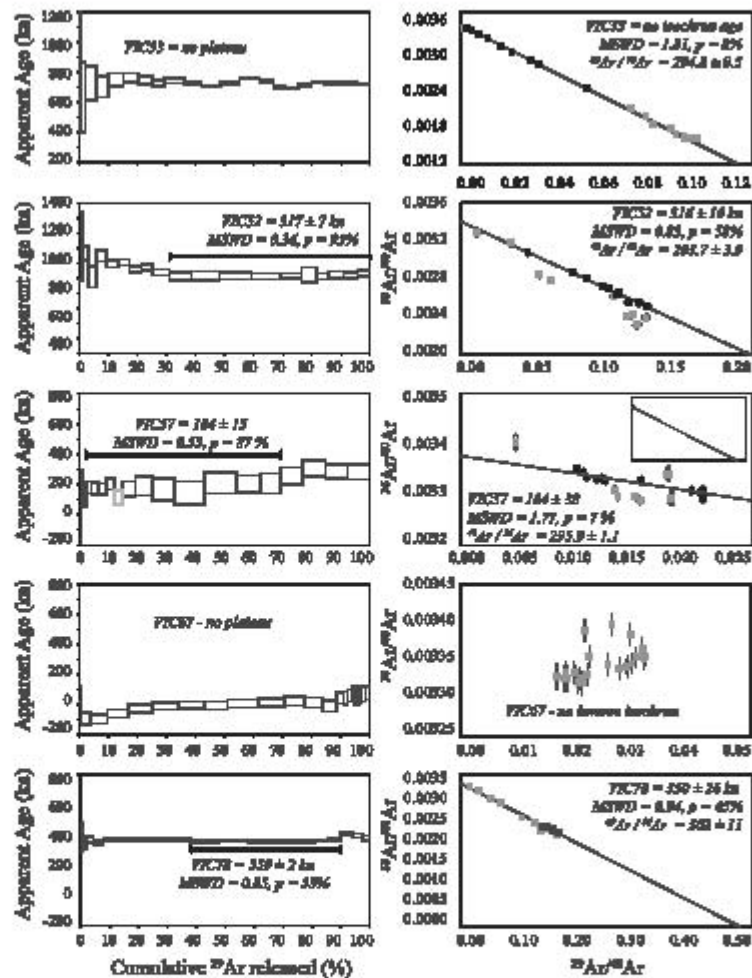


Figure 6. (continued)

**4.2.2. Newer Cones Basalt**

Nineteen of the 32 Newer Cones samples yielded statistically significant plateau ages (Figure 6 and Table 2), ranging from  $41.1 \pm 2.2$  ka (VC18A) to  $1290 \pm 20$  ka (VIC92). Replicate analyses of samples VIC17, VIC18, and VIC22 allowed us to calculate mean weighted ages of  $47.5 \pm 2.6$ ,  $41.2 \pm 1.8$ , and  $133 \pm 33$  ka, respectively. These samples yielded  $^{40}\text{Ar}/^{39}\text{Ar}$  trapped ratios ranging from  $288.9 \pm 2.5$  to  $301 \pm 8$ . Most samples are characterized by subatmospheric  $^{40}\text{Ar}/^{39}\text{Ar}$  ratios (e.g.,  $293.9 \pm 0.6$  for VIC19). Furthermore, some samples have a very low spreading factor along the inverse isochron diagram (Jourd'hean *et al.*, 2009) of only a few percent or less, for example; 0.6% for VC91. Samples VC28, VIC52, VIC57, VC78, and VIC82 only yielded

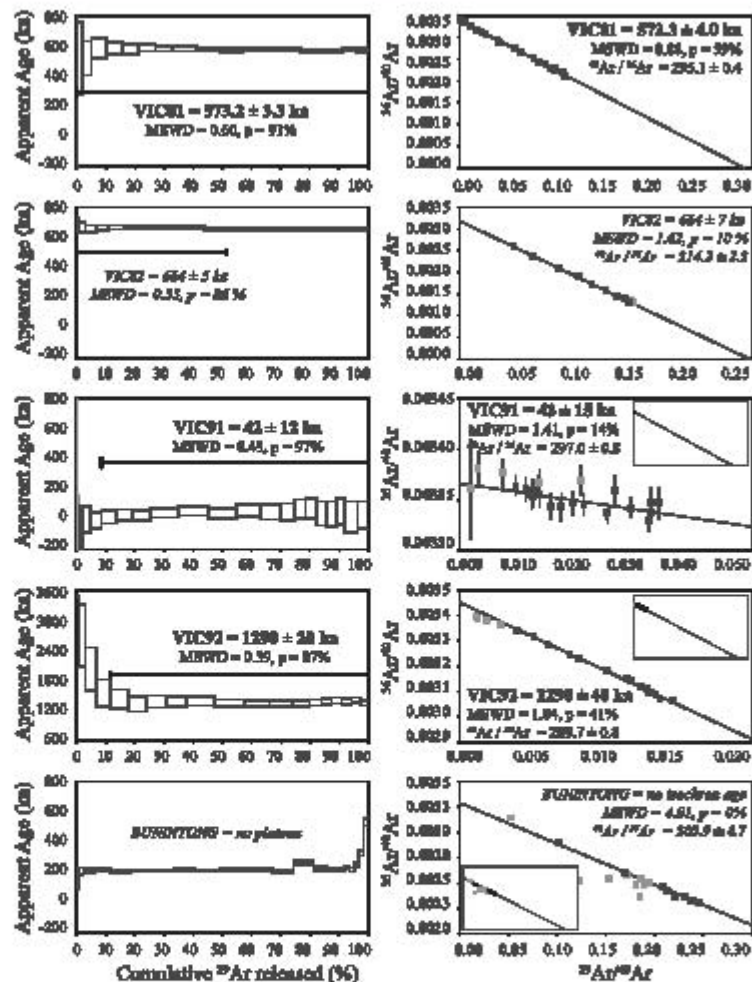


Figure 6. (continued)

miniplates as between 50% and 70% cumulative  $^{39}\text{Ar}$  released. No inverse isochron corrected plateau age could be obtained for Mt Buninyong (BUNYG), VC09, VIC19, VIC27, VIC32, and VC33 due to the statistically poor fit of their inverse isochrons. No inverse isochron or plateau age could be derived for samples VC21 and VC67. The two aliquots of sample VIC22 show indistinguishable ages of  $128 \pm 33$  ka for sample VIC22A (groundmass) and  $224 \pm 149$  ka for sample VC22B (glass). A summary of the apparent age spectra and inverse isochron diagrams for the Newer Cones basalts can be found in Figure 6, whereas full step-heating analyses and all age and isochron spectra can be found in the supporting information data set (green tabs) and supporting information Figure S2.

#### 4.2. Spatial Analysis

Regional-scale point density analysis reveals the presence of four distinct clusters of higher density within the NVP region: the Mt Gambier, Western Plains West, Western Plains East, and the Central Highlands clusters (Figure 7). GAS analysis results indicate that eruption points within all four clusters show a non-random distribution with  $R$  values of 0.581 for the Gambier cluster, 0.512 for the Western Plains West cluster, 0.447 for the Western Plains East cluster and 0.710 for the Central Highlands cluster.

Visual interpretation of individual volcanic centers shows that for all clusters, volcanic features show elongation in a preferred azimuth direction (Figures 8a–8d; Mt Gambier: 130°N–140°N ( $n = 9$ ), Western Plains West: 140°–150° ( $n = 20$ ), Western Plains East: 10°–30° ( $n = 31$ ) and Central Highlands: 0°–10° ( $n = 65$ ). These azimuth directions are confirmed in two clusters by the results of the automated two-point azimuth analysis (Figures 8e–8h: Western Plains West: 140°–150° ( $n = 6695$ ) and the Western Plains East: 10°–30° ( $n = 2371$ ). The alignment azimuth found in Mt Gambier is oriented slightly more east-west at 110°–130° ( $n = 1757$ ), whereas the Central Highland cluster shows two preferential alignment directions at 80°–90° and 140°–150° ( $n = 1151$ ).

## 5. Discussion

### 5.1. Comparison With Existing K/Ar, $^{40}\text{Ar}/^{39}\text{Ar}$ , and Cosmogenic Isotope Ages

#### 5.1.1. Newer Plains Basalts

Extensive K/Ar geochronology on the Newer Plains basalts [Atiz-ur-Rahman and McDougall, 1972; Gray and McDougall, 2009; McDougall et al., 1966; Singleton et al., 1976] has suggested ongoing volcanism from 4.6 Ma to present, with peak volcanic activity from 3 to 1.8 Ma. Our nine samples show that all ages but one (~1.8 Ma) range from 3.8 to 4.3 Ma, which is significantly older than the age range reported for the volumetric peak of Newer Plains volcanism. This could be due to the fact that most K/Ar sampling has taken place on basalt flows close to the surface which are potentially altered; from boulders in pastures as well as shallow quarries, whereas most of our samples were derived from fresh, mostly unaltered drill core. Furthermore, the degassing characteristics of our samples are important for the interpretation of published K/Ar ages, as the K/Ar dating technique is not able to recognize (and correct for) non-atmospheric  $^{40}\text{Ar}/^{39}\text{Ar}$  ratios and alteration effects. Hence, the reliability of K/Ar ages is questionable. Five out of 9 samples analyzed show non-atmospheric  $^{40}\text{Ar}/^{39}\text{Ar}$  ratios, plotting either above ( $313.5 \pm 3.5$ : VC48;  $309.9 \pm 4.9$ : VIC49) or below ( $293.8 \pm 0.5$ : VIC13;  $296.6 \pm 1.1$ : VIC14;  $297.1 \pm 0.6$ : VC39) the given atmospheric ratio of  $298.56 \pm 0.31$  [Lee et al., 2006]. Whereas supra-atmospheric values can be explained by the presence of excess  $^{40}\text{Ar}$ , sub-atmospheric values are more difficult to explain. For fresh, young volcanic rocks, this observation is best explained in terms of isotopic mass fractionation of argon of atmospheric composition during exchange with the magma before or during eruption [Jourdan et al., 2012; McDougall and Harrison, 1999; Renne et al., 2009]. Low  $^{40}\text{Ar}/^{39}\text{Ar}$  ratios can also be due to isobaric interferences during analysis on mass 36 for Cl-rich samples; however, this explanation is unlikely as (1) atmospheric  $^{40}\text{Ar}/^{39}\text{Ar}$  ratios for other young basalts are routinely obtained in this laboratory using this specific instrumental set-up; and (2) isobaric interferences are not expected to be consistent throughout the samples due to natural zoning of Cl and associated multiple isotopic reservoirs in a rock, which is not observed in the linear correlation of the inverse isochrons.

#### 5.1.2. Newer Cones Basalts

Most of the ages available for the Newer Cones basalts are based on  $^{40}\text{Ar}/^{39}\text{Ar}$  results and are hence much more reliable than the K/Ar data available for the Newer Plains. However, published  $^{40}\text{Ar}/^{39}\text{Ar}$  ages of the Newer Cones are still very scarce, with only eight ages available in the literature [Matchan et al., 2016; Matchan and Phillips, 2014, 2011]. From this restricted database, several ages have been re-investigated in this study in an attempt to directly compare with ages generated in a different laboratory. Our age of the Mt Rouse flow (VC23) is in agreement with a recently published  $^{40}\text{Ar}/^{39}\text{Ar}$  age on Mt Rouse analyzed using a similar analytical setup by Matchan and Phillips [2014]. These authors derived a weighted mean age of  $284.4 \pm 1.8$  ka from multiple aliquots, which statistically overlaps with our age of  $283.4 \pm 4.2$  ka from a single aliquot. Furthermore, our age of  $519.1 \pm 3.6$  ka for the Hopkins Falls flow (VC29) is in agreement with, and an order of magnitude more precise than, the age of  $535 \pm 27$  previously reported for the youngest of two flows at this location [Matchan and Phillips, 2011] measured using the previous generation of noble gas mass spectrometers. Our relatively imprecise but statistically correct plateau age of  $184 \pm 23$  ka for Mount

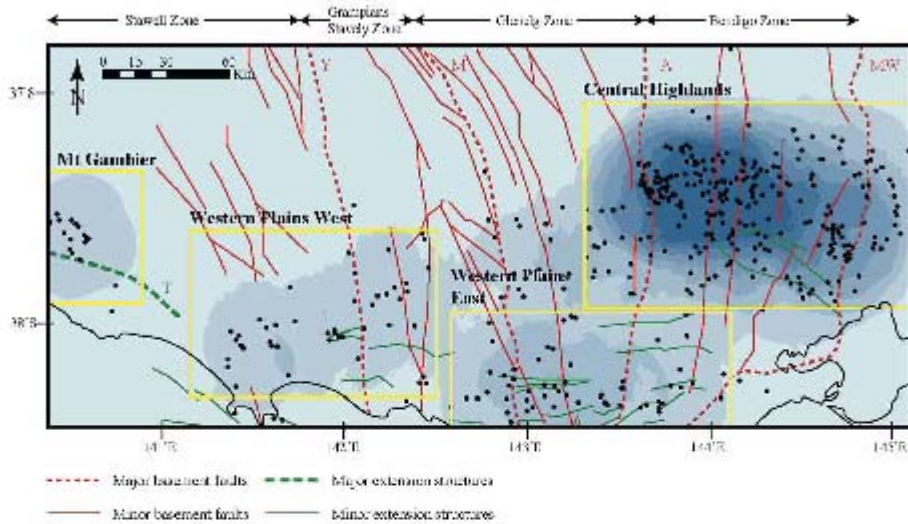


Figure 7. Qualitative Euclidean distance nearest neighbor density map of the NWV, showing the four clusters resulting from this analysis; darker colors represent higher densities. Also indicated are major and minor crustal structures as well as structural zones.

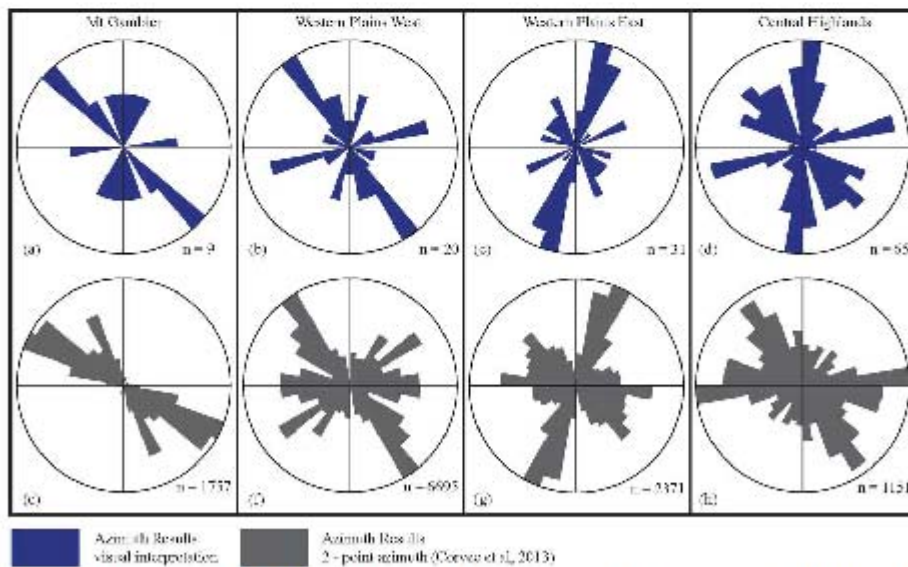
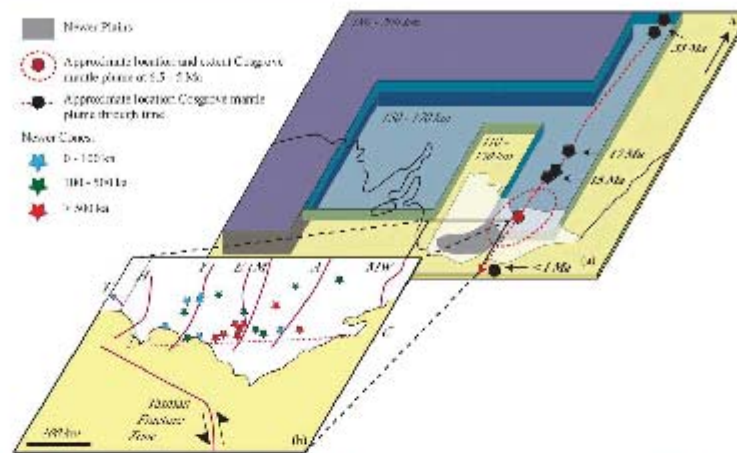


Figure 8. Rose diagrams of volcanic alignments; (a)-(d): rose diagrams of the four clusters as derived from visual interpretation of volcanic centers; (e and h) rose diagrams of the four clusters as derived from automated two-point azimuth analysis (Le Corvec et al., 2013).







**Figure 10.** Cartoon illustrating the generation of the Newer Plains (top right) due to the interplay of complex 3-D lithospheric thickness and the Cognitive track mantle plume (dashed red line) [Davies *et al.*, 2015] and the generation of the Newer Corals (lower left) as a response to movement along the Tasman Fracture Zone. Ages of the Newer Corals have been subdivided into three groups: 0–100, 100–500, and >500 ka to illustrate the age progression toward the West. Lithosphere thicknesses from Davies and Rawlinson [2014]. Note that there are much more eruption centers present (however undated) in the NVP that are not represented on this map.

section and a rate of  $115 \pm 7$  m/Ma for the upper section. The two ages of  $4.32 \pm 0.03$  Ma at 58 m (VIC38) and  $4.24 \pm 0.04$  Ma at 29.5 m (VIC39) resulted in a relatively imprecise production rate of  $356 \pm 220$  m/Ma (2 $\sigma$ ) for core Kororait-16 (Figure 2). This suggests that the production rates of volcanism throughout the NVP were relatively high before  $\sim 4$  Ma, after which a decreased rate of production is suggested by the trend recorded by PRC-006 post 4 Ma. Recent work has suggested the presence of a mantle plume ("Cognitive track") to the northeast of the NVP at around 6.5–5 Ma [Davies *et al.*, 2015]. We suggest that the potential higher production rates before  $\sim 4$  Ma could therefore be a consequence of the increased temperature of the mantle due to thermal contribution of this mantle plume. Southward migration of this mantle plume (Figure 10) over time potentially caused the thermal effects from the mantle plume to the existing process of edge-driven convection to decrease and eventually terminate. Rigorous  $^{40}\text{Ar}/^{39}\text{Ar}$  dating and eruption rate calculation of Newer Plains basalts throughout the NVP is required to further test this hypothesis.

#### 5.4. Spatial Analyses

Clustering of volcanic centers within an intraplate setting has been recorded for other volcanic provinces such as Armenia [R = 0.63], Daringanga, Mongolia [R = 0.86], Es Safa, Syria [R = 0.63], Pali Aike, Chile, Argentina [R = 0.57] and St Michael, USA [R = 0.60] [Le Corvec *et al.*, 2013a, 2013b]. The number, location and extent of our clusters does not correspond well with the six clusters proposed for the NVP by Lestif *et al.* [2008], which were based on the location of volcanic features from the database of Rosengren [1994] as well as from visual interpretation of satellite imagery. However, their interpretation of 683 volcanic points includes many circular, maar-like structures in the North West of the NVP. These features are located to the north of the northernmost extent of the sedimentary basement of the Otway basin, and are most likely not of volcanic origin, but potentially are dry salt lakes instead. Recent reassessment of volcanic features in the NVP has stressed the need for ground truthing to confirm features interpreted from satellite imagery [Boyce *et al.*, 2014]. Clustering of volcanic features on a large scale is generally interpreted to be an indication of the geological structures in the subsurface, such as the location and shape of the underlying magma source [e.g., Brenna *et al.*, 2010] and/or the (elastic) thickness of the underlying lithosphere [Vogt, 1974; Mohr and Wood, 1976; Mazzarini, 2004]. Geophysical imaging [Fishwick *et al.*, 2008; Davies and Rawlinson, 2014; Rawlinson *et al.*, 2015b] has shown that the lithosphere in southeast Australia has a complex 3-D thickness

configuration, caused by the stacking of both continental and oceanic crustal fragments in the Delamerian and Lachlan fold belts, as well as the incorporation of exotic crustal blocks such as the Selwyn Block [Cayley, 2011; Cayley *et al.*, 2011]. Magneto-telluric sounding has shown that distinct regions of partial melt are currently present in the upper mantle below the NVP [Akazpourpoigou *et al.*, 2015], spatially overlapping with our Central Highlands and Western Plains East clusters, but not with the Mt Gambier and Western Plains East cluster.

Alignment of volcanic centers in the NVP and Mt Gambier region has previously been ascribed to a dependence of magma ascent on major north-south trending basement faults as well as northwest-southeast trending Cretaceous extensional structures [Bishop, 2007; Lestl *et al.*, 2008; Holt *et al.*, 2013; Van Otterloo *et al.*, 2013]. Our results show that volcanism in the Mt Gambier region is aligned along the west northwest-east southeast Mesozoic extensional features such as the Tartwaup Fault, whereas volcanism in the Western Plains West cluster is aligned north northwest-south southeast, similar to the major basement fault direction of the Glenelg and Grampians—Stavely Zones (160°–170°). Volcanism in both the Western Plains East and Central Highlands clusters is preferentially aligned along the north-south trending basement faults of the Bendigo Zone rather than along the trend of faults (150°–160°) in the Stawell Zone (Figures 7 and 8a–8h). Our analyses using the new database and automated point pattern analysis show that volcanism in the NVP is strongly dependent on basement structures, which is in agreement with previous findings of Lestl *et al.* [2008].

## 6. Spatiotemporal Constraints on NVP Volcanism

Figure 9a shows that the predominantly tholeiitic Newer Plains erupted synchronously throughout the entire Newer Volcanic Province, starting at around 4.5 Ma. This distribution agrees with volcanism predominantly caused by edge-driven convection and aided by the thermal contribution of a migrating plume. Figure 10a provides an illustration of the potential complex interplay between lithosphere of variable thickness [Davies and Rawlinson, 2014] and the approximate location of the mantle plume at 6.5–5 Ma [Davies *et al.*, 2015].

Figure 9b shows that the predominantly alkaline Newer Cones display a potential age progression in the onset of volcanism from east to west in an otherwise much more diffuse trend of volcanism as compared to the Newer Plains. Specific space-time clusters are apparent; with a cluster of 600 ka old volcanism at longitude 143°E, ages around 40 ka at longitude 142°E and a few younger ages again at higher longitudes (around 143.5°E). Nevertheless, no older (>500 ka) ages are found in the westernmost part of the NVP (141°–143°E), and the age progression fits well with young (~5–27 ka) ages found in the westernmost Mt Gambier region [Blackburn *et al.*, 1982; Smith and Prescott, 1987]. The apparent age progression at the onset of volcanism can potentially be explained either by deep sub-surface processes such as spatial migration of the thermal mantle source or by shallow subsurface constraints such as the availability of suitable pathways for magma transport through the crust. Here we discuss some potential causes for the apparent age progression of the Newer Cones basalts. Note that our age data only represents a relatively small number of volcanic centers present in this area, and more rigorous <sup>40</sup>Ar/<sup>39</sup>Ar geochronology of other centers is required to fully investigate this hypothesis.

### 6.1. Mantle Source Migration?

Age progression of volcanic eruption centers is usually linked to migration of the plate over a static mantle plume, such as proposed for the classic Hawaiian Islands hot spot trail [Morgan, 1972]. However, for the NVP we observe an age progression (east to west) perpendicular to the direction of plate motion (south to north), thus incompatible with the hot spot track model. Furthermore, isotope geochemistry has shown that the Newer Cones most likely originated from the shallow rather than the deep asthenosphere; as distinct high (<sup>207</sup>Pb/<sup>204</sup>Pb)<sub>i</sub> ratios for a given (<sup>143</sup>Nd/<sup>144</sup>Nd)<sub>i</sub> value suggest large degrees of mixing of metasomatized Sub Continental Lithospheric Mantle into a mantle source similar to Indian MORB in composition [Oostingh *et al.*, 2016]. The distinct major and trace element and isotope signatures [Oostingh *et al.*, 2016], U-Th disequilibrium [Demidjuk *et al.*, 2007], and geophysical data [Davies and Rawlinson, 2014] of the NVP basalts are best explained by the geodynamic model of edge-driven convection [King and Anderson, 1998] aided by shear-driven upwelling [Conrad *et al.*, 2011], resulting in localized upwelling of shallow mantle at the trailing edge of an anomalous thick block of lithosphere (Figure 10a). It is still possible that the age progression is caused by a migrating roll of fertile mantle material from east to west, caused by an east to west

motion of the shallow mantle during shear-assisted upwelling caused by the complex 3-D lithospheric thickness variations below the NVP [Fishwick *et al.*, 2008; Rawlinson *et al.*, 2015b] during edge-driven convection. In such a scenario, one would expect that such a fertile mantle patch is now located in the west, at the approximate location of the youngest volcanism. However, a region of partial melt (or fertile mantle material) is currently present in the east rather than the west [Alexopoulos *et al.*, 2015] based on the identification of a low-resistivity zone beneath the Bendigo and Stawell zones by magneto-telluric sounding. Hence, migration of the mantle source fails to explain the observed age trend within the NVP.

### 6.2. Tectonic Controls?

The alignment of volcanoes along north-south trending basement structures in the east and northwest-southeast trending extension structures in the west as observed from our spatial analyses, suggests that the lithosphere had a major control on volcanism in the NVP. Such a dependence of volcanism on faults could potentially explain the age progression of the Newer Cones volcanoes from east to west in the NVP. The present-day Australian continent is not tectonically inert, and southeast Australia represents one of the regions with highest seismic activity and widespread neo-tectonism [Sandford, 2003; Hills *et al.*, 2008], which could have triggered volcanism in the NVP [Lest *et al.*, 2008]. It has been shown that this neo-tectonism initiated in the Mid-Miocene, resulting in large-scale basin inversion [Dickinson *et al.*, 2002] and continued in the Quaternary, with ~120 ka dune deposits showing evidence of deformation [Sandford, 2003], suggesting the presence of a tectonically active region during eruption of the Newer Cones volcanoes. Stress modeling has suggested that the onset of neo-tectonism can be associated with the formation of the Southern Alps in New Zealand [Sandford *et al.*, 2004]. Thermal erosion of the Sub Continental Lithospheric Mantle [Price *et al.*, 2014; Oostingh *et al.*, 2016] beneath southeast Australia could have played a role in weakening the intraplate lithosphere, facilitating neo-tectonism and allowing upwelling of magma through the crust along reactivated faults. A similar process can be observed in the northern Alpine foreland in Europe; which is an intraplate region in a compressional stress regime with active neo-tectonism [Cloetingh *et al.*, 2005] and associated volcanism. Lest *et al.* [2008] suggested that left-lateral strike-slip opening of the major north-south trending faults in the NVP caused by movement along the Tasman Fracture Zone (Figure 10b; a major sinistral transform fault) triggered magmatism in the area. Loci of maximum stress and subsequent reactivation of faults could potentially migrate from east to west throughout the NVP, due to the left-lateral nature of the Tasman Fracture Zone; resulting in the observed age progression of the onset of volcanism in the NVP. The space-time clustering of our Newer Cones age data, as well as the age progression of the onset of volcanism from east to west and recurrent volcanism around longitude 143.5°E suggests that stress derived from movement of the Tasman Fracture Zone is not accommodated evenly throughout the NVP, with data suggesting that major faults such as the Avoca fault (longitude 143°E) were reactivated multiple times (Figure 10b). The Avoca Fault—and to a lesser degree the Moyston Fault—form spatial extensions of the north-south component of the Tasman Fracture Zone [see Gibson *et al.*, 2013, Figure 1]. Therefore, movement along the Tasman Fracture Zone might have been preferentially accommodated along those two faults, explaining the frequent reactivation of these faults as reflected in the wide range of ages for volcanic features around longitude 143°E (Figure 9b).

### 7. Conclusion

$^{40}\text{Ar}/^{39}\text{Ar}$  dating of Cretaceous intraplate basalts in the Newer Volcanic Province in southeast Australia shows a rapid change in the mode of magma generation. Ages of 3.8–4.3 Ma for valley-filling tholeiitic Newer Plains basalts and relatively high production rates of volcanism prior to ~4 Ma show that these rocks were probably generated by the interplay of magma upwelling due to edge-driven convection and additional thermal contribution of the Cosgrove track mantle plume located in the northeast of the area at 6.5–5 Ma. No spatial age progression can be observed within the Newer Plains.

The stratigraphically overlying volcanic scoria cones, lava shield and associated flows as well as many of the Newer Cones are significantly younger, with ages ranging from 1.3 Ma (this work) to ~5 ka for Mt Schank [Smith and Prescott, 1987]. Detailed structural analysis of the distribution and geomorphic characteristics of these features shows a strong dependence of magmatism derived from shallow mantle melting and subsequent upwelling due to edge-driven convection with shear on existing north-south oriented Paleozoic basement faults and northwest-southeast oriented Cretaceous extension structures. An apparent age

- Gray, C. M., and I. McDougall (2008), K-Ar geochronology of basalt petrogenesis, Newer Volcanic Province, Victoria, *Aust. J. Earth Sci.*, **56**, 245–258, doi:10.1080/08120090802547066.
- Gray, D. R., et al. (2003), Structure, metamorphism, geochronology and tectonics of Palaeozoic rocks—Interpreting a complex, long-lived orogenic system, in *Geology of Victoria*, edited by W. D. Birch, pp. 15–71, Geol. Soc. of Aust., Melbourne.
- Hara, A. G., R. A. F. Cas, R. Musgrave, and D. Phillips (2005a), Magnetic and chemical stratigraphy for the Weribee Plains basaltic lava flow-field, Newer Volcanics Province, southeast Australia: Implications for eruption frequency, *Aust. J. Earth Sci.*, **52**, 41–57, doi:10.1080/08120090500100069.
- Hara, A. G., R. A. F. Cas, R. Musgrave, and D. Phillips (2005b), Magnetic and chemical stratigraphy for the Weribee Plains basaltic lava flow-field, Newer Volcanics Province, southeast Australia: Implications for eruption frequency, *Aust. J. Earth Sci.*, **52**, 41–57, doi:10.1080/08120090500100069.
- Hark, K. J. (1997), Late Quaternary vegetation and climate change in southeastern Australia: Palynological evidence from marine core ESS-6, *Paleogeography, Paleoclimatology, Paleoecology*, **131**, 465–483.
- Hark, K. J., H. Hejlskov, R. Chisari, A. P. Kershaw, U. Zoppi, and G. Jacobson (2002), A chronology for the long pollen record from Lake Wangoom, western Victoria (Australia) as derived from uranium/thorium disequilibrium dating, *J. Quat. Sci.*, **17**, 707–720, doi:10.1002/jqs.694.
- Hills, R. R., M. Sandiford, S. D. Reynolds, and M. C. Quigley (2008), Present-day stresses, seismicity and Neogene-to-Recent tectonics of Australia's "backarc" margins: Intraplate deformation controlled by plate boundary forces, *Geol. Soc. Spec. Publ.*, **304**, 71–90, doi:10.1144/SP304.3.
- Holcombe, R. (2010), *GEORIENT—Structural Geology Software*, University of Queensland, Australia. [Available at <http://www.holcombe.net.au/software/georient.html>]
- Holt, S. J., S. P. Holford, and J. Foden (2013), New insights into the magmatic plumbing system of the South Australian Quaternary Basalt province from 3D seismic and geochemical data, *Aust. J. Earth Sci.*, **60**, 797–817, doi:10.1080/08120091201865143.
- Jourdan, F., and P. R. Renne (2007), Age calibration of the Fish Canyon sanidine 40Ar/39Ar dating standard using primary K-Ar standards, *Geochim. Cosmochim. Acta*, **71**, 387–402, doi:10.1016/j.gca.2006.09.022.
- Jourdan, F., G. Féraud, H. Bieriand, and M. K. Wadsway (2007), From flood basalts to the inception of oceanization: Example from the 40Ar/39Ar high-resolution picture of the Karoo large igneous province, *Geochim. Geophys. Geophys. Res.*, **12**, Q02002, doi:10.1029/2006GC001310.
- Jourdan, F., P. R. Renne, and W. U. Reimold (2009), An appraisal of the ages of terrestrial impact structures, *Earth Planet. Sci. Lett.*, **286**, 1–13, doi:10.1016/j.epsl.2009.07.009.
- Jourdan, F., W. D. Sharp, and P. R. Renne (2012), 40Ar/39Ar ages for deep (~3.3 km) samples from the Hawaii Scientific Drilling Project, Mauna Kea volcano, Hawaii, *Geochim. Geophys. Res.*, **17**, Q05004, doi:10.1029/2011GC004017.
- King, S. D., and D. L. Anderson (1998), Edge-driven convection, *Earth Planet. Sci. Lett.*, **160**, 289–296, doi:10.1016/S0012-821X(98)00089-2.
- Koppers, A. A. P. (2002), *ArArCALC—Software for 40Ar/39Ar age calculations*, *Comput. Geosci.*, **28**, 605–619.
- La Courve, N., M. S. Babbington, J. M. Lindsay, and L. E. McGee (2013a), Age, distance, and geochemical evolution within a monogenetic volcanic field: Analyzing patterns in the Auckland Volcanic Field eruption sequence, *Geochim. Geophys. Geophys. Res.*, **14**, 3648–3665, doi:10.1002/2013JG002023.
- La Courve, N., K. B. Spörl, J. Rowland, and J. M. Lindsay (2013b), Spatial distribution and alignments of volcanic centers: Clues to the formation of monogenetic volcanic fields, *Earth Sci. Rev.*, **124**, 96–114, doi:10.1016/j.earscirev.2013.05.005.
- Lee, J. B., K. Marti, J. P. Severinghaus, K. Kawamura, H. Yoo, and J. S. Kim (2006), A re-determination of the isotopic abundances of atmospheric Ar, *Geochim. Cosmochim. Acta*, **70**, 4507–4512, doi:10.1016/j.gca.2006.05.1563.
- Lesli, C., G. Giordano, F. Salvini, and R. A. F. Cas (2008), Volcano tectonic setting of the intraplate, Pliocene-Holocene, Newer Volcanic Province (southeast Australia): Role of crustal fracture zones, *J. Geophys. Res.*, **113**, B07407, doi:10.1029/2007JB005110.
- Ludwig, K. R. (2012), *Isoplot/Ex version 3.75, a geochronological toolkit for Microsoft Excel*, Berkeley Geochronology Centre Special Publication No. 5.
- Mark, D. F., F. M. Stuart, and M. de Podesta (2011), New high-precision measurements of the isotopic composition of atmospheric argon, *Geochim. Cosmochim. Acta*, **75**, 7494–7501, doi:10.1016/j.gca.2011.09.042.
- Matchan, E. L., and D. Phillips (2011), New 40Ar/39Ar ages for selected young (<1 Ma) basalt flows of the Newer Volcanic Province, southeastern Australia, *Quat. Geochronol.*, **2**, 57–64, doi:10.1016/j.quageo.2011.03.002.
- Matchan, E. L., and D. Phillips (2014), High precision multi-collector 40Ar/39Ar dating of young basalts: Mount Rowse volcano (SE Australia) revisited, *Quat. Geochronol.*, **22**, 57–64, doi:10.1016/j.quageo.2014.02.005.
- Matchan, E. L., E. B. Joyce, and D. Phillips (2016), A new <sup>40</sup>Ar/<sup>39</sup>Ar eruption age for the Mount Widdiein volcano, Newer Volcanic Province, Australia, with implications for eruption frequency in the region, *Aust. J. Earth Sci.*, **63**, 1–12, doi:10.1080/0812009120161156576.
- Mazzanti, F. (2004), Volcanic vent self-similar clustering and crustal thickness in the northern Main Ethiopian Rift, *Geophys. Res. Lett.*, **31**, L04604, doi:10.1029/2003GL018574.
- McDougall, I., and T. M. Harrison (1999), *Geochronology and Thermochronology by the 40Ar/39Ar Method*, Oxford Univ. Press, New York.
- McDougall, I., H. L. Albee, and F. H. Chalmers (1966), Isotopic dating of the newer volcanics of Victoria, Australia, and geomagnetic polarity epochs, *J. Geophys. Res.*, **71**, 6107–6118, doi:10.1029/JZ071004p06107.
- Mohr, P. A., and C. A. Wood (1976), Volcano spacings and lithospheric attenuation in the Eastern Rift of Africa, *Earth Planet. Sci. Lett.*, **33**, 125–144, doi:10.1016/0012-821X(76)90166-7.
- Mooney, S. (1997), A fine-resolution palaeoclimatic reconstruction of the last 2000 years, from Lake Kallamata, southeastern Australia, *Holocene*, **7**, 139–149, doi:10.1177/09596369700700202.
- Morgan, W. J. (1972), Deep mantle convection plumes and plate motions, *Am. Assoc. Pet. Geol. Bull.*, **2**, 203–213.
- Niedermann, S. (2002), Cosmic-Ray-Produced noble gases in terrestrial rocks: dating tools for surface processes, *Rev. Mineral. Geochem.*, **47**, 731–784, doi:10.1385/rmg.2002.47.3.6.
- Oostingh, K. F., F. Jourdan, R. Merle, and M. Chiriac (2016), Spatio-temporal geochemical evolution of the SE Australian upper mantle deepened from the Sr, Nd and Pb isotope compositions of Cenozoic intraplate volcanic rocks, *J. Petrol.*, **57**, 1509–1530, doi:10.1093/petrology/egw048.
- Padgett, T. S., and T. J. Wilson (2010), New criteria for systematic mapping and reliability assessment of monogenetic volcanic vent alignments and elongate volcanic vents for crustal stress analysis, *Tectonophysics*, **482**, 16–28, doi:10.1016/j.tecto.2009.08.025.
- Phillips, D., and E. L. Matchan (2013), Ultra-high precision 40Ar/39Ar ages for Fish Canyon Tuff and Alder Creek Rhyolite sanidine: New dating standards required?, *Geochim. Cosmochim. Acta*, **121**, 229–239, doi:10.1016/j.gca.2013.07.003.
- Price, R. C., C. M. Gray, and F. A. Frey (1997), Strontium isotopic and trace element heterogeneity in the plains basalts of the Newer Volcanic Province, Victoria, Australia, *Geochim. Cosmochim. Acta*, **61**, 171–192, doi:10.1016/S0016-7037(96)00318-3.
- Price, R. C., I. A. Nicholls, and C. M. Gray (2003), Cenozoic igneous activity, in *Geology of Victoria*, edited by W. D. Birch, pp. 361–375, Victoria Div., Geol. Soc. of Aust., Melbourne.

- Pike, R. C., I. A. Nicholls, and A. Day (2014), Lithospheric influences on magma compositions of late Mesozoic and Cenozoic intraplate basalts (the Older Volcanics) of Victoria, southeastern Australia, *Lithos*, 206–207, 179–200, doi:10.1016/j.lithos.2014.07.027.
- Rawlinson, N., B. L. N. Kennet, M. Salmon, and R. A. Glen (2015a), Origin of lateral heterogeneities in the upper mantle beneath south-east Australia from seismic tomography, in *The Earth's Heterogeneous Mantle*, Springer Geophys., edited by A. Khan and F. Deschamps, pp. 47–78, Springer, Switzerland, doi:10.1007/978-3-319-15627-9.
- Rawlinson, N., S. Pilla, M. Young, M. Salmon, and Y. Yang (2015b), Crust and upper mantle structure beneath southeast Australia from ambient noise and teleseismic tomography, *Tectonophysics*, 689, 143–156, doi:10.1016/j.tecto.2015.11.034.
- Renne, P. R., W. S. Cassata, and L. E. Morgan (2009), The isotopic composition of atmospheric argon and  $^{40}\text{Ar}/^{39}\text{Ar}$  geochronology: Time for a change?, *Quart. Geochronol.*, 4, 288–298, doi:10.1016/j.quageo.2009.02.015.
- Renne, P. R., R. Mundl, G. Balco, K. Min, and K. R. Ludwig (2010), Joint determination of  $^{40}\text{K}$  decay constants and  $^{40}\text{Ar}/^{39}\text{Ar}$  for the Fish Canyon sandline standard and improved accuracy for  $^{40}\text{Ar}/^{39}\text{Ar}$  geochronology, *Geochim. Cosmochim. Acta*, 74, 5340–5367, doi:10.1016/j.gca.2010.06.017.
- Renne, P. R., G. Balco, K. R. Ludwig, R. Mundl, and K. Min (2011), Response to the comment by W.H. Schwarz et al. on "Joint determination of  $^{40}\text{K}$  decay constants and  $^{40}\text{Ar}/^{39}\text{Ar}$  for the Fish Canyon sandline standard and improved accuracy for  $^{40}\text{Ar}/^{39}\text{Ar}$  geochronology" by P. R. Renne et al. (2010), *Geochim. Cosmochim. Acta*, 75, 5097–5100, doi:10.1016/j.gca.2011.06.021.
- Rosengren, N. (1994), *Eruption Points of the Newer Volcanics Province—An Inventory and Evaluation of Scientific Significance*, National Trust of Australia and the Geological Society of Australia, Melbourne, Victoria, Australia.
- Sandford, M. (2003), Neotectonics of southwestern Australia: Linking Quaternary faulting record with seismicity and in situ stress, *Geol. Soc. Aust. Spec. Publ.*, 22, 101–113, doi:10.1130/00-8137-2372-8107.
- Sandford, M., M. Wallace, and D. D. Giblin (2004), Origin of the in situ stress field in south-eastern Australia, *Basin Res.*, 16, 325–338, doi:10.1111/j.1365-2117.2004.00335.x.
- Sella, G. F., T. H. Dixon, and A. Mao (2002), REVEL: A model for recent plate velocities from space geodesy, *J. Geophys. Res.*, 107(B9), doi:10.1029/2000JB000333.
- Singleton, O. P., and E. B. Joyce (1978), *Catalogue of the post-Miocene volcanoes of Victoria, Australia. Prepared for the IAGC Catalogue of post-Miocene Volcanoes of the World*.
- Singleton, O. P., I. McDougall, and C. W. Malett (1978), The Pliocene-Pleistocene boundary in Southeastern Australia, *J. Geol. Soc. Aust.*, 23, 299–311, doi:10.1080/00167617808728943.
- Smith, B. W., and J. R. Prescott (1987), Thermoluminescence dating of the eruption at Mt Schick, South Australia, *Aust. J. Earth Sci.*, 34, 335–342, doi:10.1080/08120098708729415.
- Stone, J., J. A. Peterson, L. K. Fifield, and R. G. Creaswell (1997), Cosmogenic  $^{36}\text{Cl}$  exposure ages for two basalt flows in the Newer Volcanics Province, Western Victoria, *Proc. Soc. Victoria*, 108, 121–131.
- Van Oosterloo, J., R. A. F. Cas, and M. J. Sheard (2013), Eruption processes and deposit characteristics at the monogenetic Mt. Gambier Volcanic Complex, SE Australia: Implications for alternating magmatic and phreatomagmatic activity, *Bull. Volcanol.*, 75, 1–21, doi:10.1007/s00445-013-0737-y.
- Vasconcelos, P. M., K. M. Nissen, B. E. Cohen, and J. A. Heim (2008), Geochronology of the Australian Cenozoic: A history of tectonic and igneous activity, weathering erosion, and sedimentation, *Aust. J. Earth Sci.*, 55, 865–914, doi:10.1080/08120090802120120.
- Vogt, P. R. (1974), Volcano spacing, fractures, and thickness of the lithosphere, *Earth Planet. Sci. Lett.*, 21, 235–252, doi:10.1016/0012-821X(74)90159-0.
- Wilkins, D., C. Goswami, P. De Deckker, L. K. Fifield, and J. M. Olley (2013), Holocene lake-level fluctuations in Lakes Kallabete and Grenada, southwestern Victoria, Australia, *Holocene*, 23, 784–795, doi:10.1177/09596836124471983.


# Statement of Authorship

Title of Paper	Advancements in cosmogenic $^{38}\text{Ar}$ exposure dating of terrestrial rocks.		
Publication Status	<input type="radio"/> Published <input checked="" type="radio"/> Submitted for Publication	<input type="radio"/> Accepted for Publication <input type="radio"/> Publication Style	
Publication Details	Oostingh, K.F.; Jourdan, F. and Danišík, M.; Evans, N. J.; Advancements in cosmogenic $^{38}\text{Ar}$ exposure dating of terrestrial rocks; Geochimica et Cosmochimica Acta; under review		

## Author Contributions

By signing the Statement of Authorship, each author certifies that their stated contribution to the publication is accurate and that permission is granted for the publication to be included in the candidate's thesis.

Name of Principal Author (Candidate)	Korien Oostingh		
Contribution to the Paper	Korien Oostingh produced the majority of the data and did most of the drafting of the manuscript and the interpretation of the results.		
Overall percentage (%)	60		
Signature	<i>Korien Oostingh</i>	Date	21/12/2016

Name of Co-Author	Fred Jourdan		
Contribution to the Paper	Fred Jourdan is principal supervisor and assisted with the experiments, the drafting of the document and the interpretation of the results.		
Overall percentage (%)	30		
Signature		Date	21/12/2016

Name of Co-Author	Martin Danišík		
Contribution to the Paper	Martin Danišík performed the (U-Th)/He analyses and assisted with the drafting of the manuscript		
Overall percentage (%)	5		
Signature	<i>Martin Danišík</i>	Date	21/12/2016

Name of Co-Author	Noreen Evans		
Contribution to the Paper	Noreen Evans assisted with the (U-Th)/He analyses		
Overall percentage (%)	5		
Signature	<i>Noreen Evans</i>	Date	21/12/2016

# Statement of Authorship

Title of Paper	(U-Th)/He dating of olivine phenocrysts in the K-rich Ellendale olivine lamproite, Western Australia
Publication Status	<input type="radio"/> Published <input type="radio"/> Accepted for Publication <input type="radio"/> <input checked="" type="radio"/> Submitted for Publication <input type="radio"/> Publication Style
Publication Details	Oostingh, K. F., Danišik, M., Evans, N. J., Jourdan, F., McDonald, B. J. & McInnes, B. I. A. (2017a). (U-Th)/He dating of olivine phenocrysts in the K-rich Ellendale olivine lamproite, Western Australia. Australian Journal of Earth Sciences; under revi.

## Author Contributions


By signing the Statement of Authorship, each author certifies that their stated contribution to the publication is accurate and that permission is granted for the publication to be included in the candidate's thesis.

Name of Principal Author (Candidate)	Korien Oostingh		
Contribution to the Paper	Korien Oostingh wrote the majority of the manuscript and interpreted most of the results.		
Overall percentage (%)	55		
Signature	<i>Korien Oostingh</i>	Date	21/12/2016


Name of Co-Author	Martin Danišik		
Contribution to the Paper	Martin Danišik assisted with the (U-Th)/He analysis, the interpretation of the results and the drafting of the document.		
Overall percentage (%)	15		
Signature	<i>Martin Danišik</i>	Date	21/12/2016

Name of Co-Author	Noreen Evans		
Contribution to the Paper	Noreen Evans assisted with the interpretation of the results and the drafting of the document.		
Overall percentage (%)	10		
Signature	<i>Noreen Evans</i>	Date	21/12/2016



Name of Co-Author	Fred Jourdan		
Contribution to the Paper	Fred Jourdan is a supervisor and assisted with $^{40}\text{Ar}/^{39}\text{Ar}$ analysis and the interpretation of the results as well as the drafting of the manuscript.		
Overall percentage (%)	10		
Signature		Date	21/12/2016

Name of Co-Author	Brad McDonald		
Contribution to the Paper	Brad McDonald assisted with (U-Th)/He analysis and ELA-ICP-MS analysis of the samples.		
Overall percentage (%)	5		
Signature	Brad McDonald	Date	21/12/2016

Name of Co-Author	Brent McInnes		
Contribution to the Paper	Brent McInnes is an associate supervisor and assisted in the discussions on experimental design.		
Overall percentage (%)	5		
Signature		Date	21/12/2016

APPENDIX B. SUPPLEMENTARY DATA CHAPTER 3 – MAJOR  
AND TRACE ELEMENT DATA

Latitude	dec degrees South	VIC03	VIC06	VIC09	VIC12	VIC13	VIC14	VIC16	VIC17	VIC18	VIC19	VIC20	VIC21
		-38.25	-38.30	-38.18	-37.67	-37.77	-37.92	-37.94	-37.94	-37.89	-37.89	-37.92	-38.06
Longitude	dec degrees East	143.16	143.28	142.92	141.84	142.06	141.95	141.88	141.88	142.05	142.05	142.07	141.93

**ELEMENTS UNITS DETECTION LIMITS**

<b>SiO2</b>	%	0.010	44.06	50.68	46.87	49.57	51.19	49.62	48.54	48.88	50.02	50.47	49.93	46.16
<b>Al2O3</b>	%	0.010	12.86	13.97	14.11	14.45	14.21	14.50	13.78	13.57	15.28	15.42	14.64	14.09
<b>TiO2</b>	%	0.010	3.22	2.13	2.76	1.88	1.83	1.82	2.09	2.03	2.34	2.32	2.24	2.60
<b>Fe2O3</b>	%	0.010	14.37	12.23	13.20	11.65	11.53	12.23	12.29	12.16	11.71	11.46	11.73	12.91
<b>MnO</b>	%	0.010	0.17	0.16	0.17	0.15	0.15	0.15	0.16	0.16	0.15	0.15	0.15	0.17
<b>MgO</b>	%	0.010	9.72	8.05	7.45	9.27	8.07	7.76	9.94	10.21	6.75	6.46	7.84	7.92
<b>CaO</b>	%	0.010	8.34	8.46	7.37	8.40	8.41	8.66	8.98	8.98	8.29	8.45	8.58	9.66
<b>Na2O</b>	%	0.010	4.37	3.48	4.96	3.51	3.45	3.45	3.21	3.30	4.09	3.91	3.78	3.69
<b>K2O</b>	%	0.010	2.26	1.16	2.76	1.16	0.92	0.92	1.08	1.13	1.39	1.39	1.34	1.62
<b>Cr2O3</b>	%	0.005	0.04	0.04	0.03	0.04	0.05	0.04	0.05	0.05	0.02	0.02	0.03	0.04
<b>P2O5</b>	%	0.001	1.29	0.44	1.02	0.41	0.33	0.33	0.45	0.43	0.50	0.43	0.48	0.85
<b>BaO</b>	%	0.005	0.07	0.03	0.07	0.04	0.04	0.03	0.04	0.04	0.04	0.05	0.05	0.05
<b>SO3</b>	%	0.002	0.03	0.06	0.07	0.01	X	X	0.01	0.01	X	0.01	0.01	0.04
<b>LOI</b>	%	0.01	-0.69	-0.59	-0.83	-0.35	0.02	0.25	-0.34	-0.65	-0.52	-0.44	-0.74	0.32
<b>Total</b>	%		100.10	100.30	100.00	100.18	100.19	99.77	100.28	100.30	100.06	100.09	100.06	100.11

<b>Sc</b>	ppm	10	13	18	11	19	18	18	19	18	15	16	17	19
<b>V</b>	ppm	10	197	185	161	180	153	171	192	188	192	191	191	219
<b>Cr</b>	ppm	20	236	245	176	285	308	286	293	304	101	103	171	242
<b>Co</b>	ppm	0.1	63.5	49.1	49.4	53.7	51.5	55.7	55.0	56.5	43.4	62.1	48.6	49.1
<b>Ni</b>	ppm	0.5	230.8	149.0	157.1	195.2	209.0	214.4	216.6	224.1	109.0	101.8	137.9	136.9



ELEMENTS	UNITS	DETECTION LIMITS	VIC03	VIC06	VIC09	VIC12	VIC13	VIC14	VIC16	VIC17	VIC18	VIC19	VIC20	VIC21
Mo	ppm	0.1	5.1	1.9	6.2	1.3	1.4	0.9	1.7	1.7	2.8	2.2	1.6	4.1
Sr	ppm	0.2	1044.3	477.0	1095.6	670.4	466.5	475.1	529.9	536.5	609.9	627.4	578.1	959.0
Nd	ppm	0.1	62.9	26.0	54.7	23.5	20.5	18.9	24.0	23.0	25.5	27.3	26.3	43.2
Sm	ppm	0.1	12.0	6.1	10.7	5.3	5.0	4.7	5.3	5.3	5.8	5.9	5.8	8.6
Zr	ppm	1	311	166	363	154	138	124	142	135	169	176	160	228
Hf	ppm	0.1	7.9	4.6	9.0	4.1	3.6	3.3	3.7	3.6	4.3	4.6	4.2	5.4
Eu	ppm	0.1	4.1	2.0	3.5	1.8	1.7	1.7	1.9	1.8	2.1	2.1	2.1	2.9
Sn	ppm	1	3	2	3	2	1	2	1	1	2	5	2	2
Sb	ppm	0.05	0.17	0.06	0.20	0.07	0.08	X	0.06	X	0.08	0.06	X	0.08
Gd	ppm	0.1	10.3	6.0	9.5	5.1	5.2	5.2	5.5	5.3	6.1	6.0	5.7	8.6
Tb	ppm	0.1	1.3	0.9	1.3	0.8	0.8	0.7	0.8	0.8	0.8	0.9	0.8	1.1
Dy	ppm	0.1	6.5	4.9	5.8	4.1	4.2	4.2	4.2	4.1	4.5	4.7	4.5	5.6
Li	ppm	0.1	9.7	9.8	11.2	5.7	6.4	6.8	6.1	6.4	7.2	7.8	7.3	7.6
Y	ppm	0.5	26.2	21.6	23.4	19.9	20.6	19.8	19.1	19.1	21.4	21.9	20.7	25.6
Ho	ppm	0.1	1.1	0.8	1.0	0.7	0.8	0.8	0.8	0.7	0.8	0.8	0.8	1.0
Er	ppm	0.1	2.4	2.3	2.2	2.0	2.0	2.0	1.9	1.9	2.1	2.1	2.1	2.3
Tm	ppm	0.1	0.3	0.3	0.3	0.2	0.2	0.3	0.2	0.2	0.3	0.3	0.2	0.3
Yb	ppm	0.1	1.6	1.7	1.3	1.3	1.4	1.5	1.6	1.6	1.6	1.6	1.5	1.7
Lu	ppm	0.1	0.2	0.2	0.2	0.2	0.2	0.2	0.2	0.2	0.2	0.2	0.2	0.2

Latitude	Longitude	dec degrees South	dec degrees East	<i>DETECTION</i>										
				ELEMENTS	UNITS	LIMITS	VIC22	VIC23	VIC25	VIC28	VIC29	VIC31	VIC32	VIC33
				SiO2	%	0.010	46.87	48.11	46.44	48.20	46.70	45.47	45.56	46.51
				Al2O3	%	0.010	13.35	14.15	13.78	14.11	13.19	13.19	13.18	12.88
				TiO2	%	0.010	2.36	2.29	2.46	2.22	2.45	2.81	2.76	2.40
				Fe2O3	%	0.010	13.20	12.80	13.05	12.99	13.18	12.99	12.77	13.37
				MnO	%	0.010	0.17	0.16	0.17	0.17	0.17	0.17	0.16	0.17
				MgO	%	0.010	10.10	8.87	8.86	8.68	11.01	10.60	10.48	11.12
				CaO	%	0.010	9.19	9.03	8.79	8.75	9.05	9.01	9.16	9.05
				Na2O	%	0.010	3.27	3.43	4.07	3.69	3.32	3.45	3.44	3.05
				K2O	%	0.010	1.44	1.15	2.17	1.51	1.37	1.77	1.77	1.33
				Cr2O3	%	0.005	0.05	0.04	0.03	0.04	0.05	0.04	0.05	0.05
				P2O5	%	0.001	0.61	0.45	0.82	0.58	0.58	0.62	0.62	0.57
				BaO	%	0.005	0.04	0.04	0.06	0.05	0.05	0.05	0.05	0.04
				SO3	%	0.002	0.07	0.01	0.05	0.02	0.01	0.02	0.03	0.01
				LOI	%	0.01	-0.61	-0.43	-0.52	-0.74	-0.87	-0.11	0.07	-0.47
				Total	%		100.11	100.10	100.24	100.26	100.25	100.08	100.10	100.09
				Sc	ppm	10	18	20	17	18	19	18	19	19
				V	ppm	10	203	200	194	189	208	221	231	204
				Cr	ppm	20	282	273	205	238	311	281	295	367

ELEMENTS	UNITS	DETECTION LIMITS	VIC22	VIC23	VIC25	VIC28	VIC29	VIC31	VIC32	VIC33
<b>Co</b>	ppm	0.1	60.2	55.9	53.1	49.8	62.2	63.3	60.5	64.4
<b>Ni</b>	ppm	0.5	228.8	175.7	174.1	166.3	245.6	231.8	213.9	276.7
<b>Cu</b>	ppm	0.5	67.1	47.7	49.8	57.3	53.6	59.0	52.0	49.2
<b>Zn</b>	ppm	1	112	108	127	115	115	111	106	114
<b>Ga</b>	ppm	0.1	21.0	22.4	23.8	22.4	21.1	21.6	22.5	20.6
<b>Ge</b>	ppm	0.05	0.55	0.62	0.74	0.91	0.74	0.18	0.42	0.57
<b>As</b>	ppm	0.5	1.1	0.7	1.4	X	1.5	0.9	1.6	X
<b>Be</b>	ppm	0.05	1.36	1.36	2.28	1.47	1.34	1.72	1.73	1.43
<b>Bi</b>	ppm	0.01	0.03	0.03	0.02	0.02	0.03	0.01	0.02	X
<b>Cd</b>	ppm	0.02	0.12	0.06	0.08	0.04	0.06	0.05	0.05	0.04
<b>In</b>	ppm	0.01	0.06	0.04	0.07	0.04	0.06	0.06	0.06	0.07
<b>Te</b>	ppm	0.1	0.1	0.1	X	0.3	0.1	0.1	0.1	0.1
<b>Cs</b>	ppm	0.1	0.6	0.5	0.7	0.6	0.4	0.7	0.7	0.4
<b>Tl</b>	ppm	0.02	0.04	0.03	0.07	0.03	0.03	X	0.03	X
<b>Rb</b>	ppm	0.1	27.5	21.9	44.8	30.9	25.4	33.6	35.3	23.9
<b>Ba</b>	ppm	0.5	350.3	278.2	518.5	390.6	354.9	411.8	399.8	344.9
<b>Th</b>	ppm	0.1	3.2	2.8	5.3	3.7	3.0	4.3	4.6	2.7
<b>U</b>	ppm	0.1	0.9	0.8	1.5	0.9	0.9	1.1	1.3	0.7
<b>Nb</b>	ppm	0.1	39.0	32.7	61.7	45.6	38.4	51.8	52.3	37.1
<b>Ta</b>	ppm	0.1	2.3	2.1	3.9	2.8	2.4	3.5	3.4	2.3
<b>La</b>	ppm	0.2	29.4	24.5	47.8	33.5	29.2	36.9	37.1	27.3
<b>Ce</b>	ppm	0.5	59.2	50.8	96.6	66.8	60.7	73.5	74.0	56.0

ELEMENTS	UNITS	DETECTION LIMITS										
		VIC22	VIC23	VIC25	VIC28	VIC29	VIC31	VIC32	VIC33			
<b>Pb</b>	ppm	2.3	2.2	4.0	2.9	3.1	2.8	3.1	1.6			
<b>Pr</b>	ppm	7.2	6.3	11.5	8.1	7.6	8.9	8.8	7.1			
<b>Mo</b>	ppm	3.4	2.5	4.5	2.6	1.3	3.7	3.6	2.0			
<b>Sr</b>	ppm	661.2	592.6	876.4	670.8	677.8	709.3	717.7	587.7			
<b>Nd</b>	ppm	30.5	26.2	46.0	32.9	31.4	35.2	36.6	29.1			
<b>Sm</b>	ppm	6.6	5.8	8.8	6.7	6.6	7.3	7.4	6.3			
<b>Zr</b>	ppm	169	173	279	202	168	224	225	171			
<b>Hf</b>	ppm	4.3	4.4	7.3	5.2	4.5	5.7	6.0	4.5			
<b>Eu</b>	ppm	2.3	2.0	3.0	2.4	2.3	2.4	2.5	2.3			
<b>Sn</b>	ppm	2	2	2	2	2	2	2	2			
<b>Sb</b>	ppm	0.09	0.09	0.13	0.09	0.09	0.10	0.12	X			
<b>Gd</b>	ppm	6.4	5.7	7.9	7.0	6.4	7.2	6.9	6.4			
<b>Tb</b>	ppm	0.9	0.8	1.1	0.9	0.9	0.9	0.9	0.9			
<b>Dy</b>	ppm	4.8	4.5	5.7	4.9	4.6	5.0	4.9	4.7			
<b>Li</b>	ppm	6.9	7.3	8.9	6.5	6.0	6.9	7.0	6.0			
<b>Y</b>	ppm	20.6	21.0	25.5	23.0	20.9	21.6	21.9	21.3			
<b>Ho</b>	ppm	0.8	0.8	1.0	0.9	0.8	0.9	0.9	0.8			
<b>Er</b>	ppm	2.1	2.0	2.4	2.2	2.0	2.2	2.2	2.0			
<b>Tm</b>	ppm	0.2	0.2	0.3	0.3	0.2	0.3	0.3	0.2			
<b>Yb</b>	ppm	1.5	1.7	1.6	1.8	1.2	1.5	1.5	1.4			
<b>Lu</b>	ppm	0.2	0.2	0.2	0.2	0.2	0.2	0.2	0.2			



APPENDIX C. SUPPLEMENTARY DATA CHAPTER 3 – ISOTOPE  
DATA



APPENDIX D. SUPPLEMENTARY DATA CHAPTER 4 –  $^{40}\text{Ar}/^{39}\text{Ar}$   
ISOTOPE ABUNDANCES NEWER PLAINS

Step	$^{36}\text{Ar}$ [fA]	%1s	$^{37}\text{Ar}$ [fA]	%1s	$^{38}\text{Ar}$ [fA]	%1s	$^{39}\text{Ar}$ [fA]	%1s	$^{40}\text{Ar}$ [fA]	%1s	$^{40}(\text{r})/^{39}(\text{k})$	$\pm 2s$	Age (Ka)	$\pm 2s$	$^{40}\text{Ar}(\text{r})$ (%)	$^{39}\text{Ar}(\text{k})$ (%)	K/Ca	$\pm 2s$	
<b>VIC12: J = 0.00009360 <math>\pm</math> 0.00000028 (1<math>\sigma</math>) MDF = 0.992307 <math>\pm</math> 0.00059 (1<math>\sigma</math>)</b>																			
3	0.0001	1.058	0.0014	87.935	0.0000	2071.9	0.0008	3.879	0.0376	0.828	4.70	$\pm 1.24$	0.80	$\pm 0.21$	10.29	0.12	0.25	$\pm 0.43$	
4	0.0010	0.306	0.0056	21.042	0.0000	192.05	0.0028	1.085	0.3263	0.095	10.31	$\pm 0.80$	1.74	$\pm 0.13$	8.81	0.40	0.21	$\pm 0.09$	
5	0.0030	0.249	0.0180	8.419	0.0002	26.221	0.0099	0.396	1.0067	0.031	10.38	$\pm 0.54$	1.76	$\pm 0.09$	10.22	1.42	0.24	$\pm 0.04$	
6	0.0056	0.254	0.0440	5.088	0.0005	10.781	0.0254	0.135	1.9474	0.016	10.77	$\pm 0.39$	1.82	$\pm 0.07$	14.02	3.62	0.25	$\pm 0.03$	
7	0.0054	0.245	0.0592	4.613	0.0006	2.083	0.0383	0.077	2.0080	0.008	10.82	$\pm 0.24$	1.83	$\pm 0.04$	20.63	5.47	0.28	$\pm 0.03$	
8	0.0052	0.246	0.0709	4.439	0.0006	3.838	0.0477	0.073	2.0537	0.007	10.87	$\pm 0.19$	1.84	$\pm 0.03$	25.22	6.81	0.29	$\pm 0.03$	
9	0.0039	0.243	0.0743	4.464	0.0006	3.057	0.0555	0.068	1.7596	0.008	10.93	$\pm 0.12$	1.85	$\pm 0.02$	34.42	7.92	0.32	$\pm 0.03$	
10	0.0028	0.253	0.0698	4.391	0.0004	3.873	0.0558	0.069	1.4455	0.009	10.86	$\pm 0.09$	1.84	$\pm 0.02$	41.87	7.96	0.34	$\pm 0.03$	
12	0.0034	0.244	0.0944	4.265	0.0008	1.541	0.0835	0.064	1.9248	0.006	10.85	$\pm 0.07$	1.84	$\pm 0.01$	47.03	11.92	0.38	$\pm 0.03$	
14	0.0021	0.261	0.0941	4.231	0.0005	3.760	0.0757	0.065	1.4427	0.009	10.81	$\pm 0.05$	1.83	$\pm 0.01$	56.66	10.81	0.35	$\pm 0.03$	
16	0.0016	0.253	0.1041	4.170	0.0004	4.911	0.0670	0.070	1.1944	0.010	10.72	$\pm 0.05$	1.81	$\pm 0.01$	60.05	9.56	0.28	$\pm 0.02$	
18	0.0014	0.278	0.1158	4.188	0.0003	3.960	0.0534	0.071	0.9791	0.013	10.64	$\pm 0.05$	1.80	$\pm 0.01$	57.95	7.62	0.20	$\pm 0.02$	
20	0.0014	0.285	0.1171	4.183	0.0002	19.309	0.0430	0.073	0.8505	0.062	10.61	$\pm 0.07$	1.79	$\pm 0.01$	53.46	6.13	0.16	$\pm 0.01$	
21	0.0010	0.286	0.0949	4.249	0.0002	26.946	0.0316	0.089	0.6367	0.082	10.63	$\pm 0.08$	1.80	$\pm 0.01$	52.57	4.50	0.14	$\pm 0.01$	
22	0.0008	0.328	0.0757	4.290	0.0001	66.877	0.0230	0.094	0.4803	0.109	10.61	$\pm 0.09$	1.80	$\pm 0.02$	50.73	3.28	0.13	$\pm 0.01$	
24	0.0010	0.287	0.0887	4.252	0.0001	51.449	0.0254	0.096	0.5451	0.096	10.59	$\pm 0.09$	1.79	$\pm 0.02$	49.18	3.62	0.12	$\pm 0.01$	
26	0.0009	0.278	0.0876	4.268	0.0001	20.438	0.0237	0.115	0.5135	0.061	10.56	$\pm 0.08$	1.79	$\pm 0.01$	48.66	3.38	0.12	$\pm 0.01$	
28	0.0007	0.322	0.0816	4.315	0.0001	32.631	0.0208	0.138	0.4372	0.071	10.61	$\pm 0.09$	1.79	$\pm 0.02$	50.39	2.97	0.11	$\pm 0.01$	
30	0.0006	0.339	0.0729	4.361	0.0001	38.675	0.0176	0.132	0.3734	0.083	10.59	$\pm 0.10$	1.79	$\pm 0.02$	49.87	2.51	0.10	$\pm 0.01$	
<b>VIC13: J = 0.00009320 <math>\pm</math> 0.00000019 (1<math>\sigma</math>) MDF = 0.992121 <math>\pm</math> 0.00020 (1<math>\sigma</math>)</b>																			
3	0.0511	0.081	0.0057	22.200	0.0105	0.538	0.0037	0.811	15.1399	0.003	39.03	$\pm 12.75$	6.57	$\pm 2.14$	0.96	0.74	0.28	$\pm 0.13$	
4	0.0500	0.081	0.0137	9.674	0.0103	0.556	0.0079	0.371	14.8990	0.003	28.51	$\pm 5.86$	4.80	$\pm 0.99$	1.52	1.57	0.25	$\pm 0.05$	
5	0.0490	0.081	0.0274	5.886	0.0102	0.563	0.0145	0.211	14.7761	0.002	26.43	$\pm 3.16$	4.45	$\pm 0.53$	2.58	2.86	0.23	$\pm 0.03$	

Step	<sup>36</sup> Ar [fA]	%1s	<sup>37</sup> Ar [fA]	%1s	<sup>38</sup> Ar [fA]	%1s	<sup>39</sup> Ar [fA]	%1s	<sup>40</sup> Ar [fA]	%1s	<sup>40</sup> (r)/ <sup>39</sup> (k)	Age (Ka)	± 2s	<sup>40</sup> Ar(f) (%)	<sup>39</sup> Ar(k) (%)	K/Ca	± 2s	
6	0.0408	0.082	0.0375	5.171	0.0082	0.629	0.0197	0.147	12.4599	0.007	24.96	4.20	± 0.33	3.94	3.89	0.23	± 0.02	
7	0.0323	0.084	0.0504	4.672	0.0063	0.817	0.0264	0.095	10.1586	0.008	25.14	4.23	± 0.19	6.53	5.23	0.23	± 0.02	
8	0.0261	0.082	0.0632	4.492	0.0051	1.037	0.0322	0.087	8.4715	0.010	25.27	4.25	± 0.13	9.60	6.38	0.22	± 0.02	
9	0.0203	0.084	0.0694	4.262	0.0035	1.668	0.0361	0.085	6.8670	0.011	25.58	4.31	± 0.09	13.43	7.15	0.22	± 0.02	
10	0.0160	0.084	0.0759	4.306	0.0025	2.409	0.0399	0.067	5.7072	0.013	25.74	4.33	± 0.06	17.98	7.90	0.23	± 0.02	
12	0.0186	0.087	0.1126	4.179	0.0035	1.658	0.0593	0.055	6.9807	0.011	25.66	4.32	± 0.05	21.76	11.73	0.23	± 0.02	
14	0.0161	0.086	0.1144	4.107	0.0028	3.096	0.0598	0.046	6.2367	0.003	25.28	4.26	± 0.04	24.20	11.83	0.22	± 0.02	
16	0.0140	0.091	0.1070	4.121	0.0022	3.768	0.0496	0.061	5.3350	0.003	24.96	4.20	± 0.05	23.17	9.81	0.20	± 0.02	
18	0.0104	0.088	0.0990	4.152	0.0018	4.750	0.0370	0.076	3.9686	0.004	24.74	4.16	± 0.05	23.03	7.32	0.16	± 0.01	
20	0.0093	0.098	0.1024	4.196	0.0015	5.976	0.0286	0.100	3.4117	0.013	24.40	4.11	± 0.05	20.41	5.66	0.12	± 0.01	
21	0.0079	0.087	0.0844	4.224	0.0013	6.948	0.0200	0.114	2.8130	0.015	24.57	4.14	± 0.06	17.40	3.95	0.10	± 0.01	
22	0.0071	0.094	0.0735	4.451	0.0011	8.047	0.0155	0.147	2.4610	0.018	24.52	4.13	± 0.08	15.40	3.06	0.09	± 0.01	
24	0.0063	0.096	0.0795	4.191	0.0010	5.810	0.0153	0.157	2.2394	0.026	24.98	4.20	± 0.07	17.04	3.03	0.08	± 0.01	
26	0.0058	0.089	0.0894	4.181	0.0009	6.281	0.0158	0.152	2.0722	0.028	24.37	4.10	± 0.06	18.46	3.11	0.08	± 0.01	
28	0.0067	0.102	0.0829	4.198	0.0010	5.545	0.0128	0.168	2.2675	0.025	24.34	4.10	± 0.09	13.65	2.52	0.07	± 0.01	
30	0.0043	0.092	0.0838	4.132	0.0007	7.990	0.0114	0.192	1.5100	0.038	23.59	3.97	± 0.07	17.74	2.25	0.06	± 0.00	
<b>VIC14: J = 0.00009200 ± 0.00000019 (1σ) MDF = 0.993390 ± 0.00020 (1σ)</b>																		
3	0.0088	0.090	0.0713	17.811	0.0016	1.470	0.0065	0.281	2.7022	0.013	17.10	2.84	± 0.26	4.05	1.36	0.04	± 0.01	
4	0.0085	0.089	0.0806	13.428	0.0017	1.314	0.0140	0.131	2.8147	0.013	22.34	3.71	± 0.12	11.05	2.96	0.07	± 0.02	
5	0.0073	0.097	0.0662	17.006	0.0016	1.637	0.0240	0.083	2.7288	0.014	23.17	3.85	± 0.06	20.37	5.10	0.16	± 0.05	
6	0.0061	0.117	0.0712	16.105	0.0015	1.841	0.0315	0.061	2.5331	0.014	23.28	3.87	± 0.04	28.92	6.69	0.19	± 0.06	
7	0.0042	0.106	0.0605	17.195	0.0012	2.400	0.0349	0.058	2.0484	0.018	23.32	3.87	± 0.03	39.62	7.41	0.25	± 0.09	
8	0.0033	0.106	0.0710	18.232	0.0010	3.171	0.0361	0.056	1.8255	0.019	23.35	3.88	± 0.02	46.10	7.67	0.22	± 0.08	
9	0.0024	0.131	0.0644	17.475	0.0009	2.690	0.0335	0.061	1.4869	0.024	23.32	3.88	± 0.02	52.46	7.12	0.22	± 0.08	

Step	36Ar [fA]	%1s	37Ar [fA]	%1s	38Ar [fA]	%1s	39Ar [fA]	%1s	40Ar [fA]	%1s	40(r)/ 39(k)	Age (Ka)	± 2s	40Ar(r) (%)	39Ar(k) (%)	K/Ca	± 2s
10	0.0020	0.122	0.0674	18.792	0.0007	3.738	0.0336	0.069	1.3585	0.026	23.37	3.88	± 0.02	57.76	7.14	0.21	± 0.08
12	0.0027	0.109	0.1061	11.794	0.0010	2.799	0.0438	0.050	1.8138	0.020	23.33	3.88	± 0.02	56.25	9.30	0.18	± 0.04
14	0.0023	0.116	0.1068	11.901	0.0009	2.531	0.0421	0.051	1.6490	0.021	23.29	3.87	± 0.01	59.37	8.95	0.17	± 0.04
16	0.0013	0.189	0.1034	12.200	0.0007	4.508	0.0364	0.057	1.2354	0.029	23.22	3.86	± 0.01	68.32	7.73	0.15	± 0.04
18	0.0019	0.124	0.0906	11.465	0.0007	3.032	0.0323	0.064	1.2979	0.028	23.16	3.85	± 0.02	57.54	6.86	0.15	± 0.04
20	0.0015	0.159	0.0669	15.182	0.0005	3.858	0.0266	0.079	1.0439	0.034	23.09	3.84	± 0.02	58.68	5.64	0.17	± 0.05
21	0.0012	0.134	0.0810	14.696	0.0004	5.628	0.0196	0.100	0.8007	0.044	23.26	3.87	± 0.02	56.76	4.16	0.10	± 0.03
22	0.0007	0.180	0.0489	21.455	0.0003	11.207	0.0136	0.136	0.5103	0.069	23.09	3.84	± 0.03	61.40	2.89	0.12	± 0.05
24	0.0008	0.206	0.0355	34.058	0.0003	7.131	0.0128	0.153	0.5365	0.065	23.13	3.84	± 0.03	55.26	2.73	0.16	± 0.11
26	0.0008	0.161	0.0318	38.047	0.0003	8.025	0.0113	0.171	0.4844	0.072	22.81	3.79	± 0.04	53.30	2.41	0.15	± 0.12
28	0.0006	0.169	0.0195	46.980	0.0002	12.216	0.0096	0.199	0.3917	0.089	22.96	3.81	± 0.04	56.27	2.04	0.21	± 0.20
30	0.0005	0.165	0.0292	33.037	0.0001	20.874	0.0086	0.218	0.3372	0.104	23.05	3.83	± 0.04	58.87	1.83	0.13	± 0.08

**VIC38: J = 0.00009260 ± 0.00000034 (1σ) MDF = 0.993804 ± 0.00030 (1σ)**

3	0.0031	0.171	0.0221	2.373	0.0007	4.016	0.0055	1.311	0.9753	0.058	15.73	2.63	± 0.31	8.76	0.86	0.11	± 0.01
4	0.0051	0.134	0.0426	2.169	0.0011	2.371	0.0135	0.535	1.7690	0.032	22.26	3.72	± 0.20	16.90	2.12	0.14	± 0.01
5	0.0044	0.155	0.0467	2.178	0.0011	2.597	0.0204	0.352	1.7764	0.032	24.18	4.04	± 0.12	27.73	3.21	0.19	± 0.01
6	0.0046	0.137	0.0537	2.140	0.0012	2.275	0.0295	0.244	2.0648	0.028	25.16	4.21	± 0.08	35.90	4.64	0.24	± 0.01
7	0.0039	0.156	0.0530	2.141	0.0011	2.273	0.0346	0.211	2.0336	0.028	25.77	4.31	± 0.06	43.78	5.44	0.28	± 0.01
8	0.0038	0.149	0.0558	2.148	0.0012	2.988	0.0414	0.176	2.1577	0.026	25.76	4.31	± 0.05	49.39	6.52	0.32	± 0.01
9	0.0033	0.129	0.0548	2.136	0.0012	3.110	0.0457	0.152	2.1221	0.039	25.83	4.32	± 0.04	55.60	7.19	0.36	± 0.02
10	0.0028	0.137	0.0552	2.140	0.0011	4.035	0.0501	0.139	2.1072	0.039	25.87	4.33	± 0.03	61.45	7.89	0.39	± 0.02
12	0.0033	0.150	0.0735	2.122	0.0015	2.614	0.0690	0.103	2.7461	0.030	25.82	4.32	± 0.03	64.81	10.86	0.40	± 0.02
14	0.0026	0.149	0.0733	2.130	0.0013	3.318	0.0680	0.126	2.4971	0.012	25.81	4.32	± 0.02	70.26	10.71	0.40	± 0.02
16	0.0021	0.166	0.0751	2.129	0.0011	3.857	0.0589	0.144	2.1290	0.014	25.79	4.31	± 0.02	71.27	9.27	0.34	± 0.01
18	0.0014	0.191	0.0736	2.126	0.0008	5.094	0.0449	0.187	1.5526	0.019	25.78	4.31	± 0.02	74.40	7.06	0.26	± 0.01

Step	36Ar [fA]	%1s	37Ar [fA]	%1s	38Ar [fA]	%1s	39Ar [fA]	%1s	40Ar [fA]	%1s	40(r)/39(k)	±2s	Age (Ka)	±2s	40Ar(r) (%)	39Ar(k) (%)	K/Ca	±2s
20	0.0011	0.179	0.0775	2.105	0.0007	5.561	0.0350	0.282	1.2169	0.108	25.77	±0.19	4.31	±0.03	73.97	5.50	0.19	±0.01
21	0.0007	0.278	0.0628	2.113	0.0005	8.131	0.0244	0.403	0.8252	0.159	25.74	±0.25	4.31	±0.04	75.97	3.84	0.17	±0.01
22	0.0005	0.278	0.0502	2.123	0.0003	12.166	0.0169	0.580	0.5781	0.227	25.63	±0.35	4.29	±0.06	74.86	2.66	0.14	±0.01
24	0.0004	0.282	0.0503	2.136	0.0003	13.998	0.0140	0.693	0.4865	0.216	25.73	±0.40	4.30	±0.07	73.98	2.20	0.12	±0.01
26	0.0005	0.269	0.0549	2.130	0.0003	12.709	0.0139	0.699	0.4936	0.213	25.82	±0.41	4.32	±0.07	72.64	2.19	0.11	±0.00
28	0.0003	0.320	0.0479	2.156	0.0002	15.738	0.0110	0.886	0.3760	0.280	25.86	±0.51	4.33	±0.09	75.33	1.73	0.10	±0.00
30	0.0003	0.460	0.0420	2.160	0.0002	20.769	0.0085	1.138	0.3052	0.345	26.59	±0.67	4.45	±0.11	74.01	1.34	0.09	±0.00
40	0.0006	0.304	0.0855	2.111	0.0003	9.750	0.0170	0.571	0.6008	0.175	25.85	±0.34	4.32	±0.06	73.00	2.67	0.09	±0.00
50	0.0004	0.315	0.0651	2.119	0.0002	13.978	0.0135	0.723	0.4639	0.227	25.94	±0.42	4.34	±0.07	75.03	2.11	0.09	±0.00

**VIC39: J = 0.00009170 ± 0.00000036 (1σ) MDF = 0.993804 ± 0.00030 (1σ)**

3	0.0033	0.133	0.0113	2.699	0.0007	4.251	0.0043	1.162	1.0850	0.036	26.04	±1.26	4.31	±0.21	10.35	0.73	0.16	±0.01
4	0.0051	0.137	0.0252	2.226	0.0012	2.440	0.0136	0.376	1.8596	0.021	25.57	±0.58	4.24	±0.10	18.62	2.29	0.23	±0.01
5	0.0054	0.131	0.0343	2.172	0.0014	1.709	0.0244	0.209	2.2287	0.018	25.50	±0.34	4.22	±0.06	27.89	4.13	0.31	±0.01
6	0.0058	0.125	0.0388	2.164	0.0015	1.852	0.0323	0.242	2.5499	0.005	25.49	±0.28	4.22	±0.05	32.31	5.47	0.36	±0.02
7	0.0060	0.135	0.0445	2.139	0.0016	1.677	0.0412	0.192	2.8213	0.006	25.58	±0.23	4.24	±0.04	37.32	6.97	0.40	±0.02
8	0.0048	0.136	0.0469	2.133	0.0015	2.189	0.0469	0.170	2.6105	0.005	25.61	±0.17	4.24	±0.03	46.02	7.94	0.43	±0.02
9	0.0032	0.141	0.0446	2.124	0.0012	2.274	0.0479	0.248	2.1802	0.004	25.62	±0.16	4.24	±0.03	56.29	8.11	0.46	±0.02
10	0.0026	0.165	0.0418	2.140	0.0011	2.335	0.0462	0.257	1.9595	0.006	25.64	±0.16	4.25	±0.03	60.43	7.82	0.48	±0.02
12	0.0030	0.151	0.0601	2.115	0.0013	2.079	0.0624	0.192	2.4862	0.005	25.67	±0.12	4.25	±0.02	64.42	10.56	0.45	±0.02
14	0.0019	0.141	0.0607	2.113	0.0011	2.334	0.0578	0.194	2.0365	0.045	25.61	±0.11	4.24	±0.02	72.64	9.78	0.41	±0.02
16	0.0015	0.144	0.0696	2.108	0.0008	3.107	0.0485	0.230	1.6740	0.055	25.57	±0.13	4.23	±0.02	74.00	8.20	0.30	±0.01
18	0.0010	0.197	0.0642	2.111	0.0007	3.734	0.0347	0.320	1.1868	0.078	25.55	±0.18	4.23	±0.03	74.50	5.86	0.23	±0.01
20	0.0007	0.217	0.0611	2.111	0.0005	7.819	0.0273	0.305	0.9072	0.057	25.45	±0.17	4.21	±0.03	76.39	4.61	0.19	±0.01
21	0.0004	0.276	0.0431	2.121	0.0003	9.262	0.0190	0.438	0.6117	0.084	25.50	±0.24	4.22	±0.04	79.10	3.21	0.19	±0.01
22	0.0003	0.315	0.0340	2.124	0.0002	9.638	0.0142	0.583	0.4507	0.114	25.46	±0.31	4.22	±0.05	80.15	2.40	0.18	±0.01

Step	<sup>36</sup> Ar [fA]	%1s	<sup>37</sup> Ar [fA]	%1s	<sup>38</sup> Ar [fA]	%1s	<sup>39</sup> Ar [fA]	%1s	<sup>40</sup> Ar [fA]	%1s	40(r)/39(k)	Age (Ka)	± 2s	40Ar(r) (%)	<sup>39</sup> Ar(k) (%)	K/Ca	± 2s
24	0.0003	0.421	0.0373	2.126	0.0002	11.834	0.0141	0.588	0.4482	0.115	25.38	4.20	± 0.05	79.58	2.38	0.16	± 0.01
26	0.0003	0.371	0.0382	2.134	0.0002	12.567	0.0124	0.672	0.4040	0.127	25.44	4.21	± 0.06	77.85	2.09	0.14	± 0.01
28	0.0002	0.432	0.0343	2.145	0.0002	16.871	0.0102	0.808	0.3302	0.156	25.51	4.22	± 0.07	78.95	1.73	0.13	± 0.01
30	0.0001	0.719	0.0256	2.173	0.0001	28.119	0.0070	1.183	0.2197	0.234	25.89	4.29	± 0.11	82.23	1.18	0.12	± 0.01
40	0.0004	0.352	0.0563	2.111	0.0003	7.879	0.0139	0.599	0.4573	0.113	25.80	4.27	± 0.05	78.01	2.34	0.11	± 0.00
50	0.0006	0.211	0.0473	2.119	0.0003	10.347	0.0131	0.633	0.5208	0.099	26.01	4.31	± 0.06	65.22	2.21	0.12	± 0.01
<b>VIC46: J = 0.00009300 ± 0.00000011 (1σ) MDF = 0.992527 ± 0.00120 (1σ)</b>																	
3	0.0200	0.480	0.0092	30.200	0.0038	1.193	0.0089	0.157	6.1153	0.009	19.48	3.27	± 1.57	2.82	1.93	0.41	± 0.25
4	0.0163	0.481	0.0175	16.073	0.0033	1.247	0.0216	0.131	5.3790	0.011	24.74	4.16	± 0.53	9.93	4.70	0.53	± 0.17
5	0.0069	0.481	0.0292	8.212	0.0017	2.124	0.0306	0.133	2.8574	0.042	26.22	4.40	± 0.16	28.08	6.66	0.45	± 0.07
6	0.0046	0.482	0.0485	6.385	0.0015	2.260	0.0437	0.128	2.4918	0.048	26.20	4.40	± 0.07	45.92	9.51	0.39	± 0.05
7	0.0025	0.491	0.0561	6.393	0.0011	3.336	0.0445	0.163	1.8976	0.005	26.24	4.41	± 0.04	61.47	9.67	0.34	± 0.04
8	0.0016	0.494	0.0653	7.272	0.0009	3.249	0.0476	0.158	1.7061	0.005	26.11	4.39	± 0.03	72.82	10.35	0.31	± 0.05
9	0.0017	0.486	0.0708	6.065	0.0010	3.831	0.0446	0.162	1.6506	0.004	25.96	4.36	± 0.03	70.13	9.70	0.27	± 0.03
10	0.0010	0.517	0.0703	6.174	0.0007	4.171	0.0381	0.176	1.2734	0.005	25.73	4.32	± 0.02	76.86	8.28	0.23	± 0.03
12	0.0015	0.488	0.1031	5.588	0.0009	6.255	0.0435	0.131	1.5343	0.047	25.46	4.28	± 0.03	72.08	9.45	0.18	± 0.02
14	0.0010	0.503	0.0988	5.944	0.0006	8.895	0.0333	0.133	1.1293	0.064	25.26	4.24	± 0.03	74.21	7.22	0.14	± 0.02
16	0.0008	0.532	0.1090	5.923	0.0005	10.842	0.0273	0.228	0.9211	0.010	25.17	4.23	± 0.03	74.39	5.92	0.11	± 0.01
18	0.0007	0.547	0.1175	5.540	0.0005	12.249	0.0230	0.257	0.7728	0.012	25.26	4.24	± 0.03	74.77	4.98	0.08	± 0.01
20	0.0005	0.494	0.0947	5.726	0.0003	13.664	0.0157	0.350	0.5293	0.079	25.34	4.26	± 0.04	74.69	3.40	0.07	± 0.01
21	0.0003	0.546	0.0682	6.067	0.0002	23.631	0.0102	0.517	0.3485	0.120	25.41	4.27	± 0.05	73.76	2.20	0.06	± 0.01
22	0.0002	0.638	0.0524	6.952	0.0002	27.598	0.0074	0.703	0.2501	0.167	25.46	4.28	± 0.07	74.65	1.60	0.06	± 0.01
24	0.0002	0.570	0.0496	7.894	0.0001	31.300	0.0066	0.784	0.2296	0.182	25.29	4.25	± 0.08	72.62	1.43	0.06	± 0.01
26	0.0002	0.609	0.0509	7.770	0.0001	23.129	0.0062	0.486	0.2181	0.134	25.04	4.21	± 0.06	70.99	1.35	0.05	± 0.01
28	0.0002	0.766	0.0400	10.176	0.0001	41.327	0.0044	0.662	0.1534	0.190	25.42	4.27	± 0.07	73.01	0.96	0.05	± 0.01



Step	$^{36}\text{Ar}$ [fA]	%1s	$^{37}\text{Ar}$ [fA]	%1s	$^{38}\text{Ar}$ [fA]	%1s	$^{39}\text{Ar}$ [fA]	%1s	$^{40}\text{Ar}$ [fA]	%1s	$^{40}(\text{r})/^{39}(\text{k})$	$\pm 2s$	Age (Ka)	$\pm 2s$	$^{40}\text{Ar}(\text{r})$ (%)	$^{39}\text{Ar}(\text{k})$ (%)	K/Ca	$\pm 2s$	
30	0.0001	0.774	0.0233	14.661	0.0001	45.945	0.0032	0.913	0.1132	0.259	26.01	$\pm 0.57$	4.37	$\pm 0.10$	72.96	0.69	0.06	$\pm 0.02$	
<b>VIC47: <math>J = 0.00009270 \pm 0.00000039</math> (<math>1\sigma</math>) MIDF = <math>0.992253 \pm 0.00150</math> (<math>1\sigma</math>)</b>																			
3	0.0165	0.600	0.0053	72.875	0.0032	0.844	0.0037	0.402	4.9486	0.017	20.65	$\pm 26.03$	3.46	$\pm 4.35$	1.53	1.04	0.30	$\pm 0.43$	
4	0.0127	0.601	0.0126	29.062	0.0025	1.256	0.0080	0.248	3.9318	0.021	23.36	$\pm 9.11$	3.91	$\pm 1.52$	4.77	2.29	0.27	$\pm 0.16$	
5	0.0066	0.601	0.0281	12.726	0.0014	2.502	0.0129	0.186	2.2660	0.036	25.77	$\pm 2.94$	4.31	$\pm 0.49$	14.63	3.68	0.20	$\pm 0.05$	
6	0.0040	0.602	0.0432	9.559	0.0010	2.987	0.0194	0.167	1.6716	0.048	26.21	$\pm 1.18$	4.39	$\pm 0.20$	30.40	5.54	0.19	$\pm 0.04$	
7	0.0020	0.604	0.0504	8.641	0.0006	3.848	0.0217	0.165	1.1696	0.069	26.51	$\pm 0.55$	4.44	$\pm 0.09$	49.09	6.19	0.18	$\pm 0.03$	
8	0.0017	0.608	0.0678	7.171	0.0006	3.874	0.0265	0.158	1.1980	0.068	26.61	$\pm 0.38$	4.45	$\pm 0.06$	58.74	7.55	0.17	$\pm 0.02$	
9	0.0012	0.629	0.0679	7.145	0.0005	4.270	0.0260	0.159	1.0270	0.079	26.41	$\pm 0.28$	4.42	$\pm 0.05$	66.81	7.42	0.16	$\pm 0.02$	
10	0.0011	0.624	0.0760	6.523	0.0005	4.444	0.0260	0.160	0.9875	0.082	26.31	$\pm 0.26$	4.40	$\pm 0.04$	69.22	7.42	0.15	$\pm 0.02$	
12	0.0020	0.607	0.1077	5.785	0.0008	3.239	0.0353	0.157	1.4871	0.055	26.00	$\pm 0.33$	4.35	$\pm 0.06$	61.58	10.06	0.14	$\pm 0.02$	
14	0.0015	0.613	0.1144	5.930	0.0007	3.887	0.0331	0.156	1.2765	0.063	25.95	$\pm 0.27$	4.34	$\pm 0.05$	67.09	9.43	0.12	$\pm 0.01$	
16	0.0014	0.610	0.1105	5.855	0.0006	3.778	0.0287	0.158	1.1632	0.070	26.12	$\pm 0.31$	4.37	$\pm 0.05$	64.22	8.17	0.11	$\pm 0.01$	
18	0.0014	0.614	0.1030	5.821	0.0006	4.109	0.0253	0.161	1.0462	0.077	25.80	$\pm 0.33$	4.32	$\pm 0.06$	62.22	7.21	0.11	$\pm 0.01$	
20	0.0011	0.614	0.0925	6.331	0.0005	5.662	0.0207	0.170	0.8597	0.094	25.82	$\pm 0.34$	4.32	$\pm 0.06$	62.03	5.90	0.10	$\pm 0.01$	
21	0.0009	0.619	0.0731	6.872	0.0004	7.849	0.0150	0.185	0.6456	0.125	25.92	$\pm 0.38$	4.34	$\pm 0.06$	59.94	4.26	0.09	$\pm 0.01$	
22	0.0006	0.629	0.0595	7.755	0.0003	10.743	0.0111	0.199	0.4554	0.178	25.89	$\pm 0.36$	4.33	$\pm 0.06$	63.00	3.17	0.08	$\pm 0.01$	
24	0.0006	0.641	0.0592	7.414	0.0002	10.997	0.0112	0.203	0.4750	0.170	25.93	$\pm 0.39$	4.34	$\pm 0.06$	60.84	3.18	0.08	$\pm 0.01$	
26	0.0006	0.632	0.0724	7.089	0.0003	10.990	0.0107	0.200	0.4384	0.184	25.89	$\pm 0.37$	4.33	$\pm 0.06$	62.84	3.04	0.06	$\pm 0.01$	
28	0.0005	0.628	0.0587	7.760	0.0002	14.441	0.0088	0.220	0.3690	0.219	25.94	$\pm 0.40$	4.34	$\pm 0.07$	61.48	2.50	0.06	$\pm 0.01$	
30	0.0003	0.660	0.0460	9.318	0.0002	15.963	0.0068	0.251	0.2714	0.298	25.78	$\pm 0.41$	4.32	$\pm 0.07$	64.55	1.94	0.06	$\pm 0.01$	
<b>VIC48: <math>J = 0.00009050 \pm 0.00000010</math> (<math>1\sigma</math>) MIDF = <math>0.993383 \pm 0.00030</math> (<math>1\sigma</math>)</b>																			
3	0.0037	0.187	0.0075	23.050	0.0008	5.108	0.0044	3.505	1.1512	0.189	-2.67	$\pm 7.64$	-0.4	$\pm 1.25$	-1.03	0.70	0.25	$\pm 0.12$	
4	0.0059	0.133	0.0168	17.736	0.0013	3.188	0.0094	1.759	1.9276	0.129	7.20	$\pm 5.70$	1.18	$\pm 0.93$	3.52	1.50	0.24	$\pm 0.09$	

Step	36Ar [fA]	%1s	37Ar [fA]	%1s	38Ar [fA]	%1s	39Ar [fA]	%1s	40Ar [fA]	%1s	40(r)/ 39(k)	±2s	Age (Ka)	±2s	40Ar(r) (%)	39Ar(k) (%)	K/Ca	±2s
5	0.0049	0.131	0.0192	12.013	0.0011	3.922	0.0153	0.920	1.8311	0.114	18.66	±0.48	3.05	±2.94	15.58	2.43	0.34	±0.08
6	0.0038	0.128	0.0210	12.179	0.0010	3.865	0.0231	0.609	1.7257	0.120	23.23	±0.25	3.80	±1.52	31.04	3.67	0.47	±0.12
7	0.0028	0.135	0.0228	11.603	0.0009	5.309	0.0294	0.478	1.6125	0.129	25.23	±0.15	4.12	±0.90	45.97	4.67	0.55	±0.13
8	0.0024	0.169	0.0195	13.023	0.0009	4.813	0.0354	0.398	1.6579	0.125	25.68	±0.11	4.20	±0.65	54.81	5.63	0.78	±0.20
9	0.0021	0.136	0.0225	9.801	0.0009	4.191	0.0429	0.329	1.7686	0.118	25.85	±0.08	4.22	±0.48	62.65	6.82	0.82	±0.16
10	0.0016	0.171	0.0190	12.278	0.0009	4.424	0.0470	0.300	1.7168	0.121	25.99	±0.06	4.25	±0.35	71.09	7.47	1.06	±0.26
12	0.0017	0.168	0.0367	7.674	0.0011	3.310	0.0661	0.216	2.2379	0.093	25.96	±0.04	4.24	±0.26	76.59	10.51	0.77	±0.12
14	0.0014	0.145	0.0496	6.777	0.0011	3.531	0.0714	0.199	2.2834	0.091	25.90	±0.03	4.23	±0.21	80.93	11.35	0.62	±0.08
16	0.0010	0.206	0.0607	6.856	0.0008	4.772	0.0567	0.249	1.7597	0.118	25.87	±0.03	4.23	±0.21	83.30	9.02	0.40	±0.06
18	0.0008	0.180	0.0823	5.422	0.0007	5.266	0.0477	0.296	1.4585	0.142	25.74	±0.04	4.21	±0.23	84.01	7.58	0.25	±0.03
20	0.0006	0.234	0.1035	5.377	0.0006	6.977	0.0406	0.347	1.2209	0.170	25.73	±0.04	4.20	±0.24	85.42	6.45	0.17	±0.02
21	0.0004	0.295	0.0951	5.301	0.0005	7.931	0.0318	0.442	0.9402	0.221	25.66	±0.05	4.19	±0.29	86.67	5.05	0.14	±0.02
22	0.0003	0.421	0.0806	5.698	0.0003	12.186	0.0238	0.589	0.6900	0.301	25.60	±0.06	4.18	±0.37	88.26	3.79	0.13	±0.01
24	0.0002	0.392	0.0793	5.771	0.0003	12.955	0.0225	0.625	0.6488	0.320	25.84	±0.06	4.22	±0.39	89.28	3.57	0.12	±0.01
26	0.0002	0.417	0.0934	5.360	0.0003	11.427	0.0235	0.597	0.6694	0.310	25.82	±0.06	4.22	±0.37	90.43	3.73	0.11	±0.01
28	0.0002	0.430	0.0805	5.588	0.0003	12.377	0.0197	0.714	0.5647	0.368	25.93	±0.07	4.24	±0.44	90.03	3.12	0.10	±0.01
30	0.0002	0.375	0.0706	5.648	0.0003	13.816	0.0185	0.759	0.5394	0.385	26.08	±0.08	4.26	±0.47	89.21	2.94	0.11	±0.01

**VIC49: J = 0.00009200 ± 0.00000018 (1σ) MDF = 0.993383 ± 0.00030 (1σ)**

3	0.0029	0.155	0.0070	33.748	0.0006	4.860	0.0021	4.715	0.9266	0.089	6.07	±1.15	1.01	±6.94	1.40	0.42	0.13	±0.09
4	0.0059	0.133	0.0159	21.428	0.0012	1.940	0.0066	1.529	1.8993	0.044	12.03	±0.74	2.00	±4.44	4.18	1.30	0.18	±0.08
5	0.0054	0.130	0.0288	9.350	0.0013	1.892	0.0146	0.695	1.9377	0.043	18.79	±0.31	3.12	±1.85	14.14	2.86	0.22	±0.04
6	0.0041	0.142	0.0363	7.188	0.0011	2.307	0.0220	0.460	1.7234	0.048	21.39	±0.16	3.55	±0.94	27.33	4.33	0.26	±0.04
7	0.0033	0.131	0.0365	8.217	0.0010	2.809	0.0298	0.342	1.6930	0.049	22.27	±0.10	3.70	±0.58	39.17	5.85	0.35	±0.06
8	0.0029	0.156	0.0385	7.247	0.0009	2.177	0.0348	0.293	1.6894	0.049	22.64	±0.07	3.76	±0.44	46.62	6.83	0.39	±0.06
9	0.0023	0.165	0.0358	8.612	0.0009	2.805	0.0378	0.270	1.5880	0.052	22.92	±0.06	3.81	±0.34	54.57	7.43	0.45	±0.08

Step	36Ar [fA]	%1s	37Ar [fA]	%1s	38Ar [fA]	%1s	39Ar [fA]	%1s	40Ar [fA]	%1s	40(r)/ 39(k)	± 2s	Age (Ka)	± 2s	40Ar(r) (%)	39Ar(k) (%)	K/Ca	± 2s
10	0.0018	0.139	0.0350	7.395	0.0008	2.904	0.0381	0.268	1.4261	0.058	23.03	± 0.27	3.83	± 0.04	61.45	7.48	0.47	± 0.07
12	0.0022	0.149	0.0524	6.396	0.0011	2.598	0.0557	0.184	1.9592	0.043	23.06	± 0.22	3.83	± 0.04	65.53	10.94	0.46	± 0.06
14	0.0015	0.150	0.0614	6.085	0.0009	3.252	0.0539	0.191	1.7164	0.048	23.10	± 0.17	3.84	± 0.03	72.53	10.59	0.38	± 0.05
16	0.0013	0.163	0.0744	6.035	0.0008	2.930	0.0455	0.224	1.4376	0.058	23.02	± 0.18	3.83	± 0.03	72.81	8.93	0.26	± 0.03
18	0.0010	0.199	0.0898	5.443	0.0006	3.634	0.0368	0.278	1.1509	0.072	22.89	± 0.19	3.80	± 0.03	73.03	7.21	0.18	± 0.02
20	0.0009	0.138	0.1047	5.435	0.0006	3.814	0.0321	0.318	1.0050	0.083	22.87	± 0.21	3.80	± 0.03	72.81	6.29	0.13	± 0.01
21	0.0006	0.216	0.0878	5.611	0.0004	5.979	0.0217	0.468	0.6732	0.123	22.81	± 0.27	3.79	± 0.04	73.27	4.25	0.11	± 0.01
22	0.0005	0.195	0.0750	5.533	0.0003	8.308	0.0182	0.556	0.5638	0.147	22.93	± 0.30	3.81	± 0.05	73.97	3.57	0.10	± 0.01
24	0.0004	0.194	0.0699	5.825	0.0003	6.844	0.0160	0.633	0.4864	0.170	22.88	± 0.34	3.80	± 0.06	74.99	3.13	0.10	± 0.01
26	0.0004	0.194	0.0788	5.693	0.0003	9.247	0.0176	0.576	0.5354	0.155	22.94	± 0.31	3.81	± 0.05	75.22	3.45	0.10	± 0.01
28	0.0003	0.217	0.0642	6.240	0.0002	14.712	0.0139	0.731	0.4145	0.200	22.91	± 0.38	3.81	± 0.06	76.31	2.71	0.09	± 0.01
30	0.0003	0.350	0.0613	6.141	0.0002	10.752	0.0124	0.814	0.3862	0.215	22.88	± 0.43	3.80	± 0.07	73.49	2.44	0.09	± 0.01

APPENDIX E. SUPPLEMENTARY DATA CHAPTER 3 –  $^{40}\text{Ar}/^{39}\text{Ar}$   
ISOTOPE ABUNDANCES NEWER CONES

Step	36Ar [fA]	%1s	37Ar [fA]	%1s	38Ar [fA]	%1s	39Ar [fA]	%1s	40Ar [fA]	%1s	40(r)/39(k)	±2s	Age (Ka)	±2s	40Ar(r) (%)	39Ar(k) (%)	K/Ca	±2s	
<b>Buninyong: J = 0.00009545 ± 0.00000011 (1σ) MDF = 0.993415 ± 0.00050 (1σ)</b>																			
3	0.0003	0.298	0.0029	8.408	0.0001	19.419	0.0048	0.146	0.0904	0.032	0.82	±0.30	142.0	±51.1	4.35	0.42	0.71	±0.12	
4	0.0006	0.278	0.0136	3.102	0.0004	5.929	0.0211	0.064	0.2069	0.009	1.20	±0.14	207.8	±24.1	12.25	1.86	0.66	±0.04	
5	0.0006	0.301	0.0272	2.801	0.0008	3.166	0.0414	0.055	0.2430	0.013	1.22	±0.08	211.3	±13.1	20.85	3.66	0.65	±0.04	
6	0.0007	0.262	0.0403	2.634	0.0011	2.147	0.0640	0.054	0.2997	0.009	1.23	±0.06	212.2	±9.6	26.26	5.66	0.68	±0.04	
7	0.0008	0.205	0.0464	2.587	0.0013	1.862	0.0793	0.051	0.3409	0.007	1.20	±0.05	207.9	±8.4	28.01	7.02	0.74	±0.04	
8	0.0008	0.254	0.0497	2.604	0.0014	1.621	0.0868	0.055	0.3531	0.009	1.22	±0.05	210.7	±7.9	29.98	7.67	0.75	±0.04	
9	0.0008	0.236	0.0475	2.574	0.0013	1.635	0.0815	0.053	0.3388	0.006	1.21	±0.05	208.5	±8.1	29.03	7.20	0.74	±0.04	
10	0.0008	0.246	0.0484	2.567	0.0013	1.406	0.0779	0.053	0.3270	0.022	1.24	±0.05	213.3	±8.2	29.44	6.89	0.69	±0.04	
12	0.0011	0.247	0.0716	2.551	0.0017	0.993	0.1013	0.051	0.4363	0.008	1.21	±0.05	208.3	±8.6	28.02	8.96	0.61	±0.03	
14	0.0011	0.221	0.0942	2.543	0.0018	1.630	0.1028	0.054	0.4655	0.009	1.25	±0.05	216.1	±9.0	27.64	9.09	0.47	±0.02	
16	0.0012	0.241	0.1275	2.537	0.0017	1.549	0.0980	0.052	0.4604	0.009	1.23	±0.06	211.9	±9.6	26.12	8.67	0.33	±0.02	
18	0.0010	0.240	0.1570	2.536	0.0014	1.888	0.0812	0.053	0.3891	0.011	1.21	±0.06	208.9	±10.0	25.23	7.18	0.22	±0.01	
20	0.0010	0.261	0.1832	2.534	0.0014	1.744	0.0775	0.055	0.4171	0.005	1.53	±0.06	264.3	±10.9	28.40	6.84	0.18	±0.01	
21	0.0007	0.268	0.1343	2.537	0.0010	2.991	0.0502	0.052	0.2653	0.007	1.28	±0.07	221.7	±11.4	24.25	4.43	0.16	±0.01	
22	0.0005	0.356	0.1105	2.541	0.0007	3.986	0.0386	0.059	0.1981	0.012	1.22	±0.07	211.4	±11.7	23.81	3.41	0.15	±0.01	
24	0.0004	0.291	0.0988	2.542	0.0006	3.726	0.0301	0.055	0.1619	0.007	1.23	±0.07	212.3	±12.0	22.83	2.66	0.13	±0.01	
26	0.0003	0.332	0.0766	2.554	0.0004	6.308	0.0218	0.057	0.1201	0.021	1.35	±0.07	233.8	±12.3	24.56	1.93	0.12	±0.01	
28	0.0003	0.336	0.0673	2.555	0.0004	9.543	0.0187	0.065	0.1083	0.017	1.25	±0.08	214.9	±13.5	21.38	1.65	0.12	±0.01	
30	0.0002	0.420	0.0578	2.552	0.0002	12.619	0.0136	0.070	0.0886	0.021	1.47	±0.09	254.4	±15.7	22.61	1.20	0.10	±0.01	
40	0.0005	0.288	0.1077	2.541	0.0004	5.961	0.0223	0.069	0.1820	0.022	1.89	±0.11	325.9	±18.2	23.03	1.96	0.09	±0.00	
50	0.0005	0.273	0.1034	2.537	0.0004	6.576	0.0185	0.073	0.1987	0.032	3.08	±0.13	530.7	±22.0	28.56	1.63	0.08	±0.00	
<b>VIC01: J = 0.00009510 ± 0.00000015 (1σ) MDF = 0.994750 ± 0.00020 (1σ)</b>																			
0.5	0.0000	42.731	0.0000	2245.7	0.0000	1836.31	0.0000	71.810	0.0013	37.079	3.3953	±60.094	583.7	±10330.1	6.19	0.00	1.20	±54.06	

Step	<sup>36</sup> Ar [fA]	%1s	<sup>37</sup> Ar [fA]	%1s	<sup>38</sup> Ar [fA]	%1s	<sup>39</sup> Ar [fA]	%1s	<sup>40</sup> Ar [fA]	%1s	40(r)/39(k)	±2s	Age (Ka)	±2s	<sup>40</sup> Ar(r) (%)	<sup>39</sup> Ar(k) (%)	K/Ca	±2s
1.0	0.0005	0.380	0.0002	119.43	0.0001	103.10	0.0018	1.098	0.1435	0.325	0.8733	± 0.811	150.2	± 139.4	1.09	0.14	4.54	± 10.85
2.0	0.0029	0.122	0.0041	4.620	0.0013	6.010	0.0285	0.059	0.8958	0.052	0.9607	± 0.102	165.2	± 17.5	3.06	2.28	3.03	± 0.28
3.0	0.0034	0.104	0.0097	3.116	0.0018	4.194	0.0715	0.034	1.0777	0.043	0.9639	± 0.043	165.7	± 7.4	6.40	5.71	3.16	± 0.20
3.5	0.0020	0.126	0.0099	3.105	0.0013	5.810	0.0635	0.035	0.6440	0.072	0.9628	± 0.033	165.6	± 5.7	9.50	5.08	2.76	± 0.17
4.0	0.0017	0.192	0.0123	2.741	0.0014	5.486	0.0673	0.032	0.5784	0.081	0.9505	± 0.036	163.4	± 6.2	11.06	5.38	2.35	± 0.13
4.5	0.0015	0.158	0.0136	2.794	0.0013	5.995	0.0659	0.031	0.5059	0.092	0.9428	± 0.029	162.1	± 5.0	12.28	5.26	2.08	± 0.12
5.0	0.0014	0.171	0.0150	2.691	0.0013	5.915	0.0675	0.036	0.4665	0.100	0.9434	± 0.027	162.2	± 4.7	13.66	5.40	1.94	± 0.10
5.5	0.0012	0.201	0.0152	2.625	0.0012	6.354	0.0632	0.040	0.4037	0.116	0.9381	± 0.029	161.3	± 4.9	14.68	5.05	1.79	± 0.09
6.0	0.0010	0.213	0.0144	2.682	0.0010	7.140	0.0565	0.036	0.3392	0.138	0.9600	± 0.029	165.1	± 5.0	15.98	4.51	1.69	± 0.09
6.5	0.0009	0.225	0.0145	2.804	0.0010	7.438	0.0548	0.037	0.3145	0.148	0.9449	± 0.029	162.5	± 5.0	16.46	4.38	1.62	± 0.09
7.0	0.0008	0.316	0.0145	2.660	0.0009	8.139	0.0507	0.040	0.2827	0.165	0.9356	± 0.036	160.9	± 6.2	16.77	4.05	1.51	± 0.08
7.5	0.0011	0.229	0.0165	2.697	0.0011	6.743	0.0573	0.041	0.3763	0.124	0.9473	± 0.033	162.9	± 5.6	14.42	4.58	1.49	± 0.08
8.0	0.0007	0.304	0.0136	2.713	0.0008	9.529	0.0437	0.043	0.2360	0.198	0.9402	± 0.036	161.7	± 6.2	17.40	3.49	1.38	± 0.07
8.5	0.0005	0.348	0.0130	2.711	0.0007	10.627	0.0372	0.048	0.1909	0.244	0.9679	± 0.039	166.4	± 6.8	18.88	2.97	1.23	± 0.07
9.0	0.0006	0.291	0.0139	2.721	0.0007	10.205	0.0375	0.069	0.2238	0.208	0.9396	± 0.040	161.6	± 6.9	15.75	3.00	1.16	± 0.06
9.5	0.0004	0.424	0.0117	2.890	0.0005	13.817	0.0297	0.056	0.1483	0.314	0.9488	± 0.048	163.1	± 8.2	18.98	2.37	1.09	± 0.06
10.0	0.0004	0.468	0.0119	2.982	0.0006	13.784	0.0288	0.064	0.1463	0.319	0.9535	± 0.051	163.9	± 8.8	18.75	2.30	1.04	± 0.06
10.5	0.0004	0.484	0.0124	2.905	0.0006	13.434	0.0270	0.075	0.1354	0.344	0.9196	± 0.054	158.1	± 9.2	18.33	2.16	0.94	± 0.05
11.0	0.0005	0.449	0.0143	2.662	0.0007	10.882	0.0311	0.062	0.1669	0.279	0.9574	± 0.051	164.6	± 8.7	17.85	2.49	0.94	± 0.05
11.5	0.0003	0.568	0.0121	2.998	0.0004	17.574	0.0224	0.072	0.1140	0.409	0.9884	± 0.064	169.9	± 10.9	19.38	1.79	0.79	± 0.05
12.0	0.0004	0.518	0.0153	2.714	0.0005	14.536	0.0248	0.072	0.1355	0.344	0.9470	± 0.061	162.8	± 10.5	17.31	1.98	0.70	± 0.04
14.0	0.0006	0.364	0.0391	2.404	0.0008	9.591	0.0358	0.051	0.2106	0.221	0.9476	± 0.046	162.9	± 7.9	16.09	2.86	0.39	± 0.02
16.0	0.0007	0.298	0.0724	2.367	0.0009	8.740	0.0385	0.048	0.2462	0.190	0.9759	± 0.043	167.8	± 7.4	15.25	3.07	0.23	± 0.01
20.0	0.0014	0.169	0.2324	2.351	0.0013	5.573	0.0564	0.042	0.4675	0.100	1.1419	± 0.037	196.3	± 6.4	13.72	4.49	0.10	± 0.00
25.0	0.0033	0.125	0.5204	2.350	0.0032	2.341	0.1326	0.029	1.0664	0.044	1.0380	± 0.029	178.5	± 5.0	12.86	10.56	0.11	± 0.01
30.0	0.0016	0.146	0.4171	2.350	0.0011	6.723	0.0341	0.053	0.4880	0.096	1.2388	± 0.075	213.0	± 12.9	8.57	2.70	0.03	± 0.00

Step	36Ar [fA]	%1s	37Ar [fA]	%1s	38Ar [fA]	%1s	39Ar [fA]	%1s	40Ar [fA]	%1s	40(r)/39(k)	± 2s	Age (Ka)	± 2s	40Ar(t) (%)	39Ar(k) (%)	K/Ca	± 2s
35.0	0.0008	0.268	0.1861	2.352	0.0005	13.934	0.0149	0.113	0.2476	0.188	1.9597	± 20.8	336.9	± 20.8	11.66	1.18	0.03	± 0.00
40.0	0.0005	0.392	0.1125	2.360	0.0003	23.668	0.0100	0.191	0.1610	0.290	1.7941	± 27.9	308.5	± 27.9	11.06	0.79	0.04	± 0.00

**VIC03: J = 0.00009340 ± 0.00000014 (1σ) MDF = 0.993140 ± 0.00030 (1σ)**

3	0.0010	0.173	0.0025	506.065	0.0005	16.944	0.0200	0.150	0.3228	0.081	0.88	± 20.7	148.0	± 20.7	5.44	3.13	3.40	± 34.42
4	0.0022	0.136	0.0344	36.525	0.0013	6.273	0.0713	0.054	0.7060	0.031	0.88	± 7.1	149.1	± 7.1	8.91	11.13	0.89	± 0.65
5	0.0019	0.213	0.0133	79.025	0.0015	5.283	0.0860	0.046	0.6308	0.029	0.89	± 6.2	149.6	± 6.2	12.07	13.43	2.78	± 4.39
6	0.0014	0.180	0.0321	36.420	0.0013	6.042	0.0791	0.047	0.4979	0.037	0.92	± 5.6	155.8	± 5.6	14.65	12.35	1.06	± 0.77
7	0.0011	0.200	0.0165	67.732	0.0011	7.688	0.0647	0.054	0.3948	0.047	0.94	± 6.2	159.2	± 6.2	15.45	10.11	1.69	± 2.28
8	0.0010	0.178	0.0305	48.396	0.0010	8.197	0.0602	0.060	0.3548	0.051	0.95	± 7.6	161.0	± 7.6	16.17	9.40	0.85	± 0.82
9	0.0007	0.290	0.0189	59.126	0.0007	12.599	0.0430	0.074	0.2594	0.070	0.94	± 9.0	158.0	± 9.0	15.52	6.72	0.98	± 1.15
10	0.0007	0.240	0.0213	68.776	0.0006	13.720	0.0375	0.083	0.2461	0.074	0.91	± 11.9	153.5	± 11.9	13.85	5.86	0.76	± 1.04
12	0.0012	0.178	0.0441	27.951	0.0007	11.378	0.0428	0.075	0.3818	0.050	0.89	± 9.8	150.9	± 9.8	10.00	6.68	0.42	± 0.23
14	0.0013	0.181	0.0972	13.732	0.0007	11.656	0.0334	0.091	0.4140	0.044	0.97	± 13.7	163.5	± 13.7	7.81	5.21	0.15	± 0.04
16	0.0015	0.151	0.1562	9.149	0.0006	12.311	0.0273	0.110	0.4699	0.039	0.92	± 17.7	154.5	± 17.7	5.30	4.25	0.07	± 0.01
18	0.0014	0.164	0.1803	10.199	0.0006	12.845	0.0222	0.132	0.4364	0.042	1.09	± 26.1	183.3	± 26.1	5.49	3.45	0.05	± 0.01
20	0.0011	0.199	0.1430	9.740	0.0005	15.390	0.0170	0.172	0.3421	0.055	1.31	± 27.1	220.7	± 27.1	6.45	2.64	0.05	± 0.01
21	0.0007	0.229	0.1009	14.284	0.0003	24.055	0.0100	0.292	0.2242	0.096	1.13	± 44.6	190.2	± 44.6	4.96	1.54	0.04	± 0.01
22	0.0005	0.275	0.0431	31.210	0.0003	27.635	0.0066	0.437	0.1572	0.116	1.03	± 60.9	173.9	± 60.9	4.32	1.03	0.07	± 0.04
24	0.0005	0.245	0.0505	27.955	0.0003	28.072	0.0062	0.459	0.1423	0.128	1.17	± 66.6	198.3	± 66.6	5.07	0.96	0.05	± 0.03
26	0.0005	0.327	0.0441	26.242	0.0003	30.458	0.0053	0.543	0.1423	0.129	1.54	± 68.7	259.7	± 68.7	5.64	0.82	0.05	± 0.03
28	0.0004	0.340	0.0419	31.573	0.0002	39.845	0.0048	0.600	0.1178	0.154	1.90	± 81.6	320.6	± 81.6	7.69	0.75	0.05	± 0.03
30	0.0003	0.329	0.0281	38.372	0.0002	52.865	0.0037	0.773	0.0919	0.199	1.42	± 86.4	239.2	± 86.4	5.67	0.57	0.06	± 0.04

**VIC06: J = 0.00009600 ± 0.00000016 (1σ) MDF = 0.995053 ± 0.00040 (1σ)**

2	0.0275	0.161	0.0030	27.739	0.0072	0.412	0.0016	1.170	8.1386	0.012	19.26	± 20.81	3340.2	± 3606.1	0.39	0.22	0.23	± 0.13
---	--------	-------	--------	--------	--------	-------	--------	-------	--------	-------	-------	---------	--------	----------	------	------	------	--------

Step	36Ar [fA]	%1s	37Ar [fA]	%1s	38Ar [fA]	%1s	39Ar [fA]	%1s	40Ar [fA]	%1s	40(r)/39(k)	± 2s	Age (Ka)	± 2s	40Ar(r) (%)	39Ar(k) (%)	K/Ca	± 2s
3	0.0204	0.162	0.0084	13.437	0.0057	0.549	0.0058	0.339	6.0422	0.015	4.84	± 4.43	839.2	± 768.2	0.46	0.76	0.29	± 0.08
4	0.0151	0.166	0.0210	5.981	0.0045	0.777	0.0124	0.158	4.4600	0.019	1.59	± 1.54	275.4	± 268.0	0.44	1.64	0.25	± 0.03
6	0.0177	0.165	0.0698	4.113	0.0057	0.582	0.0417	0.067	5.2289	0.016	0.50	± 0.54	87.1	± 93.1	0.40	5.53	0.26	± 0.02
8	0.0131	0.163	0.0992	4.048	0.0049	0.726	0.0697	0.052	3.8855	0.021	0.55	± 0.24	95.4	± 41.1	0.98	9.24	0.30	± 0.02
9	0.0066	0.168	0.0671	4.237	0.0028	1.179	0.0549	0.055	1.9650	0.042	0.57	± 0.16	99.5	± 27.0	1.60	7.28	0.35	± 0.03
10	0.0046	0.170	0.0606	4.254	0.0023	1.745	0.0533	0.055	1.3900	0.059	0.68	± 0.12	117.3	± 20.0	2.59	7.07	0.38	± 0.03
12	0.0049	0.181	0.0827	4.114	0.0028	1.448	0.0775	0.046	1.4754	0.056	0.65	± 0.09	113.2	± 15.0	3.42	10.28	0.40	± 0.03
14	0.0046	0.171	0.0903	4.047	0.0028	1.220	0.0839	0.050	1.4089	0.059	0.65	± 0.07	112.9	± 12.8	3.87	11.13	0.40	± 0.03
16	0.0041	0.175	0.0897	4.057	0.0025	1.450	0.0728	0.049	1.2584	0.066	0.65	± 0.08	113.7	± 13.5	3.78	9.65	0.35	± 0.03
18	0.0036	0.182	0.0915	4.058	0.0020	1.936	0.0580	0.056	1.0963	0.075	0.66	± 0.09	113.7	± 15.4	3.46	7.69	0.27	± 0.02
20	0.0035	0.184	0.1101	4.074	0.0018	2.196	0.0504	0.053	1.0458	0.079	0.69	± 0.10	119.5	± 17.2	3.31	6.68	0.20	± 0.02
21	0.0025	0.196	0.0821	4.103	0.0012	2.781	0.0333	0.074	0.7416	0.111	0.62	± 0.12	107.4	± 20.2	2.78	4.42	0.17	± 0.01
22	0.0019	0.219	0.0708	4.145	0.0010	3.233	0.0258	0.088	0.5632	0.146	0.62	± 0.13	106.9	± 22.4	2.81	3.42	0.16	± 0.01
24	0.0019	0.197	0.0850	4.058	0.0009	3.351	0.0253	0.090	0.5694	0.145	0.69	± 0.13	120.2	± 21.9	3.07	3.35	0.13	± 0.01
26	0.0018	0.206	0.0928	4.059	0.0009	3.807	0.0231	0.097	0.5385	0.153	0.83	± 0.14	143.5	± 23.6	3.53	3.05	0.11	± 0.01
28	0.0015	0.249	0.0795	4.136	0.0007	4.732	0.0189	0.111	0.4370	0.189	0.77	± 0.16	134.0	± 27.4	3.33	2.50	0.10	± 0.01
30	0.0012	0.269	0.0747	4.178	0.0006	6.256	0.0159	0.138	0.3620	0.228	0.81	± 0.17	140.9	± 30.1	3.55	2.10	0.09	± 0.01
35	0.0014	0.265	0.0939	4.115	0.0007	5.593	0.0177	0.099	0.4057	0.203	0.71	± 0.17	123.2	± 29.1	3.09	2.34	0.08	± 0.01
40	0.0009	0.287	0.0671	4.140	0.0005	6.392	0.0123	0.187	0.2819	0.292	0.68	± 0.20	118.6	± 34.7	2.97	1.63	0.08	± 0.01

**VIC07: J = 0.00009160 ± 0.00000014 (1σ) MDF = 0.993390 ± 0.00020 (1σ)**

3	0.0123	0.085	0.0129	73.384	0.0024	1.583	0.0029	0.856	3.6146	0.013	1.79	± 2.76	296.0	± 456.4	0.14	0.42	0.10	± 0.14
4	0.0182	0.084	0.0279	37.560	0.0036	1.114	0.0106	0.234	5.3803	0.014	1.82	± 1.11	300.7	± 183.9	0.36	1.53	0.16	± 0.12
5	0.0199	0.087	0.0480	16.809	0.0041	0.890	0.0250	0.101	5.9305	0.010	3.44	± 0.52	570.2	± 86.5	1.45	3.60	0.22	± 0.08
6	0.0163	0.086	0.0552	18.819	0.0034	1.186	0.0352	0.071	4.9139	0.012	3.11	± 0.30	515.0	± 50.4	2.23	5.08	0.27	± 0.10
7	0.0122	0.091	0.0618	15.801	0.0027	1.516	0.0380	0.068	3.7292	0.009	3.61	± 0.22	597.5	± 36.5	3.67	5.48	0.26	± 0.08



Step	36Ar [fA]	%1s	37Ar [fA]	%1s	38Ar [fA]	%1s	39Ar [fA]	%1s	40Ar [fA]	%1s	40(t)/39(k)	±2s	Age (Ka)	±2s	40Ar(t) (%)	39Ar(k) (%)	K/Ca	±2s
8	0.0110	0.081	0.0669	19.050	0.0026	1.623	0.0419	0.064	3.3717	0.010	3.57	± 28.3	590.5	± 28.3	4.43	6.05	0.27	± 0.10
9	0.0075	0.090	0.0394	24.563	0.0020	1.893	0.0439	0.060	2.3550	0.014	3.57	± 19.8	591.3	± 19.8	6.66	6.34	0.48	± 0.24
10	0.0049	0.087	0.0522	17.525	0.0014	2.711	0.0421	0.063	1.5804	0.021	3.60	± 14.0	595.3	± 14.0	9.56	6.07	0.35	± 0.12
12	0.0069	0.090	0.0732	14.655	0.0021	1.870	0.0627	0.047	2.2506	0.015	3.51	± 13.1	580.8	± 13.1	9.76	9.05	0.37	± 0.11
14	0.0050	0.100	0.0710	15.906	0.0018	2.457	0.0656	0.048	1.6955	0.020	3.50	± 10.2	580.1	± 10.2	13.54	9.47	0.40	± 0.13
16	0.0037	0.110	0.0738	14.277	0.0015	2.892	0.0615	0.044	1.2891	0.026	3.48	± 9.0	576.7	± 9.0	16.59	8.87	0.36	± 0.10
18	0.0026	0.116	0.1036	11.963	0.0012	3.208	0.0520	0.053	0.9626	0.035	3.69	± 9.4	611.7	± 9.4	19.93	7.50	0.22	± 0.05
20	0.0029	0.125	0.0961	12.581	0.0012	3.090	0.0455	0.059	1.0176	0.033	3.49	± 11.7	578.8	± 11.7	15.60	6.56	0.20	± 0.05
21	0.0017	0.176	0.0853	16.254	0.0007	5.304	0.0321	0.083	0.6095	0.054	3.54	± 15.5	586.9	± 15.5	18.62	4.63	0.16	± 0.05
22	0.0013	0.147	0.0717	17.264	0.0005	6.739	0.0262	0.101	0.4726	0.069	3.51	± 15.4	581.9	± 15.4	19.42	3.77	0.16	± 0.05
24	0.0020	0.107	0.1027	12.209	0.0007	5.268	0.0295	0.086	0.6722	0.049	3.51	± 14.5	580.8	± 14.5	15.34	4.25	0.12	± 0.03
26	0.0015	0.125	0.1362	9.789	0.0006	6.411	0.0300	0.086	0.5265	0.063	3.50	± 14.1	579.5	± 14.1	19.86	4.32	0.09	± 0.02
28	0.0012	0.163	0.1109	10.702	0.0004	8.752	0.0258	0.097	0.4196	0.078	3.48	± 15.0	576.1	± 15.0	21.33	3.72	0.10	± 0.02
30	0.0011	0.185	0.1251	9.828	0.0005	7.685	0.0228	0.112	0.3916	0.084	3.52	± 17.8	583.0	± 17.8	20.37	3.27	0.08	± 0.02

<b>VIC08: J = 0.00009340 ± 0.00000014 (1σ) MDF = 0.993140 ± 0.00030 (1σ)</b>																			
3	0.0114	0.138	0.0396	27.099	0.0022	4.882	0.0182	0.495	3.4243	0.062	1.33	± 0.69	224.5	± 116.1	0.70	3.10	0.20	± 0.11	
4	0.0068	0.172	0.0663	20.882	0.0016	6.997	0.0428	0.213	2.1504	0.098	2.90	± 0.22	489.5	± 37.1	5.76	7.30	0.28	± 0.12	
5	0.0034	0.266	0.0704	17.395	0.0012	9.026	0.0562	0.164	1.2007	0.175	3.21	± 0.13	542.3	± 22.5	15.00	9.59	0.34	± 0.12	
6	0.0018	0.440	0.0615	19.964	0.0009	11.882	0.0578	0.159	0.7260	0.290	3.33	± 0.12	561.8	± 19.8	26.45	9.86	0.40	± 0.16	
7	0.0009	0.870	0.0463	26.346	0.0008	13.871	0.0497	0.185	0.4272	0.492	3.36	± 0.13	567.5	± 22.4	39.06	8.49	0.46	± 0.24	
8	0.0007	1.109	0.0476	26.747	0.0006	18.544	0.0441	0.206	0.3480	0.604	3.35	± 0.15	565.3	± 25.1	42.39	7.53	0.40	± 0.21	
9	0.0005	1.493	0.0173	68.722	0.0005	20.490	0.0381	0.241	0.2777	0.757	3.30	± 0.17	557.9	± 28.9	45.36	6.52	0.95	± 1.30	
10	0.0005	1.582	0.0312	37.946	0.0005	21.809	0.0340	0.268	0.2548	0.825	3.32	± 0.19	560.8	± 32.4	44.33	5.81	0.47	± 0.36	
12	0.0008	1.014	0.0672	22.738	0.0007	14.736	0.0432	0.211	0.3629	0.579	3.32	± 0.16	560.3	± 26.3	39.49	7.38	0.28	± 0.13	

Step	36Ar [fA]	%1s	37Ar [fA]	%1s	38Ar [fA]	%1s	39Ar [fA]	%1s	40Ar [fA]	%1s	40(r)/39(k)	±2s	Age (Ka)	±2s	40Ar(f) (%)	39Ar(k) (%)	K/Ca	±2s	
14	0.0007	1.037	0.1273	11.335	0.0007	16.044	0.0419	0.218	0.3513	0.599	3.37	±0.16	569.7	±27.0	40.14	7.14	0.14	±0.03	
16	0.0009	0.905	0.1491	10.717	0.0007	14.549	0.0403	0.226	0.3771	0.558	3.35	±0.17	566.3	±28.5	35.74	6.87	0.12	±0.02	
18	0.0011	0.707	0.1399	11.656	0.0006	16.957	0.0319	0.284	0.4271	0.492	3.42	±0.22	578.1	±36.4	25.53	5.44	0.10	±0.02	
20	0.0005	1.527	0.1170	12.679	0.0005	23.202	0.0228	0.397	0.2166	0.971	3.39	±0.29	572.7	±49.7	35.52	3.88	0.08	±0.02	
21	0.0010	0.770	0.0991	12.141	0.0005	22.647	0.0189	0.476	0.3602	0.584	3.39	±0.35	572.9	±59.6	17.73	3.22	0.08	±0.02	
22	0.0007	1.124	0.0920	12.547	0.0004	28.722	0.0143	0.630	0.2448	0.859	3.35	±0.46	565.3	±77.6	19.46	2.43	0.07	±0.02	
24	0.0003	2.531	0.0664	19.870	0.0003	41.729	0.0102	0.881	0.1179	1.784	3.35	±0.65	564.9	±109.1	28.82	1.74	0.07	±0.03	
26	0.0006	1.312	0.0699	17.566	0.0003	31.130	0.0090	0.996	0.1979	1.063	3.27	±0.73	552.8	±123.2	14.87	1.54	0.06	±0.02	
28	0.0003	2.624	0.0532	22.727	0.0002	57.337	0.0066	1.354	0.1053	2.013	3.52	±0.99	594.9	±167.2	22.08	1.13	0.05	±0.02	
30	0.0008	1.003	0.0482	27.333	0.0002	48.884	0.0062	1.452	0.2405	0.875	2.90	±1.07	489.7	±180.7	7.42	1.05	0.05	±0.03	
<b>VIC09: J = 0.00009740 ± 0.00000021 (1σ) MDF = 0.994930 ± 0.00040 (1σ)</b>																			
1	0.0002	2.160	0.0001	253.509	0.0001	95.104	0.0000	1016.6	0.0575	1.402	271.10	±5754.90	47124.7	±987447.2	1.24	0.00	0.01	±0.29	
2	0.0014	0.338	0.0011	22.338	0.0003	18.865	0.0007	3.921	0.4263	0.189	0.38	±4.83	67.0	±850.7	0.06	0.07	0.29	±0.13	
3	0.0015	0.353	0.0057	4.341	0.0005	11.972	0.0041	0.602	0.4287	0.188	0.98	±0.86	173.0	±151.9	0.95	0.39	0.31	±0.03	
4	0.0007	0.611	0.0108	3.359	0.0004	13.007	0.0097	0.265	0.2254	0.358	0.30	±0.33	52.5	±58.0	1.29	0.91	0.39	±0.03	
6	0.0021	0.263	0.0273	2.508	0.0011	5.277	0.0329	0.086	0.6434	0.125	0.41	±0.12	72.5	±21.0	2.10	3.09	0.52	±0.03	
8	0.0035	0.218	0.0278	2.464	0.0016	3.639	0.0461	0.069	1.0723	0.075	0.68	±0.11	119.0	±20.1	2.90	4.33	0.71	±0.04	
10	0.0025	0.252	0.0324	2.426	0.0015	1.941	0.0553	0.056	0.7812	0.132	0.70	±0.08	123.3	±14.5	4.95	5.19	0.73	±0.04	
13	0.0093	0.170	0.0608	2.377	0.0036	0.743	0.0786	0.050	2.8585	0.036	1.03	±0.14	181.2	±25.1	2.83	7.38	0.56	±0.03	
16	0.0126	0.166	0.1021	2.364	0.0048	0.529	0.0972	0.047	3.8653	0.027	1.29	±0.15	227.4	±26.6	3.25	9.13	0.41	±0.02	
20	0.0309	0.164	0.2308	2.359	0.0098	0.251	0.1767	0.042	9.3885	0.011	1.03	±0.20	180.7	±35.4	1.93	16.59	0.33	±0.02	
23	0.0301	0.163	0.2370	2.359	0.0099	0.248	0.1783	0.042	9.1285	0.012	0.93	±0.19	163.2	±34.0	1.81	16.74	0.32	±0.02	
26	0.0075	0.175	0.1588	2.360	0.0041	0.627	0.1193	0.043	2.3222	0.044	0.87	±0.08	154.0	±13.7	4.49	11.20	0.32	±0.02	
30	0.0057	0.184	0.1253	2.364	0.0032	0.897	0.0951	0.048	1.7883	0.058	0.86	±0.08	152.0	±13.9	4.58	8.93	0.33	±0.02	
33	0.0029	0.243	0.0902	2.366	0.0020	1.537	0.0674	0.049	0.9143	0.113	0.85	±0.07	150.3	±13.1	6.28	6.32	0.32	±0.02	

Step	$^{36}\text{Ar}$ [fA]	%1s	$^{37}\text{Ar}$ [fA]	%1s	$^{38}\text{Ar}$ [fA]	%1s	$^{39}\text{Ar}$ [fA]	%1s	$^{40}\text{Ar}$ [fA]	%1s	$^{40}(\text{r})/^{39}(\text{k})$	$\pm 2s$	Age (Ka)	$\pm 2s$	$^{40}\text{Ar}(\text{r})$ (%)	$^{39}\text{Ar}(\text{k})$ (%)	K/Ca	$\pm 2s$	
36	0.0020	0.308	0.0737	2.371	0.0015	1.815	0.0556	0.049	0.6297	0.163	0.91	$\pm 0.08$	160.6	$\pm 13.7$	8.05	5.22	0.32	$\pm 0.02$	
40	0.0017	0.333	0.0644	2.372	0.0013	1.773	0.0482	0.065	0.5526	0.186	1.02	$\pm 0.09$	180.0	$\pm 15.0$	8.90	4.52	0.32	$\pm 0.02$	
<b>VIC16: J = 0.00009680 <math>\pm</math> 0.00000014 (1<math>\sigma</math>) MDF = 0.994605 <math>\pm</math> 0.00040 (1<math>\sigma</math>)</b>																			
2	0.0058	0.173	0.0065	16.211	0.0017	2.604	0.0016	1.019	1.7133	0.054	1.45	$\pm 4.46$	254.2	$\pm 780.5$	0.14	0.25	0.11	$\pm 0.03$	
3	0.0141	0.164	0.0209	5.343	0.0042	0.895	0.0066	0.272	4.1733	0.022	0.23	$\pm 2.46$	40.2	$\pm 431.0$	0.04	1.02	0.14	$\pm 0.01$	
4	0.0167	0.162	0.0508	4.228	0.0052	0.778	0.0223	0.106	4.9610	0.019	0.29	$\pm 0.86$	51.3	$\pm 149.9$	0.13	3.45	0.19	$\pm 0.02$	
6	0.0226	0.163	0.1348	3.987	0.0073	0.500	0.0812	0.051	6.7148	0.014	0.22	$\pm 0.32$	38.6	$\pm 55.6$	0.27	12.58	0.26	$\pm 0.02$	
8	0.0097	0.164	0.1263	3.984	0.0045	0.821	0.0979	0.044	2.8935	0.032	0.31	$\pm 0.11$	53.7	$\pm 20.1$	1.04	15.18	0.33	$\pm 0.03$	
9	0.0023	0.202	0.0662	4.201	0.0018	2.035	0.0591	0.056	0.6977	0.132	0.25	$\pm 0.06$	43.3	$\pm 10.8$	2.09	9.17	0.38	$\pm 0.03$	
10	0.0015	0.195	0.0510	4.315	0.0013	3.011	0.0494	0.055	0.4480	0.206	0.25	$\pm 0.05$	43.8	$\pm 9.5$	2.76	7.66	0.42	$\pm 0.04$	
12	0.0018	0.199	0.0698	4.118	0.0015	2.719	0.0619	0.055	0.5458	0.169	0.23	$\pm 0.05$	39.9	$\pm 8.7$	2.58	9.59	0.38	$\pm 0.03$	
14	0.0018	0.198	0.0767	4.047	0.0016	2.690	0.0579	0.054	0.5474	0.169	0.24	$\pm 0.05$	41.5	$\pm 9.3$	2.51	8.98	0.32	$\pm 0.03$	
16	0.0016	0.196	0.0921	4.089	0.0013	3.074	0.0473	0.070	0.4829	0.191	0.28	$\pm 0.06$	49.8	$\pm 10.6$	2.79	7.33	0.22	$\pm 0.02$	
18	0.0012	0.228	0.0937	4.043	0.0011	3.120	0.0369	0.070	0.3731	0.247	0.36	$\pm 0.07$	63.2	$\pm 12.7$	3.56	5.71	0.17	$\pm 0.01$	
20	0.0009	0.255	0.1002	4.040	0.0008	4.675	0.0265	0.100	0.2796	0.330	1.32	$\pm 0.09$	230.5	$\pm 15.9$	12.45	4.10	0.11	$\pm 0.01$	
21	0.0006	0.316	0.0825	4.109	0.0005	6.713	0.0187	0.123	0.1811	0.509	0.27	$\pm 0.12$	47.3	$\pm 21.3$	2.79	2.90	0.10	$\pm 0.01$	
22	0.0005	0.388	0.0708	4.144	0.0005	9.194	0.0142	0.140	0.1320	0.698	0.29	$\pm 0.15$	51.0	$\pm 27.0$	3.12	2.19	0.09	$\pm 0.01$	
24	0.0004	0.355	0.0840	4.091	0.0005	7.409	0.0130	0.136	0.1249	0.738	0.32	$\pm 0.17$	55.9	$\pm 29.1$	3.30	2.00	0.07	$\pm 0.01$	
26	0.0004	0.370	0.0903	4.043	0.0005	7.746	0.0119	0.192	0.1126	0.819	0.29	$\pm 0.18$	50.2	$\pm 31.6$	3.01	1.83	0.06	$\pm 0.00$	
28	0.0004	4.375	0.0813	5.639	0.0002	14.625	0.0104	3.251	0.1114	0.623	0.82	$\pm 0.94$	144.0	$\pm 164.6$	7.64	1.60	0.05	$\pm 0.01$	
30	0.0003	5.353	0.0821	5.631	0.0000	761.11	0.0090	3.736	0.0966	0.720	1.52	$\pm 1.09$	266.8	$\pm 190.1$	14.18	1.39	0.05	$\pm 0.01$	
35	0.0004	4.230	0.1004	5.123	0.0000	3428.35	0.0104	3.258	0.1175	0.594	1.19	$\pm 0.95$	208.6	$\pm 165.7$	10.45	1.60	0.04	$\pm 0.01$	
40	0.0004	4.366	0.0947	5.271	0.0001	69.218	0.0095	3.569	0.1131	0.633	1.10	$\pm 1.03$	191.8	$\pm 181.1$	9.18	1.47	0.04	$\pm 0.01$	

Step	36Ar [fA]	%1s	37Ar [fA]	%1s	38Ar [fA]	%1s	39Ar [fA]	%1s	40Ar [fA]	%1s	40(r)/39(k)	± 2s	Age (Ka)	± 2s	40Ar(r) (%)	39Ar(k) (%)	K/Ca	± 2s	
<b>VIC17A: J = 0.00009700 ± 0.00000015 (1σ) MDF = 0.994370 ± 0.00030 (1σ)</b>																			
3	0.0231	0.125	0.0415	2.511	0.0058	0.787	0.0103	1.561	6.8665	0.011	1.72	± 2.16	300.9	± 378.6	0.26	1.64	0.11	± 0.01	
6	0.0173	0.124	0.1780	2.372	0.0056	0.765	0.0851	0.191	5.1305	0.016	0.22	± 0.19	38.7	± 34.0	0.37	13.57	0.21	± 0.01	
9	0.0053	0.135	0.1371	2.377	0.0028	1.624	0.0945	0.172	1.5822	0.046	0.23	± 0.06	40.5	± 10.3	1.38	15.06	0.30	± 0.01	
12	0.0023	0.212	0.0966	2.391	0.0017	2.639	0.0746	0.217	0.7036	0.104	0.26	± 0.05	46.2	± 8.4	2.79	11.90	0.33	± 0.02	
14	0.0011	0.285	0.0739	2.410	0.0010	4.203	0.0474	0.340	0.3309	0.221	0.26	± 0.05	46.4	± 9.1	3.78	7.56	0.28	± 0.01	
16	0.0010	0.320	0.0986	2.394	0.0010	4.629	0.0494	0.326	0.3088	0.236	0.30	± 0.05	53.0	± 9.0	4.83	7.88	0.22	± 0.01	
18	0.0008	0.413	0.1104	2.389	0.0009	4.863	0.0445	0.361	0.2344	0.311	0.40	± 0.06	69.8	± 9.7	7.54	7.08	0.17	± 0.01	
20	0.0008	0.348	0.1419	2.378	0.0010	4.583	0.0488	0.330	0.2503	0.292	0.24	± 0.05	42.7	± 8.6	4.73	7.76	0.15	± 0.01	
21	0.0005	0.608	0.1010	2.399	0.0006	7.243	0.0314	0.512	0.1377	0.530	0.28	± 0.07	49.6	± 12.7	6.44	5.00	0.13	± 0.01	
22	0.0004	0.748	0.0856	2.405	0.0005	8.810	0.0259	0.618	0.1174	0.622	0.28	± 0.09	48.6	± 15.7	6.11	4.13	0.13	± 0.01	
24	0.0005	0.598	0.1005	2.393	0.0006	7.785	0.0282	0.569	0.1401	0.521	0.36	± 0.08	63.2	± 14.1	7.23	4.49	0.12	± 0.01	
26	0.0004	0.633	0.1003	2.391	0.0005	8.167	0.0253	0.635	0.1280	0.570	0.26	± 0.09	45.4	± 15.6	5.11	4.03	0.11	± 0.01	
28	0.0003	0.866	0.0883	2.404	0.0004	10.807	0.0204	0.786	0.0918	0.796	0.25	± 0.11	43.5	± 19.1	5.50	3.25	0.10	± 0.01	
35	0.0004	0.740	0.1114	2.391	0.0005	9.684	0.0232	0.692	0.1229	0.596	0.59	± 0.10	102.6	± 17.8	10.99	3.69	0.09	± 0.00	
40	0.0003	0.933	0.1000	2.393	0.0004	11.622	0.0187	0.860	0.0857	0.856	0.31	± 0.12	55.1	± 21.1	6.84	2.97	0.08	± 0.00	
<b>VIC17B: J = 0.00009700 ± 0.00000015 (1σ) MDF = 0.994370 ± 0.00040 (1σ)</b>																			
3	0.0244	0.162	0.0466	2.485	0.0061	0.487	0.0124	1.174	7.2417	0.012	0.68	± 2.59	119.4	± 454.9	0.12	2.14	0.11	± 0.01	
6	0.0143	0.165	0.1759	2.378	0.0049	0.631	0.0878	0.171	4.2421	0.021	0.19	± 0.22	33.6	± 38.0	0.40	15.14	0.21	± 0.01	
9	0.0036	0.182	0.1136	2.389	0.0022	0.989	0.0838	0.178	1.0740	0.079	0.26	± 0.06	45.9	± 11.1	2.04	14.46	0.32	± 0.02	
12	0.0021	0.230	0.0879	2.402	0.0015	1.896	0.0650	0.226	0.6263	0.134	0.37	± 0.06	64.7	± 10.1	3.82	11.22	0.32	± 0.02	
14	0.0011	0.284	0.0750	2.412	0.0009	3.812	0.0433	0.337	0.3316	0.254	0.23	± 0.06	40.2	± 11.0	2.99	7.48	0.25	± 0.01	
16	0.0011	0.307	0.1075	2.393	0.0010	2.209	0.0481	0.305	0.3425	0.246	0.26	± 0.06	46.3	± 10.5	3.70	8.29	0.19	± 0.01	
18	0.0009	0.345	0.1287	2.387	0.0009	2.687	0.0460	0.318	0.2611	0.322	0.25	± 0.06	44.7	± 10.0	4.48	7.94	0.15	± 0.01	

Step	<sup>36</sup> Ar [fA]	%1s	<sup>37</sup> Ar [fA]	%1s	<sup>38</sup> Ar [fA]	%1s	<sup>39</sup> Ar [fA]	%1s	<sup>40</sup> Ar [fA]	%1s	40Ar/ <sup>39</sup> Ar (k)	± 2s	Age (Ka)	± 2s	40Ar(r) (%)	<sup>39</sup> Ar(k) (%)	K/Ca	± 2s
20	0.0007	0.381	0.1274	2.387	0.0008	3.197	0.0402	0.365	0.2184	0.385	0.29	± 10.9	51.4	± 0.06	5.38	6.92	0.14	± 0.01
21	0.0004	0.635	0.0827	2.411	0.0005	4.848	0.0243	0.598	0.1162	0.724	0.22	± 16.6	39.2	± 0.09	4.67	4.19	0.13	± 0.01
22	0.0004	0.737	0.0762	2.412	0.0004	5.636	0.0217	0.669	0.1052	0.799	0.27	± 18.9	47.2	± 0.11	5.54	3.75	0.12	± 0.01
24	0.0004	0.629	0.0854	2.406	0.0004	6.540	0.0225	0.645	0.1223	0.688	0.26	± 18.3	45.2	± 0.10	4.74	3.88	0.11	± 0.01
26	0.0004	0.717	0.0877	2.401	0.0004	5.799	0.0213	0.689	0.1096	0.767	0.26	± 19.6	46.4	± 0.11	5.12	3.67	0.10	± 0.01
28	0.0002	0.997	0.0686	2.424	0.0003	8.836	0.0155	0.941	0.0704	1.194	0.22	± 25.5	39.0	± 0.15	4.88	2.67	0.10	± 0.01
30	0.0003	0.878	0.0663	2.427	0.0003	5.799	0.0155	0.938	0.0828	1.017	0.27	± 25.7	47.1	± 0.15	5.02	2.67	0.10	± 0.01
35	0.0003	1.024	0.0809	2.414	0.0004	6.126	0.0169	0.863	0.0753	1.119	0.27	± 24.5	47.7	± 0.14	6.07	2.90	0.09	± 0.00
40	0.0002	1.039	0.0772	2.417	0.0003	9.418	0.0156	0.931	0.0674	1.257	0.28	± 25.4	48.6	± 0.15	6.39	2.69	0.09	± 0.00

**VIC18A: J = 0.00009710 ± 0.00000017 (1σ) MDF = 0.994573 ± 0.00020 (1σ)**

2	0.0159	0.086	0.0028	30.881	0.0043	1.628	0.0012	2.131	4.6968	0.040	7.05	± 1487.5	1238.4	± 8.47	0.18	0.15	0.19	± 0.12
3	0.0337	0.082	0.0097	8.091	0.0087	0.801	0.0050	0.518	9.9758	0.019	1.19	± 683.5	209.2	± 3.89	0.06	0.61	0.22	± 0.04
4	0.0292	0.083	0.0253	5.003	0.0078	0.875	0.0145	0.177	8.6693	0.022	0.76	± 208.6	134.2	± 1.19	0.13	1.77	0.25	± 0.02
6	0.0299	0.083	0.0978	4.048	0.0087	0.814	0.0672	0.044	8.8734	0.021	0.24	± 46.0	41.6	± 0.26	0.18	8.19	0.30	± 0.02
8	0.0130	0.087	0.1168	3.998	0.0053	1.130	0.1069	0.026	3.8666	0.005	0.18	± 12.8	31.0	± 0.07	0.49	13.04	0.39	± 0.03
9	0.0043	0.125	0.0756	4.109	0.0026	2.149	0.0788	0.034	1.2710	0.008	0.21	± 7.7	36.6	± 0.04	1.29	9.61	0.45	± 0.04
10	0.0029	0.148	0.0676	4.150	0.0020	2.718	0.0718	0.035	0.8655	0.011	0.21	± 6.7	37.4	± 0.04	1.77	8.75	0.46	± 0.04
12	0.0042	0.107	0.1120	4.007	0.0032	1.790	0.1134	0.027	1.2553	0.008	0.23	± 4.7	40.0	± 0.03	2.06	13.84	0.43	± 0.03
14	0.0032	0.127	0.1144	4.034	0.0027	2.001	0.1074	0.026	0.9646	0.009	0.24	± 4.4	41.4	± 0.03	2.63	13.10	0.40	± 0.03
16	0.0026	0.116	0.0945	4.023	0.0021	2.658	0.0785	0.036	0.7686	0.011	0.24	± 4.5	42.0	± 0.03	2.44	9.57	0.36	± 0.03
18	0.0022	0.125	0.0814	4.057	0.0014	3.979	0.0325	0.041	0.6483	0.013	0.25	± 6.1	44.5	± 0.03	2.05	6.40	0.28	± 0.02
20	0.0019	0.166	0.0715	4.072	0.0011	5.701	0.0359	0.049	0.5582	0.018	0.23	± 9.8	39.5	± 0.06	1.44	4.37	0.22	± 0.02
21	0.0012	0.155	0.0493	4.293	0.0007	8.857	0.0202	0.094	0.3463	0.024	0.20	± 10.4	35.1	± 0.06	1.16	2.46	0.18	± 0.02
22	0.0008	0.211	0.0376	4.503	0.0005	12.492	0.0125	0.134	0.2349	0.035	0.27	± 15.1	47.0	± 0.09	1.42	1.52	0.14	± 0.01

Step	36Ar [fA]	%1s	37Ar [fA]	%1s	38Ar [fA]	%1s	39Ar [fA]	%1s	40Ar [fA]	%1s	40(r)/39(k)	Age (Ka)	± 2s	40Ar(r) (%)	39Ar(k) (%)	K/Ca	± 2s
24	0.0010	0.198	0.0451	4.398	0.0005	11.911	0.0120	0.162	0.2954	0.028	0.33	57.3	± 18.5	1.32	1.46	0.11	± 0.01
26	0.0010	0.184	0.0434	4.555	0.0005	11.954	0.0106	0.163	0.2937	0.028	0.28	48.5	± 19.6	0.99	1.29	0.10	± 0.01
28	0.0008	0.226	0.0388	4.549	0.0004	15.400	0.0097	0.221	0.2493	0.033	0.34	60.1	± 21.7	1.33	1.18	0.11	± 0.01
30	0.0007	0.195	0.0348	4.643	0.0002	25.316	0.0078	0.237	0.1990	0.040	0.33	58.6	± 19.3	1.31	0.95	0.10	± 0.01
35	0.0007	0.279	0.0396	4.506	0.0002	25.175	0.0074	0.204	0.2140	0.038	0.27	46.7	± 30.0	0.92	0.90	0.08	± 0.01
40	0.0005	0.297	0.0337	4.753	0.0002	27.622	0.0070	0.253	0.1475	0.056	0.24	41.6	± 23.9	1.12	0.85	0.09	± 0.01
<b>VIC18B: J = 0.00009710 ± 0.00000017 (1σ) MDF = 0.993598 ± 0.00030 (1σ)</b>																	
2	0.0206	0.124	0.0032	39.665	0.0064	0.464	0.0012	1.233	6.0879	0.019	7.77	1364.9	± 2471.9	0.16	0.17	0.17	± 0.13
3	0.0371	0.122	0.0093	11.159	0.0104	0.325	0.0051	0.286	10.9727	0.011	1.73	303.2	± 1049.3	0.08	0.69	0.24	± 0.05
4	0.0296	0.122	0.0261	5.561	0.0088	0.382	0.0150	0.150	8.7608	0.013	0.65	114.0	± 286.3	0.11	2.03	0.25	± 0.03
6	0.0314	0.124	0.0872	4.153	0.0099	0.313	0.0633	0.052	9.2900	0.012	0.28	48.7	± 72.9	0.19	8.53	0.31	± 0.03
8	0.0131	0.124	0.0987	4.238	0.0059	0.680	0.0947	0.041	3.8723	0.030	0.16	27.6	± 20.8	0.38	12.76	0.41	± 0.03
9	0.0049	0.150	0.0625	4.378	0.0029	1.056	0.0665	0.043	1.4644	0.078	0.18	31.2	± 14.1	0.80	8.96	0.46	± 0.04
10	0.0038	0.156	0.0578	4.376	0.0026	1.424	0.0633	0.050	1.1419	0.100	0.24	41.3	± 12.5	1.30	8.54	0.47	± 0.04
12	0.0048	0.144	0.0893	4.287	0.0033	1.123	0.0933	0.035	1.4489	0.079	0.24	41.4	± 9.7	1.52	12.58	0.45	± 0.04
14	0.0040	0.144	0.0937	4.209	0.0030	0.948	0.0875	0.045	1.2003	0.096	0.23	39.6	± 9.0	1.64	11.80	0.40	± 0.03
16	0.0029	0.166	0.0843	4.172	0.0025	1.480	0.0680	0.041	0.8781	0.131	0.26	46.0	± 10.1	2.03	9.16	0.35	± 0.03
18	0.0023	0.180	0.0694	4.217	0.0020	1.559	0.0470	0.046	0.6934	0.165	0.29	50.5	± 13.2	1.95	6.33	0.29	± 0.02
20	0.0020	0.200	0.0587	4.334	0.0015	2.159	0.0317	0.065	0.5804	0.198	0.24	42.7	± 18.7	1.33	4.27	0.23	± 0.02
21	0.0013	0.249	0.0437	4.607	0.0009	3.442	0.0189	0.100	0.3792	0.302	0.29	50.9	± 28.2	1.44	2.54	0.19	± 0.02
22	0.0010	0.323	0.0377	4.678	0.0008	4.839	0.0149	0.143	0.3109	0.369	0.25	43.4	± 36.5	1.18	2.00	0.17	± 0.02
24	0.0011	0.278	0.0444	4.527	0.0008	4.586	0.0156	0.105	0.3253	0.353	0.25	44.0	± 33.6	1.20	2.10	0.15	± 0.01
26	0.0012	0.271	0.0443	4.469	0.0009	4.153	0.0147	0.161	0.3574	0.321	0.31	54.3	± 36.7	1.27	1.97	0.14	± 0.01
28	0.0010	0.299	0.0389	4.926	0.0006	6.676	0.0119	0.146	0.2891	0.397	0.08	14.0	± 43.2	0.33	1.60	0.13	± 0.01

Step	<sup>36</sup> Ar [fA]	%1s	<sup>37</sup> Ar [fA]	%1s	<sup>38</sup> Ar [fA]	%1s	<sup>39</sup> Ar [fA]	%1s	<sup>40</sup> Ar [fA]	%1s	<sup>40</sup> (r)/ <sup>39</sup> (k)	Age (Ka)	± 2s	<sup>40</sup> Ar(r) (%)	<sup>39</sup> Ar(k) (%)	K/Ca	± 2s	
30	0.0009	0.333	0.0387	4.589	0.0006	6.658	0.0113	0.281	0.2523	0.454	0.27	47.8	± 44.9	1.22	1.52	0.13	± 0.01	
35	0.0009	0.321	0.0444	4.722	0.0006	6.299	0.0105	0.147	0.2677	0.428	0.22	37.8	± 48.9	0.84	1.41	0.10	± 0.01	
40	0.0006	0.451	0.0312	5.278	0.0003	14.137	0.0078	0.178	0.1757	0.652	0.35	61.7	± 63.4	1.56	1.05	0.11	± 0.01	
<b>VIC19: J = 0.00009330 ± 0.00000021 (1σ) MDF = 0.993135 ± 0.00030 (1σ)</b>																		
3	0.0195	0.121	0.0034	344.794	0.0036	4.222	0.0059	0.322	5.7440	0.004	3.20	539.0	± 521.7	0.33	1.15	0.74	± 5.08	
4	0.0275	0.121	0.0482	22.977	0.0054	2.859	0.0216	0.090	8.1127	0.003	1.00	168.7	± 200.5	0.27	4.22	0.19	± 0.09	
5	0.0197	0.121	0.0656	20.759	0.0041	3.763	0.0350	0.063	5.8063	0.003	0.51	86.0	± 89.2	0.31	6.84	0.23	± 0.10	
6	0.0126	0.124	0.0772	17.491	0.0028	5.478	0.0475	0.054	3.7163	0.004	0.38	64.5	± 42.9	0.49	9.29	0.26	± 0.09	
7	0.0073	0.127	0.0584	21.623	0.0018	8.685	0.0474	0.054	2.1520	0.005	0.40	67.1	± 25.8	0.87	9.26	0.35	± 0.15	
8	0.0066	0.137	0.0481	28.859	0.0018	8.508	0.0474	0.051	1.9623	0.005	0.33	55.8	± 24.9	0.80	9.27	0.42	± 0.24	
9	0.0050	0.144	0.0381	29.761	0.0013	13.155	0.0385	0.059	1.4834	0.017	0.42	71.7	± 24.2	1.10	7.52	0.43	± 0.26	
10	0.0040	0.139	0.0381	31.972	0.0010	17.219	0.0315	0.071	1.1680	0.022	0.25	41.7	± 24.1	0.67	6.15	0.35	± 0.23	
12	0.0063	0.134	0.0538	20.838	0.0016	11.286	0.0382	0.058	1.8666	0.014	0.43	73.2	± 28.7	0.89	7.47	0.31	± 0.13	
14	0.0048	0.135	0.0555	29.895	0.0013	8.267	0.0311	0.083	1.4243	0.020	0.55	92.3	± 29.8	1.19	6.07	0.24	± 0.14	
16	0.0038	0.129	0.0619	20.941	0.0011	10.237	0.0268	0.091	1.1155	0.025	0.50	85.0	± 26.5	1.21	5.24	0.19	± 0.08	
18	0.0045	0.127	0.0709	17.628	0.0012	9.531	0.0294	0.091	1.3388	0.021	0.46	78.3	± 27.6	1.02	5.74	0.18	± 0.06	
20	0.0018	0.171	0.0855	13.474	0.0006	25.548	0.0244	0.098	0.5248	0.017	0.43	72.5	± 19.2	2.00	4.76	0.12	± 0.03	
21	0.0012	0.155	0.0692	16.640	0.0005	31.840	0.0190	0.120	0.3707	0.021	0.54	91.1	± 20.3	2.77	3.71	0.12	± 0.04	
22	0.0010	0.168	0.0698	17.525	0.0003	42.613	0.0169	0.128	0.3092	0.025	0.47	79.8	± 22.9	2.58	3.30	0.10	± 0.04	
24	0.0011	0.143	0.0532	26.082	0.0003	32.978	0.0146	0.159	0.3150	0.030	0.54	91.5	± 28.5	2.51	2.85	0.12	± 0.06	
26	0.0009	0.207	0.0493	23.775	0.0003	34.141	0.0135	0.166	0.2772	0.034	0.51	86.7	± 28.3	2.50	2.64	0.12	± 0.06	
28	0.0008	0.208	0.0394	31.127	0.0003	42.218	0.0116	0.188	0.2321	0.042	0.39	65.5	± 32.5	1.93	2.26	0.13	± 0.08	
30	0.0009	0.239	0.0497	29.933	0.0002	49.223	0.0115	0.192	0.2588	0.036	0.60	100.6	± 40.0	2.64	2.24	0.10	± 0.06	

Step	<sup>36</sup> Ar [fA]	%1s	<sup>37</sup> Ar [fA]	%1s	<sup>38</sup> Ar [fA]	%1s	<sup>39</sup> Ar [fA]	%1s	<sup>40</sup> Ar [fA]	%1s	<sup>40</sup> (t)/ <sup>39</sup> (k)	± 2s	Age (Ka)	± 2s	<sup>40</sup> Ar(t) (%)	<sup>39</sup> Ar(k) (%)	K/Ca	± 2s	
<b>VIC20: J = 0.00009330 ± 0.00000009 (1σ) MDF = 0.992816 ± 0.00030 (1σ)</b>																			
3	0.0256	0.122	0.0264	39.984	0.0049	0.828	0.0091	0.472	7.5473	0.014	0.83	± 2.34	140.2	± 395.3	0.10	1.01	0.15	± 0.12	
4	0.0282	0.122	0.0567	20.379	0.0057	0.610	0.0318	0.137	8.3032	0.012	0.21	± 0.73	35.9	± 123.4	0.08	3.56	0.24	± 0.10	
5	0.0227	0.121	0.0767	14.594	0.0049	0.935	0.0499	0.092	6.6834	0.016	0.19	± 0.38	31.4	± 63.4	0.14	5.58	0.28	± 0.08	
6	0.0178	0.132	0.0665	14.234	0.0041	0.898	0.0622	0.076	5.2591	0.020	0.27	± 0.25	45.6	± 42.8	0.32	6.96	0.40	± 0.11	
7	0.0138	0.129	0.0813	12.439	0.0035	0.946	0.0717	0.079	4.0887	0.019	0.24	± 0.17	40.3	± 28.5	0.42	8.02	0.38	± 0.09	
8	0.0088	0.128	0.0704	13.181	0.0025	1.178	0.0686	0.081	2.6199	0.030	0.32	± 0.11	53.8	± 19.2	0.84	7.67	0.42	± 0.11	
9	0.0069	0.133	0.0692	15.723	0.0021	1.519	0.0676	0.082	2.0494	0.038	0.30	± 0.10	50.9	± 16.2	1.00	7.56	0.42	± 0.13	
10	0.0054	0.134	0.0710	16.037	0.0018	2.052	0.0634	0.087	1.5916	0.049	0.33	± 0.08	55.4	± 14.1	1.31	7.08	0.38	± 0.12	
12	0.0070	0.132	0.0838	16.232	0.0024	0.828	0.0851	0.068	2.0725	0.043	0.27	± 0.08	45.3	± 13.3	1.10	9.51	0.44	± 0.14	
14	0.0050	0.138	0.0903	15.809	0.0019	1.056	0.0816	0.068	1.4849	0.060	0.27	± 0.07	45.6	± 11.1	1.49	9.12	0.39	± 0.12	
16	0.0033	0.148	0.0962	14.210	0.0014	1.913	0.0672	0.080	0.9880	0.090	0.29	± 0.06	49.5	± 10.6	2.00	7.51	0.30	± 0.09	
18	0.0030	0.151	0.0874	14.571	0.0013	1.990	0.0575	0.093	0.8759	0.101	0.23	± 0.07	39.6	± 11.6	1.54	6.43	0.28	± 0.08	
20	0.0012	0.181	0.0989	17.257	0.0007	6.971	0.0435	0.065	0.3447	0.050	0.31	± 0.07	52.2	± 11.8	3.91	4.86	0.19	± 0.07	
21	0.0008	0.220	0.0688	22.639	0.0005	10.207	0.0293	0.088	0.2471	0.070	0.30	± 0.09	51.4	± 15.8	3.61	3.27	0.18	± 0.08	
22	0.0010	0.250	0.0672	21.098	0.0005	11.541	0.0245	0.103	0.2824	0.062	0.24	± 0.11	40.6	± 18.6	2.09	2.74	0.16	± 0.07	
24	0.0011	0.207	0.0858	18.115	0.0004	11.024	0.0211	0.116	0.3248	0.053	0.34	± 0.14	57.1	± 23.0	2.19	2.35	0.11	± 0.04	
26	0.0020	0.162	0.0968	16.846	0.0006	7.806	0.0232	0.107	0.5862	0.030	0.32	± 0.14	54.7	± 24.2	1.28	2.59	0.10	± 0.03	
28	0.0018	0.185	0.0930	16.165	0.0006	7.755	0.0198	0.123	0.5156	0.033	0.24	± 0.16	41.3	± 27.0	0.94	2.21	0.09	± 0.03	
30	0.0012	0.206	0.0871	16.541	0.0005	9.924	0.0179	0.145	0.3675	0.047	0.39	± 0.16	66.6	± 26.6	1.92	2.00	0.09	± 0.03	
<b>VIC21: J = 0.00009720 ± 0.00000036 (1σ) MDF = 0.996254 ± 0.00020 (1σ)</b>																			
2	0.0112	0.094	0.0057	3.914	0.0028	1.435	0.0050	0.349	3.3260	0.011	3.54	± 1.85	621.8	± 325.6	0.53	0.85	0.37	± 0.03	
3	0.0120	0.088	0.0228	2.568	0.0032	1.142	0.0153	0.108	3.5557	0.010	0.84	± 0.63	147.9	± 110.0	0.36	2.60	0.29	± 0.01	
4	0.0078	0.091	0.0471	2.437	0.0024	1.893	0.0289	0.089	2.3246	0.015	0.37	± 0.22	65.2	± 38.8	0.46	4.91	0.26	± 0.01	



Step	36Ar [fA]	%1s	37Ar [fA]	%1s	38Ar [fA]	%1s	39Ar [fA]	%1s	40Ar [fA]	%1s	40(r)/ 39(k)	± 2s	Age (Ka)	± 2s	40Ar(r) (%)	39Ar(k) (%)	K/Ca	± 2s	
6	0.0085	0.098	0.0999	2.411	0.0032	1.203	0.0676	0.038	2.5042	0.014	0.23	± 18.5	39.6	± 0.11	0.61	11.50	0.29	± 0.01	
8	0.0078	0.092	0.0969	2.412	0.0034	1.090	0.0901	0.030	2.3132	0.015	0.02	± 12.4	3.2	± 0.07	0.07	15.33	0.40	± 0.02	
9	0.0046	0.110	0.0532	2.436	0.0021	1.758	0.0565	0.051	1.3729	0.025	0.20	± 12.8	35.9	± 0.07	0.84	9.61	0.46	± 0.02	
10	0.0029	0.122	0.0393	2.494	0.0014	2.612	0.0400	0.045	0.8780	0.039	0.18	± 12.5	32.4	± 0.07	0.84	6.81	0.44	± 0.02	
12	0.0037	0.120	0.0611	2.426	0.0018	2.130	0.0537	0.039	1.1125	0.031	0.23	± 11.5	40.1	± 0.07	1.10	9.14	0.38	± 0.02	
14	0.0033	0.114	0.0883	2.413	0.0017	2.206	0.0501	0.045	0.9773	0.036	0.23	± 10.7	40.1	± 0.06	1.17	8.51	0.24	± 0.01	
16	0.0027	0.128	0.1194	2.411	0.0014	2.732	0.0410	0.049	0.8046	0.043	0.32	± 11.7	55.4	± 0.07	1.60	6.96	0.15	± 0.01	
18	0.0021	0.134	0.1330	2.410	0.0011	2.637	0.0312	0.117	0.6397	0.048	0.52	± 12.8	91.4	± 0.07	2.53	5.30	0.10	± 0.00	
20	0.0020	0.116	0.1330	2.408	0.0010	3.020	0.0246	0.151	0.5848	0.052	0.22	± 14.2	39.3	± 0.08	0.94	4.17	0.08	± 0.00	
21	0.0011	0.190	0.0820	2.417	0.0005	4.782	0.0137	0.256	0.3251	0.094	0.31	± 20.1	55.0	± 0.11	1.32	2.33	0.07	± 0.00	
22	0.0008	0.273	0.0676	2.421	0.0005	4.982	0.0116	0.308	0.2526	0.121	0.38	± 24.6	65.9	± 0.14	1.71	1.97	0.07	± 0.00	
24	0.0009	0.184	0.0895	2.416	0.0005	6.241	0.0132	0.274	0.2782	0.110	0.46	± 18.2	80.5	± 0.10	2.17	2.24	0.06	± 0.00	
26	0.0008	0.170	0.0832	2.415	0.0004	7.726	0.0117	0.329	0.2465	0.124	0.25	± 18.2	43.5	± 0.10	1.17	1.98	0.06	± 0.00	
28	0.0005	0.210	0.0569	2.434	0.0003	10.298	0.0070	0.492	0.1500	0.204	0.27	± 24.4	47.6	± 0.14	1.25	1.18	0.05	± 0.00	
30	0.0006	0.194	0.0534	2.426	0.0003	11.928	0.0071	0.489	0.1745	0.175	0.28	± 24.9	48.4	± 0.14	1.12	1.21	0.06	± 0.00	
35	0.0007	0.116	0.0889	2.417	0.0004	7.232	0.0103	0.379	0.2113	0.145	0.35	± 16.6	61.6	± 0.09	1.69	1.74	0.05	± 0.00	
40	0.0008	0.159	0.0739	2.426	0.0003	8.366	0.0099	0.354	0.2257	0.136	0.52	± 19.3	91.2	± 0.11	2.27	1.68	0.06	± 0.00	
<b>VIC22A: J = 0.00009320 ± 0.00000032 (1σ) MDF = 0.993931 ± 0.00040 (1σ)</b>																			
3	0.0042	1.664	0.0045	22.816	0.0004	13.308	0.0024	0.582	1.2333	1.651	3.00	± 4070.9	506.2	± 24.16	0.58	0.49	0.23	± 0.10	
4	0.0051	1.369	0.0127	8.938	0.0006	9.500	0.0069	0.278	1.4917	1.365	0.33	± 1416.7	55.0	± 8.41	0.15	1.42	0.23	± 0.04	
5	0.0104	0.681	0.0187	6.324	0.0016	3.407	0.0119	0.143	3.0681	0.664	0.19	± 840.7	31.5	± 4.99	0.07	2.45	0.27	± 0.03	
6	0.0063	1.111	0.0200	6.126	0.0011	5.202	0.0144	0.116	1.8462	1.103	0.05	± 678.6	8.1	± 4.03	0.04	2.98	0.31	± 0.04	
7	0.0062	1.118	0.0241	5.541	0.0011	4.798	0.0165	0.107	1.8463	1.103	0.81	± 594.4	136.9	± 3.53	0.72	3.40	0.29	± 0.03	
8	0.0063	1.105	0.0289	5.838	0.0011	5.031	0.0183	0.086	1.8604	1.094	0.28	± 535.9	47.4	± 3.18	0.28	3.77	0.27	± 0.03	

Step	36Ar [fA]	%1s	37Ar [fA]	%1s	38Ar [fA]	%1s	39Ar [fA]	%1s	40Ar [fA]	%1s	40(r)/39(k)	±2s	Age (Ka)	±2s	40Ar(r) (%)	39Ar(k) (%)	K/Ca	±2s
9	0.0096	0.737	0.0313	5.318	0.0017	3.255	0.0179	0.089	2.8415	0.717	0.98	± 3.29	164.3	± 554.9	0.61	3.69	0.25	± 0.03
10	0.0140	0.517	0.0450	4.670	0.0024	2.263	0.0205	0.086	4.1730	0.488	1.75	± 2.95	294.3	± 497.0	0.86	4.23	0.20	± 0.02
12	0.0497	0.212	0.1073	4.145	0.0113	0.490	0.0381	0.061	14.6511	0.139	0.13	± 2.27	22.0	± 382.4	0.03	7.86	0.15	± 0.01
14	0.0377	0.163	0.1511	4.073	0.0086	0.316	0.0488	0.050	11.1961	0.028	1.60	± 1.02	269.1	± 172.0	0.69	10.05	0.14	± 0.01
16	0.0447	0.163	0.2115	4.045	0.0106	0.263	0.0654	0.049	13.2400	0.023	0.73	± 0.90	123.2	± 151.7	0.36	13.48	0.13	± 0.01
18	0.0256	0.167	0.1950	4.051	0.0059	0.444	0.0600	0.052	7.5589	0.041	0.43	± 0.58	72.4	± 97.1	0.34	12.36	0.13	± 0.01
20	0.0157	0.177	0.1704	4.056	0.0033	1.060	0.0524	0.055	4.6516	0.066	0.58	± 0.43	97.9	± 72.2	0.65	10.79	0.13	± 0.01
21	0.0093	0.206	0.1128	4.142	0.0019	1.328	0.0341	0.066	2.7549	0.112	0.88	± 0.45	149.1	± 75.4	1.09	7.03	0.13	± 0.01
22	0.0077	0.219	0.0768	4.193	0.0015	1.561	0.0231	0.100	2.2914	0.135	0.50	± 0.59	84.3	± 99.5	0.50	4.76	0.13	± 0.01
24	0.0036	0.354	0.0588	4.285	0.0007	4.312	0.0177	0.097	1.0774	0.286	1.08	± 0.58	181.5	± 97.6	1.77	3.65	0.13	± 0.01
26	0.0021	0.564	0.0428	4.407	0.0004	7.051	0.0126	0.136	0.6205	0.497	0.72	± 0.75	120.7	± 127.1	1.45	2.59	0.13	± 0.01
28	0.0026	0.465	0.0439	4.478	0.0005	5.250	0.0127	0.126	0.7687	0.401	1.15	± 0.76	194.0	± 128.3	1.90	2.62	0.12	± 0.01
30	0.0028	0.437	0.0394	4.704	0.0004	6.510	0.0115	0.127	0.8531	0.361	3.12	± 0.85	526.4	± 144.0	4.19	2.36	0.12	± 0.01

**VIC22B: J = 0.00009230 ± 0.00000022 (1σ) MDF = 0.993846 ± 0.00020 (1σ)**

3	0.0659	0.157	0.0004	233.261	0.0146	0.329	0.0006	3.190	19.3908	0.270	283.10	± 266.96	47875.2	± 45748.3	0.93	0.11	0.62	± 2.88
4	0.0430	0.222	0.0028	41.658	0.0089	0.538	0.0012	1.142	12.5620	0.417	165.04	± 116.68	27755.3	± 19774.1	1.59	0.22	0.18	± 0.15
5	0.0513	0.190	0.0051	18.619	0.0109	0.416	0.0022	0.712	14.9974	0.349	104.17	± 69.25	17468.6	± 11668.9	1.51	0.39	0.19	± 0.07
6	0.0857	0.132	0.0091	11.113	0.0198	0.215	0.0039	0.438	25.0042	0.209	110.13	± 51.00	18473.7	± 8599.7	1.70	0.69	0.18	± 0.04
7	0.0925	0.126	0.0167	8.500	0.0208	0.223	0.0070	0.203	27.2291	0.192	31.82	± 29.44	5318.4	± 4927.6	0.82	1.27	0.18	± 0.03
8	0.1239	0.115	0.0315	4.812	0.0234	0.219	0.0122	0.136	36.7848	0.115	0.46	± 20.55	77.1	± 3429.0	0.02	2.20	0.17	± 0.02
9	0.0796	0.151	0.0437	4.578	0.0182	0.221	0.0176	0.111	23.5649	0.180	2.85	± 10.22	476.5	± 1706.7	0.21	3.17	0.17	± 0.02
10	0.0898	0.139	0.0572	4.417	0.0207	0.230	0.0231	0.081	26.5777	0.159	2.83	± 8.47	471.6	± 1414.3	0.25	4.15	0.17	± 0.02
12	0.1230	0.116	0.1135	4.117	0.0237	0.221	0.0449	0.041	36.9670	0.114	10.40	± 5.57	1735.6	± 928.9	1.26	8.06	0.17	± 0.01
14	0.0771	0.155	0.1595	4.077	0.0184	0.217	0.0619	0.036	23.0112	0.184	2.17	± 2.85	362.6	± 475.9	0.58	11.12	0.17	± 0.01

Step	36Ar [fA]	%1s	37Ar [fA]	%1s	38Ar [fA]	%1s	39Ar [fA]	%1s	40Ar [fA]	%1s	40(r)/39(k)	± 2s	Age (Ka)	± 2s	40Ar(r) (%)	39Ar(k) (%)	K/Ca	± 2s
16	0.0907	0.138	0.1905	4.069	0.0212	0.223	0.0729	0.031	27.0058	0.157	1.09	± 2.71	182.6	± 451.8	0.29	13.10	0.16	± 0.01
18	0.0599	0.188	0.1847	4.067	0.0140	0.271	0.0700	0.032	17.8390	0.237	0.89	± 2.17	148.8	± 362.6	0.35	12.57	0.16	± 0.01
20	0.0235	0.440	0.1572	4.077	0.0052	0.773	0.0597	0.033	7.0223	0.603	0.74	± 1.89	123.2	± 315.5	0.63	10.73	0.16	± 0.01
21	0.0164	0.626	0.1113	4.121	0.0029	1.256	0.0426	0.036	4.9000	0.864	0.95	± 2.55	158.5	± 425.2	0.82	7.65	0.16	± 0.01
22	0.0139	0.739	0.0871	4.163	0.0023	1.591	0.0324	0.056	4.1062	1.030	0.04	± 3.31	6.9	± 552.7	0.03	5.82	0.16	± 0.01
24	0.0124	0.825	0.0871	4.220	0.0020	1.749	0.0323	0.053	3.7295	1.135	1.61	± 3.30	269.0	± 550.6	1.40	5.81	0.16	± 0.01
26	0.0091	1.124	0.0874	4.154	0.0017	2.170	0.0322	0.054	2.8326	1.494	4.46	± 3.28	744.1	± 546.6	5.06	5.79	0.16	± 0.01
28	0.0059	1.726	0.0612	4.396	0.0010	3.835	0.0226	0.084	1.7879	2.367	1.82	± 4.78	303.8	± 797.7	2.23	3.94	0.16	± 0.01
30	0.0056	1.812	0.0488	4.378	0.0008	4.755	0.0178	0.130	1.7170	2.464	2.87	± 5.88	478.8	± 981.5	2.97	3.20	0.16	± 0.01

**VIC23: J = 0.00009230 ± 0.00000017 (1σ) MDF = 0.993390 ± 0.00020 (1σ)**

3	0.0043	0.105	0.0065	214.753	0.0008	11.675	0.0010	1.906	1.2756	0.011	2.40	± 3.85	399.7	± 641.8	0.18	0.17	0.06	± 0.27
4	0.0089	0.103	0.0059	185.409	0.0016	5.434	0.0043	0.443	2.6245	0.006	1.92	± 1.46	320.8	± 242.9	0.32	0.74	0.31	± 1.16
5	0.0098	0.091	0.0143	85.375	0.0020	4.735	0.0103	0.206	2.9191	0.005	1.35	± 0.62	225.6	± 103.2	0.48	1.77	0.31	± 0.53
6	0.0076	0.100	0.0214	50.832	0.0016	5.472	0.0162	0.119	2.2788	0.008	1.81	± 0.33	302.6	± 55.2	1.28	2.78	0.32	± 0.33
7	0.0061	0.109	0.0175	68.933	0.0014	6.529	0.0229	0.089	1.8424	0.008	1.81	± 0.21	301.5	± 34.6	2.25	3.94	0.56	± 0.77
8	0.0046	0.088	0.0291	42.501	0.0012	7.273	0.0302	0.066	1.4133	0.011	1.73	± 0.11	289.1	± 18.9	3.70	5.19	0.45	± 0.38
9	0.0035	0.155	0.0313	36.486	0.0010	4.152	0.0343	0.287	1.0913	0.058	1.77	± 0.12	295.9	± 19.7	5.57	5.91	0.47	± 0.34
10	0.0026	0.140	0.0376	21.146	0.0009	4.293	0.0357	0.275	0.8358	0.076	1.94	± 0.08	323.2	± 13.7	8.27	6.15	0.41	± 0.17
12	0.0040	0.151	0.0559	17.631	0.0014	2.855	0.0576	0.173	1.2692	0.050	1.74	± 0.07	290.8	± 12.4	7.91	9.92	0.44	± 0.16
14	0.0032	0.116	0.0697	14.322	0.0013	3.145	0.0629	0.157	1.0330	0.062	1.72	± 0.05	286.6	± 8.3	10.45	10.83	0.39	± 0.11
16	0.0030	0.154	0.0672	16.544	0.0012	3.372	0.0573	0.173	0.9700	0.066	1.66	± 0.06	277.8	± 10.5	9.82	9.86	0.37	± 0.12
18	0.0034	0.103	0.0723	14.896	0.0013	3.130	0.0518	0.191	1.0982	0.058	1.71	± 0.06	285.5	± 10.2	8.07	8.92	0.31	± 0.09
20	0.0044	0.111	0.1070	10.196	0.0014	2.883	0.0466	0.213	1.3787	0.046	1.66	± 0.08	276.9	± 13.9	5.60	8.01	0.19	± 0.04
21	0.0030	0.105	0.0763	14.840	0.0010	3.943	0.0332	0.297	0.9407	0.068	1.65	± 0.09	275.1	± 15.4	5.81	5.71	0.19	± 0.06

Step	$^{36}\text{Ar}$ [fA]	%1s	$^{37}\text{Ar}$ [fA]	%1s	$^{38}\text{Ar}$ [fA]	%1s	$^{39}\text{Ar}$ [fA]	%1s	$^{40}\text{Ar}$ [fA]	%1s	$^{40}(\text{r})/^{39}(\text{k})$	$\pm 2s$	Age (Ka)	$\pm 2s$	$^{40}\text{Ar}(\text{r})$ (%)	$^{39}\text{Ar}(\text{k})$ (%)	K/Ca	$\pm 2s$	
22	0.0028	0.138	0.0793	12.211	0.0008	5.604	0.0267	0.368	0.8768	0.073	1.65	$\pm 0.12$	275.2	$\pm 20.0$	5.01	4.59	0.14	$\pm 0.04$	
24	0.0033	0.259	0.0846	11.307	0.0009	2.945	0.0243	0.055	0.9925	0.212	1.57	$\pm 0.28$	261.3	$\pm 46.5$	3.83	4.18	0.12	$\pm 0.03$	
26	0.0039	0.219	0.0974	9.155	0.0010	2.343	0.0239	0.048	1.1837	0.178	1.61	$\pm 0.29$	268.3	$\pm 47.8$	3.24	4.10	0.11	$\pm 0.02$	
28	0.0039	0.219	0.0928	10.945	0.0010	3.370	0.0220	0.055	1.1923	0.176	1.55	$\pm 0.32$	259.4	$\pm 52.6$	2.86	3.78	0.10	$\pm 0.02$	
30	0.0038	0.221	0.0864	8.910	0.0009	3.320	0.0200	0.059	1.1475	0.183	1.47	$\pm 0.34$	245.4	$\pm 56.2$	2.56	3.44	0.10	$\pm 0.02$	
<b>VIC26: <math>J = 0.00009280 \pm 0.0000028</math> (1<math>\sigma</math>) MDF = 0.993140 <math>\pm</math> 0.00030 (1<math>\sigma</math>)</b>																			
3	0.0790	0.121	0.0967	15.899	0.0149	0.452	0.0301	0.248	23.3560	0.007	4.16	$\pm 3.23$	697.3	$\pm 542.1$	0.53	4.77	0.13	$\pm 0.04$	
4	0.0396	0.122	0.1137	13.665	0.0080	0.805	0.0700	0.111	11.6725	0.013	0.41	$\pm 0.70$	68.3	$\pm 117.2$	0.24	11.12	0.26	$\pm 0.07$	
5	0.0144	0.125	0.1273	11.457	0.0035	1.771	0.0775	0.101	4.2455	0.036	0.34	$\pm 0.24$	56.2	$\pm 39.5$	0.61	12.31	0.26	$\pm 0.06$	
6	0.0076	0.149	0.0997	13.885	0.0021	2.920	0.0693	0.113	2.2615	0.067	0.34	$\pm 0.16$	56.5	$\pm 26.2$	1.03	11.01	0.30	$\pm 0.08$	
7	0.0051	0.152	0.0641	21.618	0.0016	3.826	0.0584	0.131	1.5036	0.101	0.29	$\pm 0.13$	49.0	$\pm 22.3$	1.13	9.28	0.39	$\pm 0.17$	
8	0.0029	0.192	0.0329	55.171	0.0011	5.460	0.0479	0.158	0.8630	0.176	0.24	$\pm 0.13$	40.1	$\pm 21.2$	1.33	7.62	0.63	$\pm 0.69$	
9	0.0020	0.259	0.0483	30.539	0.0009	7.130	0.0384	0.196	0.5863	0.259	0.31	$\pm 0.14$	51.4	$\pm 22.9$	2.01	6.10	0.34	$\pm 0.21$	
10	0.0018	0.279	0.0479	35.306	0.0008	7.725	0.0345	0.218	0.5490	0.277	0.35	$\pm 0.16$	58.6	$\pm 26.1$	2.19	5.49	0.31	$\pm 0.22$	
12	0.0023	0.222	0.1108	15.289	0.0009	6.545	0.0456	0.165	0.6967	0.218	0.36	$\pm 0.12$	60.9	$\pm 20.6$	2.37	7.24	0.18	$\pm 0.05$	
14	0.0017	0.285	0.1302	12.745	0.0008	7.653	0.0392	0.193	0.5020	0.303	0.32	$\pm 0.13$	53.1	$\pm 22.3$	2.47	6.23	0.13	$\pm 0.03$	
16	0.0017	0.301	0.1401	11.182	0.0007	8.499	0.0351	0.213	0.4952	0.307	0.32	$\pm 0.15$	53.7	$\pm 24.9$	2.27	5.57	0.11	$\pm 0.02$	
18	0.0012	0.389	0.1713	10.351	0.0006	10.390	0.0294	0.254	0.3638	0.418	0.39	$\pm 0.18$	66.1	$\pm 29.7$	3.17	4.65	0.07	$\pm 0.02$	
20	0.0005	0.809	0.1166	12.900	0.0003	24.193	0.0198	0.374	0.1536	0.989	0.34	$\pm 0.24$	56.3	$\pm 39.6$	4.30	3.14	0.07	$\pm 0.02$	
21	0.0003	1.290	0.0899	16.085	0.0002	32.177	0.0131	0.567	0.0993	1.535	0.30	$\pm 0.36$	50.6	$\pm 60.1$	3.95	2.07	0.06	$\pm 0.02$	
22	0.0003	1.290	0.0488	31.548	0.0001	112.670	0.0082	0.900	0.0977	1.564	0.41	$\pm 0.57$	68.9	$\pm 96.1$	3.43	1.30	0.07	$\pm 0.05$	
24	0.0002	2.482	0.0386	40.387	0.0001	43.270	0.0058	1.287	0.0495	3.120	0.30	$\pm 0.82$	50.5	$\pm 137.7$	3.48	0.91	0.06	$\pm 0.05$	
26	0.0003	1.467	0.0305	42.704	0.0002	34.812	0.0051	1.449	0.0827	1.838	0.01	$\pm 0.88$	1.1	$\pm 147.3$	0.04	0.81	0.07	$\pm 0.06$	
28	0.0000	76.172	0.0167	80.814	0.0000	130.664	0.0015	4.974	0.0026	57.378	1.60	$\pm 3.04$	267.7	$\pm 510.5$	88.61	0.23	0.04	$\pm 0.06$	

Step	36Ar [fA]	%1s	37Ar [fA]	%1s	38Ar [fA]	%1s	39Ar [fA]	%1s	40Ar [fA]	%1s	40(r)/39(k)	± 2s	Age (Ka)	± 2s	40Ar(r) (%)	39Ar(k) (%)	K/Ca	± 2s	
30	0.0000	86.928	0.0070	197.403	0.0000	128.536	0.0011	6.911	0.0017	91.803	3.42	± 4.25	573.1	± 712.9	219.48	0.17	0.07	± 0.26	
<b>VIC27: J = 0.00009290 ± 0.00000026 (1σ) MDF = 0.993390 ± 0.00020 (1σ)</b>																			
3	0.0037	0.123	0.0136	72.157	0.0007	5.472	0.0031	1.701	1.1035	0.094	4.83	± 2.85	811.5	± 478.7	1.33	0.36	0.10	± 0.14	
4	0.0114	0.093	0.0358	24.311	0.0023	0.994	0.0115	0.457	3.3773	0.031	3.47	± 2.17	583.5	± 364.7	1.18	1.36	0.14	± 0.07	
5	0.0128	0.089	0.0613	17.296	0.0026	0.901	0.0239	0.221	3.7762	0.028	1.91	± 1.16	320.5	± 195.0	1.21	2.83	0.17	± 0.06	
6	0.0123	0.087	0.0741	13.757	0.0027	0.825	0.0371	0.143	3.6515	0.028	1.32	± 0.72	221.7	± 121.1	1.34	4.39	0.22	± 0.06	
7	0.0106	0.095	0.0716	14.732	0.0024	0.944	0.0431	0.122	3.1344	0.033	0.77	± 0.54	128.8	± 90.4	1.05	5.11	0.26	± 0.08	
8	0.0097	0.093	0.0851	13.265	0.0023	0.877	0.0469	0.114	2.8623	0.036	0.71	± 0.45	118.7	± 75.8	1.16	5.56	0.24	± 0.06	
9	0.0087	0.101	0.0734	14.944	0.0022	1.163	0.0484	0.111	2.5813	0.040	0.54	± 0.40	91.2	± 66.9	1.02	5.73	0.28	± 0.08	
10	0.0081	0.100	0.0544	17.454	0.0020	1.412	0.0465	0.116	2.3947	0.043	0.50	± 0.38	83.3	± 64.5	0.96	5.51	0.37	± 0.13	
12	0.0104	0.102	0.1032	10.585	0.0027	0.895	0.0719	0.077	3.0617	0.034	0.43	± 0.32	72.7	± 53.2	1.02	8.52	0.30	± 0.06	
14	0.0082	0.098	0.1188	9.846	0.0024	1.074	0.0710	0.078	2.4263	0.043	0.29	± 0.26	48.8	± 42.9	0.85	8.41	0.26	± 0.05	
16	0.0084	0.097	0.1396	10.218	0.0025	1.296	0.0771	0.076	2.4742	0.042	0.30	± 0.24	49.7	± 40.3	0.92	9.13	0.24	± 0.05	
18	0.0066	0.099	0.1300	9.520	0.0020	1.516	0.0652	0.086	1.9258	0.054	0.23	± 0.22	39.3	± 37.4	0.79	7.72	0.22	± 0.04	
20	0.0055	0.116	0.1439	9.733	0.0017	1.498	0.0592	0.091	1.6131	0.064	0.29	± 0.21	48.0	± 35.3	1.05	7.01	0.18	± 0.03	
21	0.0042	0.126	0.1259	10.509	0.0013	2.223	0.0469	0.115	1.2256	0.084	0.30	± 0.21	50.1	± 34.7	1.14	5.55	0.16	± 0.03	
22	0.0035	0.122	0.1069	11.714	0.0011	2.395	0.0384	0.138	1.0394	0.099	0.27	± 0.22	46.1	± 36.5	1.01	4.54	0.15	± 0.04	
24	0.0038	0.121	0.1234	10.284	0.0012	1.904	0.0404	0.133	1.1196	0.092	0.26	± 0.22	43.9	± 37.0	0.94	4.78	0.14	± 0.03	
26	0.0034	0.137	0.1623	8.098	0.0011	2.467	0.0433	0.124	1.0101	0.102	0.30	± 0.19	50.8	± 32.0	1.29	5.12	0.11	± 0.02	
28	0.0055	0.111	0.1486	9.674	0.0015	1.858	0.0366	0.144	1.6119	0.064	0.10	± 0.34	16.3	± 57.5	0.22	4.32	0.11	± 0.02	
30	0.0048	0.104	0.1443	8.973	0.0012	2.229	0.0343	0.154	1.3896	0.074	0.21	± 0.31	35.2	± 52.7	0.52	4.06	0.10	± 0.02	
<b>VIC28: J = 0.00009270 ± 0.00000013 (1σ) MDF = 0.992121 ± 0.00020 (1σ)</b>																			
3	0.0046	0.099	0.0075	12.452	0.0004	6.456	0.0049	0.690	1.3569	0.019	0.02	± 1.10	3.3	± 184.9	0.01	0.64	0.28	± 0.07	

Step	36Ar [fA]	%1s	37Ar [fA]	%1s	38Ar [fA]	%1s	39Ar [fA]	%1s	40Ar [fA]	%1s	40(f)/39(k)	±2s	Age (Ka)	±2s	40Ar(f) (%)	39Ar(k) (%)	K/Ca	±2s	
4	0.0080	0.106	0.0303	4.922	0.0012	2.046	0.0219	0.141	2.3659	0.011	0.09	±0.44	14.8	±72.9	0.08	2.89	0.31	±0.03	
5	0.0055	0.088	0.0557	4.366	0.0010	2.192	0.0476	0.066	1.6482	0.015	0.29	±0.13	47.9	±22.2	0.82	6.30	0.37	±0.03	
6	0.0032	0.109	0.0626	4.326	0.0008	3.293	0.0608	0.053	0.9566	0.027	0.24	±0.06	40.6	±10.7	1.54	8.05	0.42	±0.04	
7	0.0020	0.133	0.0594	4.460	0.0006	4.335	0.0644	0.056	0.6087	0.042	0.25	±0.04	42.1	±6.9	2.65	8.53	0.47	±0.04	
8	0.0016	0.113	0.0531	4.401	0.0005	4.959	0.0609	0.063	0.4805	0.053	0.23	±0.03	38.6	±5.5	2.92	8.07	0.49	±0.04	
9	0.0015	0.155	0.0483	4.549	0.0004	5.996	0.0562	0.056	0.4393	0.058	0.20	±0.04	33.7	±6.2	2.57	7.44	0.50	±0.05	
10	0.0008	0.178	0.0407	4.624	0.0003	7.724	0.0485	0.070	0.2436	0.104	0.24	±0.03	39.6	±4.5	4.70	6.42	0.51	±0.05	
12	0.0012	0.194	0.0668	4.360	0.0005	5.347	0.0650	0.055	0.3716	0.068	0.31	±0.03	52.4	±5.0	5.47	8.61	0.42	±0.04	
14	0.0011	0.163	0.0929	4.239	0.0005	5.150	0.0623	0.056	0.3230	0.079	0.25	±0.03	41.4	±4.5	4.76	8.24	0.29	±0.02	
16	0.0010	0.159	0.1180	4.162	0.0004	6.494	0.0548	0.060	0.2917	0.087	0.25	±0.03	42.3	±5.0	4.73	7.25	0.20	±0.02	
18	0.0009	0.173	0.1293	4.125	0.0003	8.177	0.0456	0.071	0.2533	0.100	0.25	±0.03	42.1	±5.8	4.51	6.03	0.15	±0.01	
20	0.0009	0.156	0.1285	4.128	0.0003	9.387	0.0388	0.087	0.2690	0.094	0.28	±0.04	46.6	±6.8	4.00	5.13	0.13	±0.01	
21	0.0007	0.200	0.0998	4.204	0.0002	12.490	0.0285	0.112	0.2067	0.123	0.28	±0.05	47.6	±8.0	3.91	3.77	0.12	±0.01	
22	0.0005	0.232	0.0793	4.269	0.0001	22.065	0.0217	0.142	0.1574	0.163	0.65	±0.05	109.6	±8.8	8.99	2.87	0.12	±0.01	
24	0.0004	0.234	0.0721	4.257	0.0001	20.133	0.0186	0.168	0.1332	0.198	0.48	±0.06	80.5	±9.4	6.70	2.46	0.11	±0.01	
26	0.0006	0.236	0.0846	4.195	0.0001	17.410	0.0213	0.151	0.1898	0.137	0.27	±0.06	46.1	±10.6	3.07	2.81	0.11	±0.01	
28	0.0005	0.285	0.0761	4.254	0.0001	36.801	0.0177	0.182	0.1417	0.183	0.31	±0.07	51.5	±11.3	3.82	2.33	0.10	±0.01	
30	0.0005	0.230	0.0675	4.255	0.0001	41.120	0.0162	0.197	0.1543	0.204	0.75	±0.07	125.1	±11.9	7.81	2.14	0.10	±0.01	
<b>VIC29: J = 0.00009520 ± 0.00000026 (1σ) MDF = 0.995310 ± 0.00030 (1σ)</b>																			
3	0.0072	0.125	0.0386	2.457	0.0019	1.338	0.0149	0.304	2.2170	0.048	3.85	±0.49	662.4	±84.2	2.58	2.16	0.17	±0.01	
6	0.0029	0.174	0.1726	2.386	0.0026	1.256	0.1291	0.048	1.2464	0.085	3.04	±0.03	523.0	±5.5	31.45	18.78	0.32	±0.02	
9	0.0007	0.420	0.1401	2.389	0.0024	1.083	0.1488	0.043	0.6438	0.165	3.00	±0.02	515.8	±3.3	69.23	21.65	0.46	±0.02	
12	0.0005	0.591	0.1015	2.396	0.0019	1.324	0.1190	0.049	0.4928	0.216	3.03	±0.02	521.0	±4.0	73.06	17.32	0.50	±0.02	
14	0.0003	0.832	0.0740	2.391	0.0011	1.961	0.0690	0.056	0.2936	0.202	3.02	±0.03	519.4	±4.9	70.91	10.04	0.40	±0.02	

Step	36Ar [fA]	%1s	37Ar [fA]	%1s	38Ar [fA]	%1s	39Ar [fA]	%1s	40Ar [fA]	%1s	40(t)/39(k)	±2s	Age (Ka)	±2s	40Ar(t) (%)	39Ar(k) (%)	K/Ca	±2s
16	0.0003	2.091	0.0890	2.389	0.0009	4.645	0.0535	0.045	0.2454	0.729	3.08	±0.10	529.6	±16.6	66.98	7.78	0.26	±0.01
18	0.0002	2.539	0.0937	2.392	0.0006	4.048	0.0383	0.055	0.1805	0.991	3.02	±0.14	519.3	±23.3	63.84	5.56	0.18	±0.01
20	0.0002	2.922	0.0902	2.391	0.0005	5.387	0.0284	0.063	0.1433	1.249	3.11	±0.18	534.6	±31.2	61.34	4.12	0.13	±0.01
21	0.0001	4.290	0.0633	2.397	0.0003	6.706	0.0183	0.109	0.0936	1.911	3.08	±0.28	529.7	±48.2	60.07	2.66	0.12	±0.01
22	0.0001	0.834	0.0529	2.405	0.0002	11.286	0.0137	0.325	0.0735	0.591	3.00	±0.08	516.6	±14.1	55.88	1.99	0.11	±0.01
24	0.0002	0.629	0.0737	2.389	0.0003	10.786	0.0136	0.332	0.0848	0.513	3.21	±0.08	551.9	±14.4	51.27	1.97	0.08	±0.00
26	0.0001	0.711	0.0789	2.391	0.0002	12.638	0.0113	0.391	0.0712	0.613	3.05	±0.10	524.9	±17.6	48.10	1.63	0.06	±0.00
28	0.0001	0.916	0.0564	2.405	0.0001	21.915	0.0085	0.521	0.0526	0.856	3.09	±0.13	532.5	±22.8	49.93	1.24	0.06	±0.00
30	0.0001	1.073	0.0556	2.403	0.0001	41.918	0.0071	0.617	0.0469	1.051	3.21	±0.17	552.2	±29.6	48.42	1.03	0.05	±0.00
35	0.0001	1.255	0.0693	2.394	0.0001	23.962	0.0074	0.606	0.0535	1.110	3.07	±0.21	527.6	±36.5	41.95	1.07	0.05	±0.00
40	0.0001	1.355	0.0636	2.400	0.0001	22.694	0.0069	0.653	0.0643	0.673	4.43	±0.21	763.0	±36.4	47.26	1.00	0.05	±0.00

<b>VIC32: J = 0.00009150 ± 0.00000035 (1σ) MDF = 0.993804 ± 0.00030 (1σ)</b>																			
3	0.0010	0.267	0.0059	2.952	0.0003	9.411	0.0045	0.812	0.3054	0.158	4.06	±0.59	671.0	±96.9	5.98	0.49	0.33	±0.02	
4	0.0024	0.146	0.0198	2.180	0.0007	3.745	0.0161	0.228	0.7782	0.062	3.76	±0.33	621.8	±54.3	7.76	1.76	0.35	±0.02	
5	0.0024	0.148	0.0321	2.110	0.0009	2.582	0.0283	0.131	0.8346	0.058	3.78	±0.19	626.1	±31.4	12.82	3.10	0.38	±0.02	
6	0.0025	0.167	0.0435	2.095	0.0011	2.476	0.0433	0.091	0.9208	0.052	3.79	±0.13	626.9	±21.8	17.82	4.75	0.43	±0.02	
7	0.0023	0.150	0.0460	2.110	0.0012	2.221	0.0509	0.079	0.8778	0.055	3.83	±0.10	633.1	±16.5	22.18	5.58	0.48	±0.02	
8	0.0025	0.144	0.0511	2.091	0.0014	1.693	0.0611	0.068	0.9716	0.050	3.82	±0.09	631.4	±14.7	23.99	6.69	0.51	±0.02	
9	0.0022	0.143	0.0483	2.088	0.0013	1.634	0.0594	0.071	0.8780	0.055	3.79	±0.08	627.5	±13.4	25.65	6.51	0.53	±0.02	
10	0.0022	0.144	0.0501	2.105	0.0013	1.488	0.0623	0.066	0.9064	0.053	3.82	±0.08	631.6	±13.1	26.24	6.83	0.53	±0.02	
12	0.0033	0.153	0.0786	2.080	0.0021	1.632	0.0969	0.050	1.3607	0.036	3.78	±0.08	624.7	±12.5	26.87	10.61	0.53	±0.02	
14	0.0029	0.154	0.0841	2.083	0.0019	1.093	0.0897	0.051	1.1993	0.040	3.72	±0.07	615.1	±11.8	27.78	9.82	0.46	±0.02	
16	0.0027	0.145	0.0974	2.079	0.0017	1.577	0.0783	0.057	1.0983	0.044	3.98	±0.07	658.1	±12.2	28.33	8.57	0.35	±0.01	
18	0.0023	0.143	0.1126	2.079	0.0015	1.397	0.0695	0.063	0.9681	0.050	4.18	±0.07	691.3	±11.9	29.96	7.61	0.26	±0.01	

Step	<sup>36</sup> Ar [fA]	%1s	<sup>37</sup> Ar [fA]	%1s	<sup>38</sup> Ar [fA]	%1s	<sup>39</sup> Ar [fA]	%1s	<sup>40</sup> Ar [fA]	%1s	<sup>40</sup> (r)/ <sup>39</sup> (k)	± 2s	Age (Ka)	± 2s	<sup>40</sup> Ar(r) (%)	<sup>39</sup> Ar(k) (%)	K/Ca	± 2s	
20	0.0021	0.188	0.1231	2.079	0.0013	1.793	0.0602	0.069	1.0011	0.048	6.50	± 0.08	1074.7	± 13.2	39.03	6.59	0.21	± 0.01	
21	0.0013	0.161	0.1071	2.079	0.0009	2.165	0.0423	0.091	0.5717	0.084	4.31	± 0.07	712.7	± 12.1	31.78	4.62	0.17	± 0.01	
22	0.0009	0.273	0.0818	2.085	0.0006	4.454	0.0271	0.139	0.3522	0.137	3.64	± 0.09	602.3	± 14.8	28.00	2.97	0.14	± 0.01	
24	0.0006	0.262	0.0752	2.087	0.0005	6.345	0.0209	0.179	0.2626	0.184	3.67	± 0.09	607.5	± 15.1	29.10	2.28	0.12	± 0.00	
26	0.0008	0.228	0.0778	2.084	0.0005	5.498	0.0227	0.167	0.3023	0.160	3.66	± 0.09	605.1	± 15.0	27.44	2.49	0.13	± 0.01	
28	0.0008	0.301	0.0940	2.083	0.0005	6.074	0.0230	0.163	0.3082	0.157	3.62	± 0.10	598.3	± 16.6	26.90	2.51	0.10	± 0.00	
30	0.0005	0.291	0.0807	2.086	0.0003	9.678	0.0163	0.224	0.2140	0.225	3.59	± 0.11	593.6	± 17.7	27.29	1.78	0.09	± 0.00	
40	0.0007	0.225	0.1429	2.080	0.0004	6.298	0.0221	0.166	0.2904	0.166	3.66	± 0.09	606.1	± 15.4	27.69	2.41	0.07	± 0.00	
50	0.0008	0.258	0.1491	2.080	0.0004	5.598	0.0187	0.198	0.3171	0.153	5.28	± 0.12	873.8	± 19.7	30.93	2.03	0.05	± 0.00	
<b>VIC33: J = 0.00009100 ± 0.00000020 (1σ) MDF = 0.993804 ± 0.00030 (1σ)</b>																			
3	0.0036	0.141	0.0026	5.562	0.0007	3.148	0.0017	0.678	1.0850	0.003	8.05	± 2.24	1324.8	± 368.3	1.24	0.25	0.27	± 0.03	
4	0.0173	0.127	0.0172	2.140	0.0034	0.578	0.0118	0.102	5.1685	0.010	5.05	± 1.42	830.5	± 233.7	1.15	1.75	0.29	± 0.01	
5	0.0180	0.124	0.0315	2.108	0.0038	0.730	0.0243	0.043	5.4519	0.008	5.64	± 0.70	927.3	± 115.9	2.51	3.62	0.33	± 0.01	
6	0.0135	0.124	0.0336	2.091	0.0031	0.613	0.0297	0.042	4.1356	0.005	5.50	± 0.43	904.5	± 70.7	3.94	4.41	0.38	± 0.02	
7	0.0099	0.124	0.0337	2.104	0.0023	0.820	0.0344	0.046	3.1195	0.004	5.78	± 0.27	950.2	± 44.9	6.36	5.12	0.44	± 0.02	
8	0.0065	0.138	0.0302	2.129	0.0016	1.164	0.0349	0.040	2.1206	0.005	5.86	± 0.19	963.2	± 31.1	9.63	5.19	0.50	± 0.02	
9	0.0043	0.156	0.0248	2.097	0.0012	1.887	0.0306	0.055	1.4529	0.005	5.76	± 0.16	947.4	± 25.6	12.14	4.56	0.53	± 0.02	
10	0.0030	0.151	0.0230	2.166	0.0010	2.132	0.0298	0.039	1.0367	0.005	5.64	± 0.11	927.9	± 17.6	16.18	4.43	0.56	± 0.02	
12	0.0038	0.134	0.0371	2.081	0.0014	2.011	0.0441	0.043	1.3787	0.008	5.73	± 0.09	941.9	± 14.3	18.28	6.55	0.51	± 0.02	
14	0.0019	0.158	0.0437	2.090	0.0009	3.242	0.0411	0.034	0.7947	0.005	5.67	± 0.05	932.1	± 8.6	29.26	6.11	0.40	± 0.02	
16	0.0013	0.187	0.0677	2.072	0.0008	4.760	0.0428	0.039	0.6090	0.008	5.50	± 0.04	905.4	± 6.3	38.60	6.36	0.27	± 0.01	
18	0.0012	0.174	0.0968	2.072	0.0008	3.565	0.0451	0.039	0.5915	0.003	5.64	± 0.03	927.0	± 5.2	42.91	6.70	0.20	± 0.01	
20	0.0011	0.200	0.1176	2.070	0.0008	2.585	0.0452	0.041	0.5688	0.002	5.85	± 0.03	961.8	± 5.4	46.35	6.71	0.16	± 0.01	
21	0.0006	0.208	0.0925	2.072	0.0005	4.621	0.0327	0.039	0.3675	0.011	5.72	± 0.03	941.6	± 4.7	50.80	4.86	0.15	± 0.01	



Step	36Ar [fA]	%1s	37Ar [fA]	%1s	38Ar [fA]	%1s	39Ar [fA]	%1s	40Ar [fA]	%1s	40(t)/39(k)	±2s	Age (Ka)	±2s	40Ar(t) (%)	39Ar(k) (%)	K/Ca	±2s	
22	0.0005	0.241	0.0830	2.073	0.0005	5.364	0.0284	0.045	0.2947	0.009	5.49	±0.03	902.3	±4.8	52.66	4.21	0.15	±0.01	
24	0.0005	0.267	0.0923	2.075	0.0005	6.885	0.0295	0.040	0.3025	0.008	5.46	±0.03	897.8	±5.1	53.16	4.39	0.14	±0.01	
26	0.0005	0.161	0.1021	2.074	0.0005	5.524	0.0309	0.040	0.3234	0.008	5.55	±0.02	913.2	±3.8	52.94	4.59	0.13	±0.01	
28	0.0006	0.194	0.1089	2.072	0.0005	6.407	0.0300	0.042	0.3230	0.014	5.66	±0.03	931.1	±4.5	52.37	4.45	0.12	±0.00	
30	0.0004	0.334	0.0936	2.075	0.0004	8.477	0.0243	0.046	0.2572	0.013	5.63	±0.04	926.5	±6.5	53.07	3.61	0.11	±0.00	
40	0.0010	0.222	0.2330	2.070	0.0009	3.464	0.0514	0.042	0.5565	0.007	5.64	±0.03	928.0	±5.2	51.89	7.62	0.09	±0.00	
50	0.0007	0.192	0.1434	2.072	0.0005	5.692	0.0305	0.038	0.3516	0.007	5.57	±0.03	916.4	±5.3	48.10	4.52	0.09	±0.00	
<b>VIC52: J = 0.00009270 ± 0.00000018 (1σ) MDF = 0.992527 ± 0.00120 (1σ)</b>																			
3	0.0018	0.490	0.0052	32.902	0.0005	11.473	0.0063	1.166	0.5412	0.078	3.08	±1.37	516.7	±229.7	3.60	0.84	0.53	±0.35	
4	0.0007	0.611	0.0128	16.513	0.0004	13.746	0.0152	0.494	0.2511	0.294	2.79	±0.28	467.6	±47.5	16.45	1.97	0.51	±0.17	
5	0.0019	0.487	0.0140	16.029	0.0007	7.415	0.0225	0.340	0.5898	0.113	1.83	±0.42	306.5	±70.2	6.81	2.92	0.69	±0.22	
6	0.0011	0.578	0.0184	11.398	0.0006	8.055	0.0281	0.281	0.4004	0.227	2.68	±0.23	449.8	±38.3	18.38	3.64	0.66	±0.15	
7	0.0006	0.633	0.0173	12.544	0.0006	8.685	0.0318	0.256	0.2461	0.332	2.34	±0.13	392.6	±21.3	29.52	4.12	0.79	±0.20	
8	0.0005	0.597	0.0189	10.705	0.0005	9.570	0.0297	0.272	0.2173	0.304	2.41	±0.12	404.7	±19.4	32.18	3.85	0.68	±0.15	
9	0.0005	0.675	0.0197	9.700	0.0006	8.622	0.0308	0.261	0.2142	0.302	2.14	±0.12	358.3	±19.3	29.95	3.99	0.67	±0.13	
10	0.0005	0.722	0.0221	10.721	0.0006	9.613	0.0298	0.271	0.2243	0.255	2.23	±0.13	373.4	±21.1	28.88	3.86	0.58	±0.13	
12	0.0010	0.542	0.0417	7.502	0.0008	6.075	0.0451	0.200	0.3806	0.105	2.01	±0.12	336.7	±20.8	23.20	5.84	0.46	±0.07	
14	0.0017	0.493	0.0735	5.540	0.0013	3.956	0.0579	0.173	0.5916	0.066	1.86	±0.15	311.7	±25.1	17.75	7.50	0.34	±0.04	
16	0.0025	0.486	0.1116	5.051	0.0016	1.606	0.0740	0.140	0.8494	0.013	1.89	±0.17	316.7	±28.3	16.04	9.58	0.28	±0.03	
18	0.0021	0.483	0.1353	5.037	0.0017	1.702	0.0842	0.136	0.7653	0.015	1.86	±0.13	311.7	±21.9	19.94	10.90	0.27	±0.03	
20	0.0019	0.499	0.1315	5.085	0.0016	1.336	0.0783	0.139	0.6803	0.045	1.86	±0.13	312.0	±21.0	20.90	10.15	0.26	±0.03	
21	0.0010	0.528	0.0936	5.539	0.0010	2.152	0.0550	0.157	0.3791	0.081	1.88	±0.10	314.9	±16.7	26.56	7.12	0.25	±0.03	
22	0.0024	0.486	0.0688	5.614	0.0011	2.561	0.0402	0.182	0.7683	0.038	1.93	±0.30	323.8	±49.5	9.85	5.20	0.25	±0.03	
24	0.0008	0.525	0.0598	5.638	0.0007	5.030	0.0339	0.200	0.2768	0.105	1.85	±0.12	310.1	±20.3	22.07	4.39	0.24	±0.03	

Step	36Ar [fA]	%1s	37Ar [fA]	%1s	38Ar [fA]	%1s	39Ar [fA]	%1s	40Ar [fA]	%1s	40(r)/ 39(k)	± 2s	Age (Ka)	± 2s	40Ar(r) (%)	39Ar(k) (%)	K/Ca	± 2s	
26	0.0009	0.548	0.0705	5.718	0.0008	4.494	0.0382	0.160	0.3163	0.130	1.92	± 0.12	321.4	± 20.9	22.58	4.95	0.23	± 0.03	
28	0.0007	0.558	0.0734	5.620	0.0007	4.647	0.0381	0.160	0.2749	0.149	1.88	± 0.11	315.5	± 18.2	25.44	4.94	0.22	± 0.03	
30	0.0007	0.537	0.0651	5.521	0.0007	5.775	0.0328	0.173	0.2520	0.163	1.97	± 0.11	330.1	± 19.3	24.99	4.25	0.22	± 0.02	
<b>VIC57: J = 0.00009320 ± 0.00000007 (1σ) MDF = 0.993531 ± 0.00030 (1σ)</b>																			
3	0.0015	0.205	0.0020	26.485	0.0003	7.340	0.0021	2.040	0.4397	0.102	1.54	± 1.27	258.7	± 213.8	0.72	0.22	0.43	± 0.23	
4	0.0013	0.162	0.0064	9.904	0.0003	7.608	0.0070	0.606	0.3872	0.139	1.43	± 0.31	240.4	± 51.8	2.58	0.73	0.47	± 0.09	
5	0.0022	0.209	0.0090	7.666	0.0006	4.092	0.0119	0.355	0.6680	0.070	0.62	± 0.32	104.3	± 54.0	1.10	1.24	0.57	± 0.09	
6	0.0032	0.138	0.0117	6.147	0.0009	2.752	0.0190	0.228	0.9564	0.047	1.07	± 0.23	180.0	± 39.3	2.12	1.98	0.70	± 0.09	
7	0.0035	0.145	0.0108	6.245	0.0010	3.000	0.0219	0.186	1.0531	0.030	1.04	± 0.22	175.7	± 37.8	2.16	2.28	0.87	± 0.11	
8	0.0041	0.145	0.0127	4.989	0.0011	2.328	0.0257	0.160	1.2363	0.026	1.01	± 0.22	170.9	± 37.6	2.11	2.68	0.87	± 0.09	
9	0.0043	0.134	0.0133	5.231	0.0012	2.103	0.0273	0.150	1.3112	0.024	1.22	± 0.22	205.7	± 36.4	2.54	2.85	0.88	± 0.09	
10	0.0054	0.136	0.0137	4.986	0.0014	2.399	0.0285	0.145	1.6065	0.020	0.68	± 0.26	115.3	± 43.5	1.21	2.97	0.90	± 0.09	
12	0.0091	0.128	0.0269	3.998	0.0023	1.129	0.0426	0.110	2.7393	0.064	1.01	± 0.30	169.5	± 50.2	1.56	4.44	0.68	± 0.05	
14	0.0153	0.126	0.0494	3.527	0.0037	0.683	0.0557	0.087	4.5852	0.038	1.14	± 0.37	191.9	± 62.4	1.38	5.81	0.49	± 0.03	
16	0.0234	0.124	0.0850	3.360	0.0057	0.451	0.0737	0.070	6.9919	0.025	1.00	± 0.42	167.7	± 71.2	1.05	7.67	0.37	± 0.03	
18	0.0328	0.124	0.1288	3.310	0.0076	0.345	0.0973	0.056	9.7880	0.018	0.86	± 0.45	144.4	± 75.4	0.85	10.13	0.33	± 0.02	
20	0.0328	0.123	0.1520	3.295	0.0078	0.382	0.1066	0.040	9.8379	0.003	1.24	± 0.41	209.1	± 68.6	1.34	11.10	0.30	± 0.02	
21	0.0216	0.122	0.1211	3.300	0.0053	0.640	0.0807	0.047	6.4791	0.004	1.21	± 0.35	203.4	± 59.4	1.50	8.40	0.29	± 0.02	
22	0.0192	0.126	0.1023	3.303	0.0047	0.682	0.0672	0.051	5.7542	0.005	1.23	± 0.38	206.9	± 64.0	1.43	7.00	0.28	± 0.02	
24	0.0179	0.124	0.1115	3.299	0.0045	0.830	0.0716	0.049	5.3908	0.004	1.54	± 0.33	259.1	± 55.7	2.04	7.45	0.28	± 0.02	
26	0.0182	0.121	0.1206	3.311	0.0047	0.783	0.0748	0.047	5.5267	0.005	1.83	± 0.32	308.5	± 54.0	2.47	7.78	0.27	± 0.02	
28	0.0153	0.135	0.1201	3.299	0.0040	1.446	0.0720	0.050	4.6523	0.007	1.71	± 0.29	287.8	± 48.9	2.64	7.49	0.26	± 0.02	
30	0.0164	0.125	0.1331	3.305	0.0043	0.705	0.0748	0.049	4.9662	0.004	1.67	± 0.29	281.7	± 49.1	2.51	7.78	0.24	± 0.02	

Step	<sup>36</sup> Ar [fA]	%1s	<sup>37</sup> Ar [fA]	%1s	<sup>38</sup> Ar [fA]	%1s	<sup>39</sup> Ar [fA]	%1s	<sup>40</sup> Ar [fA]	%1s	40(r)/39(k)	±2s	Age (Ka)	±2s	<sup>40</sup> Ar(r) (%)	<sup>39</sup> Ar(k) (%)	K/Ca	±2s	
<b>VIC67: J = 0.00009600 ± 0.00000023 (1σ) MDF = 0.993415 ± 0.00050 (1σ)</b>																			
3	0.0014	0.248	0.0051	5.194	0.0003	8.587	0.0067	0.247	0.4085	0.031	0.40	±0.32	68.9	±56.4	0.65	0.78	0.57	±0.06	
4	0.0042	0.208	0.0218	2.724	0.0012	2.177	0.0263	0.070	1.2344	0.016	0.55	±0.22	96.2	±38.2	1.18	3.04	0.52	±0.03	
5	0.0065	0.205	0.0361	2.567	0.0019	1.415	0.0493	0.055	1.8975	0.005	0.55	±0.18	95.0	±30.9	1.42	5.69	0.59	±0.03	
6	0.0071	0.205	0.0382	2.549	0.0022	1.375	0.0615	0.056	2.1065	0.007	0.34	±0.16	59.9	±27.4	1.01	7.11	0.69	±0.04	
7	0.0079	0.202	0.0415	2.576	0.0025	1.249	0.0727	0.054	2.3352	0.003	0.15	±0.15	26.6	±25.3	0.48	8.40	0.75	±0.04	
8	0.0084	0.206	0.0423	2.578	0.0027	1.265	0.0799	0.054	2.5112	0.004	0.06	±0.14	11.0	±25.1	0.20	9.23	0.81	±0.04	
9	0.0082	0.204	0.0374	2.581	0.0026	0.867	0.0766	0.052	2.4342	0.002	0.02	±0.15	4.1	±25.2	0.07	8.85	0.88	±0.05	
10	0.0077	0.204	0.0342	2.592	0.0025	0.921	0.0690	0.055	2.2856	0.006	0.04	±0.15	7.7	±26.2	0.13	7.97	0.87	±0.04	
12	0.0104	0.203	0.0555	2.579	0.0033	0.959	0.0910	0.053	3.0928	0.004	0.04	±0.15	7.3	±26.7	0.12	10.52	0.70	±0.04	
14	0.0090	0.205	0.0765	2.532	0.0029	0.917	0.0768	0.054	2.6793	0.003	0.09	±0.16	15.6	±27.7	0.26	8.87	0.43	±0.02	
16	0.0075	0.204	0.0968	2.528	0.0023	0.890	0.0608	0.052	2.2261	0.004	0.12	±0.17	20.0	±28.9	0.31	7.02	0.27	±0.01	
18	0.0071	0.213	0.1197	2.531	0.0022	1.169	0.0536	0.055	2.1141	0.003	0.07	±0.19	12.1	±32.4	0.18	6.19	0.19	±0.01	
20	0.0062	0.204	0.1108	2.535	0.0017	1.040	0.0410	0.053	1.8464	0.003	0.07	±0.21	12.2	±35.8	0.16	4.73	0.16	±0.01	
21	0.0034	0.212	0.0762	2.553	0.0010	1.837	0.0223	0.063	1.0200	0.006	0.24	±0.22	42.3	±37.4	0.53	2.57	0.13	±0.01	
22	0.0020	0.211	0.0481	2.587	0.0005	4.892	0.0116	0.086	0.5928	0.006	0.25	±0.24	42.6	±41.8	0.48	1.34	0.10	±0.01	
24	0.0020	0.220	0.0564	2.557	0.0006	5.446	0.0120	0.111	0.5834	0.006	0.34	±0.24	58.5	±41.0	0.69	1.38	0.09	±0.00	
26	0.0017	0.233	0.0501	2.565	0.0005	6.449	0.0107	0.095	0.5088	0.009	0.42	±0.24	73.1	±42.3	0.88	1.23	0.09	±0.00	
28	0.0017	0.242	0.0464	2.566	0.0005	5.498	0.0093	0.113	0.5143	0.005	0.28	±0.29	48.0	±50.7	0.50	1.07	0.09	±0.00	
30	0.0014	0.258	0.0407	2.616	0.0003	8.370	0.0073	0.132	0.4080	0.008	0.40	±0.31	68.8	±54.3	0.70	0.84	0.08	±0.00	
40	0.0025	0.242	0.0946	2.535	0.0006	4.178	0.0139	0.082	0.7584	0.005	0.40	±0.29	68.7	±50.2	0.72	1.60	0.06	±0.00	
50	0.0023	0.220	0.1000	2.534	0.0005	5.218	0.0137	0.080	0.6798	0.007	0.42	±0.24	73.4	±42.2	0.85	1.58	0.06	±0.00	
<b>VIC78: J = 0.00009270 ± 0.00000006 (1σ) MDF = 0.992794 ± 0.00050 (1σ)</b>																			
3	0.0009	0.348	0.0045	12.467	0.0002	12.233	0.0040	2.412	0.2701	0.224	2.30	±0.58	385.2	±96.8	3.37	0.43	0.38	±0.10	

Step	36Ar [FA]	%1s	37Ar [FA]	%1s	38Ar [FA]	%1s	39Ar [FA]	%1s	40Ar [FA]	%1s	40(r)/39(k)	± 2s	Age (Ka)	± 2s	40Ar(r) (%)	39Ar(k) (%)	K/Ca	± 2s	
4	0.0014	0.287	0.0140	5.227	0.0004	7.672	0.0125	0.766	0.4308	0.140	2.09	± 0.22	349.5	± 37.3	6.05	1.37	0.38	± 0.04	
5	0.0012	0.308	0.0225	4.392	0.0005	5.296	0.0215	0.448	0.4112	0.147	2.21	± 0.13	369.6	± 21.1	11.51	2.35	0.41	± 0.04	
6	0.0014	0.293	0.0305	3.915	0.0007	3.865	0.0340	0.286	0.4956	0.122	2.11	± 0.09	353.1	± 14.5	14.44	3.72	0.48	± 0.04	
7	0.0008	0.359	0.0315	3.759	0.0007	3.941	0.0403	0.243	0.3203	0.189	2.25	± 0.05	376.5	± 9.0	28.24	4.41	0.55	± 0.04	
8	0.0009	0.355	0.0355	3.708	0.0009	3.788	0.0469	0.210	0.3724	0.162	2.19	± 0.05	367.8	± 8.6	27.59	5.12	0.57	± 0.04	
9	0.0008	0.353	0.0362	3.695	0.0009	3.227	0.0497	0.200	0.3428	0.176	2.23	± 0.04	373.4	± 7.3	32.31	5.44	0.59	± 0.04	
10	0.0008	0.368	0.0385	3.547	0.0009	2.925	0.0522	0.190	0.3545	0.171	2.21	± 0.04	370.4	± 7.3	32.51	5.71	0.58	± 0.04	
12	0.0011	0.312	0.0696	3.374	0.0015	1.768	0.0860	0.123	0.5249	0.115	2.20	± 0.03	369.4	± 5.1	36.10	9.41	0.53	± 0.04	
14	0.0012	0.318	0.0880	3.353	0.0016	1.972	0.0883	0.120	0.5285	0.115	2.14	± 0.03	358.8	± 5.1	35.73	9.65	0.43	± 0.03	
16	0.0015	0.251	0.1226	3.335	0.0017	1.524	0.0929	0.116	0.6451	0.094	2.15	± 0.03	360.2	± 5.2	30.93	10.16	0.33	± 0.02	
18	0.0014	0.277	0.1512	3.318	0.0016	1.802	0.0885	0.120	0.5938	0.102	2.14	± 0.03	358.6	± 5.5	31.86	9.68	0.25	± 0.02	
20	0.0010	0.311	0.1580	3.314	0.0013	1.897	0.0725	0.142	0.4434	0.136	2.14	± 0.03	359.5	± 5.8	35.04	7.93	0.20	± 0.01	
21	0.0007	0.371	0.1164	3.324	0.0009	3.117	0.0510	0.194	0.3203	0.189	2.11	± 0.04	353.5	± 7.3	33.50	5.57	0.19	± 0.01	
22	0.0006	0.421	0.1003	3.338	0.0008	3.258	0.0443	0.222	0.2806	0.215	2.17	± 0.05	363.5	± 8.2	34.16	4.84	0.19	± 0.01	
24	0.0006	0.440	0.1036	3.340	0.0007	4.041	0.0377	0.259	0.2671	0.226	2.18	± 0.06	365.1	± 10.0	30.64	4.11	0.16	± 0.01	
26	0.0006	0.411	0.1206	3.324	0.0007	3.903	0.0379	0.257	0.2753	0.219	2.43	± 0.06	407.8	± 9.7	33.46	4.14	0.14	± 0.01	
28	0.0008	0.376	0.1145	3.334	0.0007	4.131	0.0305	0.318	0.2911	0.208	2.38	± 0.07	398.9	± 12.6	24.85	3.33	0.11	± 0.01	
30	0.0004	0.578	0.0990	3.356	0.0005	5.790	0.0243	0.399	0.1716	0.352	2.28	± 0.08	382.7	± 14.0	32.17	2.65	0.11	± 0.01	
<b>VIC81: J = 0.00009260 ± 0.00000012 (1σ) MDF = 0.993784 ± 0.00040 (1σ)</b>																			
3	0.0093	0.166	0.0056	10.347	0.0018	1.535	0.0024	7.090	2.7355	0.013	0.15	± 4.90	25.0	± 819.6	0.01	0.34	0.18	± 0.05	
4	0.0122	0.165	0.0188	4.422	0.0025	1.235	0.0105	1.592	3.6394	0.010	3.10	± 1.45	518.6	± 242.0	0.89	1.49	0.24	± 0.02	
5	0.0123	0.161	0.0305	3.883	0.0025	1.080	0.0226	0.742	3.6905	0.009	3.09	± 0.67	518.1	± 111.4	1.90	3.21	0.32	± 0.03	
6	0.0109	0.168	0.0431	3.632	0.0024	1.286	0.0357	0.471	3.3392	0.010	3.48	± 0.39	582.7	± 64.5	3.72	5.07	0.36	± 0.03	
7	0.0075	0.163	0.0443	3.588	0.0019	1.160	0.0397	0.424	2.3439	0.015	3.48	± 0.23	582.6	± 39.3	5.90	5.65	0.39	± 0.03	

Step	36Ar [fA]	%1s	37Ar [fA]	%1s	38Ar [fA]	%1s	39Ar [fA]	%1s	40Ar [fA]	%1s	40(r)/39(k)	Age (Ka)	± 2s	40Ar(r) (%)	39Ar(k) (%)	K/Ca	± 2s
8	0.0055	0.183	0.0402	3.636	0.0015	1.786	0.0384	0.438	1.7390	0.020	3.46	579.3	± 32.0	7.64	5.46	0.41	± 0.03
9	0.0047	0.164	0.0401	3.566	0.0014	2.020	0.0410	0.410	1.5241	0.023	3.52	588.5	± 24.3	9.45	5.82	0.44	± 0.03
10	0.0029	0.168	0.0367	3.698	0.0011	2.612	0.0398	0.424	1.0024	0.034	3.48	582.0	± 16.6	13.79	5.65	0.47	± 0.03
12	0.0045	0.172	0.0560	3.478	0.0016	1.447	0.0598	0.283	1.5219	0.023	3.47	580.9	± 16.4	13.63	8.50	0.46	± 0.03
14	0.0028	0.185	0.0604	3.480	0.0012	2.206	0.0564	0.300	1.0131	0.034	3.43	574.8	± 11.8	19.10	8.01	0.40	± 0.03
16	0.0024	0.172	0.0809	3.382	0.0012	1.999	0.0557	0.304	0.8848	0.039	3.42	572.6	± 10.0	21.52	7.91	0.30	± 0.02
18	0.0017	0.199	0.0987	3.368	0.0010	3.022	0.0505	0.334	0.6637	0.051	3.43	574.9	± 9.2	26.10	7.17	0.22	± 0.01
20	0.0015	0.208	0.1210	3.360	0.0010	2.706	0.0506	0.334	0.6174	0.055	3.43	574.8	± 8.9	28.06	7.17	0.18	± 0.01
21	0.0010	0.216	0.0987	3.369	0.0007	4.514	0.0385	0.437	0.4116	0.083	3.42	572.4	± 8.9	31.91	5.46	0.17	± 0.01
22	0.0007	0.216	0.0858	3.375	0.0005	5.065	0.0307	0.546	0.3150	0.108	3.40	568.6	± 9.7	33.07	4.36	0.15	± 0.01
24	0.0007	0.218	0.1041	3.360	0.0005	5.678	0.0332	0.506	0.3121	0.109	3.39	567.3	± 9.0	35.95	4.71	0.14	± 0.01
26	0.0010	0.219	0.1302	3.350	0.0006	4.149	0.0353	0.476	0.4005	0.085	3.41	570.1	± 10.0	29.96	5.01	0.12	± 0.01
28	0.0007	0.298	0.1249	3.372	0.0005	4.553	0.0319	0.527	0.2916	0.117	3.44	576.0	± 10.3	37.54	4.52	0.11	± 0.01
30	0.0008	0.289	0.1448	3.335	0.0005	5.352	0.0317	0.530	0.3222	0.106	3.42	573.1	± 11.1	33.55	4.49	0.09	± 0.01

<b>VIC82: J = 0.00009130 ± 0.00000026 (1σ) MDF = 0.992597 ± 0.00040 (1σ)</b>																	
3	0.0004	0.398	0.0077	6.726	0.0002	13.723	0.0071	1.224	0.1524	0.018	4.11	678.7	± 50.4	19.20	0.68	0.40	± 0.05
4	0.0009	0.232	0.0171	4.120	0.0005	4.940	0.0248	0.355	0.3816	0.010	4.03	665.0	± 31.3	25.11	2.27	0.62	± 0.05
5	0.0010	0.239	0.0274	3.733	0.0008	3.362	0.0429	0.209	0.4839	0.006	3.98	657.6	± 20.6	33.90	3.92	0.67	± 0.05
6	0.0008	0.213	0.0306	3.825	0.0008	3.991	0.0457	0.195	0.4313	0.005	4.01	662.1	± 15.8	40.87	4.19	0.64	± 0.05
7	0.0008	0.226	0.0349	3.713	0.0009	3.421	0.0531	0.169	0.4488	0.010	4.03	666.0	± 13.4	45.84	4.86	0.65	± 0.05
8	0.0007	0.257	0.0379	3.501	0.0008	3.450	0.0556	0.162	0.4268	0.007	4.05	668.4	± 11.7	50.71	5.09	0.63	± 0.04
9	0.0005	0.247	0.0340	3.535	0.0008	3.368	0.0512	0.176	0.3654	0.006	4.05	668.8	± 10.5	54.56	4.69	0.65	± 0.05
10	0.0004	0.285	0.0334	3.879	0.0007	3.316	0.0489	0.184	0.3246	0.007	4.05	668.6	± 9.6	58.56	4.47	0.63	± 0.05
12	0.0007	0.248	0.0525	3.500	0.0011	2.737	0.0737	0.125	0.5022	0.005	4.01	662.5	± 9.7	56.62	6.75	0.60	± 0.04

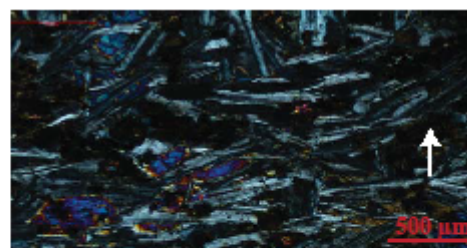
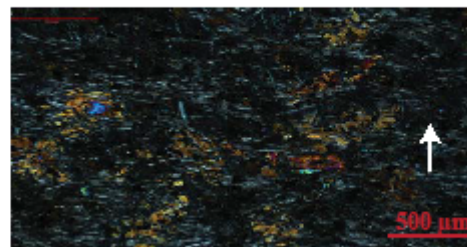
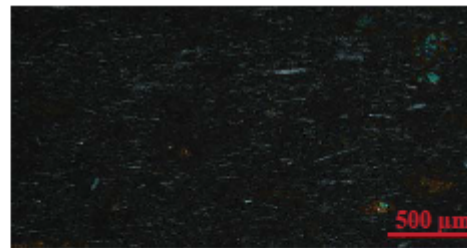
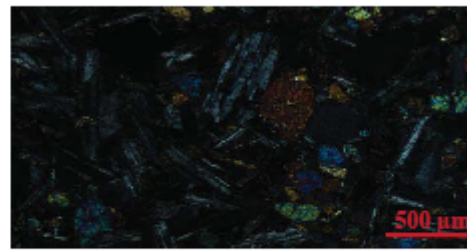
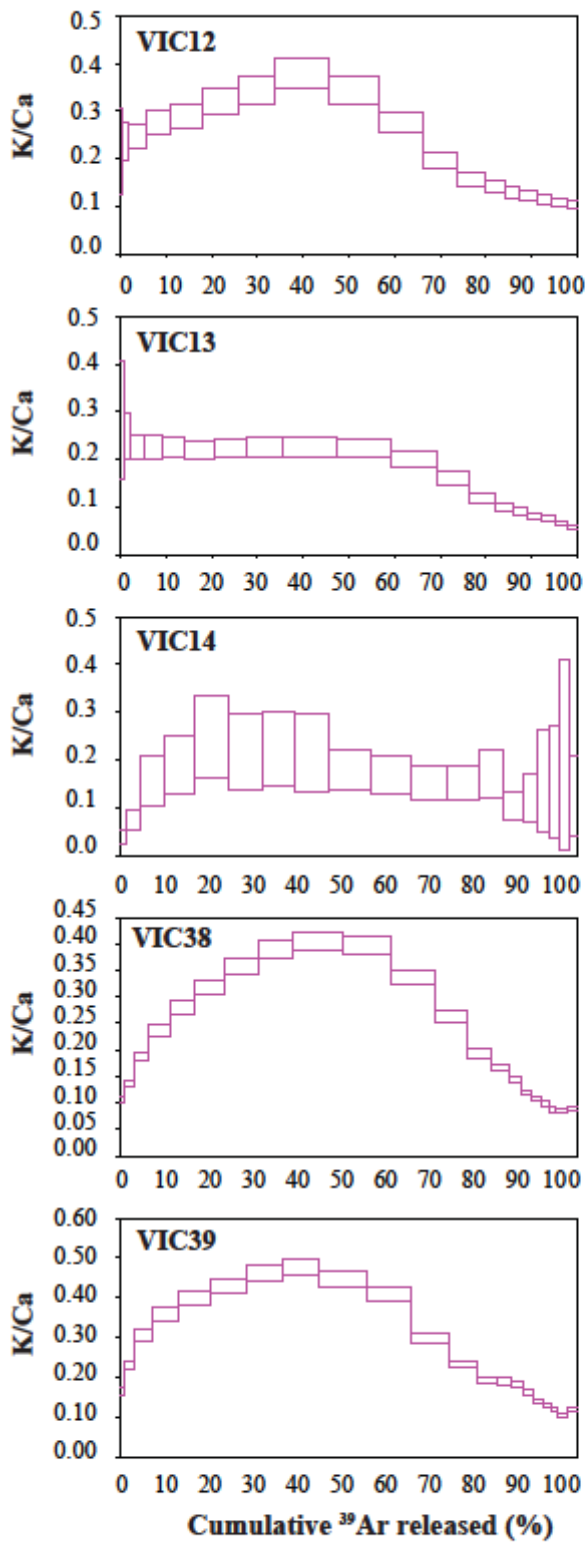
Step	36Ar [fA]	%1s	37Ar [fA]	%1s	38Ar [fA]	%1s	39Ar [fA]	%1s	40Ar [fA]	%1s	40(r)/39(k)	±2s	Age (Ka)	±2s	40Ar(t) (%)	39Ar(k) (%)	K/Ca	±2s	
14	0.0007	0.240	0.0662	3.410	0.0011	1.742	0.0774	0.107	0.5074	0.009	4.02	±0.06	663.1	±9.1	58.83	7.08	0.50	±0.03	
16	0.0007	0.256	0.0957	3.375	0.0012	1.666	0.0795	0.104	0.5219	0.008	3.98	±0.06	657.2	±9.3	58.23	7.27	0.36	±0.02	
18	0.0008	0.235	0.1348	3.349	0.0013	2.035	0.0851	0.099	0.5519	0.007	3.98	±0.06	656.7	±9.1	58.92	7.79	0.27	±0.02	
20	0.0008	0.263	0.1715	3.345	0.0014	1.836	0.0904	0.095	0.5842	0.008	3.97	±0.06	655.7	±9.2	59.02	8.27	0.23	±0.02	
21	0.0006	0.225	0.1485	3.347	0.0011	2.302	0.0697	0.118	0.4506	0.009	3.96	±0.06	653.4	±9.2	58.74	6.37	0.20	±0.01	
22	0.0005	0.239	0.1278	3.351	0.0008	3.461	0.0561	0.142	0.3636	0.010	3.95	±0.06	652.2	±9.4	58.49	5.13	0.19	±0.01	
24	0.0005	0.235	0.1337	3.347	0.0009	3.886	0.0551	0.146	0.3595	0.012	3.93	±0.06	649.2	±9.6	57.83	5.04	0.18	±0.01	
26	0.0006	0.322	0.1708	3.344	0.0011	2.677	0.0641	0.126	0.4193	0.008	3.94	±0.06	650.5	±9.9	57.80	5.86	0.16	±0.01	
28	0.0006	0.257	0.1760	3.349	0.0009	2.511	0.0606	0.133	0.3981	0.010	3.94	±0.06	650.0	±9.8	57.50	5.54	0.15	±0.01	
30	0.0005	0.256	0.1655	3.347	0.0008	3.870	0.0522	0.153	0.3436	0.014	3.94	±0.06	649.5	±10.0	57.32	4.77	0.14	±0.01	
<b>VIC91: J = 0.00009140 ± 0.00000034 (1σ) MDF = 0.993804 ± 0.00030 (1σ)</b>																			
3	0.0010	0.528	0.0011	13.006	0.0002	14.593	0.0006	4.118	0.3059	0.520	0.98	±8.24	162.2	±1361.2	0.19	0.08	0.23	±0.06	
4	0.0038	0.183	0.0055	3.080	0.0008	4.015	0.0036	0.671	1.1377	0.140	1.33	±2.28	219.6	±376.9	0.42	0.50	0.28	±0.02	
5	0.0046	0.170	0.0129	2.257	0.0010	2.945	0.0101	0.249	1.3737	0.116	0.39	±0.93	64.9	±153.4	0.29	1.41	0.34	±0.02	
6	0.0049	0.167	0.0212	2.257	0.0012	2.993	0.0197	0.129	1.4522	0.110	0.00	±0.49	0.6	±81.8	0.00	2.75	0.40	±0.02	
7	0.0043	0.177	0.0258	2.181	0.0011	2.891	0.0267	0.096	1.2892	0.123	0.03	±0.33	4.7	±55.2	0.06	3.72	0.45	±0.02	
8	0.0047	0.171	0.0325	2.131	0.0014	2.242	0.0370	0.076	1.3981	0.114	0.08	±0.26	14.0	±42.3	0.22	5.16	0.49	±0.02	
9	0.0041	0.174	0.0325	2.139	0.0013	2.562	0.0401	0.069	1.2294	0.130	0.18	±0.21	30.1	±34.9	0.59	5.60	0.53	±0.02	
10	0.0044	0.186	0.0352	2.112	0.0014	2.286	0.0445	0.063	1.3045	0.122	0.18	±0.20	29.3	±33.8	0.60	6.20	0.54	±0.02	
12	0.0069	0.145	0.0550	2.095	0.0022	1.527	0.0678	0.051	2.0639	0.077	0.26	±0.19	43.2	±31.6	0.86	9.45	0.53	±0.02	
14	0.0077	0.147	0.0628	2.097	0.0024	1.398	0.0742	0.045	2.2931	0.069	0.34	±0.19	55.7	±31.9	1.09	10.34	0.51	±0.02	
16	0.0079	0.142	0.0687	2.092	0.0024	1.199	0.0695	0.051	2.3701	0.067	0.25	±0.21	41.0	±35.0	0.73	9.69	0.43	±0.02	
18	0.0077	0.139	0.0724	2.094	0.0022	1.343	0.0584	0.054	2.3121	0.069	0.36	±0.24	59.0	±40.4	0.90	8.14	0.35	±0.01	
20	0.0078	0.143	0.0859	2.092	0.0021	1.497	0.0494	0.063	2.3209	0.069	0.30	±0.29	49.2	±48.4	0.63	6.89	0.25	±0.01	

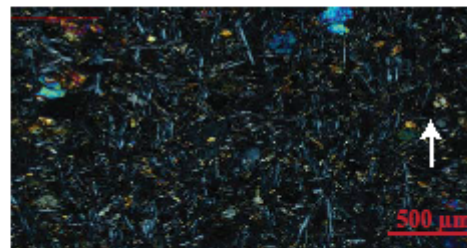
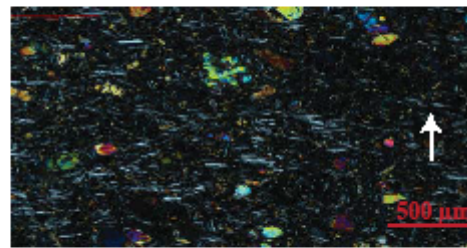
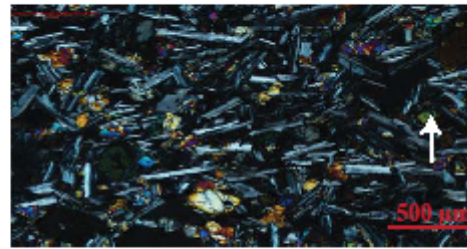
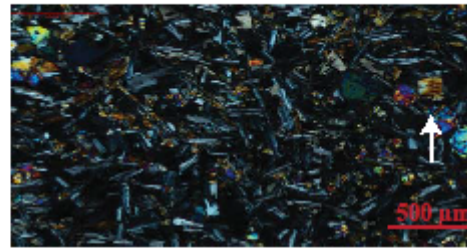
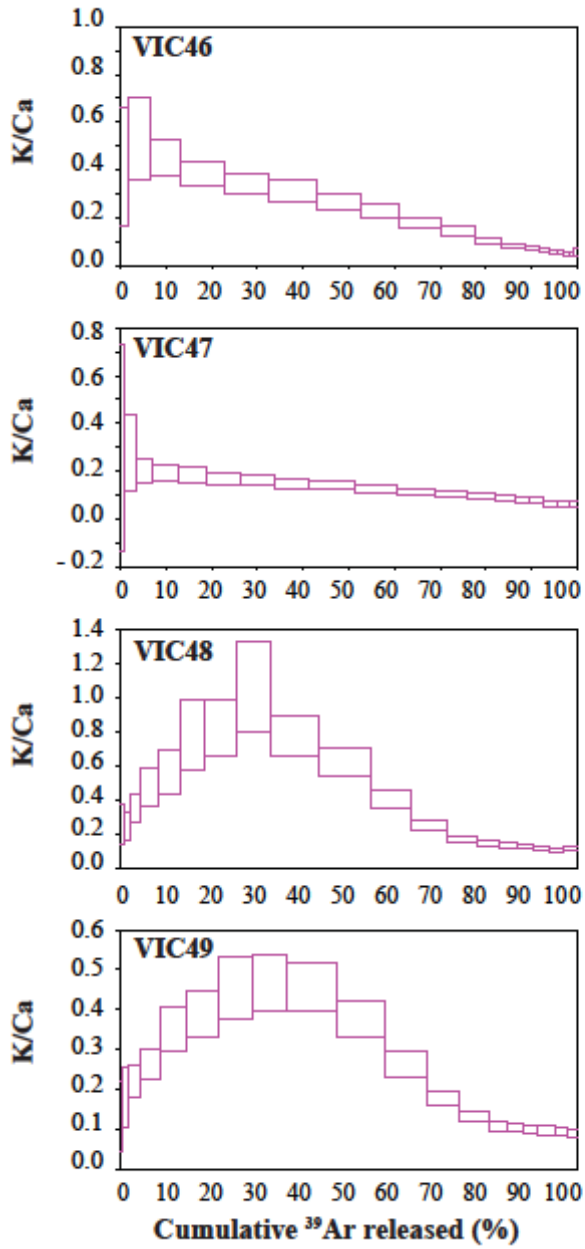
Step	36Ar [fA]	%1s	37Ar [fA]	%1s	38Ar [fA]	%1s	39Ar [fA]	%1s	40Ar [fA]	%1s	40(r)/39(k)	Age (Ka)	±2s	40Ar(r) (%)	39Ar(k) (%)	K/Ca	±2s	
21	0.0062	0.151	0.0742	2.092	0.0016	2.318	0.0355	0.075	1.8339	0.087	0.31	50.9	± 54.6	0.60	4.95	0.21	± 0.01	
22	0.0051	0.171	0.0683	2.092	0.0013	2.444	0.0265	0.098	1.5267	0.104	0.42	68.6	± 63.8	0.72	3.69	0.17	± 0.01	
24	0.0056	0.157	0.0799	2.091	0.0014	2.422	0.0261	0.101	1.6690	0.095	0.45	73.8	± 68.9	0.70	3.63	0.14	± 0.01	
26	0.0065	0.159	0.1026	2.089	0.0015	1.950	0.0265	0.102	1.9284	0.083	0.24	39.8	± 77.9	0.33	3.69	0.11	± 0.00	
28	0.0061	0.149	0.1064	2.088	0.0014	2.311	0.0228	0.112	1.8161	0.088	0.20	33.8	± 84.6	0.26	3.17	0.09	± 0.00	
30	0.0053	0.166	0.0960	2.090	0.0012	2.728	0.0195	0.132	1.5663	0.102	0.33	53.9	± 88.3	0.41	2.72	0.09	± 0.00	
40	0.0111	0.134	0.2136	2.086	0.0025	1.273	0.0317	0.083	3.2882	0.049	0.10	16.2	± 105.4	0.09	4.40	0.06	± 0.00	
50	0.0082	0.144	0.1621	2.086	0.0018	2.023	0.0276	0.095	2.4233	0.066	0.18	29.1	± 91.3	0.20	3.83	0.07	± 0.00	
<b>VIC92: J = 0.00009160 ± 0.00000015 (1σ) MDF = 0.992597 ± 0.00040 (1σ)</b>																		
3	0.0127	0.161	0.0040	19.186	0.0025	1.084	0.0041	1.314	3.7289	0.014	15.41	2.55	± 3.85	1.68	0.83	0.44	± 0.17	
4	0.0294	0.163	0.0110	7.086	0.0056	0.495	0.0107	0.502	8.6635	0.006	15.02	2.49	± 3.39	1.86	2.18	0.42	± 0.06	
5	0.0344	0.161	0.0206	4.970	0.0067	0.355	0.0186	0.292	10.1623	0.005	11.41	1.89	± 2.27	2.09	3.79	0.39	± 0.04	
6	0.0287	0.163	0.0296	4.080	0.0057	0.583	0.0240	0.228	8.5112	0.007	8.81	1.46	± 1.48	2.48	4.88	0.35	± 0.03	
7	0.0250	0.164	0.0420	3.752	0.0051	0.488	0.0295	0.188	7.4741	0.008	8.17	1.35	± 1.05	3.22	6.01	0.30	± 0.02	
8	0.0203	0.161	0.0509	3.592	0.0042	0.669	0.0311	0.180	6.1112	0.009	7.62	1.26	± 0.80	3.87	6.32	0.26	± 0.02	
9	0.0178	0.163	0.0581	3.539	0.0038	0.548	0.0326	0.171	5.4058	0.010	7.89	1.31	± 0.68	4.75	6.63	0.24	± 0.02	
10	0.0145	0.165	0.0650	3.509	0.0031	0.819	0.0337	0.165	4.4505	0.012	7.83	1.30	± 0.54	5.92	6.85	0.22	± 0.02	
12	0.0194	0.165	0.1074	3.366	0.0043	0.727	0.0489	0.078	5.9884	0.006	7.91	1.31	± 0.49	6.44	9.93	0.20	± 0.01	
14	0.0156	0.162	0.1177	3.367	0.0035	0.915	0.0494	0.075	4.8802	0.008	7.74	1.28	± 0.39	7.82	10.04	0.18	± 0.01	
16	0.0116	0.167	0.1148	3.367	0.0027	1.164	0.0425	0.081	3.6884	0.009	7.65	1.27	± 0.35	8.79	8.63	0.16	± 0.01	
18	0.0102	0.165	0.1235	3.369	0.0024	1.292	0.0381	0.094	3.2397	0.011	7.64	1.27	± 0.34	8.96	7.73	0.13	± 0.01	
20	0.0069	0.168	0.1135	3.363	0.0017	1.942	0.0282	0.115	2.1927	0.015	7.67	1.27	± 0.31	9.84	5.73	0.11	± 0.01	
21	0.0054	0.164	0.0943	3.384	0.0013	2.637	0.0216	0.151	1.7377	0.019	7.78	1.29	± 0.32	9.64	4.38	0.10	± 0.01	
22	0.0038	0.184	0.0768	3.446	0.0009	3.599	0.0162	0.191	1.2312	0.027	7.86	1.30	± 0.32	10.31	3.29	0.09	± 0.01	

Step	<sup>36</sup> Ar [fA]	%1s	<sup>37</sup> Ar [fA]	%1s	<sup>38</sup> Ar [fA]	%1s	<sup>39</sup> Ar [fA]	%1s	<sup>40</sup> Ar [fA]	%1s	40(r)/ 39(k)	± 2s	Age (Ka)	± 2s	<sup>40</sup> Ar(r) (%)	<sup>39</sup> Ar(k) (%)	K/Ca	± 2s
24	0.0040	0.180	0.0893	3.382	0.0010	4.203	0.0167	0.187	1.2897	0.026	8.03	± 0.32	1.33	± 0.05	10.36	3.39	0.08	± 0.01
26	0.0041	0.165	0.1007	3.389	0.0010	3.654	0.0177	0.176	1.3075	0.025	7.90	± 0.29	1.31	± 0.05	10.63	3.58	0.08	± 0.01
28	0.0034	0.171	0.0923	3.396	0.0008	3.639	0.0152	0.207	1.1018	0.030	8.02	± 0.29	1.33	± 0.05	11.01	3.08	0.07	± 0.00
30	0.0028	0.169	0.0910	3.385	0.0007	4.520	0.0135	0.233	0.9182	0.036	7.76	± 0.28	1.28	± 0.05	11.31	2.73	0.06	± 0.00

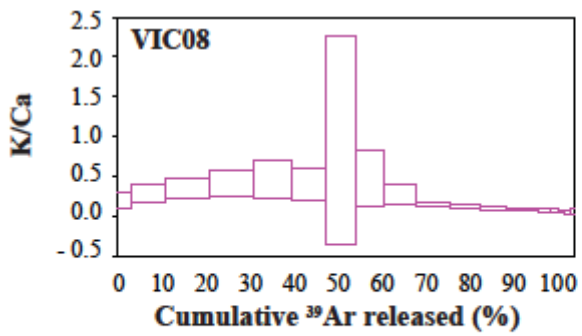
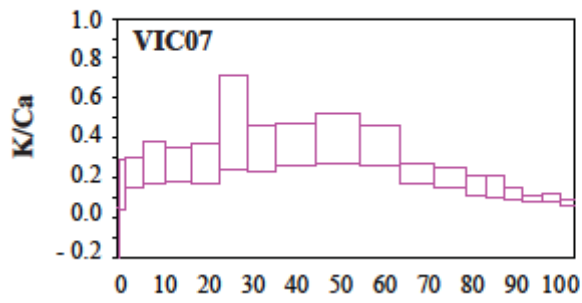
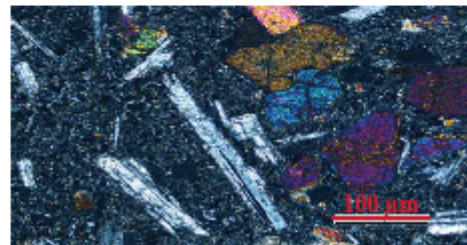
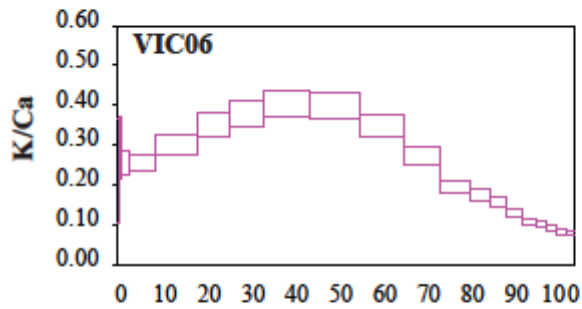
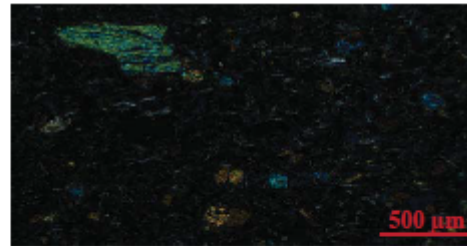
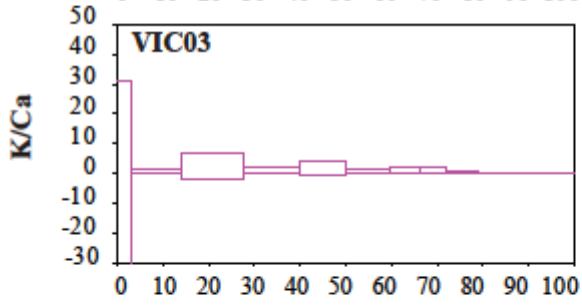
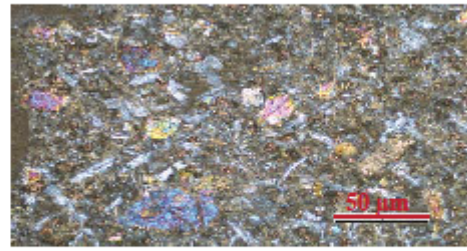
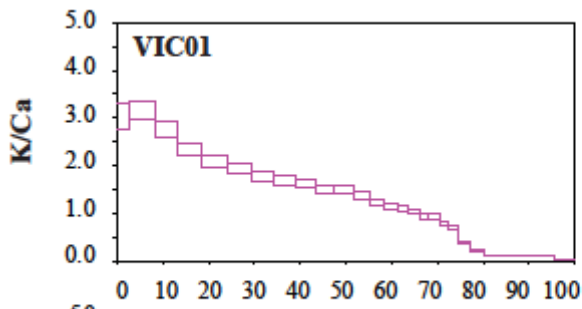


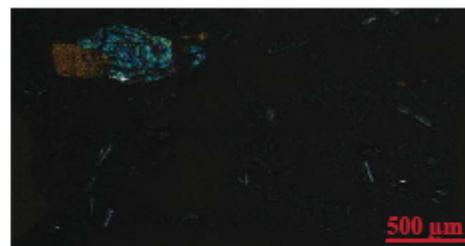
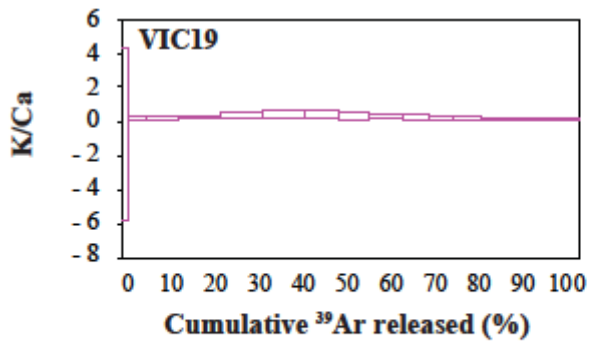
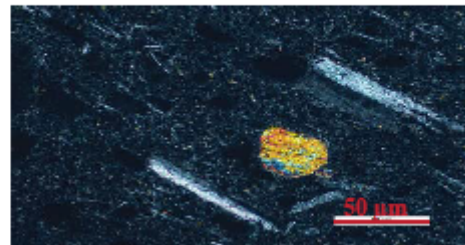
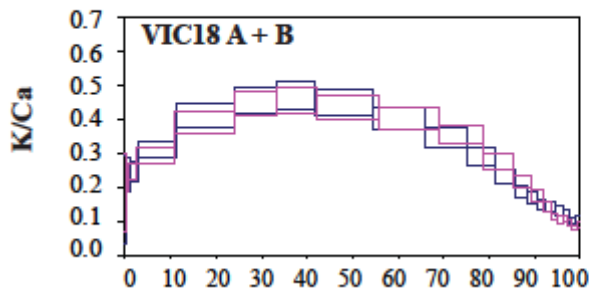
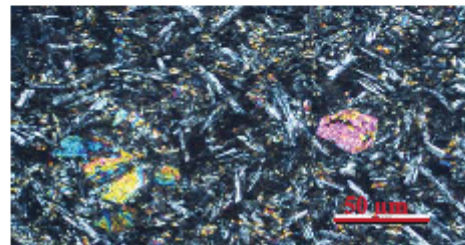
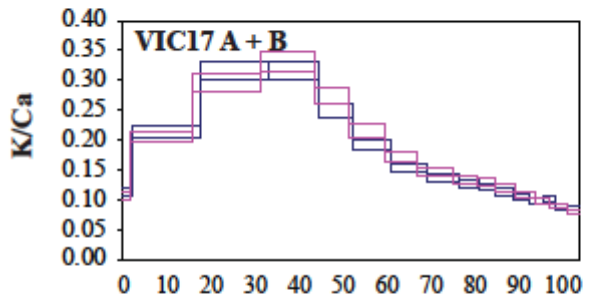
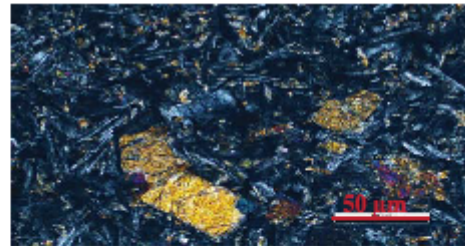
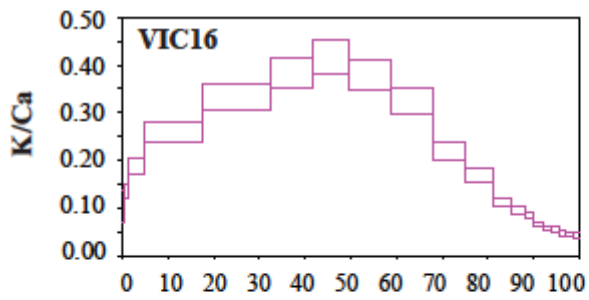
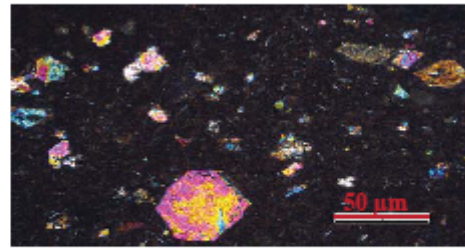
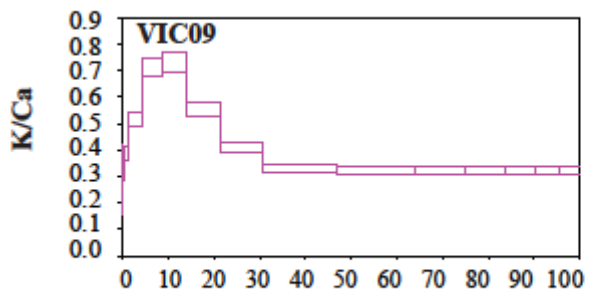
APPENDIX F. SUPPLEMENTARY DATA CHAPTER 4 - K/CA  
DIAGRAMS AND THIN SECTION PHOTOS OF THE NEWER  
PLAINS

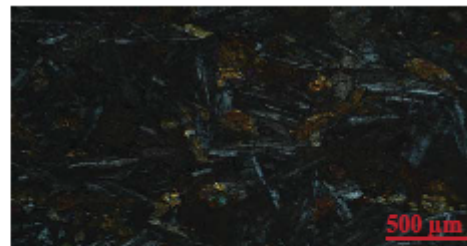
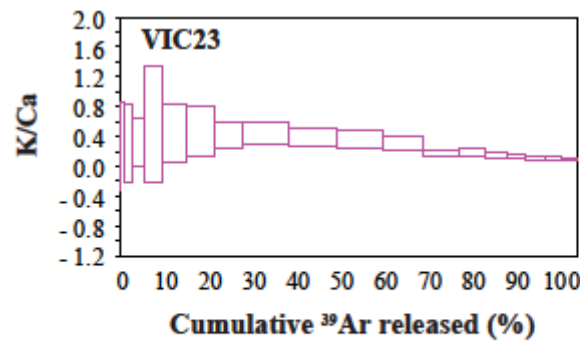
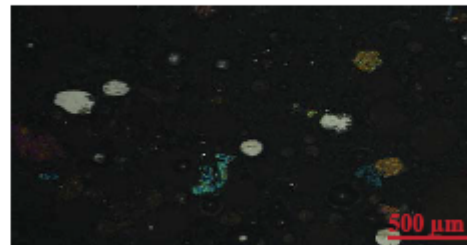
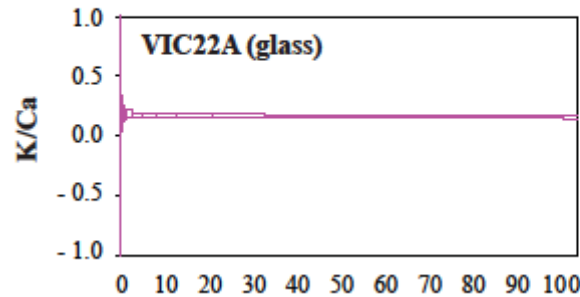
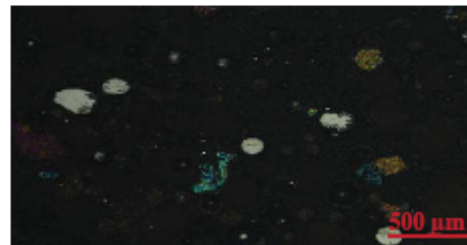
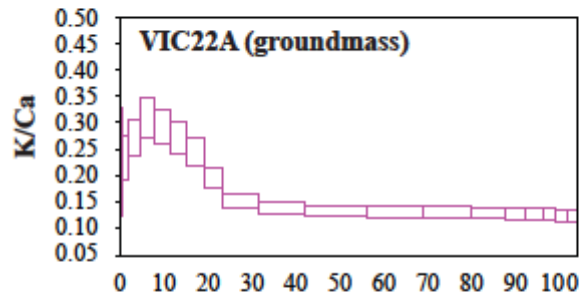
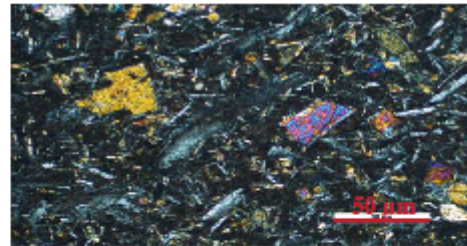
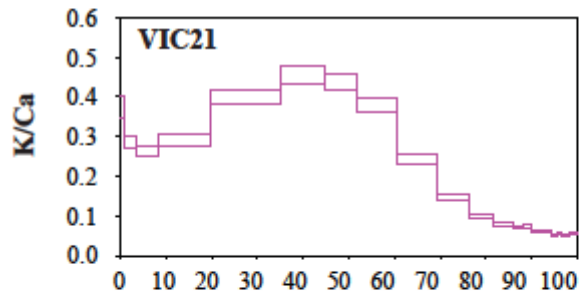
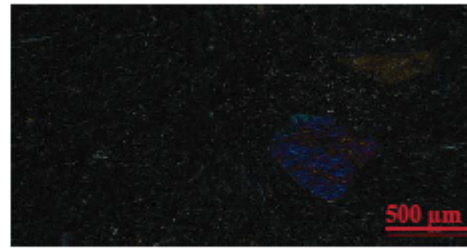
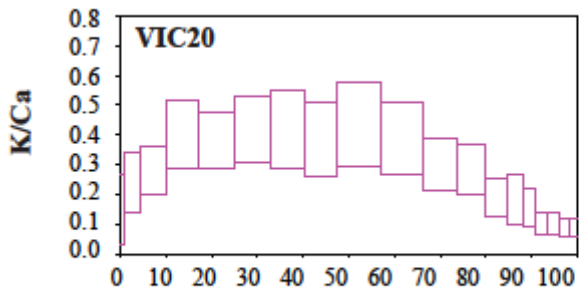


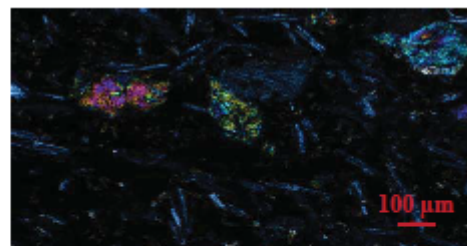
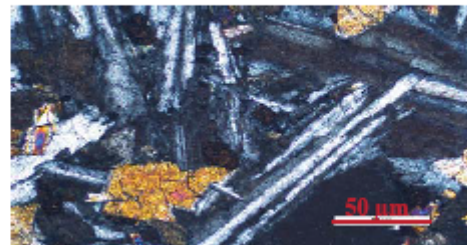
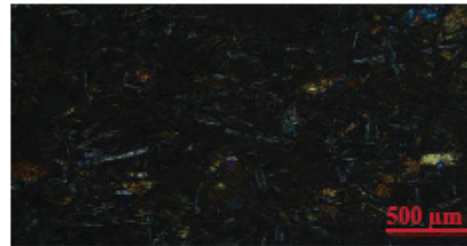
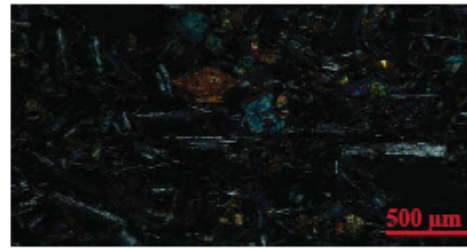
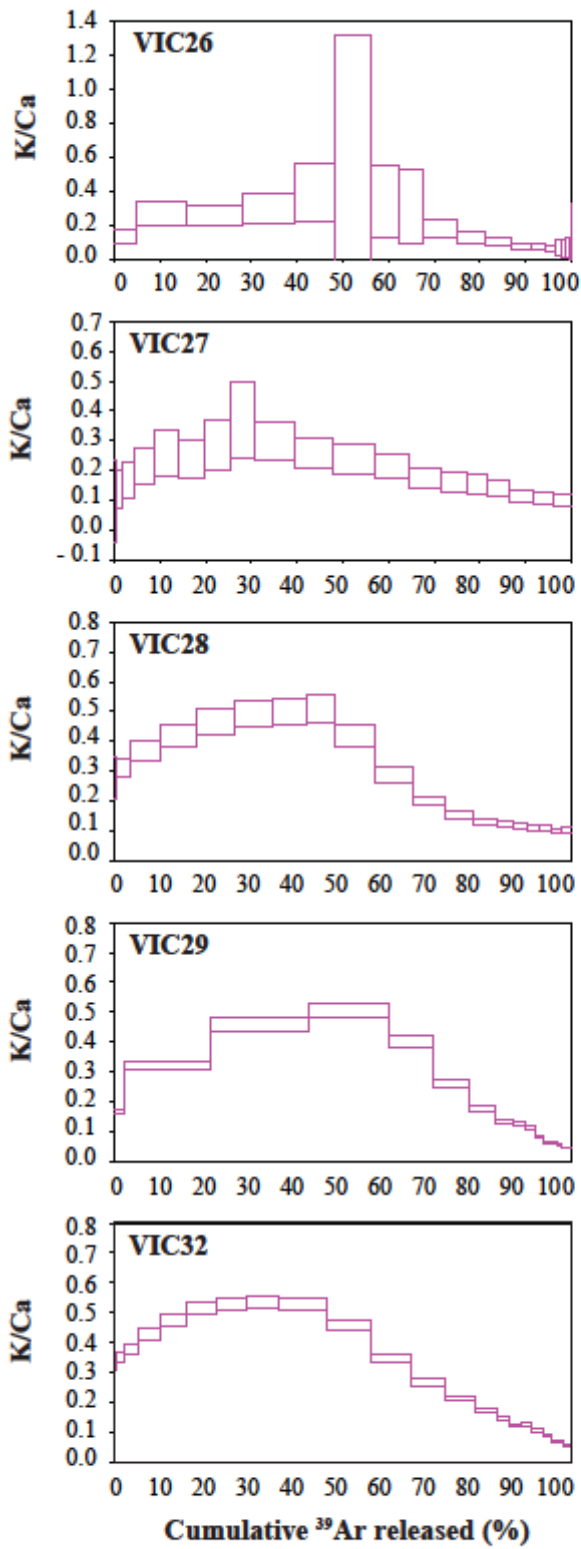


APPENDIX G. SUPPLEMENTARY DATA CHAPTER 4 - K/CA  
DIAGRAMS AND THIN SECTION PHOTOS OF THE NEWER CONES

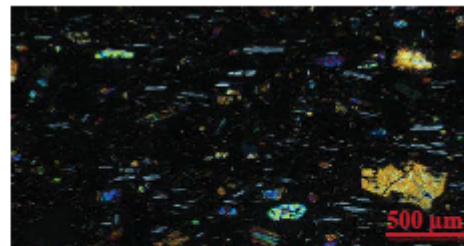
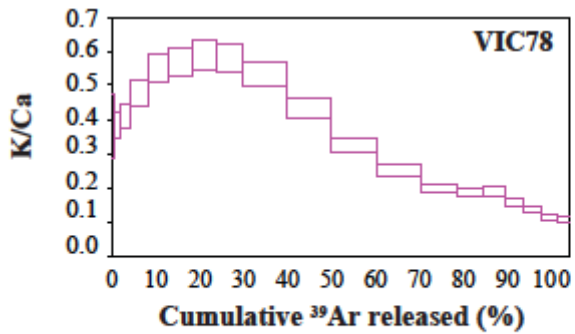
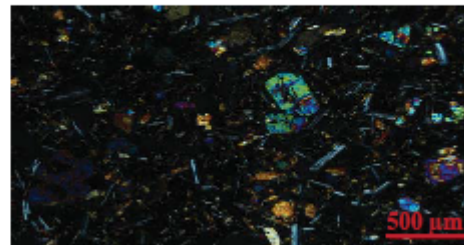
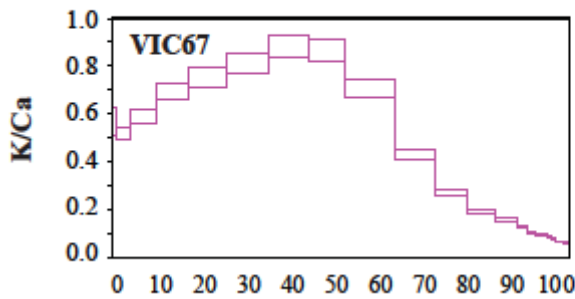
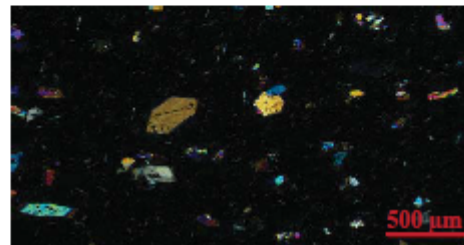
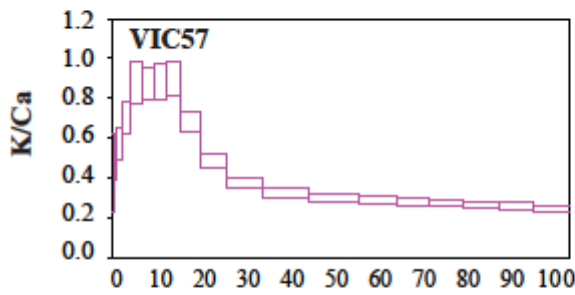
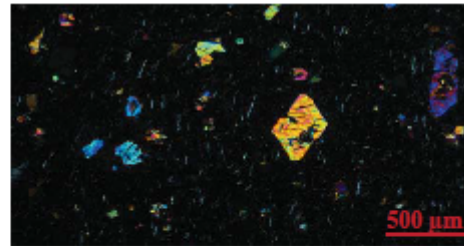
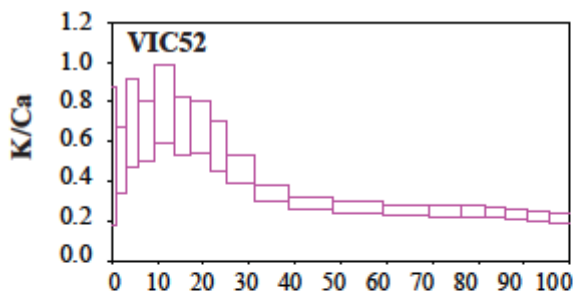
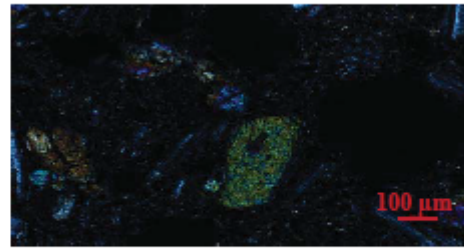
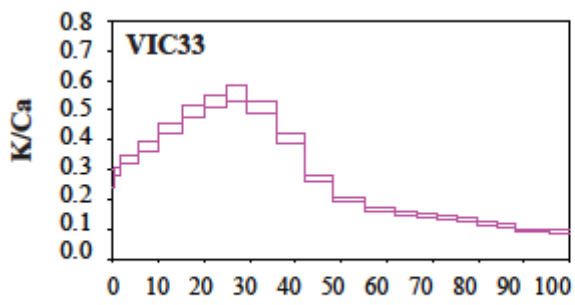


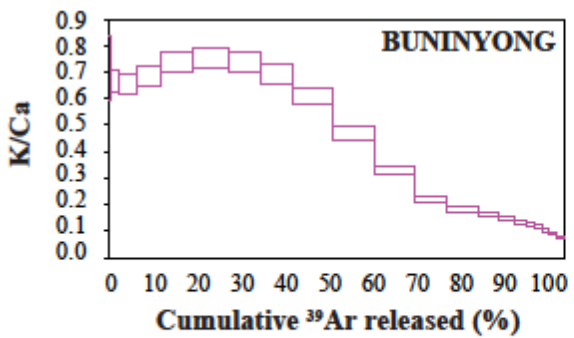
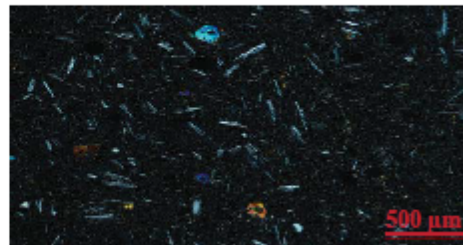
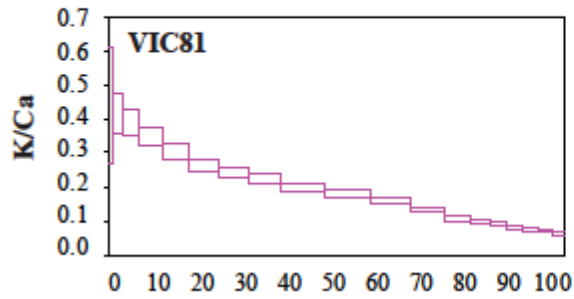
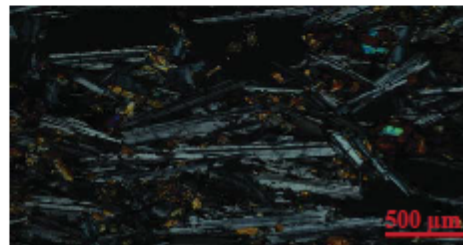
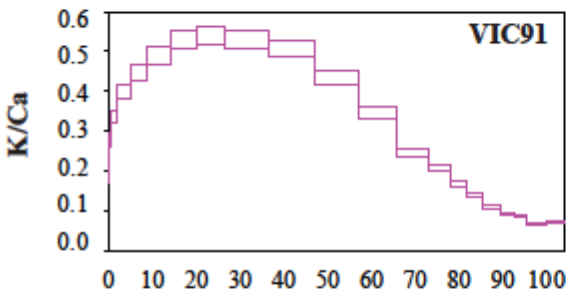
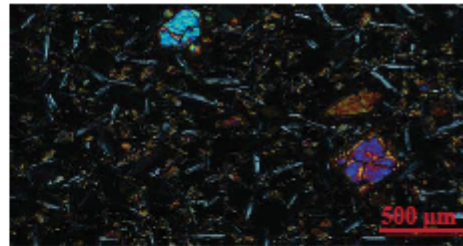
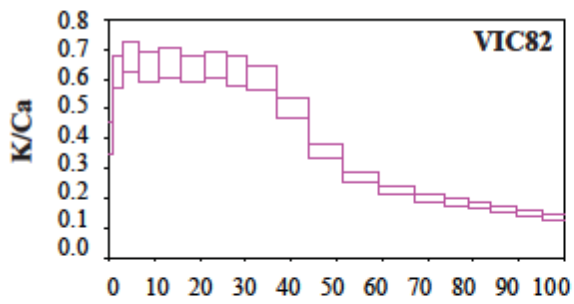
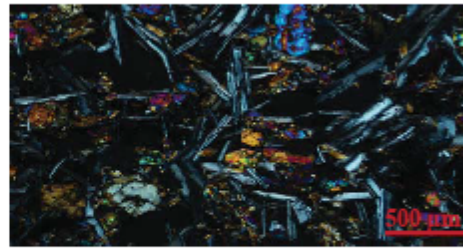
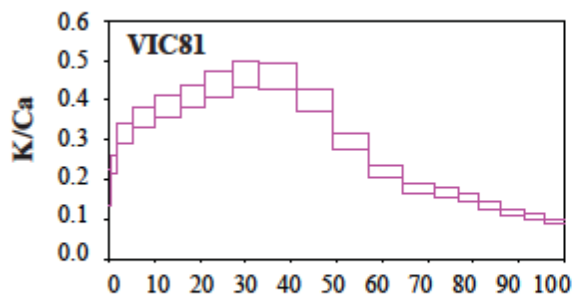




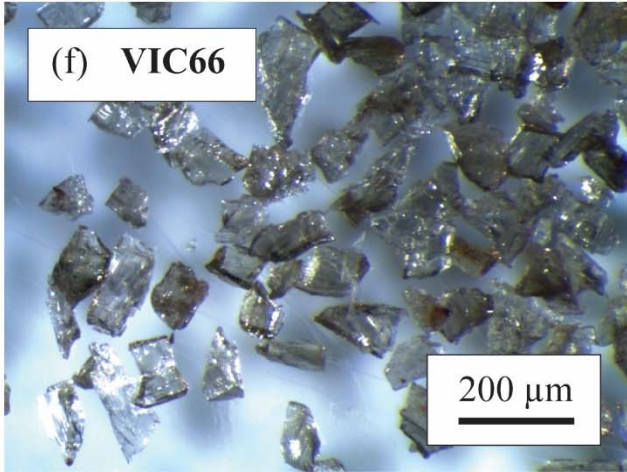
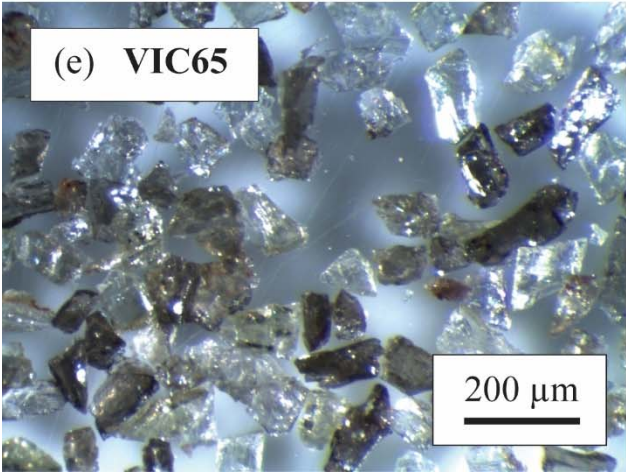
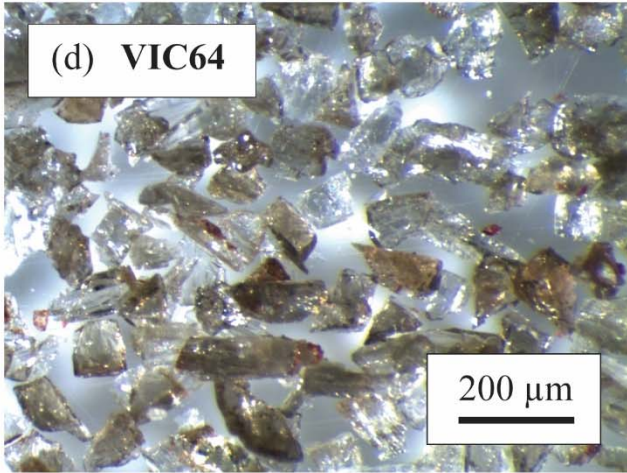
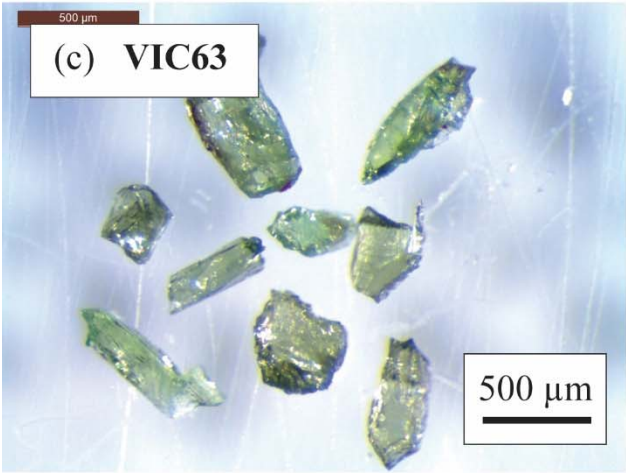
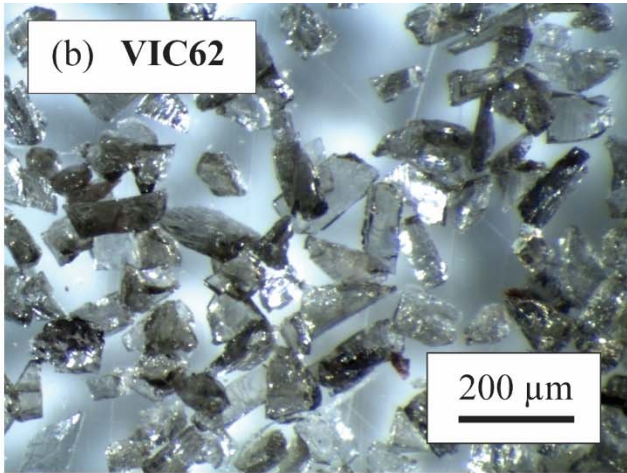
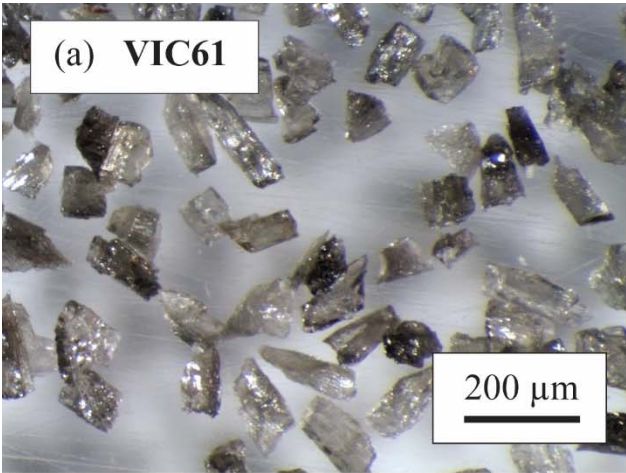




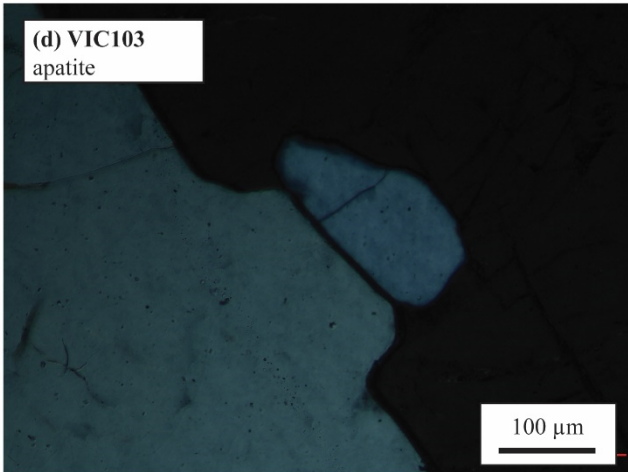
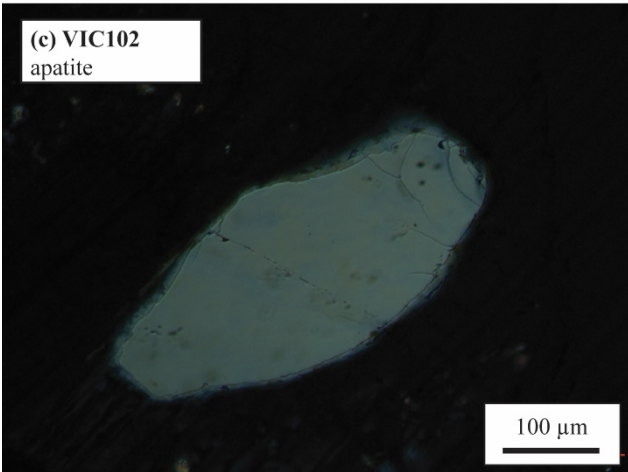
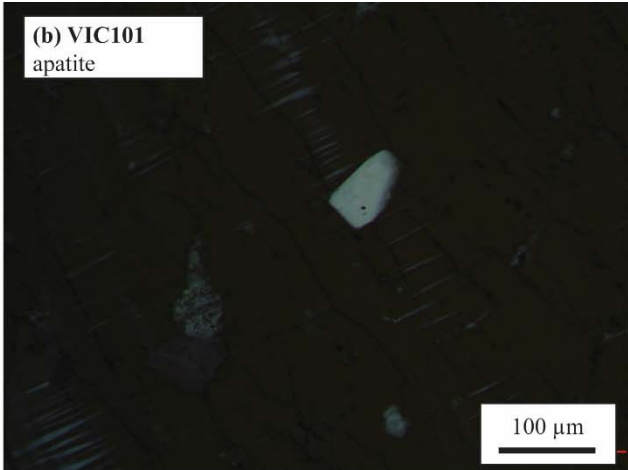
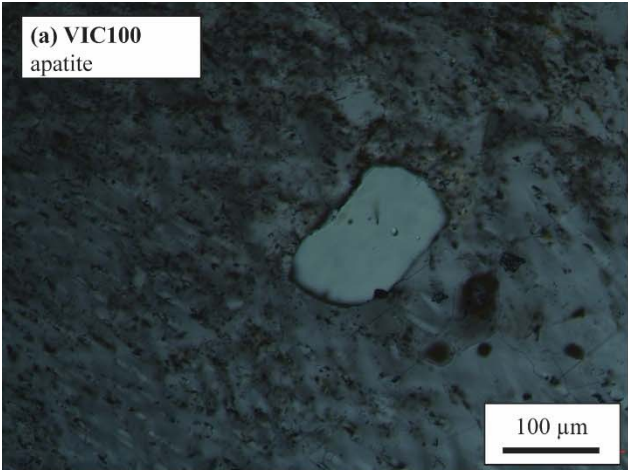




APPENDIX H. SUPPLEMENTARY DATA CHAPTER 5 – PYROXENE  
SAMPLES



APPENDIX I. SUPPLEMENTARY DATA CHAPTER 5 – APATITE  
THIN SECTIONS



APPENDIX J. SUPPLEMENTARY DATA CHAPTER 5 – ISOTOPE  
ABUNDANCES PYROXENE SAMPLES

Step	$^{36}\text{Ar}$ [V]	%1s	$^{37}\text{Ar}$ [V]	%1s	$^{38}\text{Ar}$ [V]	%1s	$^{39}\text{Ar}$ [V]	%1s	$^{40}\text{Ar}$ [V]	%1s	K/Ca	2s	$^{37}\text{Ar}/^{36}\text{Ar}$	$1\sigma$ (Abs)	$^{38}\text{Ar}/^{36}\text{Ar}$	$1\sigma$ (Abs)	
<b>VIC61: <math>J = 0.00009230 \pm 0.00000022</math> (<math>1\sigma</math>)   MDF = <math>0.992132 \pm 0.000694</math> (<math>1\sigma</math>)</b>																	
1	0.002	0.202	-0.002	186.120	0.000	0.220	0.000	22.383	0.640	0.092	-0.011	0.043	-0.78	-1.45	0.1897	0.0006	
2	0.012	0.168	0.004	94.135	0.002	0.173	0.001	1.595	3.632	0.026	0.082	0.155	0.30	0.29	0.1895	0.0005	
3	0.006	0.173	0.002	125.623	0.001	0.186	0.000	3.652	1.762	0.033	0.057	0.143	0.41	0.51	0.1897	0.0005	
4	0.004	0.190	0.000	7094.379	0.001	0.234	0.000	5.861	1.081	0.014	-1.416	200.924	-0.02	-1.17	0.1869	0.0005	
5	0.003	0.218	0.001	444.083	0.001	0.226	0.000	5.360	0.882	0.119	0.123	1.095	0.27	1.22	0.1901	0.0006	
6	0.003	0.199	0.005	73.760	0.000	0.203	0.000	2.127	0.917	0.030	0.044	0.065	1.93	1.42	0.1883	0.0006	
10	0.011	0.166	0.042	8.269	0.002	0.150	0.001	0.495	6.678	0.012	0.013	0.002	3.78	0.25	0.1888	0.0005	
15	0.022	0.163	0.233	5.060	0.004	0.106	0.003	0.396	15.010	0.009	0.005	0.000	11.02	0.14	0.1897	0.0005	
20	0.016	0.160	0.404	4.997	0.003	0.112	0.002	0.548	11.524	0.006	0.002	0.000	25.86	0.25	0.1889	0.0005	
25	0.008	0.162	0.372	4.993	0.002	0.166	0.001	0.520	5.894	0.016	0.001	0.000	45.96	0.43	0.1910	0.0005	
30	0.005	0.172	0.302	5.005	0.001	0.245	0.001	0.576	3.079	0.022	0.001	0.000	64.63	0.65	0.1891	0.0005	
35	0.003	0.179	0.265	5.090	0.001	0.265	0.001	0.763	1.745	0.022	0.001	0.000	95.18	1.30	0.1908	0.0005	

Step	$^{36}\text{Ar}$ [V]	%1s	$^{37}\text{Ar}$ [V]	%1s	$^{38}\text{Ar}$ [V]	%1s	$^{39}\text{Ar}$ [V]	%1s	$^{40}\text{Ar}$ [V]	%1s	K/Ca	2s	$^{37}\text{Ar}/^{36}\text{Ar}$	$1\sigma$ (Abs)	$^{38}\text{Ar}/^{36}\text{Ar}$	$1\sigma$ (Abs)	
<b>VIC62: <math>J = 0.00009230 \pm 0.00000022</math> (<math>1\sigma</math>)   MDF = <math>0.992503 \pm 0.000794</math> (<math>1\sigma</math>)</b>																	
1	0.000	0.425	0.000	75.153	0.000	0.555	0.000	49.619	0.108	0.026	0.072	0.129	0.23	0.17	0.1897	0.0011	
2	0.001	0.424	0.000	34.139	0.000	0.473	0.000	10.592	0.189	0.022	0.197	0.141	0.26	0.09	0.1916	0.0011	
3	0.001	0.356	0.000	169.494	0.000	0.645	0.000	10.380	0.189	0.022	0.843	2.864	0.06	0.10	0.1921	0.0010	
4	0.000	0.442	0.000	36.450	0.000	0.839	0.000	8.140	0.154	0.021	0.255	0.190	0.30	0.11	0.1965	0.0012	
5	0.000	0.360	0.000	32.026	0.000	0.815	0.000	5.318	0.139	0.019	0.207	0.134	0.67	0.21	0.1951	0.0010	
6	0.000	0.343	0.001	5.763	0.000	0.886	0.000	6.024	0.272	0.013	0.038	0.006	3.69	0.21	0.1910	0.0009	
7	0.000	0.497	0.003	2.790	0.000	1.088	0.000	5.663	0.359	0.008	0.016	0.002	8.92	0.23	0.1967	0.0014	



Step	<sup>36</sup> Ar [V]	%1s	<sup>37</sup> Ar [V]	%1s	<sup>38</sup> Ar [V]	%1s	<sup>39</sup> Ar [V]	%1s	<sup>40</sup> Ar [V]	%1s	K/Ca	2s	<sup>37</sup> Ar/ <sup>36</sup> Ar	1σ (Abs)	<sup>38</sup> Ar/ <sup>36</sup> Ar	1σ (Abs)
8	0.000	0.324	0.007	1.542	0.000	0.586	0.000	7.273	0.626	0.010	0.007	0.001	15.47	0.16	0.1898	0.0009
9	0.001	0.418	0.011	1.338	0.000	0.774	0.000	5.806	0.755	0.006	0.004	0.001	20.00	0.15	0.1938	0.0011
10	0.001	0.434	0.016	1.292	0.000	0.703	0.000	5.022	0.824	0.005	0.003	0.000	27.19	0.18	0.1905	0.0012
12	0.001	0.366	0.036	1.249	0.000	0.429	0.000	4.286	1.452	0.003	0.002	0.000	34.26	0.17	0.1943	0.0010
14	0.001	0.381	0.043	1.247	0.000	0.393	0.000	5.059	1.259	0.006	0.002	0.000	40.38	0.21	0.1891	0.0010
16	0.001	0.403	0.044	1.252	0.000	0.443	0.000	3.957	1.013	0.007	0.001	0.000	58.55	0.31	0.1883	0.0011
18	0.000	0.440	0.034	1.267	0.000	0.532	0.000	7.569	0.661	0.006	0.001	0.000	71.56	0.43	0.1881	0.0012
22	0.001	0.411	0.041	1.251	0.000	0.411	0.000	6.251	0.785	0.006	0.001	0.000	68.18	0.37	0.1880	0.0011
24	0.000	0.498	0.025	1.285	0.000	1.031	0.000	9.578	0.525	0.008	0.001	0.000	72.43	0.49	0.1897	0.0014
27	0.000	0.493	0.023	1.258	0.000	0.929	0.000	16.027	0.435	0.006	0.001	0.000	75.00	0.46	0.1917	0.0014
30	0.000	0.444	0.023	1.259	0.000	1.362	0.000	13.669	0.516	0.104	0.001	0.000	65.09	0.38	0.1869	0.0012
35	0.000	0.289	0.021	1.267	0.000	0.592	0.000	13.862	0.430	0.010	0.001	0.000	74.28	0.36	0.1869	0.0008
40	0.000	0.392	0.018	1.334	0.000	0.954	0.000	10.268	0.430	0.028	0.002	0.000	54.96	0.38	0.1869	0.0011

**VIC63: J = 0.00009230 ± 0.00000022 (1σ) | MDF = 0.991710 ± 0.000298 (1σ)**

2	0.001	0.241	0.000	32.730	0.000	0.572	0.000	4.354	0.235	0.018	0.249	0.164	0.40	0.13	0.1880	0.0007
3	0.001	0.176	0.001	16.430	0.000	0.442	0.000	1.357	0.369	0.013	0.316	0.104	0.47	0.08	0.1887	0.0005
4	0.001	0.203	0.001	13.299	0.000	0.513	0.000	1.788	0.265	0.010	0.316	0.085	1.06	0.14	0.1890	0.0006
5	0.001	0.240	0.002	5.137	0.000	0.415	0.000	1.224	0.361	0.010	0.127	0.013	2.98	0.15	0.1900	0.0007
6	0.001	0.187	0.003	2.609	0.000	0.874	0.000	1.692	0.612	0.007	0.067	0.004	4.97	0.11	0.1869	0.0005
7	0.001	0.215	0.006	1.587	0.000	0.321	0.001	1.294	1.007	0.005	0.034	0.001	8.51	0.09	0.1891	0.0006
8	0.001	0.169	0.013	1.361	0.000	0.300	0.001	1.589	1.325	0.006	0.018	0.001	10.74	0.06	0.1891	0.0005

Step	<sup>36</sup> Ar [V]	%1s	<sup>37</sup> Ar [V]	%1s	<sup>38</sup> Ar [V]	%1s	<sup>39</sup> Ar [V]	%1s	<sup>40</sup> Ar [V]	%1s	K/Ca	2s	<sup>37</sup> Ar/ <sup>36</sup> Ar	1σ (Abs)	<sup>38</sup> Ar/ <sup>36</sup> Ar	1σ (Abs)
9	0.001	0.497	0.021	1.337	0.000	0.367	0.001	1.305	1.387	0.003	0.011	0.000	17.51	0.07	0.1905	0.0005
10	0.002	0.485	0.035	1.311	0.000	0.370	0.001	0.906	1.758	0.003	0.008	0.000	20.22	0.05	0.1910	0.0004
12	0.003	0.495	0.094	1.309	0.000	0.325	0.001	0.962	2.692	0.004	0.004	0.000	37.38	0.09	0.1885	0.0005
14	0.002	0.491	0.141	1.309	0.000	0.310	0.001	1.188	2.215	0.004	0.002	0.000	65.43	0.16	0.1895	0.0005
16	0.001	0.521	0.095	1.311	0.000	0.474	0.000	1.959	1.019	0.005	0.002	0.000	94.20	0.28	0.1901	0.0007
18	0.001	0.516	0.070	1.314	0.000	0.424	0.000	2.635	0.666	0.005	0.001	0.000	108.49	0.33	0.1902	0.0007
22	0.001	0.563	0.068	1.313	0.000	0.528	0.000	3.828	0.535	0.007	0.001	0.000	142.05	0.54	0.1905	0.0009
24	0.000	0.667	0.047	1.341	0.000	1.082	0.000	6.190	0.247	0.112	0.001	0.000	155.52	0.93	0.1899	0.0013
27	0.000	0.306	0.087	1.277	0.000	0.793	0.000	4.657	0.472	0.005	0.001	0.000	203.08	0.61	0.1869	0.0007
30	0.001	0.299	0.106	1.277	0.000	0.397	0.000	3.182	0.798	0.067	0.001	0.000	116.28	0.33	0.1910	0.0006
35	0.001	0.271	0.249	1.276	0.000	0.401	0.000	1.777	1.433	0.007	0.000	0.000	198.85	0.50	0.1907	0.0005
40	0.001	0.462	0.132	1.281	0.000	0.786	0.000	3.323	0.511	0.132	0.001	0.000	213.28	1.03	0.1922	0.0012

<b>VIC64: J = 0.00009230 ± 0.00000022 (1σ)   MDF = 0.992555 ± 0.000496 (1σ)</b>																
1	0.001	0.273	0.000	1604.092	0.000	0.522	0.000	33.745	0.179	0.018	2.044	65.581	0.01	0.09	0.1925	0.0008
2	0.002	0.231	0.000	44.773	0.000	0.335	0.000	7.394	0.520	0.005	0.256	0.233	0.10	0.04	0.1892	0.0006
3	0.001	0.250	0.000	51.424	0.000	0.435	0.000	5.966	0.356	0.013	0.493	0.510	0.10	0.05	0.1893	0.0007
4	0.001	0.304	0.000	12.500	0.000	0.479	0.000	4.682	0.269	0.013	0.126	0.034	0.70	0.09	0.1907	0.0008
5	0.001	0.300	0.000	25.499	0.000	0.555	0.000	4.283	0.387	0.008	0.194	0.101	0.53	0.14	0.1889	0.0008
6	0.000	0.400	0.001	8.014	0.000	0.804	0.000	4.778	0.652	0.007	0.068	0.013	1.73	0.14	0.1919	0.0011
7	0.001	0.292	0.002	4.151	0.000	0.636	0.000	6.046	1.464	0.005	0.028	0.004	3.08	0.12	0.1907	0.0008
8	0.001	0.282	0.004	1.822	0.000	0.652	0.000	5.247	1.877	0.003	0.015	0.002	5.73	0.08	0.1904	0.0008

Step	$^{36}\text{Ar}$ [V]	%1s	$^{37}\text{Ar}$ [V]	%1s	$^{38}\text{Ar}$ [V]	%1s	$^{39}\text{Ar}$ [V]	%1s	$^{40}\text{Ar}$ [V]	%1s	K/Ca	2s	$^{37}\text{Ar}/^{36}\text{Ar}$	1 $\sigma$ (Abs)	$^{38}\text{Ar}/^{36}\text{Ar}$	1 $\sigma$ (Abs)
9	0.001	0.315	0.008	1.445	0.000	0.527	0.000	3.819	2.443	0.003	0.008	0.001	8.67	0.08	0.1893	0.0009
10	0.002	0.302	0.013	1.297	0.000	0.253	0.000	3.816	3.079	0.003	0.006	0.000	6.29	0.04	0.1882	0.0008
11	0.001	0.325	0.016	1.301	0.000	0.397	0.000	2.638	2.236	0.003	0.004	0.000	15.84	0.10	0.1889	0.0009
12	0.001	0.311	0.020	1.244	0.000	0.564	0.000	4.082	2.416	0.004	0.004	0.000	18.52	0.09	0.1890	0.0009
13	0.001	0.307	0.026	1.265	0.000	0.496	0.000	3.919	2.157	0.013	0.003	0.000	24.23	0.13	0.1904	0.0008
14	0.001	0.304	0.028	1.221	0.000	0.488	0.000	4.334	1.840	0.008	0.002	0.000	32.04	0.14	0.1897	0.0008
15	0.001	0.323	0.031	1.235	0.000	0.604	0.000	3.831	1.776	0.008	0.002	0.000	36.67	0.17	0.1882	0.0009
16	0.001	0.313	0.029	1.237	0.000	0.275	0.000	4.572	1.508	0.012	0.002	0.000	43.17	0.20	0.1920	0.0009
20	0.002	0.219	0.068	1.206	0.000	0.379	0.000	2.808	4.113	0.010	0.001	0.000	43.13	0.13	0.1892	0.0006
25	0.001	0.201	0.071	1.209	0.000	0.288	0.000	3.180	3.062	0.011	0.001	0.000	50.57	0.15	0.1903	0.0006
30	0.001	0.281	0.051	1.221	0.000	0.613	0.000	5.453	1.686	0.033	0.001	0.000	56.99	0.23	0.1902	0.0008
35	0.001	0.211	0.040	1.244	0.000	0.626	0.000	6.395	1.236	0.011	0.001	0.000	58.87	0.25	0.1903	0.0006

**VIC65: J = 0.00009230 ± 0.00000022 (1 $\sigma$ ) | MDF = 0.993138 ± 0.000695 (1 $\sigma$ )**

1	0.000	0.509	0.000	83.657	0.000	1.180	0.000	54.065	0.083	0.031	0.095	0.190	0.25	0.21	0.1869	0.0014
2	0.001	0.324	0.000	36.267	0.000	0.306	0.000	6.640	0.268	0.015	0.315	0.233	0.19	0.07	0.1936	0.0009
3	0.001	0.302	0.000	38.601	0.000	0.411	0.000	4.877	0.321	0.011	0.506	0.394	0.15	0.06	0.1904	0.0008
4	0.001	0.438	0.000	30.045	0.000	0.550	0.000	5.284	0.192	0.017	0.365	0.223	0.37	0.11	0.1869	0.0012
5	0.001	0.262	0.001	7.423	0.000	0.619	0.000	6.564	0.309	0.013	0.078	0.016	1.45	0.11	0.1917	0.0007
6	0.000	0.296	0.002	3.106	0.000	0.677	0.000	5.392	0.373	0.008	0.033	0.004	4.18	0.12	0.1933	0.0008
7	0.001	0.240	0.005	1.869	0.000	0.645	0.000	4.543	0.574	0.006	0.013	0.001	7.93	0.11	0.1903	0.0007
8	0.001	0.264	0.011	1.437	0.000	0.537	0.000	3.821	0.898	0.006	0.008	0.001	15.88	0.13	0.1894	0.0007

Step	<sup>36</sup> Ar [V]	%1s	<sup>37</sup> Ar [V]	%1s	<sup>38</sup> Ar [V]	%1s	<sup>39</sup> Ar [V]	%1s	<sup>40</sup> Ar [V]	%1s	K/Ca	2s	<sup>37</sup> Ar/ <sup>36</sup> Ar	1σ (Abs)	<sup>38</sup> Ar/ <sup>36</sup> Ar	1σ (Abs)
9	0.001	0.163	0.019	1.277	0.000	0.462	0.000	3.419	0.921	0.003	0.005	0.000	17.69	0.07	0.1903	0.0005
10	0.001	0.204	0.027	1.249	0.000	0.412	0.000	4.068	0.767	0.007	0.004	0.000	30.62	0.11	0.1890	0.0006
12	0.001	0.170	0.056	1.242	0.000	0.280	0.000	1.555	1.168	0.006	0.003	0.000	42.18	0.12	0.1905	0.0005
14	0.001	0.139	0.069	1.235	0.000	0.496	0.000	1.673	1.175	0.004	0.002	0.000	51.78	0.13	0.1894	0.0004
16	0.001	0.303	0.063	1.248	0.000	0.455	0.000	2.646	0.587	0.008	0.002	0.000	83.75	0.34	0.1934	0.0009
18	0.001	0.283	0.060	1.246	0.000	0.564	0.000	2.565	0.522	0.008	0.001	0.000	92.75	0.36	0.1869	0.0008
22	0.001	0.358	0.059	1.245	0.000	0.477	0.000	4.866	0.360	0.008	0.001	0.000	110.65	0.49	0.1909	0.0010
24	0.000	0.475	0.040	1.303	0.000	0.738	0.000	13.682	0.232	0.104	0.001	0.000	89.17	0.59	0.1900	0.0013
27	0.000	0.306	0.030	1.246	0.000	0.693	0.000	6.381	0.136	0.018	0.001	0.000	130.79	0.52	0.1872	0.0009
30	0.000	0.367	0.031	1.249	0.000	1.204	0.000	6.074	0.170	0.031	0.001	0.000	103.39	0.47	0.1912	0.0010
35	0.000	0.380	0.028	1.270	0.000	1.054	0.000	7.560	0.125	0.046	0.001	0.000	122.18	0.64	0.1938	0.0011
40	0.000	0.629	0.025	1.339	0.000	1.331	0.000	3.611	0.151	0.326	0.003	0.000	86.08	0.72	0.1869	0.0017

**VIC66: J = 0.00009260 ± 0.00000016 (1σ) | MDF = 0.993761 ± 0.000398 (1σ)**

1	0.000	0.408	0.003	78.774	0.000	1.274	0.000	19.428	0.068	0.044	-0.005	0.009	12.59	9.90	0.1869	0.0013
2	0.002	0.189	0.001	253.731	0.000	0.265	0.000	9.269	0.672	0.007	0.027	0.136	0.60	1.52	0.1877	0.0005
3	0.002	0.196	-0.002	109.932	0.000	0.200	0.000	5.134	0.554	0.068	-0.038	0.084	-1.40	-1.53	0.1908	0.0006
4	0.002	0.180	-0.003	99.141	0.000	0.269	0.000	4.851	0.602	0.063	-0.037	0.073	-1.58	-1.57	0.1899	0.0005
5	0.001	0.222	-0.001	253.554	0.000	0.327	0.000	4.708	0.617	0.061	-0.073	0.370	-1.05	-2.66	0.1907	0.0006
6	0.002	0.203	0.003	96.698	0.000	0.331	0.000	4.641	0.839	0.045	0.033	0.064	2.13	2.06	0.1906	0.0006
10	0.006	0.167	0.023	13.334	0.001	0.179	0.001	2.115	7.507	0.023	0.017	0.005	3.79	0.47	0.1902	0.0005
15	0.012	0.164	0.134	5.489	0.002	0.167	0.002	1.109	18.785	0.011	0.006	0.001	11.46	0.28	0.1900	0.0005

Step	$^{36}\text{Ar}$ [V]	%1s	$^{37}\text{Ar}$ [V]	%1s	$^{38}\text{Ar}$ [V]	%1s	$^{39}\text{Ar}$ [V]	%1s	$^{40}\text{Ar}$ [V]	%1s	K/Ca	2s	$^{37}\text{Ar}/^{36}\text{Ar}$	1 $\sigma$ (Abs)	$^{38}\text{Ar}/^{36}\text{Ar}$	1 $\sigma$ (Abs)
20	0.012	0.163	0.230	5.095	0.002	0.123	0.002	1.102	16.767	0.014	0.003	0.000	20.23	0.26	0.1902	0.0005
25	0.008	0.188	0.230	5.132	0.002	0.155	0.001	0.881	10.454	0.017	0.002	0.000	29.58	0.42	0.1895	0.0005
30	0.004	0.208	0.162	5.225	0.001	0.291	0.001	1.804	4.761	0.025	0.002	0.000	43.90	0.76	0.1907	0.0006
35	0.003	0.240	0.130	5.353	0.001	0.345	0.001	1.661	3.026	0.041	0.003	0.000	48.29	1.01	0.1906	0.0007

APPENDIX K. SUPPLEMENTARY DATA CHAPTER 5 – ISOTOPE  
ABUNDANCES APATITE SAMPLES

Step	$^{36}\text{Ar}$ [V]	%1s	$^{37}\text{Ar}$ [V]	%1s	$^{38}\text{Ar}$ [V]	%1s	$^{39}\text{Ar}$ [V]	%1s	$^{40}\text{Ar}$ [V]	%1s	K/Ca	2s	$^{37}\text{Ar}/^{36}\text{Ar}$	1 $\sigma$ (Abs)	$^{38}\text{Ar}/^{36}\text{Ar}$	1 $\sigma$ (Abs)	
<b>VIC100: J = 0.0007720 ± 0.0000010 (1<math>\sigma</math>)   MDF = 0.991815 ± 0.000298 (1<math>\sigma</math>)</b>																	
1	0.009	0.141	0.003	12.678	0.002	0.110	0.000	17.288	2.716	0.076	0.015	0.006	0.36	0.05	0.1935	0.004	
2	0.036	0.126	0.024	1.523	0.007	0.087	0.003	0.688	10.669	0.025	0.052	0.002	0.68	0.01	0.1947	0.004	
3	0.019	0.124	0.036	1.073	0.004	0.118	0.004	0.535	6.120	0.033	0.048	0.001	1.94	0.02	0.1988	0.004	
4	0.012	0.134	0.066	0.687	0.003	0.150	0.004	0.496	5.110	0.034	0.027	0.000	5.37	0.04	0.2039	0.004	
5	0.008	0.155	0.131	0.349	0.002	0.179	0.004	0.437	4.815	0.065	0.013	0.000	16.92	0.06	0.2108	0.005	
6	0.006	0.172	0.274	0.323	0.001	0.121	0.005	0.367	6.100	0.061	0.007	0.000	46.73	0.15	0.2284	0.005	
8	0.007	0.161	1.049	0.308	0.002	0.140	0.009	0.187	12.292	0.039	0.003	0.000	162.68	0.50	0.2925	0.006	
10	0.010	0.148	2.603	0.308	0.003	0.109	0.011	0.173	16.437	0.031	0.001	0.000	288.98	0.89	0.3500	0.007	
12	0.019	0.124	4.574	0.307	0.006	0.080	0.013	0.418	24.015	0.041	0.001	0.000	251.19	0.77	0.3142	0.006	
14	0.034	0.122	7.966	0.307	0.010	0.069	0.013	0.417	22.847	0.028	0.000	0.000	253.33	0.78	0.3123	0.005	
18	0.073	0.123	17.829	0.307	0.022	0.066	0.021	0.104	38.510	0.035	0.000	0.000	259.99	0.82	0.3188	0.006	
22	0.053	0.121	13.483	0.307	0.016	0.070	0.012	0.139	20.443	0.027	0.000	0.000	270.62	0.84	0.3215	0.006	
26	0.033	0.125	8.297	0.308	0.010	0.087	0.006	0.543	10.726	0.033	0.000	0.000	272.98	0.84	0.3248	0.006	
30	0.020	0.127	5.403	0.308	0.006	0.116	0.004	0.794	6.776	0.031	0.000	0.000	283.83	0.88	0.3286	0.006	
35	0.016	0.128	3.974	0.308	0.005	0.108	0.003	0.203	4.993	0.035	0.000	0.000	269.14	0.83	0.3208	0.006	
40	0.013	0.134	3.234	0.309	0.004	0.084	0.002	0.333	3.947	0.047	0.000	0.000	260.71	0.81	0.3223	0.006	
45	0.013	0.139	3.077	0.309	0.004	0.103	0.002	0.343	3.909	0.048	0.000	0.000	257.37	0.80	0.3199	0.006	
50	0.007	0.147	1.830	0.310	0.002	0.135	0.002	0.611	2.215	0.050	0.000	0.000	200.72	1.14	0.2896	0.006	
<b>VIC101: J = 0.0007720 ± 0.0000010 (1<math>\sigma</math>)   MDF = 0.990470 ± 0.000297 (1<math>\sigma</math>)</b>																	
1	0.001	0.461	0.001	60.399	0.000	1.039	0.000	247.779	0.373	0.462	-0.010	0.051	0.66	0.40	0.1923	0.013	

Step	$^{36}\text{Ar}$ [V]	%1s	$^{37}\text{Ar}$ [V]	%1s	$^{38}\text{Ar}$ [V]	%1s	$^{39}\text{Ar}$ [V]	%1s	$^{40}\text{Ar}$ [V]	%1s	K/Ca	2s	$^{37}\text{Ar}/^{36}\text{Ar}$	1 $\sigma$ (Abs)	$^{38}\text{Ar}/^{36}\text{Ar}$	1 $\sigma$ (Abs)
2	0.009	0.139	0.013	3.507	0.002	0.167	0.001	3.858	3.011	0.058	0.037	0.004	1.52	0.05	0.1918	0.0004
3	0.008	0.148	0.025	1.954	0.002	0.214	0.003	1.801	2.780	0.063	0.043	0.002	3.28	0.06	0.1969	0.0004
4	0.006	0.174	0.039	1.302	0.001	0.232	0.003	1.771	2.404	0.073	0.028	0.001	6.72	0.09	0.2018	0.0005
5	0.004	0.170	0.062	1.497	0.001	0.299	0.002	0.452	2.117	0.068	0.015	0.000	17.67	0.26	0.2123	0.0005
6	0.003	0.169	0.106	0.909	0.001	0.245	0.002	0.347	2.320	0.062	0.009	0.000	34.38	0.31	0.2232	0.0005
8	0.004	0.163	0.356	0.393	0.001	0.232	0.004	0.160	3.751	0.040	0.004	0.000	92.85	0.36	0.2430	0.0005
10	0.004	0.158	1.019	0.311	0.001	0.203	0.004	0.183	4.158	0.035	0.001	0.000	306.24	0.95	0.2893	0.0007
12	0.005	0.133	2.510	0.298	0.002	0.151	0.005	0.429	4.622	0.022	0.000	0.000	530.99	1.58	0.3370	0.0008
14	0.010	0.133	4.822	0.297	0.003	0.113	0.006	0.351	5.918	0.018	0.000	0.000	587.54	1.75	0.3446	0.0008
18	0.031	0.125	15.768	0.297	0.010	0.085	0.014	0.148	13.224	0.011	0.000	0.000	588.88	1.76	0.3425	0.0008
22	0.035	0.124	18.547	0.298	0.011	0.072	0.014	0.138	12.171	0.013	0.000	0.000	621.63	1.86	0.3524	0.0008
26	0.023	0.130	12.427	0.298	0.007	0.082	0.009	0.085	7.630	0.013	0.000	0.000	629.61	1.88	0.3496	0.0008
30	0.011	0.140	6.039	0.298	0.004	0.097	0.004	0.238	3.580	0.019	0.000	0.000	620.91	1.85	0.3475	0.0009
35	0.010	0.142	5.197	0.298	0.003	0.085	0.004	0.213	3.186	0.024	0.000	0.000	582.53	1.74	0.3417	0.0008
40	0.008	0.145	4.258	0.298	0.003	0.136	0.003	0.302	2.646	0.056	0.000	0.000	593.56	1.77	0.3409	0.0008
45	0.006	0.143	2.875	0.298	0.002	0.151	0.002	0.419	1.668	0.086	0.000	0.000	604.56	1.80	0.3403	0.0008
50	0.004	0.149	1.914	0.298	0.001	0.240	0.001	0.613	1.209	0.118	0.000	0.000	616.87	1.84	0.3442	0.0009
<b>VIC101B: J = 0.0007770 <math>\pm</math> 0.0000022 (1<math>\sigma</math>)   MDF = 0.991461 <math>\pm</math> 0.000397 (1<math>\sigma</math>)</b>																
1	0.003	0.558	0.001	37.951	0.000	2.943	0.000	595.993	0.763	0.560	-0.007	0.080	0.39	0.15	0.1904	0.0015
2	0.017	0.181	0.020	1.586	0.003	0.445	0.003	3.343	5.360	0.081	0.061	0.005	1.15	0.02	0.1915	0.0005
3	0.012	0.204	0.034	1.014	0.002	0.605	0.004	2.310	4.231	0.101	0.051	0.003	2.76	0.03	0.1952	0.0006



Step	<sup>36</sup> Ar [V]	%1s	<sup>37</sup> Ar [V]	%1s	<sup>38</sup> Ar [V]	%1s	<sup>39</sup> Ar [V]	%1s	<sup>40</sup> Ar [V]	%1s	K/Ca	2s	<sup>37</sup> Ar/ <sup>36</sup> Ar	1σ (Abs)	<sup>38</sup> Ar/ <sup>36</sup> Ar	1σ (Abs)
4	0.010	0.220	0.048	0.883	0.002	0.725	0.004	2.672	3.837	0.112	0.031	0.002	4.77	0.04	0.1948	0.0006
5	0.008	0.174	0.079	0.604	0.002	0.569	0.003	2.204	3.734	0.019	0.016	0.001	9.92	0.06	0.1968	0.0005
6	0.007	0.181	0.144	0.434	0.001	0.676	0.003	2.194	3.528	0.020	0.009	0.000	22.20	0.10	0.2036	0.0005
10	0.014	0.173	1.499	0.308	0.003	0.301	0.010	0.665	11.259	0.016	0.003	0.000	107.54	0.33	0.2392	0.0006
14	0.017	0.163	6.059	0.306	0.005	0.205	0.013	0.542	14.105	0.014	0.001	0.000	383.41	1.17	0.3103	0.0007
18	0.042	0.163	15.233	0.306	0.012	0.104	0.017	0.345	20.376	0.016	0.000	0.000	402.92	1.24	0.3003	0.0007
22	0.050	0.161	19.233	0.306	0.014	0.101	0.018	0.315	22.033	0.019	0.000	0.000	433.72	1.34	0.3055	0.0007
26	0.036	0.163	15.173	0.306	0.010	0.113	0.012	0.466	13.232	0.025	0.000	0.000	470.52	1.45	0.3129	0.0008
30	0.026	0.162	10.313	0.306	0.007	0.137	0.008	0.735	8.427	0.038	0.000	0.000	452.98	1.39	0.3063	0.0008
35	0.025	0.202	10.002	0.306	0.007	0.157	0.007	0.428	8.331	0.111	0.000	0.000	440.66	1.35	0.3035	0.0009
40	0.015	0.260	6.136	0.307	0.004	0.223	0.005	0.692	5.110	0.181	0.000	0.000	447.50	1.37	0.3042	0.0011
45	0.013	0.289	5.264	0.307	0.004	0.270	0.004	0.827	4.168	0.221	0.000	0.000	460.15	1.41	0.3094	0.0012
50	0.007	0.486	2.482	0.309	0.002	0.505	0.002	1.686	2.274	0.405	0.000	0.000	410.69	1.27	0.2982	0.0019

<b>VIC102: J = 0.0007770 ± 0.0000022 (1σ)   MDF = 0.990372 ± 0.000297 (1σ)</b>																
1	0.001	0.177	0.001	27.456	0.000	0.504	0.000	218.729	0.349	0.270	-0.008	0.036	0.81	0.22	0.1932	0.0005
2	0.006	0.132	0.015	1.832	0.001	0.108	0.001	2.551	2.342	0.042	0.039	0.002	2.35	0.04	0.2036	0.0004
3	0.006	0.155	0.027	1.097	0.001	0.292	0.002	1.400	2.576	0.086	0.047	0.002	4.73	0.05	0.2098	0.0005
4	0.004	0.202	0.034	0.809	0.001	0.290	0.004	0.938	5.733	0.040	0.055	0.001	8.54	0.07	0.2166	0.0006
5	0.003	0.147	0.054	0.745	0.001	0.255	0.004	0.297	8.731	0.012	0.042	0.001	17.00	0.13	0.2251	0.0005
6	0.003	0.168	0.094	0.501	0.001	0.285	0.002	0.490	2.206	0.011	0.013	0.000	29.90	0.15	0.2124	0.0005
8	0.005	0.132	0.338	0.318	0.001	0.194	0.004	0.352	3.996	0.015	0.006	0.000	72.78	0.23	0.2251	0.0004

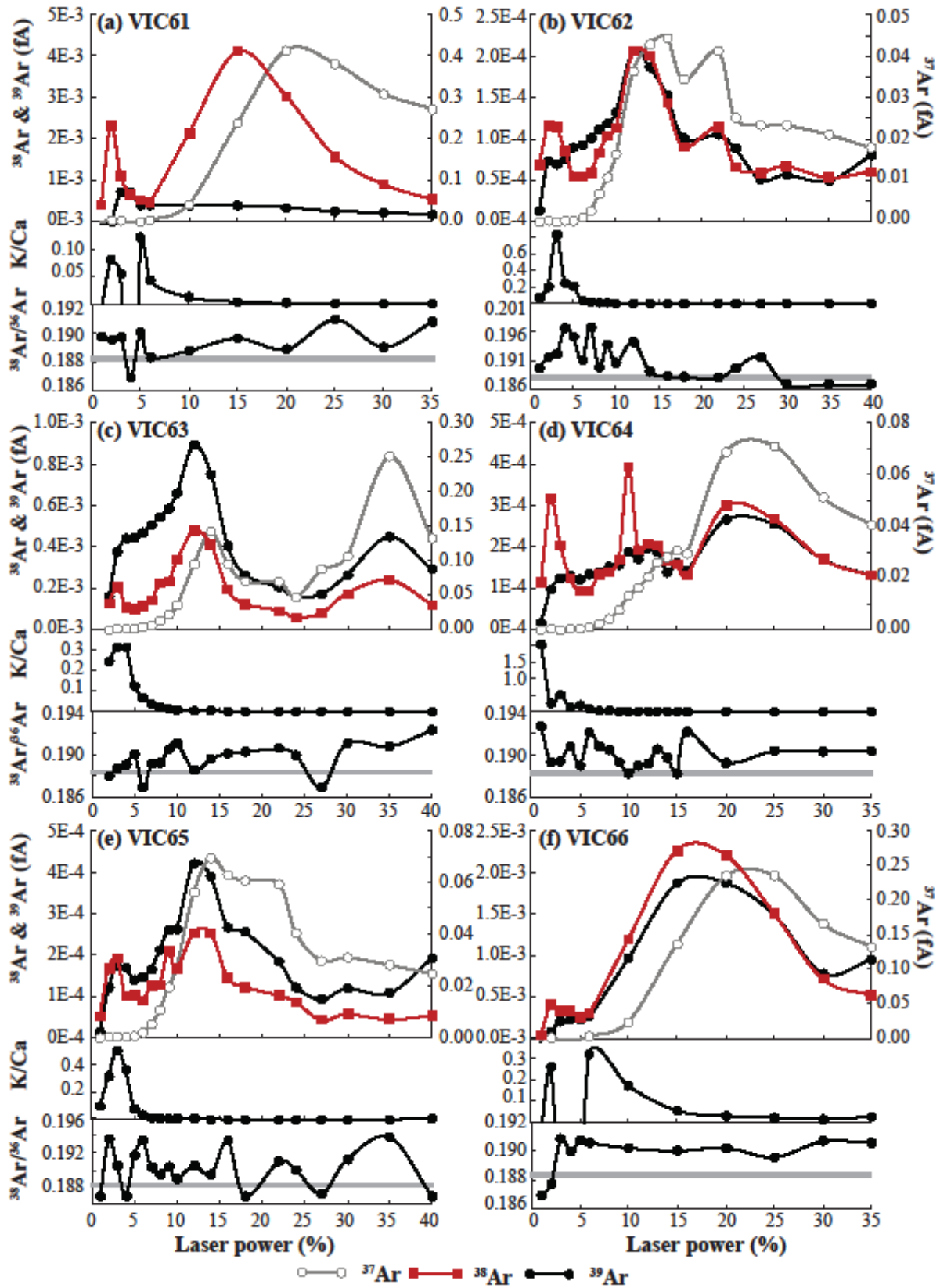
Step	<sup>36</sup> Ar [V]	%1s	<sup>37</sup> Ar [V]	%1s	<sup>38</sup> Ar [V]	%1s	<sup>39</sup> Ar [V]	%1s	<sup>40</sup> Ar [V]	%1s	K/Ca	2s	<sup>37</sup> Ar/ <sup>36</sup> Ar	1σ (Abs)	<sup>38</sup> Ar/ <sup>36</sup> Ar	1σ (Abs)
10	0.004	0.153	0.891	0.302	0.001	0.253	0.005	0.226	6.504	0.017	0.003	0.000	242.87	0.73	0.2888	0.0006
12	0.005	0.130	2.271	0.299	0.002	0.152	0.005	0.249	4.744	0.016	0.001	0.000	494.95	1.48	0.3461	0.0007
14	0.009	0.132	4.739	0.299	0.003	0.092	0.006	0.207	6.589	0.020	0.000	0.000	629.81	1.88	0.3815	0.0009
18	0.025	0.129	14.890	0.299	0.009	0.075	0.014	0.112	14.623	0.024	0.000	0.000	721.73	2.16	0.4058	0.0010
22	0.029	0.138	18.279	0.299	0.010	0.080	0.015	0.110	12.899	0.027	0.000	0.000	769.32	2.31	0.4078	0.0011
26	0.020	0.123	13.110	0.299	0.007	0.076	0.010	0.363	8.019	0.022	0.000	0.000	789.06	2.36	0.4125	0.0010
30	0.013	0.138	8.163	0.299	0.005	0.125	0.006	0.609	4.755	0.035	0.000	0.000	776.72	2.33	0.4118	0.0011
35	0.008	0.173	5.378	0.300	0.003	0.134	0.004	0.416	3.028	0.105	0.000	0.000	798.98	2.40	0.4232	0.0013
40	0.004	0.269	2.883	0.300	0.002	0.194	0.002	0.745	1.613	0.190	0.000	0.000	854.91	2.57	0.4337	0.0018
45	0.004	0.139	2.701	0.300	0.001	0.105	0.002	0.303	1.659	0.043	0.000	0.000	800.72	2.40	0.4170	0.0011
50	0.003	0.181	2.067	0.300	0.001	0.175	0.002	0.466	1.258	0.071	0.000	0.000	760.58	2.28	0.4106	0.0012

**VIC103: J = 0.0007720 ± 0.0000010 (1σ) | MDF = 0.991815 ± 0.000298 (1σ)**

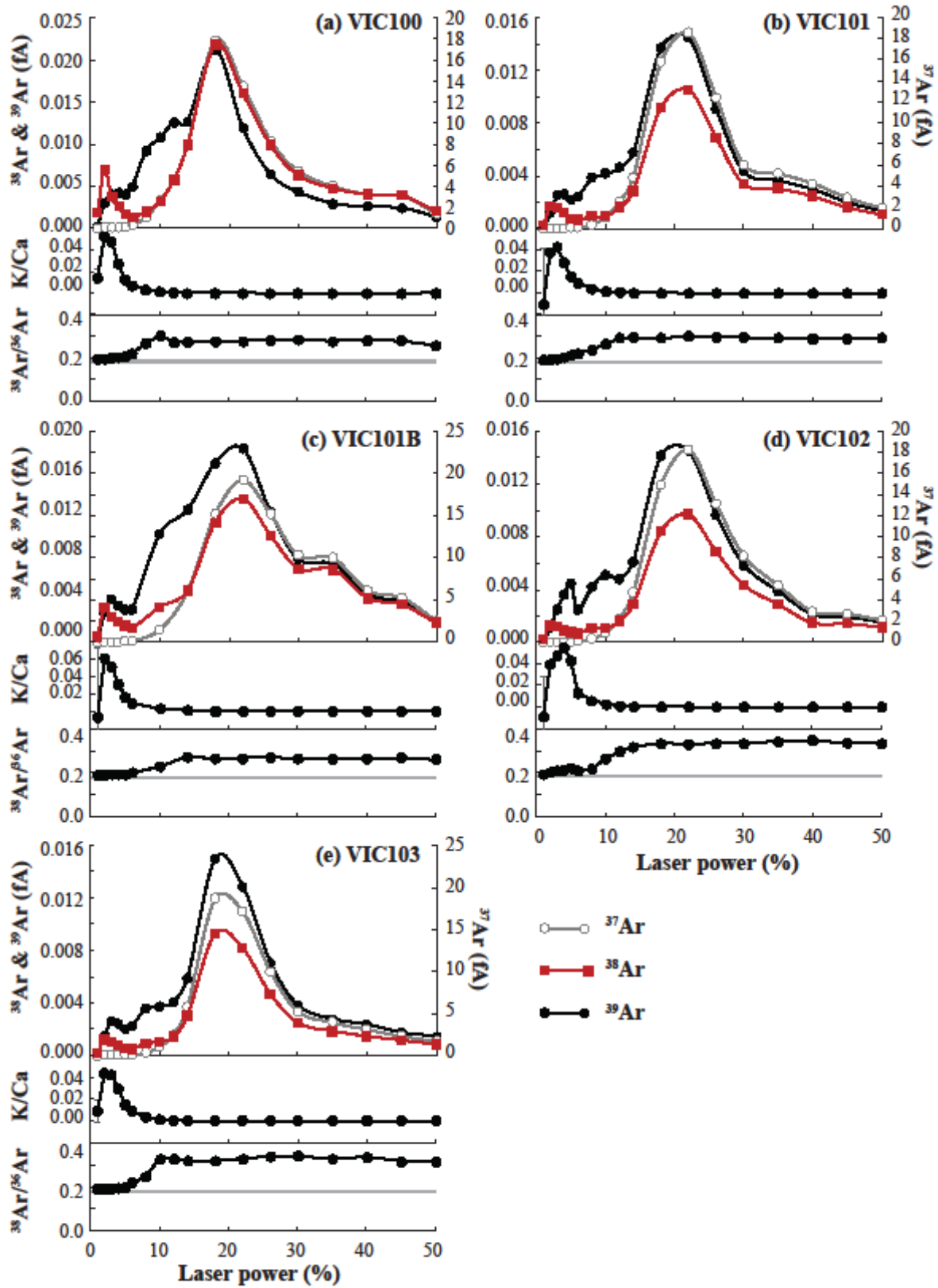
1	0.001	1.678	0.001	36.889	0.000	2.671	0.000	38.137	0.312	1.389	0.009	0.010	0.97	0.36	0.1941	0.0045
2	0.006	0.240	0.014	1.625	0.001	0.365	0.001	0.658	2.280	0.191	0.044	0.002	2.20	0.04	0.1930	0.0007
3	0.005	0.284	0.027	0.887	0.001	0.428	0.003	0.296	2.077	0.210	0.042	0.001	5.09	0.05	0.1940	0.0008
4	0.004	0.370	0.036	0.807	0.001	0.538	0.002	0.316	1.822	0.240	0.029	0.000	9.46	0.08	0.1965	0.0010
5	0.003	0.194	0.058	0.601	0.001	0.391	0.002	1.715	1.623	0.091	0.015	0.001	20.25	0.12	0.2029	0.0006
6	0.002	0.174	0.102	0.425	0.001	0.479	0.002	1.556	1.958	0.076	0.009	0.000	43.05	0.18	0.2241	0.0005
8	0.003	0.187	0.370	0.317	0.001	0.295	0.004	0.977	3.188	0.048	0.004	0.000	109.87	0.35	0.2585	0.0006
10	0.003	0.164	1.091	0.308	0.001	0.324	0.004	0.947	3.404	0.057	0.001	0.000	383.13	1.18	0.3707	0.0008
12	0.004	0.142	2.457	0.307	0.001	0.183	0.004	0.851	3.491	0.053	0.000	0.000	704.28	2.16	0.4043	0.0010

Step	$^{36}\text{Ar}$ [V]	%1s	$^{37}\text{Ar}$ [V]	%1s	$^{38}\text{Ar}$ [V]	%1s	$^{39}\text{Ar}$ [V]	%1s	$^{40}\text{Ar}$ [V]	%1s	K/Ca	2s	$^{37}\text{Ar}/^{36}\text{Ar}$	1 $\sigma$ (Abs)	$^{38}\text{Ar}/^{36}\text{Ar}$	1 $\sigma$ (Abs)
14	0.009	0.142	5.841	0.306	0.003	0.131	0.006	0.601	4.790	0.063	0.000	0.000	786.66	2.41	0.4027	0.0011
18	0.028	0.123	18.713	0.306	0.010	0.075	0.015	0.322	11.344	0.040	0.000	0.000	817.81	2.51	0.4061	0.0011
22	0.024	0.128	17.147	0.306	0.009	0.070	0.013	0.376	8.984	0.035	0.000	0.000	892.70	2.74	0.4245	0.0012
26	0.013	0.124	10.006	0.306	0.005	0.083	0.007	0.288	4.518	0.043	0.000	0.000	939.26	2.88	0.4390	0.0012
30	0.007	0.135	5.245	0.307	0.003	0.164	0.004	0.547	2.337	0.055	0.000	0.000	943.94	2.90	0.4434	0.0013
35	0.005	0.176	3.942	0.307	0.002	0.166	0.003	0.920	1.694	0.116	0.000	0.000	900.38	2.76	0.4229	0.0014
40	0.004	0.208	3.079	0.307	0.002	0.141	0.002	1.101	1.488	0.133	0.000	0.000	928.59	2.85	0.4364	0.0016
45	0.003	0.129	2.285	0.307	0.001	0.154	0.002	1.343	1.166	0.047	0.000	0.000	814.52	2.50	0.4047	0.0011
50	0.002	0.163	1.709	0.308	0.001	0.184	0.001	1.639	0.800	0.056	0.000	0.000	838.82	2.58	0.4068	0.0012

APPENDIX L. SUPPLEMENTARY DATA CHAPTER 5 – DEGASSING  
SPECTRA ALL PYROXENE SAMPLES

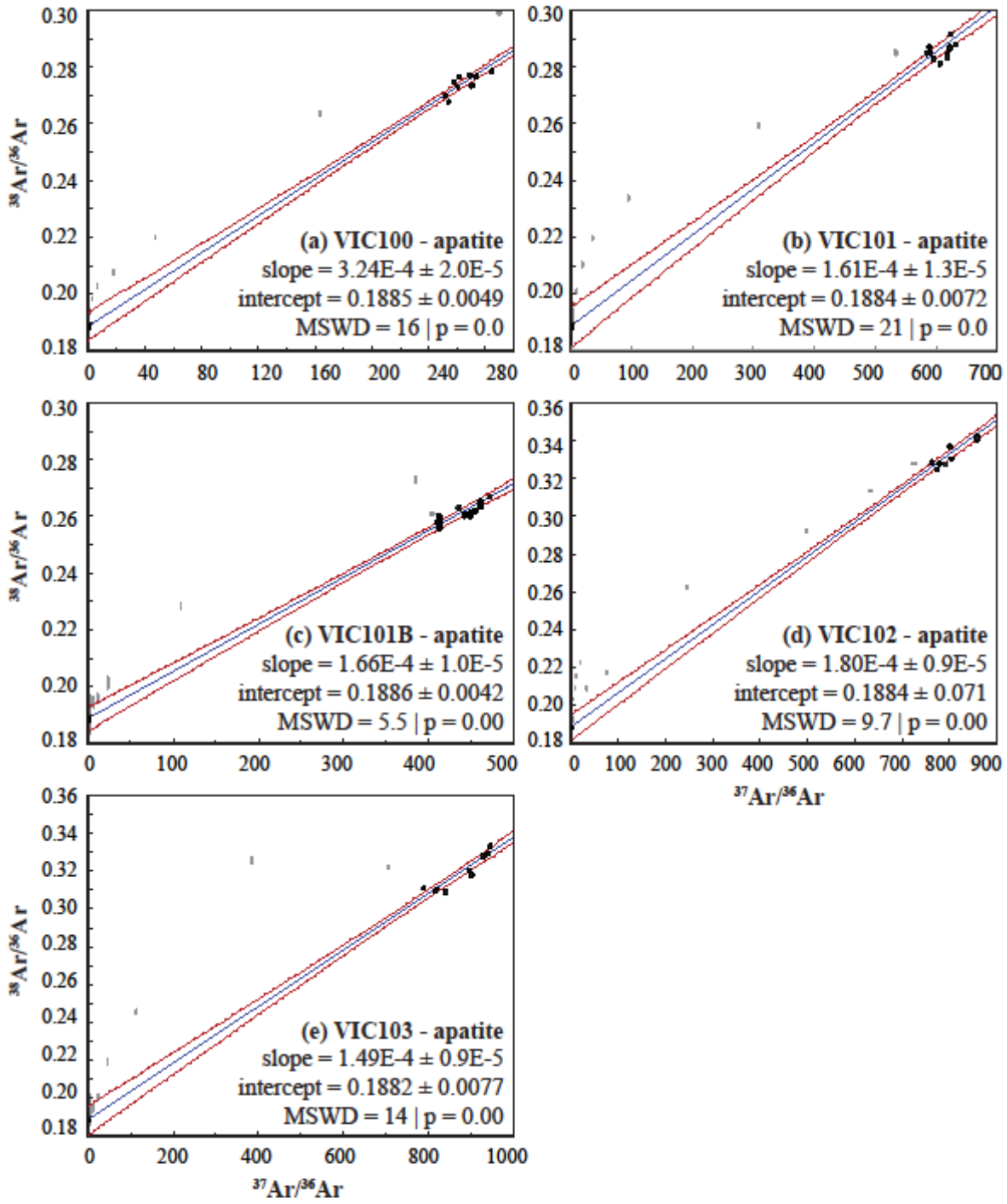


APPENDIX M. SUPPLEMENTARY DATA CHAPTER 5 –  
DEGASSING SPECTRA ALL APATITE SAMPLES



APPENDIX N. SUPPLEMENTARY DATA CHAPTER 5 –  
COSMOCHRONS ALL CL-CORRECTED APATITE SAMPLES





APPENDIX O. SUPPLEMENTARY DATA CHAPTER 6 – ISOTOPE  
ABUNDANCES E9 PHLOGOPITE

Step	36Ar [fA]	%1s	37Ar [fA]	%1s	38Ar [fA]	%1s	39Ar [fA]	%1s	40Ar [fA]	%1s	40(r)/39(k)	± 2s	Age (Ma)	± 2s	40Ar(r) (%)	39Ar(k) (%)	K/Ca	± 2s	
<b>E9 Phlogopite 1: J = 0.0008266 ± 0.00000029 (1σ) MDF = 0.993432 ± 0.00080 (1σ)</b>																			
1	0.000	0.483	0.001	22.643	0.000	43.453	0.002	0.883	0.162	0.099	11.12	0.80	16.55	1.18	14.7	0.7	0.86	0.4	
2	0.001	0.349	0.002	12.684	0.000	14.542	0.013	0.185	0.545	0.030	14.97	0.26	22.23	0.39	36.0	4.0	3.13	0.8	
3	0.001	0.474	0.002	20.872	0.000	17.048	0.019	0.115	0.449	0.036	15.08	0.11	22.40	0.16	63.2	5.8	4.68	2.0	
4	0.000	0.486	0.001	22.356	0.000	16.262	0.025	0.111	0.498	0.032	15.08	0.07	22.40	0.10	75.9	7.7	7.68	3.4	
4.5	0.000	0.634	0.001	18.132	0.000	16.840	0.026	0.114	0.461	0.035	15.11	0.06	22.45	0.08	83.9	7.9	7.74	2.8	
5	0.000	1.362	0.001	24.638	0.000	22.083	0.020	0.130	0.338	0.048	15.05	0.06	22.36	0.09	90.6	6.2	6.77	3.3	
6	0.000	1.011	0.002	18.535	0.000	20.377	0.022	0.121	0.373	0.044	15.02	0.06	22.31	0.09	88.2	6.7	5.71	2.1	
7	0.000	2.587	0.002	15.140	0.000	30.191	0.019	0.113	0.304	0.054	15.02	0.06	22.32	0.09	94.3	5.9	4.07	1.2	
7.5	0.000	1.811	0.002	13.304	0.000	26.185	0.020	0.113	0.329	0.049	15.11	0.05	22.45	0.08	93.4	6.2	4.18	1.1	
8	0.000	4.004	0.002	14.507	0.000	39.000	0.018	0.123	0.284	0.057	15.04	0.06	22.34	0.09	96.2	5.6	4.30	1.2	
9	0.000	3.880	0.002	19.138	0.000	30.613	0.021	0.121	0.321	0.050	15.04	0.06	22.34	0.08	96.7	6.3	5.31	2.0	
10	0.000	3.368	0.001	21.260	0.000	39.009	0.018	0.116	0.286	0.056	15.07	0.06	22.39	0.09	95.5	5.6	6.34	2.7	
12	0.000	3.887	0.002	14.416	0.000	29.925	0.023	0.132	0.351	0.047	15.06	0.06	22.37	0.08	97.0	6.9	4.97	1.4	
14	0.000	7.971	0.001	29.486	0.000	30.986	0.018	0.128	0.268	0.061	15.01	0.06	22.30	0.10	98.0	5.4	7.66	4.5	
16	0.000	12.614	0.001	37.551	0.000	77.616	0.011	0.194	0.167	0.097	15.03	0.10	22.33	0.15	98.0	3.3	4.96	3.7	
18	0.000	17.717	0.001	25.379	0.000	95.002	0.008	0.215	0.123	0.130	15.10	0.12	22.43	0.18	98.3	2.5	4.14	2.1	
22	0.000	15.037	0.001	25.416	0.000	121.627	0.010	0.179	0.155	0.104	15.15	0.10	22.51	0.15	98.3	3.1	3.55	1.8	
26	0.000	13.975	0.000	70.177	0.000	115.236	0.009	0.195	0.145	0.111	15.08	0.11	22.40	0.17	97.9	2.9	10.11	14.2	
30	0.000	15.494	0.001	35.471	0.000	51.897	0.005	0.284	0.082	0.195	15.05	0.18	22.36	0.27	97.0	1.6	2.38	1.7	
35	0.000	10.877	0.001	37.214	0.000	51.344	0.012	0.175	0.178	0.092	15.11	0.09	22.44	0.14	97.9	3.5	5.35	4.0	
40	0.000	8.293	0.001	42.510	0.000	29.304	0.007	0.268	0.115	0.140	14.96	0.14	22.22	0.21	95.8	2.3	5.73	4.9	

Step	36Ar [fA]	%1s	37Ar [fA]	%1s	38Ar [fA]	%1s	39Ar [fA]	%1s	40Ar [fA]	%1s	40(r)/ 39(k)	± 2s	Age (Ma)	± 2s	40Ar(r) (%)	39Ar(k) (%)	K/Ca	± 2s	
<b>E9 phlogopite 2: J = 0.0008266 ± 0.00000029 (1σ) MDF = 0.992986 ± 0.00030 (1σ)</b>																			
1	0.000	294.250	0.000	335.400	0.000	61.531	0.000	83.123	0.000	36.094	27.82	74.47	41.11	108.81	76.0	0.0	0.64	4.5	
2	0.000	5.152	0.000	777.670	0.000	355.397	0.002	0.411	0.031	0.353	14.94	0.31	22.19	0.46	85.7	1.6	267.67	4163.1	
3	0.000	1.257	0.000	1158.262	0.000	15.317	0.009	0.085	0.160	0.069	15.06	0.06	22.36	0.08	89.4	8.4	2607.78	60409.8	
4	0.000	1.606	0.000	69.529	0.000	16.025	0.014	0.078	0.217	0.051	15.07	0.04	22.39	0.06	93.9	12.0	242.29	336.9	
4.5	0.000	4.872	0.000	75.379	0.000	28.175	0.004	0.206	0.069	0.158	15.10	0.12	22.43	0.18	94.3	3.8	83.74	126.3	
5	0.000	3.506	0.000	30.656	0.000	20.041	0.011	0.095	0.164	0.067	15.06	0.05	22.37	0.08	96.5	9.3	67.56	41.4	
6	0.000	4.473	0.000	126.027	0.000	24.286	0.010	0.090	0.159	0.070	15.08	0.05	22.40	0.08	97.1	9.0	354.68	894.0	
7	0.000	13.807	0.000	61.329	0.000	116.735	0.004	0.216	0.059	0.184	15.10	0.14	22.43	0.21	97.4	3.4	46.85	57.5	
7.5	0.000	8.787	0.000	110.225	0.000	34.087	0.007	0.111	0.102	0.106	15.15	0.08	22.50	0.11	97.8	5.9	175.98	387.9	
8	0.000	8.946	0.000	281.692	0.000	42.547	0.007	0.141	0.103	0.107	15.08	0.08	22.40	0.12	97.9	5.9	469.01	2642.3	
9	0.000	9.227	0.000	205.844	0.000	43.101	0.006	0.176	0.096	0.113	14.98	0.09	22.25	0.13	97.7	5.5	-258.02	1062.2	
10	0.000	9.506	0.000	99.357	0.000	203.971	0.005	0.136	0.084	0.130	15.14	0.09	22.49	0.14	97.5	4.8	121.67	241.8	
12	0.000	11.306	0.000	105.172	0.000	29.196	0.005	0.166	0.084	0.130	15.09	0.10	22.42	0.15	97.8	4.8	107.13	225.3	
14	0.000	10.193	0.000	238.288	0.000	57.066	0.006	0.127	0.089	0.123	15.14	0.09	22.49	0.13	97.8	5.1	-305.86	1457.7	
16	0.000	15.524	0.000	264.539	0.000	48.895	0.004	0.162	0.061	0.180	14.76	0.12	21.93	0.18	97.9	3.6	266.89	1412.1	
18	0.000	12.883	0.000	89.917	0.000	119.034	0.003	0.307	0.046	0.235	15.16	0.18	22.51	0.27	96.6	2.6	-72.09	129.6	
22	0.000	11.116	0.000	232.327	0.000	36.685	0.004	0.212	0.065	0.166	15.16	0.13	22.52	0.19	97.2	3.7	-219.13	1018.2	
26	0.000	4.236	0.000	67.317	0.000	48.917	0.002	0.352	0.041	0.266	15.03	0.23	22.33	0.34	87.4	2.1	40.56	54.6	
30	0.000	8.539	0.000	280.778	0.000	26.570	0.004	0.260	0.057	0.191	15.14	0.16	22.48	0.23	95.5	3.2	-231.12	1297.9	
35	0.000	3.256	0.000	83.576	0.000	18.899	0.004	0.210	0.066	0.165	15.11	0.13	22.44	0.20	90.6	3.5	66.80	111.7	
40	0.000	2.697	0.000	221.253	0.000	19.205	0.002	0.367	0.040	0.274	15.04	0.24	22.34	0.36	81.1	1.9	125.25	554.2	
<b>E9 phlogopite 3: J = 0.0008266 ± 0.00000029 (1σ) MDF = 0.992986 ± 0.00030 (1σ)</b>																			
1	0.000	341.202	0.000	2639.790	0.000	263.269	0.000	34.302	0.000	659.170	-0.64	22.71	-0.95	33.96	-46.7	0.0	16.16	853.0	

Step	<sup>36</sup> Ar [fA]	%1s	<sup>37</sup> Ar [fA]	%1s	<sup>38</sup> Ar [fA]	%1s	<sup>39</sup> Ar [fA]	%1s	<sup>40</sup> Ar [fA]	%1s	<sup>40</sup> (r)/ <sup>39</sup> (k)	± 2s	Age (Ma)	± 2s	<sup>40</sup> Ar(r) (%)	<sup>39</sup> Ar(k) (%)	K/Ca	± 2s
2	0.000	3.482	0.000	335.296	0.000	64.923	0.002	0.596	0.028	0.843	14.69	0.42	21.83	0.62	81.4	1.3	129.01	865.1
3	0.000	1.083	0.000	208.249	0.000	18.533	0.010	0.083	0.178	0.132	15.10	0.07	22.43	0.10	88.9	8.6	462.33	1925.6
4	0.000	1.306	0.000	81.692	0.000	15.429	0.014	0.085	0.231	0.102	15.12	0.05	22.45	0.07	94.0	11.8	304.41	497.4
4.5	0.000	5.844	0.000	207.392	0.000	30.433	0.004	0.188	0.070	0.335	15.01	0.15	22.30	0.22	95.0	3.6	221.88	920.3
5	0.000	2.232	0.000	5963.180	0.000	18.394	0.011	0.092	0.180	0.131	15.12	0.06	22.46	0.09	95.8	9.4	-15303.49	1825149.4
6	0.000	3.280	0.000	149.255	0.000	19.067	0.012	0.077	0.191	0.124	15.11	0.06	22.44	0.09	96.3	10.0	400.67	1196.0
7	0.000	6.161	0.000	161.177	0.000	144.250	0.004	0.224	0.066	0.356	15.09	0.15	22.42	0.23	95.9	3.4	188.80	608.6
7.5	0.000	6.432	0.000	54.155	0.000	31.396	0.008	0.118	0.125	0.188	15.11	0.08	22.44	0.12	97.6	6.6	104.55	113.2
8	0.000	6.891	0.000	67.733	0.000	29.489	0.008	0.119	0.117	0.201	15.09	0.09	22.42	0.13	97.4	6.2	137.11	185.7
9	0.000	6.709	0.000	242.930	0.000	41.254	0.007	0.134	0.103	0.229	15.02	0.10	22.31	0.15	97.2	5.4	387.83	1884.3
10	0.000	7.554	0.000	258.512	0.000	24.946	0.007	0.129	0.109	0.217	15.06	0.10	22.37	0.14	97.6	5.8	-439.70	2273.4
12	0.000	10.035	0.000	162.638	0.000	31.566	0.006	0.165	0.099	0.237	15.11	0.11	22.44	0.16	98.2	5.3	219.81	715.0
14	0.000	11.296	0.000	190.514	0.000	32.103	0.005	0.188	0.078	0.301	15.06	0.13	22.36	0.19	97.8	4.2	-239.51	912.6
16	0.000	13.576	0.000	126.082	0.000	143.821	0.003	0.368	0.040	0.587	15.01	0.25	22.29	0.37	96.8	2.1	-78.70	198.4
18	0.000	16.448	0.000	2150.278	0.000	53.775	0.003	0.286	0.046	0.507	15.07	0.21	22.39	0.31	97.7	2.5	-1331.44	57259.5
22	0.000	15.010	0.000	139.508	0.000	161.643	0.003	0.315	0.047	0.495	15.06	0.22	22.37	0.32	97.4	2.5	-109.11	304.4
26	0.000	13.149	0.000	302.790	0.000	80.618	0.003	0.312	0.048	0.494	15.07	0.21	22.39	0.32	97.1	2.5	-264.00	1598.7
30	0.000	20.573	0.000	1667.860	0.000	37.125	0.004	0.132	0.066	0.365	14.80	0.18	21.99	0.27	97.7	3.6	-1311.43	43745.8
35	0.000	26.661	0.000	477.736	0.000	126.457	0.002	0.322	0.035	0.678	15.21	0.36	22.59	0.53	96.7	1.8	-240.16	2294.7
40	0.000	7.691	0.000	365.103	0.000	74.863	0.004	0.176	0.066	0.365	14.68	0.20	21.81	0.29	93.8	3.4	325.91	2379.8

APPENDIX P. SUPPLEMENTARY DATA CHAPTER 6 –  
ADDITIONAL  $^{40}\text{AR}/^{39}\text{AR}$  DATA SERBIAN AND SPANISH  
LAMPROITES

### Sample description.

Sample BK013/B is an Olivine-Clinopyroxene-Leucite lamproite from Boraç, Serbia and is part of the Tertiary – Quaternary Mediterranean lamproite province (Figure N.1; Prelević, 2005). These rocks are part of two types of ultrapotassic rocks of Tertiary age in the area, both with distinct isotopic signatures that were attributed to a strong contribution of variably metasomatised sub-continental lithospheric mantle melts on asthenosphere derived magmas (Prelević, 2005). A K-Ar age of  $22.78 \pm 0.88$  Ma was derived from a geochemically similar, near-by, minette (Cvetković *et al.*, 2004) and this age was adopted for the full suite of ultra-potassic rocks around Boraç (Prelević, 2005). It can be seen in thin section (Figure P.2b) that this sample contains fresh phenocrysts of phlogopite, amphibole and olivine (all  $> 100 \mu\text{m}$ ) in a very fine grained matrix containing numerous perovskite minerals.

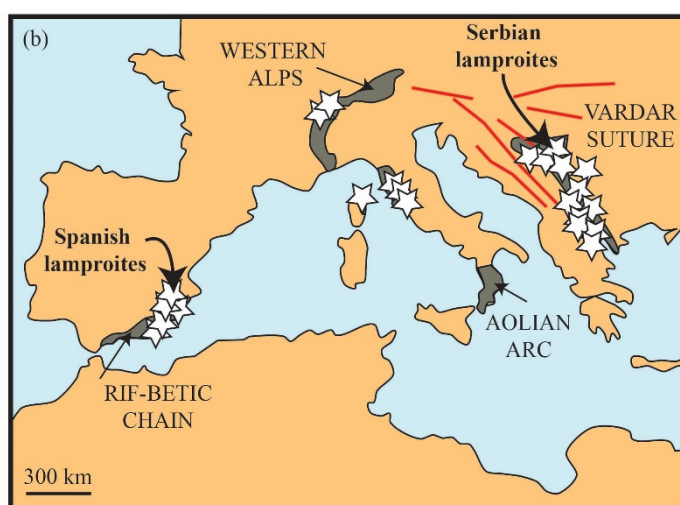


Figure P.0.1. Simplified location map of the Spanish and Serbian lamproite occurrences.

Sample 03V14 represents an Olivine-Phlogopite lamproite (Venturelli *et al.*, 1984) from the town of Vera in the Spanish Betic-Alboran Cordillera (Figure P1).  $^{40}\text{Ar}/^{39}\text{Ar}$  dating on groundmass glass has shown ages of  $6.44 \pm 0.28$  Ma and  $6.37 \pm 0.18$  Ma, whereas the age of phlogopite in these rocks

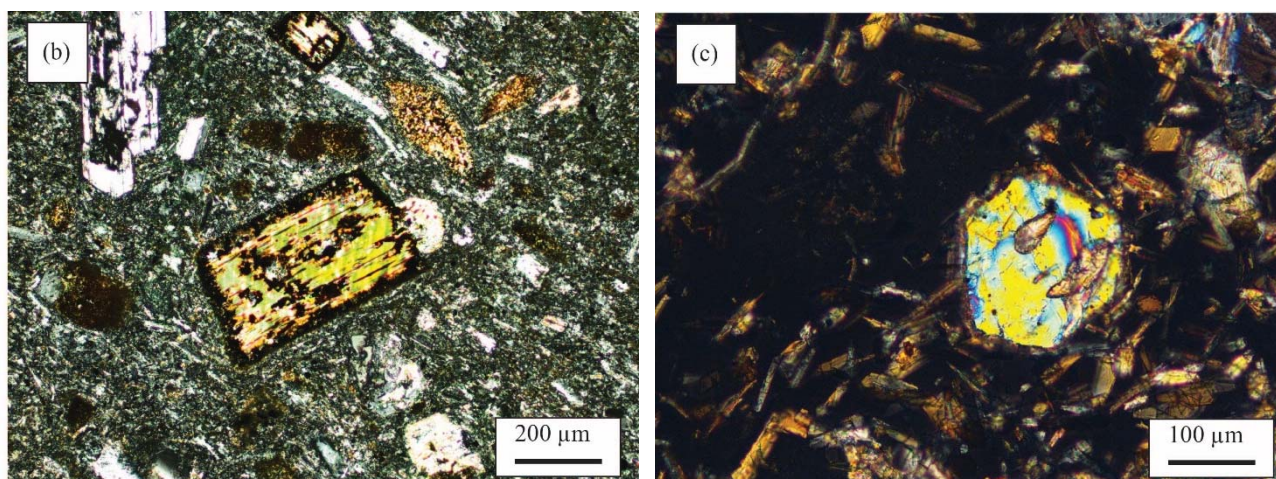


Figure P.0.2. Thin section photographs (cross polars) of (b) sample BK13/B and (c) sample 03V14.

is dated at  $7.45 \pm 0.08$  Ma (Duggen, 2005). These rocks are also part of the Tertiary – Quaternary Mediterranean lamproite province, but are geochemically very distinct from the Serbian lamproites (Prelević *et al.*, 2008, 2010), presumably explained by varying melting relations of a three-component

mantle source (Prelević *et al.*, 2008). Thin section analysis (Figure P.2c) shows that this lamproite contains fresh phlogopite as well as >100  $\mu\text{m}$  olivine phenocrysts in a glassy matrix.

### Results.

The following minerals were selected: phlogopite for sample 03V14; anorthite, K-richterite and phlogopite for sample BK013/B. Table P.1 provides a summary of the  $^{40}\text{Ar}/^{39}\text{Ar}$  geochronology results, whereas corresponding apparent age plateaus and relevant K/Ca diagrams can be found in Figure P.3. Full step-heating results can be found at the end of Appendix P. The phlogopite from sample 03V14 only yielded a mini-plateau age (between 50 – 70% cumulative  $^{39}\text{Ar}$  released) (Jourdan *et al.*, 2007) of  $\sim 7.5$  Ma, and can be considered as a maximum or minimum age only. Of the three different mineral phases analysed for sample BK013/B; K-richterite ( $32.28 \pm 0.11$  Ma) and phlogopite

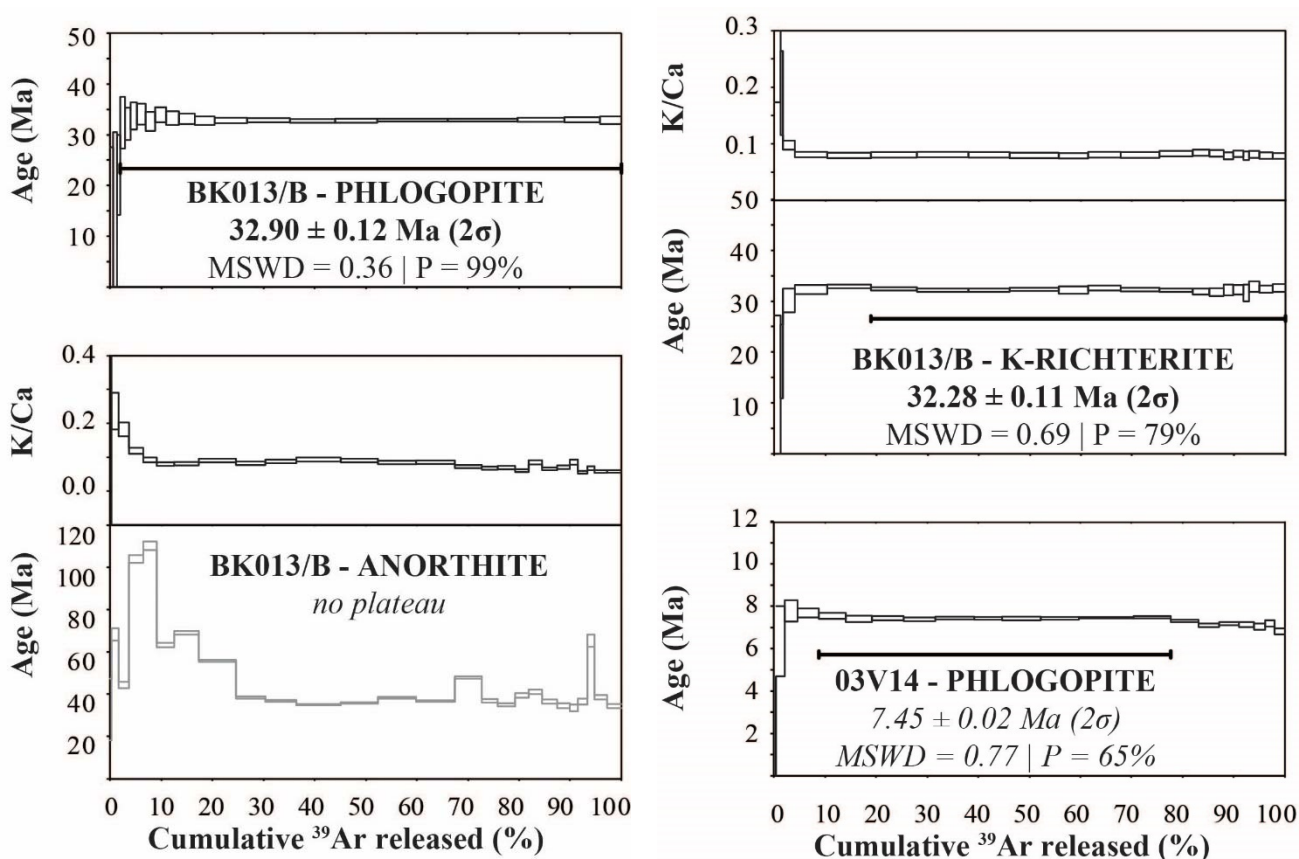


Figure P.0.3. Age spectra and K/Ca diagrams for relevant phases for K-rich phases analysed.

( $32.90 \pm 0.12$  Ma) yielded statistically significant plateau ages, however, their inverse isochron intercepts (atmospheric  $^{40}\text{Ar}/^{36}\text{Ar}$ ) are rather ill defined at  $321 \pm 28$  and  $308 \pm 39$  respectively. The mineral anorthite of sample BK013/B did not yield a plateau age or inverse isochron.



Sample	Mineral	Plateau characteristics				Inverse Isochron characteristics				
		Plateau age (Ma, $\pm 2\sigma$ )	Total $^{39}\text{Ar}$ released (%)	MS WD	P	Inverse Isochron age (Ma, $\pm 2\sigma$ )	n	$^{40}\text{Ar}/^{36}\text{Ar}$ intercept ( $\pm 2\sigma$ )	MS WD	P
BK013 /B	anorthite	<i>no plateau</i>				<i>no inverse isochron</i>				
	K-richterite	<b>32.28 <math>\pm</math> 0.11</b>	81	0.69	0.79	<b>32.27 <math>\pm</math> 0.20</b>	16	321 $\pm$ 28	0.87	0.59
	phlogopite	<b>32.90 <math>\pm</math> 0.12</b>	98	0.36	0.99	<b>32.90 <math>\pm</math> 0.16</b>	18	308 $\pm$ 39	0.41	0.98
03V14	phlogopite	<i>7.45 <math>\pm</math> 0.02</i>	<i>69</i>	<i>0.77</i>	<i>0.65</i>	<i>7.45 <math>\pm</math> 0.05</i>	<i>10</i>	<i>301.6 <math>\pm</math> 1.4</i>	<i>1.52</i>	<i>0.14</i>

Table P.0.1. Summary of  $^{40}\text{Ar}/^{39}\text{Ar}$  results of various K-rich mineral phases of the lamproite samples. Data in italics are derived from mini-plateaus (50% - 70%  $^{39}\text{Ar}$  released) and are considered minimum ages only.

### Discussion.

The  $^{40}\text{Ar}/^{39}\text{Ar}$  ages of respectively 32 Ma and 33 Ma of the K-richterite and the phlogopite from Boraç, Serbia (sample BK013/B) show that these samples are likely much older than the K-Ar age of  $\sim 23$  Ma that is currently adopted for this suite (Prelević *et al.*, 2008). This older age is still consistent with the age range of 35 Ma – 20 Ma that is generally considered for the duration of the lamproite intrusions in the Balkan region. Interestingly, the K-richterite is 1 Ma younger than the phlogopite; which is a potential indicator of a minimum magma residence time of 1 Ma before eruption, as K-richterite is a typical late-crystallizing phase (Bergman, 1987; Mitchell and Bergman, 1991) or due to the presence of xenocryst inclusions in the phlogopite.

Although the lamproite from Vera, Spain (03V14) only yielded a mini-plateau age of  $7.45 \pm 0.02$  Ma, this age is indistinguishable from the  $^{40}\text{Ar}/^{39}\text{Ar}$  plateau age of  $7.45 \pm 0.16$  Ma published for this sample as measured on a MAP 216 mass spectrometer (Duggen, 2005) which suggest that both ages represent the crystallization age of the phlogopite.

### References.

- Bergman, S. C. (1987). Lamproites and other potassium-rich igneous rocks: a review of their occurrence, mineralogy and geochemistry. Geological Society, London, Special Publications 30, 103–190.
- Cvetković, V., Prelević, D., Downes, H., Jovanović, M., Vaselli, O. & Pécskay, Z. (2004). Origin and geodynamic significance of Tertiary postcollisional basaltic magmatism in Serbia (central Balkan Peninsula). *Lithos* 73, 161–186.
- Duggen, S. (2005). Post-Collisional Transition from Subduction- to Intraplate-type Magmatism in the Westernmost Mediterranean: Evidence for Continental-Edge Delamination of Subcontinental Lithosphere. *Journal of Petrology* 46, 1155–1201.

Jourdan, F., Féraud, G., Bertrand, H. & Watkeys, M. K. (2007). From flood basalts to the inception of oceanization: Example from the  $^{40}\text{Ar}/^{39}\text{Ar}$  high-resolution picture of the Karoo large igneous province. *Geochemistry, Geophysics, Geosystems* 8.

Mitchell, R. H. & Bergman, S. C. (1991). *Petrology of Lamproites*. Plenum Press, New York.

Prelević, D. (2005). Tertiary Ultrapotassic Volcanism in Serbia: Constraints on Petrogenesis and Mantle Source Characteristics. *Journal of Petrology* 46, 1443–1487.

Prelević, D., Foley, S. F., Romer, R. L. & Conticelli, S. (2008). Mediterranean Tertiary lamproites derived from multiple source components in postcollisional geodynamics. *Geochimica et Cosmochimica Acta* 72, 2125–2156.

Prelević, D., Stracke, A., Foley, S. F., Romer, R. L. & Conticelli, S. (2010). Hf isotope compositions of Mediterranean lamproites: Mixing of melts from asthenosphere and crustally contaminated mantle lithosphere. *Lithos* 119, 297–312.

Venturelli, G., Capedri, S., Battistini, G. D. I., Crawford, A. J., Kogarko, L. N. & Celestini, S. (1984). The ultrapotassic rocks from southeastern Spain. *Lithos* 17, 37–54.

Supplementary Data – relative abundances of K-rich phases

Step	36Ar [fA]	%1s	37Ar [fA]	%1s	38Ar [fA]	%1s	39Ar [fA]	%1s	40Ar [fA]	%1s	40(r)/39(k)	±2s	Age (Ma)	±2s	40Ar(r) (%)	39Ar(k) (%)	K/Ca	±2s	
<b>BK13/B K-Richterite: J = 0.0008266 ± 0.0000029 (1σ) MDF = 0.993379 ± 0.00070 (1σ)</b>																			
5.0	0.001	0.638	0.003	17.200	0.000	12.968	0.002	1.776	0.27	0.01	7.58	10.71	11.29	15.91	5.79	1.24	0.27	0.09	
6.0	0.000	3.263	0.002	19.153	0.000	128.423	0.001	4.424	0.04	0.06	12.20	4.91	18.15	7.27	21.59	0.42	0.19	0.07	
8.0	0.000	1.501	0.017	4.039	0.000	41.361	0.004	0.779	0.14	0.02	20.34	1.57	30.14	2.31	54.65	2.27	0.10	0.01	
10.0	0.000	1.308	0.057	2.997	0.000	10.964	0.011	0.356	0.31	0.01	21.81	0.61	32.31	0.90	76.98	6.38	0.08	0.00	
11.0	0.000	2.805	0.078	2.980	0.000	9.365	0.014	0.286	0.34	0.01	22.23	0.23	32.93	0.34	92.81	8.51	0.08	0.00	
11.8	0.000	4.100	0.082	3.018	0.000	14.780	0.015	0.202	0.36	0.01	21.89	0.20	32.43	0.30	94.51	9.10	0.08	0.00	
12.6	0.000	2.913	0.090	3.016	0.000	6.543	0.017	0.221	0.39	0.01	21.69	0.21	32.13	0.30	93.18	10.01	0.08	0.00	
13.4	0.000	3.264	0.074	2.973	0.000	8.022	0.014	0.220	0.32	0.01	21.73	0.20	32.19	0.30	93.74	8.16	0.08	0.00	
14.2	0.000	3.317	0.088	2.974	0.000	11.471	0.016	0.232	0.38	0.01	21.84	0.19	32.35	0.28	94.61	9.64	0.08	0.00	
15.0	0.000	2.743	0.052	3.047	0.000	7.534	0.010	0.343	0.25	0.01	21.73	0.49	32.19	0.72	83.09	5.61	0.08	0.00	
16.0	0.000	8.667	0.057	3.167	0.000	15.543	0.011	0.362	0.25	0.01	22.01	0.34	32.61	0.50	95.05	6.36	0.08	0.01	
17.5	0.000	3.382	0.069	3.035	0.000	9.766	0.013	0.254	0.31	0.01	21.83	0.25	32.34	0.36	92.39	7.66	0.08	0.00	
19.0	0.000	8.458	0.057	3.004	0.000	8.985	0.011	0.290	0.24	0.01	21.74	0.22	32.20	0.32	97.57	6.46	0.08	0.00	
20.5	0.000	13.375	0.029	3.122	0.000	12.031	0.006	0.561	0.12	0.02	21.54	0.39	31.91	0.57	97.01	3.33	0.08	0.01	
22.0	0.000	21.899	0.024	3.376	0.000	15.600	0.005	0.671	0.10	0.02	21.49	0.52	31.84	0.76	97.64	2.78	0.08	0.01	
24.0	0.000	13.623	0.017	3.850	0.000	35.547	0.003	0.927	0.07	0.06	21.75	0.72	32.22	1.05	93.02	1.81	0.08	0.01	
26.0	0.000	24.121	0.018	3.443	0.000	30.089	0.004	0.848	0.08	0.03	21.77	0.62	32.24	0.91	97.45	2.08	0.08	0.01	
28.0	0.000	23.085	0.011	4.492	0.000	50.042	0.002	1.419	0.04	0.06	21.35	1.10	31.63	1.62	93.44	1.15	0.08	0.01	
32.0	0.000	24.726	0.017	3.652	0.000	81.471	0.003	1.047	0.08	0.04	22.18	0.71	32.85	1.04	97.34	1.95	0.08	0.01	
36.0	0.000	14.791	0.024	3.438	0.000	15.402	0.004	0.671	0.10	0.03	21.85	0.49	32.36	0.72	96.32	2.58	0.08	0.01	
40.0	0.000	20.201	0.023	3.228	0.000	33.601	0.004	0.724	0.10	0.03	22.02	0.53	32.62	0.77	97.58	2.50	0.08	0.01	

Step	$^{36}\text{Ar}$ [fA]	%1s	$^{37}\text{Ar}$ [fA]	%1s	$^{38}\text{Ar}$ [fA]	%1s	$^{39}\text{Ar}$ [fA]	%1s	$^{40}\text{Ar}$ [fA]	%1s	$^{40}(\text{r})/^{39}(\text{k})$ $\pm 2s$	Age (Ma)	$\pm 2s$	$^{40}\text{Ar}(\text{r})$ (%)	$^{39}\text{Ar}(\text{k})$ (%)	K/Ca	$\pm 2s$	
<b>BK013/B Phlogopite: <math>J = 0.0008266 \pm 0.0000029</math> (1<math>\sigma</math>) MDF = 0.992666 <math>\pm</math> 0.00090 (1<math>\sigma</math>)</b>																		
1.0	0.001	1.344	0.005	11.618	0.000	7.622	0.002	5.747	0.228	0.111	-0.51	18.92	-0.76	-0.35	0.59	0.13	0.03	
2.0	0.001	1.575	0.004	17.364	0.000	10.151	0.002	4.174	0.185	0.137	9.97	10.56	14.84	10.96	0.77	0.21	0.07	
2.7	0.000	4.549	0.003	22.420	0.000	23.988	0.002	4.729	0.085	0.296	14.88	5.32	22.11	7.86	0.67	0.24	0.11	
3.5	0.000	6.535	0.001	70.485	0.000	149.863	0.002	3.957	0.084	0.300	21.87	3.49	32.39	5.12	0.82	1.23	1.74	
4.3	0.000	10.857	0.000	179.950	0.000	193.159	0.003	2.459	0.091	0.278	21.72	2.14	32.17	3.14	1.18	-4.12	14.84	
5.0	0.000	19.549	0.000	198.947	0.000	160.863	0.003	2.313	0.088	0.285	22.78	1.86	33.72	2.72	1.25	-5.34	21.23	
5.8	0.000	22.147	0.000	181.031	0.000	296.192	0.004	1.739	0.111	0.227	23.00	1.40	34.05	2.06	1.64	-6.60	23.91	
6.5	0.000	25.898	0.000	167.494	0.000	37.685	0.005	1.558	0.120	0.210	22.07	1.27	32.68	1.87	1.87	5.87	19.66	
7.3	0.000	36.145	0.000	149.080	0.000	30.147	0.006	1.271	0.143	0.177	22.94	1.00	33.97	1.46	2.24	-7.03	20.95	
8.0	0.000	36.168	0.000	112.787	0.000	18.747	0.006	1.202	0.149	0.169	22.47	0.93	33.27	1.37	2.39	6.09	13.74	
9.0	0.000	27.238	0.000	1552.979	0.000	20.458	0.008	0.937	0.194	0.130	22.38	0.72	33.14	1.06	3.11	-105.20	3267.37	
10.0	0.000	17.811	0.001	105.918	0.000	38.948	0.010	0.732	0.244	0.103	22.13	0.58	32.77	0.85	3.93	8.90	18.86	
12.0	0.000	11.453	0.001	42.909	0.000	12.082	0.017	0.467	0.390	0.065	22.18	0.38	32.85	0.56	6.27	5.12	4.40	
14.0	0.000	12.381	0.002	34.995	0.000	11.198	0.022	0.348	0.517	0.049	22.19	0.28	32.87	0.41	8.44	6.41	4.48	
16.0	0.000	11.726	0.001	35.936	0.000	10.763	0.023	0.335	0.538	0.047	22.11	0.27	32.75	0.40	8.82	6.73	4.84	
18.0	0.000	18.934	0.000	150.499	0.000	16.432	0.022	0.358	0.497	0.051	22.12	0.28	32.77	0.41	8.23	25.92	78.03	
22.0	0.000	14.160	0.001	78.888	0.000	7.999	0.037	0.224	0.836	0.031	22.21	0.17	32.90	0.25	13.88	23.87	37.66	
26.0	0.000	16.493	0.000	159.089	0.000	7.793	0.036	0.231	0.816	0.031	22.24	0.17	32.93	0.25	13.57	45.95	146.19	
30.0	0.000	28.361	0.000	519.239	0.000	15.893	0.024	0.335	0.549	0.046	22.26	0.25	32.97	0.36	9.14	-96.09	997.90	
35.0	0.000	49.332	-0.001	80.579	0.000	31.648	0.019	0.416	0.424	0.060	22.27	0.31	32.98	0.46	7.08	-12.08	19.46	
40.0	0.000	101.978	-0.001	86.383	0.000	210.985	0.011	0.701	0.245	0.103	22.19	0.53	32.86	0.78	4.11	-7.11	12.28	

Step	36Ar [fA]	%1s	37Ar [fA]	%1s	38Ar [fA]	%1s	39Ar [fA]	%1s	40Ar [fA]	%1s	40(r)/39(k)	± 2s	Age (Ma)	± 2s	40Ar(r) (%)	39Ar(k) (%)	K/Ca	± 2s	
<b>BK013/B Anorthite: J = 0.0008266 ± 0.00000029 (1σ) MDF = 0.993379 ± 0.00070 (1σ)</b>																			
0.5	0.000	1.481	0.000	74.042	0.000	102.155	0.000	13.396	0.073	0.267	22.12	9.95	32.76	14.60	7.74	0.18	0.23	0.34	
1.0	0.001	0.569	0.004	11.323	0.000	267.821	0.002	1.783	0.311	0.064	46.53	2.03	68.24	2.93	31.76	1.45	0.24	0.05	
1.5	0.001	0.546	0.007	5.533	0.001	22.430	0.003	1.125	0.308	0.064	30.04	1.06	44.35	1.54	29.45	2.06	0.18	0.02	
2.0	0.000	0.779	0.015	3.839	0.000	40.578	0.004	0.829	0.427	0.046	71.56	1.30	103.91	1.84	68.46	2.79	0.12	0.01	
2.5	0.000	2.260	0.018	3.623	0.000	77.584	0.004	0.892	0.340	0.058	76.03	1.46	110.20	2.05	87.37	2.67	0.09	0.01	
3.0	0.000	2.687	0.026	3.260	0.000	36.423	0.005	0.733	0.241	0.082	43.05	0.76	63.23	1.09	85.85	3.28	0.08	0.01	
3.5	0.000	3.335	0.038	3.068	0.000	33.329	0.007	0.473	0.359	0.055	47.07	0.53	69.02	0.77	92.57	4.82	0.08	0.01	
4.0	0.000	1.571	0.051	3.004	0.000	32.785	0.011	0.333	0.464	0.043	37.87	0.32	55.74	0.46	87.04	7.28	0.09	0.01	
4.5	0.000	1.756	0.044	3.039	0.000	96.820	0.008	0.413	0.272	0.072	25.99	0.32	38.44	0.47	80.51	5.76	0.08	0.01	
5.0	0.000	2.525	0.044	3.030	0.000	369.664	0.009	0.401	0.260	0.076	24.86	0.30	36.77	0.44	86.23	6.15	0.09	0.01	
5.5	0.000	1.398	0.058	3.026	0.000	98.375	0.013	0.317	0.366	0.054	23.63	0.23	34.98	0.33	81.12	8.58	0.09	0.01	
6.0	0.000	1.182	0.052	3.000	0.000	118.558	0.011	0.321	0.344	0.057	24.27	0.25	35.91	0.36	76.24	7.39	0.09	0.01	
7.0	0.000	1.752	0.055	2.983	0.000	65.658	0.011	0.333	0.333	0.060	25.95	0.26	38.38	0.37	84.46	7.41	0.08	0.01	
8.0	0.000	1.576	0.057	2.983	0.000	56.023	0.011	0.310	0.337	0.058	24.85	0.24	36.76	0.35	82.85	7.68	0.09	0.01	
10.0	0.000	2.356	0.045	3.018	0.000	72.083	0.008	0.447	0.282	0.070	32.48	0.39	47.91	0.57	86.76	5.15	0.07	0.00	
12.0	0.000	3.635	0.030	3.203	0.000	44.684	0.005	0.769	0.140	0.140	24.85	0.57	36.77	0.84	82.85	3.19	0.07	0.00	
15.0	0.000	3.447	0.032	3.173	0.000	45.142	0.005	0.670	0.145	0.135	23.64	0.50	34.99	0.74	82.42	3.46	0.07	0.00	
18.0	0.000	4.855	0.027	3.231	0.000	39.662	0.004	0.888	0.118	0.166	26.66	0.71	39.42	1.04	85.01	2.58	0.06	0.00	
21.0	0.000	4.048	0.020	3.549	0.000	262.781	0.004	0.856	0.131	0.151	27.84	0.70	41.14	1.02	82.93	2.67	0.08	0.01	
24.0	0.000	5.663	0.029	3.174	0.000	164.235	0.004	0.788	0.122	0.160	24.66	0.60	36.49	0.89	87.72	2.98	0.07	0.00	
27.0	0.000	7.828	0.021	3.446	0.000	90.779	0.003	1.079	0.091	0.215	23.39	0.77	34.62	1.13	88.21	2.35	0.07	0.01	
30.0	0.000	8.381	0.012	4.150	0.000	99.306	0.002	1.384	0.065	0.300	22.63	1.03	33.51	1.51	83.87	1.65	0.09	0.01	

Step	36Ar [fA]	%1s	37Ar [fA]	%1s	38Ar [fA]	%1s	39Ar [fA]	%1s	40Ar [fA]	%1s	40(r)/39(k)	± 2s	Age (Ma)	± 2s	40Ar(r) (%)	39Ar(k) (%)	K/Ca	± 2s	
35.0	0.000	10.228	0.021	3.520	0.000	372.306	0.003	1.270	0.076	0.261	24.69	0.96	36.53	1.41	89.62	1.87	0.06	0.00	
40.0	0.000	10.034	0.012	4.013	0.000	1243.909	0.002	1.837	0.091	0.215	44.45	1.96	65.25	2.82	90.49	1.27	0.07	0.01	
45.0	0.000	6.132	0.027	3.136	0.000	311.550	0.004	0.921	0.109	0.180	26.02	0.72	38.48	1.06	87.54	2.50	0.06	0.00	
50.0	0.000	5.920	0.031	3.150	0.000	227.700	0.004	0.887	0.110	0.180	23.17	0.63	34.30	0.93	87.38	2.83	0.06	0.00	
<b>03V14 Phlogopite: J = 0.00082660 ± 0.00000029 (1σ) MDF = 0.992294 ± 0.00030 (1σ)</b>																			
1.0	0.006	0.134	0.001	32.574	0.001	19.159	0.001	1.366	1.920	0.006	-18.37	7.05	-27.67	10.70	-1.41	0.40	0.71	0.46	
2.0	0.004	0.130	0.002	15.022	0.000	62.509	0.006	0.330	1.301	0.008	4.25	1.11	6.35	1.66	1.98	1.66	1.35	0.41	
2.7	0.002	0.165	0.001	33.769	0.000	267.437	0.009	0.223	0.604	0.015	5.22	0.34	7.78	0.51	7.94	2.51	4.61	3.11	
3.5	0.001	0.169	0.001	35.142	0.000	78.014	0.015	0.131	0.460	0.020	5.15	0.14	7.68	0.21	17.32	4.23	7.58	5.33	
4.3	0.001	0.200	0.001	41.346	0.000	186.258	0.019	0.110	0.383	0.023	5.06	0.09	7.55	0.14	25.22	5.21	13.61	11.25	
5.0	0.001	0.224	0.001	45.432	0.000	630.093	0.019	0.115	0.379	0.034	4.96	0.10	7.40	0.15	24.55	5.12	9.69	8.81	
5.8	0.001	0.199	0.001	21.691	0.000	110.178	0.023	0.099	0.348	0.026	4.99	0.06	7.44	0.10	32.56	6.21	8.98	3.90	
6.5	0.001	0.270	0.000	216.423	0.000	128.078	0.023	0.096	0.277	0.033	4.95	0.05	7.39	0.08	40.69	6.22	79.35	343.46	
7.3	0.001	0.277	0.001	34.145	0.001	30.082	0.028	0.078	0.304	0.030	5.00	0.04	7.45	0.06	46.19	7.68	11.70	7.99	
8.0	0.000	0.297	0.001	25.624	0.001	35.738	0.020	0.100	0.212	0.042	4.98	0.05	7.43	0.07	46.54	5.40	7.49	3.84	
9.0	0.000	0.551	0.001	20.965	0.000	36.189	0.028	0.093	0.256	0.036	4.98	0.05	7.43	0.08	54.01	7.58	9.91	4.16	
10.0	0.001	0.302	0.001	38.918	0.001	27.393	0.027	0.089	0.296	0.030	4.98	0.05	7.43	0.07	46.02	7.46	12.31	9.58	
12.0	0.000	0.263	0.001	38.855	0.001	27.257	0.039	0.063	0.344	0.026	5.00	0.03	7.46	0.04	57.16	10.72	23.45	18.22	
14.0	0.000	0.399	0.000	148.292	0.000	50.206	0.027	0.093	0.237	0.037	5.01	0.04	7.48	0.06	56.38	7.30	57.07	169.25	
16.0	0.000	0.654	0.000	66.216	0.000	69.148	0.020	0.107	0.151	0.058	4.90	0.04	7.32	0.06	64.64	5.45	18.70	24.77	
18.0	0.000	0.508	0.000	115.911	0.000	64.878	0.015	0.181	0.144	0.063	4.76	0.06	7.10	0.09	49.50	4.08	25.70	59.57	
22.0	0.000	0.590	0.000	428.389	0.000	84.603	0.014	0.149	0.126	0.070	4.81	0.06	7.18	0.08	53.29	3.82	-66.98	573.87	
26.0	0.000	0.737	0.000	1897.776	0.000	110.102	0.011	0.222	0.100	0.088	4.79	0.08	7.14	0.12	50.14	2.87	-200.40	7606.29	
30.0	0.000	0.828	0.000	757.920	0.000	355.108	0.008	0.264	0.085	0.102	4.72	0.10	7.04	0.15	45.75	2.26	-96.27	1459.23	
35.0	0.000	0.596	0.000	368.918	0.000	740.507	0.007	0.305	0.084	0.106	4.82	0.10	7.19	0.15	39.21	1.87	-41.18	303.83	
40.0	0.000	0.748	0.000	117.951	0.000	539.646	0.007	0.284	0.070	0.126	4.57	0.09	6.82	0.13	46.59	1.95	14.36	33.87	